Search for a Standard Model Higgs Boson Decaying to Two Photons in CMS at the LHC

Thesis by

Yong Yang

In Partial Fulfillment of the Requirements

for the Degree of

Doctor of Philosophy

California Institute of Technology

Pasadena, California

2013

(Defended on November 7, 2012)

Acknowledgments

I would like to begin by thanking my Ph.D. advisor, Harvey Newman, whose broad perspective and experience in high energy physics have greatly helped and inspired me at various stages of my researches in the past seven years. I am also grateful for his careful reading and valuable suggestions of this thesis. I would like to thank Maria Spiropulu and Renyuan Zhu for their valuable and sometimes crucial and constructive criticism and suggestions during my Ph.D. period.

I want to thank Marat Gataullin and Vladimir Litvin whom I worked closely with and benefited from a lot on the π^0 calibration project, which started as early as in 2005. In particular, I thank Marat for his original contribution in developing the calibration algorithm and demonstrating it through studies in simulation. I thank Vladimir for his original contribution in developing the calibration trigger.

I want to thank Adolf Bornheim, Yousi Ma, Toyoko Orimoto, Marat Gataullin, Jan Veverka, Vladlen Timcuic and Artur Apresyan for their valuable helps on my $H \to \gamma\gamma$ analysis. In particular, I thank Adi for sharing with me his unique perspectives and his insistence on precision and correctness. I thank Yousi for his help on developing part of my analysis code. I thank Toyoko and Marat for their helps on the data production. I thank Jan for his discussions on many analysis details and his original contribution to the photon efficiency measurement. I thank Vladlen for his early and important studies on the energy scales and resolutions. I thank Artur for his valuable discussions on the analysis.

I want to thank the CMS statistic committee members for their suggestions on the statistical issue regrading two different results using two analysis methods. Especially, I thank Robert Cousins for his suggestions which led to the solution.

I want to thank all the people who worked with me on my first physics analysis of the searches for the excited leptons. In particular, I want to thank Marat Gataullin, Maria Soares, Shilpi Jain, and Elizabeth Sudano for their important contributions. I want to thank Doung Nguyen, Yuri Gershtein, and Conor Henderson for their suggestions and helps on the photon fake rate studies. I am grateful to Mikhail Dubinin for his help on the implementation of the compositeness model in the compHEP event generator.

I thank my fellow students Chris Rogan, Yi Chen, and Alex Mott for their discussions and helps in past few years. I thank Michael Thomas, Dorian Kcira, Steven Lo for their valuable support on the computing. I thank Ramiro Voicu for his help whenever my desktop had problems.

I also want to thank Si Xie for proofreading and correcting the early draft of this thesis. I thank the office of the graduate studies for the proofreading. I want to thank again Vladlen, Toyoko, and Si for sharing the office with me in the past few years.

This thesis would not be possible without the contributions from past and present CMS collaboration members. I thank all CMS members for their work.

In the end, I thank my mother and my father. I thank them for bringing me to this world. I thank them for their unconditional love and support.

Abstract

In part I of this thesis, I perform a search for the Standard Model Higgs boson decaying into two photons using 5.08 fb^{-1} of data collected by the Compact Muon Solenoid (CMS) detector in 2011 at a center-of-mass energy $\sqrt{s} = 7$ TeV.

The result of this search is interpreted as a local excess in the mass around 123 GeV/c^2 with an significance of 3.3 standard deviation. This excess was later confirmed in the data in 2012, and was an important contribution to the CMS discovery paper published in 2012.

This search makes use of the excellent energy resolution of the CMS crystal electromagnetic calorimeter (ECAL) . The energy intercalibration of approximately 76,000 crystals is crucial to improve the resolution performance. I describe in detail a novel intercalibration method using $\pi^0(\eta) \to \gamma\gamma$ decays. This method was the first one in CMS to reach 0.5% calibration precision in the central part of ECAL with $|\eta| < 1$. This calibration improved the $\text{H} \to \gamma\gamma$ search sensitivity by about 30%, compared to the precalibration performed before the installation of ECAL in CMS detector.

In part II of this thesis, I perform a search for an excited muon decaying into one muon and one photon using 36 pb^{-1} of data collected in 2010 at $\sqrt{s} = 7$ TeV. The result of this search indicates no evidence for excited muons. I report the first upper limits on single excited muon production cross section at this collision energy, and exclude a new region of the parameter space of compositeness scale and excited muon mass. Assume the compositness scale is the same as the excited muon mass, excited muons are excluded below 1090 GeV/c^2 at the 95% confidence level, representing the most stringent limits, as of the date when the analysis was first published.

Contents

List of Tables

List of Figures

Part I

Search for a Standard Model Higgs Boson Decaying to Two Photons in pp Collisions

Chapter 1

Introduction

For more than a century, the development of modern physics has brought human beings the deepest understanding of nature in terms of the building blocks of matter and their interactions. In particular, it has been established that all matter consists of a number of particles more fundamental than previously thought. From the 6th century BC [1] through the 19th century, it was believed that each element in nature consisted of atoms, named after the Greek word "atomos", meaning indivisible. In 1897 J. J. Thomson discovered the electron [2], which weighed much less than the lightest atom and was believed to be a constituent of atoms. In 1911 the discovery of nucleus in atoms by E. Rutherford [3] established the nuclear structure of atoms. In 1964 M. Gell-Mann and G. Zweig proposed the quark model to explain the constituents of atomic nuclei. At that time, only three flavors of quarks, including up, down, and strange, were proposed. The three-quark model was confirmed by deep inelastic scattering experiments [4, 5]. Three more quarks, charm [6], top, and bottom [7], were proposed and confirmed by experiments [8–11]. Quarks, together with leptons and bosons, form the elementary particles known today.

Theories to describe the interactions among elementary particles have also been developed. The electric and magnetic force have been unified as the electromagnetic force. This force was then combined with the weak force to be the electroweak force, describing the interactions among all particles except the interaction between quarks, which is described by the strong interaction force. These developments have converged to the theory of elementary particles and interactions known as the Standard Model

of particle physics. This theory has been tested experimentally to an unprecedented precision [12]. However, there is one last particle, known as the Higgs boson, that needs to be confirmed. This particle is predicted by the Higgs mechanism [13–15] which explains the origins of mass of elementary particles. The search for the Standard Model Higgs boson has been one of the main physics programs in recent collider experiments [16, 17].

This thesis describes the work related to the search for a Standard Model Higgs boson in the Compact Muon Solenoid (CMS) experiment at the Large Hadron Collider (LHC). The results of this work represent important steps toward the discovery of a Standard Model Higgs like particle in the CMS experiment in 2012 [18].

1.1 The Standard Model

The Standard Model of particle physics is a quantum field theory which describes the electromagnetic, weak and strong interactions among different fundamental particles, and the symmetries of these interactions under the gauge group $SU(3)_{\text{color}} \otimes SU(2)_L \otimes U(1)_Y$. The first step toward the Standard Model is the unification of the electromagnetic and weak interaction in the electroweak theory ($SU(2)_L \otimes U(1)_Y$) [19]. The Higgs mechanism, a mass generation mechanism based on spontaneous symmetry breaking [20], was proposed to explain the origin of masses of elementary particles. This mechanism is then incorporated into the electroweak theory, forming the basis of the Standard Model [21,22]. The complete picture of the Standard Model was formed after the theory of the strong interactions ($SU(3)_{\text{color}}$) was developed following the observation of quarks [4, 5]. The strong interactions, in the theory of the quantum chromodynamics (QCD), describe the interactions between quarks and gluons. In this thesis, we study primarily the electroweak sector of the Standard Model and the search for the Higgs boson predicted to exist as a result of its mass generation mechanism.

1.1.1 Fermions

In the Standard Model, there are three generations of leptons and quarks, each of which consists of four particles and their antiparticles. Table 1.1 lists the names and symbols of particles in each generation. All leptons and quarks have spin 1/2, and thus belong to the fermions. Each particle in a generation has a larger mass than the corresponding one of lower generations. The charged particles in the first generation are stable, and all other charged particle in the second and third generations decay. All generations of neutrinos do not decay. Each particle has its own corresponding antiparticle. All antiparticles, with the exception of neutrinos, have the opposite electric charge to its corresponding particle, while all other quantum numbers are identical. The unique feature of quarks is that they carry color charge, in analogy with electric charge. Therefore they interact with each other via gluons that mediate the strong interaction. Quarks also carry electric charge and weak isospin, thus they also interact with other fermions via both the electromagnetic and the weak interaction. The neutrinos carry neither color charge nor electric charge, thus they only interact with other particles by weak interactions. This unique feature makes neutrinos very difficult to be detected directly. In a collider experiment, the presence of neutrino is inferred from an apparent imbalance of energies measured in the detector, resulting in "missing energy".

Generation	Quark	Lepton
I	up, down quark u, d	electron, electron neutrino e^-, ν_e
II	charm, strange quark c, s	muon, muon neutrino e^-, ν_μ
III	top, bottom quark t, b	tau, tau neutrino τ^-, ν_τ

Table 1.1: Generations of leptons and quarks in the Standard Model.

1.1.2 Gauge Bosons and Higgs Boson

In analogy with fermions, there exist a class of particles with integer spin. They are called bosons. The gauge bosons in the Standard Model are bosonic particles that mediate the forces. There are three kinds of gauge bosons. The photon mediates

the electromagnetic force between charged particles. The W and Z bosons mediate the weak interactions among leptons and quarks. The gluons mediate the strong interactions between quarks. Photon and gluons are massless, while the W and Z boson are massive.

In the Standard Model, the Higgs boson is a special bosonic particle, because it explains why the gauge bosons and fermions are massive, through their interaction with the Higgs boson. The Higgs boson has zero spin and is electrically neutral. The Higgs boson is the last particle, predicted by the Standard Model, yet to be confirmed by experiments.

1.1.3 Electroweak Model

The Glashow-Salam-Weinberg theory [19, 21, 22] of weak and electromagnetic interactions among leptons was developed based on many studies of weak interactions, including the Fermi theory and the intermediate vector boson theory. Therefore, in this section we begin by introducing the two theories and their problems. Then we introduce the electroweak theory.

In 1924, Fermi proposed a theory [23] explaining the β decay of a neutron, $n \to e + \bar{\nu_e} + p$. In this theory, there is an interaction term describing the hadronic and leptonic currents

$$\mathcal{L}_F = G_F J^h J^l = G_F(\bar{u_p}\hat{O}u_n)(\bar{u_e}\hat{O}u_\nu)\,, \tag{1.1}$$

where G_F is the Fermi constant, u_p, u_n, u_e, u_ν denote the wave functions of the four particles, the bars on $\bar{u_p}$ and $\bar{u_e}$ refer to the Dirac adjoint, and $\hat{O}$ refers to the operator which characterizes the decay process. Since neutrinos are massless and the electron mass is negligible compared to the characteristic energy of the process, the theory must be formulated relativistically. Therefore the wave functions must obey the Dirac equation

$$(i\gamma^\mu\partial_\mu - m_k)u_k(x) = 0, (k = p, n, e, \nu)\,, \tag{1.2}$$

where the γ^μ are the 4×4 Dirac matrices, μ refer to the index from 0 to 3, representing

the four space-time coordinates and $\partial_\mu \equiv \frac{\partial}{\partial x^\mu}$. Therefore, the wave functions are also four-component spinors, and the operators $\hat{O}$ must be 4×4 matrices. Because the Lagrangian $\mathcal{L}_F$ must be invariant (scalar) under the Lorentz transformation, there are only five possible forms of $\hat{O}$: 1 (scalar), γ^μ (vector), $\sigma^{\mu\nu}$ (tensor) ,$\gamma^\mu\gamma^5$ (axial vector), and γ^5 (pseudoscalar), where the phrase in the parentheses refers to the transformation property of $\bar{\Psi}\hat{O}\Psi$.

By construction, the Fermi theory is a local four fermion interaction. Originally, it assumes a vector structure for both the hadronic current, $J^h_\mu = \bar{u_p}\gamma_\mu u_n$, and the leptonic current, $J^l_\mu = \bar{u_e}\gamma_\mu u_\nu$.

In 1956, Lee and Yang suggested that parity is not conserved [24] in the observation of Kaons decaying into two different final states with opposite parities, $K^+ \to \pi^+\pi^0$ and $K^+ \to \pi^+\pi^+\pi^-$. Parity violation was confirmed in 1957 [25] in the nuclear β decay, $Co \to Ni^* e^- \bar{\nu_e}$. The discovery of parity violation in weak interactions suggested a $V - A$ type [26] structure of the Fermi interaction

$$\mathcal{L}_F = G_F/\sqrt{2}[\bar{u_p}\gamma_\mu(C_V + C_A\gamma^5)u_n][\bar{u_e}\gamma^\mu(1-\gamma_5)u_\nu]\,, \tag{1.3}$$

where C_V and C_A refer to the vector and axial coupling strength among the nucleons, respectively.

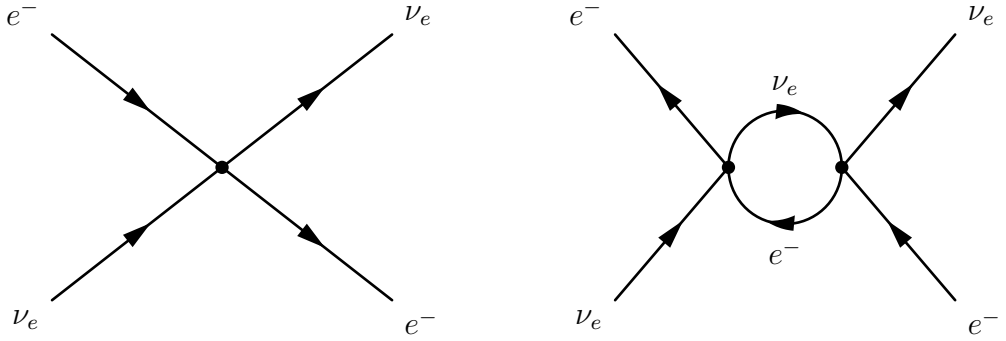

Figure 1.1: Neutrino electron scattering in Fermi theory. Left is the first order diagram. Right is the second order diagram. The scattering happens from the left to the right direction in each diagram.

The V-A Fermi theory described the known weak interactions reasonably well until the discovery of neutral currents in 1973 [27]. This type of current was not included in the Fermi theory. In addition, the major problem of the Fermi theory is that it

violates unitarity at high energies and is thus not a renormalizable theory. Based on the Fermi theory, at high center-of-mass energy $\sqrt{s} >> m_e$, the cross section of electron neutrino scattering is $\sigma(\nu_e e^- \rightarrow e^- \nu_e) = \frac{G_F^2 s}{\pi}$. However, a general partial wave analysis shows that the cross section is limited by $\frac{4\pi}{s}$. Therefore unitarity is violated when $\sqrt{s} = \sqrt{2\pi/G} = 734$ GeV.

This means that cross section calculated from perturbation theory needs to include higher-order terms of the perturbation series. Figure 1.1 shows the first and second order (multiple scattering) Feynman diagrams of the neutrino electron scattering. The cross section calculated to higher orders in perturbation theory is, however, divergent as well

$$\sigma^{(2)} \propto G_F^2 \int_0^\infty q dq \,, \tag{1.4}$$

where q is the 4-momentum exchanged in the first scattering. Such divergences in the Feynman diagrams appear as well in quantum electrodynamics (QED). For example, in the vacuum polarization of the photon, where a pair of virtual electron and position is created and annihilated through a loop diagram in the propagation of the photon, a quadratically divergent integral over the momentum q appears. This divergence, however, can be eliminated by the gauge invariance of the photon propagator [28]. The remaining logarithmic divergence $\int dq/q$ can be removed by charge renormalization. However, in the Fermi theory there is no gauge principle to reduce the order of the divergence in equation (1.4), and at higher orders even worse divergences appear.

Therefore, the Fermi theory is not renormalizable. The fundamental reason for the divergence is that the interaction between the electron and neutrino occurs at the same spcacetime coordinates. This led to the idea of having an "intermediate" boson W [29], as shown in figure 1.2. This intermediate boson W has to couple to the vector current and thus must be described by a vector field, and therefore it must be a spin-1 particle. This theory is thus called the Intermediate Vector Boson (IVB) theory.

In this theory, there is an effective Fermi coupling constant which depends on the

momentum transfer

$$G_{\text{eff}}(q^2) = \frac{g^2}{q^2 - M_W^2} \to \frac{g^2}{q^2} \quad (q \to \infty)\,, \tag{1.5}$$

where g is a dimensionless coupling constant for the interaction vertex $\nu_e - e - W$. Taking into account the contributions of both vertices, the cross section in equation (1.4) becomes

$$\sigma^{(2)} \propto g^4 \int_0^\infty \frac{dq}{q^3}\,, \tag{1.6}$$

which is no longer divergent.

To regain the Fermi theory in the limit of small momentum transfer $q^2 \to 0$, this new boson must be massive.

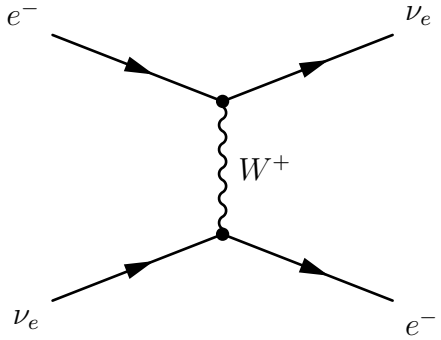

Figure 1.2: Electron neutrino scattering by means of a charged intermediate boson W.

However, the IVB theory has similar problems of nonrenormalizability and violation of unitarity at high energies, which can be easily understood by two examples. The first is the cross section of the two longitudinal W bosons from neutrino neutrino scattering: to lowest order it is $\frac{g^4}{M_W^4}s$. Therefore the the unitary bound is again violated at high energies. The second is that the W boson propagator goes to a constant at high energies

$$D^{\mu\nu}(q^2) = \frac{\frac{q^\mu q^\nu}{M_W^2} - g^{\mu\nu}}{q^2 - M_W^2} \to \frac{q^\mu q^\nu}{q^2 M_W^2} \to \frac{\text{const}}{M_W^2} \quad (q \to \infty)\,, \tag{1.7}$$

which makes the theory nonrenormalizable. The renormalizability of QED derives from the fact that the photon has zero rest mass. In the case of the photon, the

propagator is

$$D^{\mu\nu}(q^2) = \frac{\frac{q^\mu q^\nu}{q^2} - g^{\mu\nu}}{q^2} \to \frac{\text{const}}{q^2}(q \to \infty)\,. \tag{1.8}$$

Therefore to keep the IVB theory renormalizable, we would require the boson to be massless, however a massive boson is needed in order to regain the Fermi theory at low energies. Similarly, a neutral boson Z^0 proposed to describe electron neutrino scattering ($e^-\nu_\mu \to e^-\nu_\mu$) faced similar problems. One way out of the dilemma is provided by the Higgs mechanism by means of a new spin-0 field, the Higgs field, which was incorporated into the Glashow-Salam-Weinberg electroweak theory [19, 21, 22], based on the following then-established premises:

- There exist charged and neutral weak currents.
- Parity violation in β decays shows that the charged currents contain only couplings between left-handed leptons.
- The mass of the intermediate bosons must be massive, through the Higgs mechanism of electroweak symmetry breaking.

Therefore, two vector fields A^i_μ ($\mathrm{i} = 1, 2, 3$) and one single B_μ are introduced, which mix as a result of the spontaneous symmetry breaking, and finally result in the physical particles W^+, W^-, Z and γ:

$$W^\pm_\mu = \frac{1}{\sqrt{2}}(A^1_\mu \mp iA^2_\mu)\,, \tag{1.9}$$

$$Z_\mu = \cos\theta_W A^3_\mu - \sin\theta_W B_\mu\,, \tag{1.10}$$

$$A_\mu = \sin\theta_W A^3_\mu + \cos\theta_W B_\mu\,, \tag{1.11}$$

where θ_W is the Weinberg weak mixing angle, which quantifies the degree of mixing of the $SU(2)_L$ gauge fields and the $U(1)_Y$ gauge field. It is now measured to be

28.7° [30], and is related to the $SU(2)_L$ and $U(1)_Y$ coupling constants g and $g^{'}$ by

$$\sin\theta_W = \frac{g'}{\sqrt{g^2+g'^2}}\,, \tag{1.12}$$

$$\cos\theta_W = \frac{g}{\sqrt{g^2+g'^2}}\,. \tag{1.13}$$

The elementary electric charge can be expressed as

$$e = \frac{gg^{'}}{\sqrt{g^2+g'^2}}\,. \tag{1.14}$$

Up to this point, the W^+, W^- and Z all remain massless. In the next section, we will discuss how they gain masses.

1.1.4 Spontaneous Symmetry Breaking: The Higgs Mechanism

The Higgs mechanism is a mechanism for generating the masses of the W^+, W^- and Z gauge bosons in the Standard Model. This is done through a spontaneous symmetry breaking mechanism in the electroweak interactions.

To illustrate the main idea of spontaneous symmetry breaking, we consider a Lagrangian for a complex scalar field $\phi(x) = \frac{1}{\sqrt{2}}(\phi_1 + i\phi_2)$:

$$\mathcal{L} = \partial_\mu\phi^\dagger\partial^\mu\phi - U(\phi), \text{where } U(\phi) = \mu^2|\phi|^2 + \lambda|\phi|^4\,, \tag{1.15}$$

where λ is positive to ensure an absolute minimum in the Lagrangian. In terms of ϕ_1 and ϕ_2, the Lagrangian is expressed as

$$\mathcal{L}(\phi_1,\phi_2) = \frac{1}{2}(\partial_\mu\phi_1)^2 + \frac{1}{2}(\partial_\mu\phi_2)^2 - \frac{1}{2}\mu^2(\phi_1^2+\phi_2^2) - \frac{\lambda}{4}(\phi_1^2+\phi_2^2)^2\,. \tag{1.16}$$

There are two possibilities for the sign of μ^2, positive or negative. For $\mu^2 > 0$, the Lagrangian describes two massive scalar particles each with mass μ with additional

interactions

$$\mathcal{L}(\phi_1, \phi_2) = [\frac{1}{2}(\partial_\mu \phi_1)^2 - \frac{1}{2}\mu^2 \phi_1^2] + [\frac{1}{2}(\partial_\mu \phi_2)^2 - \frac{1}{2}\mu^2 \phi_2^2] + \text{interaction terms.} \quad (1.17)$$

For $\mu^2 < 0$, the minimum of the potential corresponds to an infinite number of vacuum states of ϕ_1 and ϕ_2:

$$\sqrt{\phi_1^2 + \phi_2^2} = \sqrt{\frac{-\mu^2}{\lambda}} \equiv v\,. \quad (1.18)$$

The general solution of the vacuum state of ϕ is then

$$\phi_0 = \frac{1}{\sqrt{2}} v e^{i\alpha}\,, \quad (1.19)$$

where α is an arbitrary phase. By fixing α to a particular value we have thus chosen a distinct phase. The Lagrangian is invariant under the phase transformation, while the vacuum state is not, which breaks the symmetry. This type of symmetry breaking is called spontaneous symmetry breaking.

Suppose we choose the vacuum state ϕ_0 as $\phi_1 = v$ and $\phi_2 = 0$. We can then parametrize the excitation (or perturbation) over the vacuum state as

$$\phi = \frac{1}{\sqrt{2}}(\eta + v + i\theta)\,, \quad (1.20)$$

where we have defined two shifted fields η and θ with $\eta = \phi_1 - v$ and $\theta = \phi_2$. Therefore the Lagrangian can be rewritten as

$$\mathcal{L} = [\frac{1}{2}(\partial_\mu \eta)^2 - (v^2\lambda)\eta^2] + [\frac{1}{2}(\partial_\mu \theta)^2 + 0 \cdot \theta^2] + \text{interaction terms.} \quad (1.21)$$

Therefore the field η describes a particle with mass $\sqrt{-2v^2\lambda}$, and θ is massless. This kind of massless particle produced in spontaneous symmetry breaking is called a goldstone boson [31].

To apply the idea of spontaneous symmetry breaking to the $SU(2)_L \otimes U(1)_Y$

symmetry in the electroweak interactions, we need an isodoublet of Higgs fields

$$\phi = \begin{pmatrix} \phi^+ \\ \phi^0 \end{pmatrix} = \frac{1}{\sqrt{2}} \begin{pmatrix} \phi_1 + i\phi_2 \\ \phi_3 + i\phi_4 \end{pmatrix}. \tag{1.22}$$

In order to obtain a non-vanishing vacuum expectation value of the Higgs field, we add a potential term to the Lagrangian

$$\mathcal{L} = D_\mu \phi^\dagger D^\mu \phi - U(\phi), \text{where } U(\phi) = \mu^2 |\phi|^2 + \lambda |\phi|^4, \text{with } \mu^2 < 0\,, \tag{1.23}$$

where D_μ is the covariant derivative associated to $SU(2)_L \otimes U(1)_Y$:

$$D_\mu = (\partial_\mu - ig\hat{\mathbf{T}} \cdot \mathbf{A}_\mu - ig' \frac{1}{2} \hat{Y} B_\mu)\,, \tag{1.24}$$

where $\hat{\mathbf{T}}$ are the three generators of the SU(2) group, $\hat{Y}$ is the generator of the U(1) group. As before, we can choose a particular vacuum state, for example, $\phi_1 = \phi_2 = \phi_3 = 0$ and $\phi_4 = v$:

$$\phi_0 = \frac{1}{\sqrt{2}} \begin{pmatrix} 0 \\ v + h \end{pmatrix}, \tag{1.25}$$

where h denotes the local deviation of the Higgs field from the vacuum expectation value of v. The choice for such a vacuum state is called the unitary gauge. To this end we can rewrite the covariant derivative terms in terms of the physical gauge boson fields

$$D_\mu \phi^\dagger D^\mu \phi = \frac{1}{8} v^2 [2g^2 W_\mu^{(+)} W^{(-)\mu} + (g^2 + g'^2) Z_\mu Z^\mu + 0 \cdot A_\mu A^\mu]\,. \tag{1.26}$$

Therefore, the photon remains massless, the charged gauge boson has a mass

$$M_W = \frac{1}{2} v g\,, \tag{1.27}$$

and the neutral gauge boson has a mass

$$M_Z = \frac{1}{2} v \sqrt{g^2 + g'^2}\,. \tag{1.28}$$

According to these equations and equation (1.13), the masses of the W and Z gauge bosons have the following relation to lowest order:

$$M_W = M_Z \cos\theta_W \,. \tag{1.29}$$

Comparing the coupling constant of muon decay in the Fermi theory and the IVB theory, we have

$$\frac{G_F}{\sqrt{2}} = \frac{g^2}{8M_W^2} \,. \tag{1.30}$$

Therefore the vacuum expectation value $v = \sqrt{\frac{1}{\sqrt{2}G_F}} \simeq 246$ GeV, which is also commonly known as the "electroweak scale".

The electroweak symmetry breaking also results in a term,

$$\mathcal{L}_{\rm h,free} = \frac{1}{2}(\partial_\mu h)^2 - v^2\lambda h^2 \,. \tag{1.31}$$

Therefore the mass of the Higgs boson is given by

$$m_h = \sqrt{2v^2\lambda} \,, \tag{1.32}$$

which is not known a priori in the theory since λ is a free parameter.

The interaction term between the gauge bosons and the Higgs boson is described by

$$\begin{aligned} \mathcal{L}_{\rm HG} &= D_\mu\phi^\dagger D^\mu\phi - |i\partial_\mu\phi|^2 \\ &= \frac{1}{8}(v+h)^2[2g^2W_\mu^{(+)}W^{(-)\mu} + (g^2+g'^2)Z_\mu Z^\mu] \,, \end{aligned} \tag{1.33}$$

which shows that the coupling of the Higgs boson to the gauge bosons is proportional to the square of the mass of the gauge boson.

The masses of quarks and leptons are generated by the so-called Yukawa couplings [32] between the fermions and the Higgs boson, with the strength of the coupling proportional to the fermion's mass. To explain this we begin with a $SU(2)_L \otimes$

$U(1)_Y$ invariant Lagrangian that couples the Higgs doublet to the fermion field which only generates masses for down-type fermions

$$\mathcal{L}_{\text{fermion}} = -\lambda_f(\bar{\psi}_{\text{L}}\phi\psi_{\text{R}} + \bar{\psi}_{\text{R}}\bar{\phi}\psi_{\text{L}})\,, \tag{1.34}$$

where ψ_{L} refers to the isospin doublets of left-handed fermions, for example $\binom{\nu}{e}_{\text{L}}$, and ψ_{R} refers to the isospin singlet of righted-handed fermions like e_{R}.

After the spontaneous symmetry breaking, this Lagrangian can be rewritten as

$$\begin{aligned}\mathcal{L}_{\text{e}} &= -\lambda_e\frac{1}{\sqrt{2}}[(\bar{\nu},\bar{e})_{\text{L}}\begin{pmatrix}0\\ v+h\end{pmatrix}e_{\text{R}} + \bar{e}_{\text{R}}(0,v+h)\begin{pmatrix}\nu\\ e\end{pmatrix}_L] \\ &= -\frac{\lambda_e v}{\sqrt{2}}\bar{e}e - \frac{\lambda_e v}{\sqrt{2}}h\bar{e}e\,,\end{aligned} \tag{1.35}$$

where the first term is the electron mass term and the second term the electron-Higgs interaction term. Therefore, the electron mass is $m_e = \frac{\lambda_e v}{\sqrt{2}}$, which is not predicted since λ_e is a free parameter. The coupling of the fermions to the Higgs field is proportional to the fermion mass, $\frac{\lambda_e}{\sqrt{2}} = \frac{m_e}{v}$. In general, the coupling between the fermions and the Higgs boson is called the Yukawa coupling.

As we have shown, the above Lagrangian does not give mass to up-type fermions. To allow all possible fermion mass terms in the Lagrangian, we need the general form of the Yukawa interactions. First we define the quark and lepton weak eigenstate $SU(2)$ doublet as $Q_L = \binom{u_L^I}{d_L^I}$ and $L_{\text{L}}^I = \binom{l_{\text{L}}}{\nu_{\text{L}}}$, where the superscript I means that the fermion fields are expressed in the *interaction (flavor)* basis. Then the Yukawa interaction terms can be written as [33]

$$\mathcal{L}_{\text{Yukawa}} = Y_{ij}^{\text{d}}\bar{Q}_{\text{L}i}^I\phi d_{\text{R}j}^I + Y_{ij}^u\bar{Q}_{\text{L}i}^I i\sigma_2\phi^* u_{\text{R}j}^I + Y_{ij}^{\text{l}}\bar{L}_{\text{L}i}^I\phi l_{\text{R}j}^I + \text{hermitian conjugate}\,, \tag{1.36}$$

where Y_{ij}^{d} (Y_{ij}^{u}) are the matrices of Yukawa coupling constants between the down-type (up-type) quarks and the Higgs boson, l_{Rj}^I refers to the right-handed isospin singlet of leptons (without neutrinos), and σ_2 is the second Pauli matrix, $\sigma_2 = \binom{0\ -i}{-i\ 0}$, the subscript i,j stands for the three generations.

If the Higgs field is excited over its vacuum expectation value, $\phi = (1/\sqrt{2})\binom{0}{v+h}$, the terms from $\mathcal{L}_{\rm Yukawa}$ involving the vacuum expectation value will become the fermion mass terms of the form

$$\mathcal{L}^{\rm quarks}_{\rm Yukawa} = \bar{\rm d}^I_{{\rm L}i} M^d_{ij} d^I_{{\rm R}j} + \bar{\rm u}^I_{{\rm L}i} M^u_{ij} u^I_{{\rm R}j} + \text{hermitian conjugate} + \text{interaction terms}\,, \quad (1.37)$$

where $M_{ij} = (v/\sqrt{2})Y_{ij}$. The quark mass eigenstates can obtained by diagonalizing the matrices M with unitary matrices ($V^\dagger V = 1$)

$$M^d_{\rm diag} = V^d_{\rm L} M^d V^{d\dagger}_{\rm R}\,. \quad (1.38)$$

The Lagrangian can be expressed in terms of the quark mass eigenstates

$$\mathcal{L}^{\rm quarks}_{\rm Yukawa} = \bar{d}_{{\rm L}i}(M^d_{ij})_{\rm diag} d_{{\rm R}j} + \bar{u}_{{\rm L}i}(M^u_{ij})_{\rm diag} u_{{\rm R}j} + \text{hermitian conjugate} + \text{interaction terms}\,, \quad (1.39)$$

where

$$d_{{\rm L}i} = (V^d_{\rm L})_{ij} d^I_{{\rm L}j} \quad d_{{\rm R}i} = (V^d_{\rm R})_{ij} d^I_{{\rm R}j}\,, \quad (1.40)$$

$$u_{{\rm L}i} = (V^u_{\rm L})_{ij} u^I_{{\rm L}j} \quad u_{{\rm R}i} = (V^u_{\rm R})_{ij} u^I_{{\rm R}j}\,. \quad (1.41)$$

Now we can also express the charged current interaction between quarks in terms of the quark mass eigenstates instead of the weak eigenstates, for example

$$\begin{aligned} \mathcal{L} &= \frac{g}{\sqrt{2}} \bar{d}^I_{{\rm L}i} \gamma_\mu W^{+\mu} u^I_{{\rm L}i} \\ &= \frac{g}{\sqrt{2}} \bar{d}_{{\rm L}i} (V^d_{\rm L} V^{u\dagger}_{\rm L})_{ij} \gamma_\mu W^{+\mu} u_{{\rm L}i}\,, \end{aligned} \quad (1.42)$$

where the matrix $V^d_{\rm L} V^{u\dagger}_{\rm L}$ is a unitary 3×3 matrix, known as the Cabibbo-Kobayashi-Maskawa (CKM) mixing matrix. In general, the mass eigenstates and the weak eigenstates are chosen to be the identical for up-type quarks, whereas for the down-

type quarks, the two eigenstates are related by the CKM matrix V_{CKM}

$$\begin{pmatrix} d^I \\ s^I \\ b^I \end{pmatrix} = \begin{pmatrix} V_{ud} & V_{us} & V_{ub} \\ V_{cd} & V_{cs} & V_{cb} \\ V_{td} & V_{ts} & V_{tb} \end{pmatrix} \begin{pmatrix} d \\ s \\ b \end{pmatrix} . \tag{1.43}$$

One important aspect of the CKM matrix is that the off-diagonal terms allow weak-interaction transitions between different quark generations.

1.1.5 Problems of the Standard Model

Despite its great success so far, the Standard Model of particle physics is not deemed to be ultimate and perfect, from both the experimental and theoretical points of view. On the experimental side, there are a number of facts that the Standard Model does not explain:

- The Standard Model does not unify gravitational forces into the theory.
- In the Standard Model, neutrinos are massless particles. The observation of neutrino oscillations [34] requires that neutrinos have nonzero masses.
- The Standard Model predicts the same amount of matter and antimatter. However, the fact is that the universe primarily consists of matter.

On the theoretical side, the major problem of the Standard Model is the so-called hierarchy problem of the Higgs boson mass. The Higgs boson mass is subject to very large corrections, arising from virtual fermion loops, dominated by the top quark

$$m_h = m_h^{\mathrm{bare}} + \delta m_h^{\mathrm{corr}} , \tag{1.44}$$

where the first term refers to the Higgs boson mass in the free field, and the second term refers to the correction to the mass when the Higgs boson interacts with other particles.

The top loop correction, when expressed in terms of the loop momentum cutoff Λ, is

$$(\Delta m_h^2)^{\text{top}} = \frac{-3}{8\pi^2}\lambda_t^2\Lambda^2\,, \tag{1.45}$$

to the leading order, where Λ is the energy scale below which the Standard Model is valid, which is unknown at present. However, it must be at least of the order of TeV, which is the energy scale of the current collider experiments. Precision electroweak measurements [12] constrain the Higgs boson mass to be of the order of the electroweak scale. Therefore, both the bare mass and the correction must be very large compared to the electroweak scale. It is unnatural to have a Higgs boson mass which is much smaller than 1 TeV/c^2. This problem in the Standard Model is called the hierarchy problem.

One solution to the hierarchy problem is the Supersymmetry theory [35]. In this theory, there is a boson (fermion) as the partner of every fermion (boson). Therefore, the leading order top and stop (the supersymmetric partner of top) loop corrections cancel.

There are also other unsolved problems in the Standard Model. For example, there is no explanation for the existence of three generations of fermions. This particular question is solved by the compositeness model [36]. We will present a search for evidence of this model in part two of this thesis (chapter 16).

1.2 Higgs Boson Searches

The phenomenological studies of the production and decays of the Standard Model Higgs boson have started as early as the 1970s [37], followed by the studies in e^+e^- collisions [38] and $p\bar{p}$ and pp collisions [39, 40]. Searches for the Standard Model Higgs boson started at the Large Electron-Positron (LEP) collider at CERN which started to run in 1989. Initially the LEP collider operated at $\sqrt{s}$ = 91 GeV, to produce the Z bosons. About 17 M Z events were collected from 1990 to 1995, which were studied in detail by the four experiments at LEP [41]. In 1995, the machine

was upgraded to enable pair production of W bosons. At LEP, precision electroweak measurements were performed, providing various indirect tests of the electroweak theory and constraints on the Higgs boson [12]. In 2000, the $\sqrt{s}$ increased to 209 GeV, with the goal of a direct observation of the Higgs boson. However, despite some hints, no definitive evidence was established, and a lower limit on the Higgs boson mass $M_H > 114.4$ GeV/c^2 at 95 % Confidence Level (CL) was extracted [42].

In 2010, the precision electroweak measurements [12] from the LEP and Tevatron experiments set an upper limit on the Higgs boson mass of 158 GeV at 95% CL. In December 2011, both experiments, ATLAS and CMS at the LHC found preliminary evidence of a "Higgs-like" sboson at the mass around 125 GeV/c^2. ATLAS observed an excess of events with a local significance of 3.1 standard deviation (σ) at a mass around 126 GeV/c^2 [43], and CMS observed 3.1 σ at a mass around 124 GeV/c^2 [44].

The searches continued at the LHC and the Tevatron. At the end of July, the two experiments at Tevatron, CDF and D0, observed an excess of events over a large range of mass range between 120 and 135 GeV/c^2, with a most significant excess of 3.3 σ at $M_H = 135$ GeV/c^2 [45]. The observation of a new particle was finally established by the two experiments at the LHC. With the data from 2011 and first half of 2012, the ATLAS experiment observed a significance of 5.9 σ at $M_H = 126$ GeV/c^2 [46], and the CMS experiment observed a significance of 5.0 σ at $M_H = 125$ GeV/c^2 [18].

Though the new particle was found to be consistent with the production of a Standard Model Higgs boson, more studies are needed to confirm if it is really the Higgs boson predicted by the Standard Model, or if it implies new physics beyond the Standard Model.

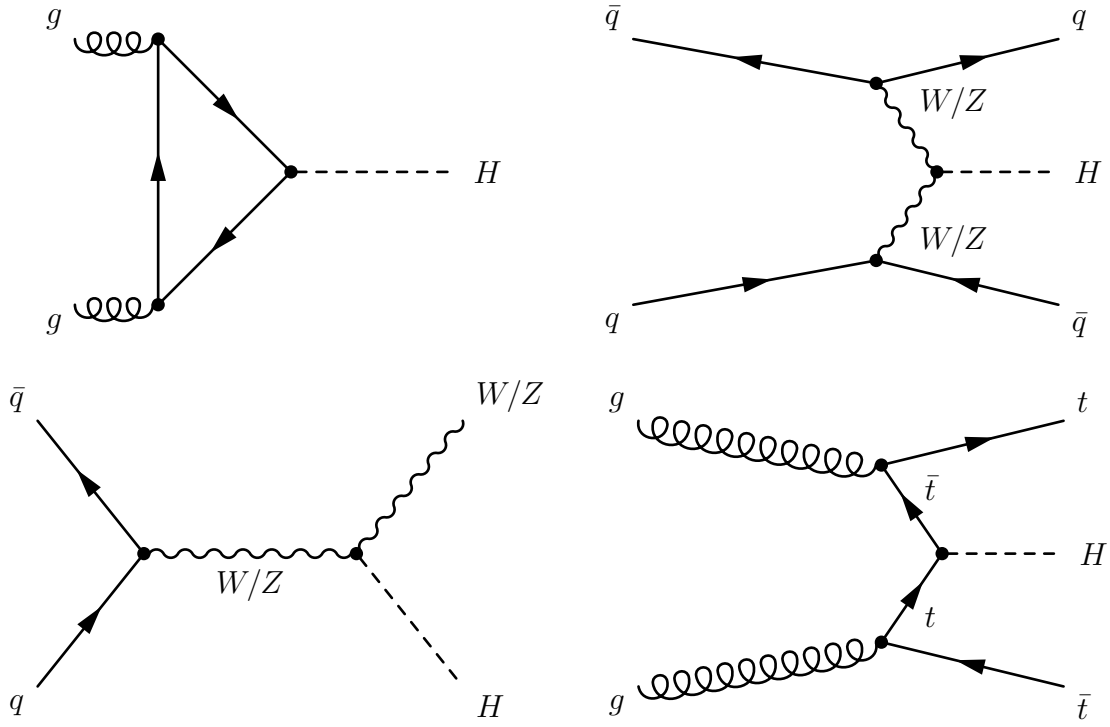

Figure 1.3: Feynman diagrams for the main production mechanisms of the Standard Model Higgs boson at the LHC.

1.3 Standard Model Higgs Boson Production and Decays at the LHC

1.3.1 Higgs Boson Production and Decays

At the LHC, the Standard Model Higgs boson is produced by four processes, as shown by the Feynman diagrams in figure 1.3. The dominant one is gluon gluon fusion (ggF), where the Higgs boson is produced by the fusion of two initial state gluons, mediated by a virtual heavy fermion loop or a W loop, that couples to the Higgs boson. The next most dominant process is the vector boson fusion (VBF) process. This process has a production cross section roughly an order of magnitude lower than ggF. The Higgs boson can also be produced through the radiative "Higgs-strahlung" process, leading to associated production with a W or Z boson (VH). This process has a cross section about a factor of 1-2 lower than VBF in the mass range between 110 and 150 GeV/c^2. The last small contribution to the Higgs production is associated production with a top-antitop pair (ttH). The cross section of this process is roughly

an order of magnitude smaller than VH.

The production cross sections of these processes at $\sqrt{s}$ =7 TeV and 14 TeV at the LHC are shown in figure 1.4 as a function of the Higgs boson mass.

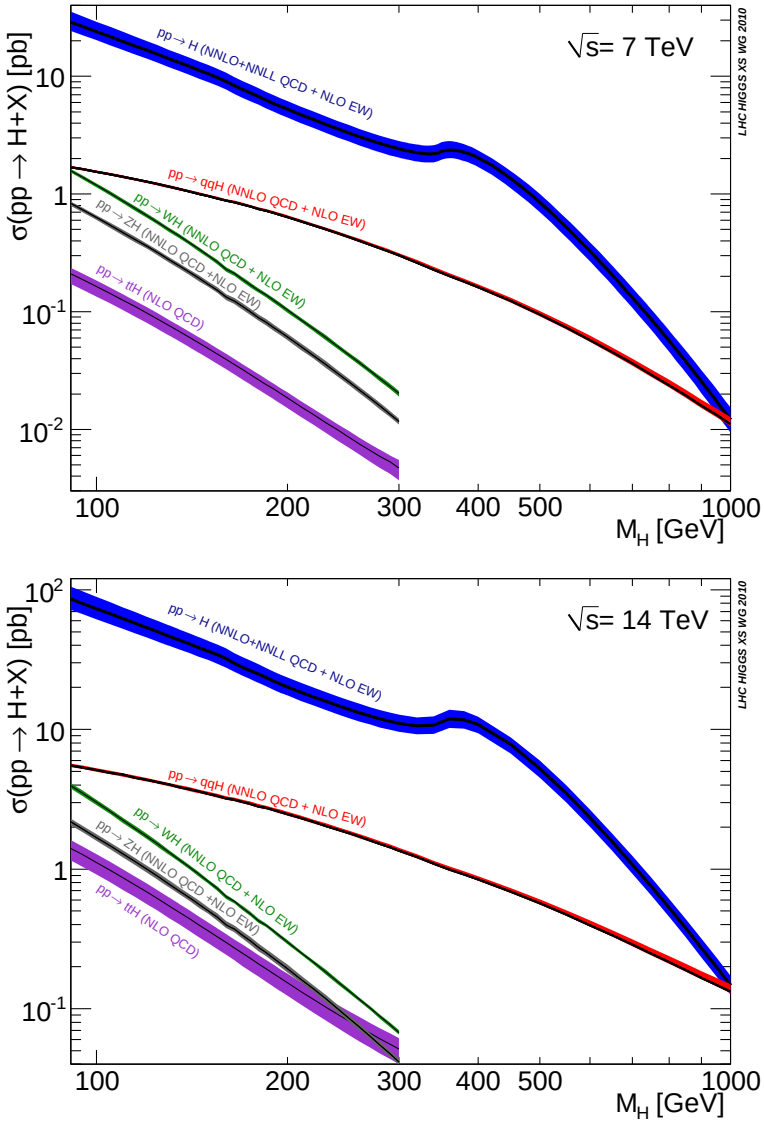

Figure 1.4: Standard Model Higgs boson production cross sections at $\sqrt{s}$ = 7 (top) and 14 TeV (bottom).

The Higgs boson decays immediately after its production. Due to its coupling to the fermions and bosons, the Higgs boson decays into a pair of W bosons, a pair

of Z bosons, or a pair of massive fermions at the tree level. [1] It also decays, via internal loop diagrams, into a pair of gluons, a pair of photons, or a Z boson and a photon. However these decay modes are suppressed because the loop diagrams are higher order. Figure 1.5 [47] shows the branching ratio of the various decay modes. It is dominated by $b\bar{b}$ for Higgs boson masses below 135 GeV/c^2, and dominated by WW for higher masses.

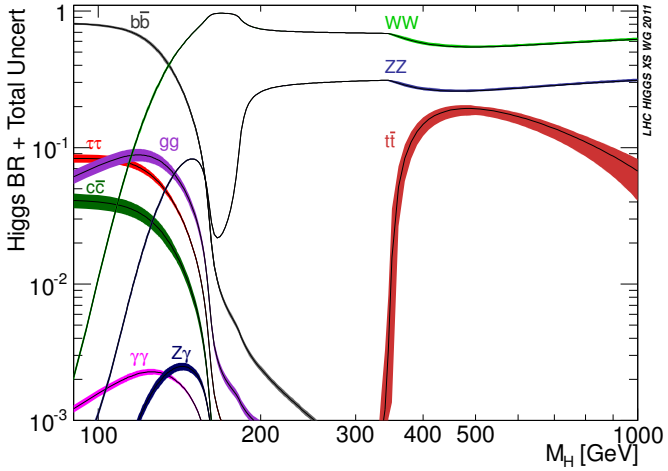

Figure 1.5: Standard Model Higgs decay branching ratios as a function of its mass.

1.3.2 The H $\to \gamma\gamma$ Decay Mode

This thesis presents my search for the Higgs boson in the H $\to \gamma\gamma$ channel in the low mass range between 100 and 150 GeV/c^2. In this range, the branching ratio is only about 2×10^{-3}. However, this channel has distinguishing features, making it very important for this mass range. The invariant mass of the two photons from a Higgs boson could present itself as a narrow $\gamma\gamma$ resonance in the data, on top of a smoothly falling background. With sufficient data and sufficiently good energy resolution, this resonance becomes well pronounced. This channel is thus one of the channels with the greatest discovery potential, due to the excellent energy resolution of the crystal calorimeter of CMS.

[1] Tree level here means there are no loops in the Feynman diagrams.

Chapter 2

Experimental Apparatus

In this chapter we introduce the experimental apparatus used to perform the studies in this thesis, including the Large Hadron Collider and the Compact Muon Solenoid detector.

2.1 The Large Hadron Collider

The Large Hadron Collider (LHC) is a particle accelerator installed in a tunnel with a circumference of 27 km, 50 to 175 meters underground, located at CERN on the border between Switzerland and France. The LHC is the last part of the CERN accelerator complex, shown in figure 2.1, which consists of a succession of accelerators for increasingly higher energies. The main LHC accelerator consists of 1232 superconducting dipole magnets, which can accelerate a proton to the energy of 7 TeV when operated at a magnetic field of 8.33 tesla, which is approximately 200,000 times the Earth's magnetic field.

The design center-of-mass energy ($\sqrt{s}$) of the LHC for pp collisions is 14 TeV. In 2010 and 2011, $\sqrt{s}$ was 7 TeV. In 2012, this was increased to 8 TeV. After the long shutdown planned in 2013 and 2014, the center-of-mass energy will be raised to 13-14 TeV, close to the design value.

In pp collisions at the LHC, the instantaneous luminosity is given by

$$L = \frac{N_p^2 n_b f_{\mathrm{LHC}} \gamma_r}{4\pi \epsilon_n \beta^*} F \,, \tag{2.1}$$

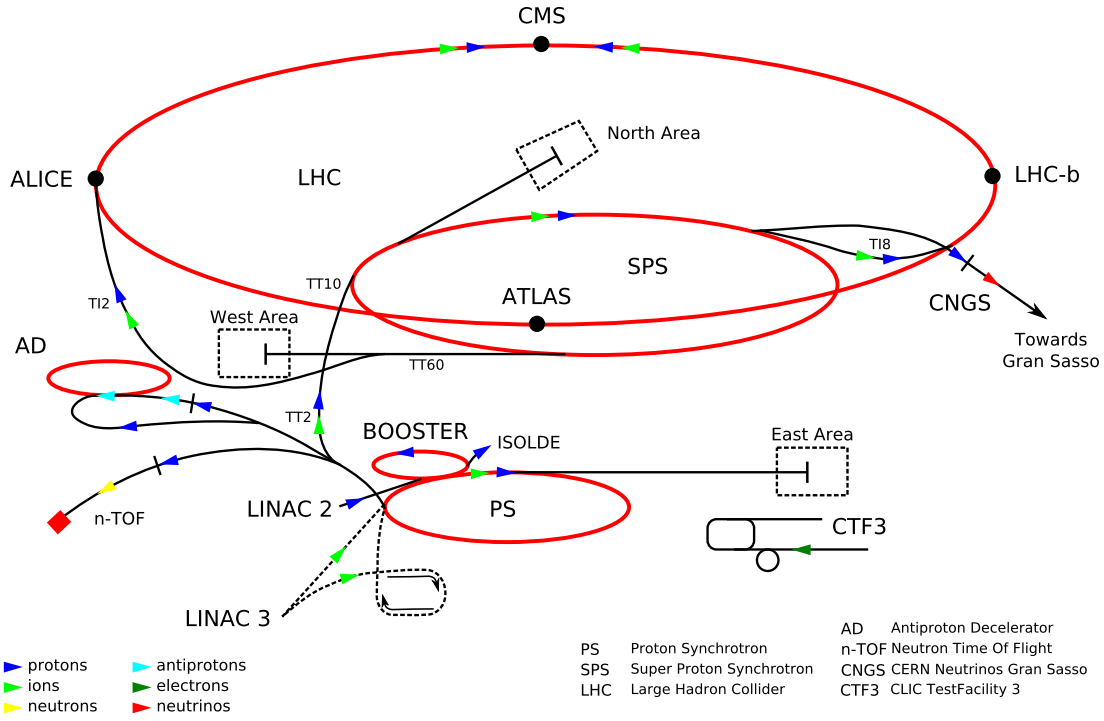

Figure 2.1: A schematic diagram of the LHC accelerator complex [48]. Protons are first accelerated in the linear accelerator (LINAC) and injected into the PS Booster to reach a kinetic energy of 1.4 GeV. Then, they enter the Proton Synchrotron (PS) ring, are accelerated to 25 GeV, and are further accelerated to 450 GeV in the Super Proton Synchrotron (SPS). Finally they are injected into the LHC, and there they are accelerated to the maximum energy.

where N_p is the number of protons per bunch, n_b is the number of bunches per beam, and f_{LHC} is the LHC revolution frequency 11.245 kHz. γ_r is the relativistic gamma factor, ϵ_n is the normalized transverse beam emittance, and β^* is the value of the beta function at the collision point which relates to the transverse size of the beams at the interaction point, and F is the geometric factor due to the crossing angle of the two beams.

Table 2.1 lists the design parameters of the LHC, and the corresponding values realized in 2010, 2011 and 2012. The intensity per bunch has exceeded the design. The product of the emittance and the value of the beta function at the CMS interaction regions have also exceeded the design, resulting in a smaller beam size at the collision

Parameter	2010	2011	2012	design
N_p (10^{11} proton/bunch)	1.2	1.5	1.6	1.15
n_b (bunches/beam)	368	1380	1368,1374,1380	2808
Bunch spacing (ns)	150	75, 50	50	25
ϵ_n (mm rad)	2.4-4	1.9-2.4	2.2-2.5	3.75
β^* (m)	3.5	1.5-1	0.6	0.55
peak L ($\mathrm{cm}^{-2}\mathrm{s}^{-1}$)	2×10^{32}	4×10^{33}	7.6×10^{33}	10^{34}
$< N_{\mathrm{evt}} >$ per bunch crossing	3	19	35	23

Table 2.1: LHC key parameters in 2010, 2011, 2012, compared to design values.

points. The LHC has been operating with a bunch spacing of 50 ns in 2011 and 2012, in order to reduce the electron cloud effects of the proton beams and pileup effects due to multiple inelastic interactions. At the LHC, the average number events per bunch crossing is given by

$$< N_{\mathrm{evt}} > \; = \frac{\sigma_{\mathrm{inel}} L}{n_b f_{\mathrm{LHC}}} \,, \tag{2.2}$$

where σ_{inel} is total inelastic cross section, which is about 70 mb for pp collisions at $\sqrt{s} = 7$ TeV [49]. Analysis sensitive to pileup needs to consider its impact. For example, the isolation variable, usually defined as the sum of the energies measured inside a cone around the direction of the particle of interest, increases with the pileup. Energies from pileup need to be removed or corrected for, in order to maintain the selection efficiency, and to reconstruct the event without bias. We will discuss in details the pileup subtraction for photon identifications in section 7.2.

During the data taking period in 2011, LHC has delivered a total integrated luminosity to CMS 6.1 fb^{-1}, out of which 5.6 fb^{-1} was recorded by the CMS detector, as shown in figure 2.2. A peak luminosity of 4×10^{33} $\mathrm{cm}^{-2}\mathrm{s}^{-1}$ was recorded in 2011, as shown in figure 2.3.

In a collider experiment, the production rate of a process is given by the product of the instantaneous luminosity L and the production cross section σ

$$d\mathrm{N}/d\mathrm{t} = L \cdot \sigma \,. \tag{2.3}$$

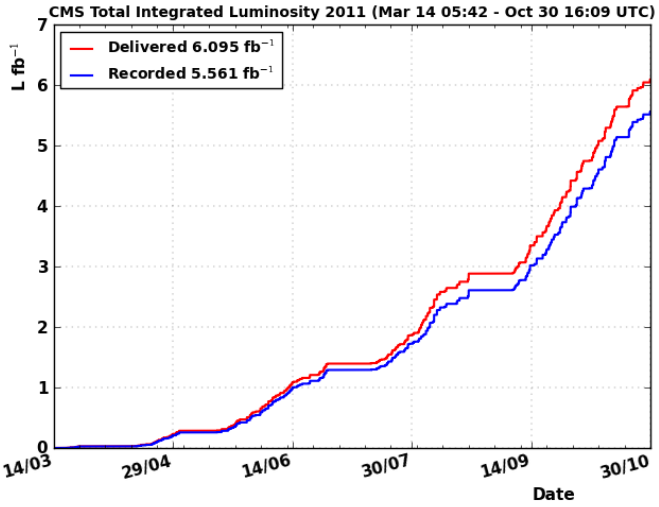

Figure 2.2: Integrated luminosity vs time delivered by LHC and recorded by CMS during 2011.

To calculate the expected number of events for a given period of data taking, it is more convenient to use the integrated luminosity, because of the varying instantaneous luminosity during LHC operations

$$\mathrm{N} = \mathrm{L} \cdot \sigma = \int L d\mathrm{t} \cdot \sigma \,. \tag{2.4}$$

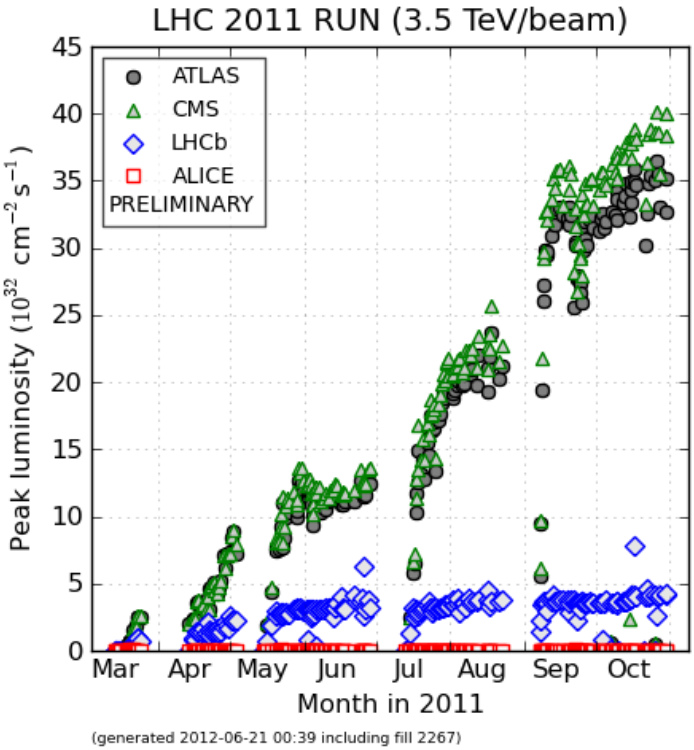

Figure 2.3: Peak luminosity recorded at the LHC experiments during 2011.

2.2 The Compact Muon Solenoid

2.2.1 Introduction

The CMS detector is a general purpose particle physics detector, located at the interaction point 5 in the LHC tunnel. Being general, it is able to detect a wide range of particles with energy from a few MeV up to a few TeV. It mainly consists of a silicon based tracker detector, a scintillating crystal electromagnetic calorimeter (ECAL), a sampling hadronic calorimeter (HCAL), a superconducting solenoid, and muon detectors. The overall layout of the various subdetectors in CMS is shown in figure 2.4. The solenoid, one unique feature of the CMS detector, generates a powerful magnetic field of 3.8 tesla, which is used to measure the momentum of charged particles. The tracker and the calorimeters are compact enough to fit inside the solenoid. The muon detectors are outside the solenoid and inside the steel return yoke of the magnet. A

transverse slice of CMS, showing the various subdetectors is shown in figure 2.5.

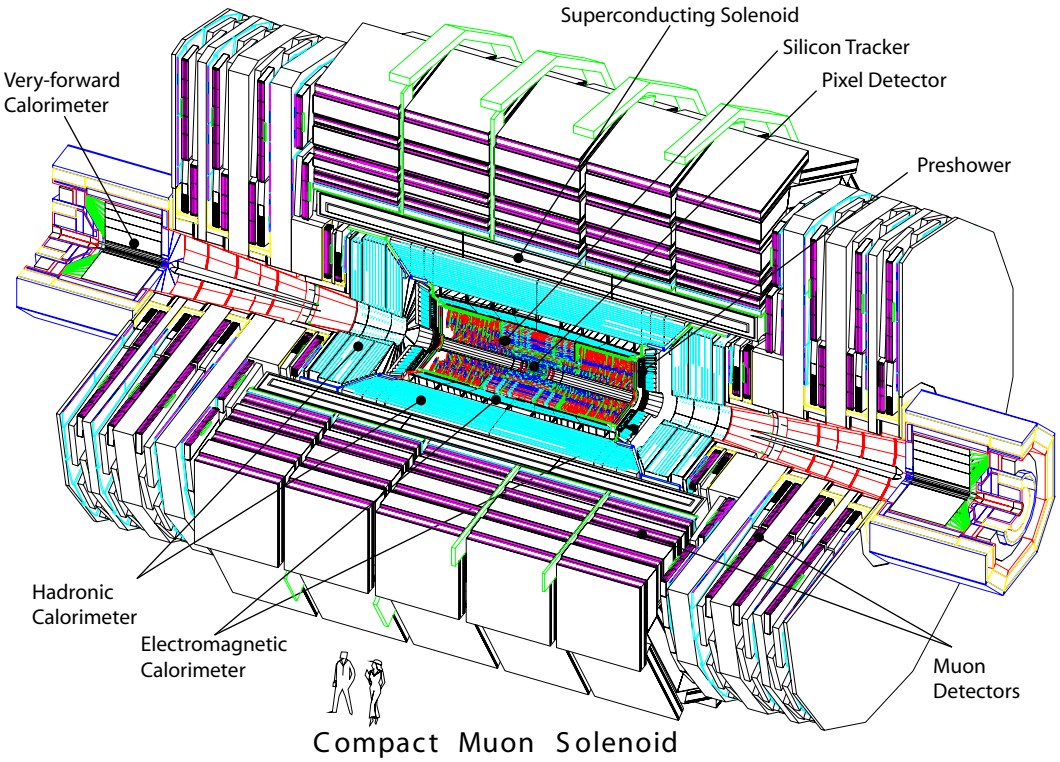

Figure 2.4: The 3D view of the CMS detector [50]. Various subdetectors are shown.

In CMS, the coordinate system has its origin centered at the nominal collision point. The y-axis points vertically upward and the x-axis points radially inward toward the center of the LHC tunnel. The z-axis points along the beam direction. The azimuthal angle ϕ is measured from the x-axis in the x-y plane. The polar angle θ is measured from the z-axis. In experiments at a hadron collider another quantity, pseudorapidity is more generally used instead of θ and it is defined as

$$\eta = -\ln(\tan\frac{\theta}{2})\,. \tag{2.5}$$

The pseudorapidity η is preferred over the polar angle because the rate of production of relatively light particles such as pions and kaons at hadron colliders is approximately constant over a wide range of η. The momentum and energy mea-

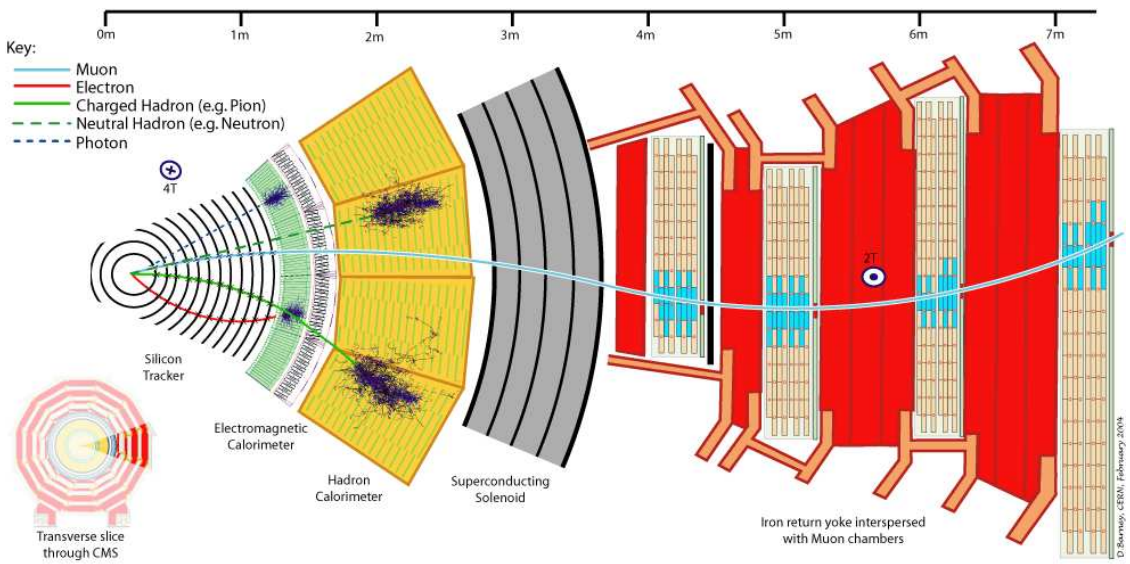

Figure 2.5: A transverse slice of the CMS subdetectors with a representative detection of a particle in each subdetector. Animated version for particles passing through each part can be found in [51].

sured transverse to the z-axis is denoted as p_{T} and E_{T}, respectively.

2.2.2 Tracking System

The innermost subdetector in CMS is the pixel detector, surrounded by a tracker detector. The two subdetectors together make the inner tracking system of CMS. The inner tracking system provides a precise and efficient measurement of the trajectories of charged particles as well as a precise reconstruction of interaction vertices, which are critical in many physics programs of CMS. For example, in the analysis of $h \to \gamma\gamma$, the tracker-based isolation quantity is an efficient discriminating variable to separate real photons from Higgs boson decays and fake photons from jet backgrounds. Knowledge of the primary interaction point where the Higgs boson decays is also important to reduce its impact on the invariant mass resolution, especially in the high instantaneous luminosity operations at the LHC, where multiple vertices are present for every collision because of multiple interactions.

At the design instantaneous luminosity of 10^{34} $\mathrm{cm}^{-2}\mathrm{s}^{-1}$, there are on average

about 1000 particles traversing the tracker per LHC bunch crossing (25 ns). That requires a tracker detector with a high granularity and fast response. The intense particle flux causes sever radiation damage to the tracker detector. Considering those requirements of granularity, fast speed and radiation hardness, CMS experiment built its tracker detector entirely based on the silicon detector technology. These features require a high power density of electronics which in turn require an efficient cooling in the operations.

A schematic cross section view of the tracking system is shown in figure 2.6 [52]. The pixel detector has three horizontal layers at radii r between 4.4 cm and 10.2 cm and 2 vertical layers extending z to 46 cm from the collision center. In total there are about 66 million pixels with an area of about 1 m^2. In the radial region between 20 cm and 116 cm, the strip tracker is used. It consists of three subsystems, covering different r and z regions. The Tracker Inner Barrel and Disks (TIB/TID) have 4 barrel layers extending r up to 55 cm, supplemented by 3 disks at both sides along the z direction. The TIB/TID is surrounded by the Tracker Outer Barrel (TOB) which extends z to 118 cm. The Tracker EndCaps (TEC) covers the region of r between 22.5 cm and 113.5 cm and the region of z between 124 cm and 282 cm. The strip tracker has 9.3 million strips with an area of about 198 m^2. The whole inner tracking system covers $|\eta|$ up to 2.5.

The large usage of silicon and supporting electronics and structure has an big impact on the material budget of the CMS tracker. Figure 2.7 [52] shows the material budget in units of the radiation length. It is about $0.4X_0$ at $\eta = 0$ and increases to about $1.8X_0$ at $\eta = 1.4$, and decreases to about $1X_0$ at $\eta = 2.5$. The material budget has an important impact on the performance of the electron and photon measurement. The energy resolution of converted photons is worse than that of unconverted ones. This is because the tracks of the electron pairs from conversion bend in the presence of 4 T magnetic field, and thus the energy deposit at the ECAL is spread along the direction of ϕ. The conversion probability depends on the radiation length

$$p_{\text{conv}} = 1 - e^{-\frac{7X}{9X_0}} . \tag{2.6}$$

Therefore, the photon conversion probability is about 27% at $\eta = 0$, and increases to about 75% at $|\eta| = 1.4$. In the region of $|\eta| > 1.5$ the probability increases before photon reaches ECAL crystals because of the preshower detector in front. In the H $\rightarrow \gamma\gamma$ analysis, we will categorize photons based on the energy resolution. One variable used for the categorization is highly correlated with the conversion probability, as we will discuss in section 7.2.

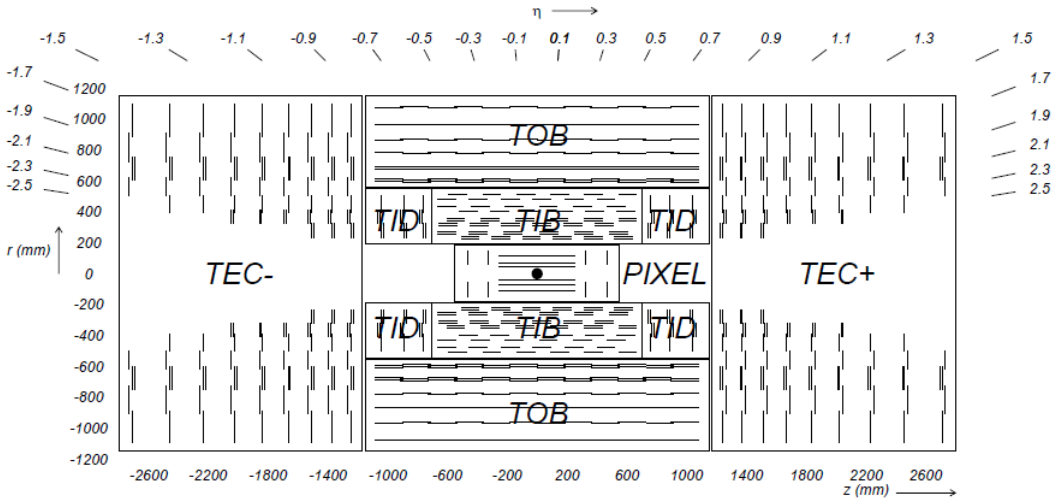

Figure 2.6: Schematic cross section of CMS tracker detectors. Each line represent a detector module or layer.

Figure 2.8 shows the tracker p_{T} resolution for single muons at different p_{T}, as a function of η. For high p_{T} tracks, the resolution increases from about 1.5% at $\eta = 0$ to about 7% at $|\eta| = 2.5$.

2.2.3 Electromagnetic Calorimeter

The electromagnetic calorimeter (ECAL) of CMS is a hermetic and homogeneous calorimeter. It measures the energy of electromagnetic showers from electrons or photons. It consists of 61,200 lead tungstate ($PbWO_4$) crystals in the barrel, covering $|\eta| < 1.48$, and 14,648 crystals in two endcaps at both sides, covering $1.5 < |\eta| < 3.0$. In addition, a preshower detector is mounted in front of each endcap, covering $1.65 <$

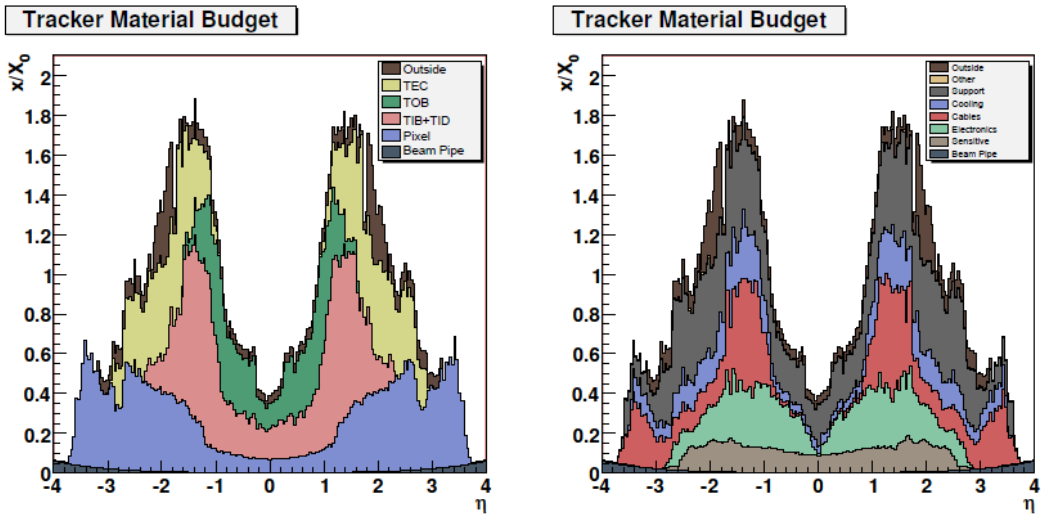

Figure 2.7: CMS tracker material budget in units of radiation length as a function of η. Left figure shows the contribution from different subdetectors. Right figure breaks down according to the functionality.

$|\eta| < 2.6$.

The detection of the two photons from Higgs boson decay is the main benchmark to test the performance of the design of ECAL, driven by its energy resolution. Crystal calorimeters have been known for decades for their excellent energy resolution [53]. CMS experiment uses the $PbWO_4$ crystals based on their desiring characteristics. They have a high density (8.28 g/cm^3), short radiation length (0.89 cm), and small Moliere radius (2.2 cm). These features lead to a compact calorimeter with fine granularity. The decay time of scintillation light in $PbWO_4$ is very short, the same order of magnitude as the LHC bunch crossing time, therefore, about 80% of the light is collected. One major disadvantage of $PbWO_4$ crystal is its relative low light yield, about 4.5 photoelectrons per MeV. However this can be compensated by gains of the photodetectors, the avalanche photodiodes (APD) in the barrel and vacuum phototriodes (VPT) in the endcaps. Figure 2.9 shows the picture of one barrel and endcap crystal with photodetectors attached [52].

In the barrel, each crystal has a cross section approximately 0.0173×0.0173 in

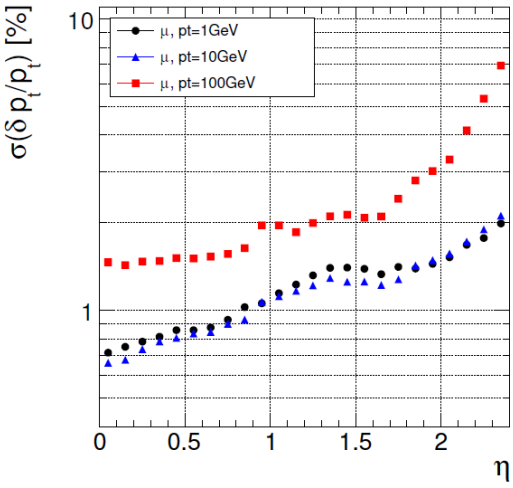

Figure 2.8: CMS tracker transverse momentum resolution as a function of η for muons at different transverse momentum: 1, 10, and 100 GeV.

$\eta - \phi$ coordinates or 22×22 mm^2 at the front face, which faces the interaction point, and 26×26 mm^2 at the rear face. Crystals are tapered such that all crystals point roughtly to the beam interaction point. Each crystal is 23 cm in length, corresponding to a radiation length $25.8X_0$. The CMS ECAL has a modular design, resulting in an relatively easy production and installation. Sets of 2×5 crystals are grouped in a thin-walled alveolar structure (submodule). Each alveole is 0.1 mm in thickness and consists of one aluminum layer (inner) and two layers of glass fibre-epoxy resin. The submodules are then assembled into larger modules, containing 400 or 500 crystals. Four modules, separated by aluminum nets, are assembled in one supermodule (SMod) which contains 1700 crystals, arrayed as 85×20 in η and ϕ direction. There are in total 36 SMods in the barrel. Half of them are in the negative side, covering -1.5$< \eta <$0, and the rest in the positive side, covering 0$< \eta <$1.5.

The modular construction causes sizable gaps between modules and cracks between SMods. The size of a gap between modules is about 6 mm along η and the crack size is about 5 mm between SMods along ϕ. These gaps or cracks cause energy loss of the electromagnetic showers. These loss needs to be corrected for when deriving the intercalibration constants, which we will discuss in section 4.3.3. In

the supercluster energy correction which we will discuss in section 5.5, we will use variables which are sensitive to the gaps or cracks to correct the energy loss.

In the endcaps, each crystal has a cross section 28.62×28.62 mm^2 at the front face and 30×30 mm^2 at the rear face. Each crystal is 22 cm in length, corresponding to a radiation length of $24.7X_0$. Array of 5×5 crystals is grouped in a carbon-fiber alveola structure, making one supercrystals (SC). A total number of 138 standard SCs and 18 special partial ones on the inner and outer circumference make up one-half of one endcap, named the "Dee". Each Dee contains 3662 crystals.

Figure 2.10 shows the layout of the ECAL. It shows the modules, SMods in the barrel and Dees in endcaps with preshowers in front. Figure 2.11 shows the barrel when it is installed inside the CMS detector. Figure 2.12 shows a Dee when it is fully equipped with SCs.

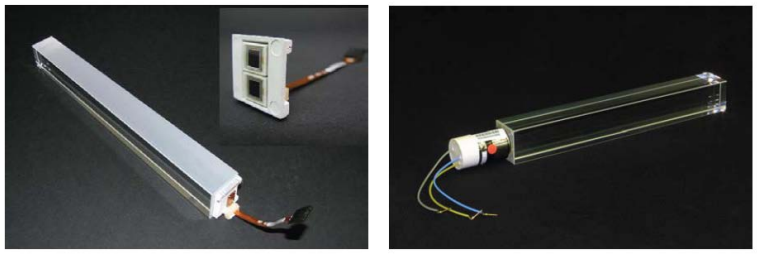

Figure 2.9: $PbWO_4$ crystals with photodetector attached. Left, a barrel crystal with the upper face depolished and the APD capsule. In the upper-right corner of the figure, a capsule with two APDs is shown. Right, an endcap crystal with VPT.

The ECAL energy resolution is usually parametrized as a function of energy [54],

$$\frac{\sigma(\mathrm{E})}{\mathrm{E}} = \frac{S}{\sqrt{\mathrm{E(GeV)}}} \oplus \frac{N}{\mathrm{E}} \oplus C\,, \tag{2.7}$$

where $\frac{S}{\sqrt{\mathrm{E}}}$ stands for the stochastic term (photoelectron statistics), $\frac{N}{\mathrm{E}}$ the electronic readout noise term, and C the constant term. The symbol of $\oplus$ means adding in quadrature. Detailed contributions [54] to each term are discussed below.

- **Stochastic term**. There are three main contributions. First, fluctuations on the lateral containment gives about 1.5%. Second, fluctuations on the energy

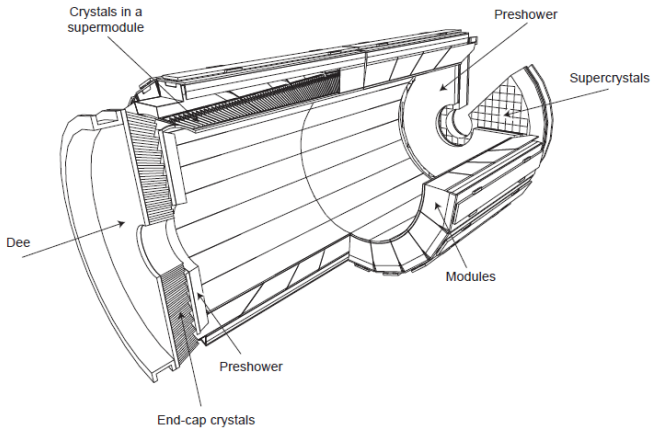

Figure 2.10: Layout of the CMS ECAL, showing arrangement of modules, SMods in the barrel and one Dee and the preshower detector in front of the endcap.

deposited in the preshower absorber with respect to what is measured give a sampling term of about 5%. Third, the photostatistics gives a contribution of about 2.3%.

- **Noise term**. It contains contributions from preamplifier and digitization noise from readout electronics as well as pileup noise from multiple inelastic collisions.

- **Constant term**. It is dominated by the crystal-to-crystal intercalibration errors and nonuniformity of the longitudinal light collection. Other small contributions ($< 0.2\%$) include variation of energy leakage, e.g., from the back of the crystal, and geometrical effects.

CMS ECAL has a very ambitious energy resolution design goal [54]. Table 2.2.3 shows the design parameters for the energy resolution at the center of barrel and endcaps.

Figure 2.13 left shows the different contributions to the designed energy resolution of the $PbWO_4$ crystals in the barrel. In the high energy regime of E $>$ 50 GeV, the constant term dominates the energy resolution. Figure 2.13 right shows the obtained energy resolution in the barrel from a test beam study. The result agrees with the design. However, it should be noted that the results are obtained under an

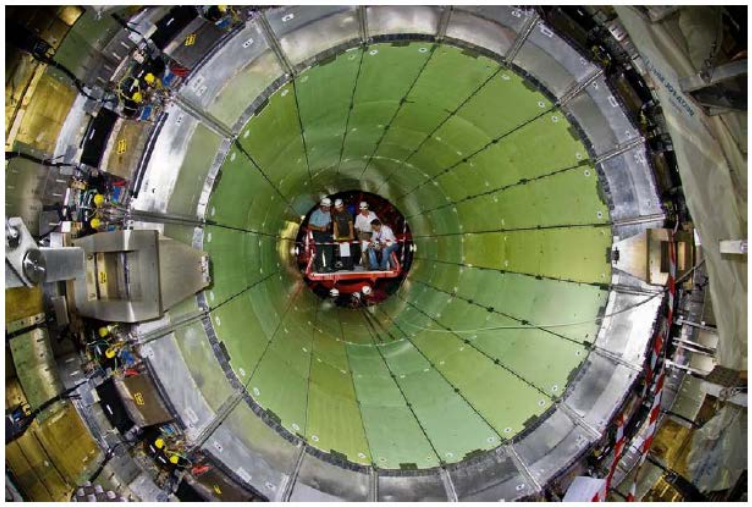

Figure 2.11: A photo of barrel ECAL when it is fully installed in CMS detector.

almost perfect conditions of test beam, with no material in front of ECAL and with stringent requirement of choosing only electrons incident close to the center of the crystal. Therefore, the measurement does not take into account the variation from the containment variations and intercalibration errors, which are important contributions in the pp collisions at the LHC. This result, however, shows the excellent performance of the $PbWO_4$ crystals.

We will continue the discussions in chapter 9 about the photon energy resolution from $H \to \gamma\gamma$ decays in realistic CMS simulation.

Besides the good energy resolution, another desirable characteristic of the CMS ECAL is the small nonlinearity of the energy response as a function of the energy. Here, the response refers to the peak of the distribution of the measured energy over the true energy: $E_{measured}/E_{true}$. There are mainly three factors which cause the nonuniform response as a function of the energy. The first one is energy leakage at the back of the crystal. At high energies, typically above 100 GeV, about 1% of the energy is lost due to the leakage. The second one is the dependence of the light collection efficiency and the longitudinal shower maximum on the energy. The tapered shape of the crystal causes a focusing effect, which leads to a higher light

Figure 2.12: An endcap Dee, fully equipped with supercrystals.

collection efficiency for scintillation light produced closer to the front of the crystal. This is why one side of the crystal was roughened to improve the uniformity of the light yield along the length of the crystals. *in situ*, the formation of the color center inside the crystal due to radiation damage (more discussion later in this section) can cause additional nonuniformity. The last one is the dependence of shower containment on energy because the energy is usually measured in a limited number of crystals. At very low energy, typically below 5 GeV, some channels are suppressed due to the selective readout (see section 4.3.1) implemented on ECAL detector *in situ*. This causes additional nonlinearity as well.

At test beams [55], the nonlinearity from 2 GeV to 100 GeV was found to be about 1%, where the energy was measured from a 5×5 array. The nonuniform response on energy has two potentially important impact. One potential impact is that this might cause the degradation of the performance when the intercalibration constants derived from low energy photons from $\pi^0(\eta)$ decays (see chapter 4) are applied to the reconstruction of the high energy electromagnetic showers. In the test beam studies in 2006 [56], we have found that the obtained intercalibration constants successfully

Contribution	Barrel ($\eta = 0$)	Endcaps ($\eta = 2.5$)
Containment	1.5%	1.5%
PhotoStatistics	2.3%	2.3%
Preshower sampling	–	5%
Stochastic term	2.7%	5.7%
Electronic noise at low (high) luminosity	0.15 (0.18) GeV	0.75 (0.77) GeV
Pileup noise at low (high) luminosity)	0.03 (0.095) GeV	0.175 (0.525) GeV
Noise term at low (high) luminosity	0.16 (0.21) GeV	0.77 (0.92) GeV
Intercalibration	0.4%	0.4%
Longitudinal nonuniformity	0.3%	0.3%
Others	$< 0.2\%$	$< 0.2\%$
Constant term	0.55%	0.55%

Table 2.2: Designed ECAL energy resolution parameters, as in Eq. 2.7.

improved the energy resolution of 50 GeV electrons, without noticeable degradation of the intercalibration precision. The improvement of *in situ* $\pi^0(\eta)$ intercalibration is also validated using $Z \to e^+e^-$ data, as will be discussed in section 4.8. Another potential impact is the determination of the energy scale at high energies. *in situ*, the ECAL energy scale can be determined using electrons from $Z \to e^+e^-$ decays or radiative photons from $Z \to \mu\mu\gamma$ decays, for energies up to O(100) GeV. Above that, extrapolation, determined from simulation, can be used. The lack of validation of the energy scale at very high energies is a potentially important systematic uncertainty for many searches using very high energy electrons or photons, for example, $Z' \to e^+e^-$.

Despite their superb intrinsic energy resolution, crystal calorimeters suffer from the radiation damage [57] [58], which can lead to degraded performance over time. The predominant radiation damage effect is radiation-induced absorption, caused by color center [59] formation inside the crystals. The formation of the color center causes self-absorption of a fraction of the scintillation light when it transports inside the crystal untill it reaches the photodetector. Therefore, the measured light output is reduced, which degrades the energy resolution.

When there are no collisions at the LHC, the crystals recover from radiation damage due to color center annihilation or annealing [57]. The balance of creation and annihilation of the color center results in a dose-rate dependent equilibrium of the light

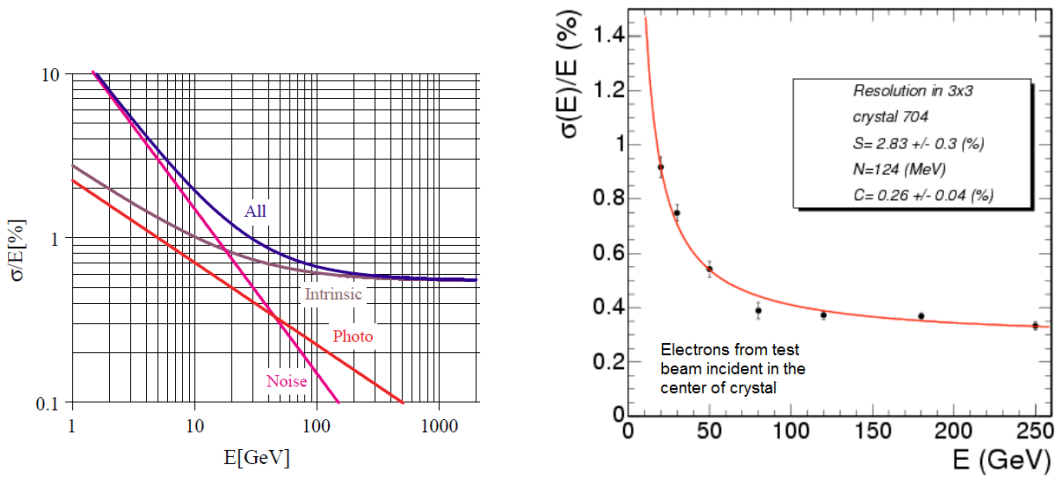

Figure 2.13: Left, different contributions to the energy resolution of the $PbWO_4$ calorimeter. Right, measured resolution as a function of the electron energy measured in a 3×3 array of crystals with beam incident in an area of 4×4 mm^2 around the crystal cross section center.

transmission. In the operations of the LHC, the typical result is a cyclic transparency behavior between collisions and no-collisions, as illustrated by a simulation study shown in figure 2.14 [52].

In order to maintain the ECAL energy resolution over time, a light monitoring system is designed to monitor the variation of the transparency of each crystal during the data taking at the LHC. To illustrate the effects of the transparency loss to the physics data and the correction based on the laser system, figure 2.15 shows the evolution of the $\pi^0(\eta) \to \gamma\gamma$ invariant mass peak positions reconstructed in the ECAL barrel, from September 22nd to October 30th in 2010, with and without applying the laser correction. The invariant mass is normalized to unity at the start of the run period considered. Without applying the laser correction, there is about 1% drop in the invariant mass peaks over this period. After applying the laser corrections, the invariant mass peaks are stable within 0.3%.

During 2011, the instantaneous luminosity at LHC is increased compared to 2010, resulting in more severe transparency loss. Figure 2.16 left shows the relative laser response changes, measured by the ECAL laser monitoring system, averaged over all

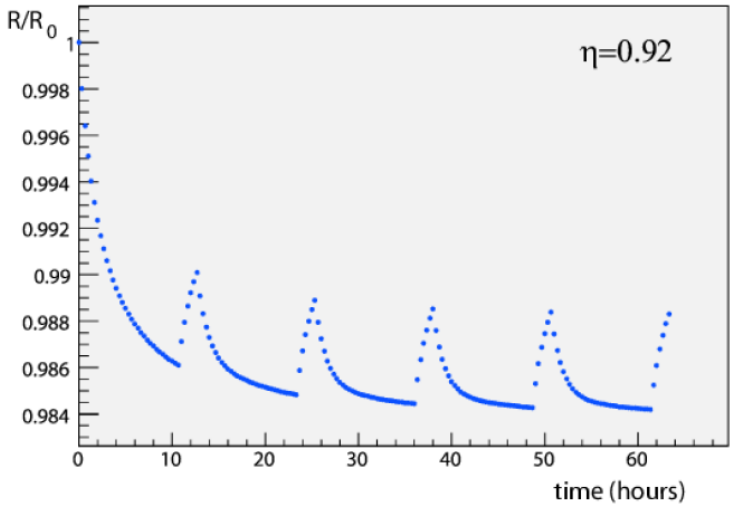

Figure 2.14: Simulation of crystal transparency variation. A LHC running cycle consists of 10 hours data taking followed by 2 hours filling time is assumed. The simulation model is based on data taken during a crystal irradiation in test beam.

crystals in bins of $|\eta|$, during the full 2011 data taking period. The response change is at the order of a few percent in the barrel, and is as high as about 15% in the most forward endcap regions used by analysis with electrons and photons ($|\eta| \leq$ 2.4-2.5). The change is upto about 40% for crystals closest to beam pipe. The recovery from radiation damge when no collisions is also clearly visible. Figure 2.17 shows that on average the ECAL energy scale is stable within 0.12% and 0.45% in barrel and endcaps, respectively.

In summary of this section, CMS ECAL is built with $PbWO_4$ crystals, which provide an excellent energy resolution. At high energy, the expected energy resolution for unconverted photons is dominated by the constant term, which is dominated by the intercalibration errors. All crystals of ECAL have been precalibrated with test beams electrons or cosmic ray muons [60]. However, the ultimate intercalibrations have to be measured *in situ*, for example, using photon pairs from neutral pion or eta decays, which we will discuss in chapter 4. The laser monitoring system is indispensable to monitor and correct for the transparency variation due to the radiation damage and recovery. Therefore, with proper calibration and monitoring, the CMS

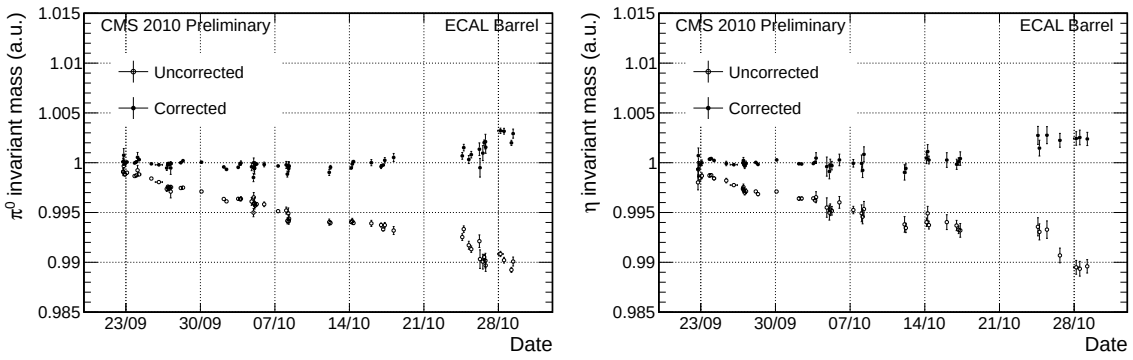

Figure 2.15: Effect of the laser correction on the $\pi^0 \to \gamma\gamma$ (left) and $\eta \to \gamma\gamma$ (right) invariant mass peak during about 5 weeks of data taking in 2010.

crystal calorimeter is an excellent calorimeter to search for new physics involved with electrons or photons, especially the search for a Higgs boson in the decay channel of two photons, $H \to \gamma\gamma$.

2.2.4 Hadron Calorimeter

The CMS Hadron calorimeters (HCAL) in conjunction with the ECAL form a complete calorimetry system to measure the energies and direction of jets and missing transverse energy [61]. The active material of the HCAL consists of plastic scintillator tiles with wave length shifting fibers for light readout. The tiles are interleaved with layers of brass alloy or stainless steel absorber to from a sampling calorimeter. Brass was chosen due to its nonmagnetic property and short nuclear interaction length $\lambda_{\text{int}} = 16.42$ cm. The energy is summed up over many layers of tiles in depths, called a tower.

Figure 2.18 [62] shows the CMS HCAL detector. It consists of four subsystems. The barrel HCAL (HB) covers $|\eta| < 1.4$ and consists of 2304 towers arranged in a projective geometry pointing back to the interaction point. Each HCAL tower consists of 15 layers of brass and one layer of stainless steel in the innermost and outermost radius for a better structural strength. Each tower covers 0.087×0.087 in η and ϕ, matched with a 5×5 array of crystals in the ECAL, forms a caloTower. Energies of the

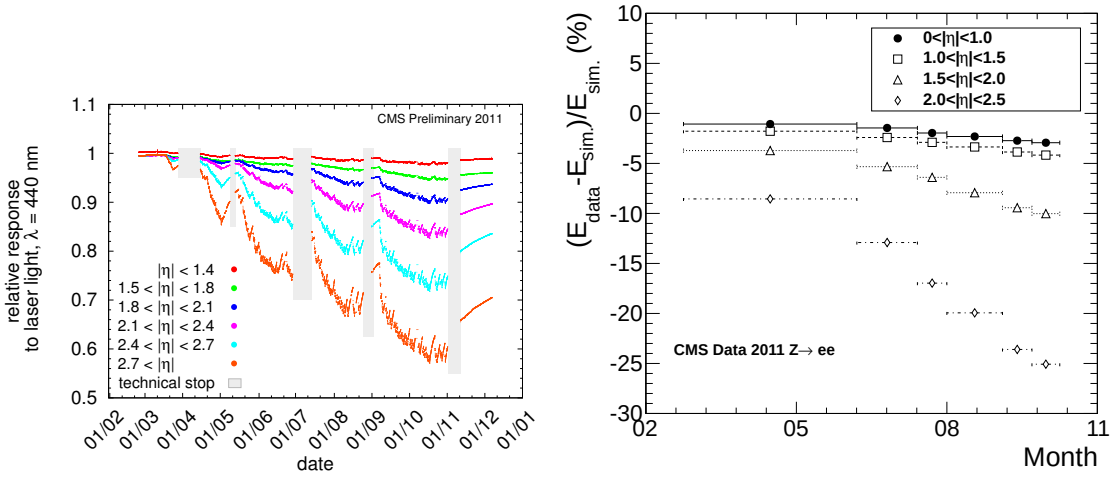

Figure 2.16: Left, relative response to the laser light (wavelength at 440 nm) measured by the ECAL laser monitoring system, averaged over all crystals in bins of pseudorapidity $|\eta|$, during the 2011 data taking period. Right, ECAL energy scale determined from $Z \to e^+e^-$ as a function of time in different regions of ECAL. See also figure 5.16 which has the same meaning, showing improved energy scale dependence over time after applying the laser correction.

jet are normally measured by summing up the energies in a few caloTowers. Another layer of scintillators, the outer hadron calorimeter (HO), is placed outside the solenoid, resulting an improvement of the energy and missing transverse energy resolution. The endcap HCAL (HE) covers $1.3 < |\eta| < 3.0$ and use only brass as the absorber. One tower in η and ϕ is 0.087×0.087 except for $|\eta| > 1.74$, where the η segmentation varies from 0.09 to 0.35 and the ϕ segmentation is 0.175. The forward calorimeters (HF) are located 11.2 m from the interaction point, covering $3.0 < |\eta| < 5.2$ and use steel as absorber. HF has a tower segmentation of 0.1075×0.0175 except for $|\eta| > 4.7$, where the segmentation is 0.0175×0.35.

The hadronic energy resolution of the HCAL and ECAL combined calorimeter is parametrized as

$$\frac{\sigma(\mathrm{E})}{\mathrm{E}} = \frac{S}{\sqrt{\mathrm{E(GeV)}}} \oplus C\,, \tag{2.8}$$

where S is the stochastic term and N the constant term. They have been measured in test beams [63] to be $S = 0.85 \pm 0.02\sqrt{\mathrm{GeV}}$ and $C = 0.074 \pm 0.008\%$ in HB and HE. The corresponding values for HF are $S = 1.98\sqrt{\mathrm{GeV}}$ and $C = 0.09\%$ [64].

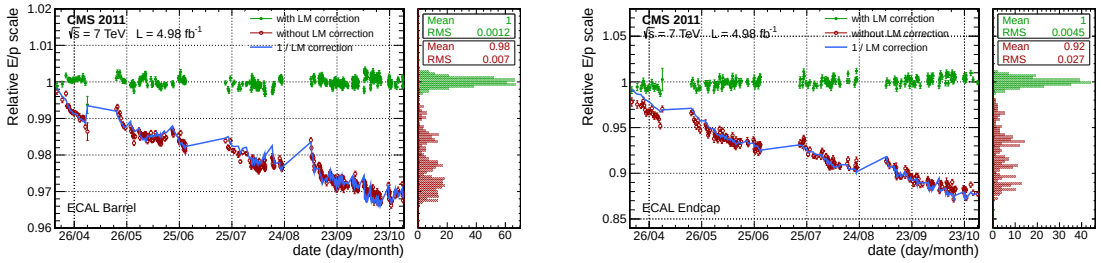

Figure 2.17: The ratio of the electron energy with and without laser correction, measured in the ECAL, to the electron momentum p, measured in the tracker as a function of time, in the barrel (left) and endcaps (right). The continuous blue line indicates the magnitude of the average transparency correction.

2.2.5 Muon Detectors

The muon detector [65] is the outermost detector in CMS to detect and measure muons. Most particles produced in pp collisions, for example, electrons, photons, pions or kions in jets are stopped by materials in the calorimeter. Muons, however, traverse the calorimeter with minimal loss of energy and easily reach the muon system. This unique feature result in the muon detection and identification with a very high efficiency and with a very low background contamination. One so-called golden channel for the search of the Higgs boson is by its four lepton decay, $H \rightarrow ZZ^* \rightarrow 4\mu$ because of its very clean signature.

The muon system consists of three types of gaseous detectors, driven by the very large surfaces to be covered and by the different radiation environments at different $|\eta|$. Drift tude (DT) chambers are used in the barrel of $|\eta| < 1.2$, where the neutral induced background is relatively small, the muon rate is relatively low and the residual magnetic field is relatively low. DT consisting of 4 layers of stations placed inside the magnet return yoke, at different radii from the beam axis. Each of 5 wheels of DT is divided into 12 sectors, each of which covers $\frac{\pi}{6}$ in ϕ. In 2 endcaps, cathode strip chambers (CSC) are used because of higher particle flux and higher magnetic field. It extends the $|\eta|$ coverage up to 2.4. Resistive plate chambers (RPC) are used both in the barrel and endcaps, providing a fast time response, comparable to scintillators, but with a coarser position resolution than DTs or CSCs. Thus RPCs can be used as

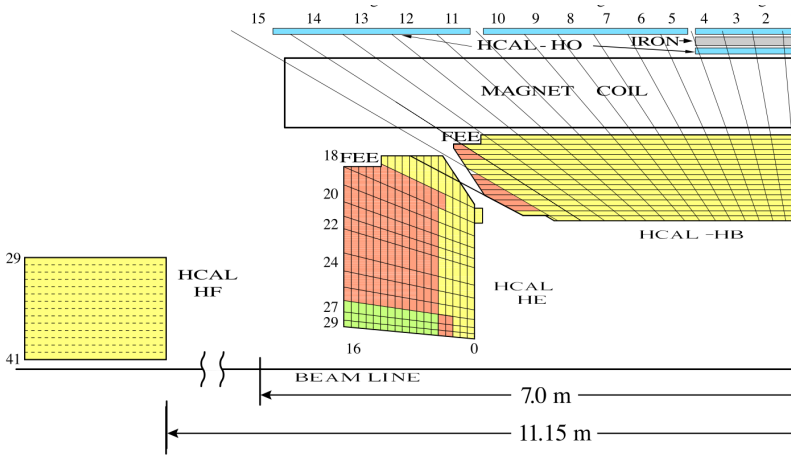

Figure 2.18: The CMS HCAL detector for one-fourth of the HB, HO, HE and HF. The number on the top (1 - 15) and on the left (18 - 29) refer to the tower numbers. The number on the right and on the bottom (0 - 16) refers to the scintillator layers. Different shading color represents independent optical readouts. "FEE" indicates the locations of the Front End Electronics for HB and HE.

a fast dedicated trigger which identifies muon candidates within one bunch crossing with a high efficiency.

Muons are not only measured in muon system, but also in the inner tracking system, resulting in an improved momentum resolution. The resolution of muon momentum measured by muon system is dominated by the multiple scattering in the material before the first muon station for $p_{\mathrm{T}} < 200$ GeV, when the chamber spatial resolution starts to dominate. Momentum measured with the inner tracking system thus has a better resolution for p_{T} up to hundreds of GeV. A combined measurement, refitting the trajectory in both the muon and the inner tracking system, improves the muon resolution at high p_{T}. Figure 2.20 left and right show the performance of the muon system, inner tracking system and the combined system in terms of the muon momentum resolution, in $0 < |\eta| < 0.2$ and $1.8 < |\eta| < 2.0$ regions, respectively. At this low η, the momentum resolution measured in the combined system increases from 0.7% at few GeV to 4% at 1 TeV. At the high η, the resolution increases from 1.5% at few GeV to 6% at 1 TeV.

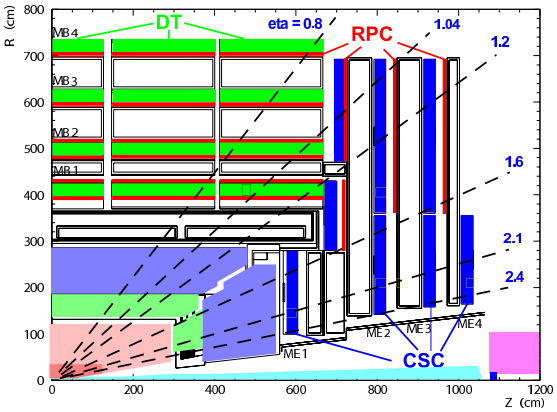

Figure 2.19: The layout of one quarter of the CMS muon systems, showing the positions of three subsystems, DT, CSC and RPC. 4 stations (labeled MB1-4) of DT are shown in green, CSC in blue and RPC in red.

2.2.6 Data Acquisition and Trigger System

The expected event rate from pp collisions at the LHC is very high. At $\sqrt{s} = 7$ TeV, the total inelastic cross section is about 70 mb [49]. Therefore, at a typical instantaneous luminosity 3×10^{33} cm^{-2}s^{-1} during the data taking in 2011, there are about 2×10^{8} events produced per second. However, the cross sections of most new physics channels are rather small. For example, the process of a 125 GeV Standard Model Higgs boson decaying to two photons has a cross section of only 3.94 pb. Thus the event rate of this process is about 1.18×10^{-4} Hz, which is an order of 10^{12} times smaller compared to the total event rate. The primary goal of the CMS Data Acquisition (DAQ) and Trigger system is to reduce the total event rate from collisions to a manageable level of a few hundred hertz while keeping the most interesting and precious events with a high efficiency.

Because of the required high event rejection power, CMS performs the full online selection in two steps. The first step is performed by the Level-1 (L1) Trigger systems. The L1 system is designed to reduce the total rate to less than 100 kHz based on detector electronics. It uses only coarsely segmented data from calorimeter and muon detectors in order to make a fast decision to keep or reject one particular event for further processing. The second step is performed by the High Level Trigger (HLT).

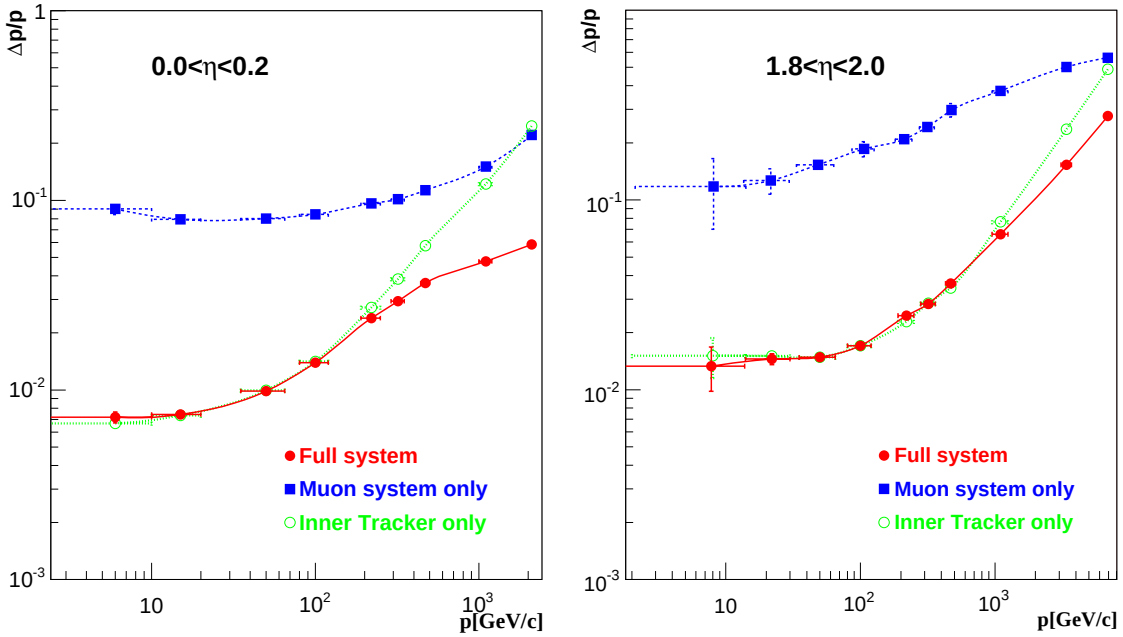

Figure 2.20: Muon momentum resolution as a function of p, measured from muon system only, inner tracking system only or combined ("full system" indicated in the figures), in two η bins, $0 < |\eta| < 0.2$ (left) and $1.8 < |\eta| < 2.0$ (right).

The HLT system is designed to reduce the L1-accepted events to a rate of O(10^2) Hz. It is based on the reconstruction and selection algorithms performed in a large farm of processors. The algorithms are quite close to the one used by the offline analysis, however, the selection criteria are usually less stringent than what are used offline. Events accepted by the HLT system are stored for end-user analysis or reprocessing with updated algorithms.

For ease of the analysis, HLT-accepted data are split into different primary datasets, based on the event trigger information. For example, photon datasets consist of events in which at least one or two photons passed some defined HLT photon selection criteria. This dataset is then a suitable dataset to search for a Higg boson in the diphoton decay channel.

Chapter 3

Data and MC samples for $\mathrm{H} \to \gamma\gamma$ Analysis

In this chapter we describe the data and Monte Carlo (MC) simulation samples used in the $\mathrm{H} \to \gamma\gamma$ search. We discuss the list of triggers used in data to select di-photon events, and conditions used in data reconstruction and MC simulation.

3.1 Data and Trigger

The dataset we used in the $\mathrm{H} \to \gamma\gamma$ analysis consists of a list of certified good runs taken by the CMS detector during 2011. The total integrated luminosity is $5.08\mathrm{fb}^{-1}$. The primary dataset, a concept that is defined in section 2.2.6, consists of events that passed any one of a list of di-photon triggers. The double-electron and double-muon primary datasets which consist of events passing the double-electron and double-muon triggers respectively are used to measure the ECAL performance and photon identification efficiency.

Table 3.1 lists the primary datasets used in this analysis, where the label "AOD" is a name that refers to a particular data structure format of the events in these datasets used in CMS. The label "Photon", "DoubleElectron", and "DoubleMuon" refer to the primary datasets. The label "Run2011AB16Jan2012v1" refers to the run periods and data reprocessing date (or version).

Table 3.2 shows the list of the High Level Trigger (HLT) paths used in each data taking period of 2011. Different trigger paths are used in different data taking periods

to take into account the rapid increase of the instantaneous luminosity at the LHC, in order to keep the total rate of photon trigger paths below about 30 Hz, the allocated rate from the CMS HLT. In this table, the number in the trigger path name following the "Photon" labels refers to the p_{T} thresholds. The labels follows that indicate specific cuts applied on the photon HLT objects. These cuts are listed in detail in table 3.3.

In all these triggers, events are selected with at least two photon candidates. These two photons are required to pass some separately defined p_{T} threshold. Each photon is required to pass some loosely defined isolation criteria or a loose requirement on the shower shape variable r_9 and $\sigma_{\mathrm{i}\eta\mathrm{i}\eta}$. These requirements are summarized in table 3.3, where r_9 is defined as the sum of energy inside a 3×3 crystal centered on the most energetic crystal divided by the sum of energy of all crystals associated to the photon

$$r_9 = \frac{\mathrm{E}_{3\times3}}{\mathrm{E}_{\mathrm{sc}}^{\mathrm{raw}}}\,, \tag{3.1}$$

where $\mathrm{E}_{\mathrm{sc}}^{\mathrm{raw}}$ refers to the raw energy, namely the total energy of all crystals, measured by the superclustering algorithm, which we will describe in section 5.2. The shower shape variable $\sigma_{\mathrm{i}\eta\mathrm{i}\eta}$ is defined in section 7.2. Isolation observables are computed from the sum of the transverse energy of calorimeter deposits or the transverse momentum of tracks within a geometric cone around the photon direction defined by $\Delta R = \sqrt{(\Delta\eta)^2 + (\Delta\phi)^2} < 0.3$, and proper inner veto cones are used to exclude the photon energy from the sum. Similar isolation variables used for offline photon identification are defined more precisely in section 7.2.

Table 3.4 shows the the overall trigger efficiency for di-photon events passing the offline photon identifications which we will describe in section 7.2. The trigger efficiency is very close to 100%, measured with $\mathrm{Z} \to \mathrm{e}^+\mathrm{e}^-$ events where electrons are reconstructed as photons.

Dataset	Use
/Photon/Run2011AB16Jan2012v1/AOD	Main analysis
/DoubleElectron/Run2011AB16Jan2012v1/AOD	ECAL performance
/DoubleMuon/Run2011AB16Jan2012v1/AOD	Photon identification

Table 3.1: Primary datasets used in the $H \to \gamma\gamma$ analysis.

Trigger path	run period
HLT_Photon26_CaloIdL_IsoVL_Photon18_CaloIdL_IsoVL	160404-161176
HLT_Photon26_CaloIdL_IsoVL_Photon18_CaloIdL_IsoVL HLT_Photon26_CaloIdL_IsoVL_Photon18_R9Id HLT_Photon26_R9Id_Photon18_CaloIdL_IsoVL HLT_Photon20_R9Id_Photon18_R9Id	161216-165633
HLT_Photon26_CaloIdL_IsoVL_Photon18_CaloIdL_IsoVL HLT_Photon26_CaloIdL_IsoVL_Photon18_R9Id HLT_Photon26_R9Id_Photon18_CaloIdL_IsoVL HLT_Photon26_R9Id_Photon18_R9Id HLT_Photon36_CaloIdL_IsoVL_Photon22_CaloIdL_IsoVL HLT_Photon36_CaloId_IsoVL_Photon22_R9Id HLT_Photon36_R9Id_Photon22_CaloIdL_IsoVL HLT_Photon36_R9Id_Photon22_R9Id	165970-166967
HLT_Photon26_CaloIdL_IsoVL_Photon18_CaloIdL_IsoVL HLT_Photon26_CaloIdL_IsoVL_Photon18_R9Id HLT_Photon26_R9Id_Photon18_CaloIdL_IsoVL HLT_Photon26_R9Id_Photon18_R9Id HLT_Photon36_CaloIdL_IsoVL_Photon22_CaloIdL_IsoVL HLT_Photon36_CaloIdL_IsoVL_Photon22_R9Id HLT_Photon36_CaloIdL_IsoVL_Photon22_CaloIdL_IsoVL HLT_Photon36_R9Id_Photon22_R9Id	167039-173198
HLT_Photon26_CaloIdXL_IsoXL_Photon18_CaloIdXL_IsoXL HLT_Photon26_CaloIdXL_IsoXL_Photon18_R9Id HLT_Photon26_R9Id_Photon18_CaloIdXL_IsoXL HLT_Photon26_R9Id_Photon18_R9Id HLT_Photon36_CaloIdL_IsoVL_Photon22_CaloIdL_IsoVL HLT_Photon36_CaloIdL_IsoVL_Photon22_R9Id HLT_Photon36_R9Id_Photon22_CaloIdL_IsoVL HLT_Photon36_R9Id_Photon22_R9Id	173236-178380
HLT_Photon26_CaloIdXL_IsoXL_Photon18_CaloIdXL_IsoXL_Mass60 HLT_Photon26_CaloIdXL_IsoXL_Photon18_R9IdT_Mass60 HLT_Photon26_R9IdT_Photon18_CaloIdXL_IsoXL_Mass60 HLT_Photon26_R9IdT_Photon18_R9IdT_Mass60 HLT_Photon36_CaloIdL_IsoVL_Photon22_CaloIdL_IsoVL HLT_Photon36_CaloIdL_IsoVL_Photon22_R9Id HLT_Photon36_R9Id_Photon22_CaloIdL_IsoVL HLT_Photon36_R9Id_Photon22_R9Id	178420-180252

Table 3.2: The full list of triggers in each run period of 2011 used in the H $\rightarrow \gamma\gamma$ analysis.

Trigger name label	Requirement for barrel (endcaps) photons
CaloIdL	$H/E < 0.15(0.10)$ $\sigma_{i\eta i\eta} < 0.014$ (0.035)
CaloIdXL	$H/E < 0.10(0.10)$ $\sigma_{i\eta i\eta} < 0.014$ (0.035)
Trigger name label	Requirement
IsoVL	$E_T^{ECAL} < 6.0 + 0.012E_T$ $E_T^{HCAL} < 4.0 + 0.005E_T$ $E_T^{TRK} < 4.0 + 0.005E_T$
IsoXL	$E_T^{ECAL} < 4.0 + 0.012E_T$ $E_T^{HCAL} < 4.0 + 0.005E_T$ $E_T^{TRK} < 4.0 + 0.005E_T$
R9ID	$r_9 > 0.8$ $r_9 > 0.9$,if "Mass60" is required
Mass60	$m_{\gamma\gamma} > 60$ GeV/c^2

Table 3.3: Definitions of the photon trigger path labels, where the abbreviations in the labels represent: VL=Very loose, L=Loose, XL= Extra loose.

Both photons in barrel		One or more in endcap	
$min(r_9)$ >0.94	$min(r_9)$ <0.94	$min(r_9)$ >0.94	$min(r_9)$ <0.94
100.00±0.01±0.00%	99.3±0.04±0.10%	100.00±0.02±0.00%	98.8±0.06±0.4%

Table 3.4: Trigger efficiency for events where two photons passing offline identification, measured with $Z \to e^+e^-$ events.

3.2 Monte Carlo (MC) Simulation Sample

The signal samples used in this analysis were generated with the POWHEG generator at Next-to-Leading order (NLO) in α_s for the gluon fusion and the vector boson fusion [66, 67], whereas the associated production process was simulated with PYTHIA [68] at leading order (LO). For the gluon fusion process the Higgs boson p_T spectrum is reweighted to the Next-Next-to-Leading order (NNLO) + Next-to-Leading Log (NLL) prediction computed using the HqT program [69, 70].

We use the cross sections and branching ratios recommended by the LHC Cross Section Working Group [47]. The gluon fusion cross section has been calculated to the NNLO+NNLL order for perturbative QCD and NLO for electroweak (EWK) contributions. The vector boson fusion cross section has been computed at NNLO for QCD and NLO for Electroweak contributions. The associated production cross sections have been computed at NLO QCD. Table 3.5 lists the signal mass points we used in this analysis and the corresponding cross section of each production mode and the $H \to \gamma\gamma$ branching ratio.

The major irreducible backgrounds to $H \to \gamma\gamma$ signals are the di-photon production from quark-antiquark and gluon-gluon annihilation, shown in Figure 3.1. The former is known as the born process and the later as the box process. The main reducible backgrounds include γ+jet and di-jet process, shown in Figure 3.2, where the jet is misidentified as the photon.

The background Monte Carlo samples were generated with PYTHIA release 6.4 or with the LO matrix-element generator MADGRAPH [71] interfaced with PYTHIA. Table 3.6 shows the background samples and their LO cross sections and the corresponding k-factors applied to scale the cross sections to NLO. In QCD samples, a k-factor of 1.3 is used for events with one real and one fake photons and a k-factor of 1.0 is used for events with both fake photons. In both the QCD and γ+Jets samples, events with two real photons are not used since they are already contained in the di-photon sample. The POWHEG $Z \to ee$ sample is used to derive the electron energy correction, which we will discuss in section 5.5.

M_H (GeV/c^2)	Gluon Fusion	Vector Boson Fusion	$W \to WH$, $Z \to ZH$	$t\bar{t} \to H$	Branching Fraction
110	19.8	1.40	1.35	0.126	1.97×10^{-3}
115	18.1	1.33	1.16	0.111	2.13×10^{-3}
120	16.6	1.27	1.02	0.098	2.25×10^{-3}
130	14.1	1.15	0.78	0.076	2.26×10^{-3}
140	12.1	1.05	0.60	0.061	1.93×10^{-3}
150	10.5	0.96	0.47	0.049	1.36×10^{-3}

Table 3.5: Standard Model Higgs boson production cross sections (pb) for different production mechanisms and the H $\to \gamma\gamma$ branching ratios at different Higgs boson masses.

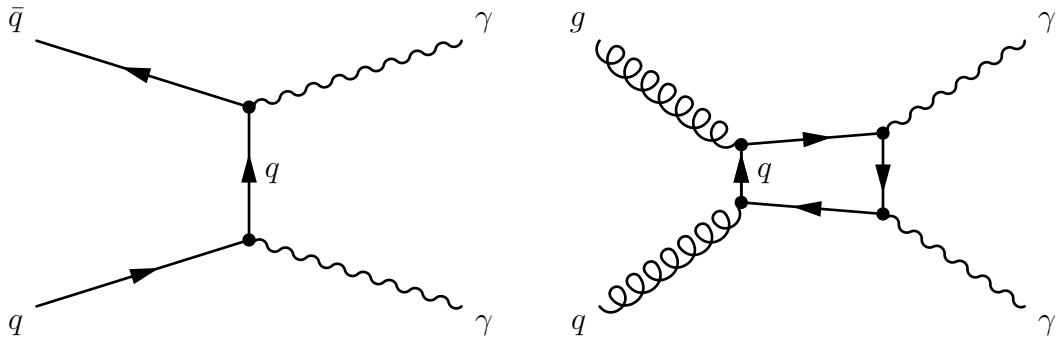

Figure 3.1: Feynman diagrams for the main $\gamma\gamma$ production mechanisms at the LHC, representing the irreducible backgrounds to H $\to \gamma\gamma$ signals. Left is the born process and right is the box process.

Process	Generator Order	$\hat{p_T}$ Bins	LO Cross Section (pb)	k-factor	$\int Ldt$ (fb^{-1})
$\gamma\gamma$+Jets	LO-MADGRAPH	-	154.7	1.15	7.4
$\gamma\gamma$ (Box)	LO-PYTHIA	10–25	358.2	1.3	2.23
		25–250	12.37	1.3	41.9
		250–∞	2.08×10^{-4}	1.3	3.8×10^6
$Z \to l^+l^-$ +jets	LO-MADGRAPH	50–∞	2475.0	1.15	14.
$Z \to e^+e^-$	NLO-POWHEG	20–∞	1666 (NLO)	-	17.7
QCD di-jet	LO-PYTHIA	30–40	10870	see text	0.56
		40–∞	43571	see text	0.92
γ+Jets	LO-PYTHIA	20–∞	493.44	1.3	2.4

Table 3.6: Standard Model background samples with the corresponding production cross sections and equivalent integrated luminosity.

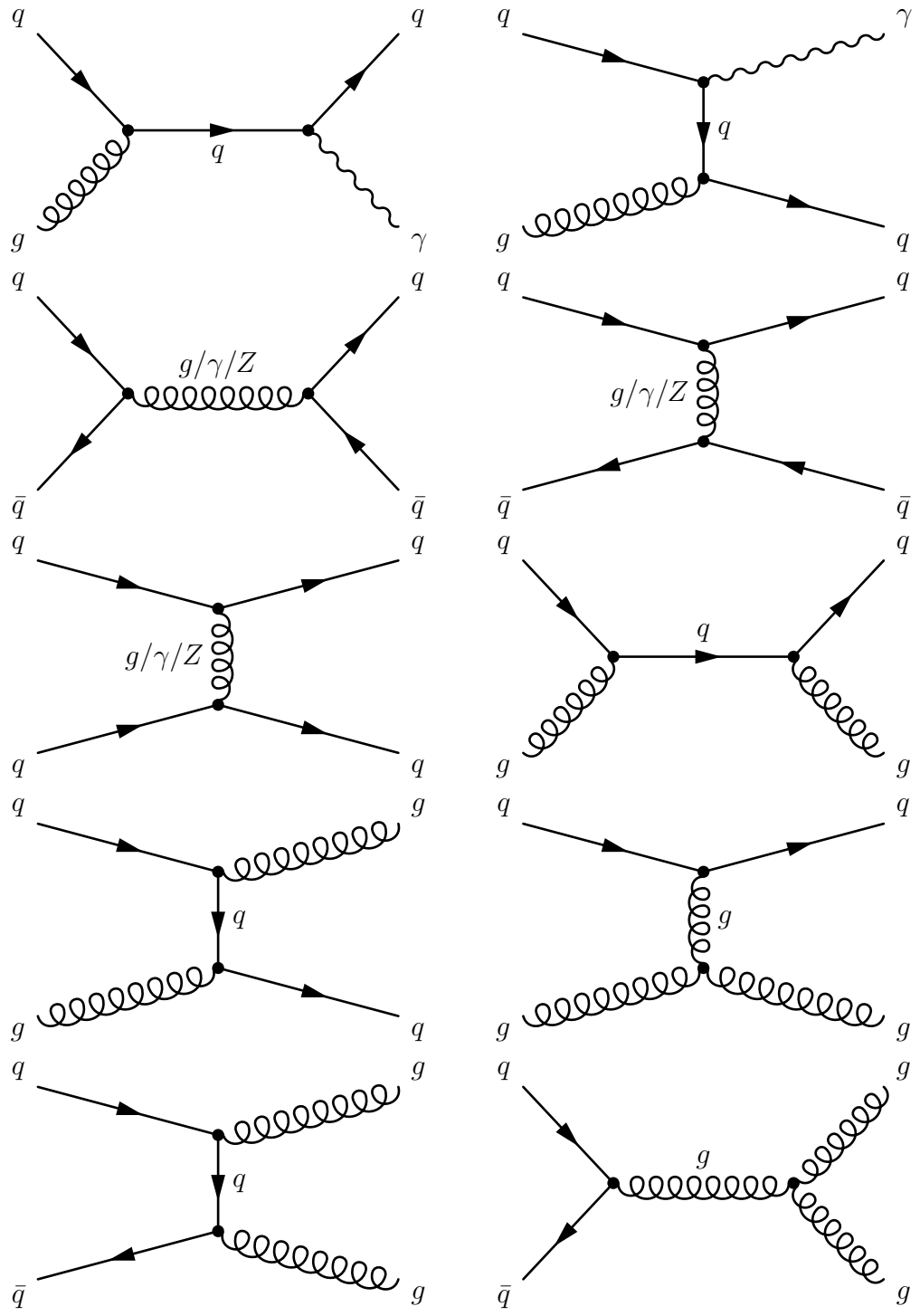

Figure 3.2: Feynman diagrams for the main γ+jet and di-jet production mechanisms at the LHC, representing the reducible backgrounds to $H \to \gamma\gamma$ signals.

3.3 Data and Simulation Conditions

Two of the keys to obtain the high mass resolution required for the $H \to \gamma\gamma$ analysis are precise ECAL calibration condition and laser monitor-based corrections of the crystals' transparency loss under irradiation. Calibration and laser correction will be discussed in detail in chapter 4. The datasets listed in table 3.1 were reconstructed with the best ECAL calibration available at the end of 2011. This ECAL calibration is provided by the $\pi^0(\eta) \to \gamma\gamma$ intercalibration, electron and $\phi-$symmetry calibration method with full 2011 calibration sample.

In simulation, in general the best known conditions were applied when the signal and background samples were generated. The MC samples used in this analysis have properly -correlated in-time and out-of-time pileup simulated. All MC samples are reweighted to match the actual pileup distribution observed in the data by applying an event weight based on the number of simulated pileup events and the instantaneous luminosity per bunch-crossing averaged pileup over the data taking period considered in this analysis. Figure 3.3 shows the number of pileup interactions per bunch crossing for the first and second half of the data taking in 2011. Figure 3.3 shows that the distributions of number of vertices in $Z \to e^+e^-$ events from simulation are in good agreement with data after applying the pileup reweighting.

The best 2010 *in situ* ECAL calibration conditions were used in simulation in 2011. Figure 3.3 shows the energy smearing applied to the ECAL simulation at the crystal level, which corresponds to the *in situ* intercalibration precision the ECAL calibration group achieved in 2010.

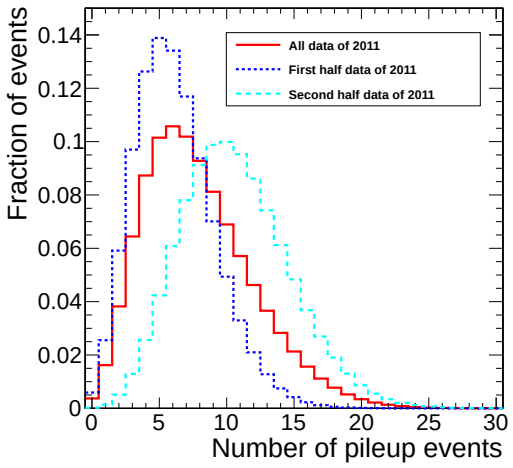

Figure 3.3: Number of pileup interactions per bunch crossing for different periods of data taking in 2011.

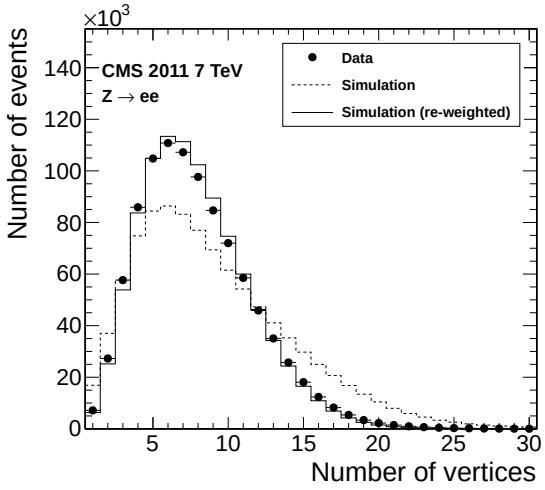

Figure 3.4: Comparison between the distributions of number of vertices in selected $Z \to e^+e^-$ events in data and simulation with or without pileup reweighting.

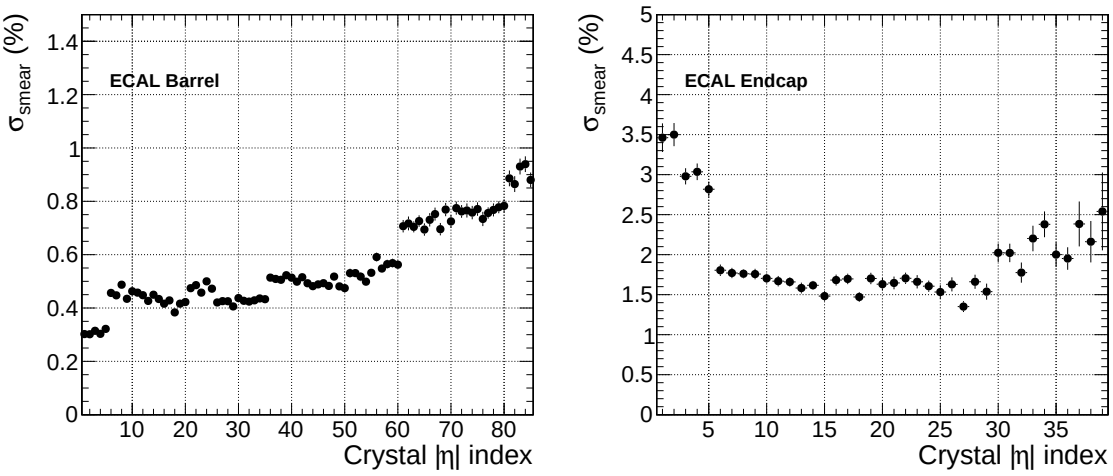

Figure 3.5: The amount of smearing applied in the 2011 ECAL simulation for crystals in the barrel ($|\eta|$ <1.5) and endcaps (1.5<$|\eta|$ <3).

Chapter 4

Energy Intercalibration of the ECAL Crystals

4.1 Introduction

As shown in equation (2.7), the ECAL energy resolution for unconverted photons at high energies is dominated by the constant term. The largest contribution to the constant term is the crystal-to-crystal response variation. In the barrel, this is dominated by the variation of the scintillation light yield of individual crystals, which has a RMS of about 15%. In the endcaps, this is dominated by the gain spread, quantum efficiency and photocathode area of the photodetectors, which has a RMS of about 25%. Corrections and calibrations of these variations are thus used to significantly improve the ECAL performance.

During the construction and commissioning phase of the CMS ECAL, different calibration procedures [60] have been performed to reduce these variations. All barrel crystals have been intercalibrated with cosmic ray muons to a precision of about 1 to 4%. Nine Sumpermodules (SMods) in the barrel have been intercalibrated with high energy electron beams to sub-percent precision. Another method, based on $\pi^0 \to \gamma\gamma$, was also studied. These π^0s were produced during a special run at the CERN H2 beam line with one SMod where a π^- beam was incident on an aluminum target. Due to the limited π^0 event sample, only a 9×8 crystal matrix around the beam axis was intercalibrated with this method. A precision of approximately 1% was

achieved, consistent with the expected statistical precision. Due to the limited time prior to installation at LHC Point 5, endcap crystals were only intercalibrated with laboratory measurements of the crystal light yield and photodetector response. The precision was 10 - 15%. Use of "beam slash" data, which was taken during the LHC runs in 2008, where the beam was dumped upstream of CMS, improved the precision to about 7%.

Different calibration methods have been proposed using the LHC data to further improve the intercalibration precision.

- $\phi-$symmetry method. This method uses the uniformity of the energy flows along the ϕ direction. It was expected to provide a fast intercalibration with a 1 - 2% precision within each ϕ ring in the barrel [72].

- $\pi^0(\eta) \rightarrow \gamma\gamma$ method. This method uses photon pairs from low mass resonance decays $\pi^0(\eta) \rightarrow \gamma\gamma$ [73–75]. It was expected that the majority of the barrel crystals can be intercalibrated to a precision of 0.5% with 5 - 10 pb^{-1} at the low luminosity scenario $L = 2 \cdot 10^{30}\,\mathrm{cm}^{-2}\,\mathrm{s}^{-1}$.

- E/p method. It uses energetic electrons from $\mathrm{W} \rightarrow \mathrm{e}\nu$ decays and was expected to provide a precision of 0.5% in the low pseudorapidity region of $|\eta| < 1.0$, after collecting about 5 fb^{-1} data [76].

- $Z \rightarrow ee$ method. This method uses electron pairs from $\mathrm{Z} \rightarrow \mathrm{e}^+\mathrm{e}^-$ decays and was expected to provide a ring-to-ring calibration with a precision of about 1% after collecting 2 fb^{-1} data [77].

The $\phi-$symmetry and $\pi^0(\eta) \rightarrow \gamma\gamma$ method have been used to derive a first *in situ* intercalibration with the data taken during 2010 [78]. In the barrel, 0.5% precision has been achieved in the pseudorapidity region $|\eta| < 1$ and better than 1% everywhere else, combining the *in situ* calibration with the precalibrations from test beam and cosmic ray measurements. In the endcaps, about 2% precision was achieved in most of the region up to $|\eta| < 2.5$, combining *in situ* with precalibration.

The intercalibation was repeated with the data taken during 2011 [79]. This was necessary for two reasons. First, the laser correction is normalized to the beginning of the data taking in 2011, and it was expected that this normalization would introduce an unwanted variation in the response among all channels. Second, the laser correction is not perfect and also introduces crystal-to-crystal response variations. Intercalibrations partially account for these two effects and improve the overall resolution. In 2011, the E/p method was also employed to derive another set of intercalibration constants, which was then combined with constants derived with the $\pi^0(\eta)$ and ϕ symmetry method. The estimated intercalibration precision from 2011 is about the same for $|\eta| < 1$ compared to 2010 and a little worse in other parts of the ECAL.

In the following sections, we first describe the ECAL laser monitoring and the correction for crystal transparency changes. Then we describe the $\pi^0(\eta) \to \gamma\gamma$ calibration, including the studies on the trigger, the studies in simulation as well as the calibration method. In particular, we use the first half of the 2010 data to study the systematic uncertainties of this calibration method. After that, we describe the intercalibration performed in 2011 and the performance on $Z \to e^+e^-$. Afterward, we show the performance with the combined intercalibration constants derived from the $\phi-$symmetry, $\pi^0(\eta) \to \gamma\gamma$, and E/p methods.

4.2 Laser Monitoring and Correction for the Transparency Change in ECAL Crystals

During LHC operations the CMS detector is exposed to a severe radiation environment. In this environment the $PbW0_4$ crystals suffer from radiation induced damage, which can be separated in two major contributions: electromagnetic damage induced mainly by electrons and photons [57] [58], and hadronic damage resulting from nuclear interactions in the crystals [80]. While hadronic damage, which causes crystal lattice deformations that reduce crystal transparency, does not recover at the ECAL oper-

ating temperatures, the contribution of this effect was negligibly small at the instantaneous luminosities at which the LHC was operating during 2011. Electromagnetic damage causes formation of color centers that produce absorption bands that reduce crystal transparency to the scintillation photons. The color centers in $PbWO_4$ are subject to thermal annealing at room temperature creating an equilibrium between center formation and dissociation, thus introducing a dose-rate dependent response in crystal transparency. The effect of electromagnetic damage, while recoverable, has to be monitored closely during the operation as it can significantly affect the transparency of the crystals at the operating luminosities during 2011, especially at the high η regions of ECAL.

The CMS ECAL utilizes a laser monitoring system [81] [82] to continuously monitor the crystal transparency change. To provide continuous monitoring, about 1% of the 3.17 μs beam gap in every 88.924 μs LHC beam cycle is used to inject the laser light. A full laser pulse injection sequence for the entire set of ECAL crystals, where each of 88 subsets of the crystals received laser light pulses in turn, takes about 30 minutes.

The correction for the transparency change is based on the relation between the crystal response to an electromagnetic shower and to the injected laser light, which can be parametrized by a power law, for the small changes in transparency [83]:

$$\frac{\mathrm{S}}{\mathrm{S}_0} = \left(\frac{\mathrm{R}}{\mathrm{R}_0}\right)^{\alpha}, \tag{4.1}$$

where S/S_0 is the normalized crystal response to electromagnetic shower and R/R_0 normalized response to the laser light. The initial values S_0 and R_0 correspond to measurements taken prior to the irradiation. There are two groups of crystals based on the manufacturing origin, and α values differ between them. Crystals were produced at two plants using different techniques. The majority of crystals were produced at the Bogoroditsk Techno-Chemical Plant in Tula, Russia, where the Czochralski method of crystal growing was used. The remaining crystals were supplied by Shanghai Institute of Ceramics, Shanghai, China, where the Bridgman-Stockbarger technique

was employed. We refer to the former as the Russian crystals and to the latter as the Chinese crystals. The α value on average for Russian crystals is 1.52, while α for Chinese crystals is 1.0 [84].

The imprecise knowledge of the α values for each crystal degrades the ECAL energy resolution, and is parameterized by

$$\frac{\Delta \mathrm{E}}{\mathrm{E}} = \ln(\frac{\mathrm{S}}{\mathrm{S}_0})\frac{\Delta\alpha}{\alpha}\,. \tag{4.2}$$

Thirty-five Russian crystals in the barrel have been exposed to electron irradiation from test beams. The measured α values have a spread of about 6%. During the data taking in 2011, the overall ECAL response to electrons have been reduced by about 3% in the barrel (see figure 2.16). Therefore, there is a contribution of about 0.2% to the energy resolution in the barrel due to the uncertanties in the α values. For crystals in the ECAL endcaps, the transparency loss is much larger, and the approximation given by equation (4.1) becomes less accurate.

4.3 Intercalibration With $\pi^0(\eta) \to \gamma\gamma$

4.3.1 The $\pi^0(\eta)$ Calibration Trigger

The CMS ECAL consists of 75,848 crystals. *In situ* intercalibration of this large number of crystals using low energy photons from $\pi^0(\eta)$ decays has never been previously performed at a hardon collider experiment. In the CMS experiment, there are a number of particular challenges. As described below, these challenges have been met by use of a special calibration trigger.

First, the typical energy of selected photons from $\pi^0(\eta)$ decays is 2 - 5 GeV. Therefore the intercalibration performed with this method must be validated *in situ* for objects with a much higher energy. For example, electrons from $\mathrm{Z} \to \mathrm{e}^+\mathrm{e}^-$ decays, which have comparable energy to photons from the decays of a Standard Model Higgs boson, can be used.

Next, the typical energy of photons from $\pi^0(\eta)$ decays is well below the threshold

used for the standard photon reconstruction in CMS, which is optimized for high p_{T} physics. Therefore, a special low energy photon reconstruction method is needed.

Finally, collecting a sufficiently large data sample to reach the systematic limit of the method is a major challenge. In the barrel, about 3000 $\pi^0 \to \gamma\gamma$ per crystal is necessary to reach the statistical precision about 0.5%. The CMS physics High Level Trigger (HLT) has a maximum output rate of about 300 Hz. Even with extremely naive assumptions, it would take about 70 days of continuous data taking to collect a sufficiently large data sample, taking into account the selection efficiency of approximately 10% for π^0 and about 1% for $\eta \to \gamma\gamma$.

Therefore, we have developed a special calibration stream to select π^0 and η candidates directly from Level-1 triggered events. In events passing a list of L1 triggers, only potentially interesting regions of the ECAL are used to select $\pi^0(\eta) \to \gamma\gamma$ candidates. Only information from crystals within a limited geometric area around the $\pi^0(\eta) \to \gamma\gamma$ candidate are saved. This significantly reduces the event size and allows the rate of this calibration stream to be as high as 15 kHz during physics runs, with an average of about 7 kHz during most runs in 2011.

The list of L1 triggers used for this calibration stream has been updated several times since the first data taking in 2010, in order to take into account the changes in the L1 configuration with increasing instantaneous luminosity at the LHC. Table 4.1 shows the list of L1 triggers used for this calibration stream in 2012 and the efficiency of the π^0 and η calibration trigger in the barrel and endcaps. In the L1 algorithm names, "EG", "Mu" and "Jet" refer to electromagnetic, muon and jet objects, respectively. The numbers following the object labels refer to the p_{T} thresholds. "MuOpen" refers to muon candidates without p_{T} threshold. "JetC" refers to jet candidates in the central region of $|\eta| < 2.8$, while "VBF" refers to forward region of $3.2 < |\eta| < 4.7$. "HTT" refers to the total hadronic transverse energies. "Single","Double", "Triple" or "Quad" means at least one, two, three or four candidates satisfying the requirements. The label "p5" in "DoubleMu3p5" means that the a prescale factor of 5 is applied to the algorithm "DoubleMu3", namely it only accepts 1 out of 5 events which passed the "DoubleMu3" trigger.

Due to the stringent processing time requirements at the HLT of CMS, a regional unpacking method is used to select $\pi^0 \to \gamma\gamma$ and $\eta \to \gamma\gamma$ decays in some potentially interesting regions of the ECAL. Each interesting region consists of a few Supermodules (SMod) around any L1 electromagnetic objects with E_{T} above 2 GeV. In a typical event, information from about one fourth of the ECAL crystals are used.

	π^0		η	
L1 Algorithm	Barrel	Endcap	Barrel	Endcap
L1_SingleEG5	20.8 ± 0.1	3.1 ± 0.0	6.6 ± 0.0	1.2 ± 0.0
L1_SingleEG7	20.6 ± 0.1	3.5 ± 0.0	7.9 ± 0.1	1.4 ± 0.0
L1_SingleEG12	20.9 ± 0.3	4.9 ± 0.1	10.7 ± 0.2	1.7 ± 0.1
L1_SingleEG20	17.1 ± 0.6	4.9 ± 0.3	8.0 ± 0.4	1.5 ± 0.2
L1_SingleEG22	16.3 ± 0.6	4.8 ± 0.4	7.3 ± 0.4	1.4 ± 0.2
L1_SingleEG24	16.3 ± 0.7	4.7 ± 0.4	6.2 ± 0.5	1.3 ± 0.2
L1_SingleEG30	15.9 ± 1.0	5.6 ± 0.6	5.9 ± 0.6	1.0 ± 0.3
L1_DoubleEG_13_7	28.6 ± 0.9	7.0 ± 0.5	13.3 ± 0.7	2.3 ± 0.3
L1_TripleEG7	32.0 ± 2.3	9.3 ± 1.4	13.6 ± 1.7	2.9 ± 0.8
L1_TripleEG_12_7_5	31.1 ± 1.8	8.2 ± 1.0	13.4 ± 1.3	2.4 ± 0.6
L1_DoubleEG5	35.1 ± 0.3	6.0 ± 0.1	12.7 ± 0.2	2.3 ± 0.1
L1_TripleJet_64_44_24_VBF	20.6 ± 1.3	6.7 ± 0.8	8.3 ± 0.9	2.4 ± 0.5
L1_TripleJet_64_48_28_VBF	20.7 ± 1.5	5.9 ± 0.9	7.8 ± 1.0	2.0 ± 0.5
L1_TripleJetC_52_28_28	26.7 ± 0.8	7.2 ± 0.5	10.0 ± 0.5	2.2 ± 0.3
L1_QuadJetC32	20.6 ± 1.8	6.1 ± 1.1	8.3 ± 1.2	2.6 ± 0.7
L1_QuadJetC36	17.5 ± 2.3	7.3 ± 1.6	6.9 ± 1.5	2.9 ± 1.0
L1_QuadJetC40	13.2 ± 2.7	5.3 ± 1.8	6.6 ± 2.0	3.9 ± 1.6
L1_DoubleEG6_HTT100	22.1 ± 1.9	8.1 ± 1.3	8.1 ± 1.3	1.3 ± 0.5
L1_DoubleEG6_HTT125	20.1 ± 2.6	6.6 ± 1.6	8.2 ± 1.8	1.6 ± 0.8
L1_EG8_DoubleJetC20	28.3 ± 0.3	5.7 ± 0.1	12.4 ± 0.2	2.1 ± 0.1
L1_Mu12_EG7	22.5 ± 1.7	5.0 ± 0.9	10.3 ± 1.3	2.1 ± 0.6
L1_MuOpen_EG12	22.4 ± 1.2	5.6 ± 0.7	11.1 ± 0.9	1.6 ± 0.4
L1_DoubleMu3p5_EG5	23.1 ± 2.2	4.3 ± 1.1	9.1 ± 1.5	0.5 ± 0.4
L1_DoubleMu5_EG5	19.3 ± 2.9	3.7 ± 1.4	8.6 ± 2.0	0.0 ± 0.0
L1_Mu12_EG7	22.5 ± 1.7	5.0 ± 0.9	10.3 ± 1.3	2.1 ± 0.6
L1_Mu5_DoubleEG5	35.5 ± 1.9	7.5 ± 1.0	11.9 ± 1.3	2.4 ± 0.6
L1_Mu5_DoubleEG6	35.8 ± 2.7	6.8 ± 1.4	13.2 ± 1.9	2.6 ± 0.9
L1_MuOpen_EG5	23.0 ± 0.3	3.9 ± 0.1	7.6 ± 0.2	1.3 ± 0.1

Table 4.1: Trigger efficiency (%) for selecting $\pi^0(\eta) \to \gamma\gamma$ candidates in the barrel and endcaps, for each L1 algorithm used in 2012 for the calibration stream.

As we discussed earlier, a special low energy photon reconstruction algorithm is needed. We developed a simple 3×3 window clustering algorithm. In this algorithm, the first step is to identify a list of seed crystals in the order of decreasing energies. The energy threshold for a seed crystal is 0.5 GeV in the barrel, and 1 GeV in the

endcaps. The second step is to make clusters sequentially, starting from the first seed crystal. The first cluster is made by clustering all crystals inside a 3×3 crystal matrix around the first seed. The second cluster is then seeded by the next available seed crystal which has not been used by the first cluster. This algorithm continues until all seed crystals have been used.

The clustering method is illustrated in Figure 4.1. By construction, there is no single crystal which can be assigned to more than one cluster, and some clusters contain less than nine crystals because their 3×3 matrices overlap with other such matrices containing seed crystals with higher energies. Besides the clustering algorithm, the selective readout schema implemented in the ECAL L1 readout system [85] also cause some clusters to contain less than nine crystals. The main purpose of the selective readout is to reduce the ECAL raw data size to a level acceptable by the CMS data acquisition system. It directs the ECAL readout electronics to apply predefined zero suppression levels to the crystal data, depending on whether the crystals fall within the ECAL regions with energy deposition satisfying certain programmable criteria.

The cluster energy is computed as the sum of the energy deposited in each crystal of the cluster

$$\mathrm{S_9} \equiv \sum_{3\times3} \mathrm{LC_i} \cdot \mathrm{c_i} \cdot \mathrm{G} \cdot \mathrm{ADC_i}\,, \tag{4.3}$$

where $\mathrm{c_i}$ denotes the crystal's intercalibration constant, $\mathrm{LC_i}$ denotes the laser correction to the crystal transparency change, ADC refers to the measured value in the Anology-to-Digitcal Converter, and G refers to the conversion factor from the ADC value to the energy in GeV.

The pseudorapidity and azimuthal angle of the photon candidate are obtained by calculating the weighted averages of the positions of the constituent crystals, where the weight is given by the logarithm of the crystal energy [86].

To suppress backgrounds, a number of simple selection cuts are used, based on quantities computed using per-crystal information from a localized region surrounding each $\pi^0(\eta)$ candidate. These selection cuts, described below, have been optimized in simulated Minimum Bias events. Only the barrel is considered below.

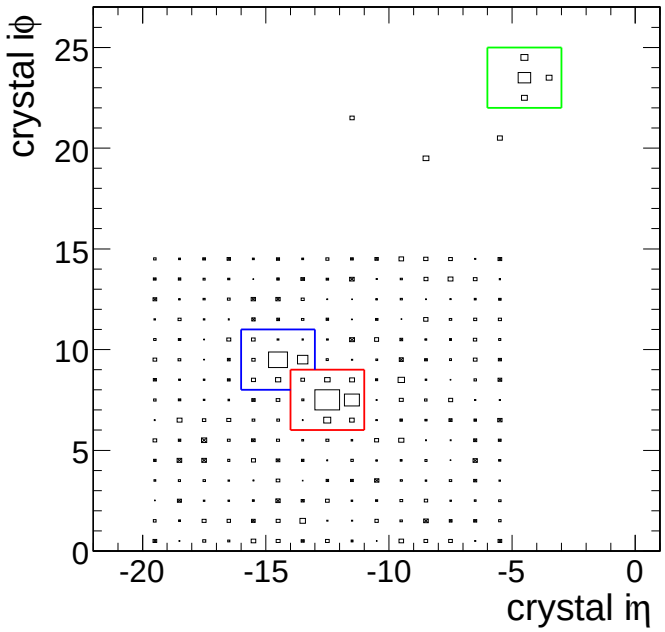

Figure 4.1: The 3×3 clustering method. The first cluster in the bottom box contains nine crystals, while the second one contains only eight crystals due to overlap with the first cluster. The third cluster in the top box contains only four crystals due to the selective readout. The size of the box is proportional to the energy deposited in that crystal.

First, to be considered in the combinatorial selection of $\gamma\gamma$ pairs, a photon candidate is required to have a p_{T} greater than a certain threshold. The $\pi^0(\eta)$ candidates are then selected by requiring the reconstructed p_{T} of the candidate to be above a certain threshold.

Second, the shape of cluster energy deposition should be consistent with that of an electromagnetic shower produced by photons. The ratio $\mathrm{S}_4/\mathrm{S}_9$ is required to be above a certain threshold. Here, the quantities S_9 correspond to the total energy deposited in the cluster. The quantity S_4 is the highest value of energies deposited in the four possible combinations of 2×2 crystal matrices containing the seed crystal inside the cluster. For selecting $\eta \to \gamma\gamma$, the ratio $\mathrm{S}_9/\mathrm{S}_{25}$ is also required to be above a certain threshold. Here the quantity S_{25} is the total energy deposited in the 5×5 crystal matrix centered on the seed crystal.

Thirdly, to further improve the expected calibration performance of the selected

sample, the following isolation cut is applied: the sum of p_{T} of all clusters (excluding the two forming the candidate) found within $\Delta R \equiv \sqrt{(\Delta\phi)^2 + (\Delta\eta)^2} < 0.2(0.3)$ and $\Delta\eta < 0.05(0.1)$ from the $\pi^0(\eta)$ candidate is required to be less than 50% of the p_{T} of the reconstructed $\pi^0(\eta)$ candidate. Only clusters with a p_{T} above 0.5 GeV are included in the sum. This isolation scheme is illustrated in Figure 4.2.

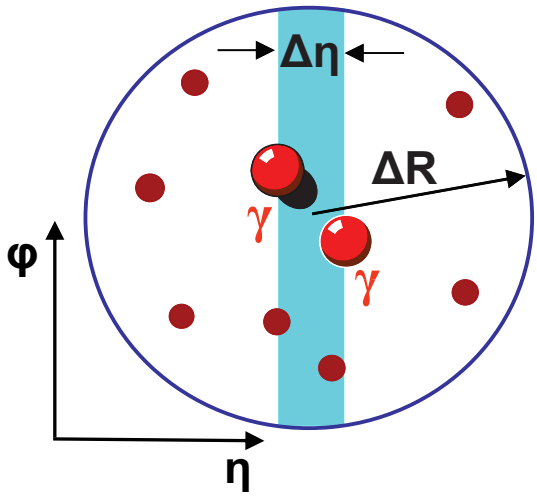

Figure 4.2: A schematic drawing of the isolation band around π^0 candidate.

The four selection variables in the barrel, mentioned above, for $\pi^0 \to \gamma\gamma$ are shown in Figure 4.3. In those figures, signal π^0 candidates are identified by matching the η and ϕ coordinates of the both reconstructed photons to those of the photons from "generator-level" π^0 decays, as obtained from the `PYTHIA` event record. Only the photon pairs whose invariant mass within the $\pm 2\sigma_{fit}$ of mass peak are used in those figures. Similarly, the selection variables are shown in Figure 4.4 for $\eta \to \gamma\gamma$.

Variable	Cut (2010)		Cut (Since 2011)	
	barrel	endcaps	barrel	endcaps
p_{T}	0.8	η dependent, see text	1.3	see text
$p_{\mathrm{T}}^{\gamma\gamma}$	1.6	see text	2.6	see text
$\mathrm{E_4/E_9}$	0.83	0.90	0.83	0.90
Isolation	0.50	0.50	0.50	0.50

Table 4.2: Online selection cuts for $\pi^0 \to \gamma\gamma$.

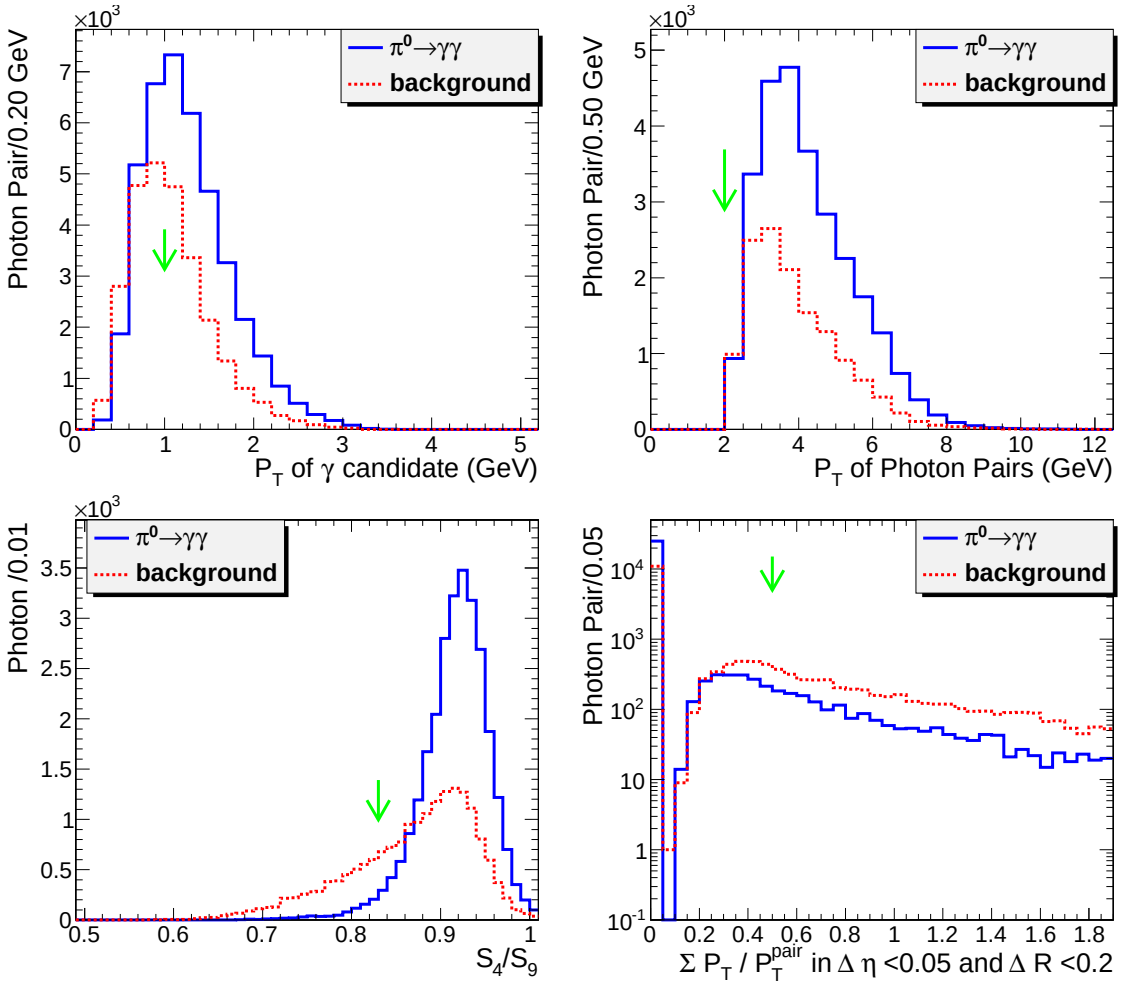

Figure 4.3: "N-1" distributions for the cuts used in the online selection of $\pi^0 \to \gamma\gamma$ decays. Each distribution is obtained after all other cuts have been applied. The solid curve indicates the signal and the dashed line indicates the background. The arrow indicates the cut value.

Tables 4.2 and 4.3 list the online selection cuts used for π^0 and η, respectively. The actual cuts used online for π^0 are slightly different from what we have initially developed from studies in the simulation, and the cuts have been tightened since 2011 because of the increased instantaneous luminosity at the LHC. In the endcaps, the p_{T} and $p_{\mathrm{T}}^{\gamma\gamma}$ cuts have been optimized in different $\eta^{\gamma\gamma}$ regions. For selecting $\pi^0 \to \gamma\gamma$, in the case of $|\eta^{\gamma\gamma}| < 2.5$, p_{T} is required to be above 0.6 GeV, $p_{\mathrm{T}}^{\gamma\gamma}$ is required to be above 2.5 GeV, otherwise, p_{T} is required to be above 0.5 GeV, $p_{\mathrm{T}}^{\gamma\gamma}$ is required to be above 1.0 GeV and below 2.5 GeV. The upper cut on $p_{\mathrm{T}}^{\gamma\gamma}$ is useful to reject backgrounds and

very high energy π^0s which usually decay into two photons with very small opening angle. For selecting $\eta \to \gamma\gamma$, in the case of $|\eta^{\gamma\gamma}| < 2.5$, p_{T} and $p_{\mathrm{T}}^{\gamma\gamma}$ is required to be above 1.0 and 3.0 GeV, respectively. In other cases, the p_{T} cut value is relaxed to 0.7 GeV, while the $p_{\mathrm{T}}^{\gamma\gamma}$ cut value stays the same.

Variable	Cut	
	barrel	endcaps
p_{T}^{γ}	1.2	η dependent, see text
$p_{\mathrm{T}}^{\gamma\gamma}$	4.0	η dependent, see text
$\mathrm{E_4/E_9}$	0.87	0.90
$\mathrm{E_9/E_{25}}$	0.80	0.85
Isolation	0.50	0.50

Table 4.3: Online selection cuts for $\eta \to \gamma\gamma$.

4.3.2 Intercalibration Method

Intercalibration using photon pairs from $\pi^0(\eta)$ decays utilizes the correlation of the reconstructed invariant mass peak positions and the intercalibration constants on individual crystals. The invariant mass of the $\pi^0(\eta)$ candidate is reconstructed as

$$\mathrm{M_{inv}} = \sqrt{2\mathrm{E_1E_2}(1-\cos\theta_{12})}\,, \tag{4.4}$$

where $\mathrm{E_1}$ and $\mathrm{E_2}$ are the energies of the two photons and θ_{12} is the opening angle between them. Therefore, by uniformizing the peak positions reconstructed on each individual crystal, we obtain the intercalibration constant for each crystal. We use two iterative algorithms to derive the intercalibration constants.

4.3.2.1 L3 Method

This method was developed for the intercalibration of the crystal electromagnetic calorimeter of the L3 experiment [87]. We use the same principle with minor changes.

In this method, before deriving the intercalibration constants, some initial value for each crystal needs to be set. In simulation, this value can be set to be one,

referring to a perfect intercalibration, or some Gaussian distributed value, referring to misintercalibration. In data, the initial value is the precalibration constant measured from test beam or cosmic rays, or *in situ* intercalibration measured with previous data. However, the obtained intercalibration precision is found to be independent of the initial value, as shown in figure 4.7b from the study in simulation. The definition of the precision is given in section 4.4.

The calibration constants are then obtained from an iterative method,

$$\mathrm{c_N(i\eta, i\phi) = c_{N-1}(i\eta, i\phi) \times \frac{1}{\sum_{i=1}^{n_{phot}} w_i^2} \sum_{i=1}^{n_{phot}} \left(\frac{M_0}{M_{inv}}\right)^2 w_i^2 \,, } \tag{4.5}$$

where

- N is the number of the iteration step.
- $\mathrm{c(i\eta, i\phi)}$ is the calibration constant of a crystal with integer coordinates $\mathrm{i}\eta$ and $\mathrm{i}\phi$ in the global ECAL crystal matrix.
- $\mathrm{n_{phot}}$ is the number of selected photon candidates containing this crystal in the 3×3 crystal matrix.
- $\mathrm{w_i}$ is the weight assigned to the ith photon candidate, calculated as the ratio of the energy deposited in this crystal to the total energy deposited in the 3×3 crystal matrix; these energy quantities are computed with calibration constants from the previous iteration step, $\{c_{N-1}\}$.
- $\mathrm{M_{inv}}$ is the reconstructed invariant mass of the corresponding $\gamma\gamma$ pair, also computed with $\{c_{N-1}\}$.
- $\mathrm{M_0}$ is the $\pi^0(\eta)$ mass peak reconstructed from all crystals, representing the mean value.
- In the L3 paper [87], there is no power of two in the formula. We find there is no effect inn the final calibration precision, but the convergence speed is improved if the power of two is used.

In the L3 algorithm, only photon pairs with a reconstructed invariant mass in the range of $[\mathrm{M_{fit}} - 2\sigma_{\mathrm{fit}}, \mathrm{M_{fit}} + 2\sigma_{\mathrm{fit}}]$ are used. After each step, the energy and direction of flight of each photon are recalculated using the updated calibration constants. The iterations are repeated until the calibration constants converge.

4.3.2.2 Fit Method

This algorithm makes use of the whole invariant mass distributions collected for individual crystals, rather than the event-by-event photon information as used in the L3 method.

For a given crystal, a corresponding histogram is filled with the invariant masses of all $\pi^0 \to \gamma\gamma$ candidates for which one of the photons is centered on this crystal. The obtained distributions are then fitted with the sum of a polynomial for background and a Gaussian for the signal peak. The intercalibration constants are then calculated iteratively,

$$\mathrm{c_N}(\mathrm{i}\eta, \mathrm{i}\phi) = \mathrm{c_{N-1}}(\mathrm{i}\eta, \mathrm{i}\phi) \times \left(\frac{\mathrm{M_0}}{\mathrm{M_{fit}}}\right)^2, \tag{4.6}$$

where $\mathrm{M_{fit}}$ is the fitted peak position and all other variables are the same as in equation (4.5). The fitted $\pi^0(\eta)$ mass peak for a given crystal is largely unaffected by the errors on the calibration constants of other crystals since they are averaged over and only contribute to the width of the peak. Thus, the new calibration constants will shift the individual peaks closer to the nominal value. As in the L3 method, after each calibration step, the energy and the direction of flight of each photon are recalculated using the updated calibration constants. The method is then iterated until the calibration constants converge.

The two calibration methods are found to give the same precision, as shown in Figure 4.7c. The fit method provides faster convergence, but yields less robust results in the case of very low statistics where a certain number of fits fail. As a result, the L3 method is more often used for the crystal-to-crystal intercalibration.

4.3.3 Correction For Intercalibration

In deriving the intercalibration constants, a few steps are needed to ensure that the obtained constants are not compensating effects which are beyond the scope of the intercalibration. The photon energy measurement defined in equation (4.3) is affected by a number of factors:

- There is some energy loss in module or submodule gaps or supermodule cracks. Therefore, the energy reconstructed in crystals next to the gaps or cracks tend to give systematically smaller values than others.
- There exists some dependence of the shower containment on energy and pseudorapidity. Therefore, energies reconstructed at different pseudorapidities are systematically different with respect to the nominal energies.
- Energy in dead or masked crystals are not measured. There are about 1.0% such crystals in the barrel and 1.7% in the endcaps.

Without taking into account these effects, the obtained intercalibration constants cause degraded performance for photons at higher energies. Higher energy photons, reconstructed with a different clustering algorithm, have different shower containment dependence on energy and pseudorapidity, and different biases of the energy measurement due to gaps or cracks or dead crystals. The correction for this dependence, or bias, is derived as part of the energy correction procedure which we will discuss in section 5.5. Therefore, the intercalibration constants derived from low energy photons from $\pi^0(\eta)$ decays that attempt to account for these biases, using only low energy data, do not correctly compensate for these biases at higher energies.

In the following subsections, we describe the supermodule scale corrections, which can be thought of as a SMod-to-SMod intercalibration, and other corrections to avoid the above biases. These corrections are then applied to data before deriving the crystal-to-crystal intercalibration constants.

The following corrections are for the barrel only. For the endcaps, the SMod correction and the iϕ correction are not necessary. However, very similar iη and dead

crystal corrections are needed.

4.3.3.1 Supermodule Scale Correction

The studies of the Supermodule scale in the barrel has been performed with the first 250 nb^{-1} of data, both with the ϕ-symmetry and π^0 calibration methods [88]. In the π^0 method, the correction is derived from the invariant mass peaks reconstructed in individual SMods,

$$\text{Corr}_\text{j} = \frac{\bar{\text{M}}}{\text{M}_\text{j}}\,, \tag{4.7}$$

where j refers to the SMod number, M_j is the peak in an individual SMod, and $\bar{\text{M}}$ is the average.

The derived SMod scale corrections have been propagated via the *in situ* inter-calibration into later versions of the offline reconstruction, but these corrections were not used in the HLT reconstruction which affects the calibration data, up until the run period of 2010B (from September 22 to October 31 2010).

Figure 4.5 shows the reconstructed $\pi^0 \to \gamma\gamma$ peak positions obtained in each SMod in the calibration data from run periods of 2010A (from June 24 to August 30, 2010) before and after applying the SMod scale correction.

4.3.3.2 The iη and iϕ Correction

Due to the first two effects listed at the beginning of section 4.3.3, the reconstructed $\pi^0(\eta)$ invariant mass peak shows a dependence on the index of the seed crystal, both in the η and ϕ directions. We use iη and iϕ to refer to the crystal index. At each iη value, there are 360 crystals in the ϕdirection. At each iϕ number, there are 2×85 crystals, along the positive and negative η directions, centered on $\eta = 0$.

Firstly, we derive a correction as a function of the iη number, based on the invariant mass peaks reconstructed at each iη. The correction is derived iteratively,

$$\text{Corr}^\text{N}_{\text{i}\eta} = \frac{\bar{\text{M}}}{\text{M}^\text{N}_{\text{i}\eta}}\,, \tag{4.8}$$

where N is the iteration step, $M_{i\eta}^{N}$ is the peak at each iη, and $\bar{M}$ is the average. After each step, the obtained correction factors are applied to each crystal. The iterations stop when the correction factors have converged.

After the correction, the obtained invariant mass peaks should be flat as a function of the iη number, as shown in Figure 4.6 left.

Secondly, we derive a correction as a function of the iϕ number, $\mathrm{Corr}_{i\phi}$. The method is quite similar. In the end, the obtained mass peaks should have no dependence on the iϕ number, as shown in Figure 4.6 right.

The iη and iϕ corrections have a large impact on the intercalibration precision, as shown in Figure 4.7a. The precision improves by more than a factor of two with these corrections.

4.3.3.3 Dead Crystal Correction

The energy measurement is biased if the 3×3 cluster contains one or more dead crystals where the deposited energies are not measurable. The intercalibration constants as determined above compensate for the bias, but incorrectly, which is an undesirable feature.

To correctly remove the bias in the intercalibration constants, we correct the photon energy based on the number of dead crystals next to the seed crystal. We separate the dead crystals into two classes, according to their contributions to the total energies in the 3×3 cluster. On average, the unmeasurable energy is larger if the dead crystal is in the side of the 3×3 matrix, thus sharing an edge with the seed crystal in the matrix, instead of in the corner. Figure 4.8 shows possible locations of the dead crystals in the cluster, when the number of dead crystals is up to 4. According to this, we can classify each crystal based on the number of each type of dead crystals surrounding this crystal in a 3×3 crystal matrix. For example, if there is no dead crystals next to one crystal, then this crystal is in the first category. If there is one dead crystal in the corner of the 3×3 crystal matrix centered on this crystal (as in the first plot in Figure 4.8), then this crystal is in the second category.

Table 4.4 shows the resulting dead-crystal categories in the barrel, and the recon-

structed $\pi^0 \to \gamma\gamma$ peak positions in each crystal class normalized to the peak of the first class, as well as the total number of crystals in each category. The result is from the calibration data of run period 2010A.

Dead-crystal category	Next to dead crystals?	m_0/m_{fit}	Total count
0	No	1	59417
1	1 corner	1.005	531
2	1 side	1.017	466
3	2 corner	0.987	6
4	2 side	1.019	4
5	1 corner + 1 side	1.034	159
6	3 corner	–	0
7	3 side	1.074	1
8	1 corner + 2 side	–	0
9	2 corner + 1 side	1.040	242
10	4 corner	–	0
11	4 side	–	0
12	2 corner + 2 side	1.063	4
13	1 corner + 3 side	–	0
14	3 corner + 1 side	1.051	2
15	is dead itself	–	638

Table 4.4: Dead-crystal categories in the barrel, the reconstructed $\pi^0 \to \gamma\gamma$ peak in each crystal class normalized to the peak in the first class, and the total number of crystals in each category.

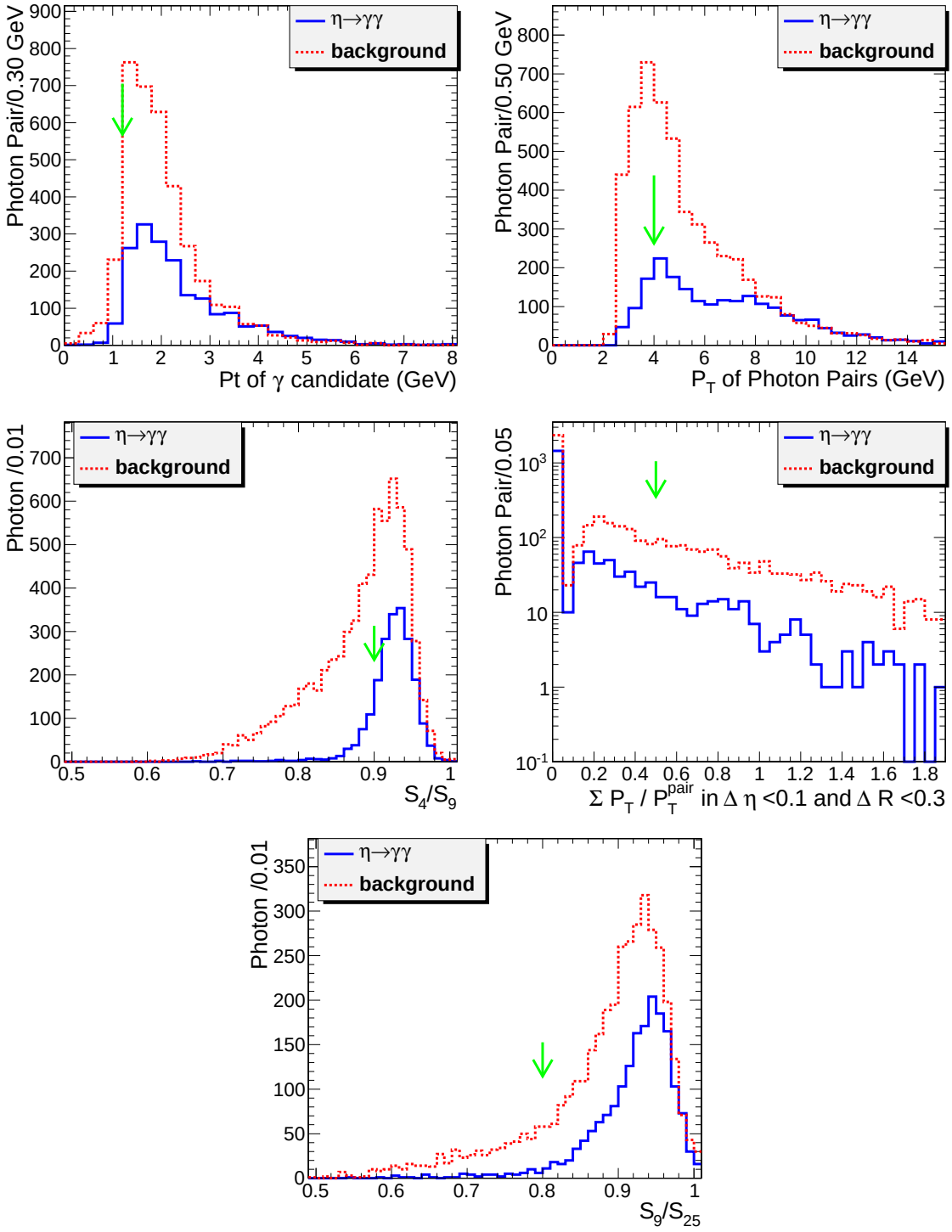

Figure 4.4: "N-1" distributions for the cuts used in the selection of $\eta \to \gamma\gamma$ decays. Each distribution is obtained after all other cuts have been applied. The solid curve indicates the signal and the red line indicates the background. The arrow indicates the cut value.

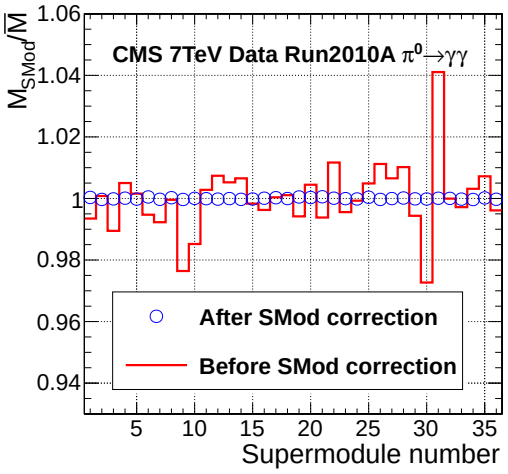

Figure 4.5: Reconstructed $\pi^0 \to \gamma\gamma$ peak positions obtained within each SMod in the ECAL barrel before and after applying the SMod scale correction.

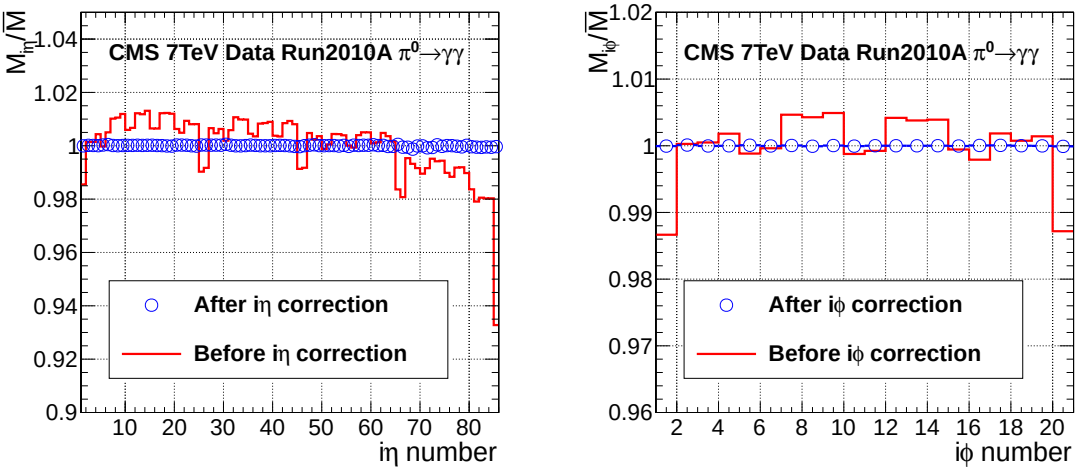

Figure 4.6: The $\pi^0 \to \gamma\gamma$ invariant mass peak as a function of the iη number (left) and iϕ number (right), before and after applying the corresponding corrections.

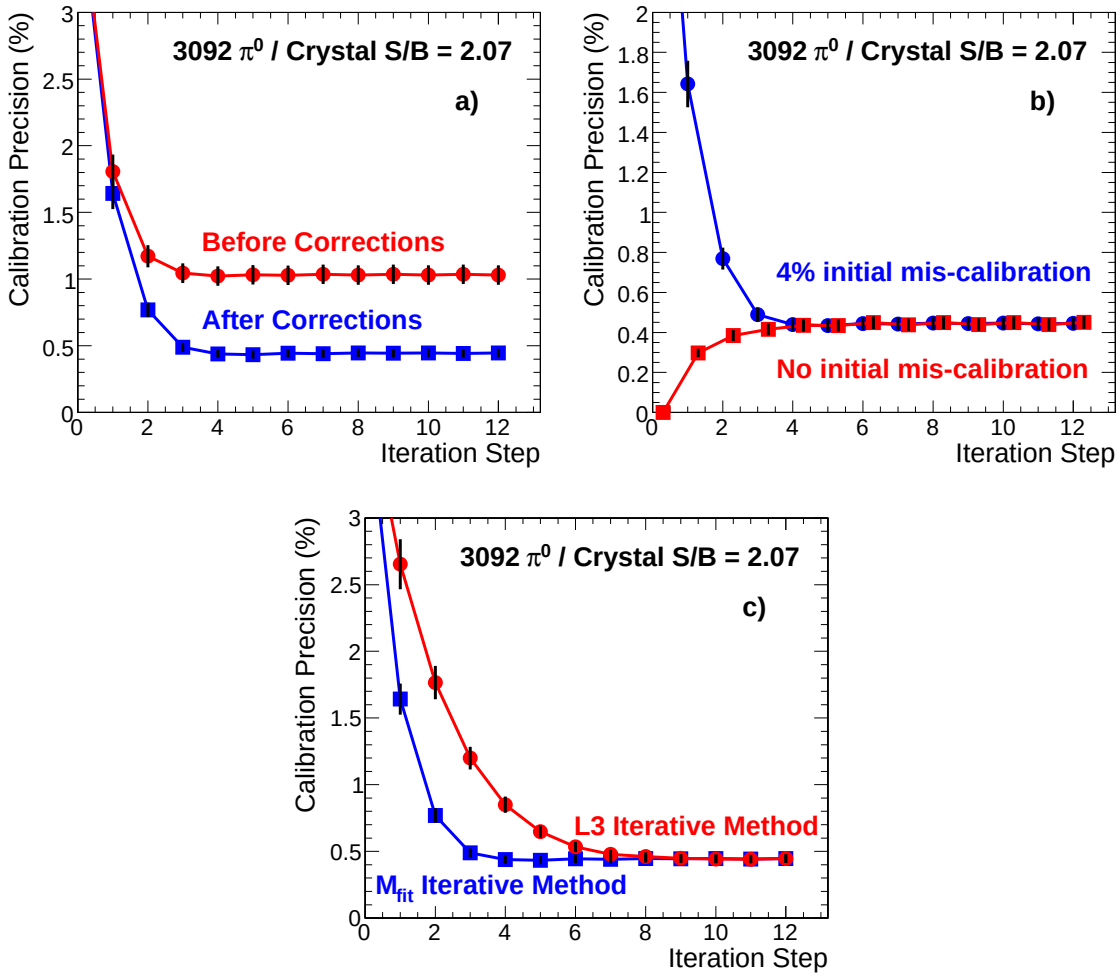

Figure 4.7: Calibration precision as a function of the iteration step. a) Improvement in the calibration precision after applying corrections for the gaps between the ECAL supermodules/baskets and shower containment variations. b) Comparison of the calibration precisions obtained with a 4% initial miscalibration and without any initial miscalibration, showing that an initial miscalibration has no effect on the final results. c) Comparison between the L3 and $M_{\rm fit}$ methods, showing the obtained calibration precision agrees. Results are from simulation studies.

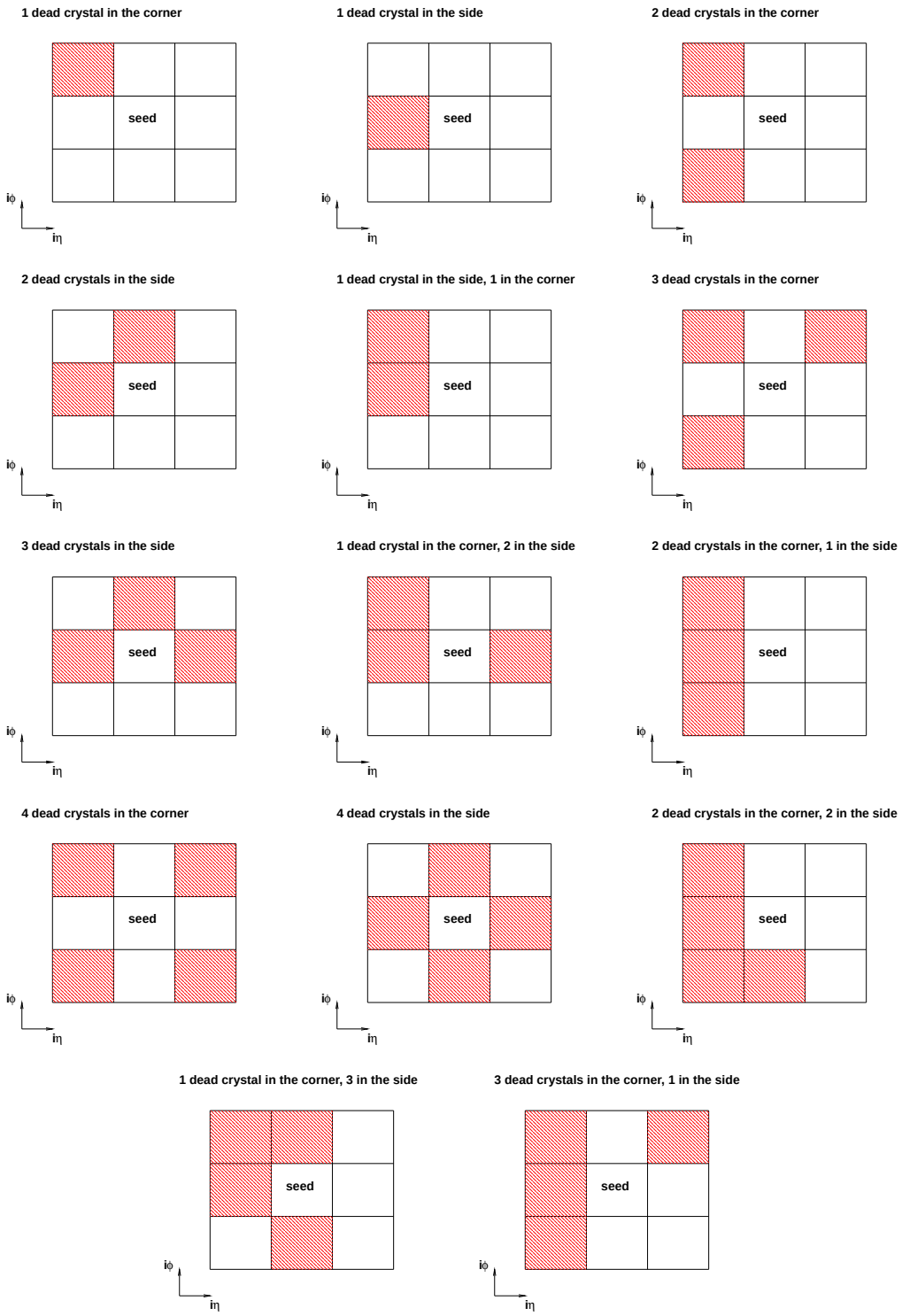

Figure 4.8: Illustration of the 3×3 clusters containing different number of dead crystals. On each plot, the box in the center refers to the seed crystal. The boxes with shaded red color refer to the dead or masked crystals which provide no measurement of the energies.

4.4 Intercalibration Studies in Simulation

To study the performance of the π^0 intercalibration method, we use simulated events. In particular we studied the dependence of the intercalibration precision on the number of signal π^0s and the signal-over-background yield ratio. Due to the limited available samples from simulation, to achieve the necessary level of statistical precision, we fold the entire barrel onto a 10×10 ($\eta \times \phi$) crystal matrix. This is done by assuming that the intercalibration constants are periodic:

$$C_N(n_\eta, n_\phi) = C_N(n_\eta + 10\,m, n_\phi + 10\,n)\,, \tag{4.9}$$

where m and n are integers.

For a perfectly calibrated crystal, the product of the obtained intercalibration constant and initial miscalibration constant should be equal to one. The intercalibration precision is then estimated as the RMS width of the distribution of such products that remain after the folding onto a 10×10 crystal matrix.

In order to investigate the dependence of the calibration precision on the number of collected $\pi^0 \to \gamma\gamma$ decays, we split the calibration sample into several subsamples of varying sizes. As shown in Figure 4.9 left, this dependence can be described by the following function:

$$\frac{\sigma_C}{C} = \frac{a}{\sqrt{n_{\pi^0}}} \oplus b\,, \tag{4.10}$$

where a and b are parameters and n_{π^0} denotes the average number of $\pi^0 \to \gamma\gamma$ decays per crystal. The fits are performed for two cases "signal-only" and Signal-over-Background yield ratio (S/B) = 2.1, calculated inside the $\pm 2\sigma$ around the peak,

These fits produce the following results:

$$\begin{aligned} \frac{\sigma_C}{C}(\text{signal only}) &= \frac{(17.6 \pm 0.7)\%}{\sqrt{n_{\pi^0}}} \oplus (0.2 \pm 0.1)\%\,, \\ \frac{\sigma_C}{C}(\text{S/B} = 2.07) &= \frac{(23.4 \pm 0.5)\%}{\sqrt{n_{\pi^0}}} \oplus (0.0 \pm 0.1)\%\,. \end{aligned} \tag{4.11}$$

In the case of no backgrounds, the best possible value of the "stochastic" constant

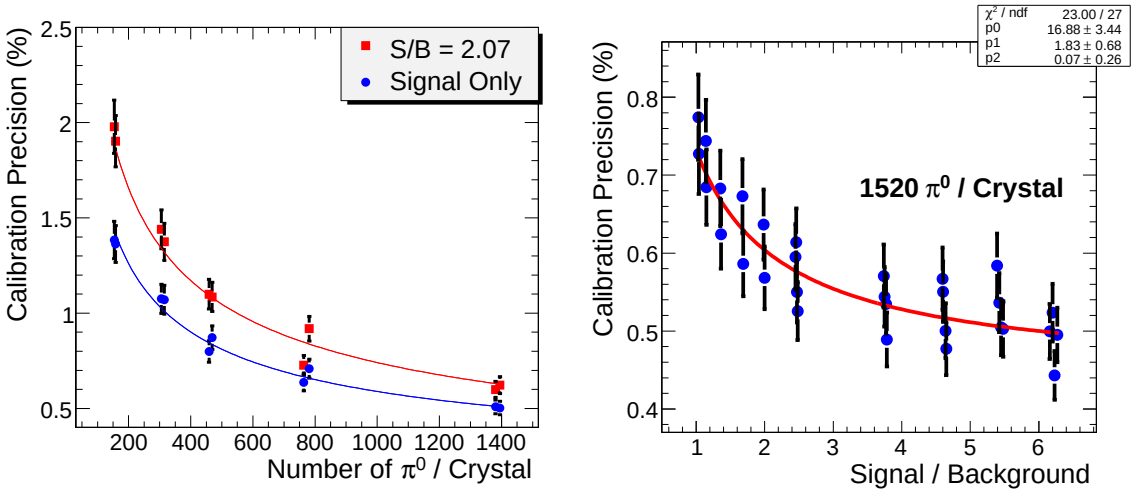

Figure 4.9: Left, the obtained calibration precision as a function of the number $\pi^0 \to \gamma\gamma$ decays per crystal. Right, the calibration precision as a function of S/B value, superimposed on the function $\frac{p_0 \times \sqrt{1+p_1/(S/B)}}{\sqrt{n_{\pi^0}}} \oplus p_2$. In this figure there are different data points with about the same S/B value due to the different ways in which the whole selected sample has been split.

a in equation (4.10) can be expressed as

$$\mathrm{a_{ideal}} = \frac{\sqrt{2}\,\sigma_{\mathrm{M}}/\mathrm{M}_{\pi^0}}{\sqrt{<\sum \mathrm{w_k^2}>}}\,, \tag{4.12}$$

where $\sigma_{\mathrm{M}}/\mathrm{M}_{\pi^0}$ is the π^0 peak resolution, $\mathrm{w_k}$ is the fraction of the cluster energy deposited in the kth crystal of the cluster, and the summation is performed over all the constituent crystals. In this calibration sample $\sigma_{\mathrm{M}}/\mathrm{M}_{\pi^0} \simeq 7.4\%$ and $\sqrt{<\sum \mathrm{w_k^2}>} \simeq 71\%$, giving $a_{\mathrm{ideal}} \simeq 15\%$. The observed value $a = 17.6 \pm 0.7\%$ is consistent with this theoretical limit.

It is worth noting that the intercalibration precision, σ_C/C, is expected to affect the ECAL energy resolution as

$$\delta(\sigma_E/E) = \frac{\sigma_C}{C} \times \sqrt{<\sum w_k^2>}\,, \tag{4.13}$$

where $\delta(\sigma_E/E)$ denotes the contribution in quadrature to the constant term in equation (2.7) and $\sqrt{<\sum w_k^2>}$ is the same as in equation (4.12). This is due to the fact

that not all of the shower energy is contained in the central crystal.

In summary, the results from simulation show that the there is no limit in the intercalibration precision. The precision approaches very near to zero in the infinite statistics limit. However, one should always be cautious to use results obtained from simulation to project the result to data. In simulation, we have a very controlled calibration region, namely the 10×10 crystal matrix. In data, we cannot do this: each crystal is unique and has its own unique intercalibration constant. Besides, we know that the simulation cannot represent the real CMS experiments. For example, in the simulation used for the intercalibration study, we assumed that the tracker material was uniformly distributed along ϕ. However, this is not true in reality.

Therefore, to more realistically understand the systematical limit of this calibration method, we need to use real data. In section 4.6 we will describe this study.

4.5 First π^0 and η Results From Minimum Bias Data

The first LHC data was important to understand the π^0 and η reconstruction and to validate the calibration trigger.

The first collisions in 2010 at 7 TeV were collected with very low instantaneous luminosity, at the order of 10^{27} cm^{-2} s^{-1}. Therefore, the data is dominated by minimum bias events. This kind of data is actually an ideal sample to reconstruct $\pi^0(\eta) \to \gamma\gamma$ candidates, because of relatively low backgrounds. In this study, we used a sample of 2.4×10^8 minimum bias events accepted by the minimum bias trigger. Without the stringent timing and bandwidth constraints which exist on the CMS online filter farm, less stringent cuts on transverse energies of the photon candidates can be applied. In the $\pi^0 \to \gamma\gamma$ selection, we require $E_T^{\gamma} > 0.3$ GeV and $E_T^{\gamma\gamma} > 0.9$ GeV, while the other cuts are the same as in section 4.3.1.

Figure 4.10 left and right show the invariant mass distributions of the selected π^0 candidates in the barrel after all selection cuts from data and from simulated

minimum bias events, respectively. The π^0 peak width is found to be 10.0% in data, in good agreement with the simulation. The S/B is about 0.8. Here and throughout this section, PYTHIA8 is used in the simulation.

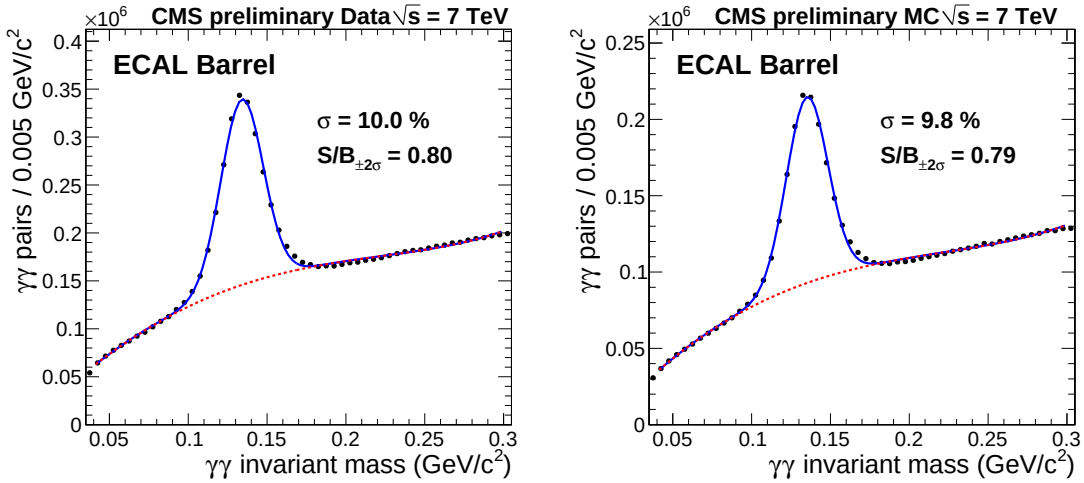

Figure 4.10: The $\pi^0 \to \gamma\gamma$ invariant mass distributions selected in a minimum bias data sample (left) and in simulation (right).

Figure 4.11 shows the average number of $\pi^0 \to \gamma\gamma$ decays and S/B as a function of the crystal η index. The selected number of candidates decreases quickly with increasing $|\eta|$, mainly due to the selection cuts. In particular, the shower shape cut which is used to reduce converted photons. At higher $|\eta|$, the conversion probability increases due to the increased material budget, which we have discussed in section 2.2.2. The combinatorial backgrounds, on the other hand, are less sensitive to the selections. Therefore, the S/B also decreases with increasing $|\eta|$.

Figure 4.12 shows the invariant mass distributions of the selected $\eta \to \gamma\gamma$ candidates from the same minimum bias sample. Here, looser cuts are also used than what was described in section 4.3.1. We require E_T^{γ} >0.5 GeV and $E_T^{\gamma\gamma} > 2.5$ GeV. The η peak width is found to be 6.0% in data, in agreement with the simulation. However, the S/B value is significantly larger in data than in simulation, indicating that the η production cross section in the PYTHIA simulation is too low.

The minimum bias trigger at higher instantaneous luminosities is highly prescaled in order to allocate more rate to high p_T physics triggers, and it thus becomes less

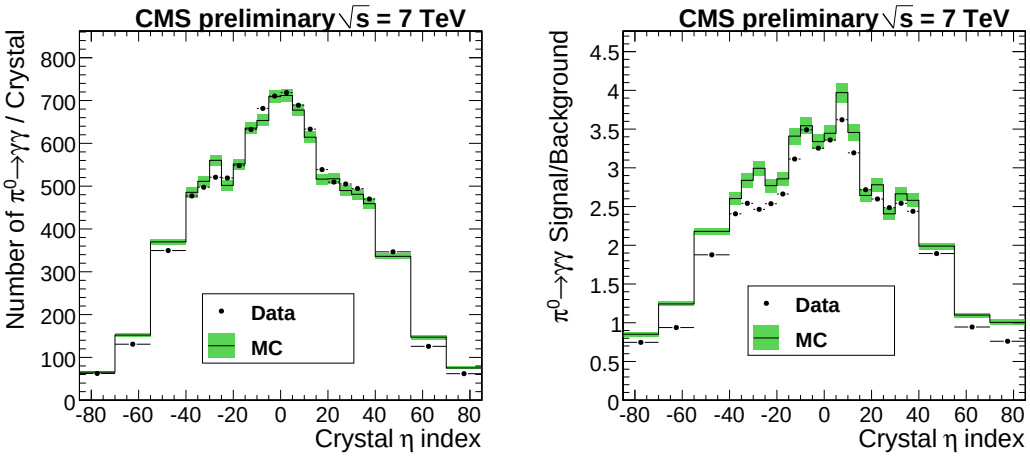

Figure 4.11: Average number of $\pi^0 \to \gamma\gamma$ decays selected by the online stream and S/B as functions of the crystal η index. The η indexes of the two seed crystals from both photons forming each selected $\pi^0 \to \gamma\gamma$ candidate are used. To avoid double counting, each entry is therefore assigned a weight of 0.5. On the left, the total Monte Carlo rate is normalized to that obtained in data. The shaded bands correspond to the statistical uncertainty due to the limited size of the MC sample.

useful for selecting $\pi^0 \to \gamma\gamma$ and $\eta \to \gamma\gamma$ decays. On the other hand, the calibration trigger starts to play a more important role at higher instantaneous luminosities ($L > 5 \times 10^{28}$ cm^{-2} s^{-1}). As shown in Figure 4.13, the measured signal rate from the calibration stream increases rapidly with the instantaneous luminosity, while the equivalent rate from the minimum bias trigger sample decreases drastically due to prescales.

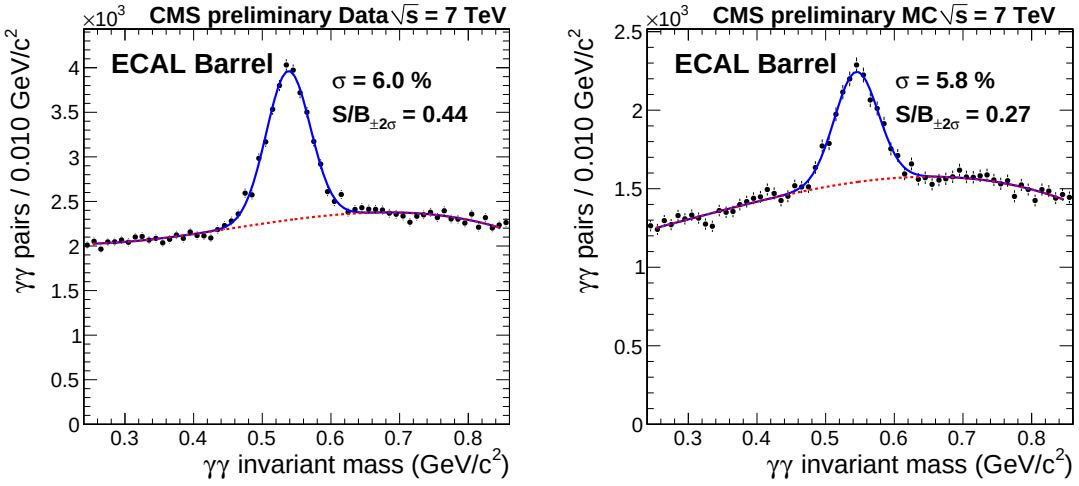

Figure 4.12: The $\eta \to \gamma\gamma$ invariant mass distributions selected in a minimum bias data sample (left) and in simulation (right).

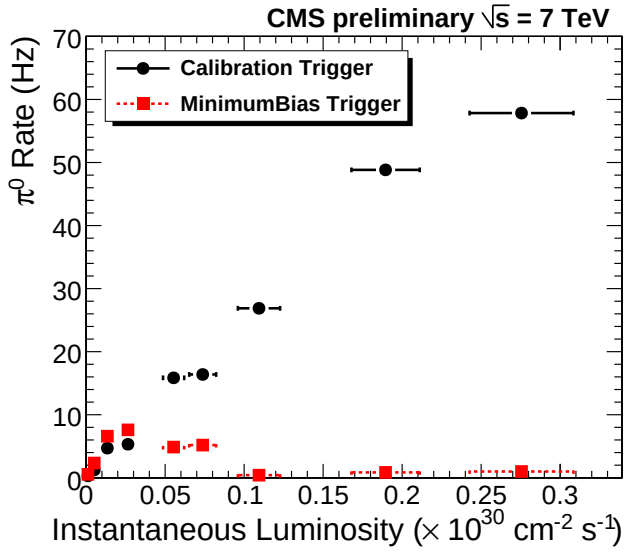

Figure 4.13: Measured signal rate as a function of the instantaneous luminosity shown both for the online calibration stream and for the events accepted by the minimum bias trigger and selected by applying the same selection cuts as those in the online calibration stream. For the minimum bias trigger sample, the π^0 rate decreases at higher instantaneous luminosities ($L > 5 \times 10^{28}$ cm^{-2} s^{-1}) due to the incremental prescaling of the minimum bias triggers.

4.6 The π^0 and η Intercalibration Precision

To study the intercalibration systematic uncertainty of this method, we use the first half of the calibration data taken in 2010 (Run2010A). During this period, the instantaneous luminosity was relatively low and the transparency change in ECAL crystals is found to be negligible. Figure 4.14 shows the collected number of $\pi^0 \to \gamma\gamma$ and $\eta \to \gamma\gamma$ decays per crystal and S/B during the period of Run2010A and Run2010B, respectively. Both $\pi^0 \to \gamma\gamma$ and $\eta \to \gamma\gamma$ have an S/B that is smaller in the second period, due to the increasing prescales of the L1 triggers with low p_{T} thresholds. The number of selected $\pi^0 \to \gamma\gamma$ decays is about the same in the two periods. The number of selected $\eta \to \gamma\gamma$ decays, however, decreases by about 20%. This is due to the difference in the fraction of $\pi^0 \to \gamma\gamma$ and $\eta \to \gamma\gamma$ decays selected in these prescaled triggers.

As discussed in section 4.1, nine ECAL barrel SMods were intercalibrated with high precision with an electron beam. As a result of the analysis outlined below, three of them (Smods 1, 11, 24) achieved a precalibration precision of 0.4%, which is sufficient to be used as a reference in estimating the $\pi^0(\eta)$ intercalibration precision *in situ* at the LHC. Other SMods at the test beam had worse precision, and the rest of the SMods that were tested with cosmic rays only had a precalibration precision of 1 - 4%, so that these SMods had insufficient precision to test the $\pi^0(\eta)$ intercalibration.

Since all ECAL crystals had already been intercalibrated with the precalibration constants, the π^0 calibration constant was then applied as a multiplicative correction to the precalibration constant for each crystal:

$$\mathrm{c_i} = \mathrm{c_{precalib,i}} \cdot \mathrm{c_{\pi^0,i}}\,, \tag{4.14}$$

where i refers to crystal numbering.

The precalibration precision is estimated by comparing two sets of intercalibration constants derived from (1) the π^0 intercalibration data set and (2) beam-splash events obtained during the beam commissioning runs in late 2009. Since the two

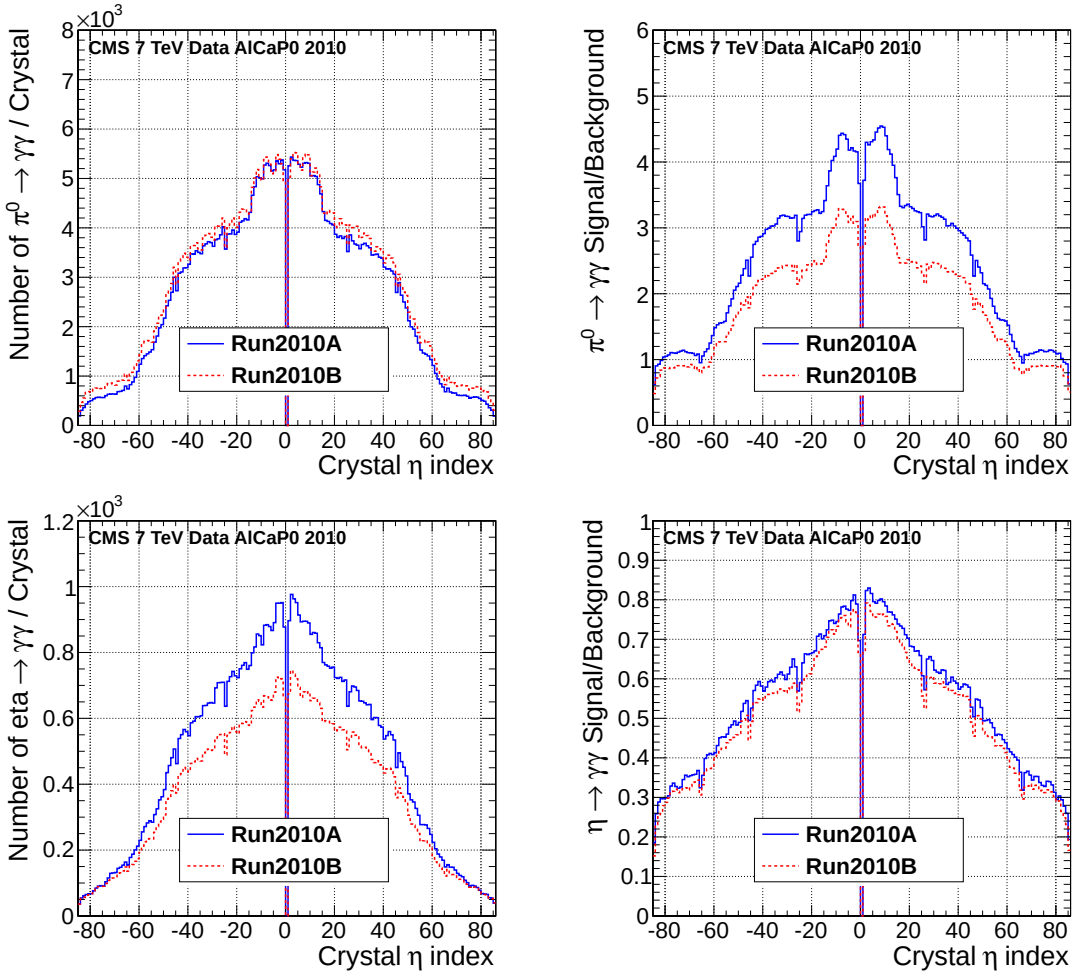

Figure 4.14: The average numbers of photons (left column) from $\pi^0 \to \gamma\gamma$ (top row) and $\eta \to \gamma\gamma$ (bottom row) decays selected by the on-line stream, and the S/B (right column) as functions of the crystal η index. Here, data taken during the two periods in 2010 is considered.

intercalibrations have no correlated systematic uncertainties, the following equations hold:

$$\frac{1}{\sigma^2_{\text{comb}} - \delta^2_{\text{precalib}}} = \frac{1}{\sigma^2_1 - \delta^2_{\text{precalib}}} + \frac{1}{\sigma^2_2 - \delta^2_{\text{precalib}}}\,, \tag{4.15}$$

$$\sigma^2_{\text{sum}} - \sigma^2_{\text{diff}} = 4\ \delta^2_{\text{precalib}}\,, \tag{4.16}$$

where δ_{precalib} denotes the precalibration precision. In general, σ_{x} denotes the width of the distribution concerned. For example, $\sigma_{\text{sum(diff)}}$ means the width of the sum

(difference) of the two constants. $\sigma_{\rm comb}$ means the width of the distribution of the weighted average constants, where the weight is the estimated precision of each intercalibration. Equation (4.15) is solved iteratively, starting from an estimate of the precalibration precision. Equation (4.16) directly gives $\delta_{\rm precalib}$. Consistent results are obtained by solving the two equations.

Figure 4.15 and 4.16 show the distributions of the sum and the difference of the π^0 and beam-splash intercalibration constants in SMod 1 and 9, respectively. The width of these distributions are then fed into equation (4.16) to estimate the precalibration precision of the corresponding SMod. Figure 4.17 left shows the width of the sum and difference of the π^0 and beam-splash intercalibration constants in each SMod. Figure 4.17 right shows the resultant precalibration precision.

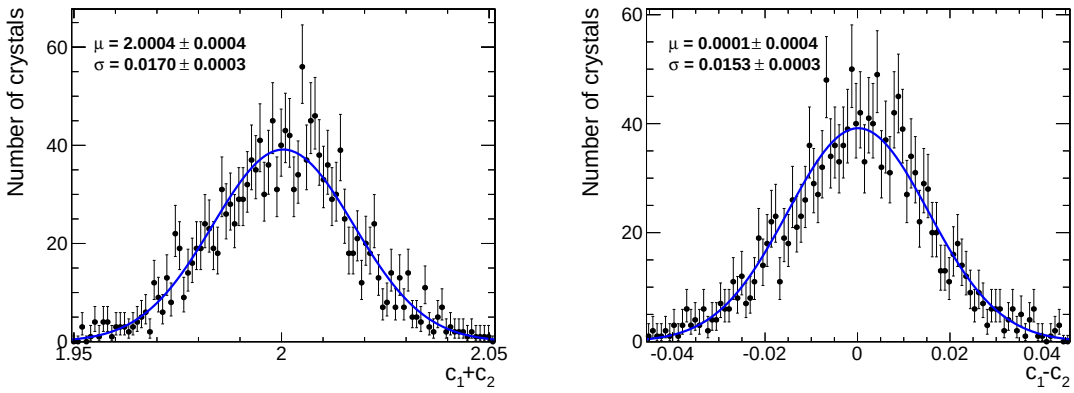

Figure 4.15: The distributions (black circles with error bars) of the sum (left) and difference (right) of the π^0 and beam-splash intercalibration constants in SMod 1, which has been intercalibrated with a high precision (about 0.4%) with the test beam electrons. The overlaid curve on each plot is from the unbinned Gaussian fit to the distributions.

SMod 1, 11 and 24 is measured to have the best precalibration precision about 0.4%. Figure 4.18 left shows the estimated precalibration precision in each module in each of three SMods. The precision varies about 0.2% among SMmods. We consider this variation as a systematic uncertainty on the precalibration precision estimation on the three SMods. Figure 4.18 right shows the estimated precalibration precision in each module of the three SMods. In summary, the test beam precalibration precision

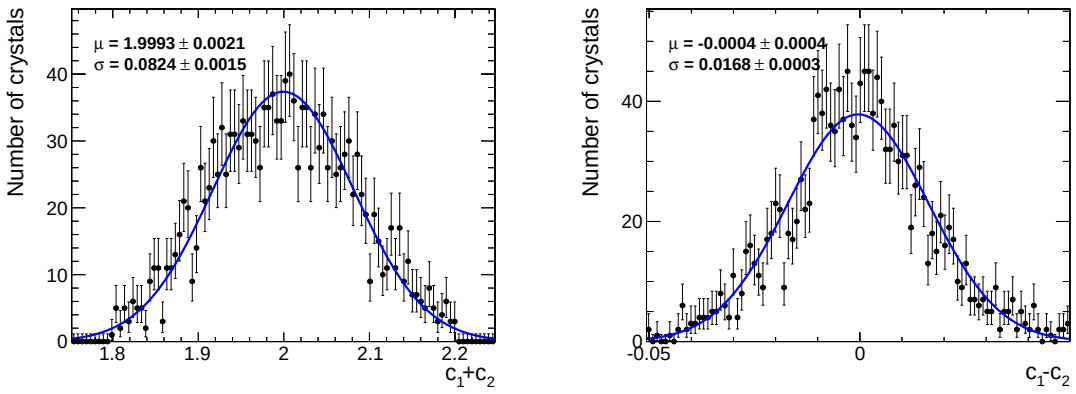

Figure 4.16: The distributions (black circles with error bars) of the sum (left) and difference (right) of the π^0 and beam-splash intercalibration constants in SMod 9, which has been intercalibrated with comic muons with a worse precision (few%). The overlaid curve on each plot is from the unbinned Gaussian fit to the distributions.

in the three best SMods is estimated to be $\delta_{\text{precalib}} = 0.4 \pm 0.03 \pm 0.2\%$.

The $\pi^0(\eta)$ intercalibration precision of all ECAL barrel crystals (represented by those with the best precalibration precision in SMods 1, 11, 24) is then estimated to be the width of the distribution of the intercalibration constants inside the three SMods, subtracted in quadrature by the test beam precalibration precision of 0.4%.

The estimated precision consists of two contributions: the systematic uncertainty of this calibration method and the statistical uncertainty due to the limited calibration sample size. We have shown in section 4.4 the dependence of the statistical uncertainty on the number of $\pi^0 \to \gamma\gamma$ decays and S/B in simulation. In data, the statistical uncertainty can be estimated by splitting the whole calibration sample into two halves and deriving one set of intercalibration constants from each half. Subtracting the two intercalibration constants fully cancels any systematic biases, so that the width of the distribution of the differences between the two intercalibration constants can be used to estimate the statistical uncertainty in the calibration for the full sample, $\sigma_{\text{stat}} = \sigma_{c_1 - c_2}/2$. Then the systematic uncertainty is estimated as the difference in quadrature between the total precision and the statistical uncertainty.

Figure 4.19 show the π^0 and η intercalibration precision obtained from two subsamples of Run2010A. Figure 4.20 and figure 4.21 show the statistical and systematic

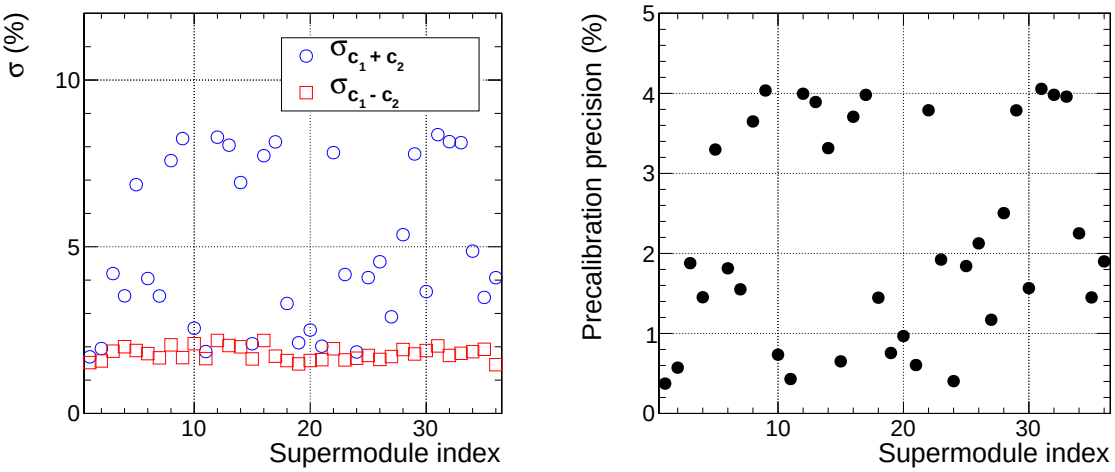

Figure 4.17: Left: The Gaussian width of the distribution of the sums (blue circles) and differences (red squares) of the π^0 and beam-splash intercalibration constants for each SMod. Right: The estimated precalibration precision for each SMod.

uncertainties obtained from π^0 and η calibration samples of Run2010A, respectively. The statistical uncertainty agrees with the expectation from the intercalibration studies with simulated events (see section 4.4). The estimated systematic uncertainty is estimated to be 0.4 - 0.5% in the central barrel ($|i\eta| < 60$) and 0.9 - 1.0% in the outer barrel.

Figure 4.22 shows the precision of the combined intercalibration constants derived from the $\pi^0 \to \gamma\gamma$ and $\eta \to \gamma\gamma$ calibration samples collected in 2010. In the central part of ECAL barrel, the precision obtained is close to the design precision of 0.5%. In the outer barrel, the precision is worse and includes a nonnegligible statistical uncertainty.

In section 4.3.3 we have described the iη and iϕ-dependent correction needed to reduce the bias on the energy measurement due to cracks or gaps. In the barrel, there are some crystals which are closest to the largest cracks between modules along η. These crystals have $|\mathrm{i}\eta| = 1, 25, 26, 45, 46, 65, 66, 85$. Along ϕ, crystals with iϕ mod $20 = 0, 1$ are next to the gaps between SMods. Here, we explicitly check the π^0 intercalibration precision for these crystals. Figure 4.23 shows the distributions of the π^0 intercalibration constants for these crystals next to cracks, gaps, or far away from

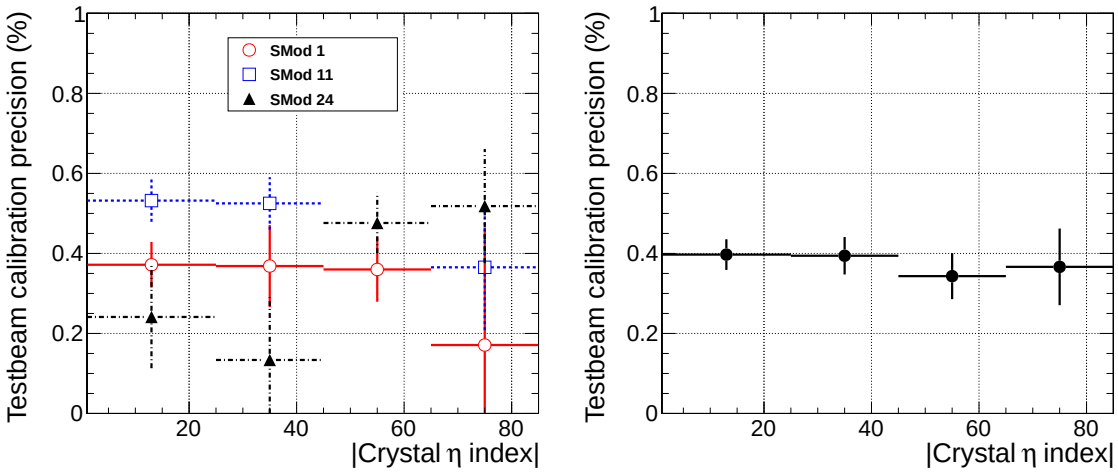

Figure 4.18: The estimated precalibration precision for SMods 1, 11 and 24 versus the module number. Left: Separately for each SMod. Right: Combined.

cracks and gaps in the first two modules ($|i\eta| \leq 45$) in the three best precalibrated SMods, where both the systematical and statistical uncertainties are smaller than for the other two modules. Subtracting the estimated precalibration precision of 0.4%, the intercalibration precision is about 0.51% for these crystals which are not next to cracks or gaps. The precision is 0.63% for crystals next to the ϕ gaps. Such a loss of precision on these crystals is tolerable given that they comprise only 10% of all crystals. There is no significant loss of precision for crystals next to the η cracks.

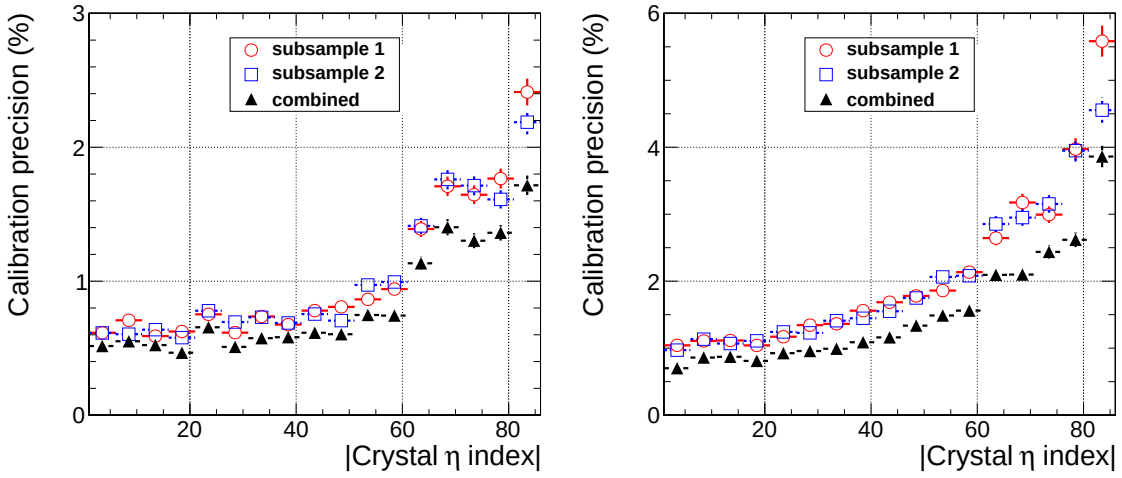

Figure 4.19: Precision of the intercalibration constants derived from two subsamples in the run period Run2010A, from $\pi^0 \to \gamma\gamma$ (left) and $\eta \to \gamma\gamma$ (right).

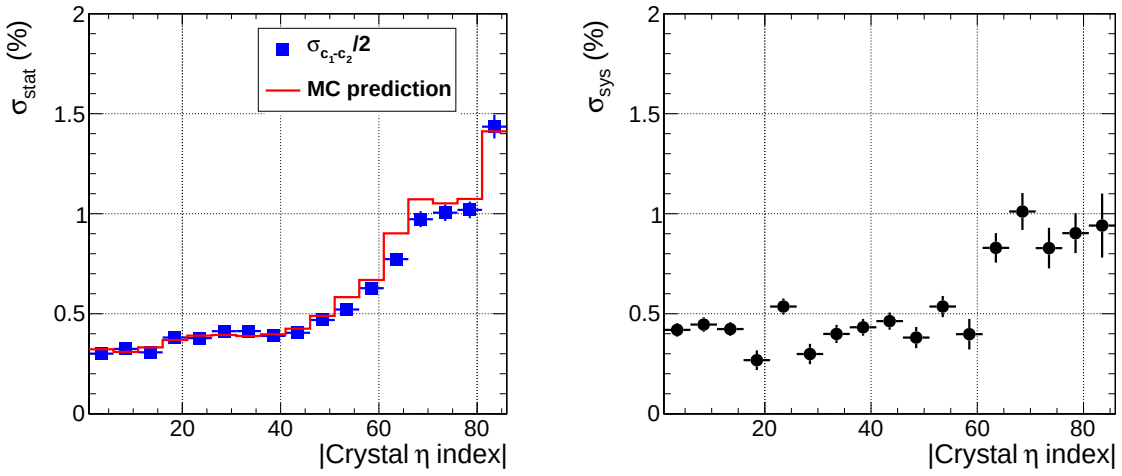

Figure 4.20: Statistical (left) and systematic uncertainty (right) of the intercalibration constants derived from $\pi^0 \to \gamma\gamma$ decays, collected during the run period Run2010A.

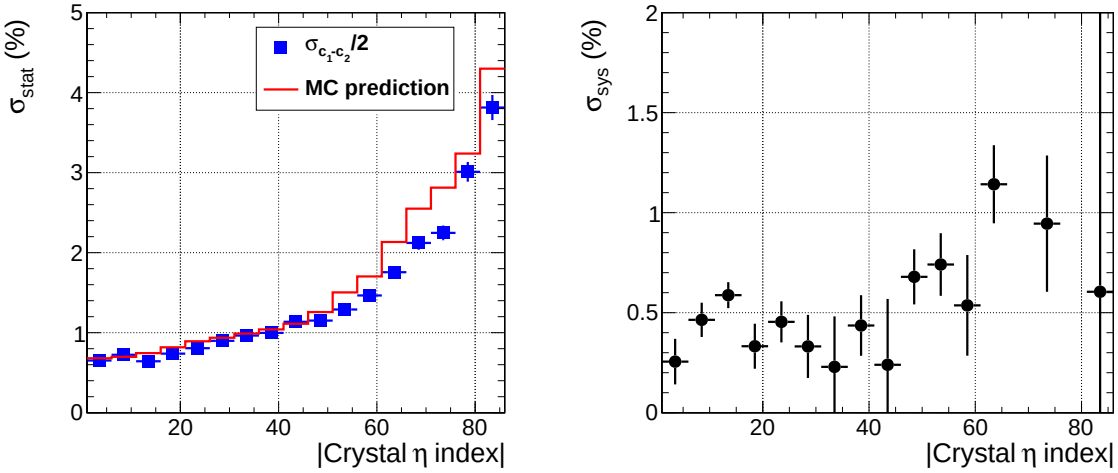

Figure 4.21: Statistical and systematic uncertainty of the intercalibration constants derived from $\eta \to \gamma\gamma$ decays, collected during the run period Run2010A.

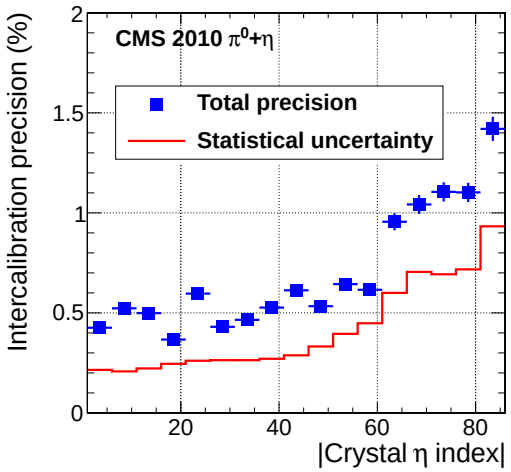

Figure 4.22: The intercalibration precision of the combined constants derived from the 2010 π^0 and η calibration samples. Also shown is the statistical uncertainty due to the limited sample sizes.

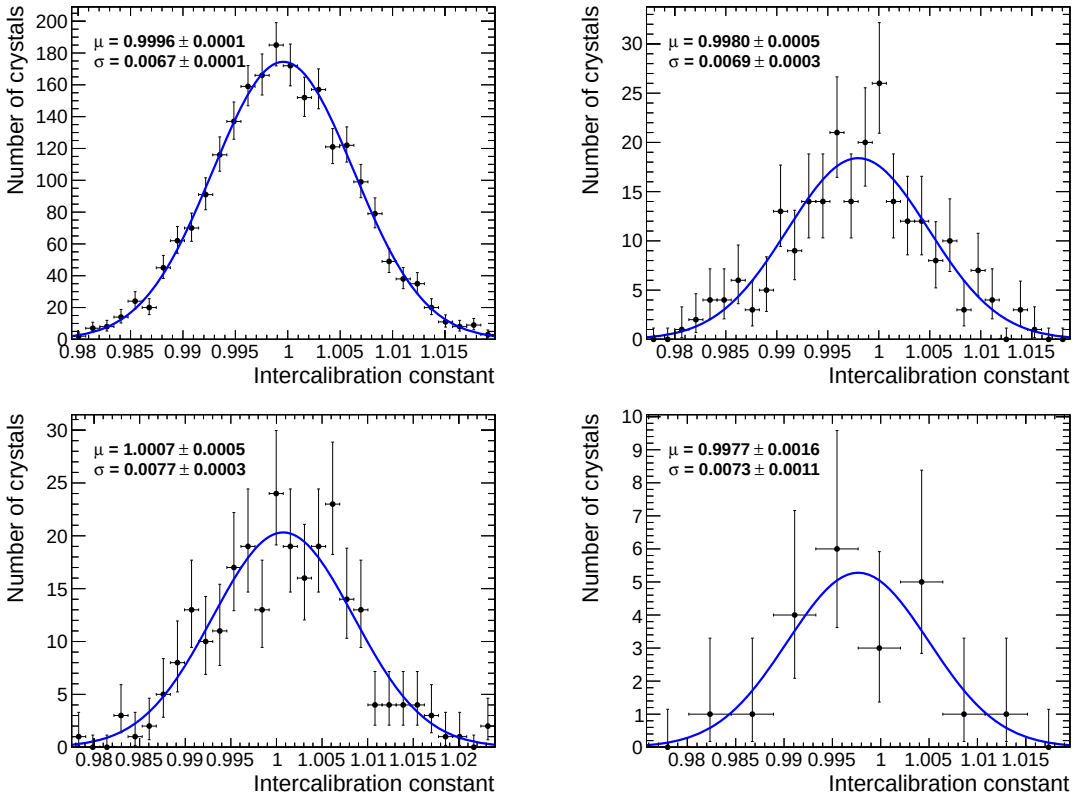

Figure 4.23: The distribution of the π^0 intercalibration constant derived from the Run2010A period, for crystals in module 1 and 2 of SMod 1,11, and 24. Top left, not next to η cracks or ϕ gaps; top right, next to η cracks; bottom left, next to ϕ gaps; bottom right, next to both η cracks and ϕ gaps. The superimposed curve on each distribution is a Gaussian fit to the data.

4.7 The π^0 and η Intercalibration From 2011 Data

As we discussed in section 4.1, the intercalibration constants needed to be rederived in 2011. During the data taking in 2011, the average rate from the π^0 and η calibration stream was increased, relative to 2010. Figure 4.24 and 4.25 show the selected number of $\pi^0(\eta) \to \gamma\gamma$ decays per crystal and S/B as a function of the crystal η index, from different run periods in 2011. We split the 2011 data-taking into seven run periods. The data from each period is used to derive one set of intercalibration constants. The variation on the number of $\pi^0 \to \gamma\gamma$ and $\eta \to \gamma\gamma$ decays from period to period is due to the size of the collected data sample. The first period has the best S/B compared to the others, due to the lower luminosity and hence smaller prescales on the L1 triggers with low p_{T} thresholds.

Due to the large calibration sample collected in 2011, the combined statistical uncertainty of the intercalibration constants from $\pi^0 + \eta$ is negligible compared to the systematic uncertainty of this calibration method.

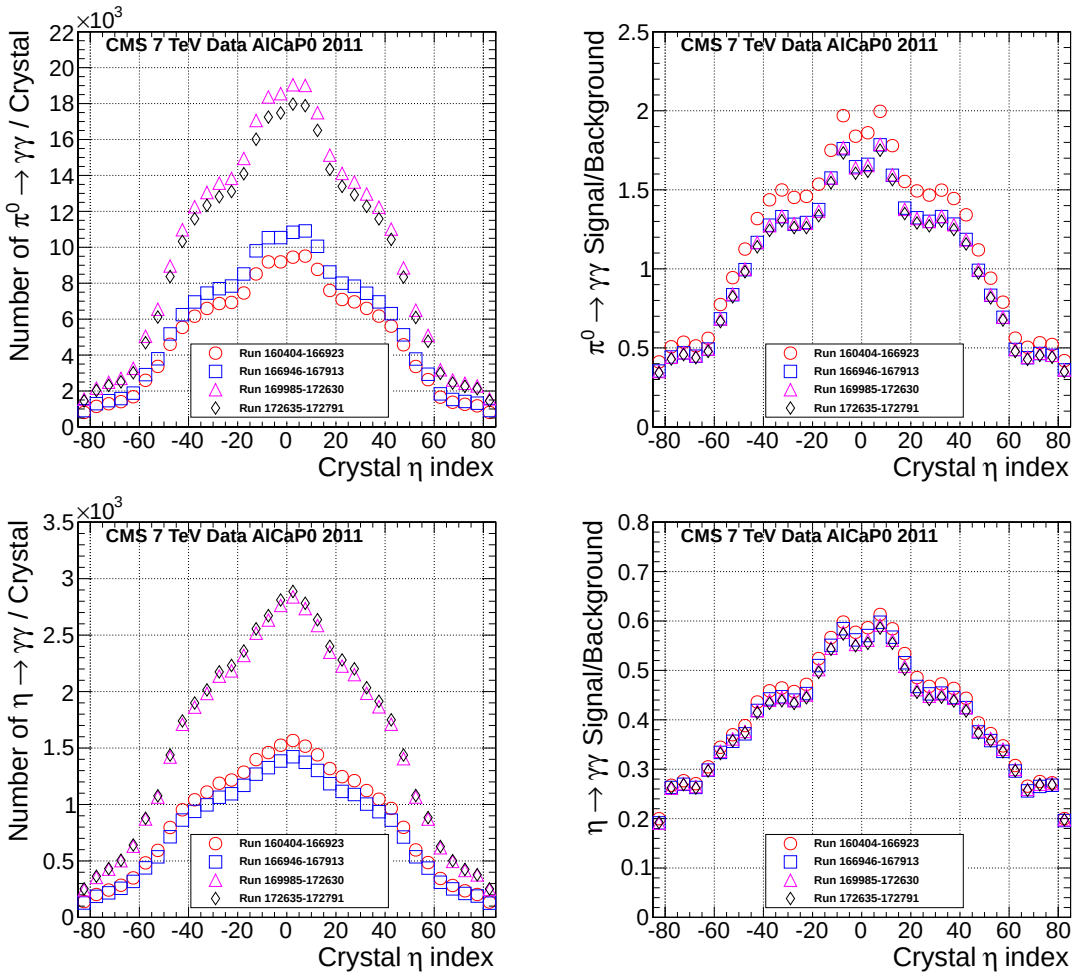

Figure 4.24: The average number of photons (left column) from $\pi^0 \to \gamma\gamma$ (top row) and $\eta \to \gamma\gamma$ (bottom row) decays selected by the online stream, and the S/B (right column) as functions of the crystal $|\eta|$ index. Here, data taken during the Run2011A period is considered (from run number 160404 to 172791).

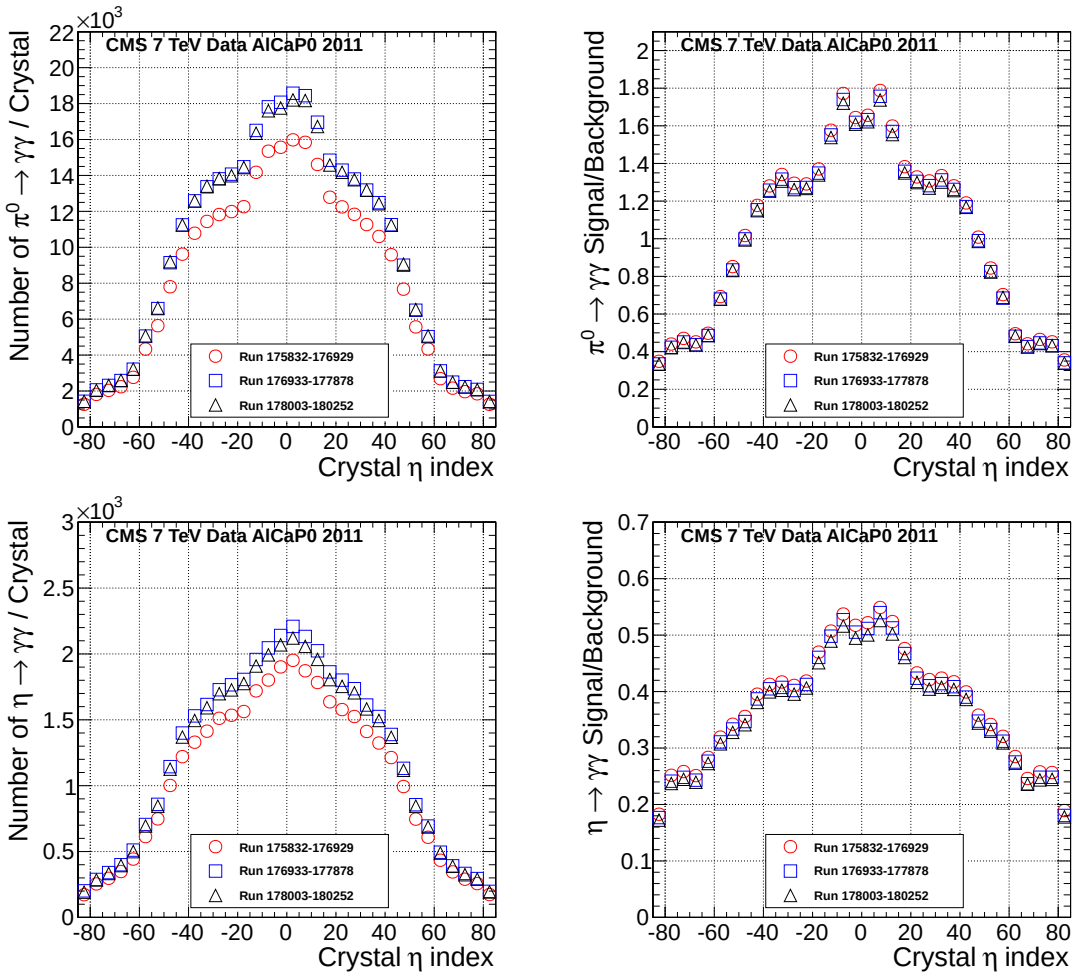

Figure 4.25: The average numbers of photons (left column) from $\pi^0 \to \gamma\gamma$ (top row) and $\eta \to \gamma\gamma$ (bottom row) decays selected by the on-line stream, and the S/B (right column) as functions of the crystal $|\eta|$ index. Here, data taken during the Run2011B period is considered (from run number 175832 to 180252).

4.8 Combined Intercalibration In 2011

The intercalibration constants derived from three methods with 2011 data, including $\pi^0(\eta)$, $\phi-$symmetry and electron (E/p) calibrations, are combined to give the best set of intercalibration constants. The combination is based on the estimated precision of each method, as shown in Figure 4.26. The $\pi^0 + \eta$ method gives the best intercalibration precision for all regions of the barrel and endcaps up to $|\eta| \approx 2$.

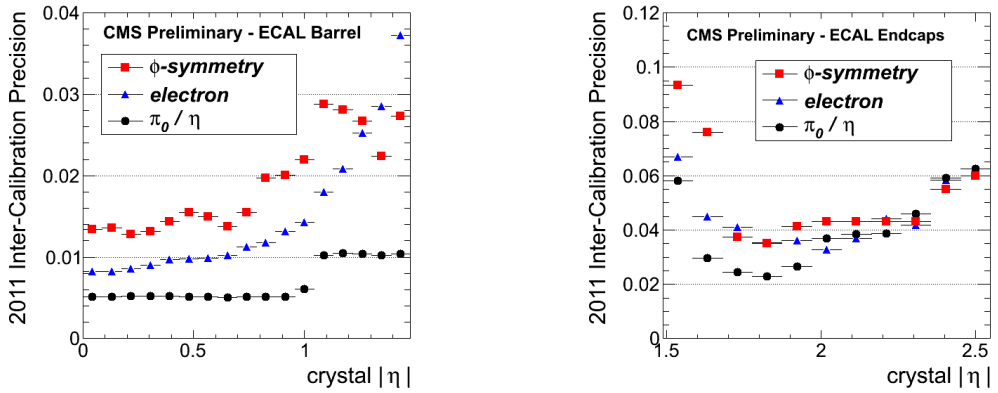

Figure 4.26: Estimated intercalibration precision from the $\pi^0(\eta) \to \gamma\gamma$ (black circles), electron E/p (blue triangles), and ϕ-symmetry (red squares) calibration methods as functions of $|\eta|$ in the ECAL barrel (left) and the endcaps (right) using the 2011 calibration data.

Figure 4.27 shows the comparisons of the $Z \to e^+e^-$ invariant mass distributions between data re-reconstructed with the $\pi^0 + \eta$ intercalibration constants and data re-reconstructed with the combined constants, in different event categories according to the r_9 and η values of two electrons. The first category, when two electrons are both in the barrel and have r_9 greater than 0.94, has the best mass resolution and is thus the most important category for the $H \to \gamma\gamma$ search. When one of the electrons in the barrel has r_9 less than 0.94, the event is in the second category. The third and fourth categories contains events in which at least one of the two electrons is in the endcaps. In the third category, both electrons have r_9 greater than 0.94. The same definition of the event categories will be used for di-photon event classification for $H \to \gamma\gamma$ search in chapter 8 (see table 8.1). There is some improvement by combining the $\phi-$symmetry and E/p intercalibration constants with the $\pi^0 + \eta$ constants. The

improvement in the barrel is very small, especially in the first category. In section 13.1 we will compare the two set of calibration constants in terms of the energy smearing, which accounts for the width difference in the $Z \to e^+e^-$ invariant mass distributions between data and simulation.

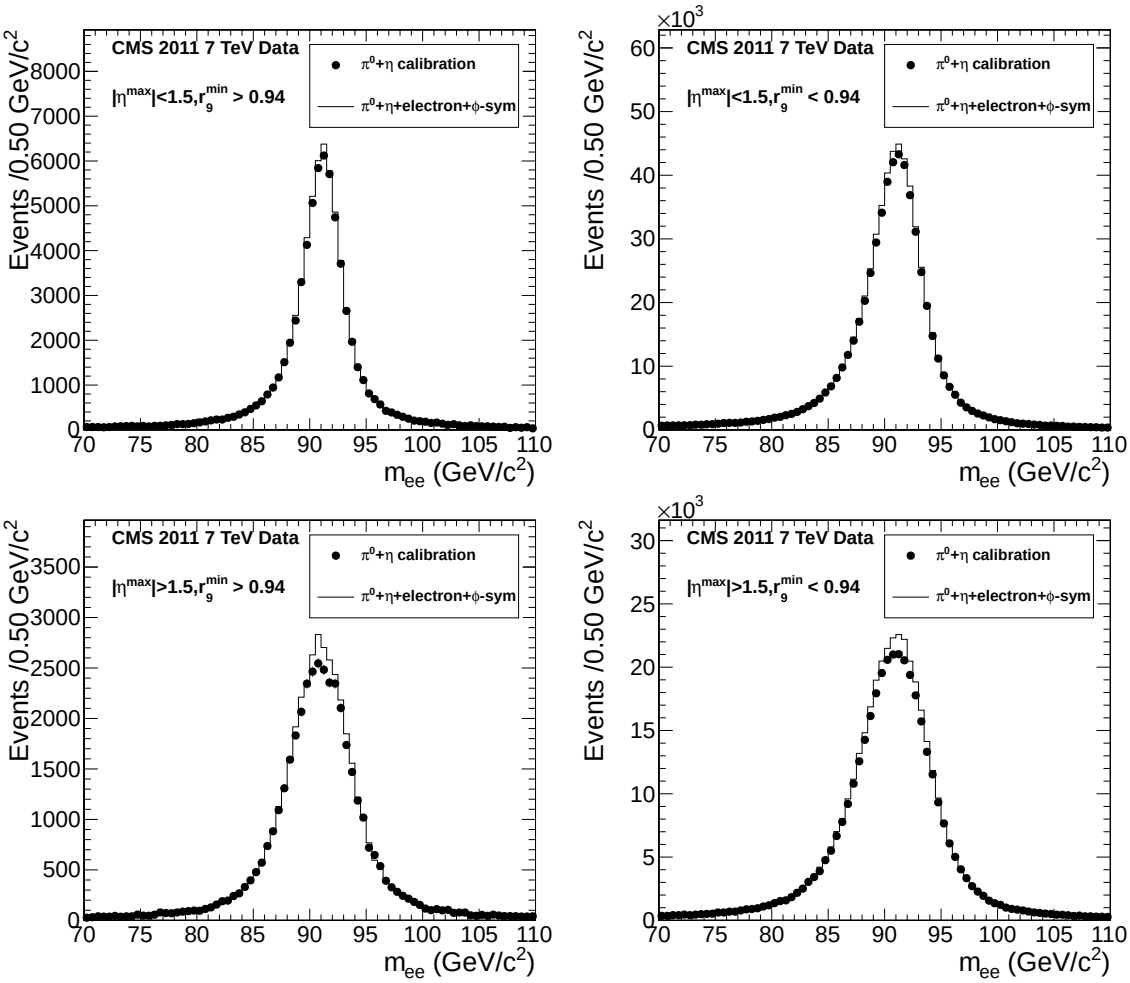

Figure 4.27: Comparison of the $Z \to e^+e^-$ invariant mass distributions between data re-reconstructed with the intercalibration constants derived from the $\pi^0 + \eta$ methods only (black circles) and the combined intercalibration (histograms), in different event categories indicated on each figure (see text for description).

As we have discussed at the beginning of this chapter, at high energies, the intercalibration precision is the key contribution to the ECAL energy resolution, which drives the $H \to \gamma\gamma$ search sensitivity. We will discuss in chapter 13 the impact of the *in situ* intercalibration on the $H \to \gamma\gamma$ search.

Chapter 5

Electron and Photon Measurement and Correction

5.1 Introduction

The energy of electromagnetic showers from electrons or photons incident on the ECAL crystals is measured as the sum of the energies deposited in a number of crystals which are grouped together by a supercluster algorithm (described in more detail in section 5.2),

$$\mathrm{E} = \mathrm{f(e/\gamma)} \sum_{\mathrm{i}} \mathrm{ADC_i} \cdot \mathrm{G} \cdot \mathrm{c_i} \cdot \mathrm{LC_i(t)}\,. \tag{5.1}$$

In simulation, there is no laser correction $\mathrm{LC_i}$, and the intercalibration constant $\mathrm{c_i}$ is a Gaussian random number for each crystal. This is needed to simulate the effects due to imperfect *in situ* intercalibration. $\mathrm{c_i}$ is distributed as a Gaussian with a mean of one and a width equal to the precision of the intercalibration constants. In the simulation of 2011, the precision is taken from the intercalibration precision achieved in 2010. The Gaussian width is shown in figure 3.3. The term $\mathrm{f(e/\gamma)}$ refers to the correction for the energy measured by the supercluster algorithm for electron or photon.

For illustration, figure 5.1 shows the effect of the energy correction on the energy resolution and the scale for electrons in the barrel and in the endcaps. The energy resolution corresponds to the width of the distribution and the scale corresponds to

its peak. Here, the standard energy correction, which we will describe in section 5.4, is used. Clearly, there is some improvement after correction in terms of both the energy resolution and the scale. In the barrel, the overall scale is precise at the level of 1%. In the endcaps, the scale without energy correction is about 7% lower because the energy measured in the preshower detector is not taken into account by the supercluster algorithm. After the correction, however, the scale is overcorrected by approximately 3%.

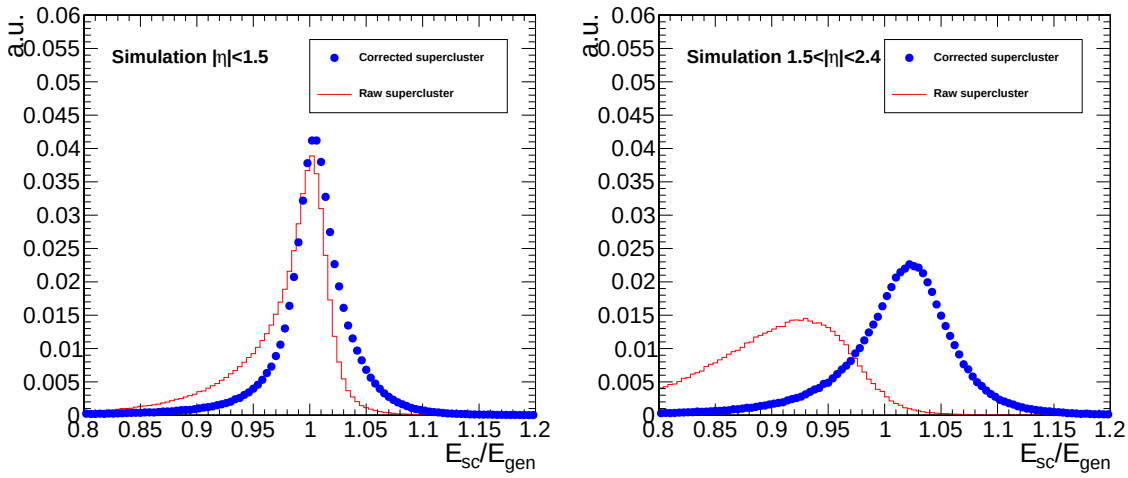

Figure 5.1: Ratio of the raw and the corrected supercluster energy (standard method) over the generated energy from simulation for the barrel (Left) and the endcaps (right).

The purpose of the energy correction is to correct the raw energy determined by the supercluster algorithm back to the true energy of the particles when produced at the collision point. There are a few main reasons that the raw energy needs to be corrected:

- There exist gaps between the ECAL crystals, and cracks between the modules or super-modules in which some of the energy is lost. The energy reconstruction performance is worse for electrons near gaps or cracks. This is illustrated in figure 5.2.

- Electron might radiate photons when it is deflected by an atomic nucleus in the material. This process is called "bremsstrahlung". Photon might convert into

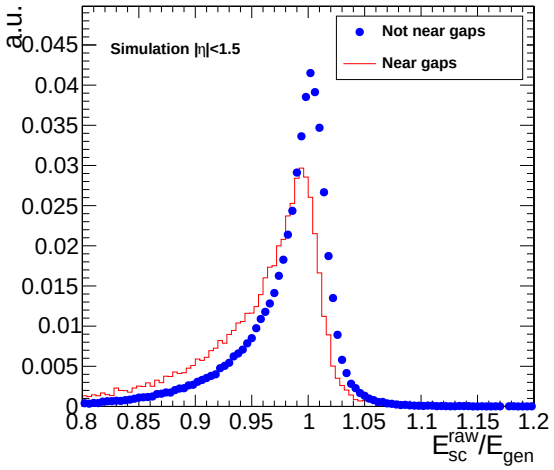

Figure 5.2: Comparison of the distribution of raw supercluster energy normalized to the generated energy, for electrons near gaps or not near gaps in the barrel.

e^+e^- pairs when it travels through the tracker material. Due to the solenoidal magnetic field, the bremsstrahlung photons or e^+e^- pairs spread out in the ϕ direction.

The variable, r_9, defined in equation (3.1), is thus a good variable for discriminating bremsstrahlung electrons from nonbrem electrons or converted photons from non-converted photons. A higher value of r_9 means a smaller probability that a photon has converted in the tracker.

Another variable brem, characterizing the electron bremsstrahlung, is defined as ratio of the shower width along ϕ and η,

$$brem = \frac{\sigma_\phi}{\sigma_\eta}\,, \tag{5.2}$$

where σ_η is defined as

$$\sigma_\eta = \sum_{\mathrm{i}} \sqrt{\frac{\mathrm{E_i}}{\mathrm{E_{raw}}}(\eta_\mathrm{i} - \eta_\mathrm{sc})^2}\,, \tag{5.3}$$

and σ_ϕ is defined as

$$\sigma_\phi = \sum_{\mathrm{i}} \sqrt{\frac{\mathrm{E_i}}{\mathrm{E_{raw}}}(\phi_\mathrm{i} - \phi_\mathrm{sc})^2}\,, \tag{5.4}$$

where the sum is over all constituent crystals in the supercluster, $\mathrm{E_i}$ is the energy measured in each crystal, and $\mathrm{E_{raw}}$ is the raw supercluster energy. σ_η describes the natural shower size. The normalization of σ_ϕ with σ_η allows one to treat the showers in various energy ranges in one single approach. Figure 5.3 shows that the energy reconstruction performance of electrons with larger bremsstrahlung is worse.

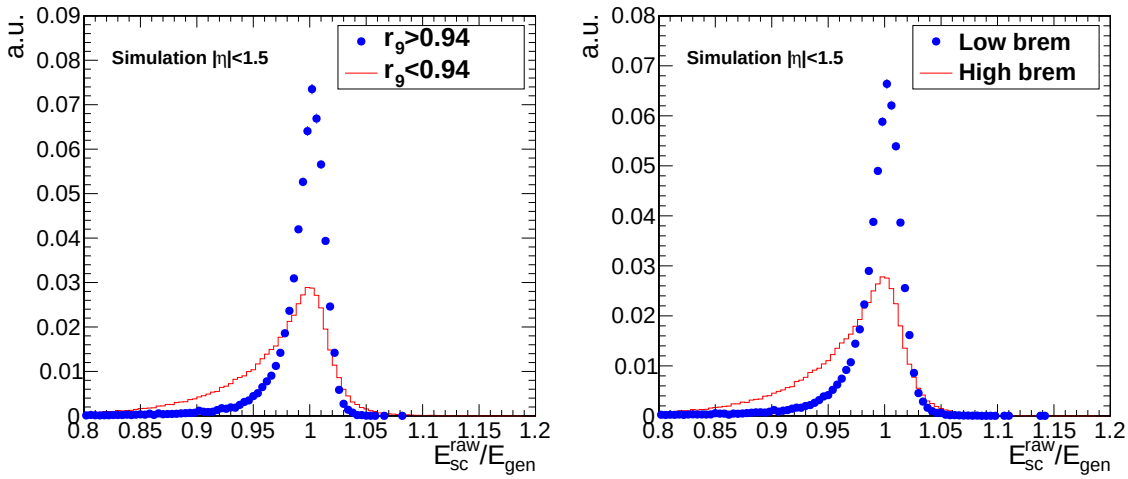

Figure 5.3: Comparison of the distribution of raw supercluster energy normalized to the generated energy, for electrons with low and high bremsstrahlung in the barrel. Two variables, both related to bremsstrahlung, are considered: r_9 (left) and brem (right).

- The tracker material is not uniformly distributed, especially in η. Figure 5.4 left shows that the energy reconstruction performance for electrons is worse at higher $|\eta|$.

- Energies from pileup collisions could be added into the supercluster. Figure 5.4 right shows that the energy reconstruction performance for electrons is worse in events with a larger number of vertices, corresponding to higher pileup.

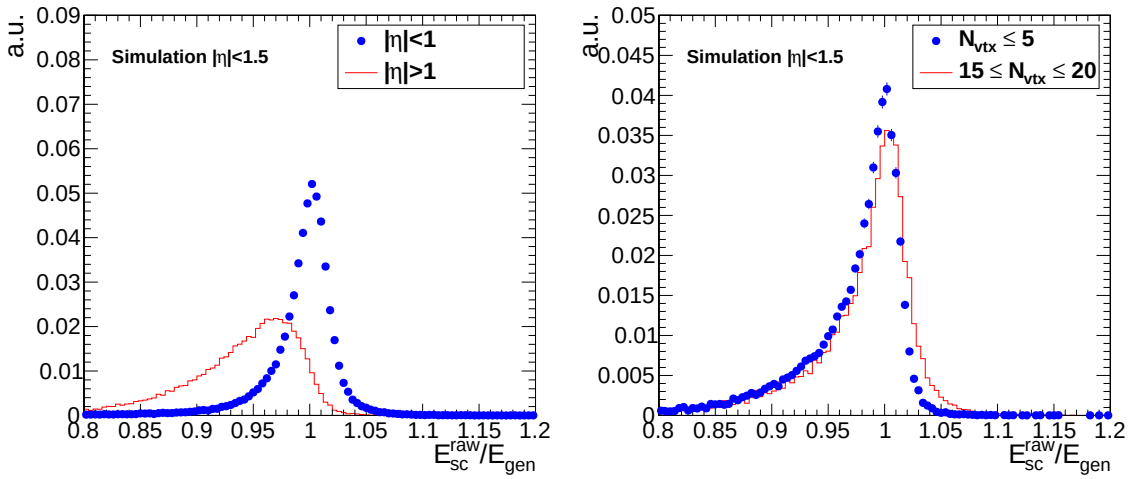

Figure 5.4: Comparison of the distribution of raw supercluster energy normalized to the generated energy, for electrons at low and high pesudorapidity in the barrel (left), and in events with low and high number of vertexes (right).

5.2 Energy Clustering Algorithm

The energy measurement of electromagnetic showers induced from electron or photon interactions with ECAL crystals starts by building an object which consists of a collection of crystals in which the showers deposited some energy [86]. Building such an object can be realized by a pattern recognition procedure, considering the physical behavior of electrons and photons once they reach ECAL crystals.

The electromagnetic shower appears as a local maximum in a spatial array of energy deposits in individual crystals. The local maximum is identified by looking for a single crystal with the largest deposited energy, among a contiguous set of crystals, which has an energy above a certain threshold. Such crystals are called seed crystals. Energies from other crystals close to the seed crystal are added to recover the original shower energy as much as possible. This process of combining crystals close to a seed crystal is called clustering.

In most physics analyses, only high energy electrons or photons are used. Electrons with very low energy might not reach the ECAL crystals at all because of the bending of its trajectory along the ϕ direction in the 3.8 T magnetic field. This could happen as well for e^+e^- pairs from photon conversions. So we will only consider electrons or

photons which have energy deposited in ECAL crystals.

Approximately 94% of the incident energy of a single electron or photon is contained in the 3×3 crystal matrix, and 97% in the 5×5 crystal matrix, as illustrated in figure 5.5. Summing the energy measured in such fixed arrays gives the best performance for unconverted photons, or for electrons in the test beam conditions, where there is no material present in front of ECAL.

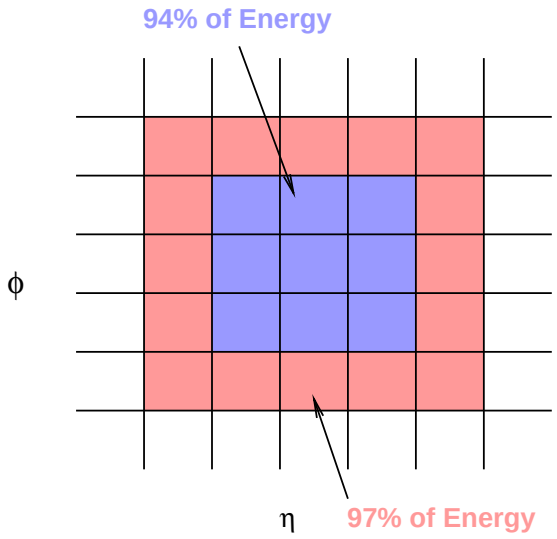

Figure 5.5: Illustration of a fixed array clustering algorithm.

In CMS, however, electrons might radiate photons as they travel through the tracker material between the interaction point and the ECAL. Bremsstrahlung photons may also contribute to the observed energy if they reach ECAL. Because of the bending of the electron's trajectory, radiated photons (tangent to the electron's trajectory) will spread out along the ϕ direction. These radiative energy deposits should by considered in the pattern recognition procedure. The photons might convert into e^+e^- pairs in the tracker material, and these electrons will also spread out along the ϕ direction.

It is thus natural dynamically search among the energy deposits in the ϕ direction while take a fixed interval of crystals in η, as illustrated in figure 5.6 [86]. This algorithm is called the Hybrid superclustering, which is used for electron and pho-

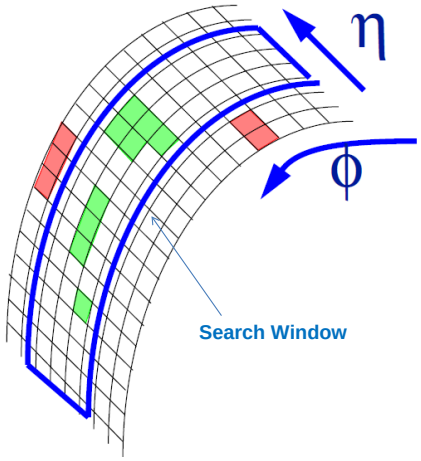

Figure 5.6: Illustration of the Hybrid supercluster algorithm used for barrel.

ton reconstruction in the barrel. It starts with a cluster, for example, made from the energy deposits of the electron which carries most of the original energy after bremsstrahlung, and adds other clusters from radiative photons. In other words, a supercluster is a cluster of clusters. The cluster with the highest energy is called the seed cluster.

In the endcaps, due to the different geometry, a "Multi5×5" supercluster algorithm is used. It starts with a 5×5 seed cluster and adds in more 5×5 clusters to form one supercluster.

5.3 Position Measurement

The ECAL is not only used to measure the energies of electromagnetic showers, but also their positions. This is important in many aspects. For example, the direction of a photon is determined from the vertex position to the position at the ECAL.

For a first and simple consideration, the position of the electromagnetic shower can be measured by calculating the energy-weighted mean position of the constituent crystals in the supercluster. In CMS however, this is complicated by two factors:

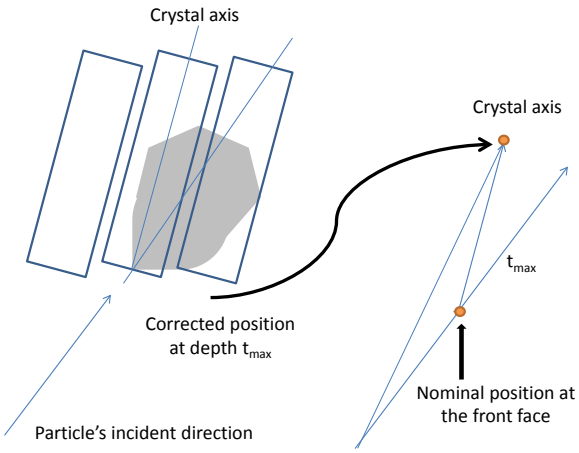

Figure 5.7: Illustration of the ECAL crystal offpoint in CMS.

- The position of the crystal should take into account the longitudinal showering depth (t_{max} in figure 5.7). By design, the ECAL crystals do not exactly point to the nominal interaction point [54]. Therefore, the lateral position (η, ϕ) of the crystal axis depends on the showering depth, as illustrated in figure 5.7 [86].

- A simple energy weighted mean of the crystal energies would cause a bias in the position measurement, because the electromagnetic shower energy falls exponentially with the transverse distance from the shower axis. The bias in position tends to be towards the axis of the crystal with the largest energy deposit (the seed crystal) in the supercluster.

  A logarithmic weighted average is therefore used [86]

$$x = \frac{\sum_i x_i \cdot w_i}{\sum_i w_i}, \tag{5.5}$$

  where

$$w_i = w_0 + \log\frac{E_i}{E_{raw}}, \tag{5.6}$$

  where E_i is the measured energy in each crystal and E_{raw} is the raw super-

cluster energy. The parameter w_0 controls the smallest fractional energy to be considered in the position measurement, which is about 1.5%.

5.4 Factorized Energy Correction

5.4.1 The Method

The standard and traditional electron or photon energy correction scheme in CMS is to factorize the correction into a few individual energy corrections applied sequentially to the supercluster energy. In the barrel, three sequential corrections are applied to the Hybrid supercluster energy. In the endcaps, two corrections are applied to the Multi5×5 supercluster energy, and the energies measured in preshower clusters are added.

In general, the correction is determined from simulation by measuring the peak of the distribution of the reconstructed energy over the generated or true energy. We discuss the correction procedure in more detail below.

- In step one, for the barrel only, an energy correction as a function of η, f(η), is used to compensate for the lateral energy leakage from the exposed faces near the front of the crystals. In the endcaps, the crystals are oriented such that the area of the sidefaces exposed is much less so that no such correction is needed.

- In step two, after applying the correction derived in step one (for the barrel only), a correction as a function of brem is used to correct for the varying response of the supercluster algorithm to the showers.

- In step three, after applying the previous corrections, the last correction, as a function of E_{T} and η, is applied to correct for the nonlinear distribution of material in the detector and of the energy dependence. A correction factor is calculated as a function of η, in bins of 2 GeV of E_{T}.

The factorized approach is relatively simple, as it only uses two or three variables. The correction is parametrized as a function of just one variable, in steps of the other

one or two variables. But since the correlations among the variables are not fully taken into account, this method is not expected to give an optimal correction.

In the standard photon reconstruction in CMS, the above correction is only applied to photons with r_9 below a certain threshold which are considered as converted photons; otherwise, above the threshold, the corrections described above are not needed. The threshold is 0.94 and 0.95 for the barrel and endcaps, respectively. Above the threshold, the total energy measured in the 5×5 crystal matrix around the seed crystal, $E_{5\times5}$, is used as the photon energy in the barrel. The preshower energy is added into $E_{5\times5}$ in the endcaps. In section 7.2, we will use r_9 to categorize photons. The cut chosen on r_9 is 0.94 for both the barrel and endcaps. Therefore, in this thesis, only electrons or photons with $r_9 < 0.94$ have the factorized correction applied.

5.4.2 Performance of the Factorized Correction on $Z \to e^+e^-$

Figures 5.8 and 5.9 show a comparison of the reconstructed $Z \to e^+e^-$ invariant mass distributions with and without the factorized correction, in simulation and data, respectively.

There is clearly an improvement after applying the correction, both in simulation and real data: the width of the distribution is narrower, and the peak position is also closer to the nominal Z mass.

To quantitatively study the performance of the correction, we perform an unbinned maximum likelihood to the $Z \to e^+e^-$ invariant mass. The fit function is a Breit-Wigner (BW) convoluted with a Crystal Ball (CB). This type of function is usually used to model the shape of a resonance in the presence of a finite detector resolution. The functional form of BW is

$$f_{\mathrm{bw}}(x) = \frac{1}{(x - x_0)^2 + \frac{1}{4}g^2}\,, \tag{5.7}$$

where x_0 and g is the mean and width of the BW function. In the case of $Z \to e^+e^-$,

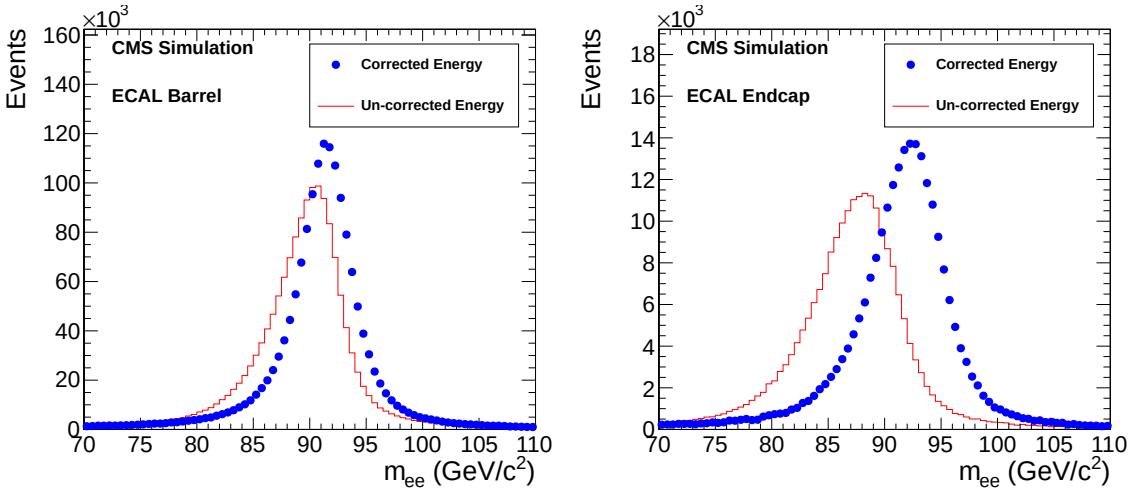

Figure 5.8: Performance of the factorized energy corrections in simulated $Z \to e^+e^-$ data in the barrel (left) and endcaps (right), by comparing the reconstructed invariant mass distributions with and without the correction.

$x_0 = 91.1876$ GeV and $g = 2.4952$ GeV [30]. The functional form of CB is

$$f_{\rm cb}(x) = \begin{cases} \frac{(\frac{n}{|a|})^2 e^{-\frac{1}{2}a^2}}{(\frac{n}{|a|} - |a| - n)^n} & \text{if } x < -|a| \\ e^{-\frac{1}{2}(\frac{x-\Delta_m}{\sigma_{\rm cb}})^2} & \text{if } x > -|a| \end{cases} . \tag{5.8}$$

The CB function consists of a Gaussian core portion, the width of which is controlled by the parameter $\sigma_{\rm cb}$, and a power low-end tail below a certain threshold, the size of which is controlled by two parameters a and n. The parameter Δ_m determines the shift of the peak position with respect to the nominal Z mass.

Figure 5.10 left and right shows the fitted functions on the invariant mass distributions in simulation and data, respectively. When fitting to data, the CB shape parameters a and n are fixed to the values obtained from the simulation, and the energy scale in data is corrected to match to that in simulation; such corrections will be discussed further in section 5.6. In addition to $\sigma_{\rm cb}$, we also compare the values of effective sigma, $\sigma_{\rm eff}$, which is defined as the half of the shortest interval which covers 68.3% of the integral of the fitted function over the mass range considered. In the case of a Gaussian distribution, $\sigma_{\rm eff}$ is equivalent to one standard deviation. In the case of the fit function we consider here, $\sigma_{\rm eff}$ takes into account the asymmetric shape

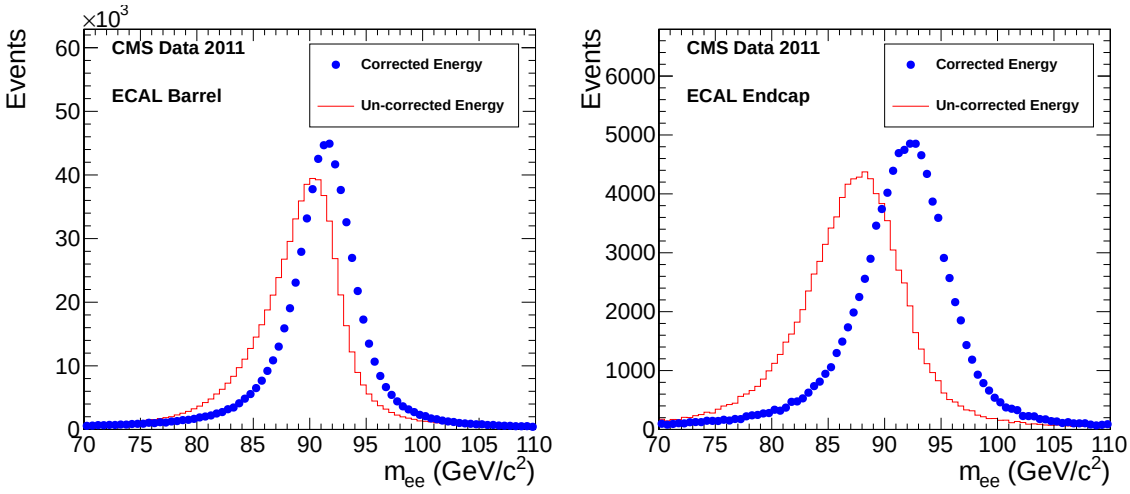

Figure 5.9: Performance of the factorized energy corrections in real $Z \to e^+e^-$ data in the barrel (left) and endcaps (right),by comparing the reconstructed invariant mass distributions with and without the correction.

better.

The comparison of σ_{cb} or σ_{eff} between data and simulation indicates that the energy resolution in data is worse than that in simulation. There are a few main reasons. First of all, the simulation-based correction is not expected to work equally well when applied to data since simulation cannot model perfectly each of the variables used for deriving the correction and their correlations. Second, the *in situ* intercalibration precision obtained in 2011 is worse than that obtained in 2010, which was assumed in the 2011 simulation. Thirdly, the laser corrections in data are not perfect, and that degrades the resolution in data.

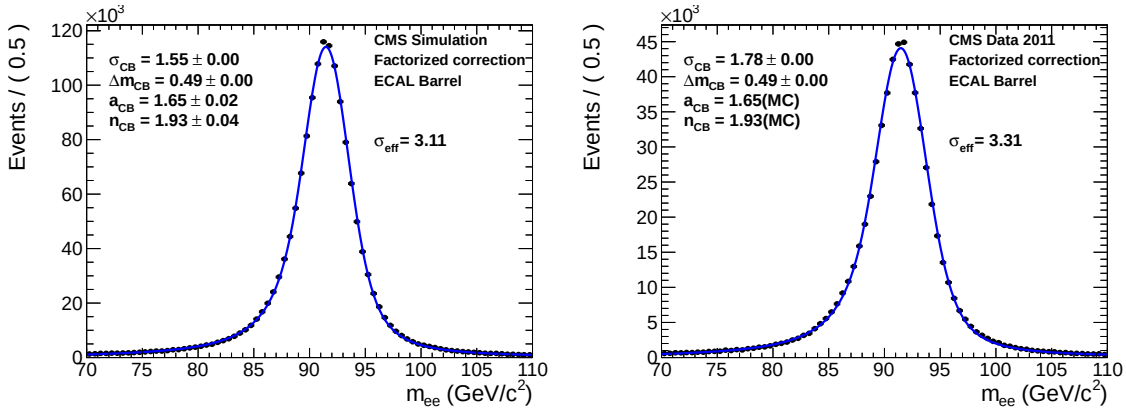

Figure 5.10: Unbinned maximum likelihood fit to the $Z \to e^+e^-$ invariant mass distributions in simulation (left) and data (right). The factorized correction, discussed in the text, is applied as needed to the electron and positron energies used to construct the Z mass.

5.5 Regression Energy Correction

5.5.1 Introduction to Regression

The factorized energy correction we discussed in the last section is relatively simple. It is based only on three variables, so the power of the correction is limited, and the correlations among variables are not taken fully into account. Besides, there is no explicit correction for the intercrystal gaps or the (sub)module cracks, and no explicit correction for pileup. In this section, we will investigate a more advanced technique: multivariate regression.

In general, regression analysis is a statistical technique to determine the dependence among variables. It relates the dependent (or output) variable y to the set of input variables $\mathbf{x} = x_1, x_2, ..., x_n$,

$$y = f(\mathbf{x}, \phi)\,, \tag{5.9}$$

where ϕ represents the set of input parameters to the function.

In our case, the output variable is the energy correction we want to derive. In simulation, we know the true energy of electron or photon from the event generator,

and we also know the raw supercluster energy, therefore, we can define the output variable to be

$$y = \mathrm{E_{true}}/\mathrm{E_{sc}^{raw}}\,, \tag{5.10}$$

where the preshower energy is added into the raw supercluster energy for the endcaps.

The set of input variables can include in principle any which are correlated with the energy measurement; for example, those variable we have introduced in previous sections: r_9, η, brem, number of vertices, etc. Figure 5.11 shows the nonlinear dependence of the energy correction on the variables η and brem, illustrating the complexity of the correction.

The goal of regression analysis is to obtain a function f to map a set of input variables to the output variable. Actually, the factorized approach can be considered as a one dimensional nonlinear regression; since it parametrizes the energy correction as a nonlinear function of η or brem or E_{T}.

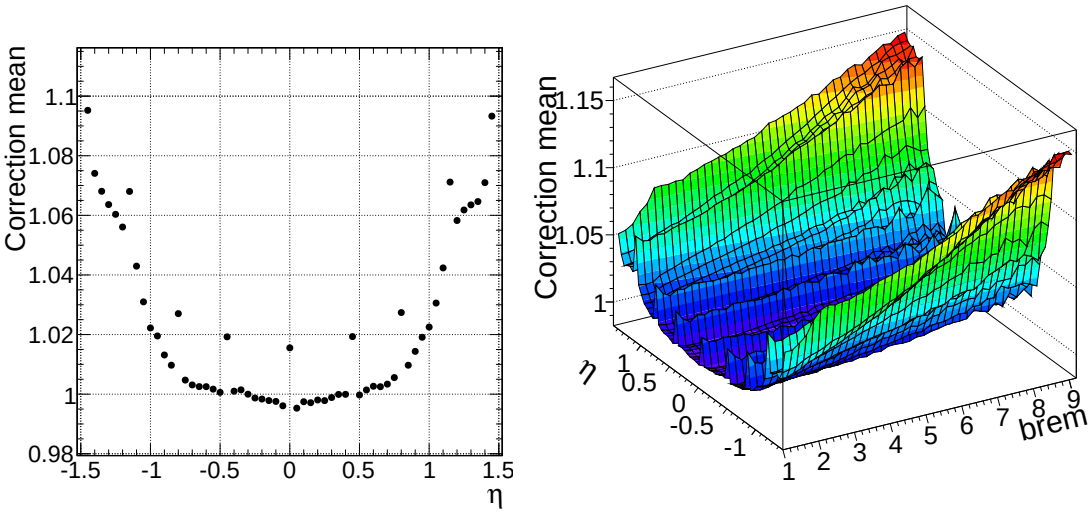

Figure 5.11: The energy correction as a function of η (left) and as a function of η and brem (right), illustrating the one and two dimensional nonlinear dependence of the correction on related variables.

Implementing regression with multiple variables is challenging, both mathematically and technically. In general, the true function $f(\mathbf{x})$ is unknown, and only an approximate function $\hat{f}(\mathbf{x})$ can be obtained. We use the regression technique of Gra-

dient Boosting Decision Trees (GBDT) [89, 90]. This has been implemented in the `TMVA` package [91].

Table 5.1 shows the list of input variables used for regression energy correction for ECAL barrel. Only the first seven rows of variables are used for the endcaps. Adding the rest does not improve the performance in data. In the barrel, the large intermodule gaps at $i\eta = 25, 45, 65$ are explicitly taken into account by the variable $(|i\eta| \leq 25)i\eta \mod 25 + (|i\eta| > 25)(i\eta - 25\frac{|i\eta|}{i\eta}) \mod 20$. The cracks between two supermodules along ϕ are explicitly taken into account by the variable $i\phi \mod 20$.

In this thesis, all real photons with $E_{\mathrm{T}} > 20$ GeV in the γ+jet MC sample are used to train the multivariate regression for the photon energy correction. The same number of events is used to the train the regression for electron, for which we use the POWHEG $\mathrm{Z} \to \mathrm{e}^{+}\mathrm{e}^{-}$ sample. In the common analysis [92], the photon regression is trained with real photons with $E_{\mathrm{T}} > 25$ GeV and only events with even event number in the MC sample are used, while the other half events are used to train another regression. Besides, the input variables are not exactly the same. In this analysis we use less number of variables for the barrel but more for the endcaps. However, the two regressions give very similar performance, as shown in figure 5.12. In this thesis, there is no reason to use only half of the available training statistics. In addition, we observed some differences in the results in terms of the observed exclusion limits and signal significance using one half or the other half. We will discuss in chapter 14 the studies related to the regression energy correction trained with limited number of events.

In figure 5.12 and throughout the thesis, the variable r_9 in simulation is scaled in order to better match the distribution in data, as shown in figure 5.13. A factor of 1.004 is multiplied to the value r_9 for electrons or photons in the barrel. The factor 1.005 is used for endcaps. However, the agreement is not perfect after rescaling. This causes difference in the efficiency if using r_9 cut to select events. This difference, as a systematic uncertainty, needs to be taken into account in the $\mathrm{H} \to \gamma\gamma$ signal modeling, where r_9 is used to category events, and thus events can migrate into another because of the uncertainty.

Variables	Descriptions
$E_{sc}^{raw}, \eta_{sc}, \phi_{sc}$	basic kinematic quantities
$E_{5\times5}, E_{3\times3}, E_{ps}/E_{sc}^{raw}$	basic shower shape variables, last one only for endcaps.
$\sigma_{i\eta i\eta}$	local $i\eta$ covariance of the seed cluster (bc)
σ_η, σ_ϕ	η, ϕ width of the supercluster(sc)
$E_{2\times5left/right/top/bottom}/E_{sc}^{raw}$	more shower shape variables
$E_{max,l/r/t/b}/E_{sc}^{raw}$	more shower shape variables
n_{vtx}	N.b. of vertexes.
$i\eta, i\phi$, and see text.	seed crystal η and ϕ index
$\eta(\phi)_{bc}^{local}$	local η, ϕ coordinates of the seed bc
$\delta_{bc,sc}^{\phi/\eta}$	relative η, ϕ coordinates of the seed bc to the sc
$(E_{top} - E_{bottom})/(E_{top} + E_{bottom})$	energy asymmetry
$(E_{left} - E_{right})/(E_{left} + E_{right})$	energy asymmetry
$\eta_{Gap}^{c,s,m}, \phi_{Gap}^{c,s,m}$	crystal, submodule and module relative coordinates
H/E	hadronic over electromagnetic energy

Table 5.1: The list of variables used for the regression energy correction.

5.5.2 Performance of the Regression Correction on $Z \to e^+e^-$

We use the $Z \to e^+e^-$ invariant mass distributions to compare the regression and the standard energy correction methods. Figures 5.14 and 5.15 show the comparison in simulation and data, respectively. Clearly, the regression method improves the performance, both in terms of the energy scale and the energy resolution. The electron energy scale, in the data distributions, has been corrected to match the simulation, using the method we will discuss in the next section.

In chapter 13 we will discuss the impact of the energy resolution improvement on the $H \to \gamma\gamma$ analysis.

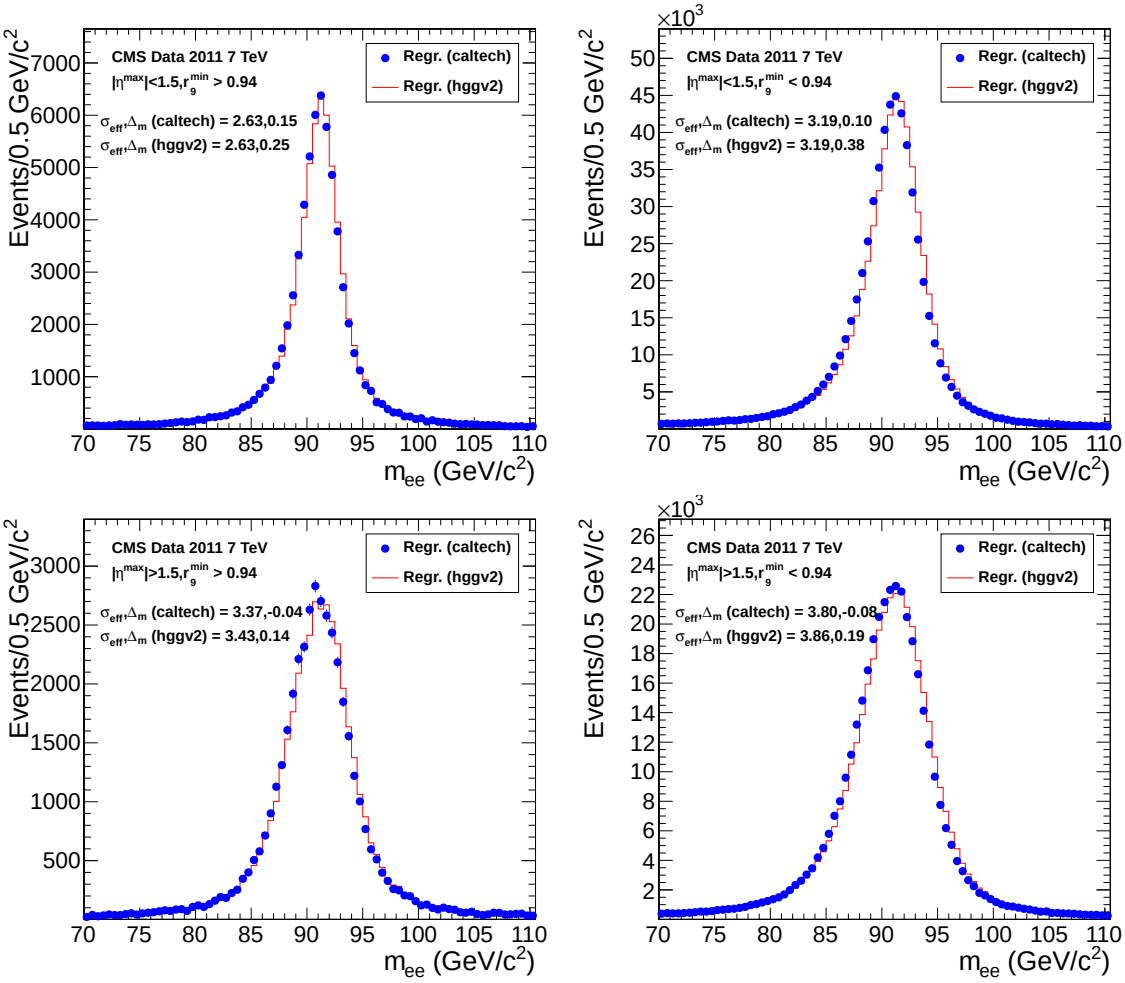

Figure 5.12: Comparison of the $Z \to e^+e^-$ invariant mass distributions in data between two versions of regression-based electron energy correction, one used in this thesis (labeled "caltech") and the one used in the so-called common analysis of the CMS Higgs analysis group (labeled "hggv2"), in each event category.

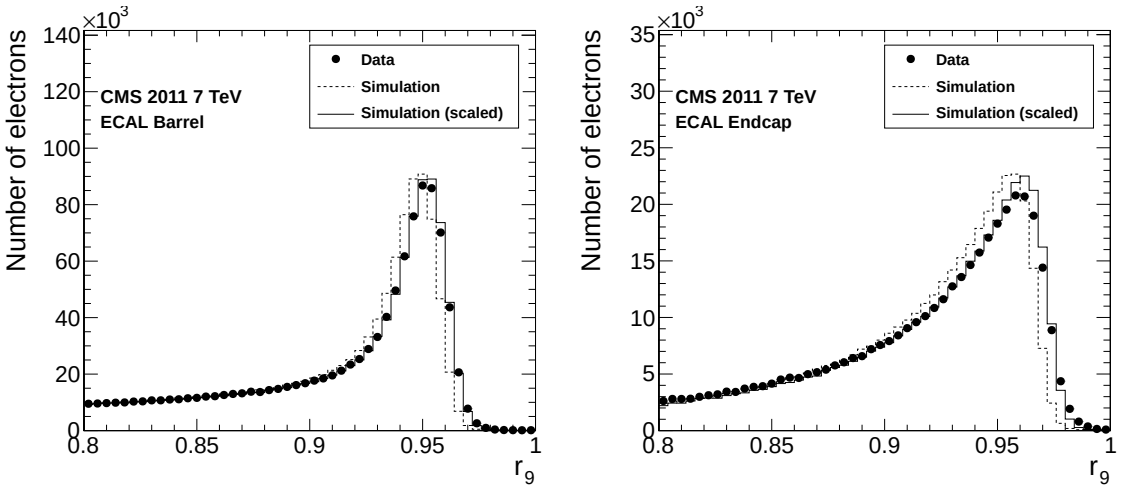

Figure 5.13: Electron r_9 distributions in data and simulation before and after the rescaling.

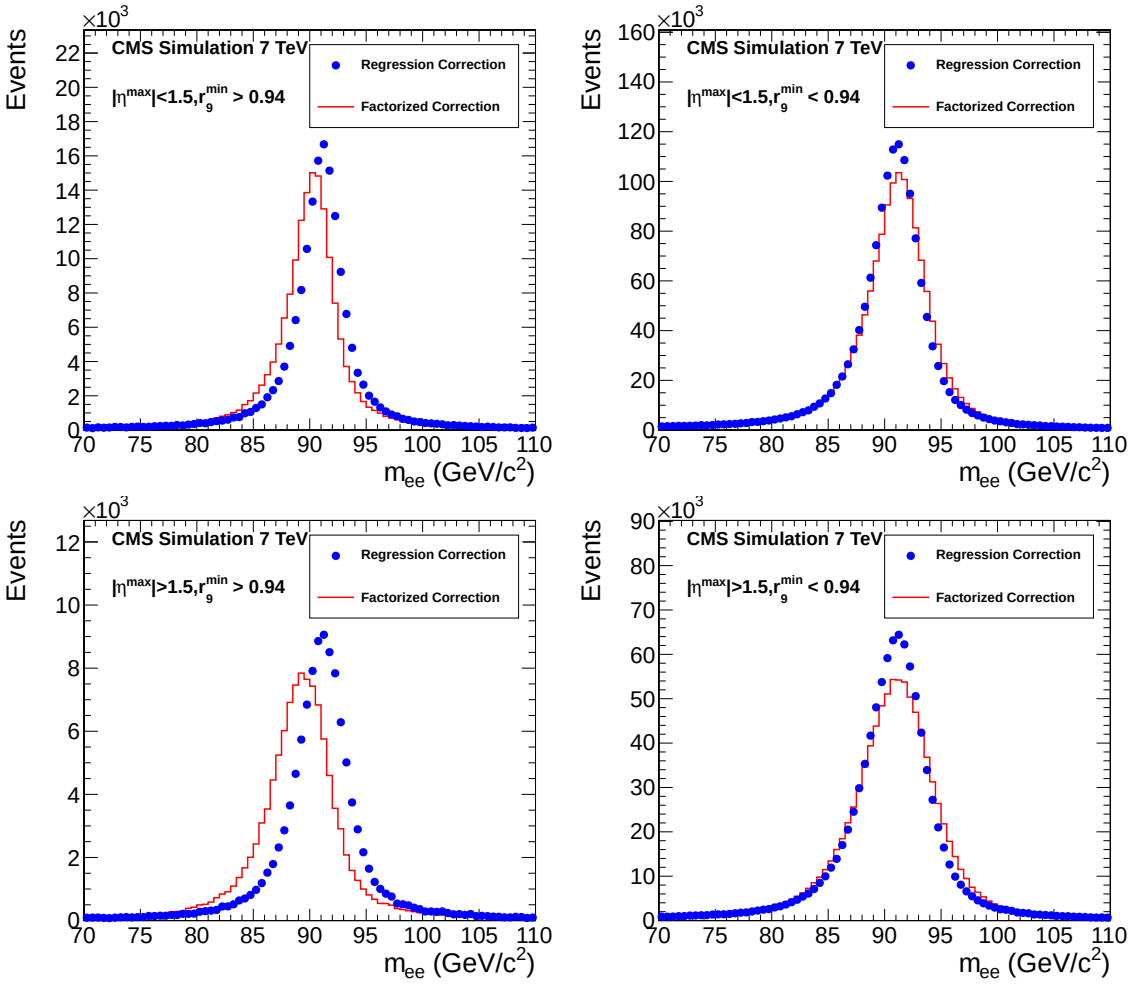

Figure 5.14: Comparison of the $Z \to e^+e^-$ invariant mass distributions in the simulation with the electron energies corrected with the factorized method, and with the regression technique, in each event category.

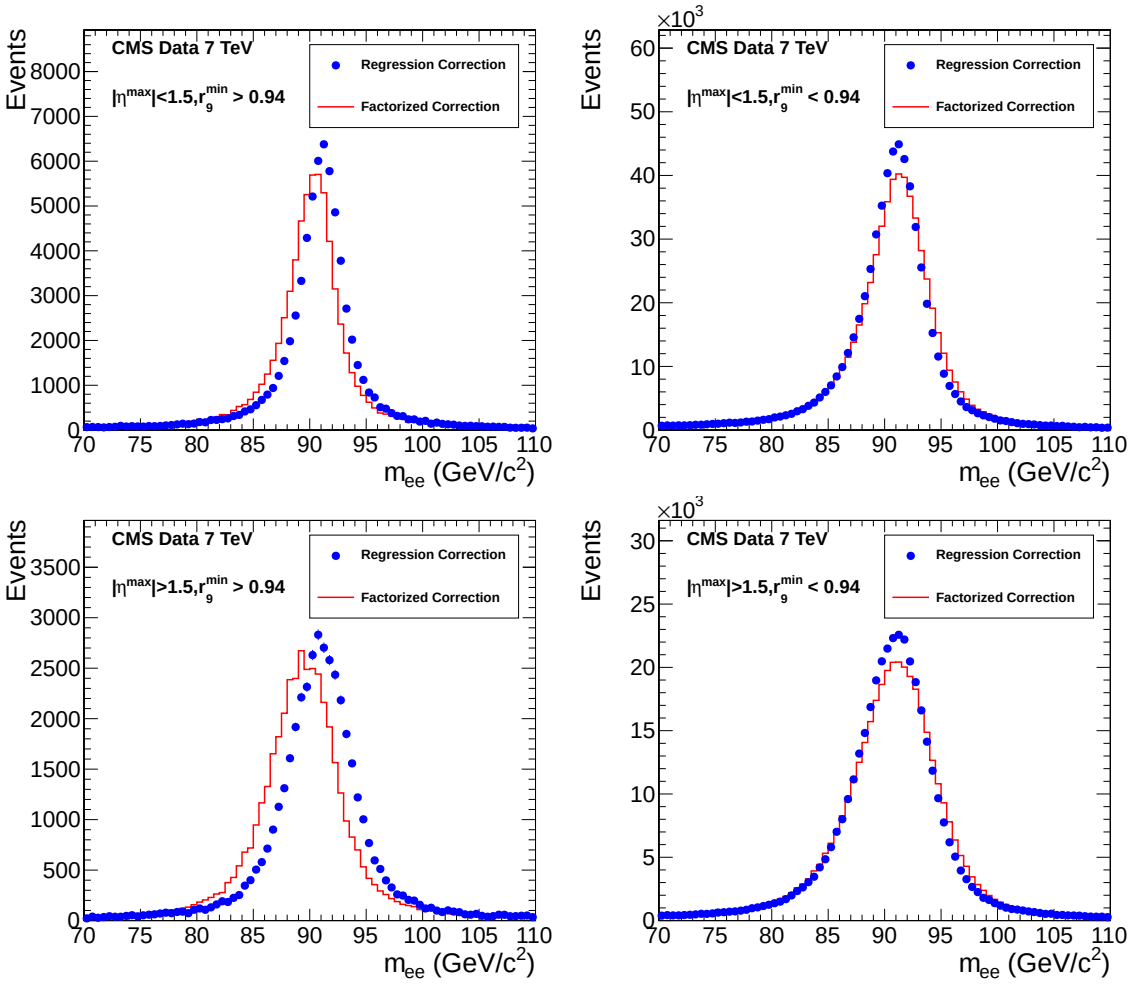

Figure 5.15: Comparison of the Z $\rightarrow e^+e^-$ invariant mass distributions in the data with the electron energies corrected with the factorized method, and with the regression technique, in each event category.

5.6 Energy Scale Correction

Correct determination of the ECAL energy scale is important for an accurate measurement of the mass for a potential $H \to \gamma\gamma$ signal, among many other aspects. To measure the mass, the energy scale in the data must be matched with that in the simulation because we model the signal distributions from the simulation.

We derive the energy scale correction for the data by comparing the fitted $Z \to e^+e^-$ peak values in data and simulation as follow:

$$\delta_E = \frac{E^{scale}_{data} - E^{scale}_{sim.}}{E^{scale}_{sim}} = \frac{\Delta m^{data}_{cb} - \Delta m^{sim}_{cb}}{m_Z + \Delta m^{sim}_{cb}}, \tag{5.11}$$

where E^{scale}_{data} and E^{scale}_{sim} denote the ECAL energy scale in data and simulation, respectively. If we precisely know the energy of the incident particle, the scale in data can be corrected by comparing the peak values of $E^{data}_{rec}/E^{data}_{true}$ and $E^{sim}_{rec}/E^{sim}_{true}$, where E^{data}_{rec} and E^{sim}_{rec} denote the reconstructed energy in the data and in the simulation, respectively.

This is the case in a test beam study where the electron's momentum is precisely measured. In simulation, we know the true electron energy E^{sim}_{true} from generator level. Therefore, the energy scale correction can be derived based on

$$\delta_E = \frac{(\frac{E^{data}_{rec}}{E^{data}_{beam}})_{peak} - (\frac{E^{sim}_{rec}}{E^{sim}_{gen}})_{peak}}{(\frac{E^{sim}_{rec}}{E^{sim}_{gen}})_{peak}}. \tag{5.12}$$

In situ, we can measure the reconstructed $Z \to e^+e^-$ peak and compare that with the simulation and derive the energy scale correction as in equation (5.11).

There are two main reasons that the scale in the data needs to be corrected. First of all, the response of each ECAL crystal varies as a function of time because of the radiation damage. While the laser correction is applied, it might not be perfect. On average, it might introduce an energy scale shift from run to run. Secondly, the detailed material representation in the simulation might not precisely match the real detector, which could introduce an energy scale difference between the data and the

simulation, for example as a function of η or r_9.

Therefore, the energy scale correction for data is derived in two steps, factorizing the time and material dependence.

- In step one, the 2011 runs are divided into six run periods. For each period, the scale correction is derived for each η category: $|\eta| < 1$, $1 < |\eta| < 1.5$, $1.5 < |\eta| < 2.0$ and $2 < |\eta| < 2.5$. The correction is derived for both sides of the ECAL ($\eta < 0$ and $\eta > 0$) separately to correct for a possible asymmetry. Figure 5.16 shows the time dependent correction in each η region. In the barrel, there is a trend that the energy scale in the data drops along time, and the outer barrel ($|\eta| > 1$) needs a larger corrections than the central barrel ($|\eta| < 1$). In the endcaps, the scale asymmetry is more pronounced, and there is a clear trend in the region of $1.5 < |\eta| < 2.0$ that the scale in the data increases with time.

- In step two, after applying the scale corrections from step one, the scale in each r_9 category is corrected separately in each $|\eta|$ category, using the 2011 data in its entirety. Figure 5.17 shows the r_9-dependent correction in each $|\eta|$ region. The amount of the correction is within 0.4%, except for the case of the outer barrel and high r_9.

The determination of the energy scale is subject to a number of systematic uncertainties. The r_9 distributions do not perfectly agree between data and simulation, even after the rescaling in simulation. The energy scale might also depend on the energy. To estimate these uncertainties we vary the r_9 and p_{T} cuts and rederive the energy scale corrections. The resultant differences are considered as the systematic uncertainties due to the r_9 difference and the p_{T} dependence. When applying the energy scale determined from $\mathrm{Z} \to \mathrm{e}^+\mathrm{e}^-$ to photons in the $\mathrm{H} \to \gamma\gamma$ search, there might be some systematic uncertainties related to the difference between the reconstruction of electrons and photons, and electron identification versus photon identification. To estimate these uncertainties, we apply the photon-tuned regressions to $\mathrm{Z} \to \mathrm{e}^+\mathrm{e}^-$, or vary the electron identification cuts and rederive the energy scale corrections. The resultant differences are added into the systematic uncertainties in quadrature.

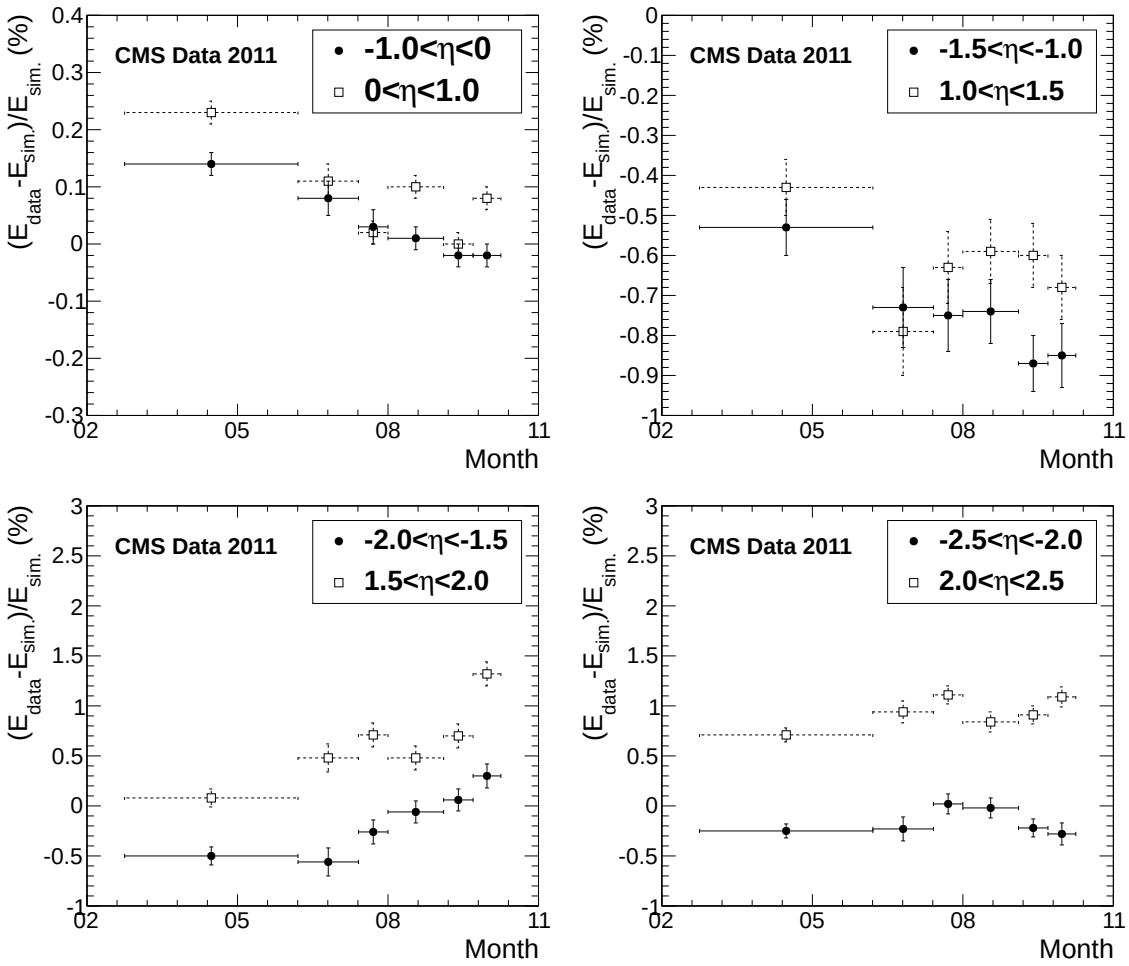

Figure 5.16: Energy scale correction derived from $Z \to e^+e^-$ for 6 time periods of 2011 in each η region of ECAL.

Table 5.2, second column, shows the total systematic uncertainty [92] of the energy scale correction in each $\eta \times r_9$ category.

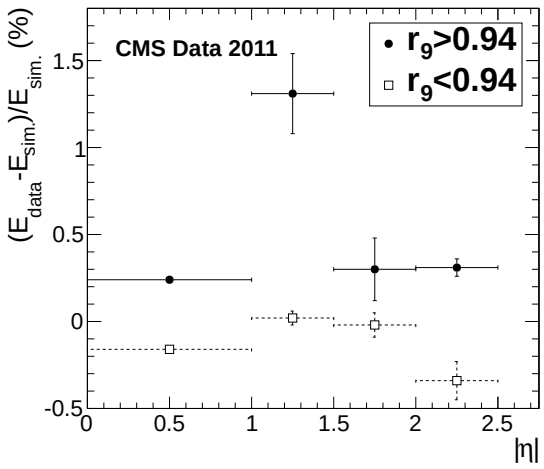

Figure 5.17: Energy scale correction derived from Z $\rightarrow$ e^+e^- for low and high r_9 electrons in different η regions of the ECAL.

Category	$\Delta E/E$ Syst (%)	σ_s Syst (%)
$\|\eta\| < 1, r_9 > 0.94$	0.19	0.22
$\|\eta\| < 1, r_9 < 0.94$	0.13	0.24
$1 < \|\eta\| < 1.5, r_9 > 0.94$	0.71	0.60
$1 < \|\eta\| < 1.5, r_9 < 0.94$	0.51	0.59
$1.5 < \|\eta\| < 2.0, r_9 > 0.94$	0.88	0.90
$1.5 < \|\eta\| < 2.0, r_9 < 0.94$	0.18	0.30
$2.0 < \|\eta\| < 2.5, r_9 > 0.94$	0.19	0.34
$2.0 < \|\eta\| < 2.5, r_9 < 0.94$	0.28	0.52

Table 5.2: Systematic uncertainties on the energy scale and energy smearings in different categories.

5.7 Energy Smearing in Simulation

We have shown in previous sections, e.g. figure 5.10, that the energy resolution in data is worse than that in simulation. This means that the crystal-to-crystal calibration condition we assumed in simulation, or the energy correction derived from simulation is overly optimistic. This has to be corrected for, in order to realistically model the H $\rightarrow$ $\gamma\gamma$ distributions starting from the simulation. Changing the calibration conditions in the simulation might improve the agreement, but it is not expected to be sufficient, since the energy correction is applied at the supercluster level. Unless

we tuned the simulation such that all input variables to the energy correction are well modeled, it is not likely that the $Z \to e^+e^-$ invariant mass distributions would agree between the data and the simulation.

Therefore, instead of tuning the simulation, we directly smear the reconstructed energy in the simulation. We derive the smearing for each category needed in the simulation in order to match the $Z \to e^+e^-$ mass distribution in the data as follows. Given the nominal electron energy in simulation E and the smearing σ_s, the smeared energy is a Gaussian-distributed random number,

$$E_{smeared} = Gaus(E, \sigma_s E) \,. \tag{5.13}$$

To derive the energy smearing, we perform a binned maximum likelihood fit to the $Z \to e^+e^-$ invariant mass distributions. The fit is done for the barrel and the endcaps separately. Because of the energy resolution dependence on η and r_9, we derive a energy smearing for each category of $\eta \times r_9$, as shown in table 5.3.

The procedure to perform the fit is the following:

- First of all, each e^+e^- pair is categorized based on the categories of the electron and positron. For example, if both the e^+ and e^- are in the same category (diagonal category) of low η and high r_9, then the pair is in category one. e^+ and e^- can be in different $\eta \times r_9$ categories (non-diagonal categories). This adds more statistics to the fit. In total, there are ten categories of e^+e^- pair with four categories for the individual electrons or positrons. The invariant mass distribution of $m_{e^+e^-}$ in data is then obtained for each of the ten categories.

- Secondly, in the simulation, for the current estimate of the extra smearing σ_s^i, where i refers to the e^+ or e^- category, the invariant mass distribution for each m_{ee} category is obtained. The likelihood is built, assuming Poisson fluctuations, as

$$L = P(\text{observed}|\text{expected}) = \prod_k \prod_b \frac{\mu_b^{n_b} e^{-\mu_b}}{n_b!} \,, \tag{5.14}$$

where k refers to the $m_{e^+e^-}$ category, b refers to the bin of the invariant mass distribution, and μ_b and n_b are the expected and observed number of events in that bin in the simulation and the data, respectively. The parameters σ_s^i are obtained when the likelihood function is maximized.

Table 5.3 shows the energy smearing obtained for each electron category. We have checked both the electron-tuned regression and photon-tuned regressions. The results agree within statistical errors.

Category	$\sigma_s(\%)$ (e-regression)	$\sigma_s(\%)$ (γ-regression)
$\|\eta\| < 1, r_9 > 0.94$	0.71 ± 0.03	0.73 ± 0.04
$\|\eta\| < 1, r_9 < 0.94$	0.89 ± 0.03	0.93 ± 0.03
$1 < \|\eta\| < 1.5, r_9 > 0.94$	1.38 ± 0.11	1.44 ± 0.11
$1 < \|\eta\| < 1.5, r_9 < 0.94$	2.08 ± 0.03	2.01 ± 0.04
$1.5 < \|\eta\| < 2.0, r_9 > 0.94$	2.43 ± 0.15	2.42 ± 0.16
$1.5 < \|\eta\| < 2.0, r_9 < 0.94$	2.41 ± 0.08	2.39 ± 0.08
$2.0 < \|\eta\| < 2.5, r_9 > 0.94$	2.80 ± 0.06	2.83 ± 0.06
$2.0 < \|\eta\| < 2.5, r_9 < 0.94$	2.51 ± 0.09	2.52 ± 0.08

Table 5.3: Energy smearing for each electron category. Electron-tuned and photon-tuned regressions give consistent results.

Figures 5.18 and 5.20 show the $Z \to e^+e^-$ invariant mass comparison between the data and the nominal simulation (before smearing), and between the data and realistic simulation (after smearing) in each $m_{e^+e^-}$ category in the barrel and end-caps, respectively. After applying the energy smearing, good agreement between the simulation and the data is observed. Here we compare the distributions in each of the ten $m_{e^+e^-}$ categories.

Figure 5.22 shows similar comparisons, in each event category defined according to the maximum value of η and minimal value of r_9 of the electron and positron. Figure 5.23 shows similar comparisons as well, but with photon-tuned regression correction applied to electrons or positrons. Good agreement with data is observed after energy smearing in simulation.

We have shown the way to realistically model the $Z \to e^+e^-$ invariant mass distributions from simulation. In the $H \to \gamma\gamma$ analysis, the photon energy is corrected with

the photon-tuned regression. The energy needs to be smeared as well to realistically model the $H \to \gamma\gamma$ invariant mass distributions.

In the $H \to \gamma\gamma$ analysis, we will use the energy smearing numbers from the electron-tuned regression, because those numbers are derived from $Z \to e^+e^-$ samples. To do this, we assume that the difference between the data and the simulation is the same for electrons and photons. This assumption is reasonable since the energy smearing is trying to account for two factors which are common to electrons and photons. First, the *in situ* crystal-to-crystal intercalibration is taken into account in the simulation, but might be overly optimistic. This contributes to the raw supercluster energy. Electrons and photons use the same supercluster algorithm. Therefore, any miscalibration effects contribute equally to the electron or photon energy measured as the raw supercluster energy. Second, the simulation-based energy correction in data does not work as well in the data as it does in the simulation, due to the fact that not all input variables for the energy corrections are well modeled by the simulation. In addition, the level of disagreement between the data and the simulation for electrons and photons should be similar, since (1) nearly all variables are electromagnetic shower based and electrons and photons have similar electromagnetic behavior in the ECAL crystals, and (2) electron and photon-tuned regressions are trained with the same list of input variables and with the same number of events. Therefore we conclude that the energy smearing from electron-tuned regression, derived from $Z \to e^+e^-$, is applicable to photons from $H \to \gamma\gamma$ decays.

We have discussed in the previous section the systematic uncertainties related to the energy scale. The systematic uncertainties of the energy smearing are studied in similar ways. Table 5.2, third column, shows the total systematic uncertainty [92] of the energy smearing in each $\eta \times r_9$ category.

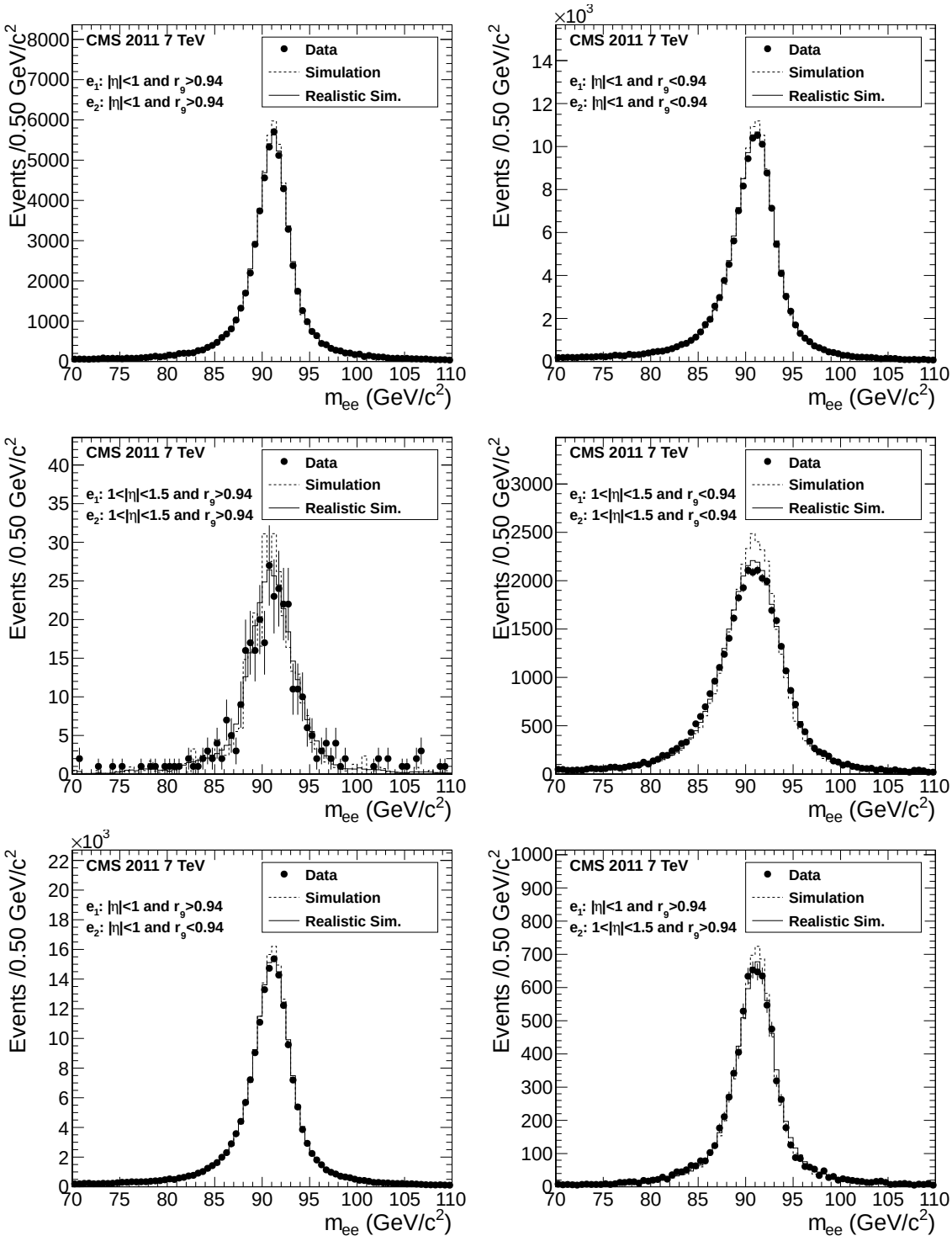

Figure 5.18: Comparison of $Z \to e^+e^-$ invariant mass distributions between the data and the nominal or realistic simulation in different $m_{e^+e^-}$ categories, where the e^+ and e^- are both in the barrel. The e^+ and e^- energies are corrected using electron-tuned regression.

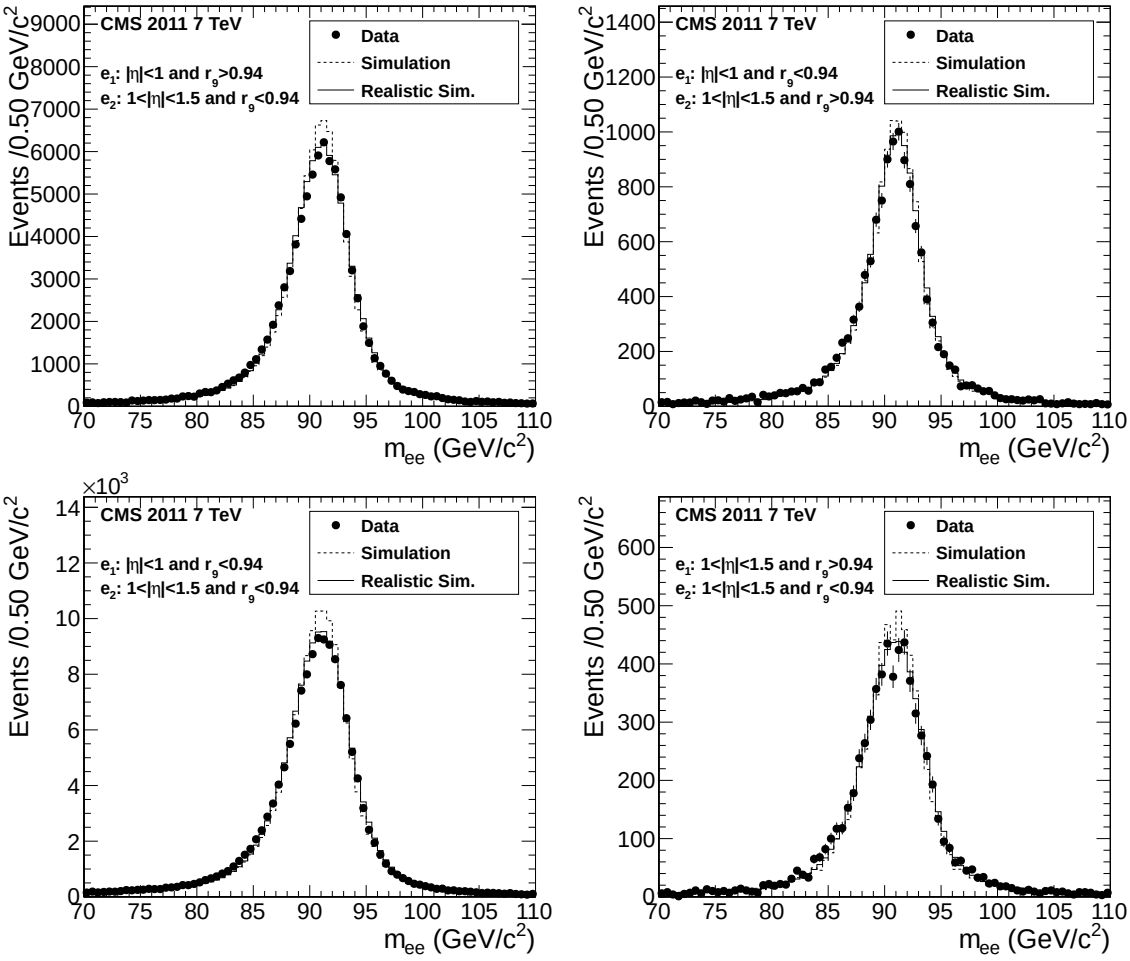

Figure 5.19: Same meaning as the caption of figure 5.18, the remaining 4 $m_{e^+e^-}$ categories are shown.

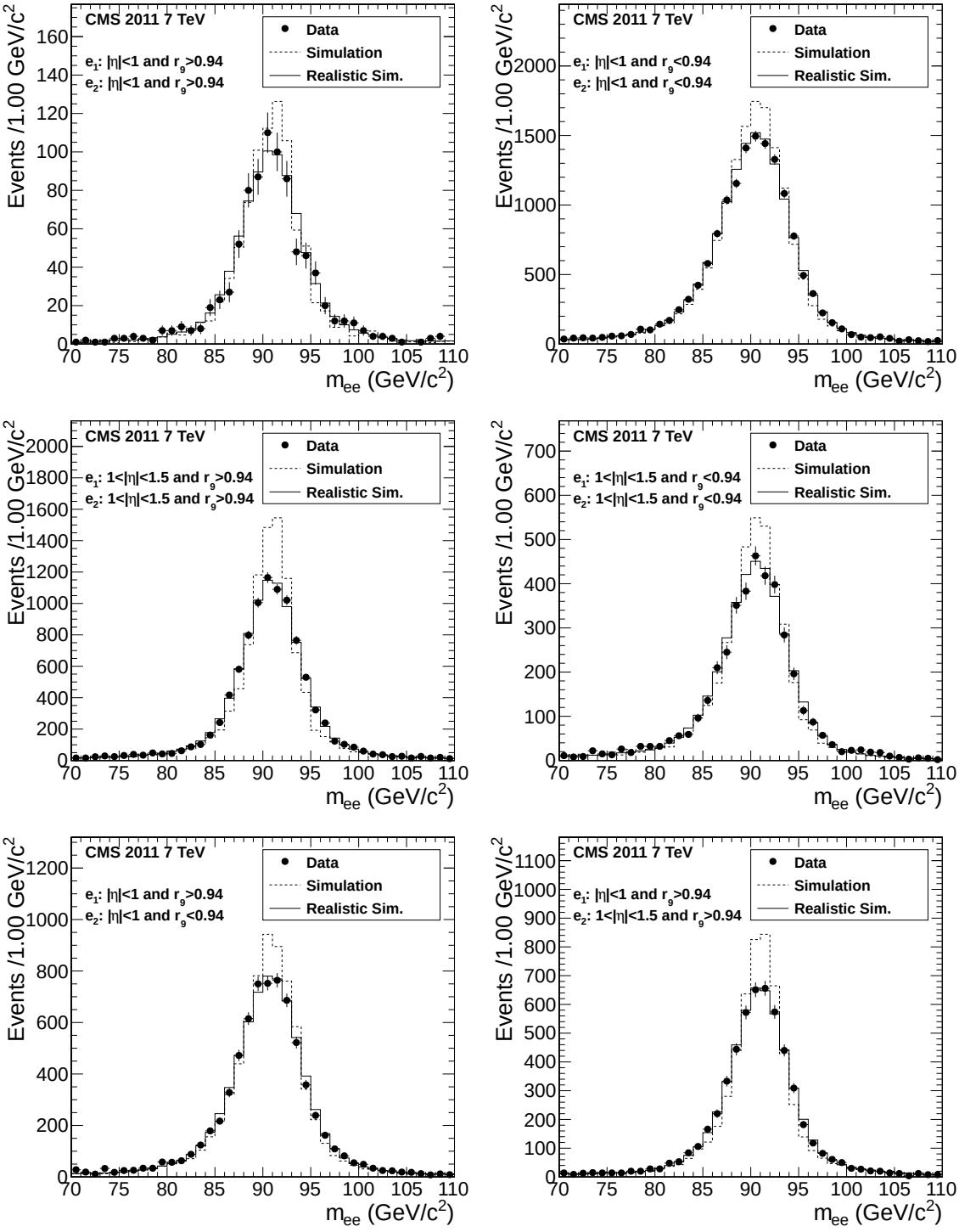

Figure 5.20: Same meaning as the caption of figure 5.18, except that endcaps are considered here.

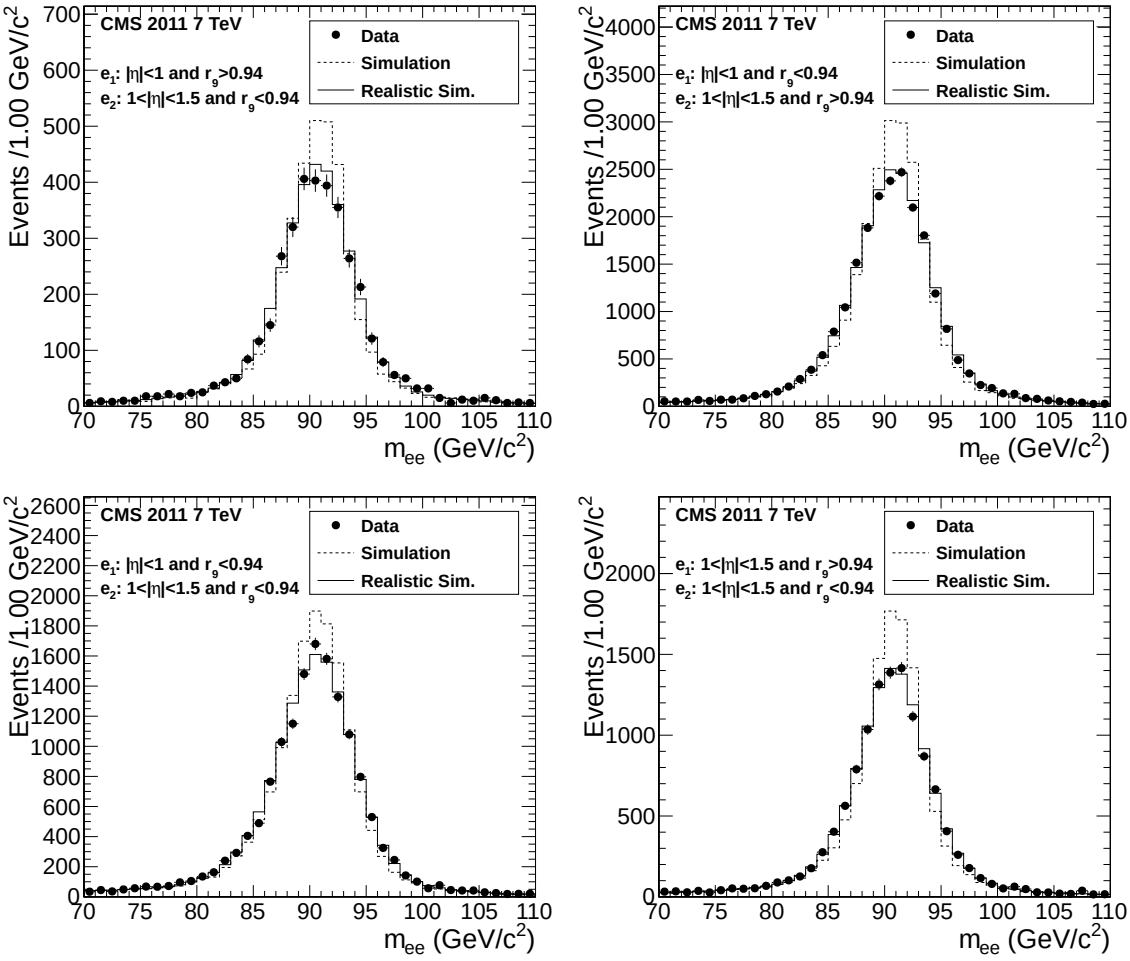

Figure 5.21: Same meaning as the caption of figure 5.20, the remaining 4 $m_{e^+e^-}$ categories are shown.

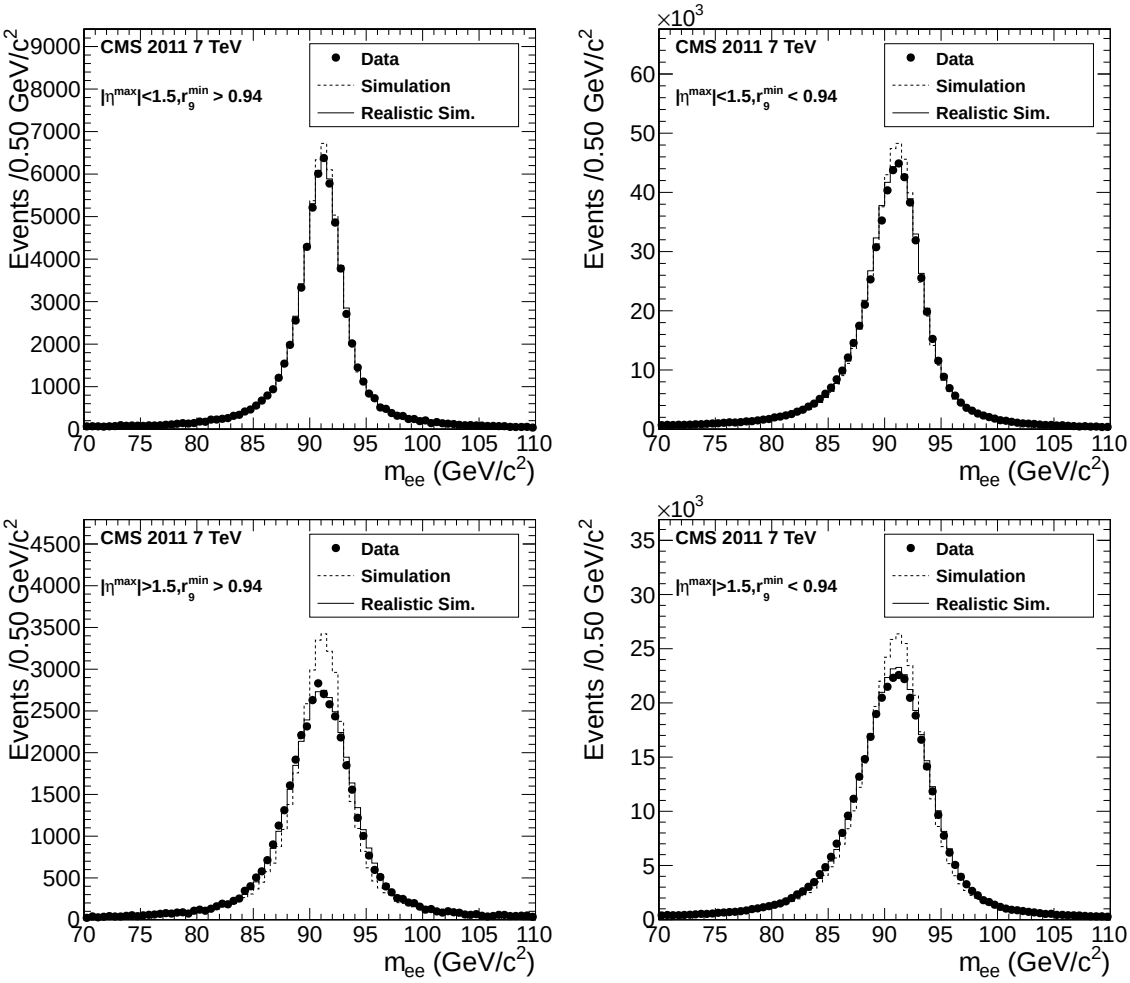

Figure 5.22: Same meaning as the caption of figure 5.18, except that here the comparison is made for each event category, indicated on each figure, also described in section 4.8.

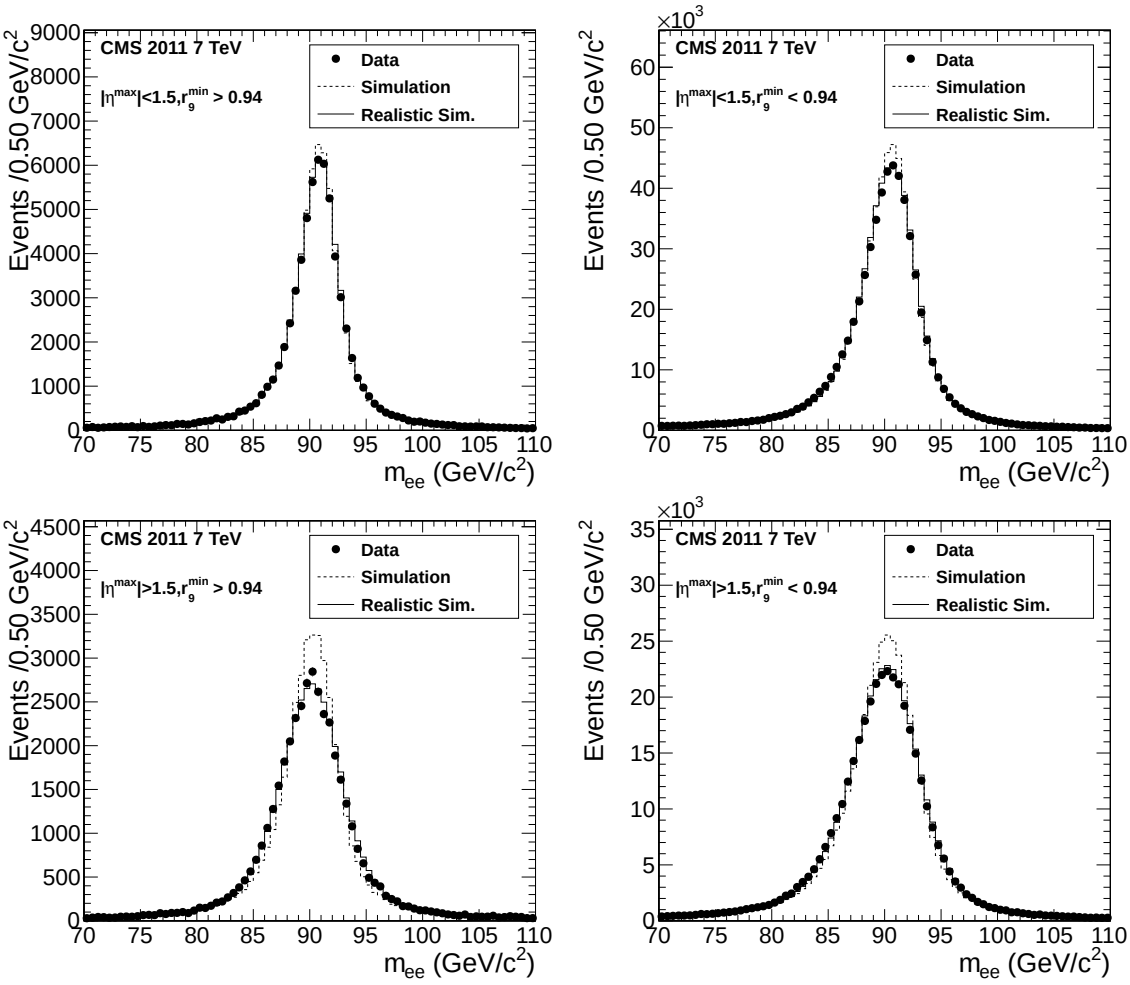

Figure 5.23: Same meaning as the caption of figure 5.22, except that here photon-tuned regression is used.

Chapter 6

Vertex Identification for $\mathrm{H} \to \gamma\gamma$

In order to reconstruct the invariant mass of $\mathrm{H} \to \gamma\gamma$ decays, the location of the Higgs boson production vertex is required. Misidentification of the true interaction vertex degrades the mass resolution. In events with multiple pileup interactions, it is challenging to correctly determine the Higgs boson production vertex.

The standard vertex identification algorithm used in CMS is based on the sum of the p_{T}^2 of all tracks associated with each reconstructed vertex. The primary vertex is identified as the one which has the largest $\sum p_{\mathrm{T}}^2$. As shown in figures 6.1 and 6.2, the probability to find the correct vertex, when the identified vertex is within 0.1 cm of the generated vertex of the Higgs boson, for $\mathrm{H} \to \gamma\gamma$ events increases with increasing $p_{\mathrm{T}}^{\gamma\gamma}$ and decreases with increasing pileup.

In order to improve the vertex finding efficiency, a multivariate (MVA) algorithm was developed [92]. The following variables are used to train the MVA algorithm to identify the correct vertex for $\mathrm{H} \to \gamma\gamma$ events:

- *sumpt2* $= \sum_i |\vec{p}_{\mathrm{T}}^{\,i}|^2$: the sum of the p_{T}^2 of all tracks associated with each reconstructed vertex, where $\vec{p}_{\mathrm{T}}^{\,i}$ is the momentum vector of the i^{th} track, projected on a plane transverse to the beam line.

- *ptbal* $= -\sum_i (\vec{p}_{\mathrm{T}}^{\,i} \cdot \frac{\vec{p}_{\mathrm{T}}^{\,\gamma\gamma}}{|\vec{p}_{\mathrm{T}}^{\,\gamma\gamma}|})$: the transverse momentum balance, removing tracks in a cone of $\Delta R < 0.05$ around each photon.

- *ptasym* $= |\sum_i \vec{p}_{\mathrm{T}}^{\,i}| - p_{\mathrm{T}}^{\gamma\gamma})/(|\sum_i \vec{p}_{\mathrm{T}}^{\,i}| + p_{\mathrm{T}}^{\gamma\gamma}$: the transverse momentum asymmetry, removing tracks near photons as above.

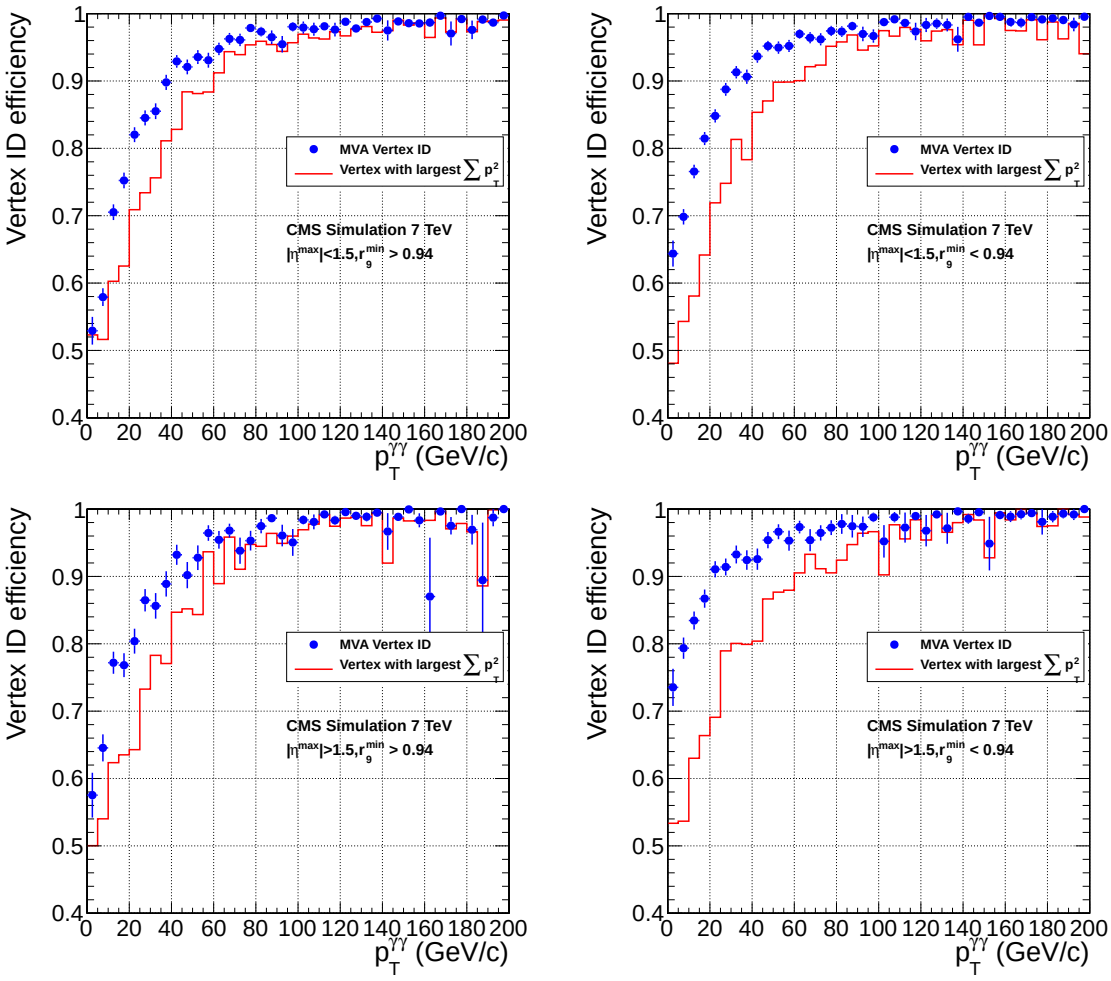

Figure 6.1: Standard and MVA vertex identification efficiencies as functions of the reconstructed p_T of the Higgs boson in different di-photon categories.

- *convpull* $= |z_{vertex} - z_{conv}|/\sigma_{conv}$: the compatibility between the estimated z position from the tracks of the photon conversions z_{conv} and the z position of each reconstructed vertex z_{vertex}, where σ_{conv} is the resolution on z_{conv} measured in the data.

Figures 6.1 and 6.2 show the improvement of the vertex identification efficiency using the MVA algorithm in different di-photon categories, as a function of $p_T^{\gamma\gamma}$ and the number of vertexes, respectively. The improvement is larger at small $p_T^{\gamma\gamma}$. The average improvement for $p_T^{\gamma\gamma}$ below 60 GeV is approximately 12% in all categories. Above 60 GeV, the improvement is approximately 3% on average.

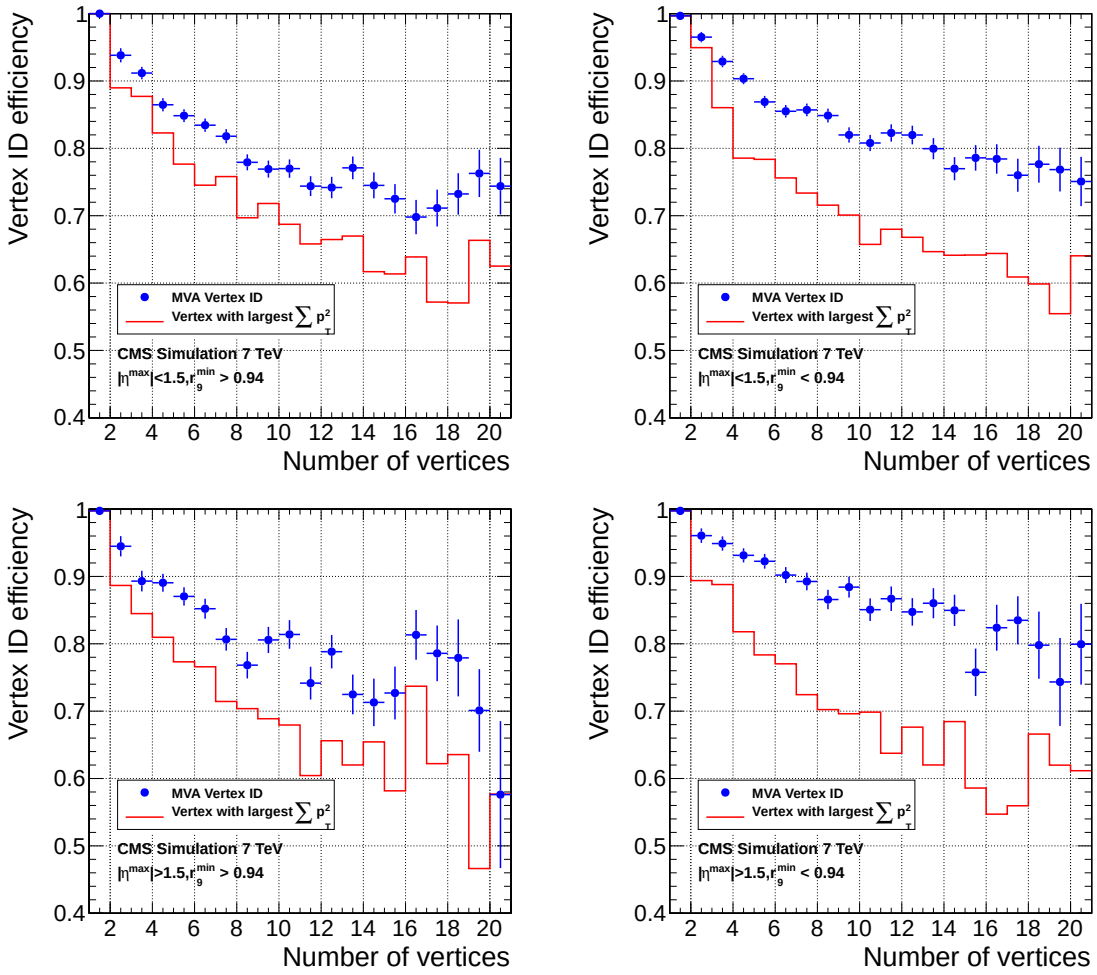

Figure 6.2: Standard and MVA vertex identification efficiencies as functions of the number of reconstructed vertices in the different di-photon categories.

Figure 6.3 shows the MVA vertex ID efficiency as a function of the Higgs boson mass. As shown, the overall efficiency is fairly high, varying between 80% and 90% among the di-photon categories. The di-jet category has highest efficiency among all categories, because on average $p_{\mathrm{T}}^{\gamma\gamma}$ in those events is higher. In general, the low r_9 categories have higher efficiencies than the high r_9 categories, due to the use of the conversion-related variable in the MVA.

Figure 6.4 shows the $\mathrm{H} \to \gamma\gamma$ mass resolution in events with a correct vertex, compared to events with a wrongly identified vertex. The resolution on average degrades by about 80% when the vertex is misidentified.

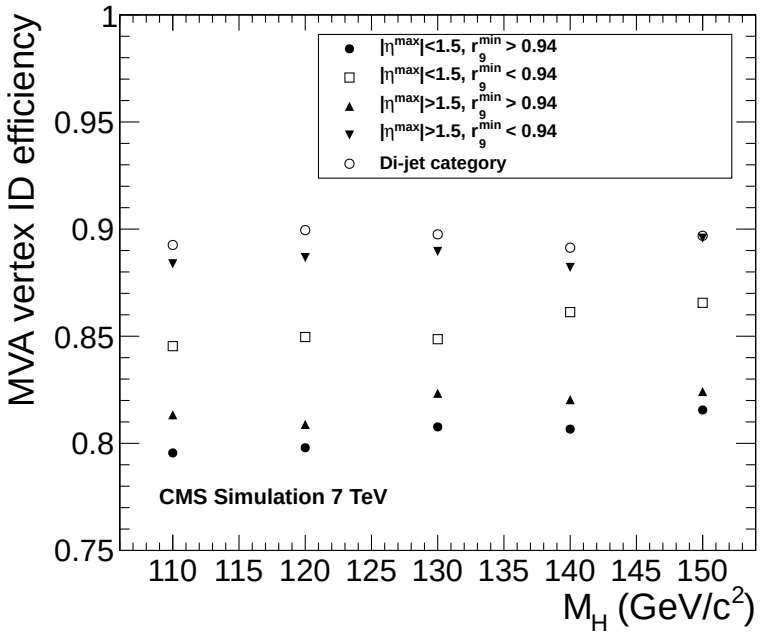

Figure 6.3: The MVA vertex ID efficiency as a function of the Higgs boson mass in the different di-photon categories.

In chapter 13 we will further discuss the improvement of the H $\rightarrow \gamma\gamma$ mass resolution, and its impact on the search sensitivity.

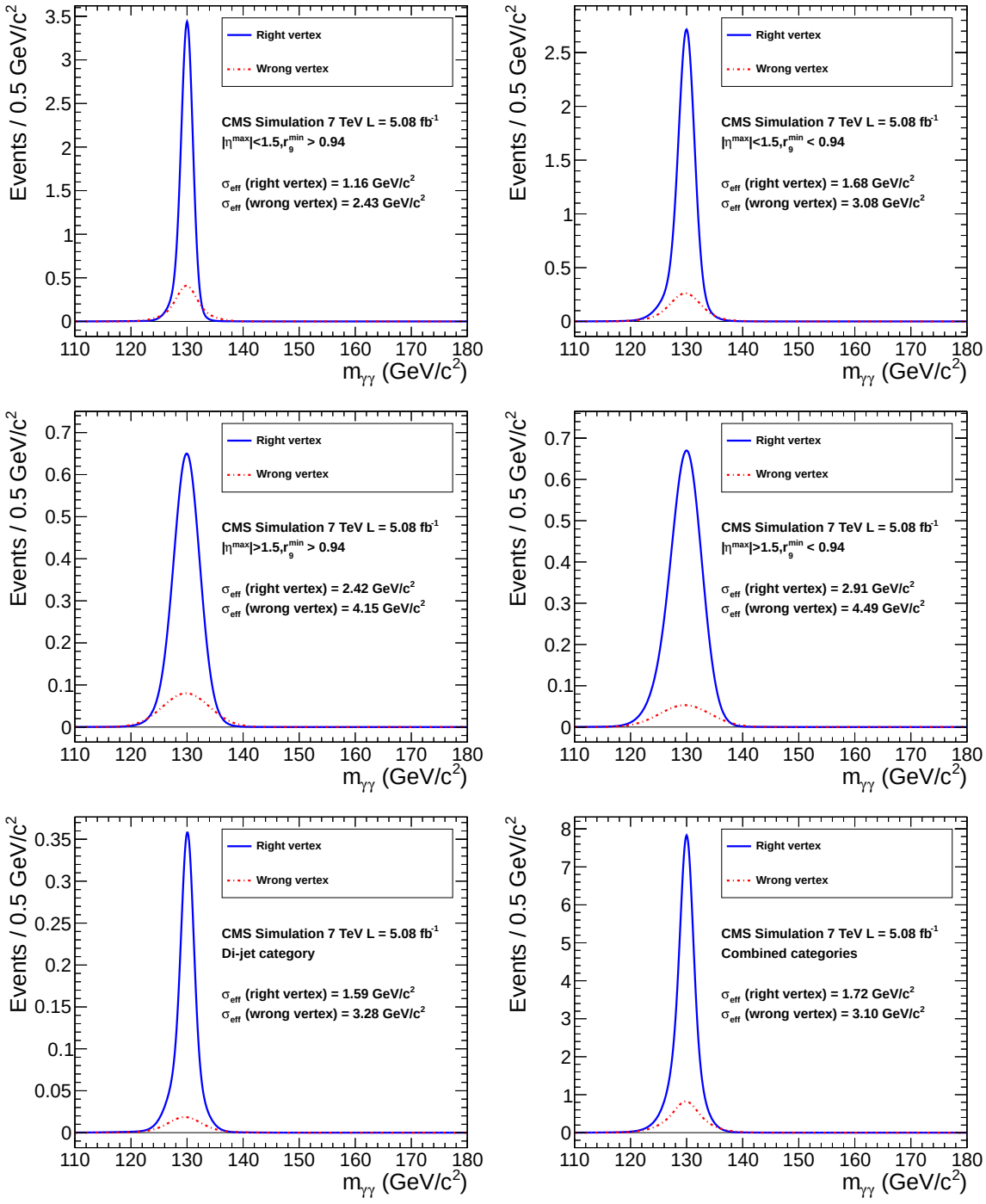

Figure 6.4: Expected H $\rightarrow \gamma\gamma$ invariant mass distributions at $M_H = 130$ GeV/c^2 in different di-photon categories, for events with a correct vertex, compared to events with a wrongly identified vertex.

Chapter 7

Photon Reconstruction and Identification

7.1 Photon Reconstruction

In CMS, standard photon objects are reconstructed starting from superclusters passing very loose identification criteria: of $E_{\mathrm{T}} > 10$ GeV and H/E < 0.2. In this analysis, instead of using the standard vertex identification, we use the MVA algorithm described in chapter 6 to identify the best vertex for a given event. The regression technique described in section 5.5 is used to correct the raw energy measurement from the supercluster algorithm, which provides an improvement over the standard factorized supercluster energy correction discussed in section 5.4. In the data, additional energy scale corrections, described in section 5.6, are applied to data to match the energy scale in the simulation.

The tracking system in CMS has $|\eta|$ coverage up to 2.4, thus to ensure an effective track isolation requirement only photons with $|\eta_{\mathrm{sc}}| < 2.5$ are considered, where η_{sc} is the measured pseudorapidity of the supercluster with respect to center of the CMS detector. Photons whose trajectory point to the transition region between the barrel and the endcaps, with $1.4442 < |\eta_{\mathrm{sc}}| < 1.566$, are not used in this analysis due to the poor energy resolution.

Category	Photon requirement	Common name
1	$\|\eta\|$ <1.4442, r_9 >0.94	Barrel, high r_9
2	$\|\eta\|$ <1.4442, r_9 <0.94	Barrel, low r_9
3	1.566< $\|\eta\|$ <2.5, r_9 >0.94	Endcap, high r_9
4	1.566< $\|\eta\|$ <2.5, r_9 <0.94	Endcap, low r_9

Table 7.1: Photon categories used for the "Cuts in Categories" selection.

7.2 Photon Identification

In the H $\to \gamma\gamma$ analysis, the main reducible background comes from γ+jet and multijet processes where jets are misidentified as photons. Their cross sections are many orders of magnitude larger than the H $\to \gamma\gamma$ signal. These backgrounds therefore must be suppressed by many orders of magnitude in order to achieve any sensitivity to the signal.

We use the "Cuts in Categories"(CiC) strategy, where cuts are applied in different photon categories, as defined in table 7.1. The categories are defined according to the photon energy resolution, which drives the sensitivity of the H $\to \gamma\gamma$ search. Cuts in different categories are separately tuned. In general, looser cuts are applied to the high r_9 categories, maintaining a higher efficiency because of the expected better resolution in those categories.

In general, isolated prompt photons from H $\to \gamma\gamma$ decays and electromagnetic showers from jets have very different properties. Photons are usually produced accompanied by no or little energy at angles close to the photon trajectory. Jets are produced in the fragmentation of quarks or gluons, consisting of many particles, mostly pions or kaons in a conelike geometrical configuration around the direction of the partons. Therefore, the shower width from a real photon is usually narrower than a jet. And more energies are expected in a cone around the photon direction if the photon is misidentified from a jet. These energies can be measured in both the tracker and the calorimeter systems, and are used to build highly discriminating variables to identify real photons.

The following variables are used to distinguish isolated prompt photons from back-

ground photons:

- Relative combined isolation using the selected vertex. This is defined as

$$\mathrm{Iso}^{\mathrm{rel}}_{\mathrm{vtx}} = \frac{\mathrm{Iso}^{\mathrm{track}} + \mathrm{Iso}^{\mathrm{ECAL}} + \mathrm{Iso}^{\mathrm{HCAL}} - \rho \mathrm{A}_{\mathrm{eff}}}{\mathrm{p}^{\gamma}_{\mathrm{T}}/50}\,, \tag{7.1}$$

  where $\mathrm{Iso}^{\mathrm{track}}$ is the scalar sum of the transverse momenta of tracks originating from the vertex identified by the algorithm described in chapter 6 and lying within a hollow cone of size $\Delta R < 0.3$ centered around a line joining the identified vertex to the ECAL supercluster. Only tracks whose trajectory are within ± 1 cm along the beam direction and within ± 0.1 cm transverse to the beam direction are considered, to reduce contamination from charged particles produced from pileup interactions. Tracks within an inner cone satisfying $\Delta R > 0.02$ are excluded, to avoid tracks produced by a conversion of the prompt photon.

  $\mathrm{Iso}^{\mathrm{ECAL}}$ is computed as the transverse energy sum of ECAL energy deposited in crystals located within a cone of size $\Delta R < 0.3$, centered around the supercluster position, excluding an inner veto cone of $\Delta R > 3.5$ crystals and an eta-slice of $\Delta\eta > 2.5$ crystals, in order to exclude the footprint of the signal photon, which can be extended in the ϕ direction in the case of converted photons. $\mathrm{Iso}^{\mathrm{HCAL}}$ is the sum of the energies of HCAL towers contained within an annulus of outer radius $\Delta R < 0.4$ and inner radius $\Delta R < 0.15$, centered on the ECAL supercluster position. The variable p^{γ}_{T} in equation (7.1) is scaled by 50 so that the denominator is close to 1 for a typical signal photon transverse momentum.

  The energy deposited within the isolation cone defined above is contaminated by energies from pileup (i.e., by the energy deposited by particles from other interactions in the same bunch crossing) and from the underlying event. Therefore, the efficiency of this isolation cut decreases with increasing pileup. In order to maintain the selection efficiency, the contribution to $\sum$Iso from pileups and the underlying event is estimated on an event-by-event basis, as the product of the measured energy density ρ of the event determined using the FastJet

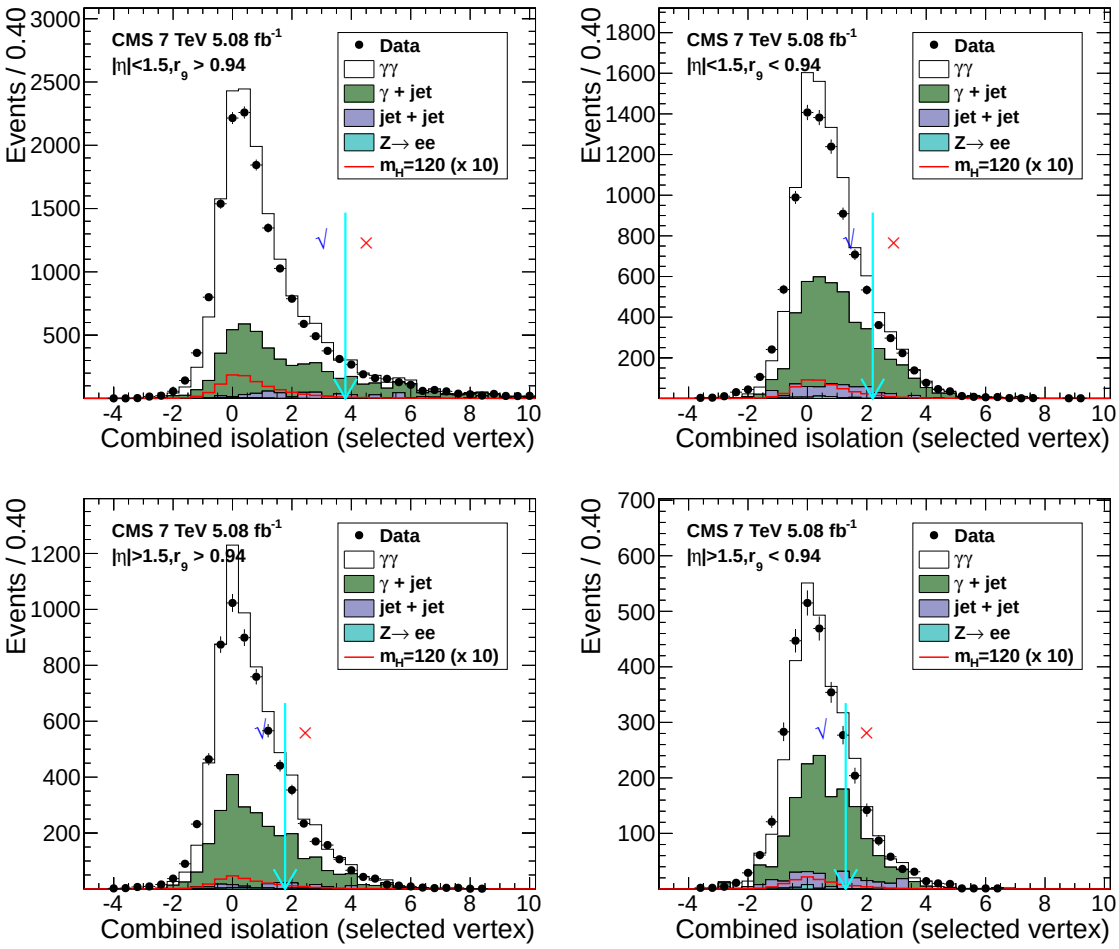

Figure 7.1: Distributions of the photon combined isolation for different photon categories, with $n-1$ cuts applied.

algorithm [93] and an effective area A_{eff}. A_{eff} is determined empirically as the ratio of the slope resulting from a linear fit of the mean value of $\sum$Iso as a function of the number of primary vertices, to the slope resulting from a linear fit of the value of ρ as a function of the number of primary vertices in $Z \to e^+e^-$ events. The value of A_{eff} for the definition of isolation described here is found to be 0.17.

Figure 7.1 shows the distributions of the isolation variable Iso^{rel}_{vtx}. Good agreement between data and simulation is observed. In this and all the following plots of photon identification variables, all other cuts are applied except the

one plotted. In addition, the invariant mass of two photons is required to be between 100 to 150 GeV/c^2.

- Relative combined isolation using the vertex giving highest Iso^{track}. This is defined as

$$\mathrm{Iso}^{\mathrm{rel}}_{\mathrm{worst\ vtx}} = \frac{\mathrm{Iso}^{\mathrm{track}}_{\mathrm{worst\ vtx}} + \mathrm{Iso}^{\mathrm{ECAL}} + \mathrm{Iso}^{\mathrm{HCAL}} - \rho \mathrm{A}_{\mathrm{eff}}}{\mathrm{p}^{\gamma}_{\mathrm{T}}/50}\,, \tag{7.2}$$

  where the three isolations have the same definition as in equation (7.1), except that the outer cone size ΔR is set to be 0.4. The value of the effective area $\mathrm{A}_{\mathrm{eff}}$ is 0.52 for this isolation variable definition. p^{γ}_{T} is recalculated with respect to the vertex giving the highest track isolation.

  Figure 7.2 shows the distributions of this isolation variable, with $n-1$ cuts applied.

- $\mathrm{Iso}^{\mathrm{track}}_{\mathrm{rel}}$. Relative tracker-only isolation, defined as

$$\mathrm{Iso}^{\mathrm{track}}_{\mathrm{rel}} = \frac{\sum \mathrm{Iso}^{\mathrm{track}}}{\mathrm{p}^{\gamma}_{\mathrm{T}}/50}\,, \tag{7.3}$$

  where $\mathrm{Iso}^{\mathrm{track}}$ is defined in equation (7.1). No pileup subtraction is required since only tracks which are consistent with the selected vertex are included in the sum. Figure 7.3 shows the distributions of the track-only isolation.

- H/E. The ratio of the hadronic energy to the electromagnetic energy is calculated as the ratio of the sum of HCAL tower energies within a cone of size $\Delta R < 0.15$ centered on the ECAL supercluster position, to the energy of the supercluster. Due to the 25 radiation length thickness of the ECAL crystals, signal photons have a value close to or equal to zero.

  Figure 7.4 shows the H/E distributions, with $n-1$ cuts applied.

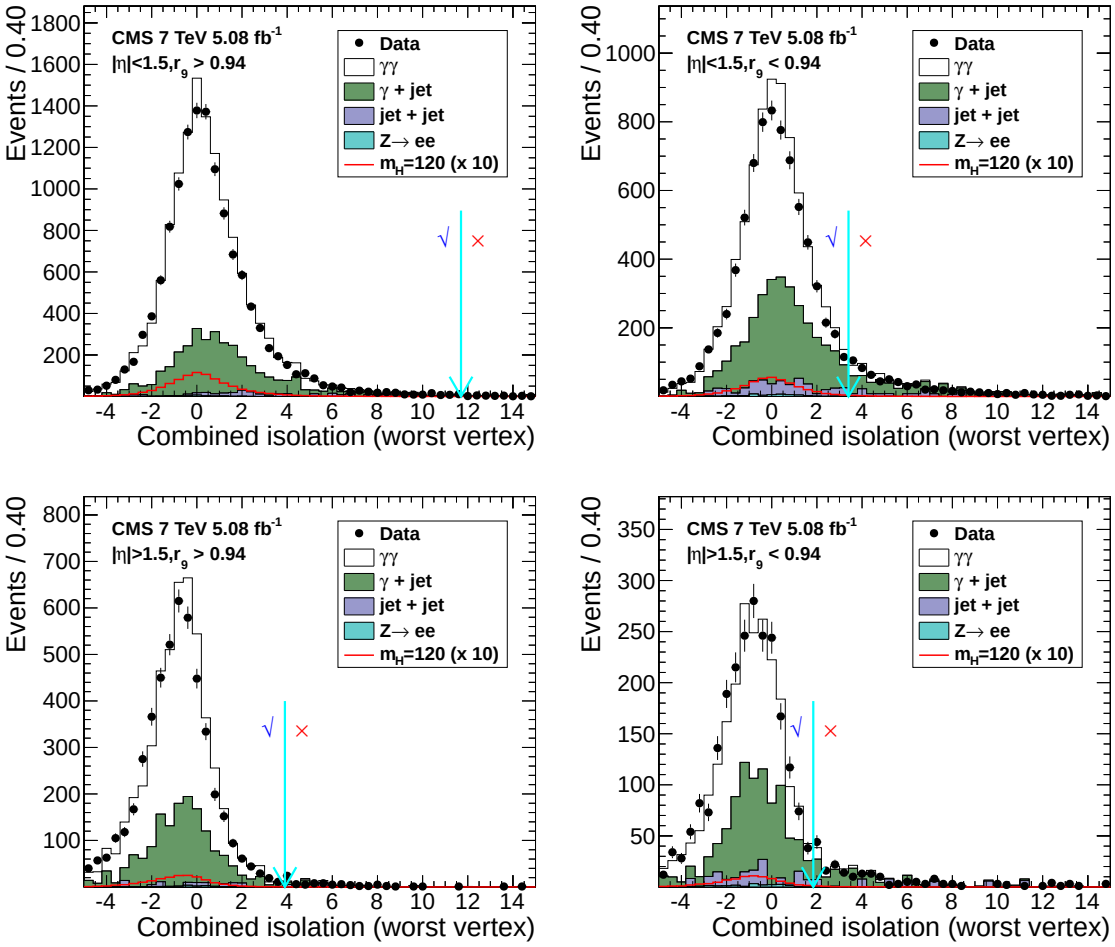

Figure 7.2: Distributions of the photon combined isolation (worst vertex) in different photon categories, with $n-1$ cuts applied.

- $\sigma_{i\eta i\eta}$. The transverse shape of the electromagnetic shower, which is defined as

$$\sigma^2_{i\eta i\eta} = \frac{\sum_i^{5\times5} w_i(\eta_i - \bar{\eta}_{5\times5})^2}{\sum_i^{5\times5} w_i}, \; w_i = \max\left(0, 4.7 + \ln\frac{E_i}{E_{5\times5}}\right), \qquad (7.4)$$

where E_i and η_i are the energy and pseudorapidity of the i^{th} crystal within the 5×5 electromagnetic cluster and $E_{5\times5}$ and $\eta_{5\times5}$ are the energy and η of the entire 5×5 cluster. The value of 4.7 in w_i controls the minimal energy fraction of individual crystals to be used in the calculation. For $E_{5\times5}$ =100 GeV, the minimal energy corresponds to approximately 0.9 GeV. The value of $\sigma_{i\eta i\eta}$ tends

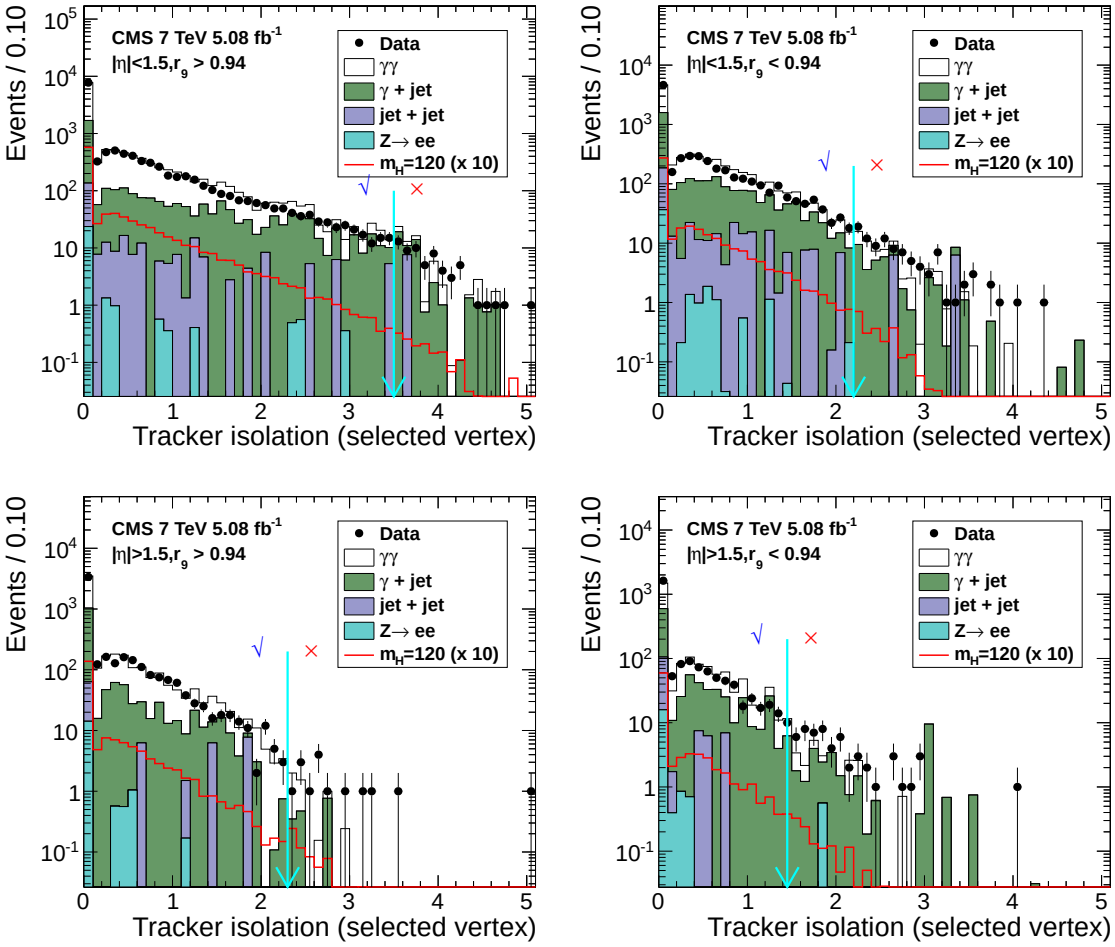

Figure 7.3: Distributions of the photon track isolation in different photon categories, with $n-1$ cuts applied.

to be smaller for isolated photons than for the background which is dominated by jets consisting of multiple π^0s each decaying to two photons.

Figure 7.4 shows the $\sigma_{i\eta i\eta}$ distributions, with $n-1$ cuts applied. There is an noticeable disagreement between data and simulation, especially for photons with $r_9 > 0.94$ both in the barrel and endcaps. At the time of the writing of this thesis, this difference is not completely understood, but it is believed to be caused mainly by the imperfect model of the electromagnetic showers in the GEANT4 simulation [94].

- r_9. A minimum threshold on r_9 is applied to photons in the ECAL endcaps in

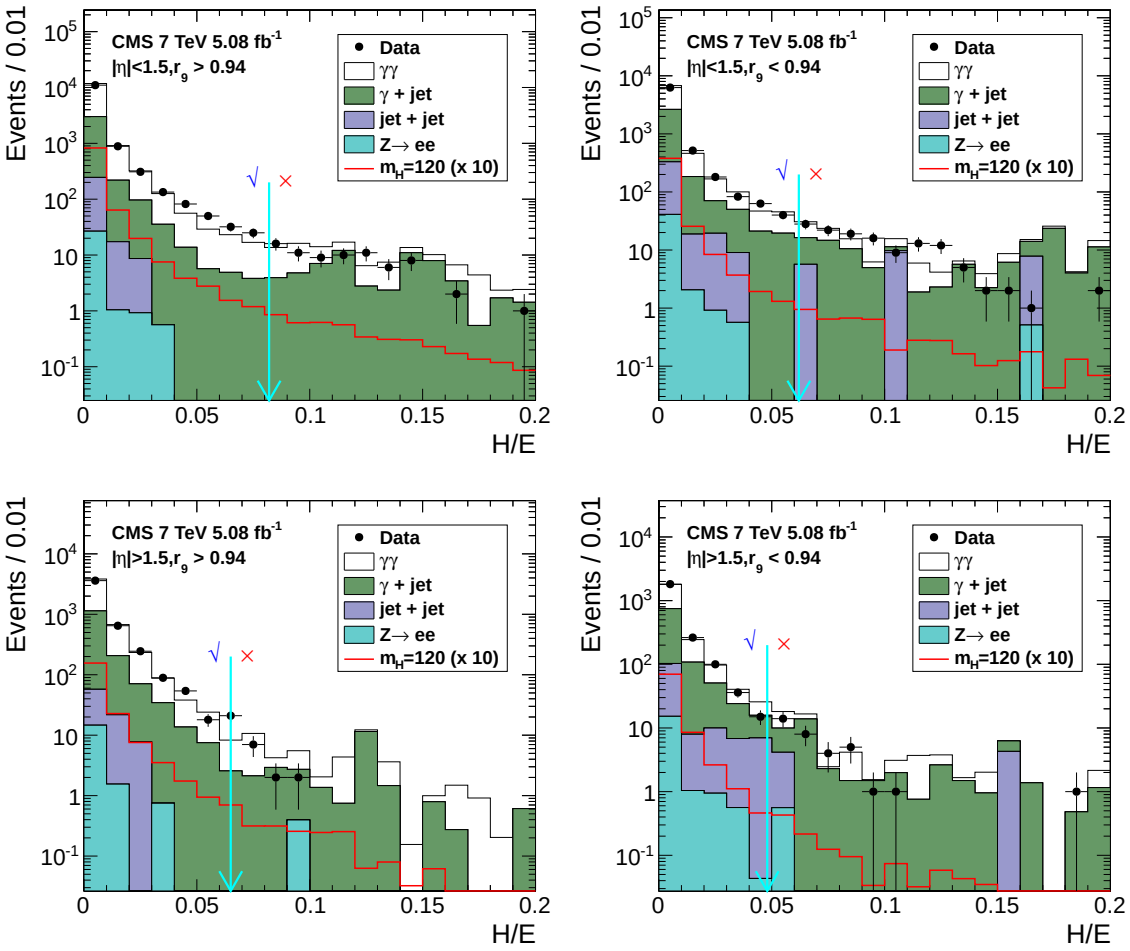

Figure 7.4: Distributions of the photon H/E in different photon categories, with $n-1$ cuts applied.

order to exclude very poorly reconstructed photons.

- $\Delta R_{e,\gamma}$. This is calculated as the minimal ΔR between the photon and every reconstructed electron's track in the event. If a photon is actually reconstructed from an electron, this variable is peaked at zero, while a real signal photon is usually far from an electron track. In the case of no reconstructed electrons in an event, this variable is set to be some large number, e.g., 99. Figure 7.7 shows the $\Delta R_{e,\gamma}$ distributions.

Figure 7.8 shows the photon identification efficiency in each photon category as a function of p_{T} or η for the leading and trailing photon from $\mathrm{H} \to \gamma\gamma$ decays.

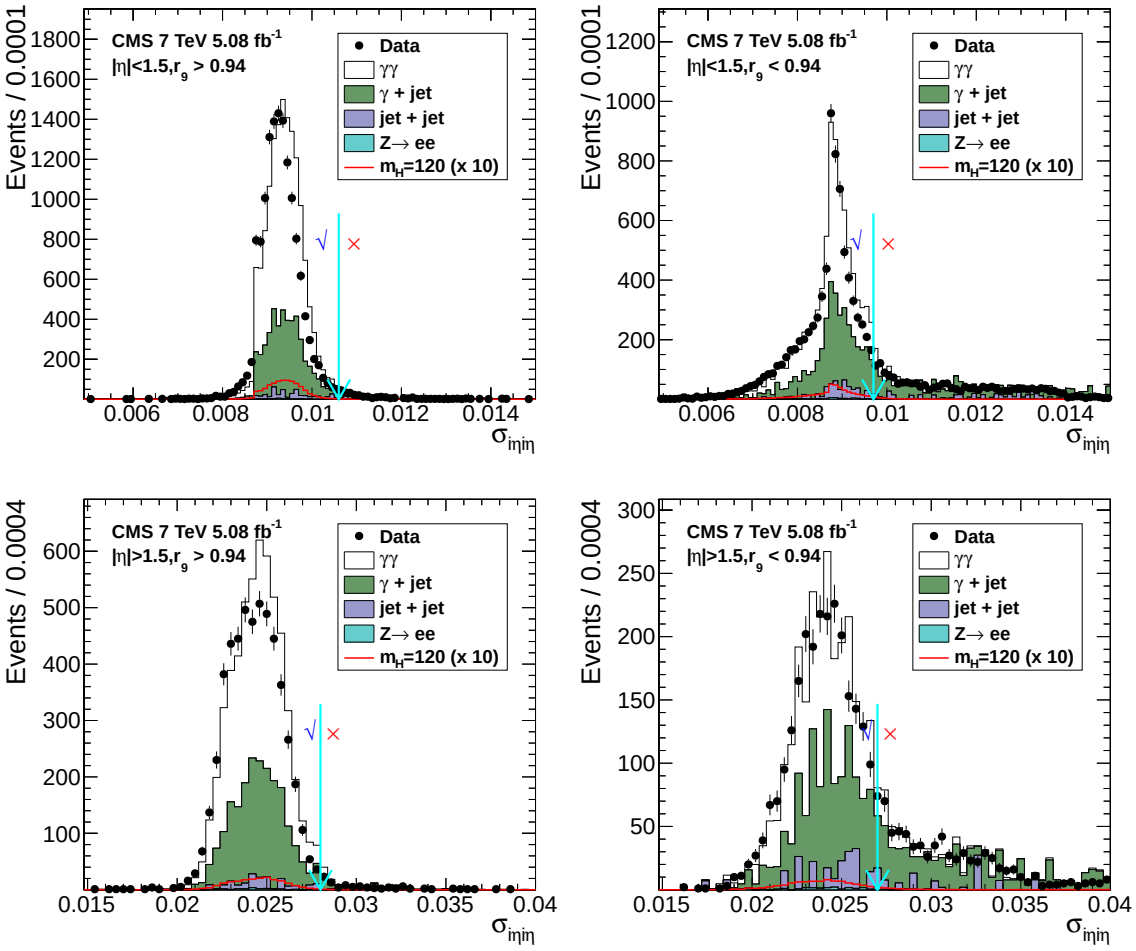

Figure 7.5: Distributions of $\sigma_{i\eta i\eta}$ in different photon categories, with $n-1$ cuts applied.

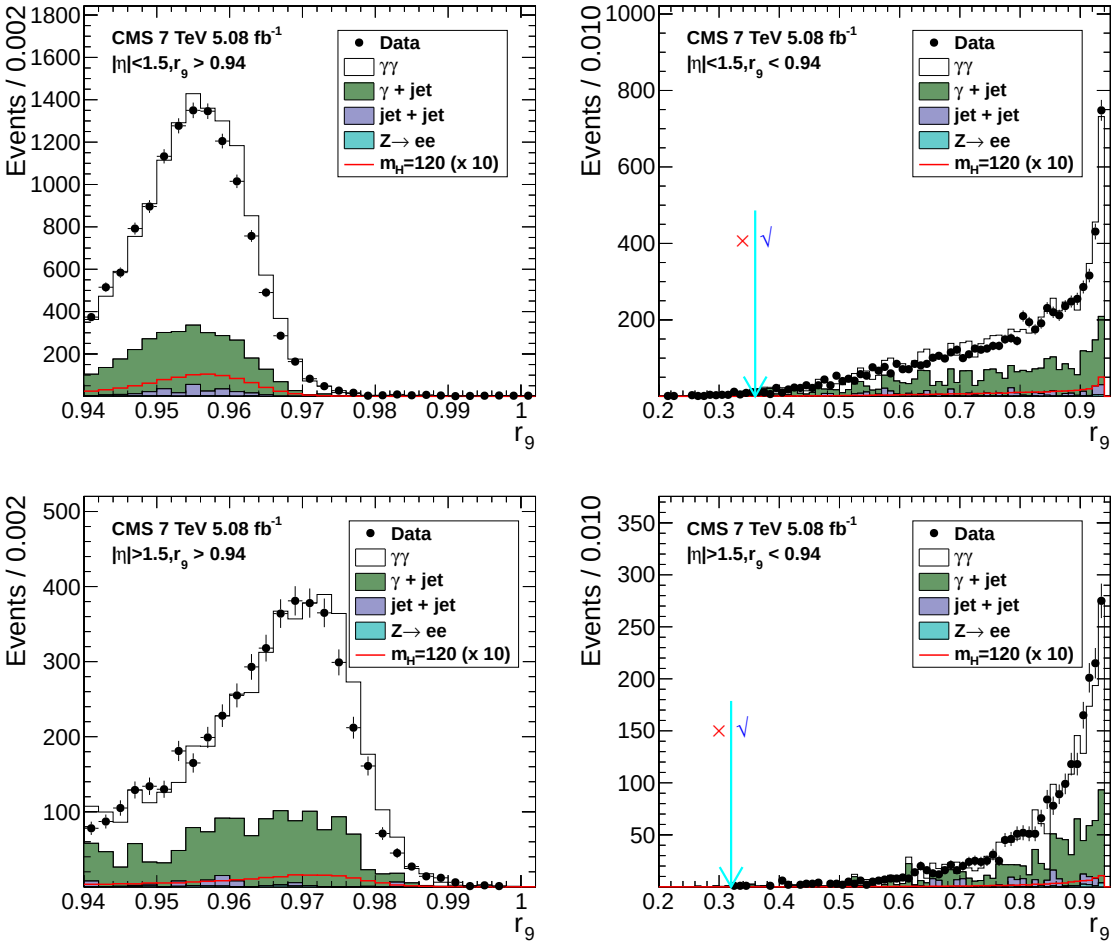

Figure 7.6: Distributions of the photon r_9 in different photon categories, with $n-1$ cuts applied.

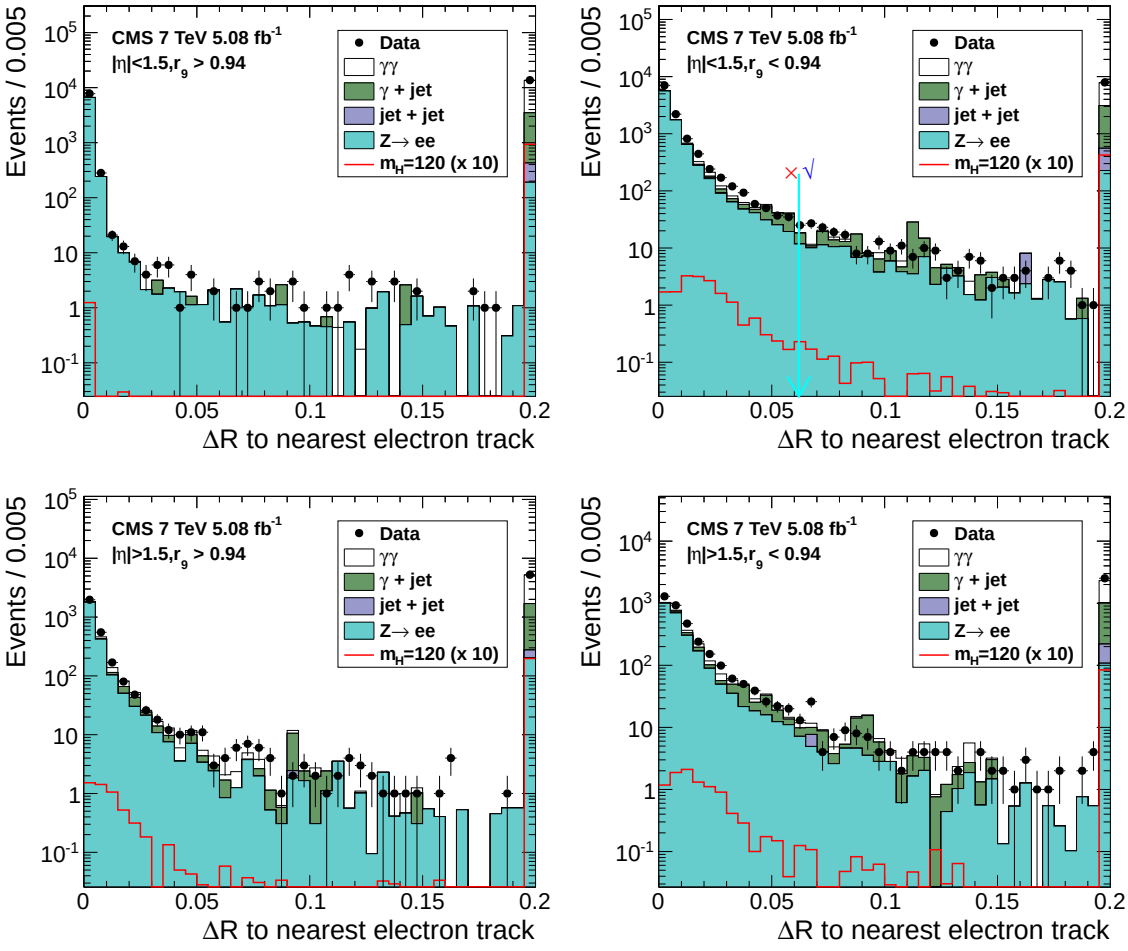

Figure 7.7: Distributions of photon $\Delta R_{e,\gamma}$ in different photon categories, with $n-1$ cuts applied.

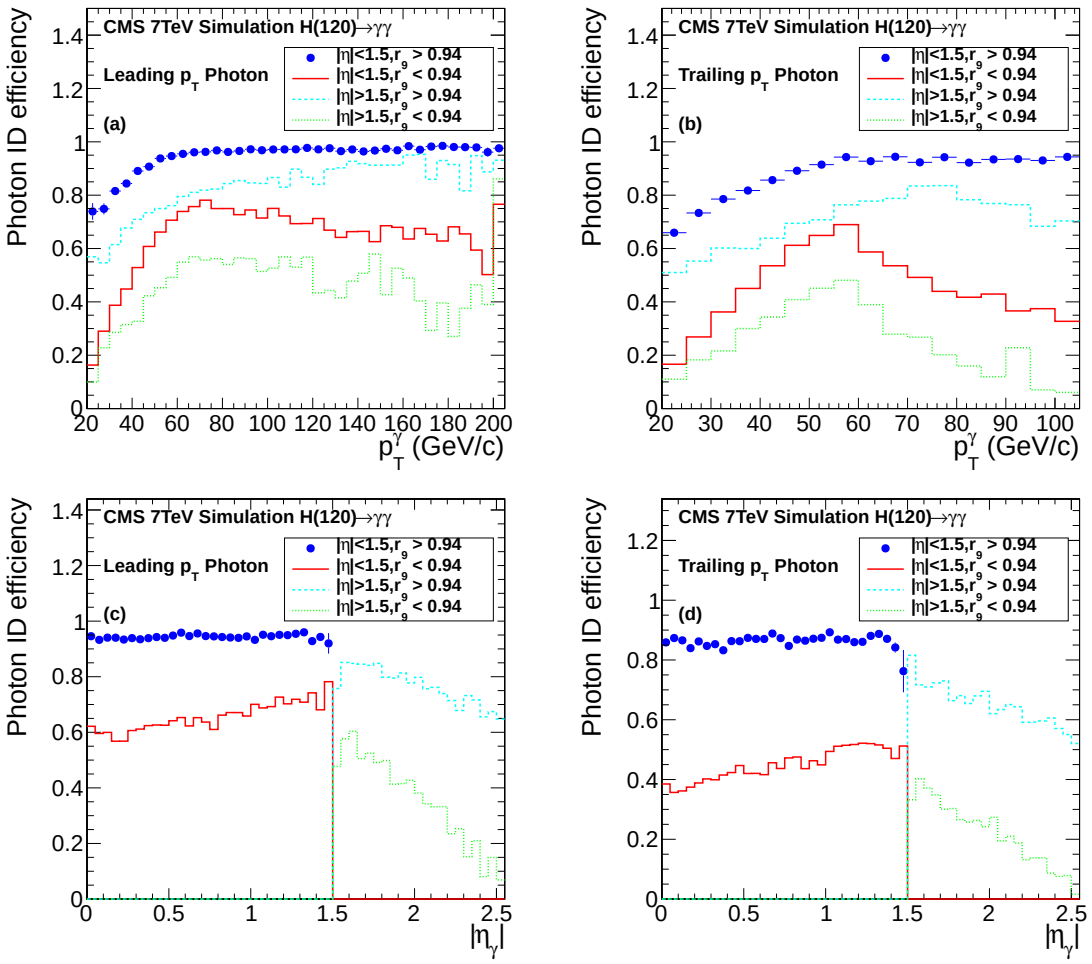

Figure 7.8: Photon identification efficiency in each photon category measured in H $\rightarrow \gamma\gamma$ simulation with mass 120 GeV/c^2. (a) Efficiency as a function p_{T} of the leading photon. (b) Efficiency as a function p_{T} of the trailing photon. (c) Efficiency as a function $|\eta|$ of the leading photon. (d) Efficiency as a function $|\eta|$ of the trailing photon.

7.3 Photon Identification Efficiency Correction

The efficiency of the CiC photon ID is measured with the Tag-and-Probe (TnP) technique, described further in section 16.4.1. We factorize the overall efficiency into two parts: the first part is the electron veto efficiency, and the second part is the combined efficiency of the remaining identification requirements.

We use photons from $Z \to \mu^+\mu^-\gamma$ decays to measure the first part, and electrons from $Z \to e^+e^-$ decays to measure the second part.

Figures 7.9 and 7.10 show the TnP $Z \to \mu^+\mu^-\gamma$ invariant mass distributions for the passing and failing probes in the four photon categories defined in table 7.1.

Table 7.3 [95] shows the TnP electron veto efficiencies in the data and in the simulation, ϵ_{data} and ϵ_{MC}, and their ratio $\epsilon_{\text{data}}/\epsilon_{\text{MC}}$, in the four photon categories. Table 7.3 [92] shows the TnP efficiencies of the second part measured with $Z \to e^+e^-$. The total uncertainties [92] on the photon ID efficiency correction are estimated to be 1% and 2.6% for barrel and endcaps, respectively.

The ratio of the TnP efficiency between the data and the simulation in each photon category is applied to the $H \to \gamma\gamma$ simulation when estimating the expected $H \to \gamma\gamma$ yield in each event category.

Category	ϵ_{data} (%)	ϵ_{MC} (%)	$\epsilon_{data}/\epsilon_{MC}$
1	$99.45^{+0.11}_{-0.12}$	$99.74^{+0.03}_{-0.04}$	$0.9971^{+0.0011}_{-0.0013}$
2	$97.21^{+0.41}_{-0.42}$	$98.14^{+0.08}_{-0.09}$	$0.9905^{+0.0042}_{-0.0043}$
3	$98.63^{+0.27}_{-0.33}$	$99.08^{+0.13}_{-0.14}$	$0.9954^{+0.0030}_{-0.0036}$
4	$91.85^{+0.75}_{-0.78}$	$92.67^{+0.27}_{-0.27}$	$0.9912^{+0.0080}_{-0.0083}$

Table 7.2: CiC photon ID TnP electron rejection cut efficiency measured in $Z \to \mu^+\mu^-\gamma$ events, in four different categories, using the 2011 data and MC simulation.

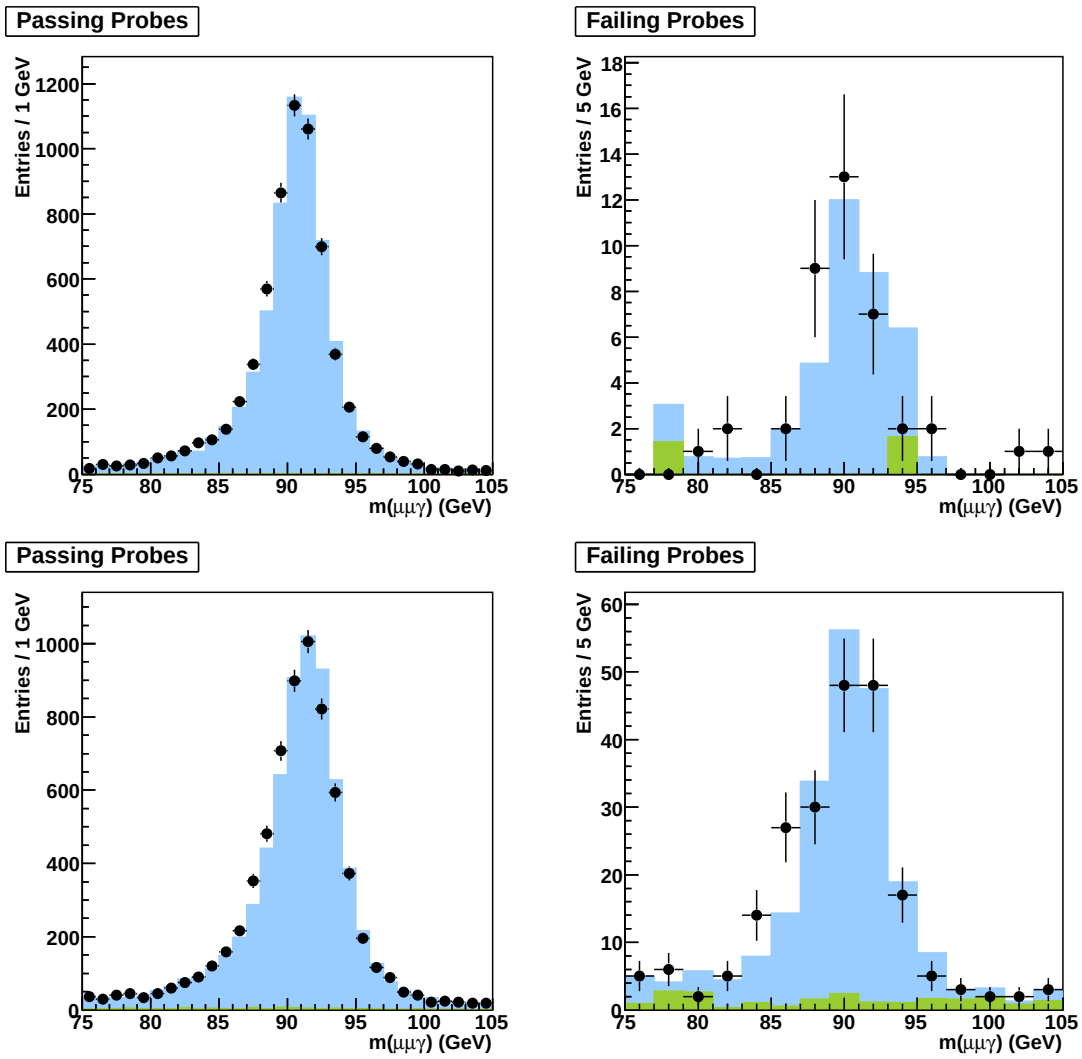

Figure 7.9: "Tag and probe" invariant mass distributions for the electron rejection cut in the ECAL barrel, obtained with $Z \to \mu^+\mu^-\gamma$ events. Black dots are data, solid blue histogram is the signal Monte Carlo, solid green the background (mostly Z+jets). The left column shows the distribution for the passing probes; the right column shows the failing probes. Top row shows photons in category 1 ($r_9 > 0.94$); bottom row shows photons in category 2 ($r_9 < 0.94$).

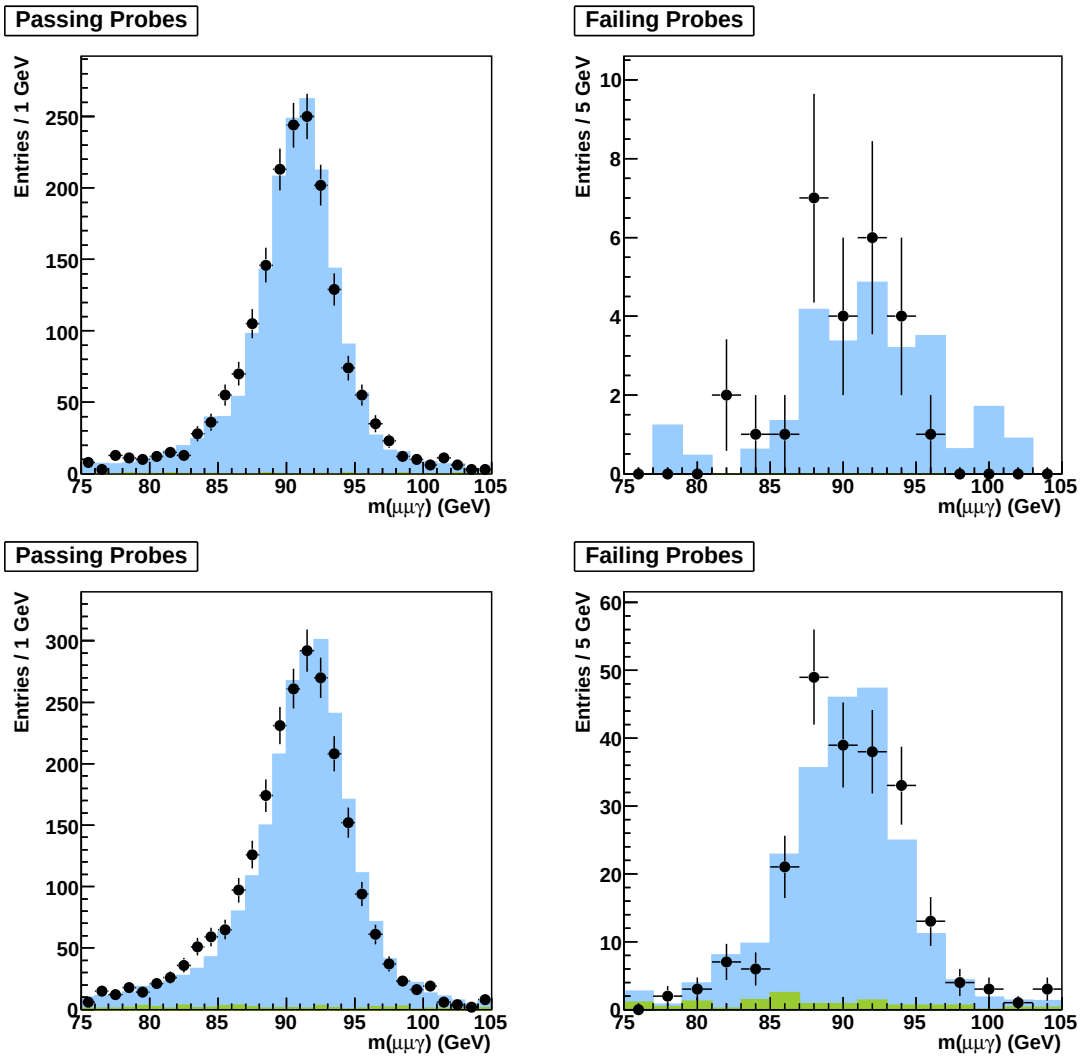

Figure 7.10:]
Same as figure 7.9 but for the photon probes in the endcaps instead of the barrel. Top row shows photons in category 3 ($r_9 > 0.94$), bottom row shows photons in category 4 ($r_9 < 0.94$).

Category	ϵ_{data} (%)	ϵ_{MC} (%)	$\epsilon_{data}/\epsilon_{MC}$
1	89.26±0.06±0.04	90.61±0.05	0.985±0.001
2	68.31±0.06±0.55	68.16±0.05	1.002±0.008
3	73.65±0.14±0.39	73.45±0.12	1.002±0.006
4	51.25±0.11±1.25	48.70±0.08	1.052±0.026

Table 7.3: CiC photon ID TnP efficiency measured in Z $\rightarrow$ e^+e^- events, in four different categories, using the 2011 data and MC simulation.

Chapter 8

Event Selection and Classification

8.1 Inclusive Categories

The signal significance in the search for a Higgs boson decaying to two photons is sensitive to the mass resolution and the signal-to-background yield ratio (S/B). The search sensitivity can be enhanced by subdividing the selected events into classes according to the indicators of mass resolution and predicted S/B, and combining the results of the search in each class.

Two simple classifiers are used: the minimum r_9 of the two photons, and the maximum pseudorapidity ($\eta_{\rm sc}$) of the two photons in the ECAL. Both classifiers are found to be effective in separating di-photon events with good mass resolution from those with worse resolution, and in separating events with a higher S/B from those with a lower S/B.

The selected events are split into four categories, discussed in section 4.8. Table 8.1 summarizes the requirements of each category. The four categories we considered in this section all select two photons without any other requirements on other objects in the events. Therefore they are called "inclusive" categories. The other type of category, selecting two jets in the events, is called the "di-jet" category, which we will describe in the next section.

In selecting events in the "inclusive" categories, additional cuts on the $p_{\rm T}^{\gamma 1}$ and $p_{\rm T}^{\gamma 2}$ of any two photons passing the photon ID are applied to further suppress backgrounds. To obtain similar invariant mass shapes over the different inclusive categories to

Event Category	Requirement
Inclusive 1	Both $\|\eta\|$ <1.4442, both r_9 >0.94
Inclusive 2	Both $\|\eta\|$ <1.4442, not both r_9 >0.94
Incluisve 3	Not both $\|\eta\|$ <1.4442, both r_9 >0.94
Inclusive 4	Not both $\|\eta\|$ <1.4442, not both r_9 >0.94
Di-jet tag	two jets

Table 8.1: Event categories used in the $H \to \gamma\gamma$ analysis.

simplify the background modeling, we apply cuts on $p_T^\gamma/m_{\gamma\gamma}$ instead of p_T^γ. Therefore, the photon transverse momentum cut is not a fixed value but depends on $m_{\gamma\gamma}$. These cuts on the leading and subleading photon are fixed to be 1/3 and 1/4, respectively. For a Higgs boson with mass 120 GeV/c^2, the cuts on the p_T of the leading photon and subleading photon become 40 and 30 GeV respectively. If in one event there are more than two photons satisfying these requirements, the pair with highest scalar sum of the p_T^γ of the two photons is finally selected.

Figure 8.1 shows the $p_T^{\gamma\gamma}$ distributions from the data and the simulation after the event selections described above, in different "inclusive" categories. In these plots and all others in this section, the invariant mass of the two photons is required to be between 100 and 150 GeV/c^2. Figures 8.1, 8.2, and 8.3 show the $p_T^{\gamma\gamma}$, $\eta^{\gamma\gamma}$, and $\Delta\phi^{\gamma\gamma}$ distributions, respectively. Figures 8.4 and 8.5 show the p_T distributions of the leading and the trailing photon, respectively. Figure 8.6 shows the invariant mass distributions in each event category. In each of these plots, the irreducible background from prompt di-photon production, as well as the reducible γ+jet and multijet and $Z \to e^+e^-$ backgrounds are shown. The simulated distribution of a 120 GeV/c^2 Standard Model Higgs boson decaying into two photons is also shown, magnified by a factor of 10 for visibility. In general, the prediction from the simulation is consistent with the observed data. However, one should note that the determination of the backgrounds for $H \to \gamma\gamma$ is fully data driven, which we will describe in following chapters of this thesis.

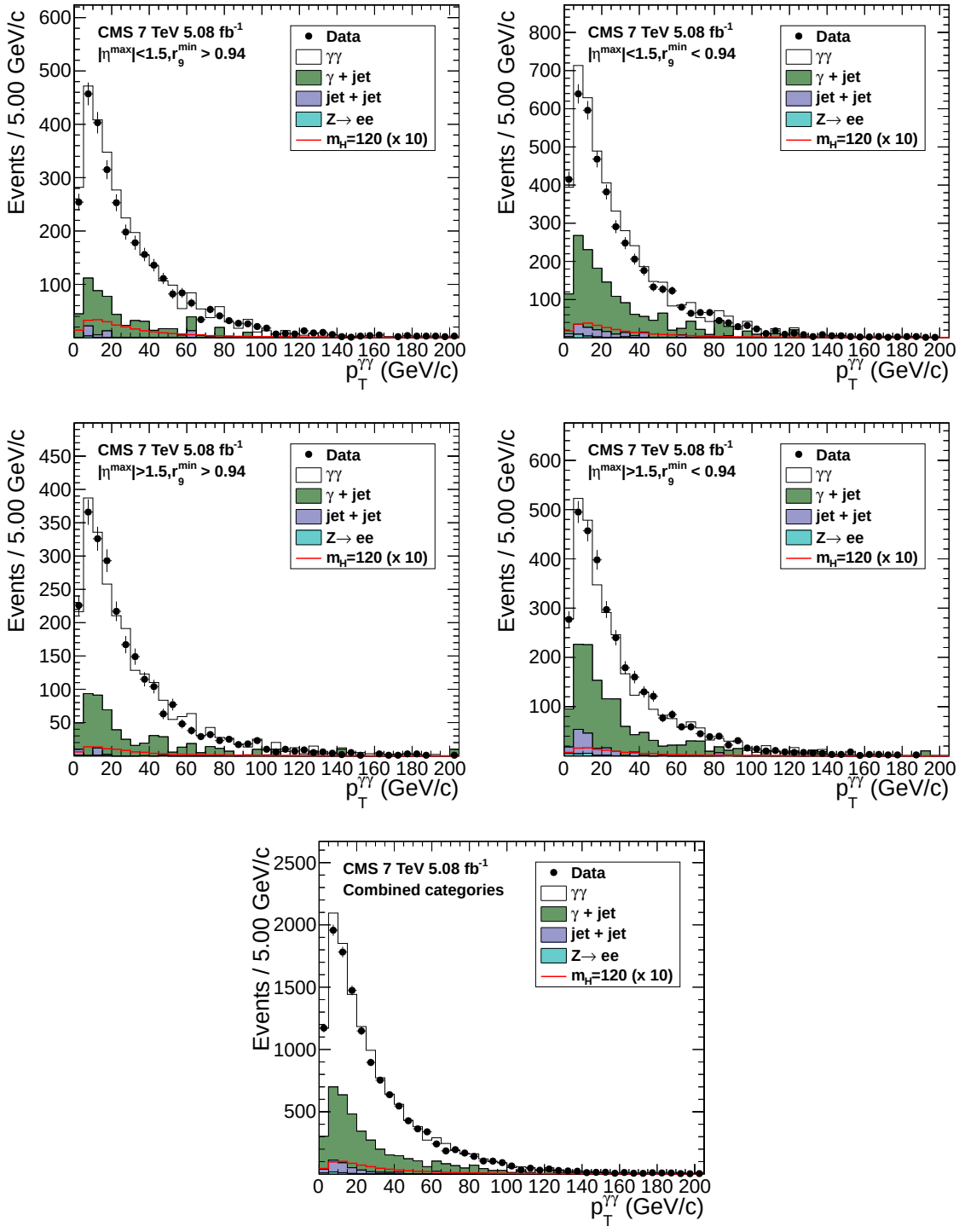

Figure 8.1: $p_{\mathrm{T}}^{\gamma\gamma}$ distributions after the event selections in different inclusive categories are applied.

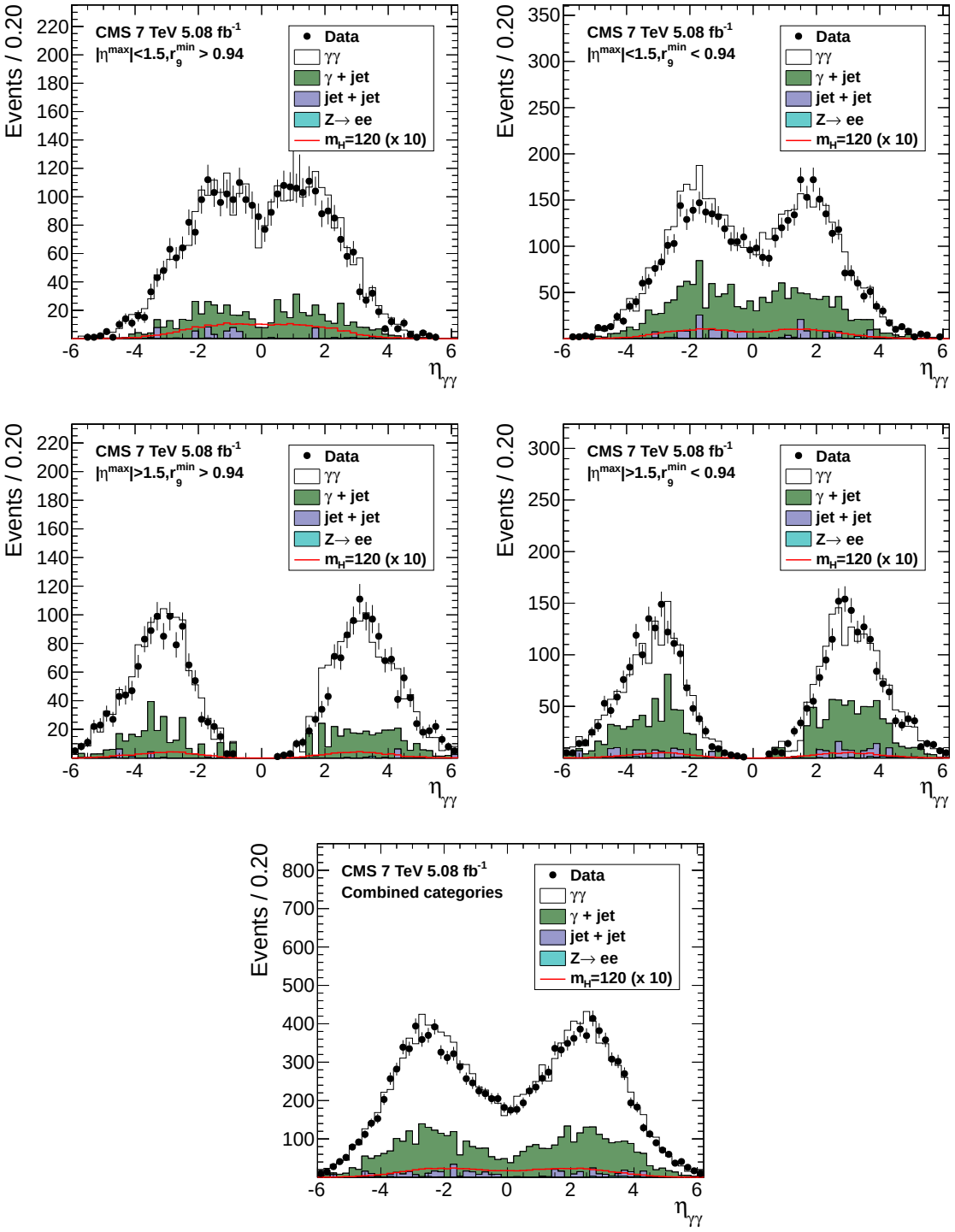

Figure 8.2: $\eta_{\gamma\gamma}$ distributions after the event selections in different inclusive categories are applied.

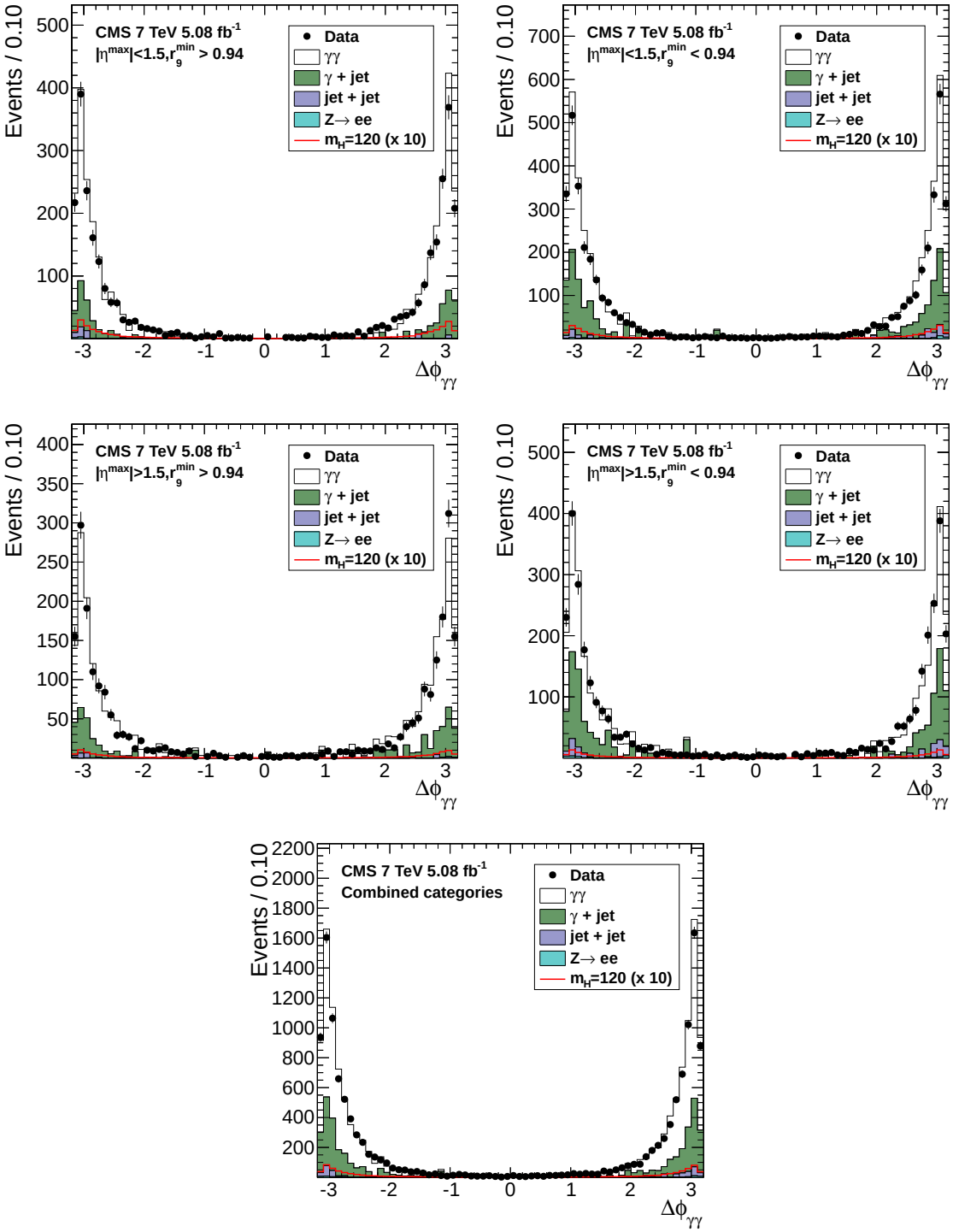

Figure 8.3: $\Delta\phi_{\gamma\gamma}$ distributions after the event selections in different inclusive categories are applied.

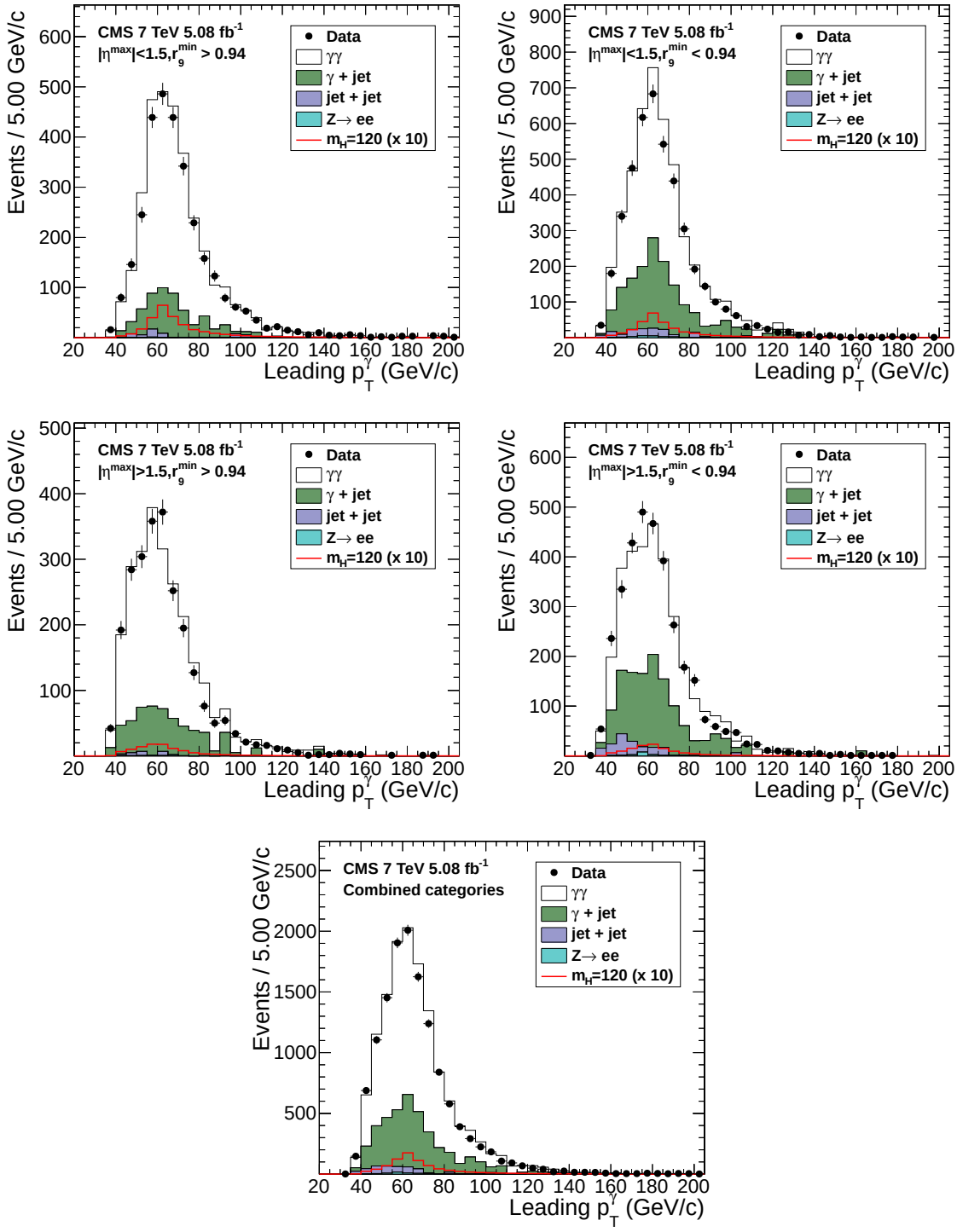

Figure 8.4: p_{T} distributions of the leading photon after the event selections in different inclusive categories are applied.

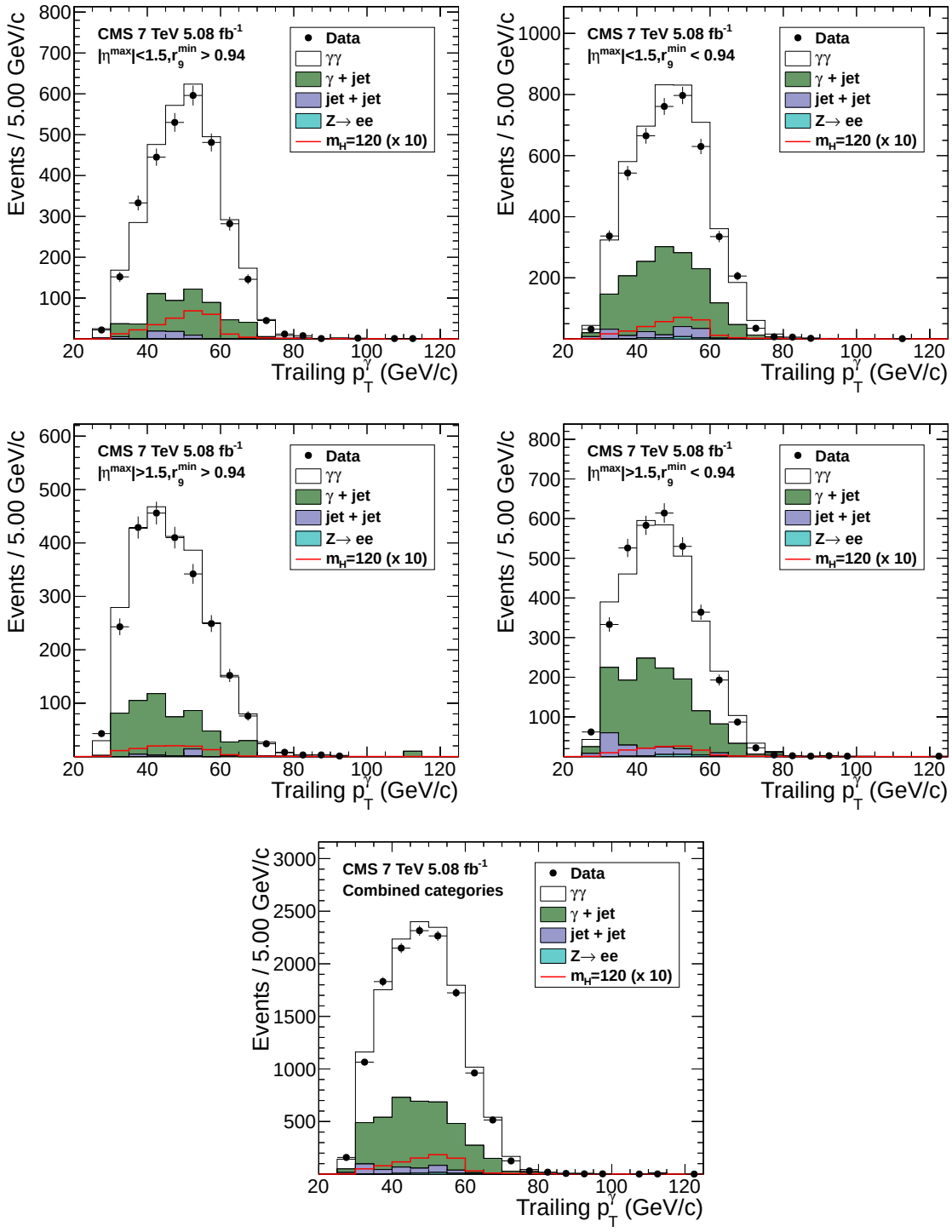

Figure 8.5: p_{T} distributions of the trailing photon after the event selections in different inclusive categories are applied.

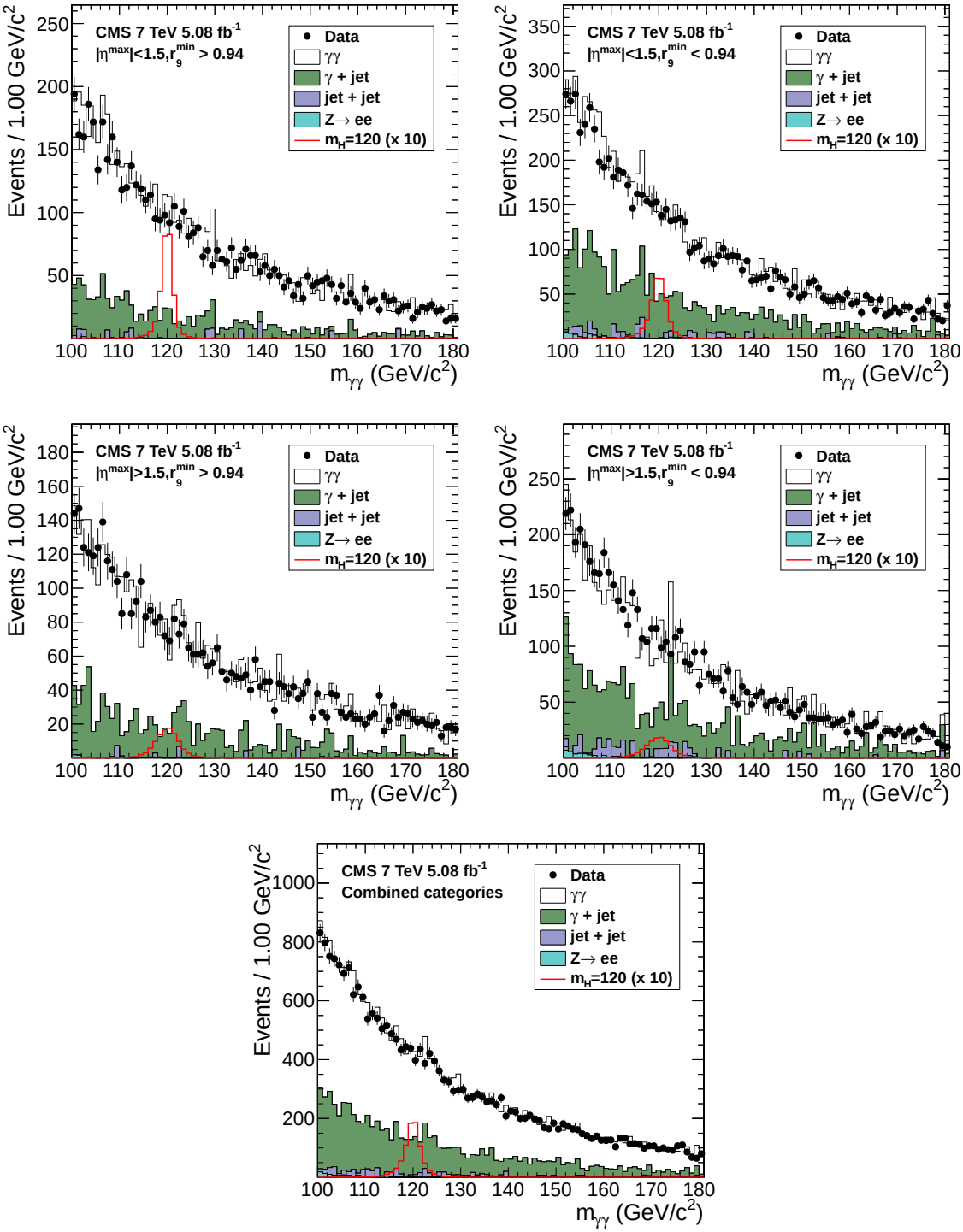

Figure 8.6: $m_{\gamma\gamma}$ distributions after the event selections in different inclusive categories are applied.

8.2 Di-jet Category

Higgs boson production is dominated by the gluon fusion process. The Vector Boson Fusion (VBF) process contributes less than 10 % to the total cross section. However, this process produces two additional jets, mostly in the forward region at high η. With appropriate selections on the two jets, this process yields a much better S/B than the inclusive categories. Events passing these selections are classified into the "di-jet" category. Combining this category with the inclusive categories enhances the sensitivity of the analysis.

In this analysis, we use corrected anti-k_T [96] Particle Flow (PF) [97] jets with cone size $\Delta R = 0.5$. The pileup correction is performed using the FastJet algorithm [93,98]. CMS standard jet energy corrections are applied to both the simulation and the data, and a residual calibration as a function of η and p_{T} is applied to data only which fixes the small difference between the data and the simulation.

To select "di-jet" events, any two photons passing the photon ID are selected. A cut on $p_{\mathrm{T}}^{\gamma}/m_{\gamma\gamma}$ is then applied to the leading photon, requiring $p_{\mathrm{T}}^{\gamma}/m_{\gamma\gamma} < 55/120$. For the subleading photon, $p_{\mathrm{T}}^{\gamma} > 25$ GeV/c is required. Again, if in one event there are more than one pair of photons satisfying these requirements, the pair with highest scalar sum of the p_{T}^{γ} of the two photons is finally selected.

Next, two jets are selected. First, jets are required to have $|\eta|$ less than 4.7, which is within the acceptance of the hadron calorimeter. Secondly, they are required not to overlap with any of the two selected photons, by requiring $\Delta R = \sqrt{\Delta\eta^2_{\mathrm{jet},\gamma} + \Delta\phi^2_{\mathrm{jet},\gamma}} > 0.5$. The two jets with highest p_{T} are selected if more than two jets passed these requirements.

Finally, the following selection criteria are applied to the two jets.

- The transverse momenta of the leading and subleading jets are required to be above 30 and 20 GeV/c, respectively. Figure 8.7 left and right shows the p_{T} distributions of the selected leading and trailing jets, respectively. In these plots and the following ones showing the distribution of one particular selection variable, all other cuts are applied except the cut on the variable being plotted.

In addition, the invariant mass of two photons are required to be between 90 and 190 GeV/c^2. This range is set to be larger than the invariant mass range used for the search, in order to allow more events to be selected, to get a better comparison between the data and the simulation.

- The di-jet invariant mass, $M_{j_1 j_2}$ is required to be above 350 GeV/c^2. Figure 8.8 left shows the di-jet invariant mass distributions.

- The difference in pseudorapidity between the two jets, $|\Delta\eta(j_1 j_2)|$ is required to be above 3.5. Figure 8.8 right shows the $|\Delta\eta|$ distributions.

- The *Zeppenfeld* variable, defined below, is required to be smaller than 2.5.

$$Z = \eta_{\gamma\gamma} - (\eta_{j_1} + \eta_{j_2})/2\,. \tag{8.1}$$

  Figure 8.9 left shows the $|Z|$ distributions.

- The difference in azimuthal angle between the di-jet system and the di-photon system, $\Delta\phi((j_1 j_2, \gamma\gamma))$ is required to be above 2.6. Figure 8.9 left shows the $\Delta\phi$ distributions.

Figure 8.10 left shows the di-photon invariant mass distributions after the di-jet selections. Figure 8.10 right shows the $p_{\mathrm{T}}^{\gamma\gamma}$ distributions for selected events with $m_{\gamma\gamma}$ between 100 and 150 GeV/c^2.

In combining the di-jet category with the inclusive ones, events passing the di-jet selection are excluded from the inclusive categories.

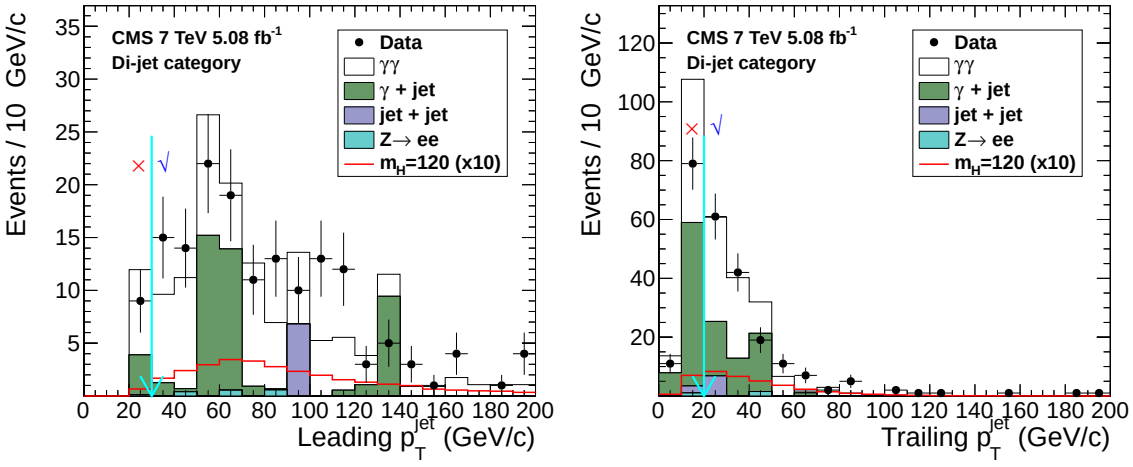

Figure 8.7: p_{T} distributions of the leading and trailing jets, with $n-1$ cuts applied.

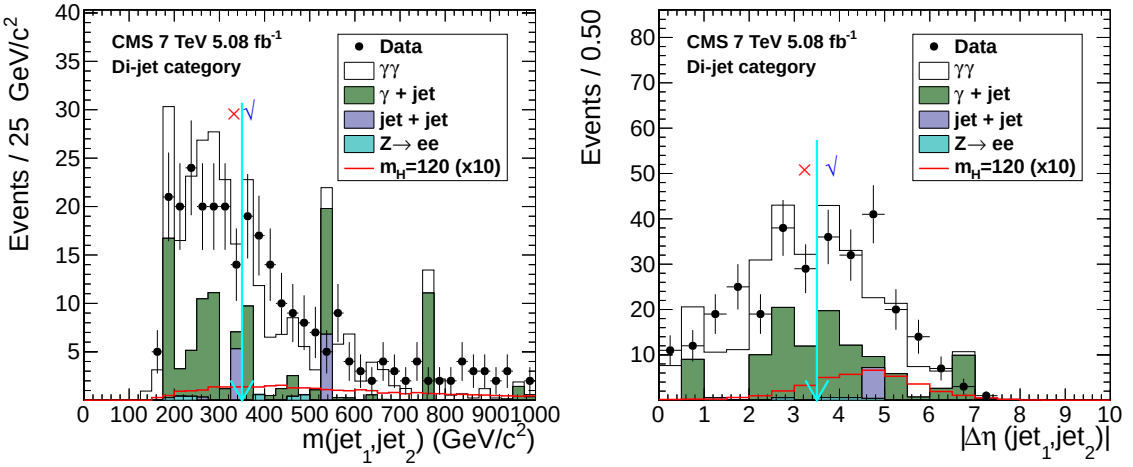

Figure 8.8: Invariant mass and $\Delta\eta$ distributions of the two jets, with $n-1$ cuts applied.

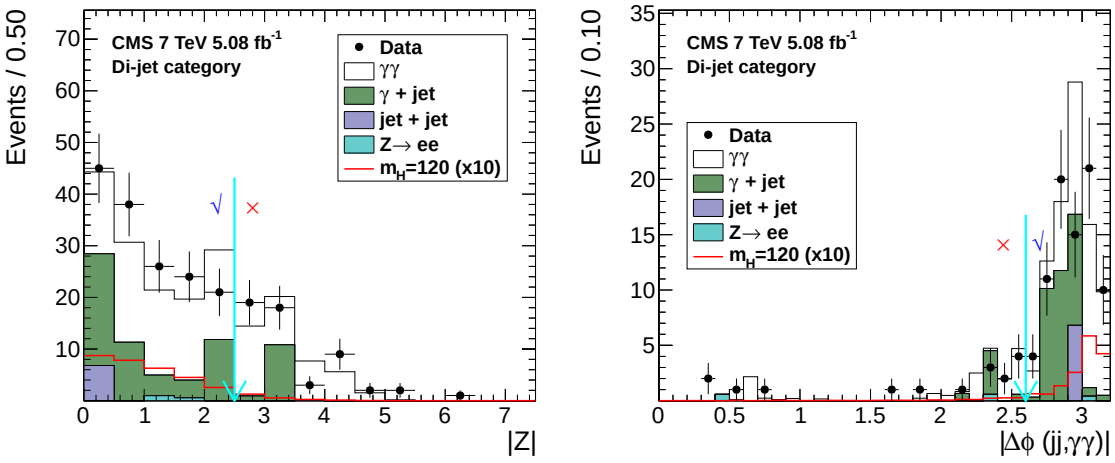

Figure 8.9: Left, *Zeppenfeld* variable distributions. Right, $\Delta\phi((j_1 j_2, \gamma\gamma))$ distributions. Both plots are with $n-1$ cuts applied.

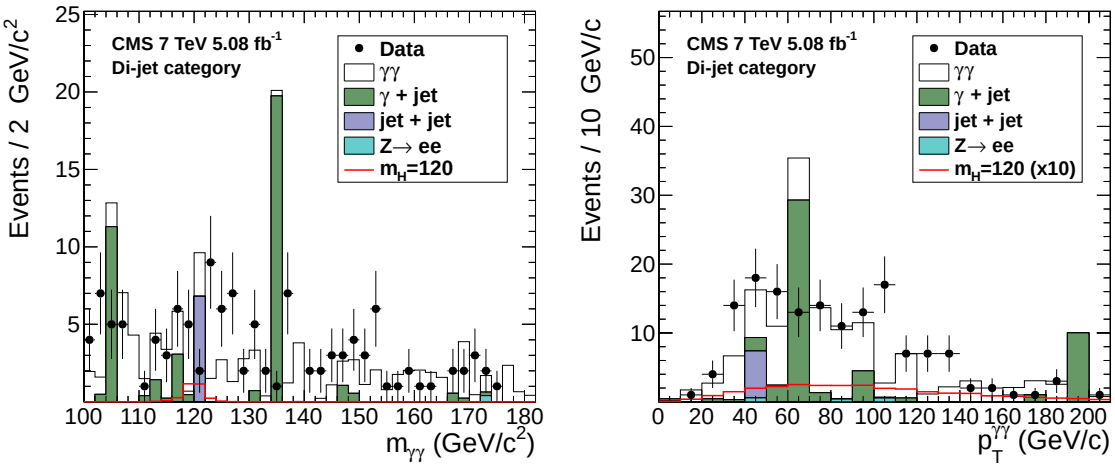

Figure 8.10: Left, $m_{\gamma\gamma}$ distributions after the di-jet selection. Right, $p_{\mathrm{T}}^{\gamma\gamma}$ distributions after the di-jet selection, where $m_{\gamma\gamma}$ is required to be between 100 and 150 GeV/c^2.

8.3 Signal Efficiency and Yield

Figure 8.11 shows the acceptance times the selection efficiency as a function of the Higgs boson mass in each inclusive category and di-jet category. Table 8.2 shows the expected number of H $\rightarrow \gamma\gamma$ events at mass 125 GeV/c^2 in each category with an integrated luminosity L=5.08 fb^{-1}. The table also shows the contribution from each Higgs boson production mode. In all "inclusive" categories, the gluon fusion contributes about 90%. In the di-jet category, the vector boson fusion contributes about 70%.

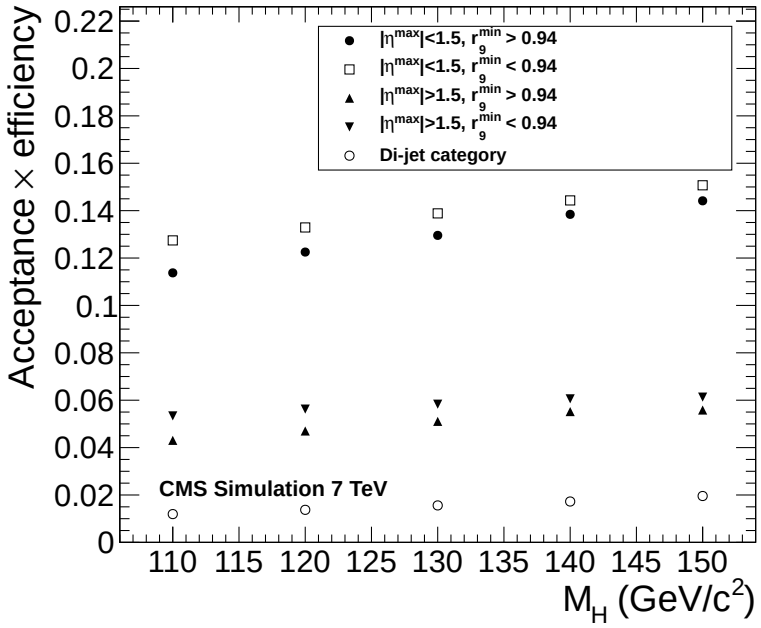

Figure 8.11: The acceptance times selection efficiency as a function of the Higgs boson mass in different di-photon categories.

Event Category	all production modes	ggH	VBF	$t\bar{t}H$	WH,ZH
Both $\|\eta\|$ <1.4442, both r_9 >0.94	25.8	23.2	1.28	1.15	0.122
Both $\|\eta\|$ <1.4442, not both r_9 >0.94	27.9	25.3	1.35	1.19	0.11
Not both $\|\eta\|$ <1.4442, both r_9 >0.94	10.1	9.01	0.533	0.553	0.0247
Not both $\|\eta\|$ <1.4442, not both r_9 >0.94	11.8	10.6	0.594	0.597	0.0296
Di-jet tag	2.96	0.838	2.11	0.017	0.000663
Total	78.6	68.9	5.87	3.5	0.287

Table 8.2: The expected Standard Model H $\rightarrow \gamma\gamma$ signal yield after the event selections, from each production mode with an integrated luminosity L= 5.08 fb^{-1} in each di-photon event category, for a Higgs boson mass of 125 GeV/c^2.

Chapter 9

$H \to \gamma\gamma$ Photon Energy Resolution

In this chapter, we study the energy resolution for photons from $H \to \gamma\gamma$ decays in realistic CMS simulation, namely the photon energies have been smeared in each category, shown in table 5.3, to take into account the $Z \to e^+e^-$ invariant mass resolution difference between the data and the simulation.

The photon identification cuts and event selections, discussed in the previous chapters, have been applied to the $H \to \gamma\gamma$ events in simulation.

We perform the resolution measurements in each "smearing category" defined in table 5.3 as a function of the photon transverse energy E_T. The reason to use E_T instead of E is that the latter has strong dependence on η, as shown in figure 9.1 left, while E_T has almost no correlation with η (figure 9.1 right).

We define the energy resolution to be the effective sigma σ_{eff}, as defined in Section 5.4.2, of the distribution of reconstructed energies normalized to the true energy.

To measure the effective sigma, we fit the distributions with a sum of a Crystal Ball (CB) and a Gaussian function for the first two smearing categories, and a CB function for other categories.

Figures 9.2 to 9.17 show the results of the fit in different energy intervals for each category. The photon energy indicated in each figure represents the mean and RMS of the energy distribution in each interval.

The results of the energy resolution as a function of the E_T are shown in figures 9.18 and 9.19 for different categories. We fit the results with the function $\frac{\sigma_E}{E} = \frac{S}{\sqrt{E_T}} \oplus \frac{N}{E_T} \oplus C$. In some categories, either S or N is fixed to zero to allow a better parametrization.

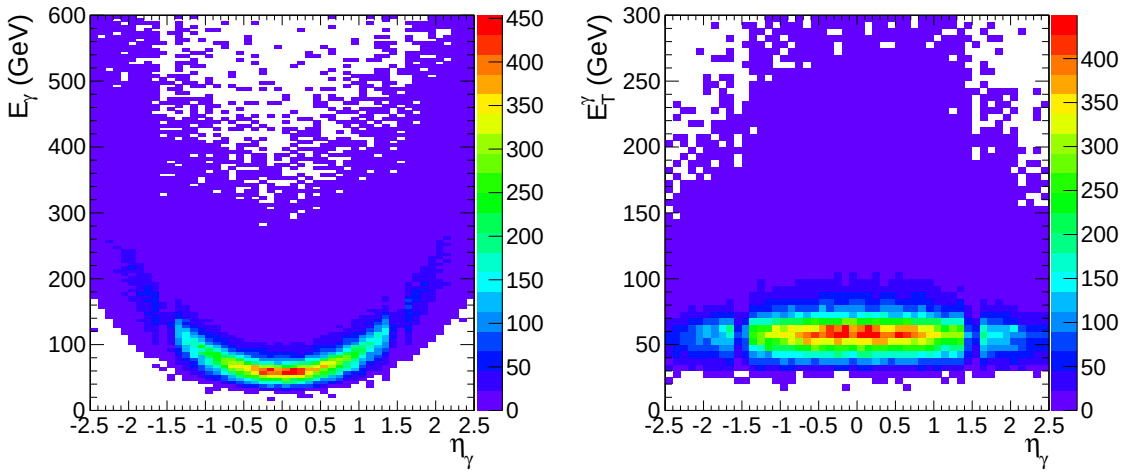

Figure 9.1: The photon energy (left) or transverse energy (right) vs pesudorapidity from H $\rightarrow \gamma\gamma$ decays at mass 125 GeV/c^2.

In general, the fit results shows that the design performance of the ECAL is not yet reached at this writing. Based on the current understanding, this is mostly due to the imperfect simulation of the tracker material present in front of the ECAL and the imperfect cluster corrections derived from simulation. These imperfections are also the dominant contributions to the energy smearing.

The result in the fist category shows that for photons at high energies in the central barrel and with $r_9 > 0.94$, the energy resolution approaches to 1%. The main contributions to this number is the energy smearing of 0.71% (table 5.3), the intercalibration precision of about 0.5% (figure 3.3), and the intrinsic energy resolution of the $PbWO_4$ crystals of about 0.5% (figure 2.13).

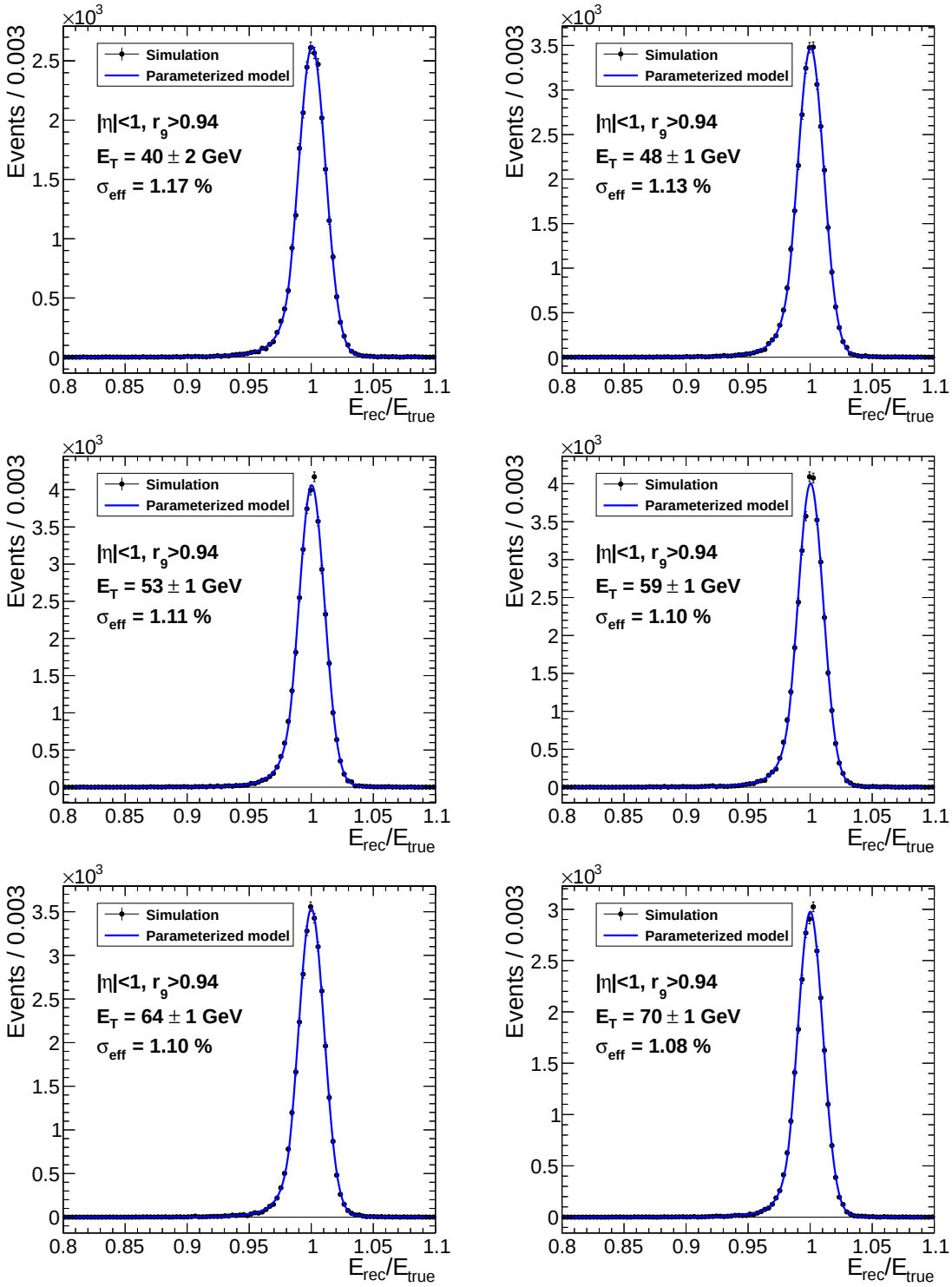

Figure 9.2: The distributions of the reconstructed photon energy normalized to the true energy in H $\rightarrow \gamma\gamma$ simulation at different energies, indicated in each figure. Here, only photons in the central barrel ($|\eta| < 1$) and with $r_9 > 0.94$ are considered.

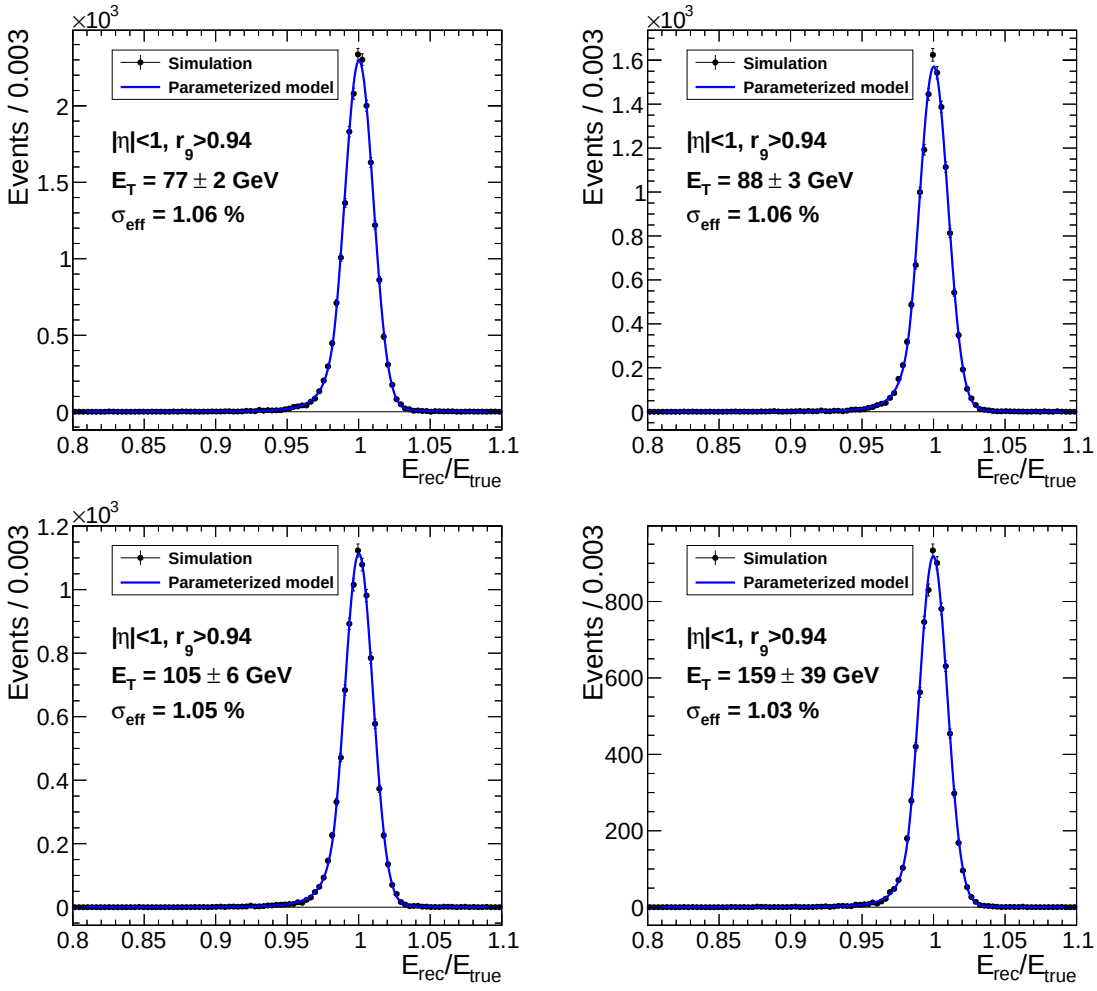

Figure 9.3: Same as figure 9.2, four more E_T bins.

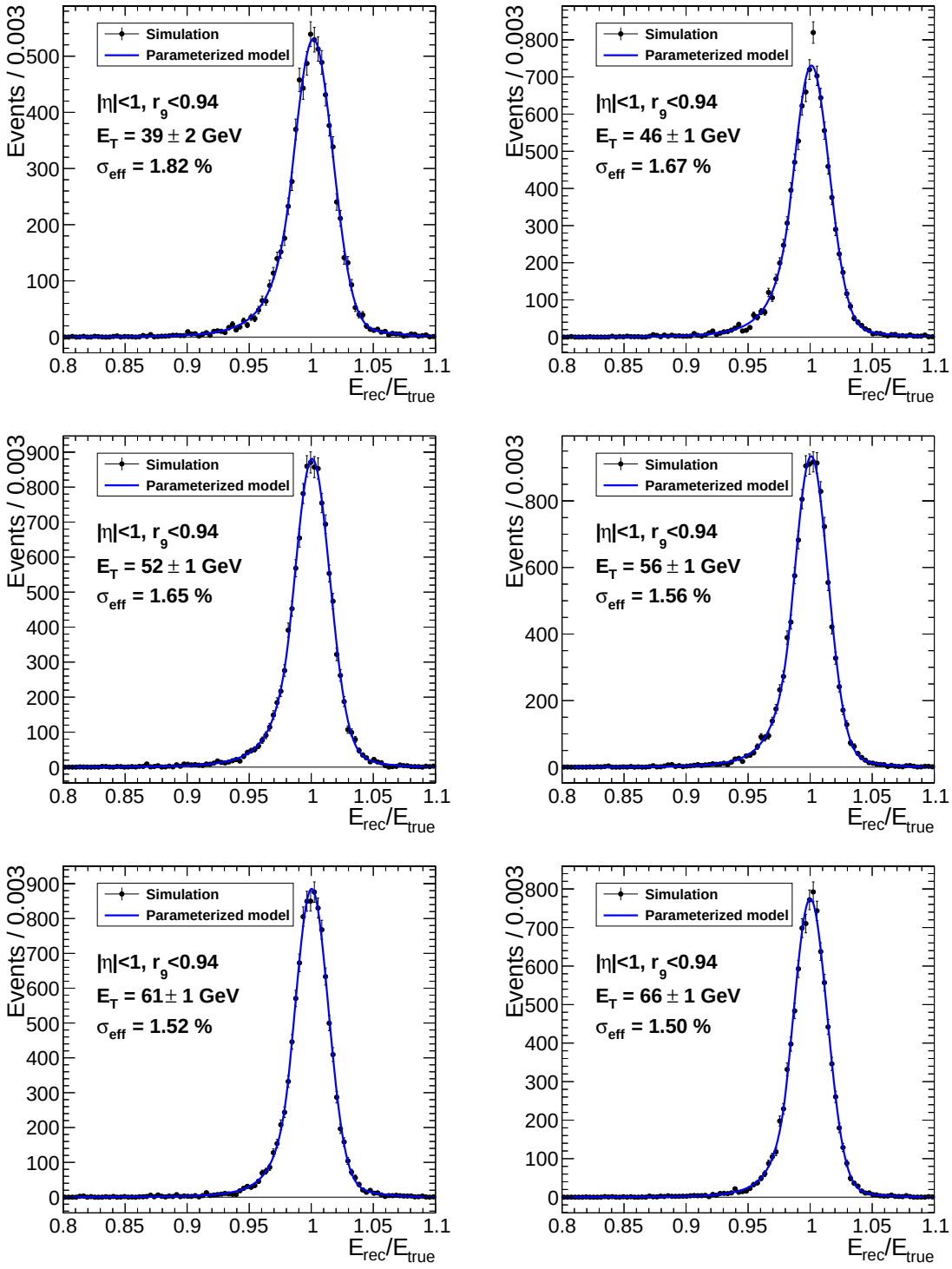

Figure 9.4:]
The distributions of the reconstructed photon energy normalized to the true energy in H $\rightarrow \gamma\gamma$ simulation at different energies, indicated in each figure. Here, only photons in the central barrel ($|\eta| < 1$) and with $r_9 < 0.94$ are considered.

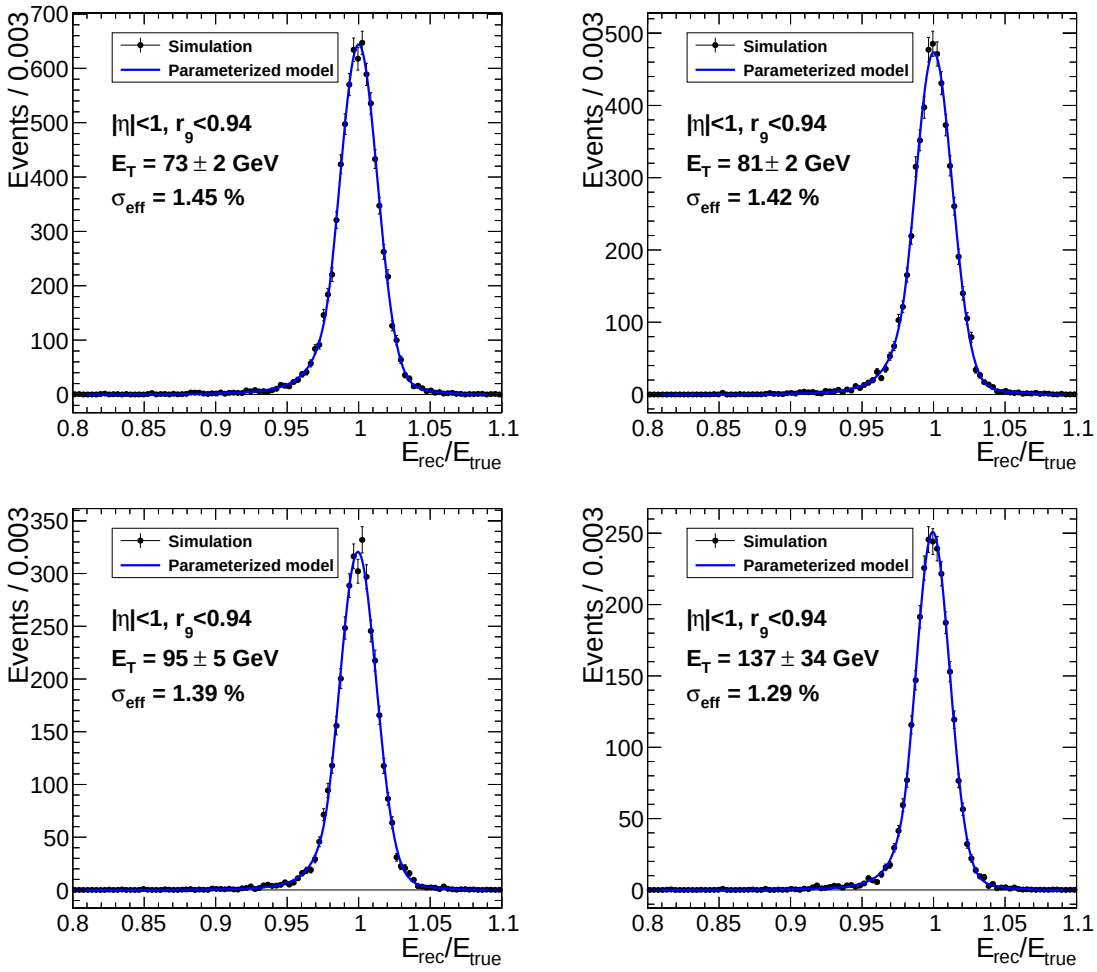

Figure 9.5:]
Same as figure 9.4, four more E_T bins.

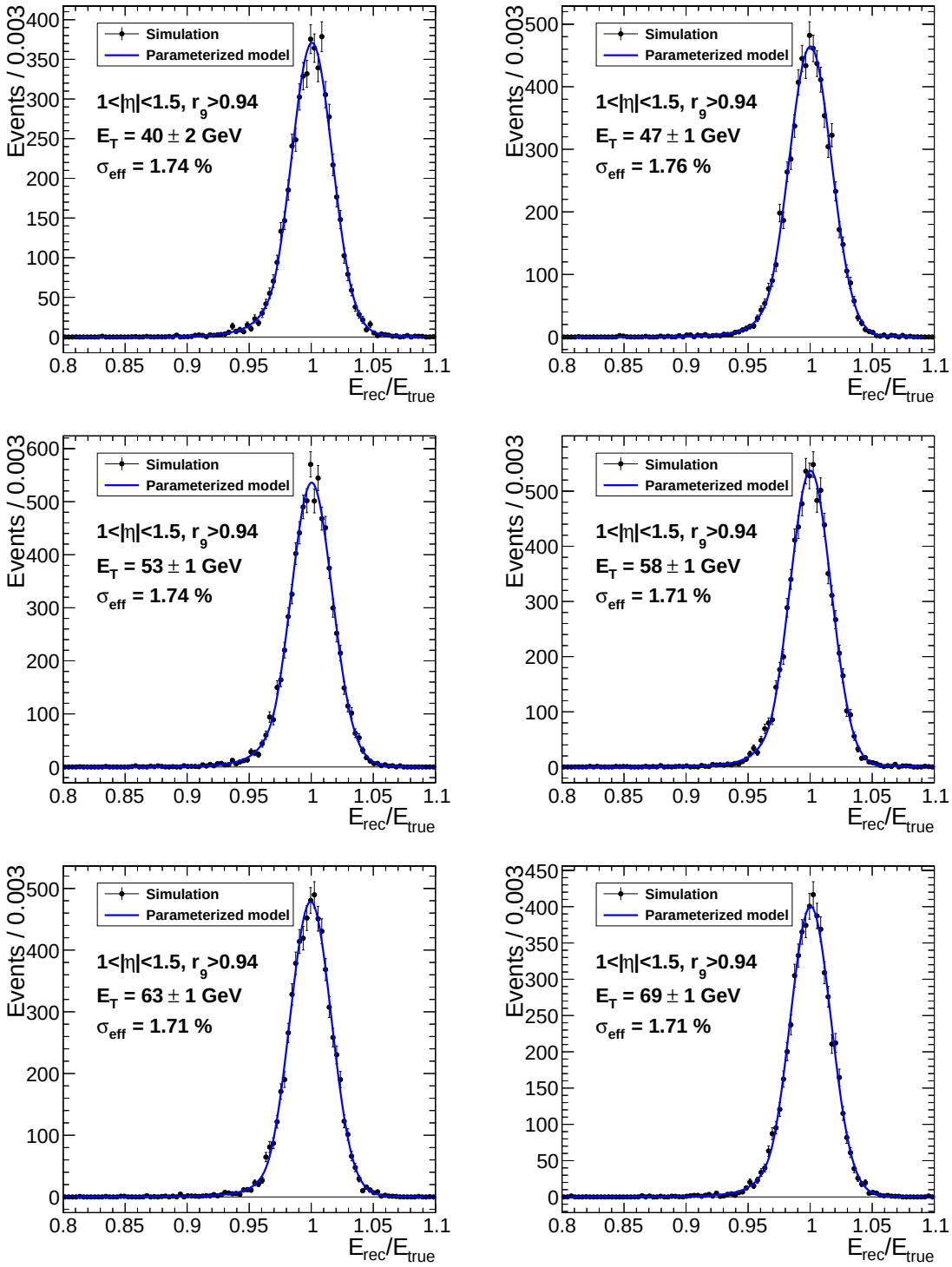

Figure 9.6:]
The distributions of the reconstructed photon energy normalized to the true energy in H $\rightarrow \gamma\gamma$ simulation at different energies, indicated in each figure. Here, only photons in the outer barrel ($1 < |\eta| < 1.5$) and with $r_9 > 0.94$ are considered.

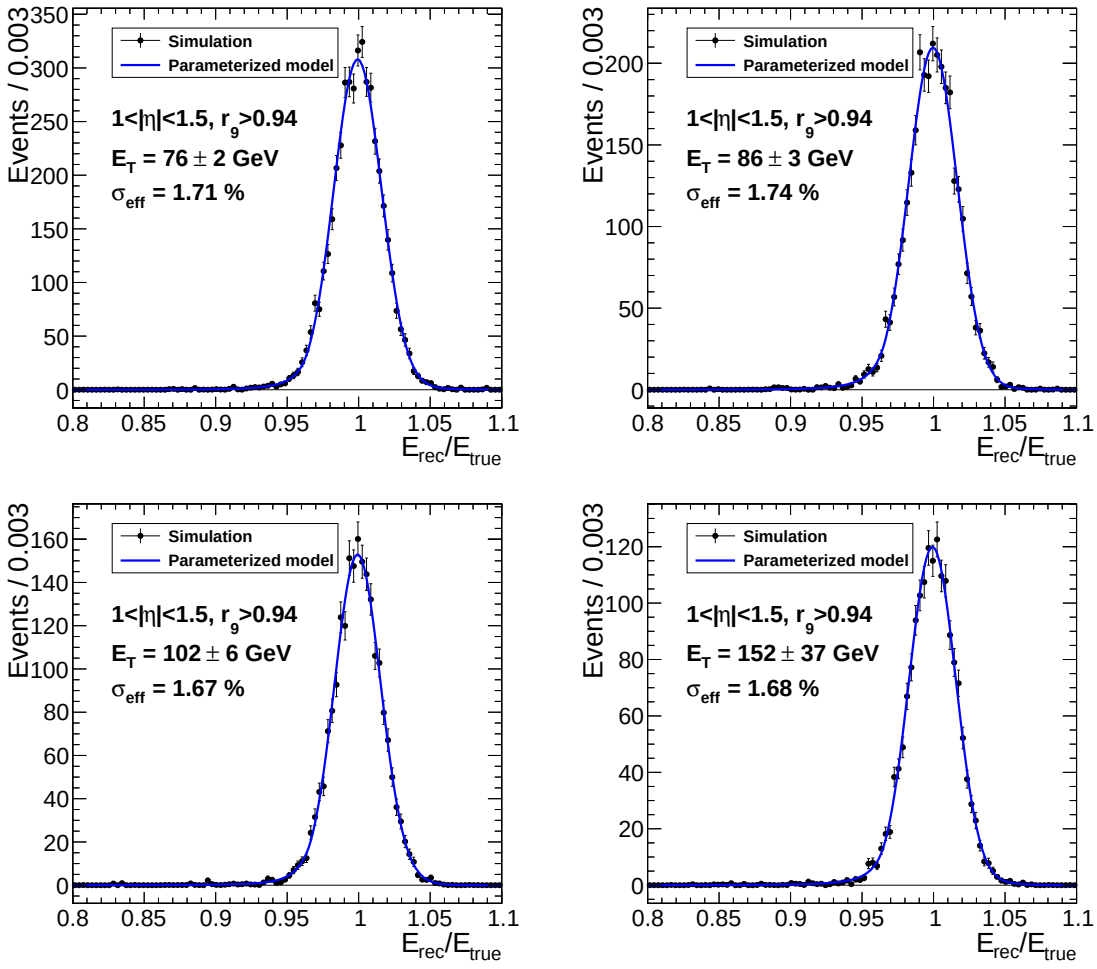

Figure 9.7: Same as figure 9.6, four more E_T bins.

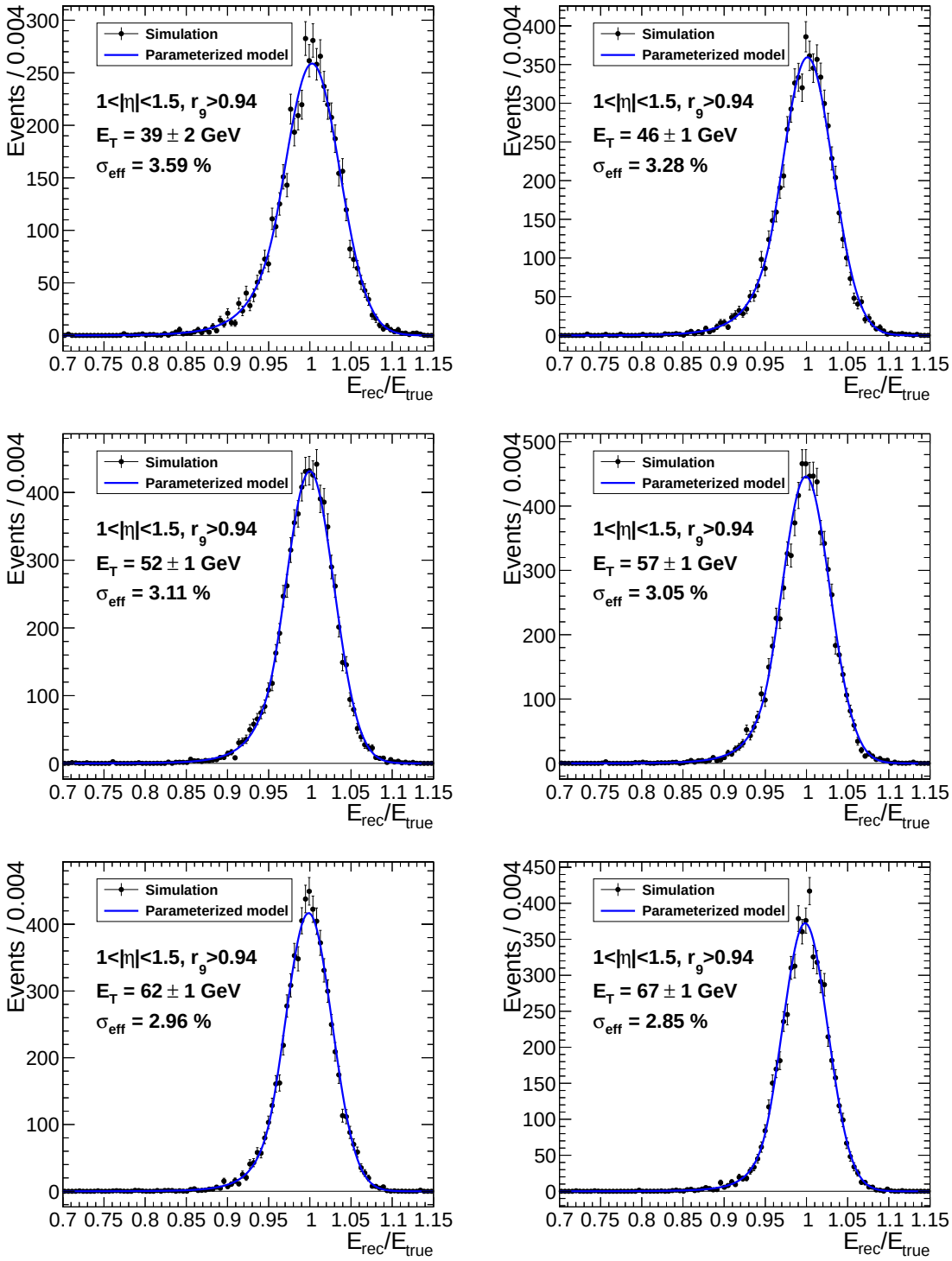

Figure 9.8:]
The distributions of the reconstructed photon energy normalized to the true energy in H $\to \gamma\gamma$ simulation at different energies, indicated in each figure. Here, only photons in the outer barrel ($1 < |\eta| < 1.5$) and with $r_9 < 0.94$ are considered.

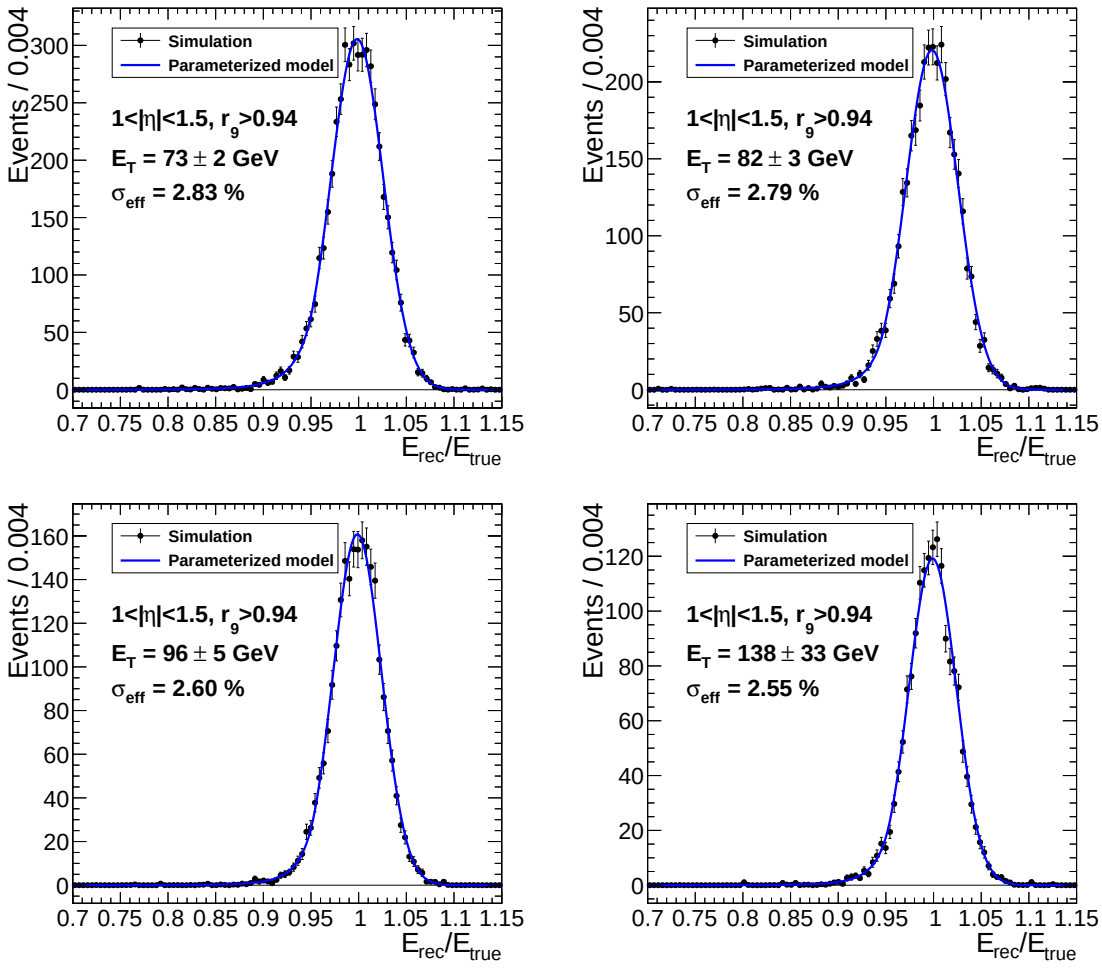

Figure 9.9: Same as figure 9.8, four more E_T bins.

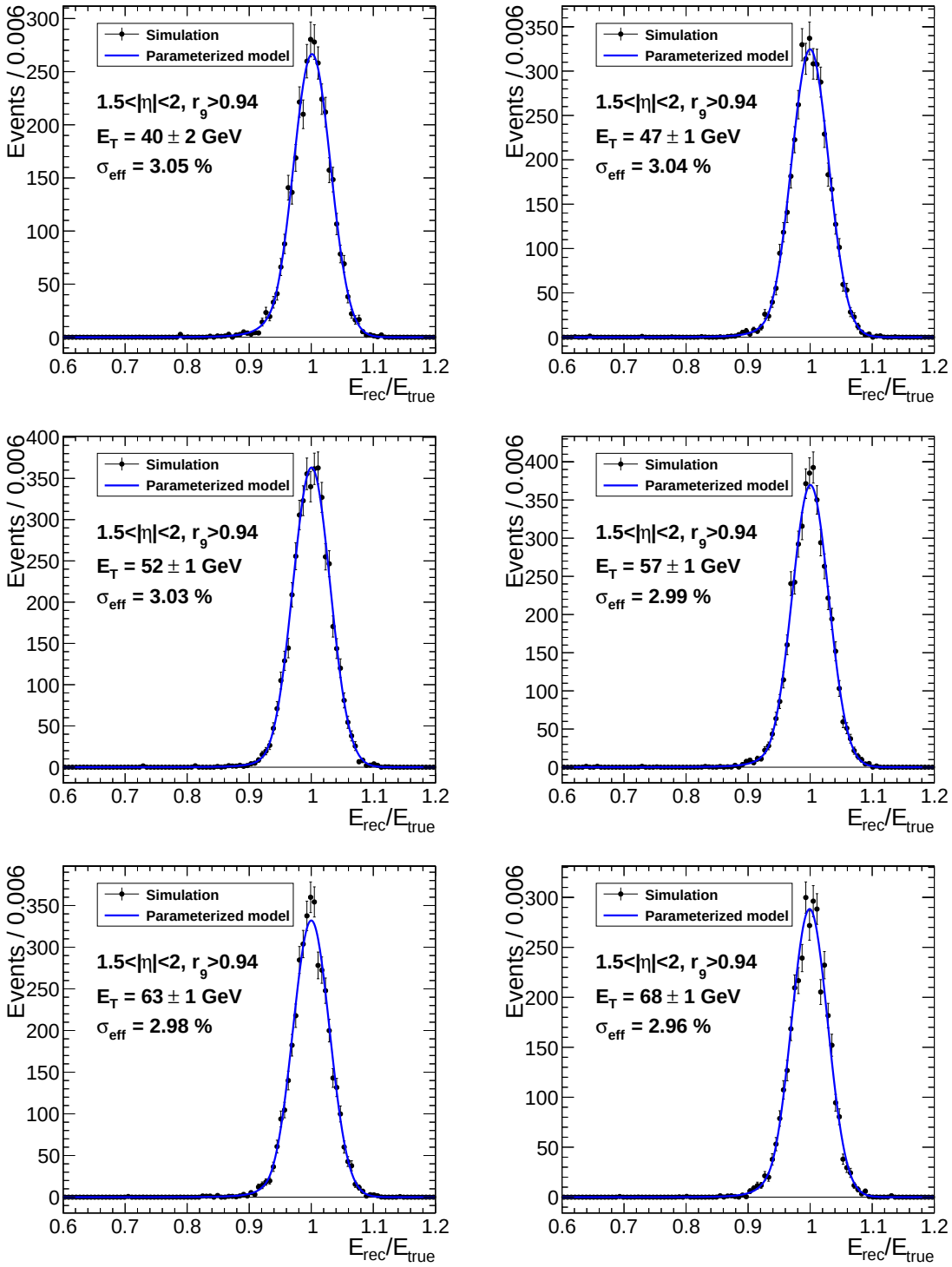

Figure 9.10: The distributions of the reconstructed photon energy normalized to the true energy in H $\rightarrow \gamma\gamma$ simulation at different energies, indicated in each figure. Here, only photons in the central endcaps ($1.5 < |\eta| < 2$) and with $r_9 > 0.94$ are considered.

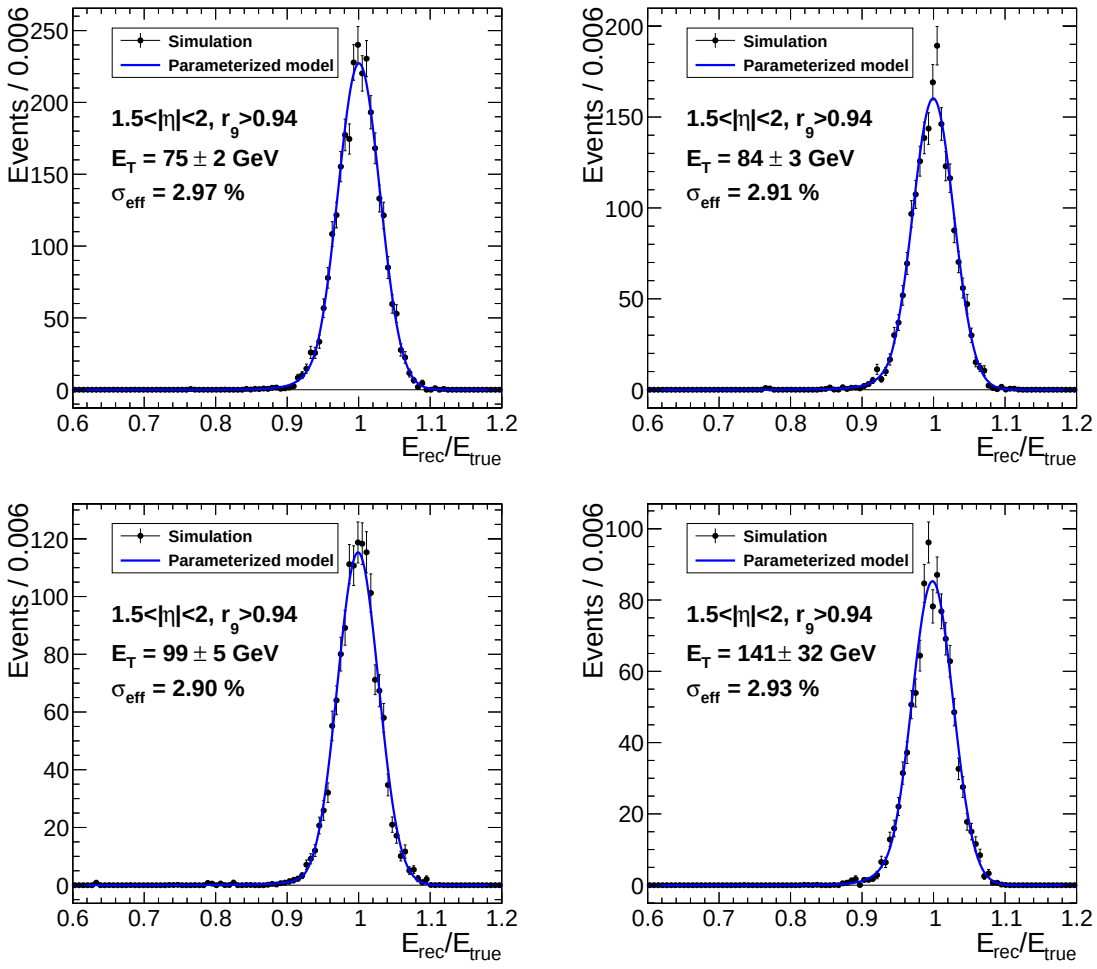

Figure 9.11: Same as figure 9.10, four more E_T bins.

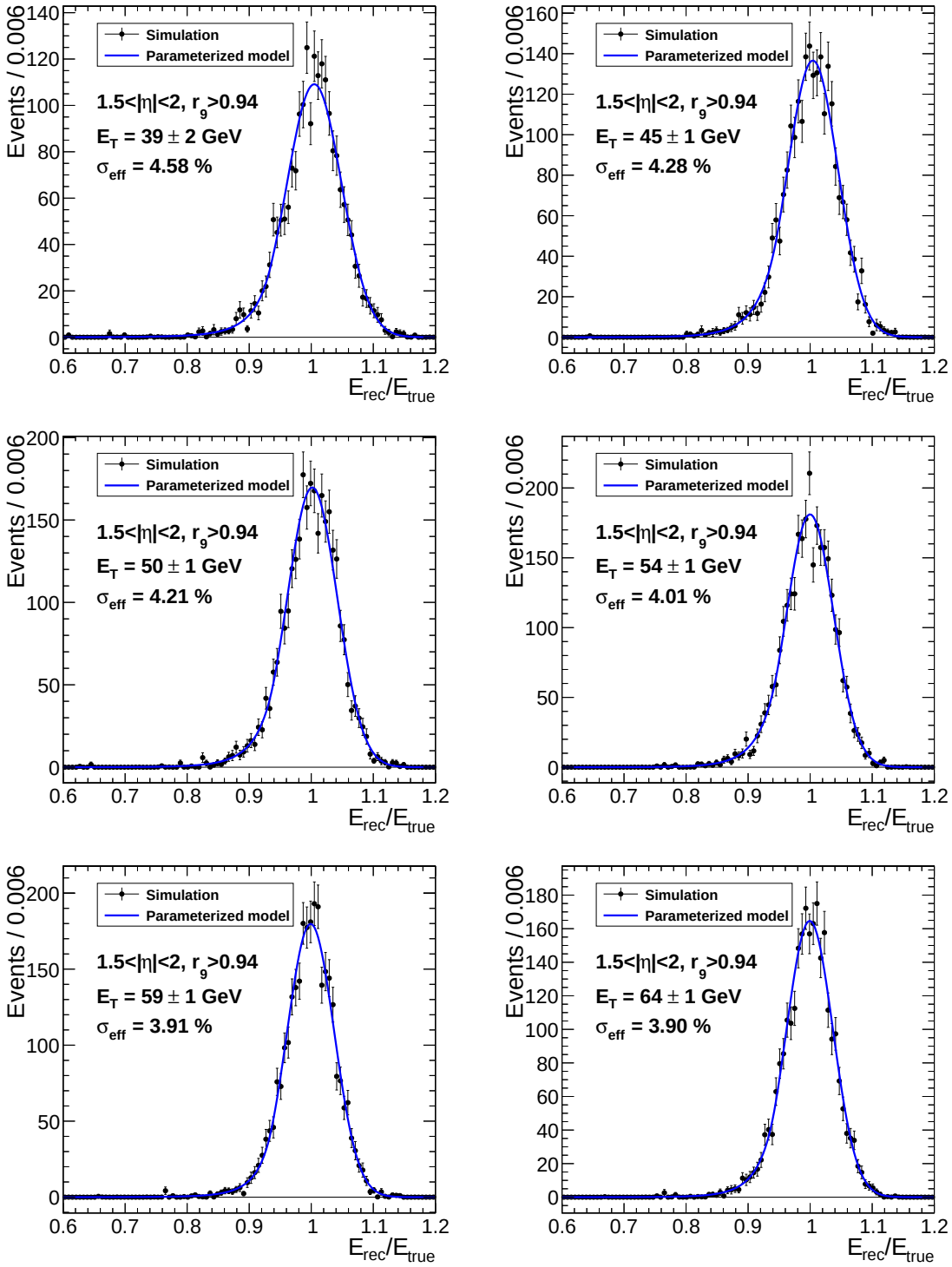

Figure 9.12: The distributions of the reconstructed photon energy normalized to the true energy in H $\to \gamma\gamma$ simulation at different energies, indicated in each figure. Here, only photons in the central endcaps ($1.5 < |\eta| < 2$) and with $r_9 < 0.94$ are considered.

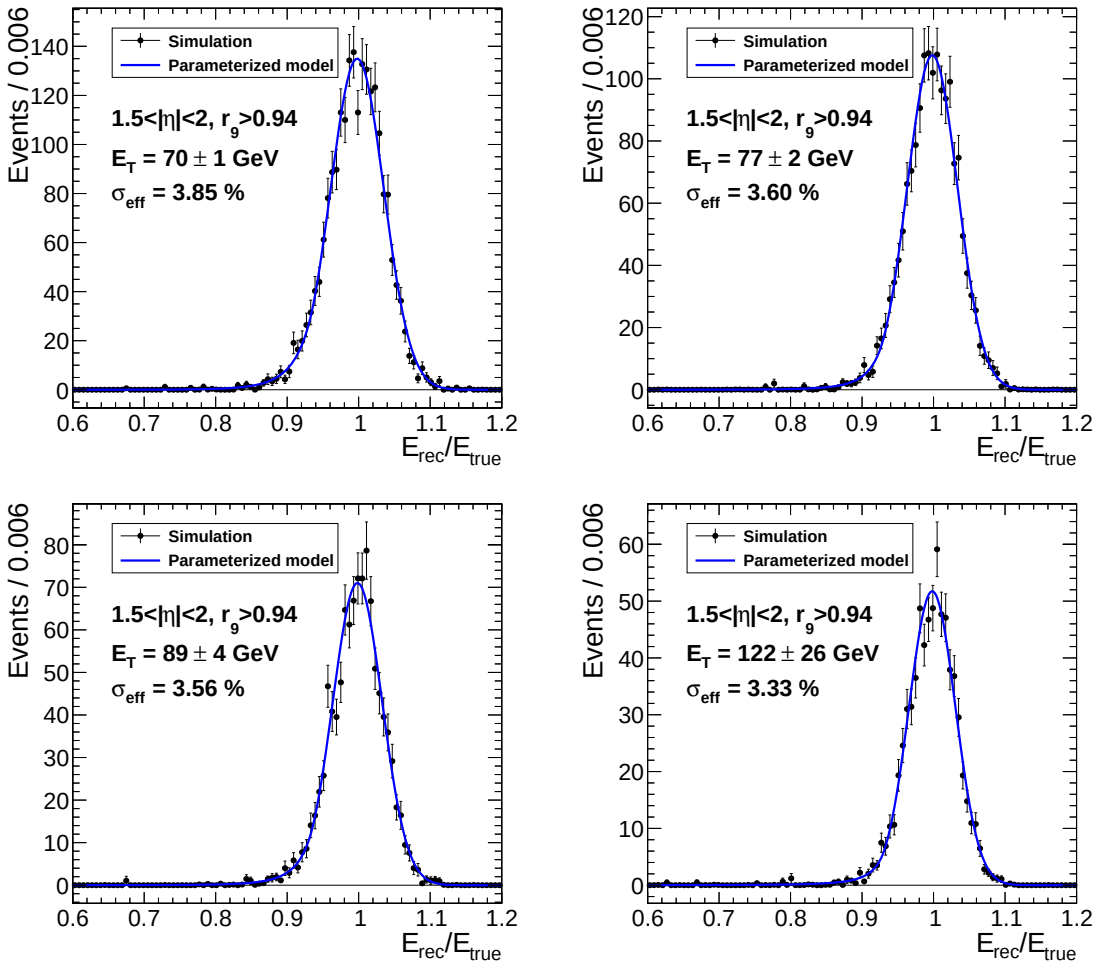

Figure 9.13: Same as figure 9.12, four more E_T bins.

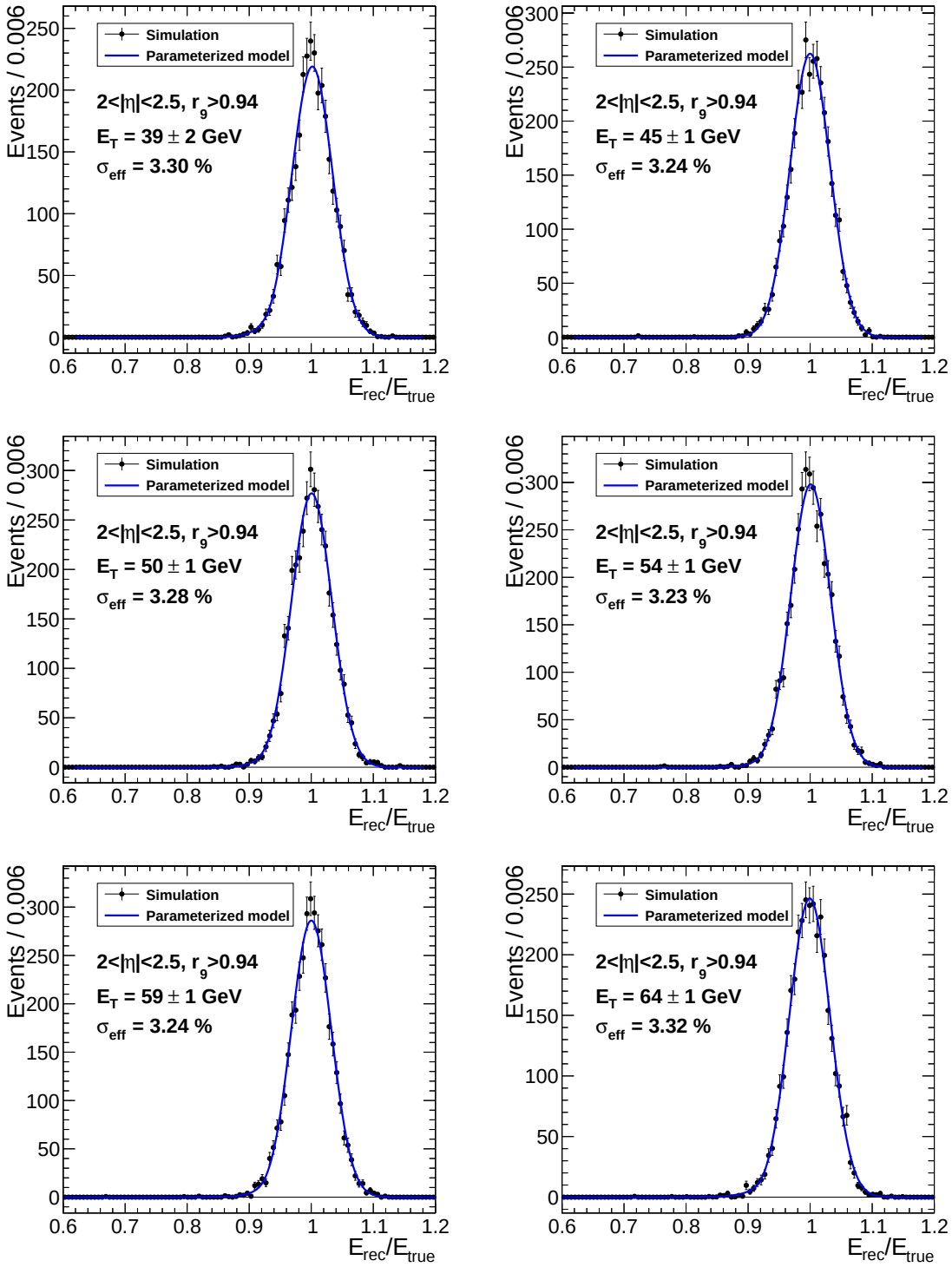

Figure 9.14: The distributions of the reconstructed photon energy normalized to the true energy in H $\rightarrow \gamma\gamma$ simulation at different energies, indicated in each figure. Here, only photons in the outer endcaps ($2 < |\eta| < 2.5$) and with $r_9 > 0.94$ are considered.

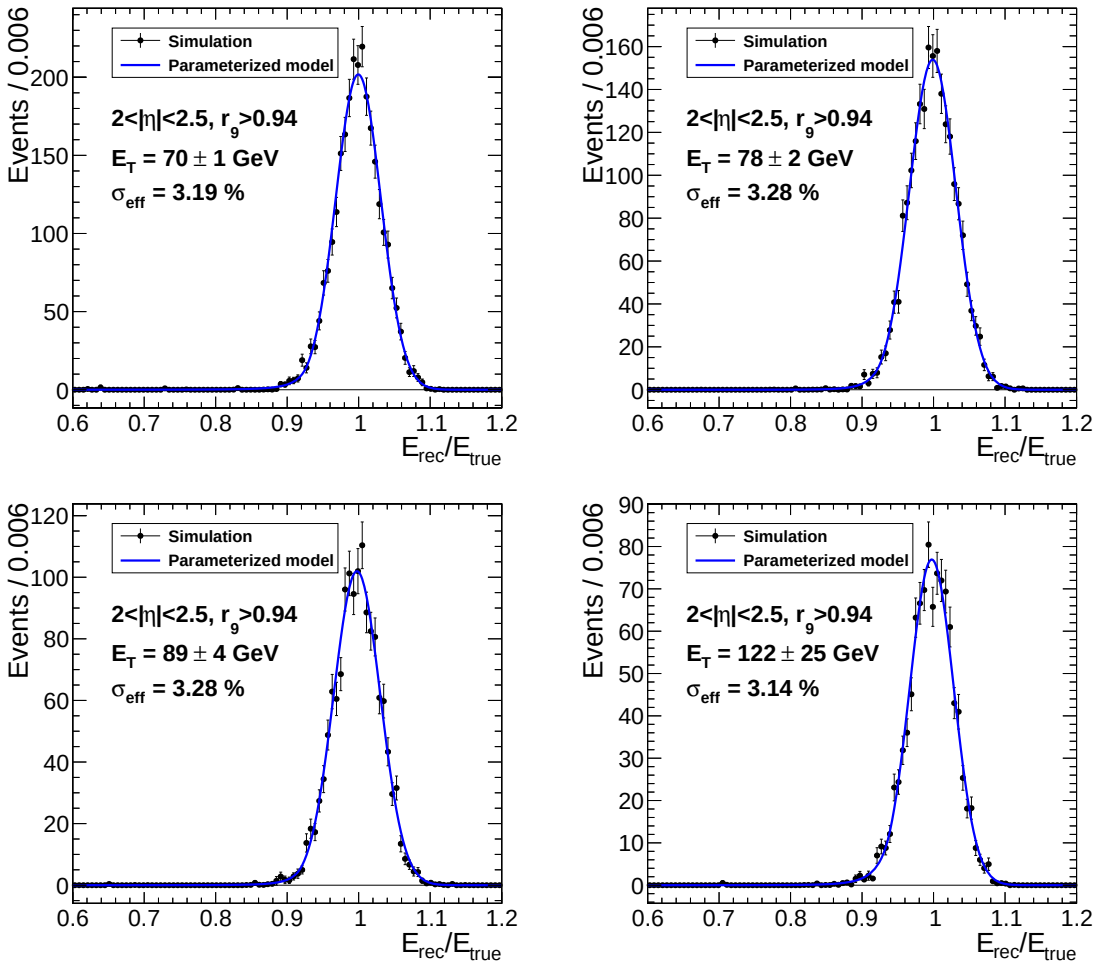

Figure 9.15: Same as figure 9.14, four more E_T bins.

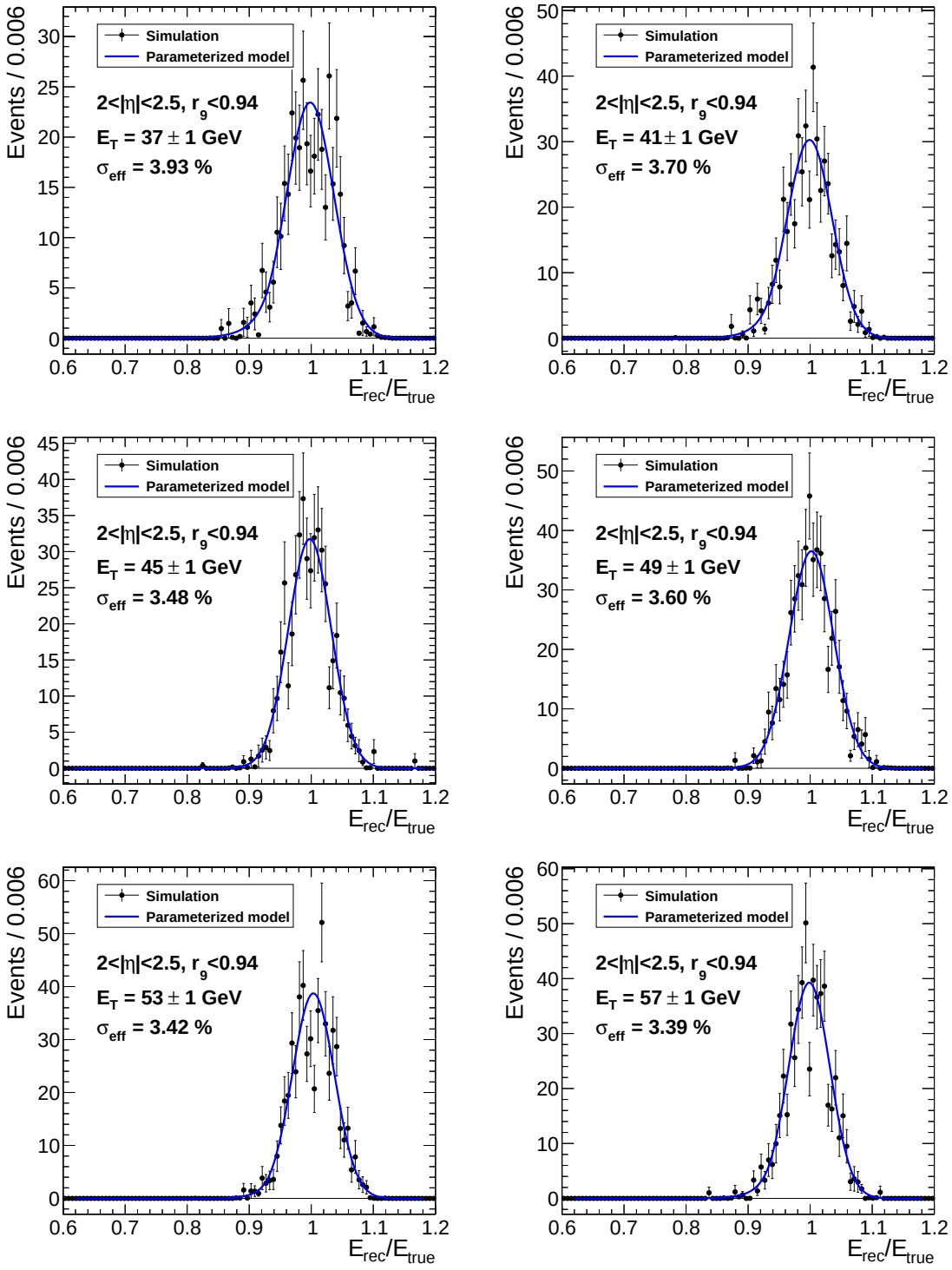

Figure 9.16: The distributions of the reconstructed photon energy normalized to the true energy in H $\rightarrow \gamma\gamma$ simulation at different energies, indicated in each figure. Here, only photons in the outer endcaps ($2 < |\eta| < 2.5$) and with $r_9 < 0.94$ are considered.

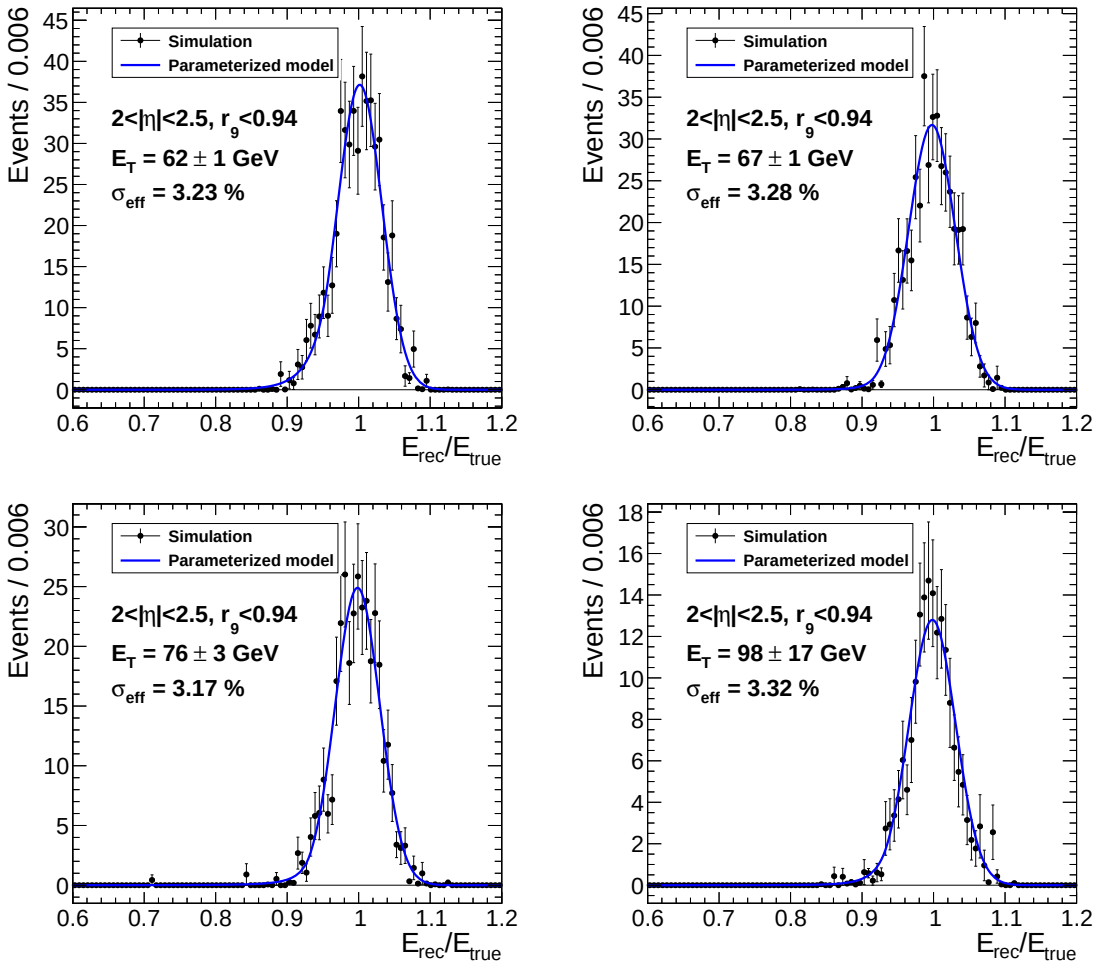

Figure 9.17: Same as figure 9.16, four more E_T bins.

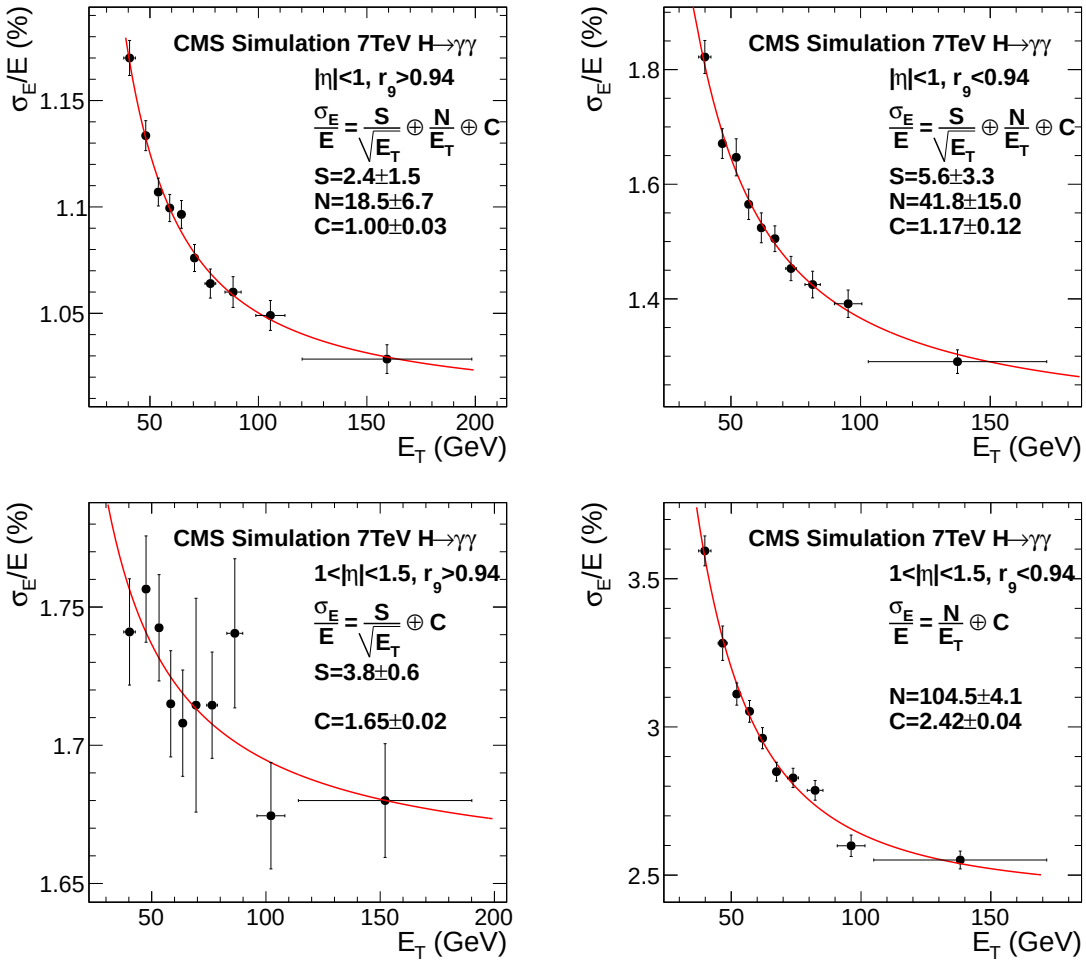

Figure 9.18: Photon energy resolution as a function of E_{T}, in four $\eta \times r_9$ categories in the barrel.

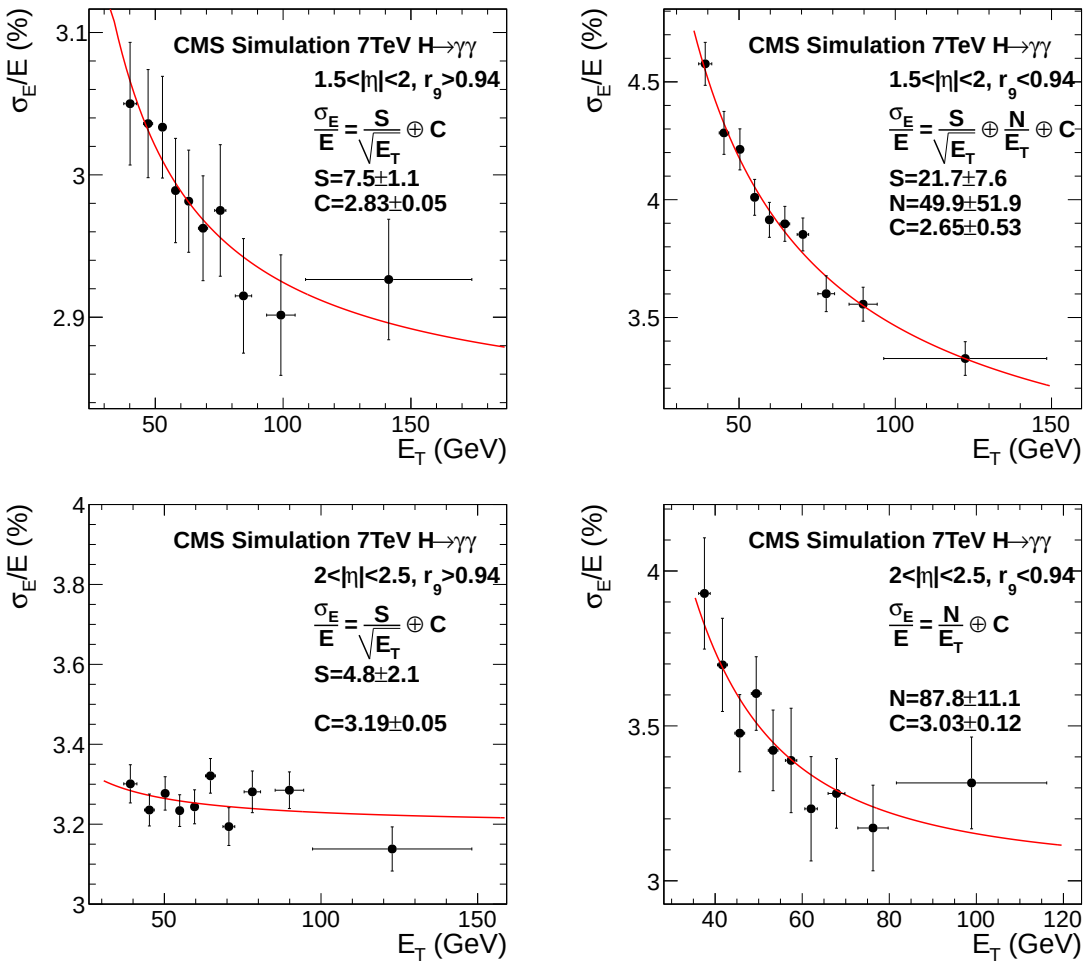

Figure 9.19: Photon energy resolution as a function of E_{T}, in four $\eta \times r_9$ categories in the endcaps.

Chapter 10

Signal and Background Modeling

In this chapter, we discuss the signal and background modeling. The signal model is used to predict the Standard Model H $\to \gamma\gamma$ signal yield and shape at any given mass point in the range of interest, from 100 to 150 GeV/c^2. Similarly, the background model is used to predict the background yield and shape. These models are the inputs needed to perform the hypothesis test from which we extract the exclusion limits or signal significance from the data, as discussed in chapter 12.

10.1 Signal Modeling

The H $\to \gamma\gamma$ signal shape is modeled from simulation. The energy of photons in the simulation are smeared to account for the differences in resolution between the data and the simulation, as was discussed in section 5.7.

At the generator level, the H $\to \gamma\gamma$ has nearly zero width in the mass range of interest. The observed width is broadened by detector effects, mostly due to the non-zero ECAL energy resolution. To the first order, the resolution can be described by a Gaussian distribution. More realistically, the energy resolution contains non-Gaussian tails on both sides. Wrong identification of the event vertex also degrades the mass resolution, and introduces additional non-Gaussian tails to the overall distribution.

Therefore, in order to model well both the core part and the tails of the H $\to \gamma\gamma$ shape, we use a sum of two or three Gaussians to model the distribution, depending on the category and whether the correct vertex was selected. The fit is done separately

for events with a correctly identified vertex and for events with a wrong vertex. In this way, the systematic uncertainties from the multivariate vertex ID are taken into account through a "nuisance parameter"[1] which changes the fraction of events with the correct vertex. For events with a correct vertex, we use the sum of three Gaussians. For events with a wrong vertex, two Gaussians are used for the first two inclusive categories and the di-jet category and one Gaussian is used for the remaining two inclusive categories.

Figure 10.1 and figure 10.2 show the fit results for a Higgs boson mass at 120 GeV/c^2 in events with a correct vertex and with a wrong vertex, respectively. The same fit procedure is performed for four other mass points, in 10 GeV/c^2 intervals from 100 to 150 GeV/c^2. For a given hypothesized signal Higgs boson mass, we perform a piece-wise linear interpolation between the two nearest mass points for which Monte Carlo simulation samples were produced for the relevant parameters, including the mean and width of each Gaussian and the corresponding fractions. The signal model is then built as the sum of the two or three Gaussians with the interpolated parameters. As an example of the interpolation, we show the widths of the two Gaussian for events with a correct vertex as a function of the hypothesized Higgs boson mass in figure 10.3. The models with the correct and wrong vertex are built separately and then combined into the final model, with the fraction of correct vertices obtained from simulation, as we have shown in figure 6.3. The same interpolation among the simulated mass points is used to obtain the fraction of events with the event vertex correctly selected.

Therefore, for a given Higgs boson mass $\mathrm{M_H}$, the signal model can be written as

$$G_s^i(m_{\gamma\gamma}, \mathrm{M_H}) = N_s^i(f_{\mathrm{vtx}} g_{\mathrm{rv}}(\mathrm{M_H} + \delta_M, \sigma_M) + (1 - f_{\mathrm{vtx}}) g_{\mathrm{wv}}(\mathrm{M_H} + \delta_M, \sigma_M)), \quad (10.1)$$

where $G_s^i(\mathrm{M_H})$ is the parametrized model function for the $m_{\gamma\gamma}$ distribution in each category for a given Higgs boson mass $\mathrm{M_H}$, i refers to the category number, f_{vtx} refers to the fraction of events with a correctly selected vertex. The two functions g_{rv} and

[1]Nuisance parameters refer to those parameters which are not of primary interest in an analysis, but must be accounted for in extracting the parameters of primary interest.

$g_{\rm wv}$ are the probability density functions for the diphoton mass built from the the sum of Gaussians, described above, for events with correct and wrong vertex, respectively. $\sigma_{\rm M}$ is the width of each Gaussian, and $\delta_{\rm M}$ refers to the shift of the mean of each Gaussian with respect to the nominal Higgs boson mass $\rm M_H$.

The number of events in each category i is

$$N_s^i(\mathrm{M_H}) = \mu \cdot \sigma_{\mathrm{H}\to\gamma\gamma} \cdot L \cdot (A \cdot \epsilon^i_{\rm sel})\,, \tag{10.2}$$

where μ is the signal strength modifier on the cross section of Standard Model $\mathrm{H} \to \gamma\gamma$, which is the primary parameter of interest in the statistical analysis of this thesis (see chapter 12). $(A \cdot \epsilon^i_{\rm sel})$ is the acceptance times selection efficiency calculated from simulation and corrected for differences in efficiency between the simulation and the data, as we have shown in figure 8.11. L is the integrated luminosity.

Figure 10.4 shows the combined model for a Higgs boson mass at 120 GeV/c^2. Figure 10.5 shows the comparison between the parametrized model and the interpolated model for the mass point 125 GeV/c^2. Good agreement is obtained in general, though in a few categories there are some minor visible differences in the peak or in the tails. Only a difference of 0.3% on the expected asympotoic limit is found between the interpolated model and the parametrized model at the mass point 125 GeV/c^2. This small difference is neglected in this analysis.

Other systematic uncertainties which affect the signal shape are also parametrized through the model function defined in equation (10.1). For example, the energy smearing systematic uncertainties are propagated by a nuisance parameter on the Gaussian width $\sigma_{\rm M}$. The energy scale uncertainties are propagated by another nuisance parameter on the Gaussian mean $\delta_{\rm M}$. Systematic uncertainties in r_9 are also taken into account by adding a nuisance parameter to the yield of each category N_s^i. We will discuss in more detail, in chapter 12 which deals with the statistical analysis, how each nuisance parameter is taken into account in the likelihood function to extract limits on the signal cross section or p-values.

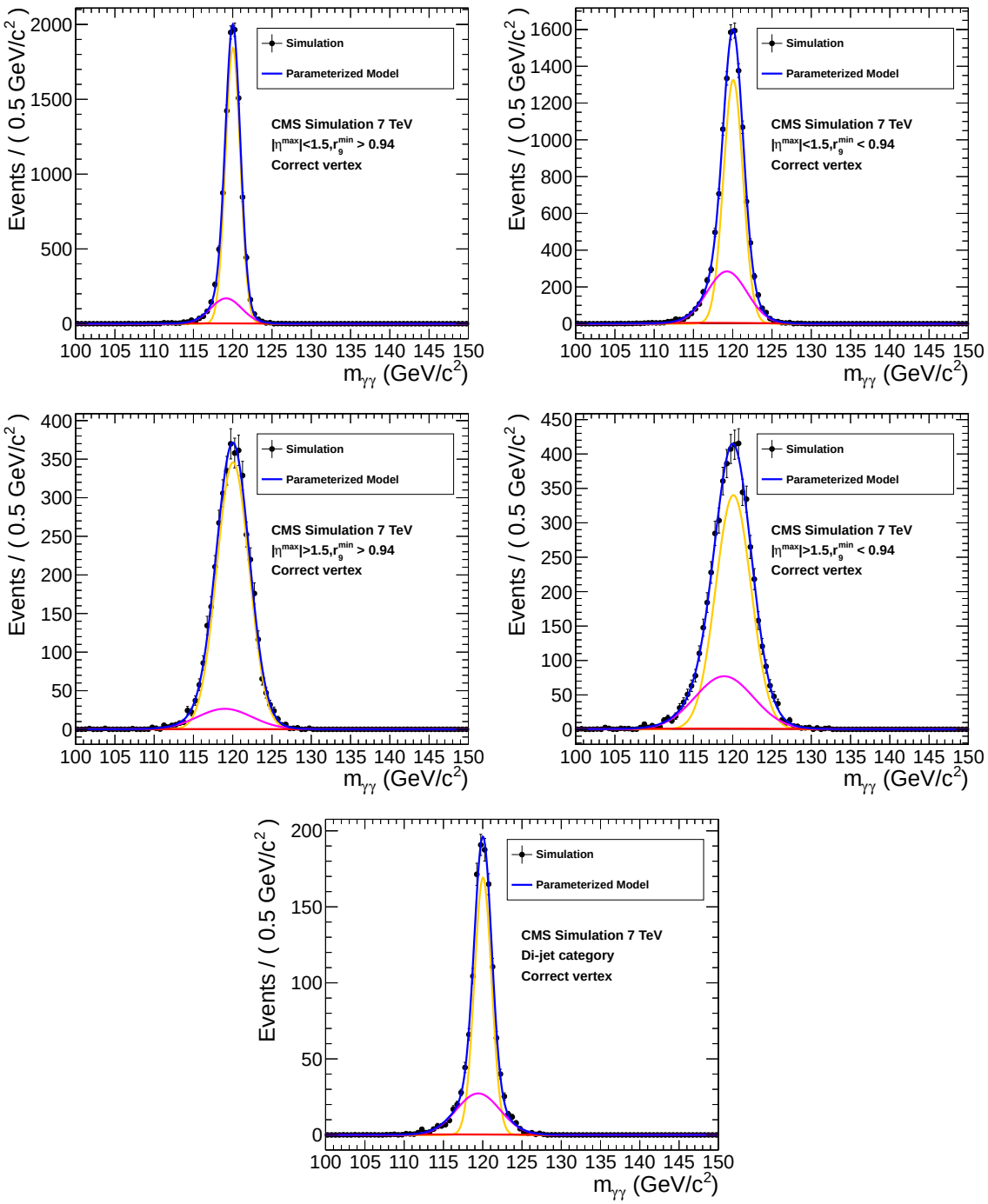

Figure 10.1: H $\rightarrow \gamma\gamma$ signal mass distribution in each diphoton category. The overlaid curve in blue on each distribution is the parametrized model. In these distributions, events with a correct vertex are selected. The other curves with different colors represent the Gaussian components of the model.

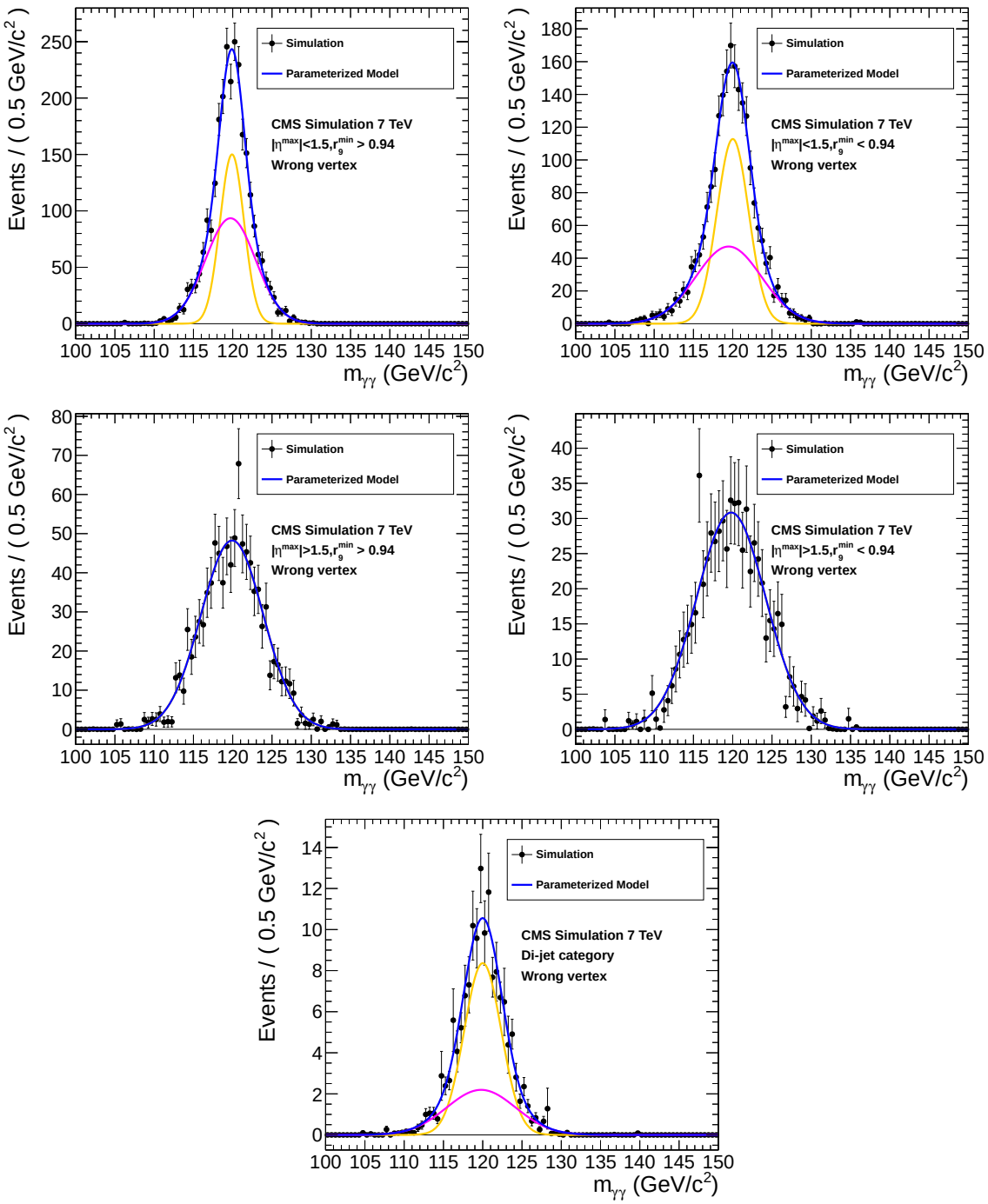

Figure 10.2: H $\rightarrow \gamma\gamma$ signal mass distribution in each diphoton category. The overlaid curve in blue on each distribution is the parametrized model. In these distributions, events with a wrong vertex are selected. The other curves with different colors represent the Gaussian components of the model.

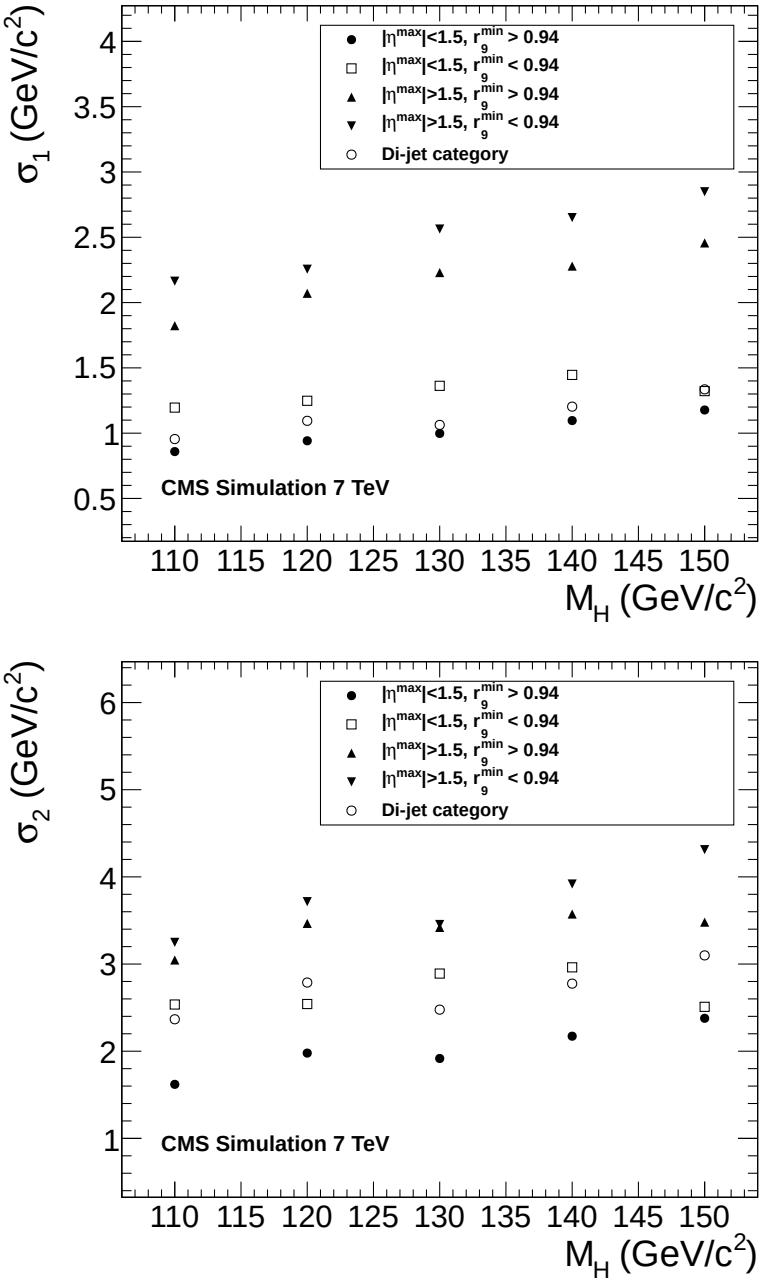

Figure 10.3: The width of the two Gaussian components σ_1 and σ_2 in the model used to fit the invariant mass distributions, for events with a correct vertex. These parameters, obtained from the five mass points, are used to predict the corresponding parameters for any given mass.

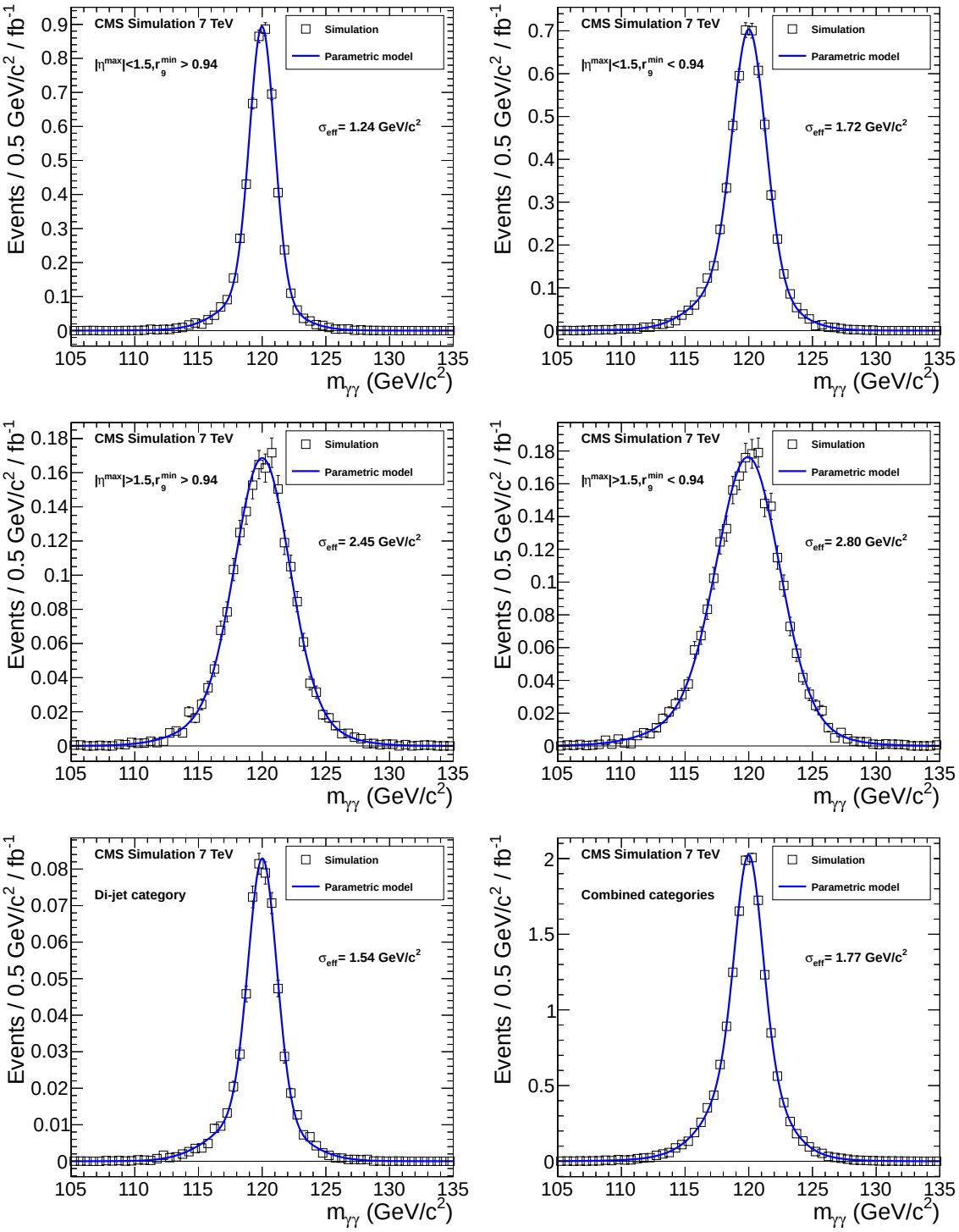

Figure 10.4: H $\rightarrow \gamma\gamma$ signal mass distribution in each diphoton category, and combined. The overlaid curve on each distribution is the parametrized model. The value of σ_{eff} represents the half of the shortest interval which contains 68.3% of the whole area under the curve.

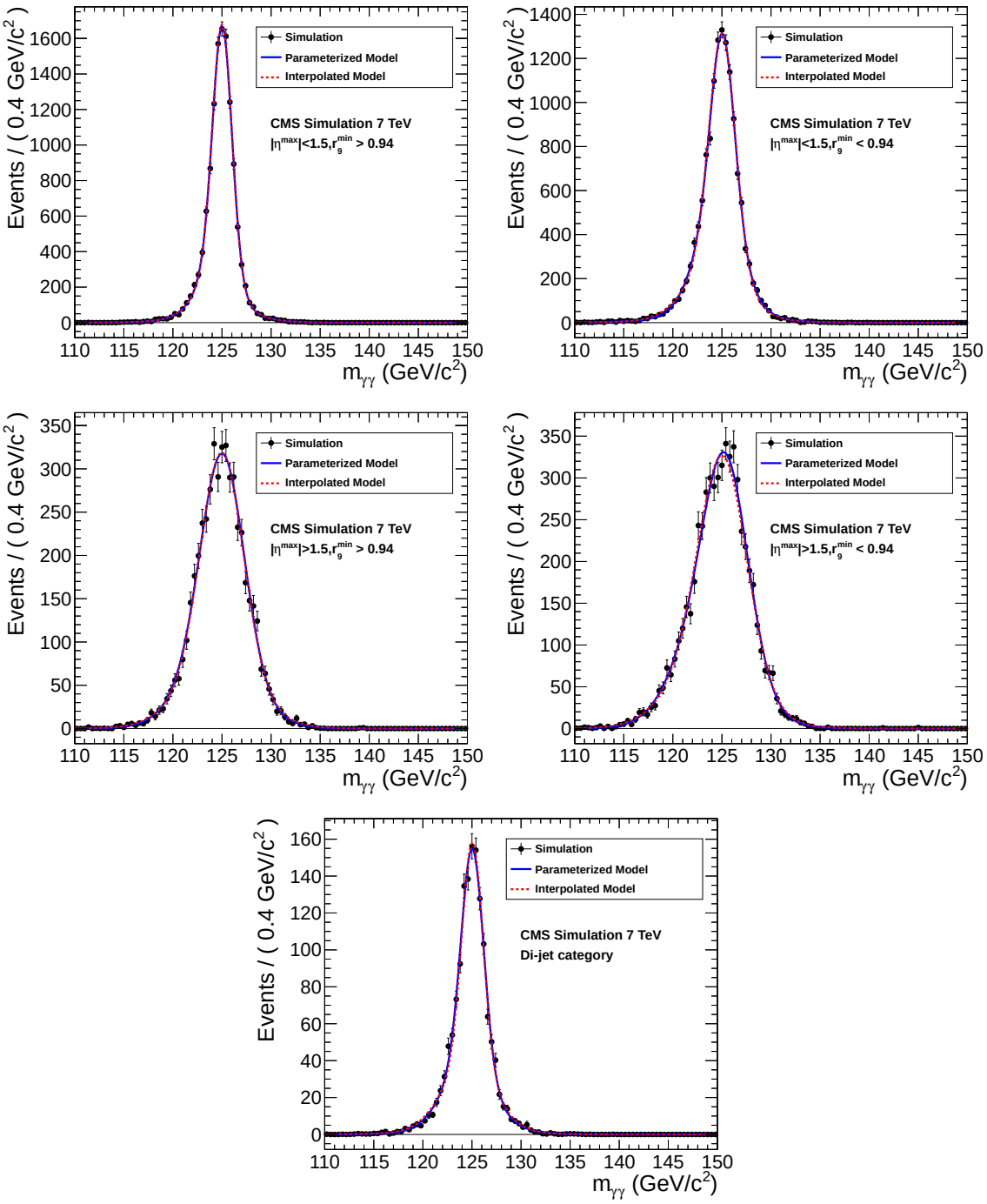

Figure 10.5: Comparison between the parametrized and interpolated H $\to \gamma\gamma$ model in each diphoton category.

10.2 Background Modeling

10.2.1 Introduction

The background to the H $\to \gamma\gamma$ signal is dominated by three processes, $\gamma\gamma$, γ+jet, and jet+jet, which were introduced in section 3.2. These processes are all generated at leading order, therefore the kinematics distributions are not precisely modeled. In addition, the process of jets misidentified as photons is complex and subject to many details in the simulation, and therefore this process may not be well modeled in the simulation. However, simulation can give us some idea of the possible functional forms that can be used to represent the real data.

In this section we study the possible functional forms to model the background distributions in the inclusive category. Given that we do not know what the true functional form is, the goal is to find the one which minimizes the bias on the fitted signal strength μ for a number of different assumed truth models. The set of truth models that we test are intended to be representative of the set of possible functional forms that the actual background shape in the data may take. In practice, the set of functional forms that we test are intended to yield conservative estimates of the uncertainty on the background, and therefore certain functional forms that do not closely fit the simulation shape, as well as other functional forms, are also considered. Figures 10.6 to 10.9 show the background fit with a variety of functional forms to the invariant mass distributions in each diphoton category from the simulation, normalized to an integrated luminosity of 5.08 fb^{-1}.

The following background models have been studied:

- Bernstein polynomials with degree N,

$$N\text{Pol}(x) := B(x) = \sum_{n=1}^{N} \beta_n b_{n,N}(x)\,, \tag{10.3}$$

  where β_n is the Bernstein coefficient and

$$b_{n,N}(x) = C_N^n x^n (1-x)^{N-n}, n = 0, ..., N\,, \tag{10.4}$$

where C_N^n is the binomial coefficient.

- Power law function,

$$1\text{Pow}(x) := cx^{-n}\,, \tag{10.5}$$

  where c is the normalization and n is the power index which controls the decline of the distributions.

- Exponential function,

$$1\text{Exp}(x) := ce^{-nx}\,, \tag{10.6}$$

  where c is the normalization and n is the parameter which controls the decline of the distributions.

- Laurent series with 4 terms,

$$4\text{Lau}(x) := c(f_1x^{-3} + f_2x^{-4} + f_3x^{-5} + (1 - f_1 - f_2 - f_3)x^{-6})\,, \tag{10.7}$$

  where $f_{1,2,3}$ refer to the fraction of the first three components.

Though we have chosen these function forms to fit the distributions, we do not conclude that any of them represents the true background model in the real data. The study only results in an estimate of the amount of bias that remains if a background model that is different from the true model is chosen. Given that the set of functional forms that we test are intended to be representative of the range of possible background shapes, the bias estimate is assumed to provide the proper uncertainty coverage.

The rest of this chapter is organized as follows. In the next section we study the bias on the signal strength μ due to a wrong choice of background model, and then study the sensitivity loss on the exclusion limit on μ. The same study is performed for the signal significance. In this chapter, we do not consider any systematic uncertainties related to the signal modeling, since they are not correlated with any possible systematic uncertainties in the background modeling.

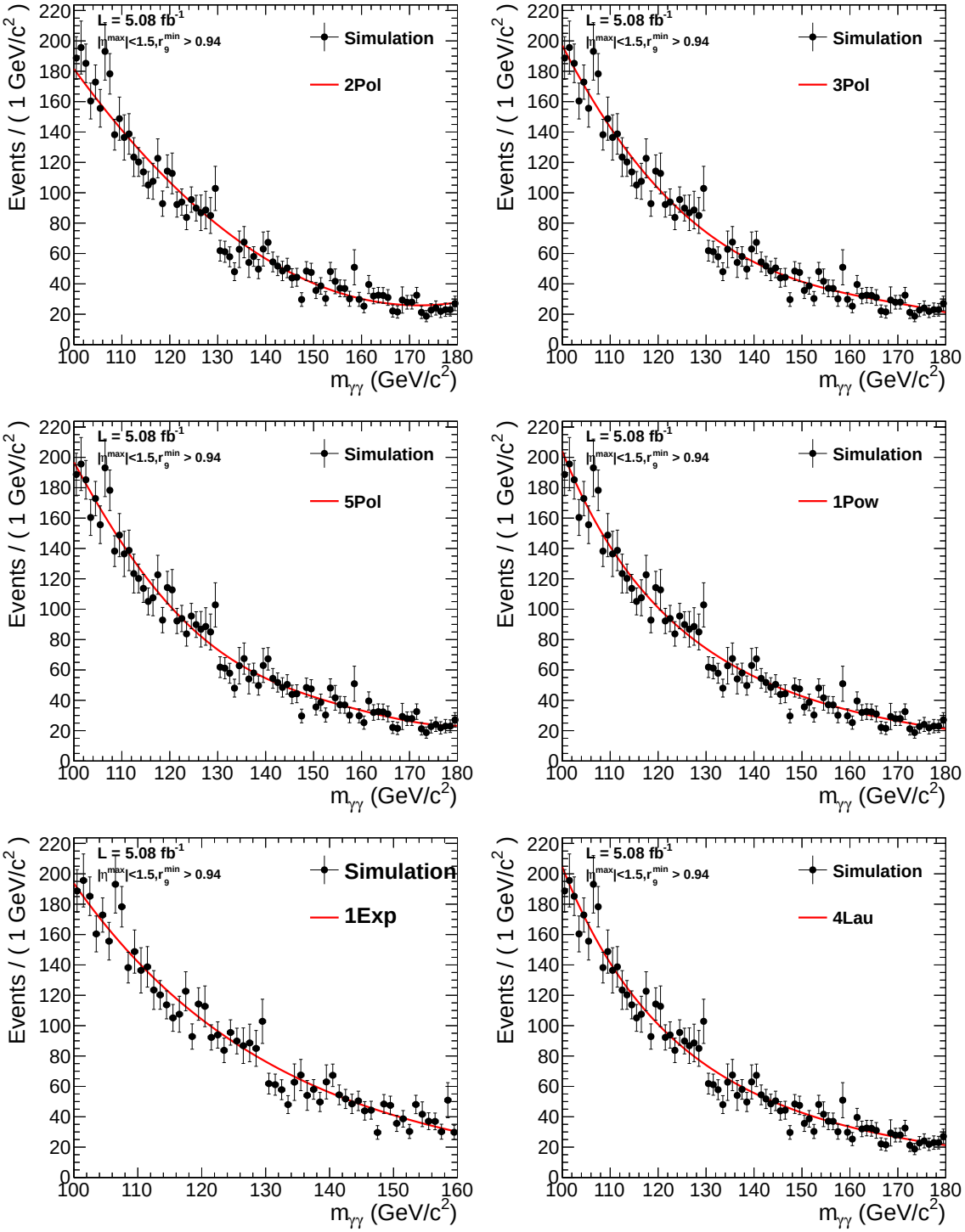

Figure 10.6: Background fit to the invariant mass distribution of events in the first category, from simulated events normalized to 5.08 fb^{-1}. Each plot shows a different choice of the functional form of the background model.

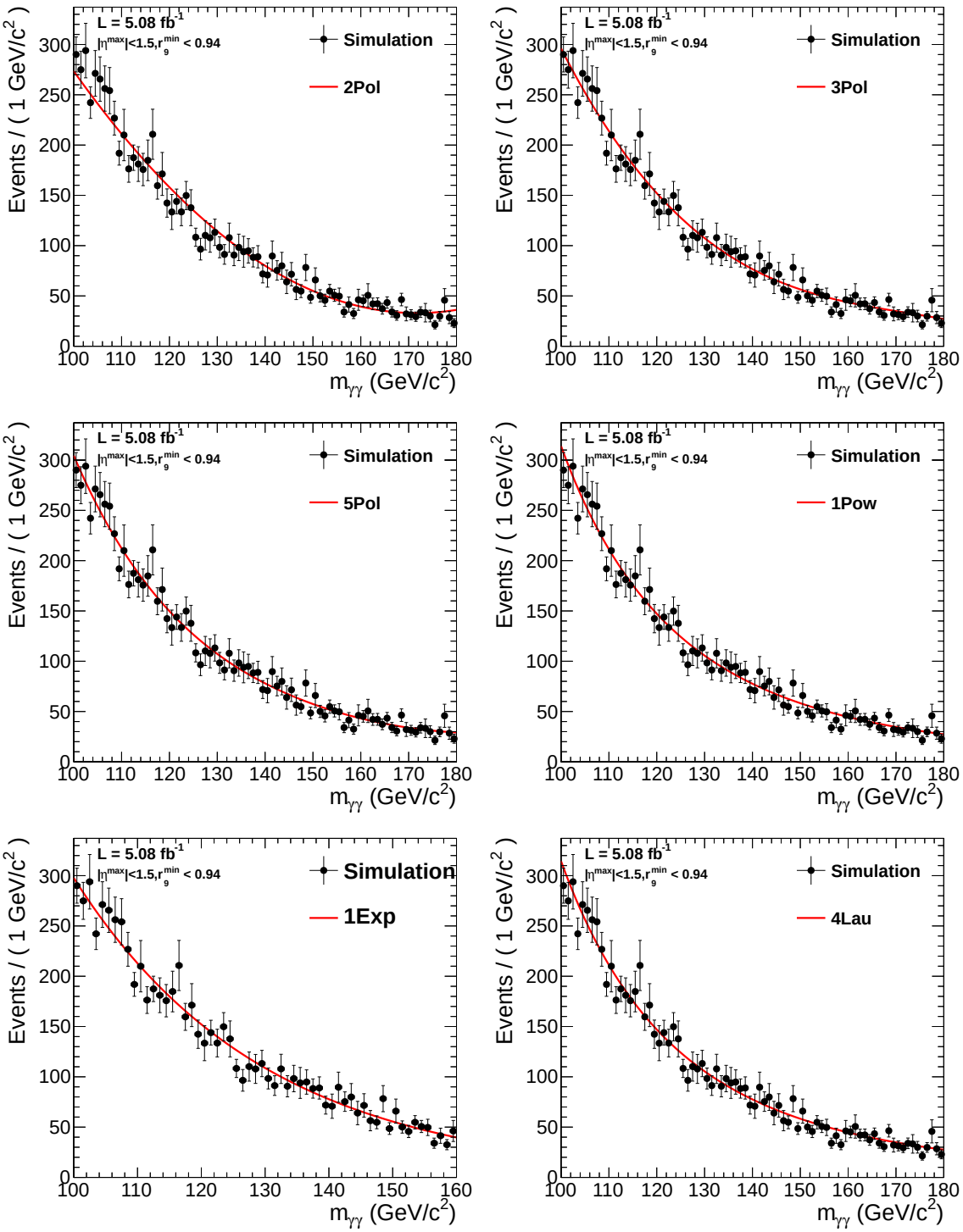

Figure 10.7:]
Background fit to the invariant mass distribution of events in the second category, from simulated events normalized to 5.08 fb^{-1}. Each plot shows a different choice of the functional form of the background model.

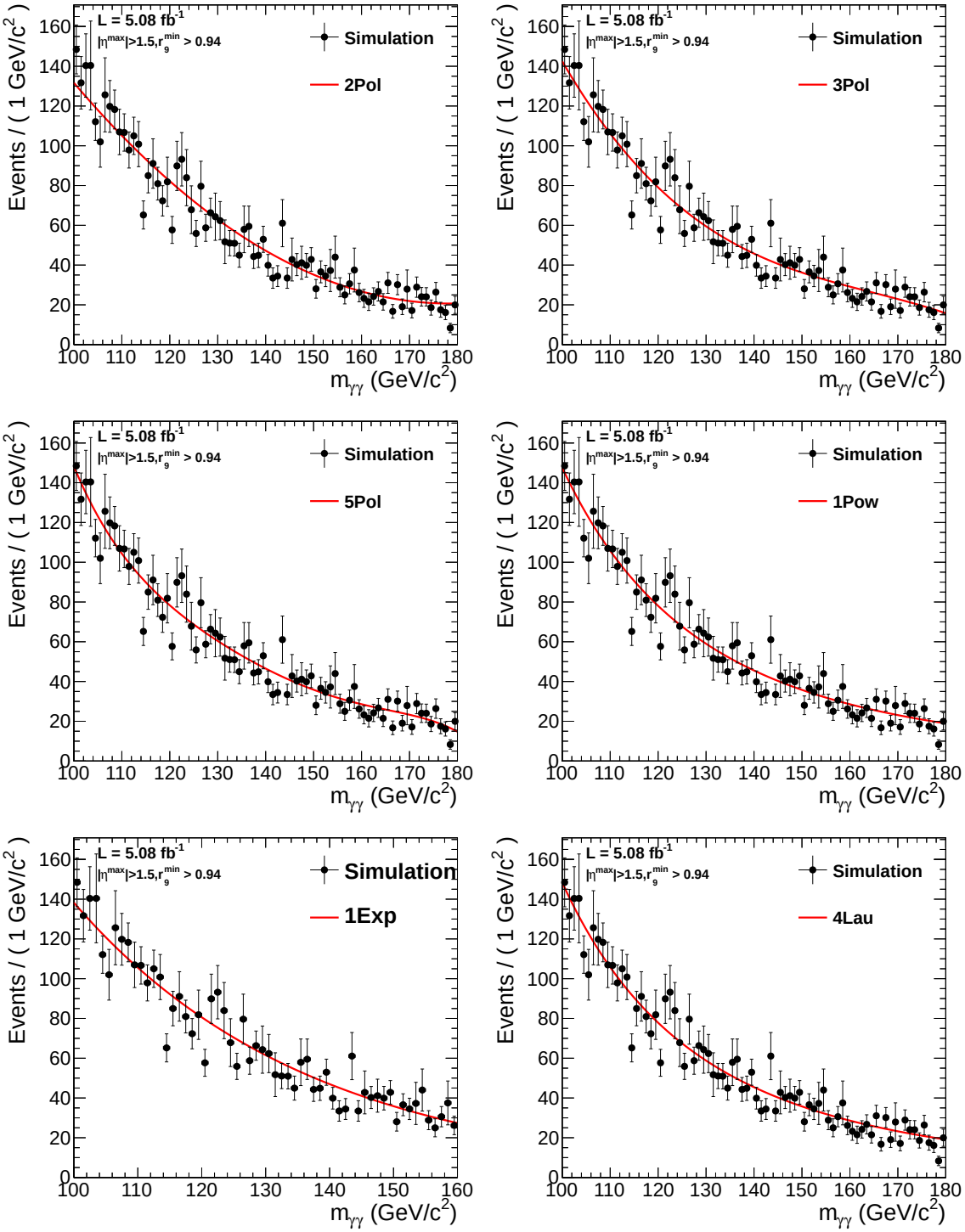

Figure 10.8: Background fit to the invariant mass distribution of events in the third category, from simulated events normalized to 5.08 fb^{-1}. Each plot shows a different choice of the functional form of the background model.

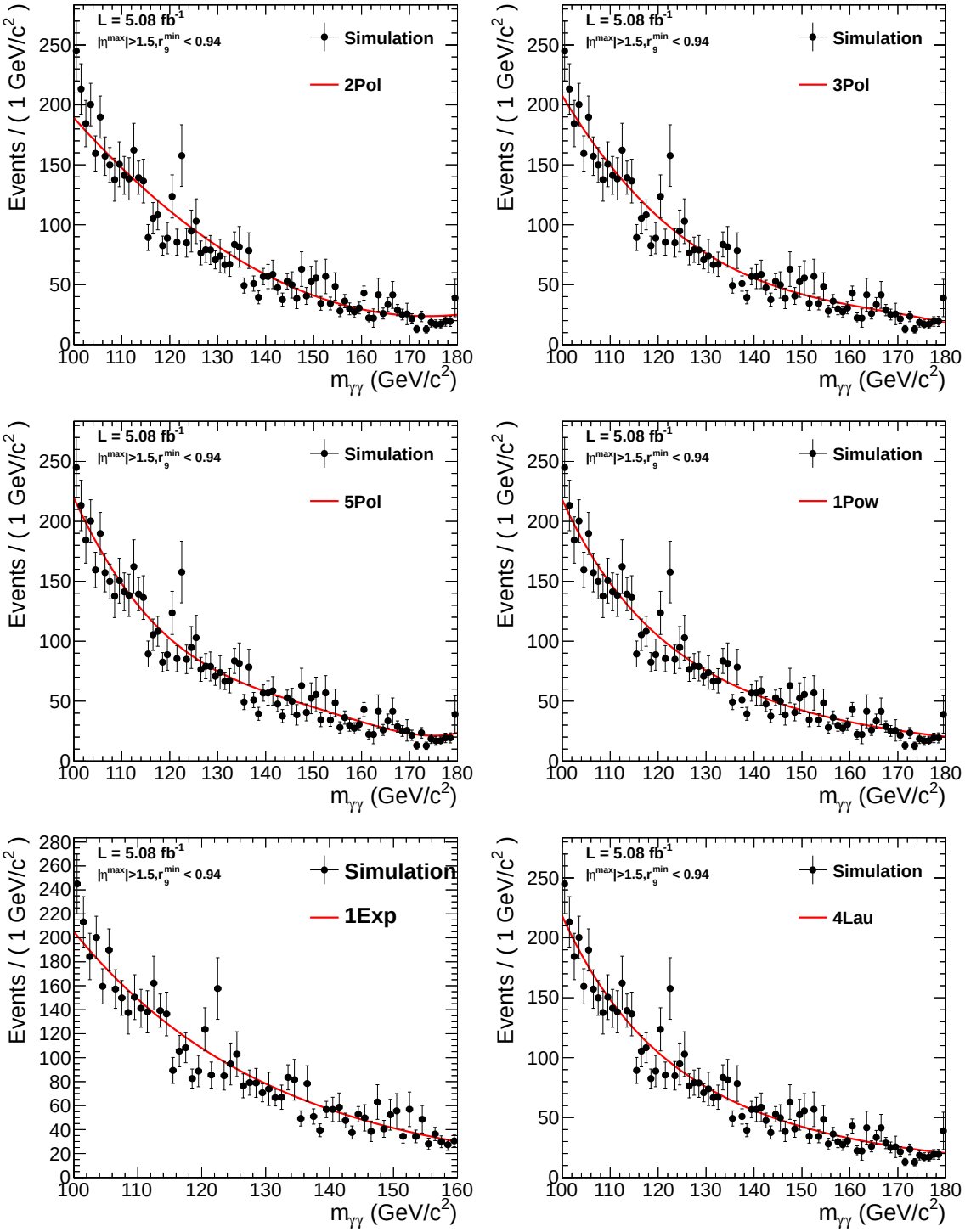

Figure 10.9: Background fit to the invariant mass distribution of events in the fourth category, from simulated events normalized to 5.08 fb^{-1}. Each plot shows a different choice of the functional form of the background model.

10.2.2 Bias on the signal strength

In this section we study the bias on the signal strength modifier μ induced by using a different background model than the true one. First we generate a pseudo-dataset from one particular model, which we call the "truth model", and the Standard Model $H \to \gamma\gamma$ signal model at a particular mass point. Then we fit the pseudo-data with a background model, which we call the "fit model". The fit model for the background and the signal model are then used to extract μ. The difference in the mean value of the best fitted μ over the set of pseudo-experiments from 1 is thus the bias due to the chosen fit model:

$$\text{Bias} = \bar{\mu}_{fit} - 1\,. \tag{10.8}$$

In this section, the signal $H \to \gamma\gamma$ is fixed at $M_H = 130$ GeV/c^2. To check the above procedure, we use the same fit model as the truth model. The obtained mean value should be consistent with one. The results are shown in figure 10.10, where we use the 5^{th} order polynomial for the background model. The left plot shows that the mean value of the fitted μ is consistent with one, indicating that there no bias on the mean. The right plot shows the distribution of the pull, defined as $(\mu - 1)/\sigma_\mu$. Its width is also consistent with unity, indicating no bias on the estimation of the fit uncertainty. In these pseudo-experiments, we have chosen the fit range of the invariant mass between 100 and 180 GeV/c^2. In addition, we compare the bias study results with a different choice of the mass fit range: 100 and 160 GeV/c^2. Figure 10.11 to figure 10.12 show the distributions of the fitted signal strength and its pull, where the 1Pow, 1Exp, and 4Lau truth background models are used to test the fit model of 5Pol in the fit range between 100 and 180 GeV/c^2. Appendix A shows all the remaining distributions for other choices of the fit models, and a different fit range between 100 and 160 GeV/c^2.

Table 10.1 summarizes the largest observed bias on the fitted signal strength for each fit model. In general, the power-like functions, 1Pow or 4Lau, or exponential function give large biases on the signal strength. The model with smallest bias is 5Pol. 4Pol is also comparable when the fit range is from 100 to 160 GeV/c^2.

Fit model	fit range 100 to 160 GeV/c^2	fit range 100 to 180 GeV/c^2
2Pol	-60%	-30%
3Pol	28%	14%
4Pol	3.1%	14%
5Pol	2%	2.5%
1Pow	84%	150%
1Exp	-41%	-40%
4Lau	83%	200%

Table 10.1: Summary of the largest bias on the signal strength with the choice of a particular background model.

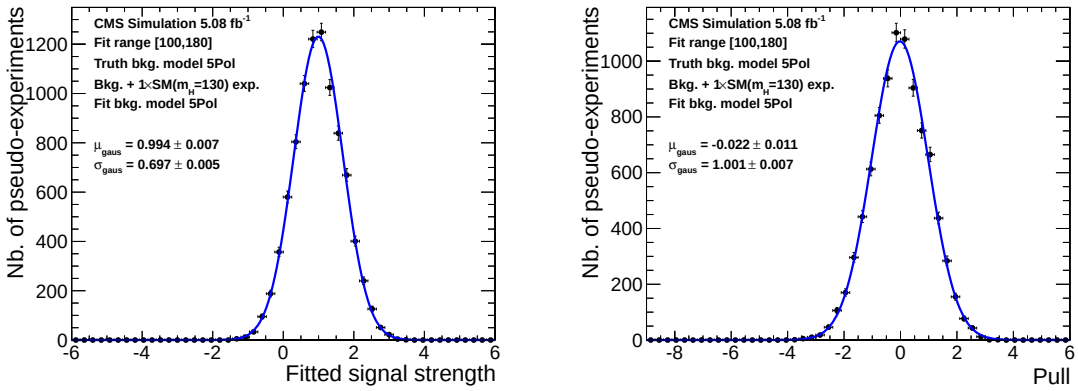

Figure 10.10: Left: distributions of the fitted signal strength from pseudo-experiments. Each pseudo-experiment is drawn from a 5^{th} order polynomial background plus a Standard Model H $\rightarrow \gamma\gamma$ with M_H = 130 GeV/c^2, in the invariant mass range from 100 to 180 GeV/c^2, and fitted with the same model. The Gaussian mean is consistent with unity, which means there is no bias. The Gaussian width represents the statistical error of the signal strength due to limited statistics in each pseudo-experiment. Right: the pull distribution. The width is consistent with unity, indicating that the procedure gives a reliable estimation of the statistical error.

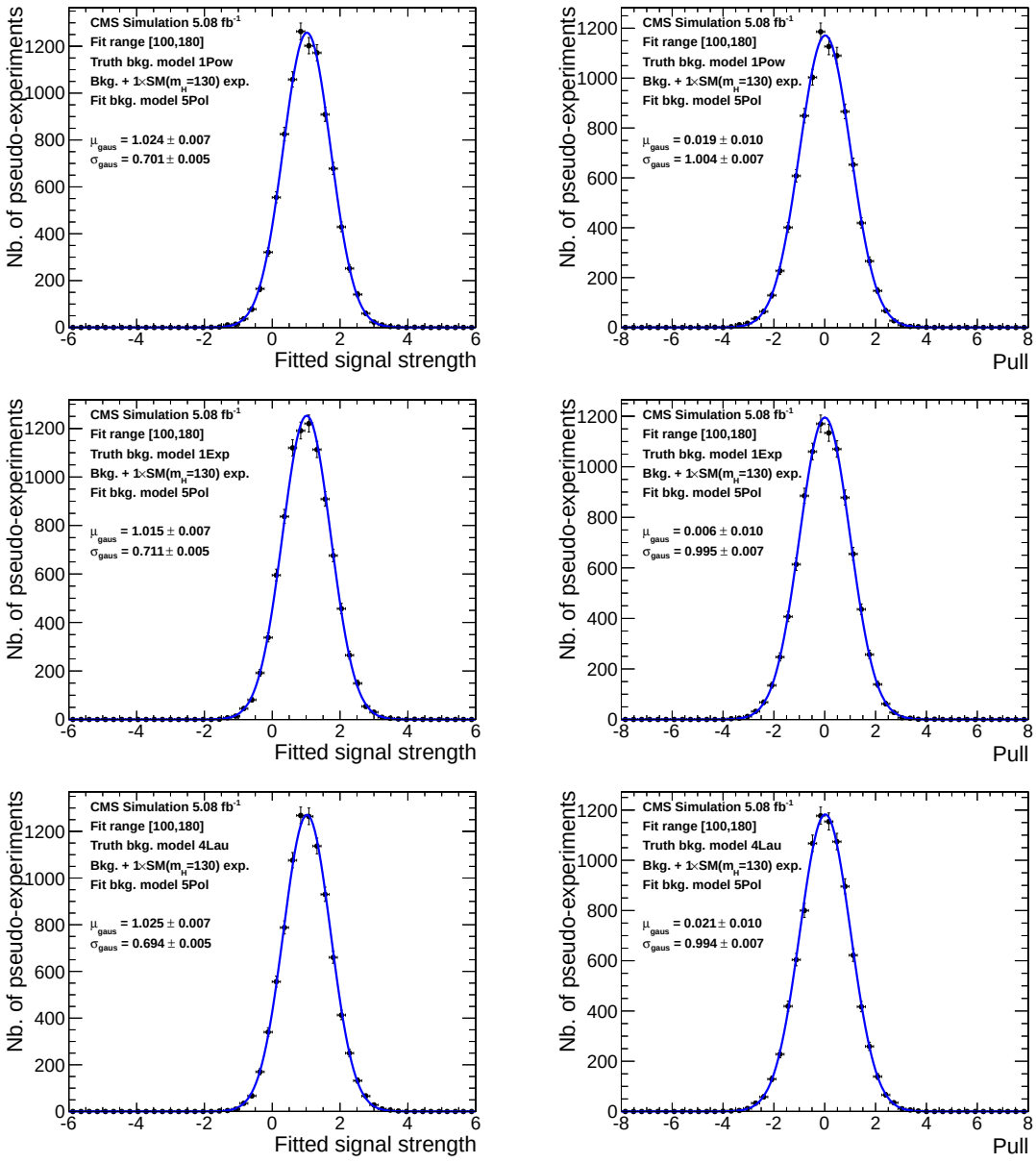

Figure 10.11: Distributions of the fitted signal strength and the pull from pseudo-experiments. Different truth background models, 1Pow, 1Exp, and 4Lau, are tested against the fit model of a 5^{th} order polynomial. The invariant mass range is chosen to be 100 to 180 GeV/c^2.

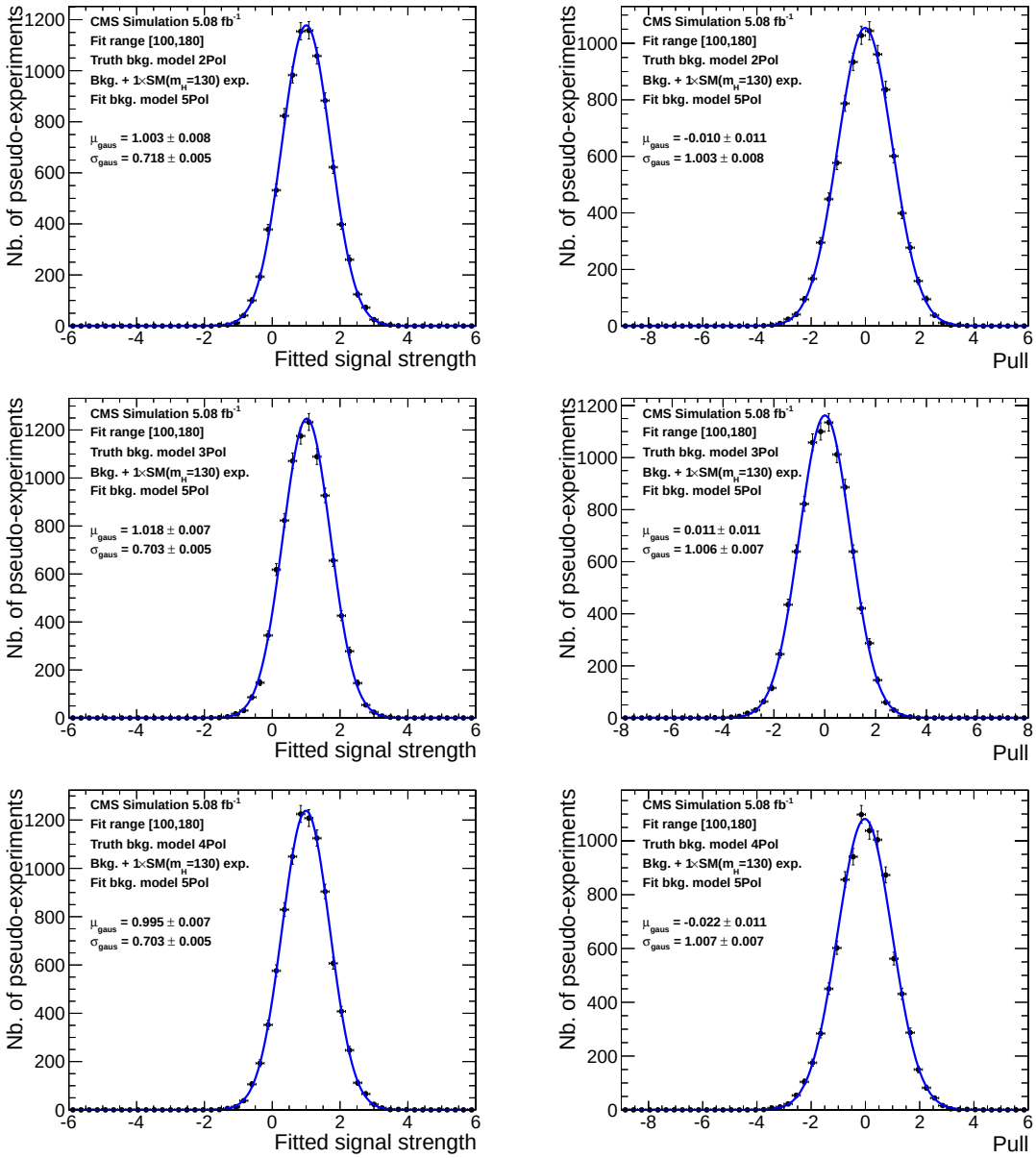

Figure 10.12: Same as figure 10.11, except that 2Pol, 3Pol, and 4Pol truth background models are used here.

10.2.3 Sensitivity loss on the exclusion limits

We have found in the previous section that the function of the 4th order polynomial, with fit range from 100 to 160 GeV/c^2, and the 5th order polynomial, give relatively small bias on the signal strength among the tested functions. In this section we study the loss of the expected sensitivity in terms of the median expected exclusion limits at the 95% Confidence Level (CL). For a chosen fit model under study, we generate a number of background-only pseudo-experiments with different truth models. In each pseudo-experiment, two values of the median expected exclusion limits at a given Higgs boson mass point are then extracted, with the truth model and with the fit model, from the pseudo data. The relative difference on average indicates the loss in the sensitivity that results from choosing a different model than the truth one

$$\text{Sensitivity Loss(SL)} = \frac{1}{N}\sum_{n=1}^{N}(\mu_{\text{fit}}^{\text{med. 95CL}} - \mu_{\text{truth}}^{\text{med. 95CL}})/\mu_{\text{truth}}^{\text{med. 95CL}}. \qquad (10.9)$$

SL being positive means that the chosen fit model would give less sensitive results than the truth model, which means that the results are conservative. Negative SL means the results are overly optimistic, in the sense that the signal strength would be overestimated.

Figures 10.13 and 10.14 show the sensitivity loss when the 5th order polynomial is used for the background model, when the fit range is from 100 to 180 and 100 to 160 GeV/c^2, respectively. Figure 10.15 shows the sensitivity loss when the 4th order polynomial is used, when the fit range is from 100 to 160 GeV/c^2.

In general, we observed a positive SL, except for the case when the 4th order polynomial is used while the truth model is 5th order polynomial. There is at most a 25% SL when the 5th order polynomial is used when the fit range is from 100 to 160 GeV/c^2. The sensitivity loss reduces to about 15% if the fit range is from 100 to 180 GeV/c^2, due to the additional constraints from the data in the mass range between 160 and 180 GeV/c^2. Therefore, we choose the 5Pol function as the background model for the inclusive categories, with the fit range from 100 to 180 GeV/c^2. For the di-jet

category, we use the 2Pol function [92].

10.2.4 Bias on the signal significance

In this section we study the bias on the signal significance induced by using the 5th order polynomial. We use the asymptotic formula which we will discuss in section 12.4.1 to calculate the local significance. Without systematic uncertainties on the signal model, the significance can be estimated as

$$Z = \sqrt{-2\ln(\frac{L(\text{data}|0,\hat{\tau}_b)}{L(\text{data}|\hat{\mu},\hat{\tau}_b)})}, 0 \leq \hat{\mu}\,, \tag{10.10}$$

where $\hat{\tau}_b$ represents the values of the parameters in the background model when the likelihood function L in the denominator is maximized under the signal+ background hypothesis. Here $\hat{\tau}$ is different from $\hat{\theta}$ in section 12.4.1. The former refers to the background parameters which are determined directly from data or pseudo-data. The latter includes the nuisance parameters related to the signal modeling as well.

To measure the bias on the signal significance, we perform pseudo-experiments, similarly as in section 10.2.2. Each pseudo-experiment is generated with a particular truth background model summed with the Standard Model H $\rightarrow \gamma\gamma$(130 GeV/c^2) signal model. Then the signal significance is evaluated according to equation (10.10) separately using the truth model or the 5th order polynomial at the mass point 130 GeV/c^2. The difference between the two signal significances averaged over many pseudo-experiments represents the bias from using the 5th order polynomial.

According to equation (10.10), any bias on the signal significance comes from the bias in the difference between the two $-$log likelihood values under the background-only and signal+background hypothesis. The biases in these two values are highly correlated, as shown in figure 10.16, and thus taking the difference reduces the bias. Figure 10.16 right shows the signal significance distributions. The average signal significance is 1.75 if the truth model is used to fit each pseudo-experiment. The average value is 1.83 if the 5th order polynomial is used. Therefore there is about

+4% relative bias. A positive value of the bias means that the obtained significance is more optimistic than it should be, which could potentially lead to an early or false claim of a discovery, if the bias is not taken into account.

Figure 10.17 shows the bias for different truth background models. Among these truth models, the largest negative bias is -0.14 when the truth model is 4Lau. The fact that the bias is negative means that the obtained signal significance is conservative. The largest positive bias is 0.08 when the truth model is 1Pow. Given the expected signal significance has a mean about 1.8 and a RMS width about 0.8, which is a factor of 10 larger than the bias, we consider this bias small and neglect it.

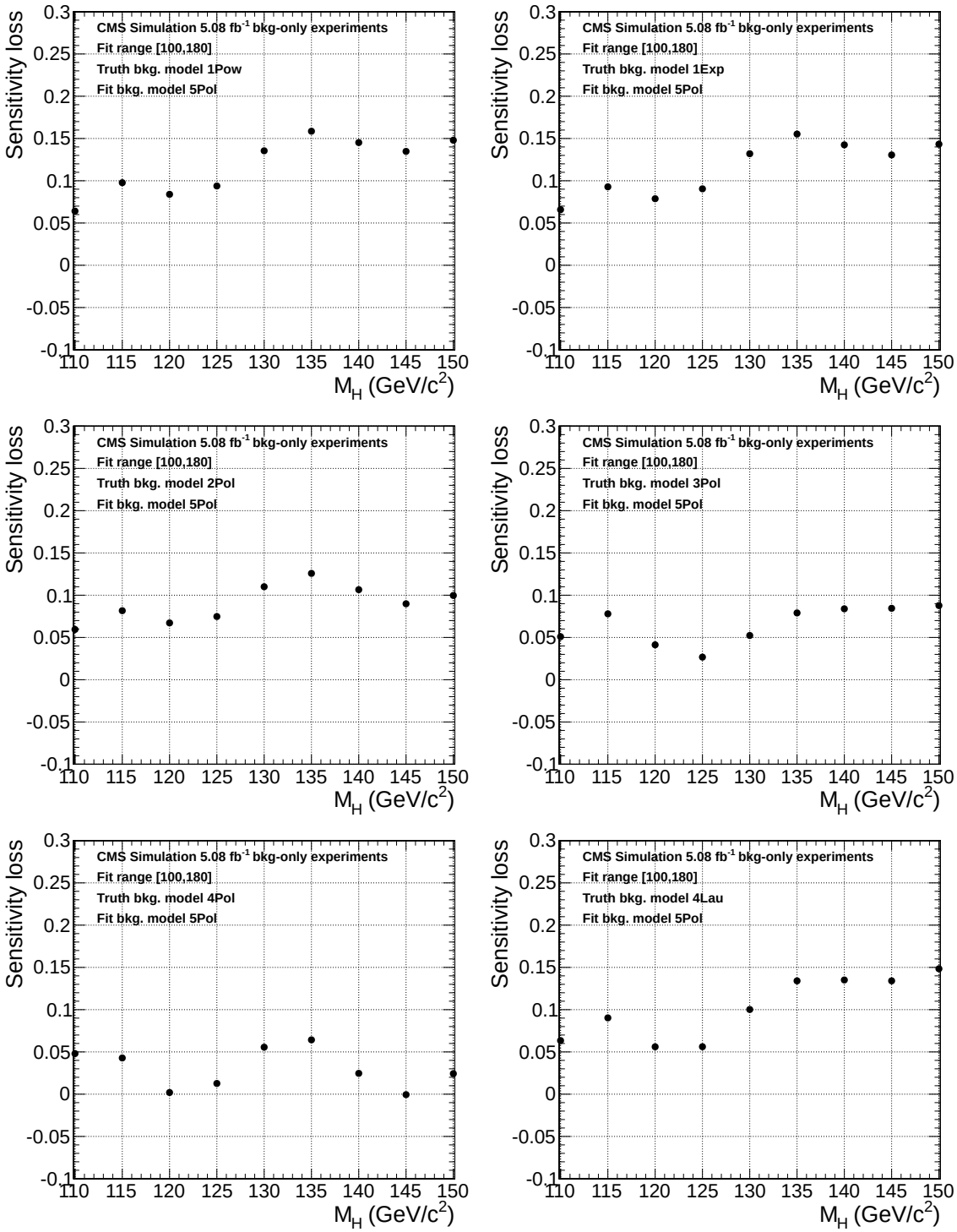

Figure 10.13: Sensitivity loss as a function of the Higgs boson mass, if the 5th order polynomial is used for the background model while the truth background model is different, indicated on each plot. Fit range is from 100 to 180 GeV/c^2.

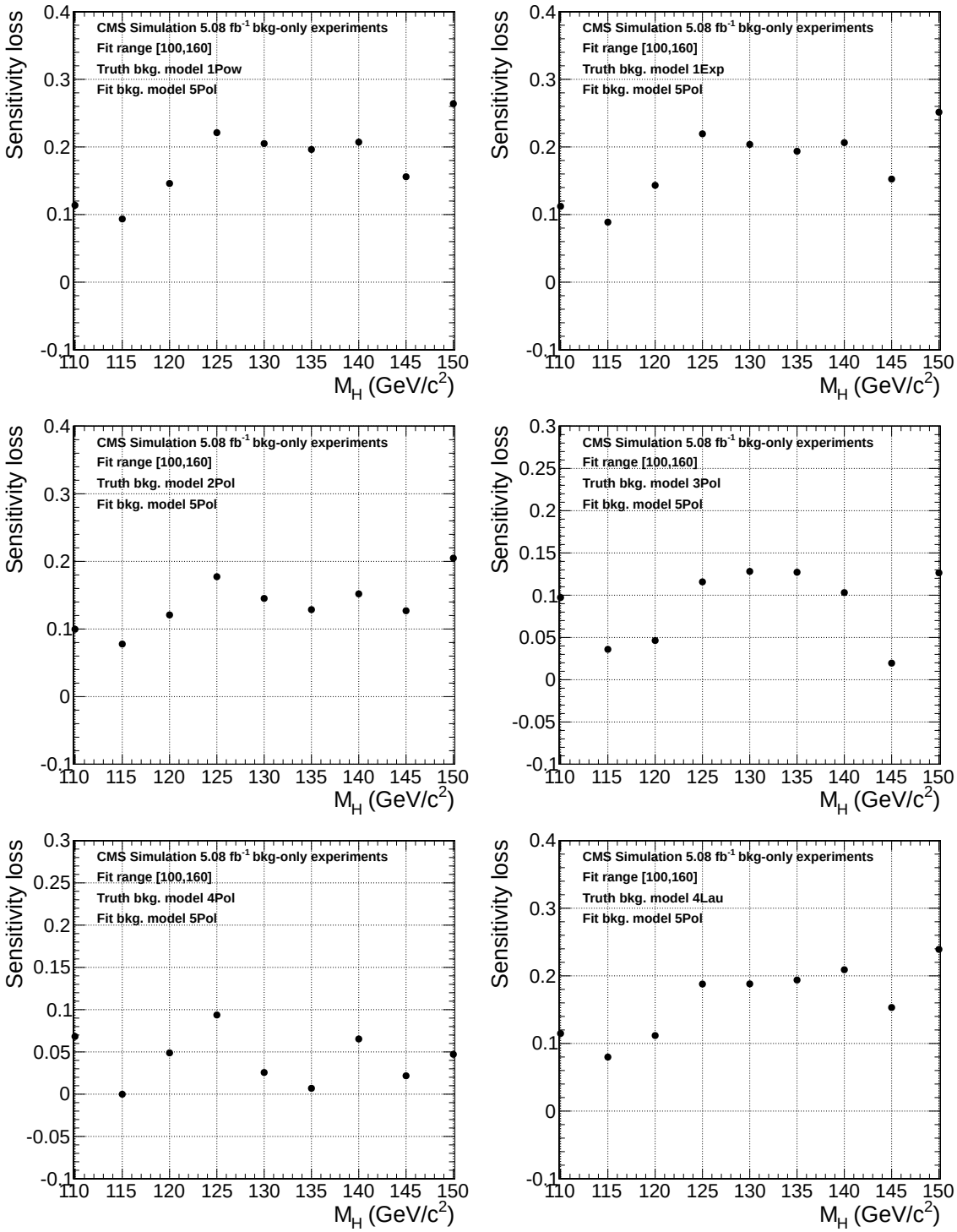

Figure 10.14: Sensitivity loss as a function of the Higgs boson mass, if the 5th order polynomial is used for the background model while the truth background model is different, indicated on each plot. Fit range is from 100 to 160 GeV/c^2.

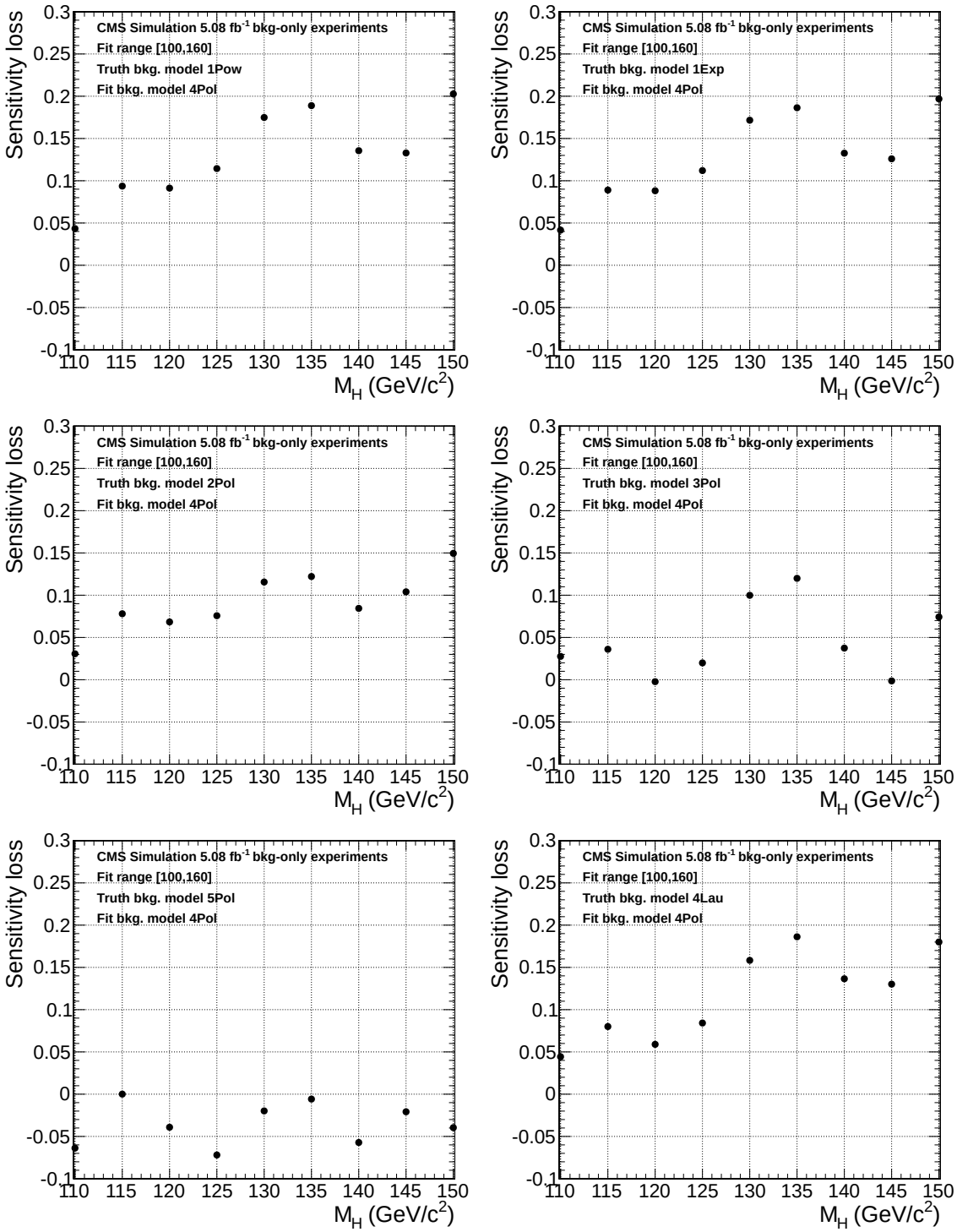

Figure 10.15: Sensitivity loss as a function of the Higgs boson mass, if the 4th order polynomial is used for the background model while the truth background model is different, indicated on each plot. Fit range is from 100 to 160 GeV/c^2.

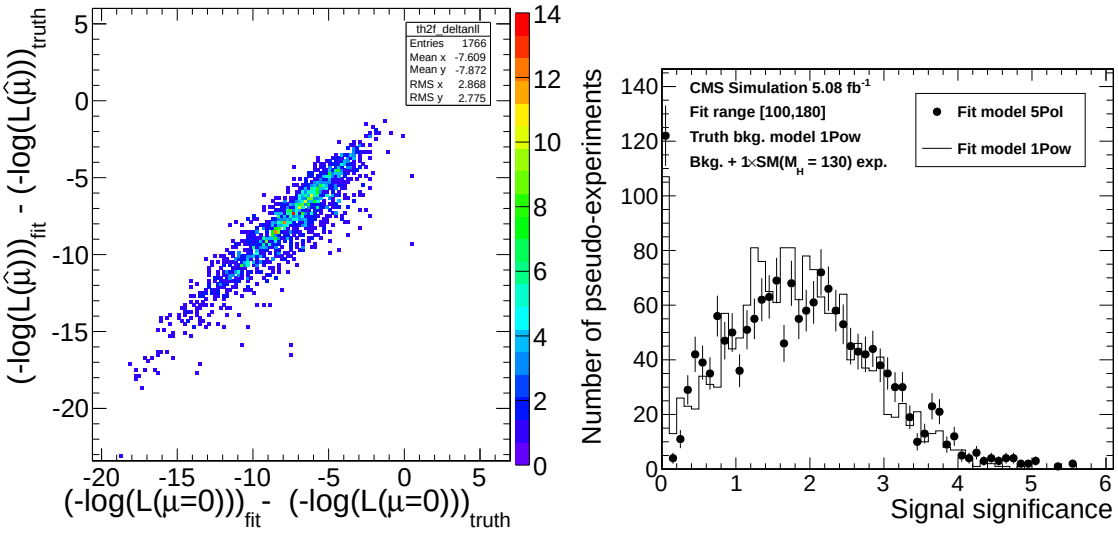

Figure 10.16: Left, correlation between the bias on the $-\log$ likelihood values under the signal+background and the background-only hypothesis from pseudo-experiments. Each pseudo-experiment is generated with a power low function (truth model) + H $\rightarrow \gamma\gamma$ (130GeV/c^2) signal model. The bias on the likelihood values, under each hypothesis, is the difference between the values obtained from the truth background model and the 5th order polynomial. Right, distributions of the signal significance from pseudo-experiments.

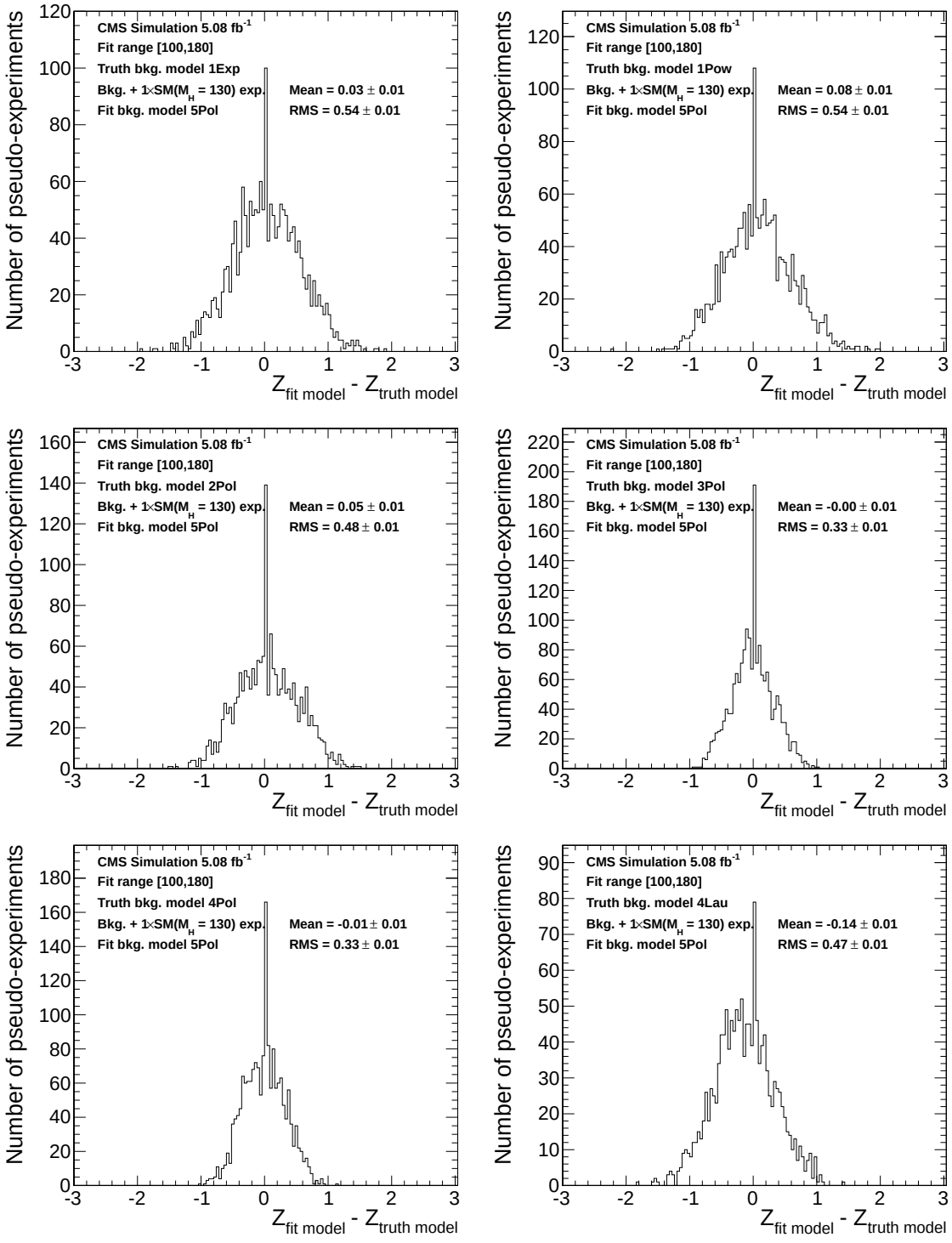

Figure 10.17: Bias of the signal significance for the 5th order polynomial from pseudo-experiments. On each figure, pseudo-experiments are generated with a background model (truth model) + H $\rightarrow \gamma\gamma$(130 GeV/c^2) signal model, and two values of signal significance are obtained, with the truth background model and the 5Pol. The difference between these two significances on average represents the bias of the 5Pol. The peak at zero means a downward statistical fluctuations in the pseudo-experiment, thus no significance is observed.

Chapter 11

Systematic Uncertainties

In this chapter we discuss all systematic uncertainties considered, related to the H $\rightarrow$ $\gamma\gamma$ search.

The background mass spectrum and yield of each di-photon category is determined by fitting the corresponding data with a 2nd order polynomial function in the di-jet category and a 5th order polynomial in the other inclusive categories. The normalization and polynomial coefficients are allowed to float unconstrained in the fit. The statistical uncertainties on these parameters represent the full set of systematic uncertainties on the background model.

The signal model, based on the simulation, suffers from a variety of systematic uncertainties. From Eq. 10.1, which defines the signal model for each category, there are two types of systematic uncertainties. The first type are systematic effects that affect the signal yield, for example systematic uncertainties on the luminosity and the selection efficiency. Uncertainties related to the r_9 categorization induce event migration among different categories, except for the di-jet category. The other type of systematic uncertainties are ones that change the signal shape. Examples include the energy scale and energy smearing which directly affect the Gaussian model defined in Eq. 10.1. Table 11.1 summarizes all the systematic uncertainties considered in this analysis.

- Integrated luminosity. 2.2% uncertainty measured by the luminosity group [99].
- Theoretical calculations on the cross section of H $\rightarrow$ $\gamma\gamma$ have systematic uncer-

tainties due to uncertainties on the QCD scale and Parton Distribution Function (PDF). The systematic uncertainties due to the QCD scale are assumed to be uncorrelated among different production modes, while the systematic uncertainties due to the PDF uncertainties are assumed to be correlated for processes with the same initial states and uncorrelated for processes with different initial states. Taking into account the relative contribution to the yield from different production modes, the total cross section systematic uncertainties from the QCD scale are estimated to be 11.4% and 3.8% for the inclusive and di-jet category, respectively. The corresponding systematic uncertainties from the PDF are estimated to be 6.6% and 1.6%, respectively.

- Trigger efficiency uncertainties [92]. An uncertainty of 0.4% is assigned for the 4th inclusive category and 0.1% for other categories.

- r_9 disagreement between the data and simulation. This results in an 8% migration between the first two inclusive categories (barrel) and 11.5% between the other two inclusive categories (barrel and endcaps mixed).

- Photon identification efficiency uncertainties. The uncertainty of 1% in the identification efficiency in the barrel results in an uncertainty of 2% on the signal yield for the first two inclusive categories, an uncertainty of 0.8% for the other two inclusive categories, and an uncertainty of 1.65% for the di-jet category. The 2.6% efficiency uncertainty in the endcap results in an uncertainty of 3% on the signal yield for the last two inclusive categories, and an uncertainty of 1.5% for the di-jet category.

- Energy smearing uncertainties. These uncertainties affect the mass resolution σ_M/M_H, where σ_M refers to the Gaussian width defined in equation (10.1). The uncertainties on the energy smearing, shown in table 5.2, result in uncertainties of 0.22%, 0.26%, 0.37%, 0.30% and 0.26% on σ_M/M_H for each of the four inclusive and di-jet category, respectively.

- Energy scale uncertainties. These affect the shift in the location of the mass

peak, δ_M/M_H, with respect to the nominal Higgs boson mass defined in equation (10.1). The uncertainties on δ_M/M_H are 0.28%, 0.28%, 0.47% 0.33% and 0.31% on δ_M/M_H for each of the four inclusive categories and the di-jet category, respectively.

- Event migration between the inclusive and di-jet categories, due to the systematic uncertainties related to the di-jet selection. These uncertainties result in a 28% uncertainty on the yield for the di-jet category, and a 1% uncertainty on the yield for each of the inclusive categories [92].

Source		**Uncertainty**	
Photon identification efficiency:	barrel	1.0%	
	endcap	2.6%	
r_9 >0.94 efficiency	barrel	4%	
(results in class migration)	endcap	6.5%	
		$r_9 > 0.94$	$r_9 < 0.94$
Energy resolution ($\Delta\sigma/E_{MC}$):	barrel low η, high η	0.22%, 0.61%	0.24%, 0.59%
	endcap low η, high η	0.91%, 0.34%	0.30%, 0.53%
Energy scale ($(E_{data} - E_{MC})/E_{MC}$)	barrel low η, high η	0.19%, 0.71%	0.13%, 0.51%
	endcap low η, high η	0.88%, 0.19%	0.18%, 0.28%
Integrated luminosity		2.2%	
Trigger efficiency: One or more photons $r_9 < 0.94$ in endcap		0.4%	
Other events		0.1%	
Vertex finding efficiency		0.4%	
Di-jet selections	inclusive category	1%	
(results in class migration)	di-jet category	28%	
Gluon fusion process cross section (scale)		+12.5%, -8.2%	
Gluon fusion process cross section (PDF)		+7.9%, -7.7%	
Vector boson fusion process cross section (scale)		+0.5%, -0.3%	
Vector boson fusion process cross section (PDF)		+2.7%, -2.1%	
Associated production with W/Z cross section (scale)		+1.8%, -1.8%	
Associated production with W/Z cross section (PDF)		+4.2%, -4.2%	
Associated production with $t\bar{t}$ cross section (scale)		+3.6%, -9.5%	
Associated production with $t\bar{t}$ cross section (PDF)		+8.5%, -8.5%	

Table 11.1: Separate sources of systematic uncertainties for the H $\rightarrow \gamma\gamma$ signal modeling. The magnitude of the variation of the source is shown in the right column.

Chapter 12

Statistical Analysis

12.1 Introduction

The statistical analysis of the H $\rightarrow \gamma\gamma$ search answers quantitatively two main questions given the observed yield and the distributions in data. In the case of no excess over the expected background, we measure the upper limit of the H $\rightarrow \gamma\gamma$ production cross section relative to the Standard Model H $\rightarrow \gamma\gamma$ cross section, namely μ. If the observed limit on μ is below one at one particular mass, then the Standard Model H $\rightarrow \gamma\gamma$ is excluded at that mass. This means that data is consistent with the hypothesis that the Standard Model Higgs boson does not exist. This hypothesis is referred to as the "background-only hypothesis". The hypothesis that the Standard Model Higgs boson does exist is refereed to as the "signal+background hypothesis". In the case where an excess is observed, we want to infer whether it is a result of a signal process or from background-only fluctuations. To this end we calculate the probability of this excess due to background-only fluctuations, which is called the background p-value. From the p-value, the significance Z, under the convention of a one-sided Gaussian tail, is calculated from the following equation

$$\mathrm{p} = \int_{\mathrm{Z}}^{\infty} \frac{1}{\sqrt{2\pi}} \mathrm{e}^{-\frac{\mathrm{x}^2}{2}} \mathrm{dx} = \frac{1}{2} \mathrm{P}_{\chi^2_1}(\mathrm{Z}^2)\,, \tag{12.1}$$

where $\mathrm{P}_{\chi^2_1}$ is the survival function of a χ^2 function with one degree of freedom. A smaller p-value corresponds to a higher probability that the excess is from a signal.

In high energy physics, usually, the discovery of a new signal can be claimed when the p-value is below 2.87×10^{-7}, corresponding to a significance of 5.

A number of statistical procedures [100–102] have been used to quantitatively measure the existence or nonexistence of hypothesized particles. These procedures, which can be very different in the details of their assumptions or implementations, can be classified into two approaches: Bayesian and Frequentist. The fundamental difference between the two approaches is in the way to interpret the probability. The Bayesian approach interprets the probability as a measure of the degree of belief about the value of the parameter of interest. The frequentist approach regards the probability as the frequency of occurrence in a large number of repeated experiments.

For ease of comparisons and combinations of the Higgs results, the ATLAS and CMS collaborations have arrived at a common statistical procedure [103] in 2011, based on a full frequentist approach. This approach is known as the LHC-style $CL_{\rm s}$.

In the next section, we introduce the $CL_{\rm s}$ procedure. After that, we introduce the asymptotic $CL_{\rm s}$ approach which has the advantage that it requires much less computation. Then we discuss how to quantify an excess using the $CL_{\rm s}$ approach.

12.2 Likelihood Construction and Statistical Procedure: $\mathbf{CL_S}$

In the $CL_{\rm s}$ approach, first we define a test statistic q, a quantity which is sensitive to the presence of the signal. Then we build the probability density function (*pdf*) for q in the background-only hypothesis and the signal+background hypothesis, using pseudo-experiments. The upper limits are extracted from these *pdf*s.

The test statistic is constructed to discriminate between the background-only and signal+background hypothesis. In the case of no other unknown parameters, a likelihood ratio gives the highest discriminating power, justified by the Neyman-Pearson lemma [104].

The likelihood is a quantity which tells how likely the observed data is compatible

with the prediction from a particular model. It is constructed as follows:

$$L(\text{data}|\mu,\theta) = L(\text{data}|\mu \cdot s(\theta) + b(\theta)) \cdot L(\theta)\,, \tag{12.2}$$

where "data" represents either the actual experimental data or pseudo-data, μ is the signal strength modifier[1] and θ represents the full set of nuisance parameters, which are used to parametrize the systematic uncertainties related to modeling of the signal and background. The first part of the likelihood is the product of the *pdf* of the model, evaluated for every event in the data:

$$L(\text{data}|(\mu s + b) = N_{\text{data}}^{-1} e^{-(\mu N_s + N_b)} \prod_i (\mu N_s(\theta) pdf_s(\theta) + N_b(\theta) pdf_b(\theta))\,, \tag{12.3}$$

where i refers to each event, pdf_s and pdf_b the signal and background *pdf*, respectively, and N_{data} is the total number of events in data. N_s is the expected signal yield assuming the Standard Model hypothesis, and N_b is the expected background yield. The second part of the likelihood is the product of each nuisance *pdf*,

$$L(\theta) = \prod_i L(\theta^i) = \prod_i Gaus(\theta_0^i, \sigma_\theta^i)\,, \tag{12.4}$$

where i refers to each nuisance parameter, θ_0^i and σ_θ^i refer to the central value and relative uncertainty of each nuisance parameter, respectively. Here we have assumed that the nuisance *pdf* is a Gaussian. The effect of the uncertainty on the signal yield is parametrized by $e^{1+\theta^i}$. For example, the luminosity measurement has an uncertainty of 2.2%, the central value θ_0 is zero, and σ_θ is 0.022. A nonzero value of θ will change the signal yield prediction by about 2.2θ%.

In CMS, following the agreed upon procedure in [103], the test statistic is defined to be a particular modification of the profile likelihood ratio [105], requiring the signal

[1] where the prediction corresponding to the Standard Model signal gives $\mu = 1$.

strength μ not to be negative:

$$\tilde{q_\mu} = -2\ln(\frac{L(\text{data}|\mu,\hat{\theta}_\mu)}{L(\text{data}|\hat{\mu},\hat{\theta})}), 0 \leq \hat{\mu} \leq \mu\,, \tag{12.5}$$

where $\hat{\theta}_\mu$ represent the values of the nuisance parameters for which the likelihood is maximized with the given data and the value of the signal strength fixed to μ, and $\hat{\mu}$ and $\hat{\theta}$ are the values of the signal strength and the nuisance parameters, respectively, for which the likelihood is globally maximized with the data. The lower constraint on $\hat{\mu}$ implies that physics signal rate is always non-negative, while the upper constraint $\hat{\mu} \leq \mu$ guarantees the obtained limits to be one-sided. This also means that upward fluctuations in the data such that $\hat{\mu} > \mu$ are not considered as the evidence against a signal hypothesis with signal strength μ. Another advantage of this definition of the test statistic is that its *pdfs* can be approximately described by the asymptotic formulas, which we will discuss in the next section.

For each given signal strength μ under test, a value of the test statistics $\tilde{q}_\mu^{obs}$ is obtained when the two likelihoods in equation (12.5) are maximized in the data. Simultaneously, the corresponding nuisance parameters $\hat{\theta}_0^{obs}$ and $\hat{\theta}_\mu^{obs}$ are obtained.

The next step is to generate a large number of pseudo-experiments to construct two *pdf*s of the test statistics, one for the background hypothesis, $f(\tilde{q_\mu}|0,\hat{\theta}_0^{obs})$, another one for the signal+background hypothesis, $f(\tilde{q_\mu}|\mu,\hat{\theta}_\mu^{obs})$. In generating pseudo-experiments, the nuisance parameters are fixed at the values obtained from the data.

From the two constructed *pdf*s, we obtain two p-values for data for signal+background and background-only hypotheses:

$$p_s(\mu) = P(\tilde{q}_\mu \geq \tilde{q}_\mu^{\text{obs}}|\text{signal strength } \mu, \hat{\theta}_\mu^{\text{obs}}) = \int_{\tilde{q}_\mu^{\text{obs}}}^{\infty} f(\tilde{q}_\mu|\mu,\hat{\theta}_\mu^{\text{obs}})d\tilde{q}_\mu\,, \tag{12.6}$$

$$1-p_b(\mu) = P(\tilde{q}_\mu \geq \tilde{q}_\mu^{\text{obs}}|\text{background only}, \hat{\theta}_0^{\text{obs}}) = \int_{\tilde{q}_\mu^{\text{obs}}}^{\infty} f(\tilde{q}_\mu|0,\hat{\theta}_0^{\text{obs}})d\tilde{q}_\mu\,, \tag{12.7}$$

where the p-value is the probability of obtaining a test statistic value that is at least as "extreme" as the observed value in the experimental data, for each hypothesis.

Finally we define $\mathrm{CL_s}(\mu)$ as the ratio of these two probabilities:

$$\mathrm{CL_s}(\mu) = \frac{p_s(\mu)}{1 - p_b(\mu)}\,. \tag{12.8}$$

Therefore the confidence level (CL) for the exclusion of a signal with signal strength μ is equal to $1 - \mathrm{CL_s}(\mu)$. The upper limit on the signal strength at the 95% CL, μ_{up}, is obtained when $\mathrm{CL_s}(\mu) = 0.05$ is satisfied.

12.3 Asymptotic CL_{S}

The procedure discussed in the previous section can be very computationally intensive. For each signal strength μ being tested, one needs to generate a large number of pseudo-experiments to construct the *pdf* of the test statistics under the background and the signal+background hypotheses. An asymptotic formula [106] is thus derived, justified by Wilks theorem [107] which states that the distribution of the test statistic approaches a particular analytical form in the regime of a large number of events.

Without the constraint of $0 \leq \hat{\mu}$, q_μ is expected to form one-half times a χ^2 distribution with one degree of freedom. With the physics requirement of $0 \leq \hat{\mu}$, the asymptotic formula is given by

$$f(\tilde{q}_\mu|\mu) = \frac{1}{2}\delta(\tilde{q}_\mu) + \begin{cases} \frac{1}{2}\frac{1}{\sqrt{2\pi\tilde{q}_\mu}}\exp^{-\tilde{q}_\mu/2} & 0 < \tilde{q}_\mu \leq \mu^2/\sigma^2 \\ \frac{1}{\sqrt{2\pi}(2\mu/\sigma)}\exp\left[-\frac{1}{2}\frac{(\tilde{q}_\mu+\mu^2/\sigma^2)^2}{(2\mu/\sigma)^2}\right] & \tilde{q}_\mu > \mu^2/\sigma^2 \end{cases}, \tag{12.9}$$

where δ is the Dirac delta function, and

$$\sigma^2 = \frac{\mu^2}{q_{\mu,\mathrm{asimov}}}\,. \tag{12.10}$$

The value $q_{\mu,\mathrm{asimov}}$ is the test statistic evaluated on the Asimov dataset [106], which is defined as the dataset with the expected signal and background yields and the nominal values of the nuisance parameters.

The background-only asymptotic formula is **??**,

$$f(\tilde{q}_0|0) = \frac{1}{2}\delta(\tilde{q}_0) + \frac{1}{2}\frac{1}{\sqrt{2\pi\tilde{q}_0}}\exp^{-\tilde{q}_0/2} \ . \tag{12.11}$$

From these formulas we can solve for the 95% confidence level upper limit in the $CL_{\rm s}$ method:

$$CL_s = 0.05 = \frac{1-\Phi(\sqrt{q_\mu})}{\Phi(\sqrt{q_{\mu,\rm asimov}}-\sqrt{q_\mu})}\,, \tag{12.12}$$

where Φ is the cumulative distribution of the standard Gaussian. The median and expected $N\sigma$ error bands are calculated as

$$\mu_{up+N} = \sigma(\Phi^{-1}(1-\alpha\Phi(N)+N)\,. \tag{12.13}$$

with $\alpha = 0.05$. For $N = 0$, the median expected $CL_{\rm s}$ limit is

$$\mu_{up}^{\rm median} = \sigma\Phi^{-1}(1-0.5\alpha) = \sigma\Phi^{-1}(0.975)\,. \tag{12.14}$$

In practice, the bands based on the asymptotic approximation are found to give slightly optimistic results (too narrow uncertainty bands) for situations with a small number of events.

12.4 Quantifying an Excess: Background-only p-value

In this section we discuss the procedure to quantify an excess in the data, based on very similar approaches discussed in the previous sections. Since the Higgs boson mass in the Standard Model is unknown, the p-value obtained needs to taken into account the mass search region, in our case, from 100 to 150 GeV/c^2.

12.4.1 Fixed Higgs Boson Mass M_H

As in section 12.2, we build a test statistic for a given Higgs boson mass hypothesis M_H

$$q_0 = -2\ln(\frac{L(\text{data}|0,\hat{\theta}_0)}{L(\text{data}|\hat{\mu},\hat{\theta})}), 0 \leq \hat{\mu}\,. \tag{12.15}$$

Compared to equation (12.5), the signal strength μ in the numerator is fixed to zero, corresponding to the background-only hypothesis.

Next we build the *pdf* of the test statistic by generating a large number of pseudo-experiments with nuisance parameters θ_0^{obs} maximizing the background-only likelihood defined in equation (12.15). From the obtained *pdf*, we evaluate the p-value corresponding to the observed q_0^{obs}

$$p_0 = P(q_0 \geq q_0^{\text{obs}}) = \int_{q_0^{\text{obs}}}^{\infty} f(q_0|0,\theta_0^{\text{obs}})dq_0\,. \tag{12.16}$$

Then the significance Z is calculated by equation (12.1).

In practice, for a very low p-value it is also very computationally expensive to build the *pdf* of q_0. In the asymptotic regime, a fairly accurate estimate of the p-value can be obtained from the observed value q_0^{obs} directly

$$p_0^{\text{estimate}} = \frac{1}{2}(1 - \text{erf}(\sqrt{q_0^{obs}/2}))\,. \tag{12.17}$$

In this case, the significance Z is simply $\sqrt{q_0^{\text{obs}}}$.

12.4.2 Look-elsewhere Effects of Unknown M_H

The p-value calculated in the previous section corresponds to a fixed Higgs boson mass M_H. This p-value is thus referred to as a local p-value. However the parameter M_H is not known in the Standard Model. Therefore we need to scan the mass region. The scanning results in a dilution effect, known as a trial factor or the look-elsewhere effect. The resulting p-value taking into account the look-elsewhere effect, corresponding to the probability of obtaining a value of the test statistic at least as large as the observed

value, anywhere in the mass interval of interest, is thus called a global p-value.

To estimate the look-elsewhere effect, the local test statistic defined in equation (12.15) can be used to build the global test statistic in the scanned mass points within the range of interest,

$$q_0^{\text{global}} = \max\, q_0(\mathrm{M_H})\,. \tag{12.18}$$

Again, building the *pdf* of the test statistics with a large number of pseudo-experiments can be very time consuming. In the asymptotic regime and for very small p-values, a simplified procedure has been proposed in [108]. In this approach, the p-value of the global test statistics is given by

$$p_0^{\text{global}} = P(q_0^{\text{global}} > u) \leq \langle N_u \rangle + p_0\,, \tag{12.19}$$

where $\langle N_u \rangle$ is the average number of up-crossings of q_0 at a level u, which is the largest observed value q_0^{obs} within the scanned mass range. That is the look-elsewhere effect we want to estimate for this particular level of local significance.

The average number of up-crossing at the level u can be estimated from a lower level u_0

$$\langle N_u \rangle = \langle N_{u_0} \rangle e^{-(u-u_0)/2}\,. \tag{12.20}$$

In chapter 15, we will report the CL_{s} exclusion limits and local p-value both under the asymptotic assumptions. The global p-value will be estimated with the method described in this section.

Chapter 13

Impact of ECAL Energy Calibration, Correction and Vertex Identification on the $\mathrm{H} \to \gamma\gamma$ Search

We have discussed in previous chapters various improvements in the energy measurement and vertex identification. Therefore in this chapter we show the impact of these improvements on the $\mathrm{H} \to \gamma\gamma$ search. In particular, we discuss the improvement in the search sensitivity from the ECAL *in situ* intercalibration and laser monitoring corrections (chapter 4), from the regression energy correction (chapter 5), and from the multivariate vertex identification (chapter 6).

The figure of merit that we use for the search sensitivity is the median expected exclusion limit at 95 % Confidence Level (CL) on the signal strength modifier μ to the Standard Model $\mathrm{H} \to \gamma\gamma$ cross section, discussed in section 12.2.

13.1 Impact of ECAL Calibration

In this section we study the impact of the ECAL calibration, including laser monitoring corrections, on the $\mathrm{H} \to \gamma\gamma$ analysis. We consider a few different ECAL calibration scenarios, and in each scenario we rederive the energy smearing numbers from $\mathrm{Z} \to \mathrm{e}^+\mathrm{e}^-$ events and apply them to the $\mathrm{H} \to \gamma\gamma$ simulation. Then we compare the resulting sensitivities. The following calibration scenarios are compared:

- No calibration. Crystal-to-crystal intercalibration constants and laser correc-

tions are not applied to the energy reconstruction in the ECAL crystals.

- Precalibration. Only crystal-to-crystal precalibration constants are applied to the crystal energy reconstruction.

- Precalibration and Laser correction. Crystal-by-crystal precalibration constants and laser corrections are applied.

- *In situ* π^0 calibration and Laser correction (LC). Crystal-to-crystal *in situ* $\pi^0+\eta$ intercalibration constants and laser corrections are applied.

- *In situ* calibration and Laser correction. Crystal-to-crystal *in situ* combined intercalibration and laser corrections are applied.

Figure 13.1 shows the reconstructed $Z \to e^+e^-$ invariant mass distributions in the data under these ECAL calibration scenarios. In all these distributions, the simulation-based energy correction with regression technique is applied to the raw supercluster energy. The run-by-run energy scale correction, described in section 5.6, is not applied in order to more clearly show the energy scale effects due to the laser correction.

Table 13.1 shows the energy smearing in each category under different ECAL calibration scenarios. Here, run-by-run energy scale corrections are rederived and applied. Figure 13.2, 13.3 and 13.4 shows that the $Z \to e^+e^-$ invariant mass distributions in the simulation after the smearings are applied agree with the data under different calibration scenarios.

Category	No calibration	Precalibration	Precalib + LC	π^0 calib + LC	comb. calib + LC
$\|\eta\| < 1, r_9 > 0.94$	8.85 ± 0.03	2.93 ± 0.02	2.47 ± 0.02	0.74 ± 0.03	0.71 ± 0.03
$\|\eta\| < 1, r_9 < 0.94$	8.69 ± 0.02	2.69 ± 0.02	2.29 ± 0.02	0.97 ± 0.03	0.89 ± 0.03
$1 < \|\eta\| < 1.5, r_9 > 0.94$	8.65 ± 0.14	3.08 ± 0.09	2.70 ± 0.12	1.35 ± 0.10	1.38 ± 0.11
$1 < \|\eta\| < 1.5, r_9 < 0.94$	8.32 ± 0.04	3.26 ± 0.03	3.00 ± 0.03	2.10 ± 0.03	2.08 ± 0.03
$1.5 < \|\eta\| < 2.0, r_9 > 0.94$	14.4 ± 0.03	5.44 ± 0.15	5.10 ± 0.14	2.65 ± 0.14	2.43 ± 0.15
$1.5 < \|\eta\| < 2.0, r_9 < 0.94$	13.7 ± 0.16	5.17 ± 0.08	4.91 ± 0.07	2.75 ± 0.04	2.41 ± 0.08
$2.0 < \|\eta\| < 2.5, r_9 > 0.94$	17.3 ± 0.02	7.88 ± 0.07	6.49 ± 0.07	3.06 ± 0.06	2.80 ± 0.06
$2.0 < \|\eta\| < 2.5, r_9 < 0.94$	17.0 ± 0.03	7.70 ± 0.08	6.02 ± 0.09	2.85 ± 0.10	2.51 ± 0.09

Table 13.1: Energy smearing (%) in each category under different ECAL calibration scenarios.

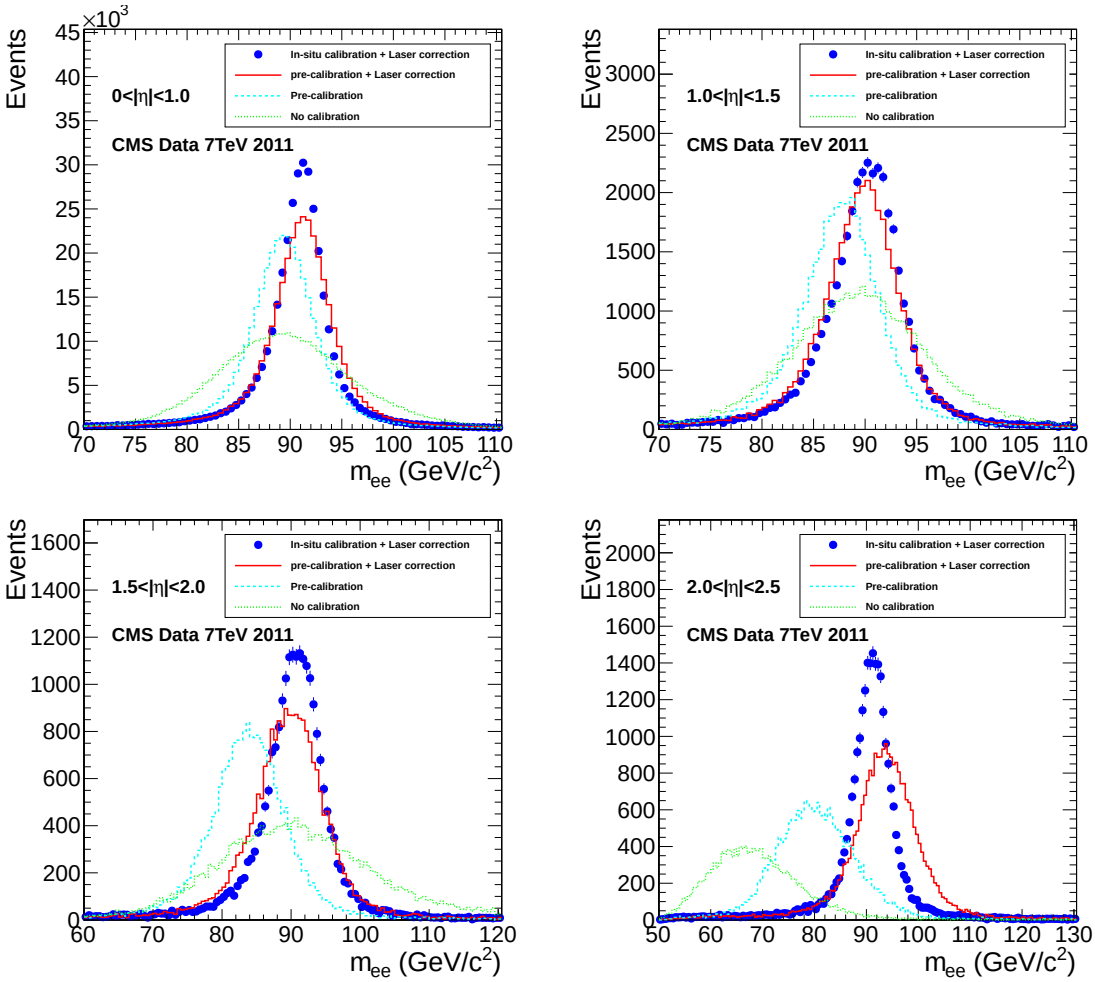

Figure 13.1: Comparison of the Z $\rightarrow$ e^+e^- invariant mass distributions obtained with the ECAL energies reconstructed without calibration, with precalibration, with precalibration and laser correction, and with *in situ* calibration and laser correction.

In each scenario, the corresponding energy smearings are applied to the H $\rightarrow \gamma\gamma$ simulation. Figure 13.5 shows the expected H $\rightarrow \gamma\gamma$ distributions at a Higgs boson mass $M_H = 125$ GeV/c^2 in different scenarios.

Figure 13.6 shows the improvement of the exclusion limit in different ECAL calibration scenarios. The improvement from precalibration to *in situ* calibration with laser correction is about 38% at the Higgs boson mass 125 GeV/c^2.

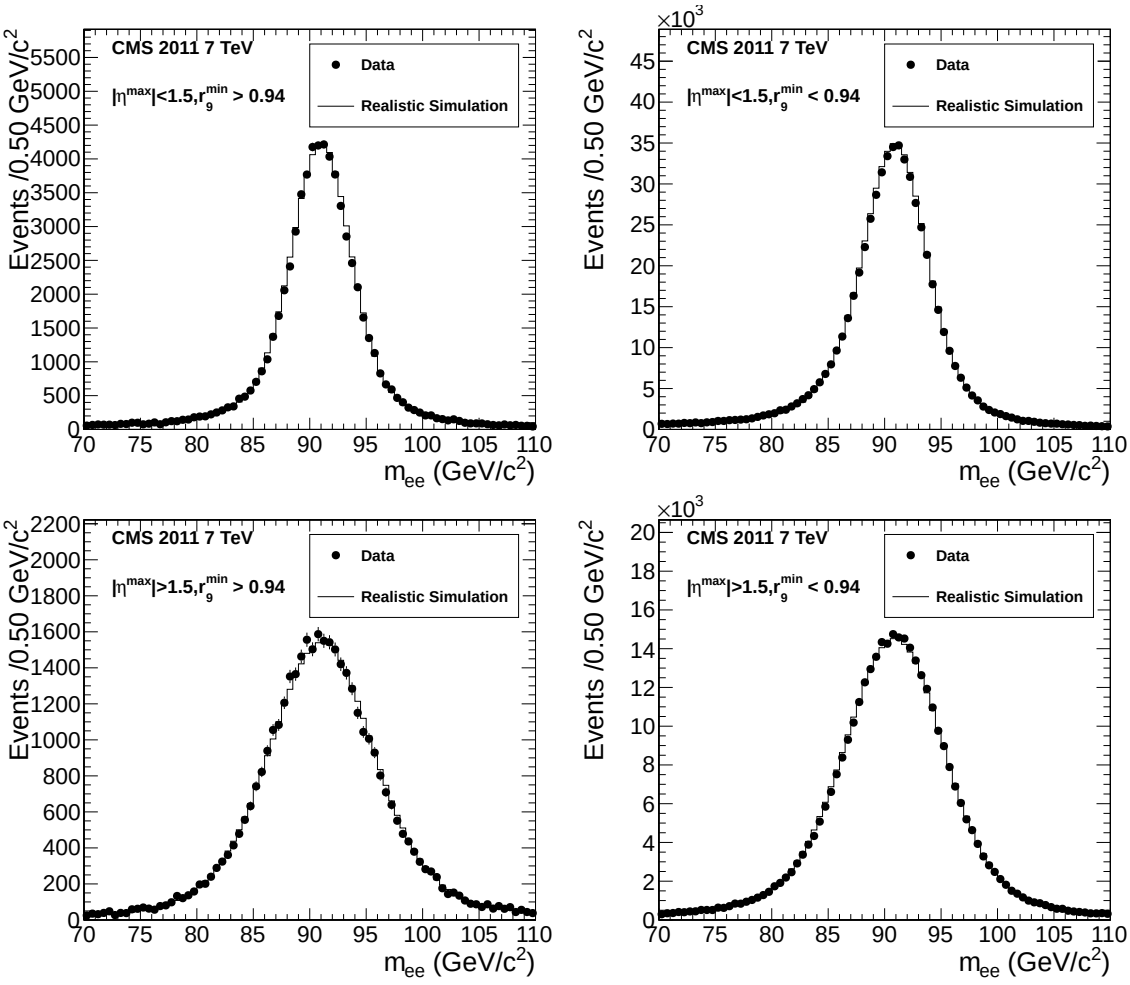

Figure 13.2: Comparison of the $Z \to e^+e^-$ invariant mass distributions between the data and a realistic simulation (after smearing) under the precalibration-only scenario.

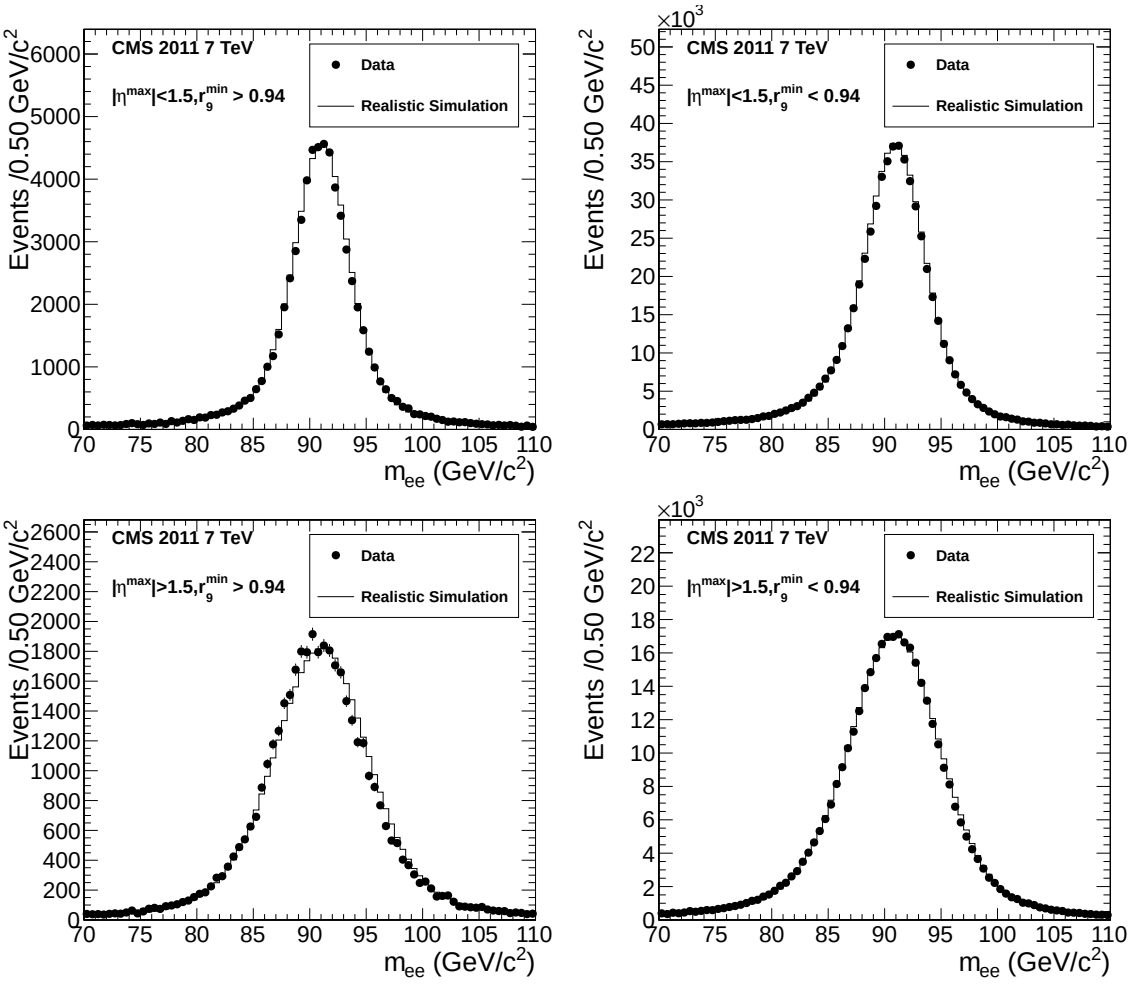

Figure 13.3: Comparison of the $Z \to e^+e^-$ invariant mass distributions between the data and realistic simulation (after smearing) under precalibration + LC scenario.

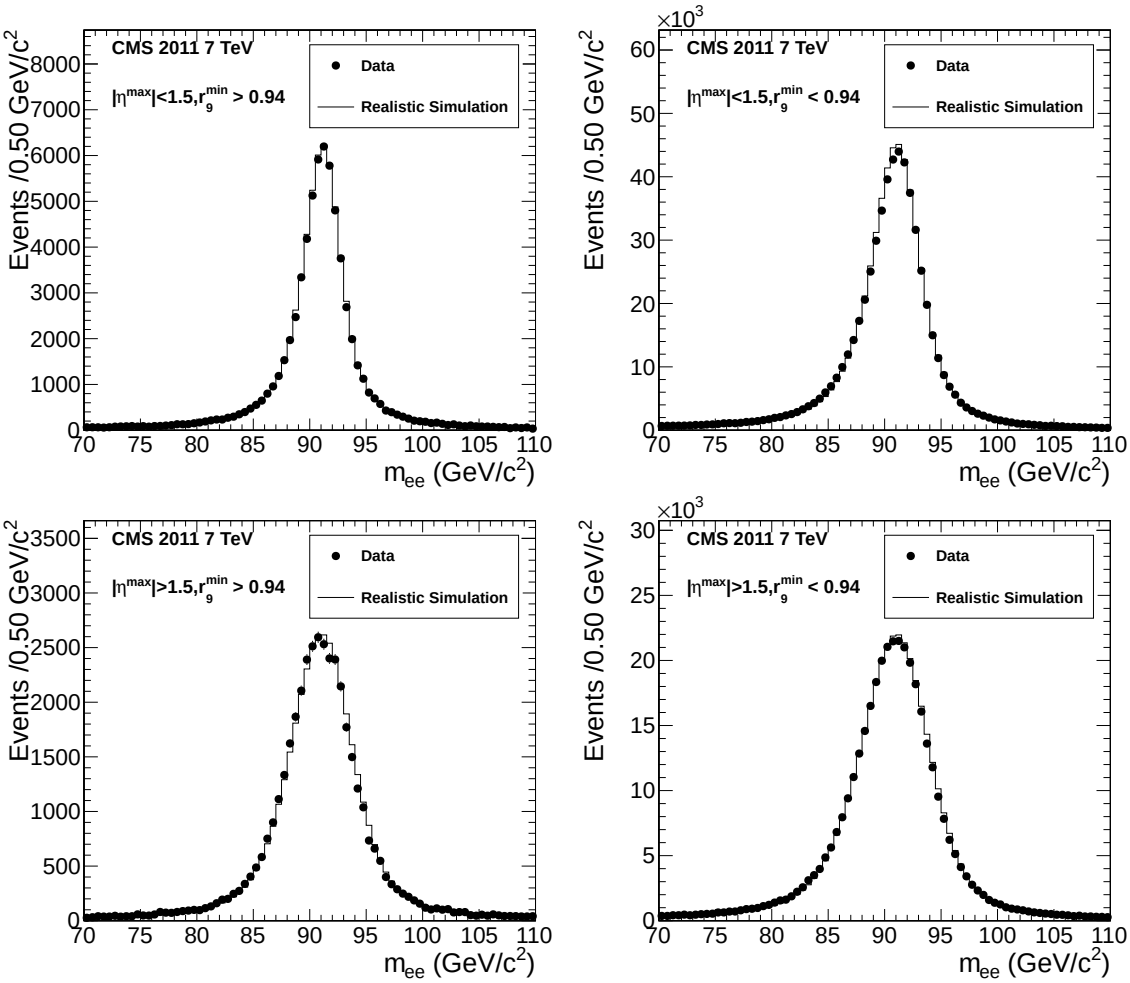

Figure 13.4: Comparison of the $Z \to e^+e^-$ invariant mass distributions between the data and a realistic simulation under the π^0 calibration + LC scenario.

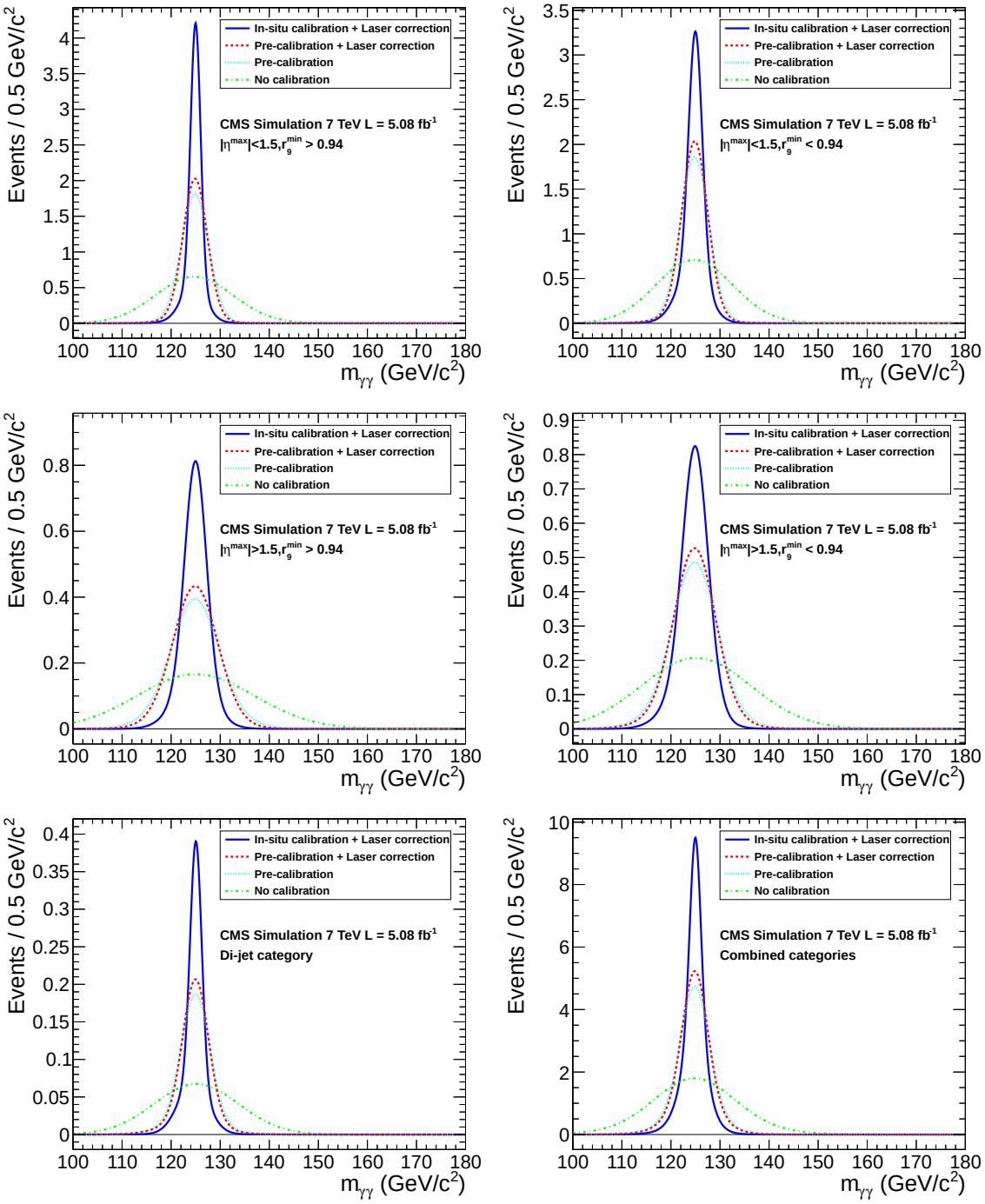

Figure 13.5: Expected H $\rightarrow \gamma\gamma$ mass distributions at $M_H = 125 GeV/c^2$ in different categories under different ECAL calibration scenarios.

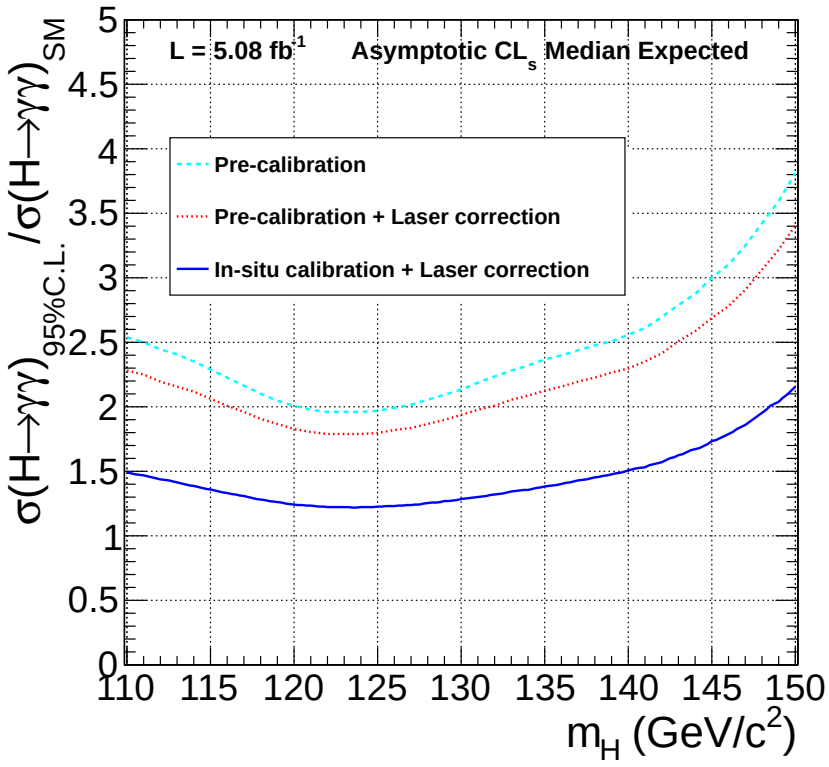

Figure 13.6: Comparison of the median expected 95% CL exclusion limits on the cross section relative to the Standard Model cross section in the asymptotic CL_{s} approximation, under different ECAL calibration scenarios.

13.2 Impact of the Regression Energy Correction

We have discussed in section 5.5 the improvement in the energy resolution resulting from the use of the multivariate regression technique to correct the supercluster energy. To study the improvement in the sensitivity of the H $\rightarrow \gamma\gamma$ analysis, we rederive the energy smearings for the standard energy correction. The results are shown in table 5.3 Figure 13.7 shows the comparison of the Z $\rightarrow e^+e^-$ invariant mass distributions in the data and the simulation, where these smearing have been applied to the corrected electron energy. Good agreement is observed.

Category	$\sigma_s(\%)$
$\lvert\eta\rvert < 1, r_9 > 0.94$	0.82 ± 0.04
$\lvert\eta\rvert < 1, r_9 < 0.94$	0.93 ± 0.04
$1 < \lvert\eta\rvert < 1.5, r_9 > 0.94$	1.49 ± 0.12
$1 < \lvert\eta\rvert < 1.5, r_9 < 0.94$	2.28 ± 0.04
$1.5 < \lvert\eta\rvert < 2.0, r_9 > 0.94$	2.21 ± 0.15
$1.5 < \lvert\eta\rvert < 2.0, r_9 < 0.94$	1.93 ± 0.08
$2.0 < \lvert\eta\rvert < 2.5, r_9 > 0.94$	2.48 ± 0.06
$2.0 < \lvert\eta\rvert < 2.5, r_9 < 0.94$	2.15 ± 0.09

Table 13.2: Energy smearing in each electron category. Standard supercluster corrections are applied to electrons with $r_9 < 0.94$.

Figure 13.8 shows the expected H $\rightarrow \gamma\gamma$ invariant mass distributions at $M_H = 125$ GeV/c^2 with the regression or the standard energy corrections, where the corresponding energy smearings are applied. The improvement due to the regression energy correction in the invariant mass resolution is found to be between 10% to 20% in different categories.

Figure 13.9 shows the improvement in the median expected exclusion limits as a function of the Standard Model Higgs boson mass. The improvement is approximately 14% at a Higgs boson mass of 125 GeV/c^2.

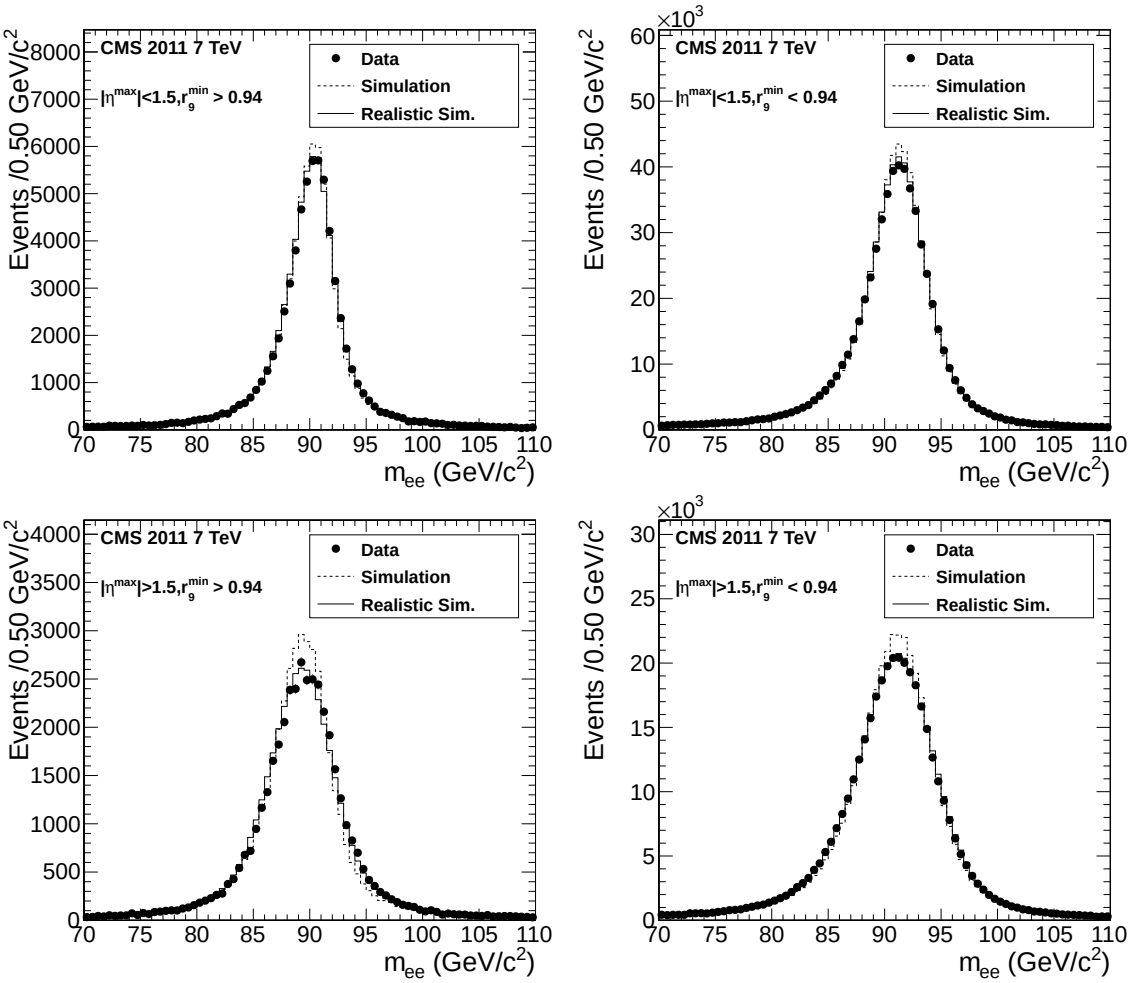

Figure 13.7: Comparison of $Z \to e^+e^-$ invariant mass distributions between the data and nominal or realistic simulation in each event category. Standard supercluster energy correction is used. In realistic simulation, the energy smearings in table 13.2 are applied.

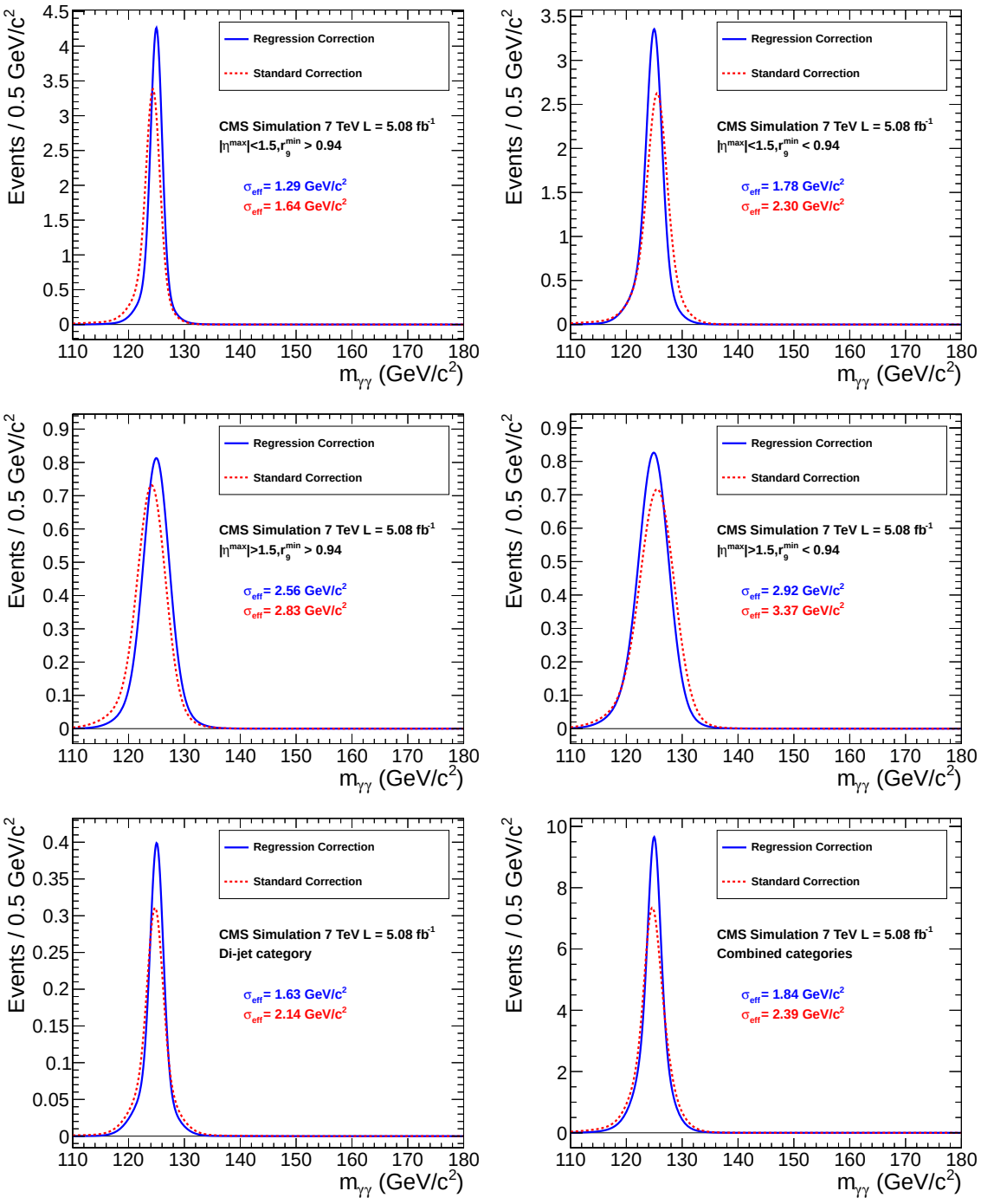

Figure 13.8: Expected H $\rightarrow \gamma\gamma$ invariant mass distributions at $M_H = 125$ GeV/c^2 in different event categories, with the regression corrections and the standard supercluster corrections applied.

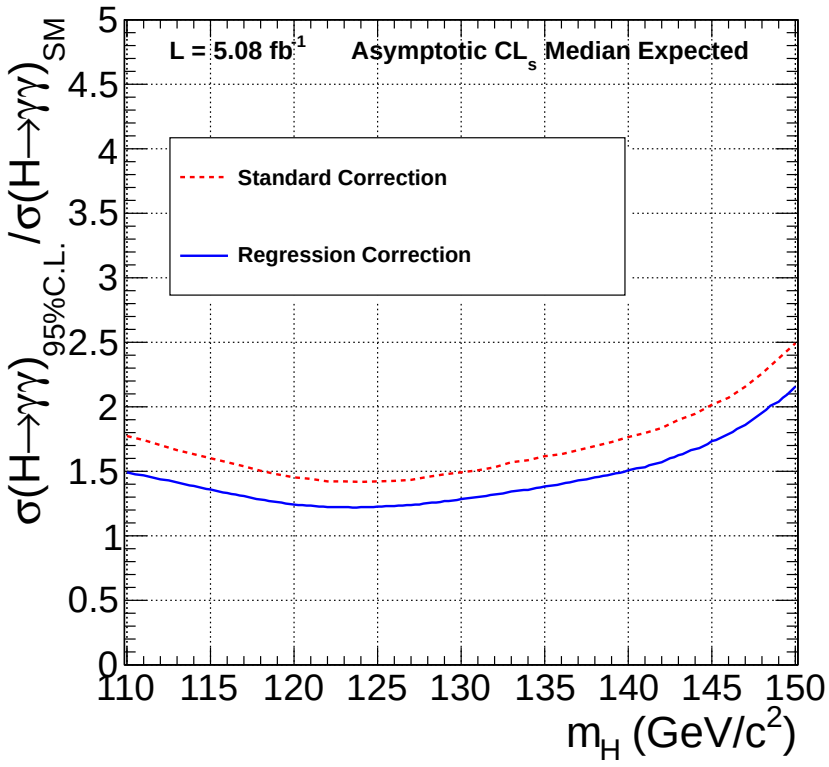

Figure 13.9: Comparison of the 95% CL exclusion limits on the cross section relative to the Standard Model cross section in the asymptotic CL_s approximation, with the standard or the regression supercluster energy correction applied.

13.3 Impact of the MVA Vertex Identification

Figure 13.10 shows the improvement on the H $\rightarrow \gamma\gamma$ resolution with the MVA vertex identification. There is about a 5% improvement in the first category. The improvement is about 8.5% in the second category where at least one photon has very likely been converted (low r_9). In this case, the MVA algorithm improves more because it explicitly uses the conversion information. Similarly, the improvement for the fourth category is larger than for the third category, 6.7% versus 4.3%. In the di-jet category, the improvement is smaller, only about 1.7%. This is due to the fact that in those events the Higgs boson has higher p_{T} than in other categories, where the improvement from the MVA is smaller.

Figure 13.11 shows the improvement from the MVA vertex ID on the median expected exclusion limits as a function of the Standard Model Higgs boson mass. The improvement is about 4% at the Higgs boson mass of 125 GeV/c^2.

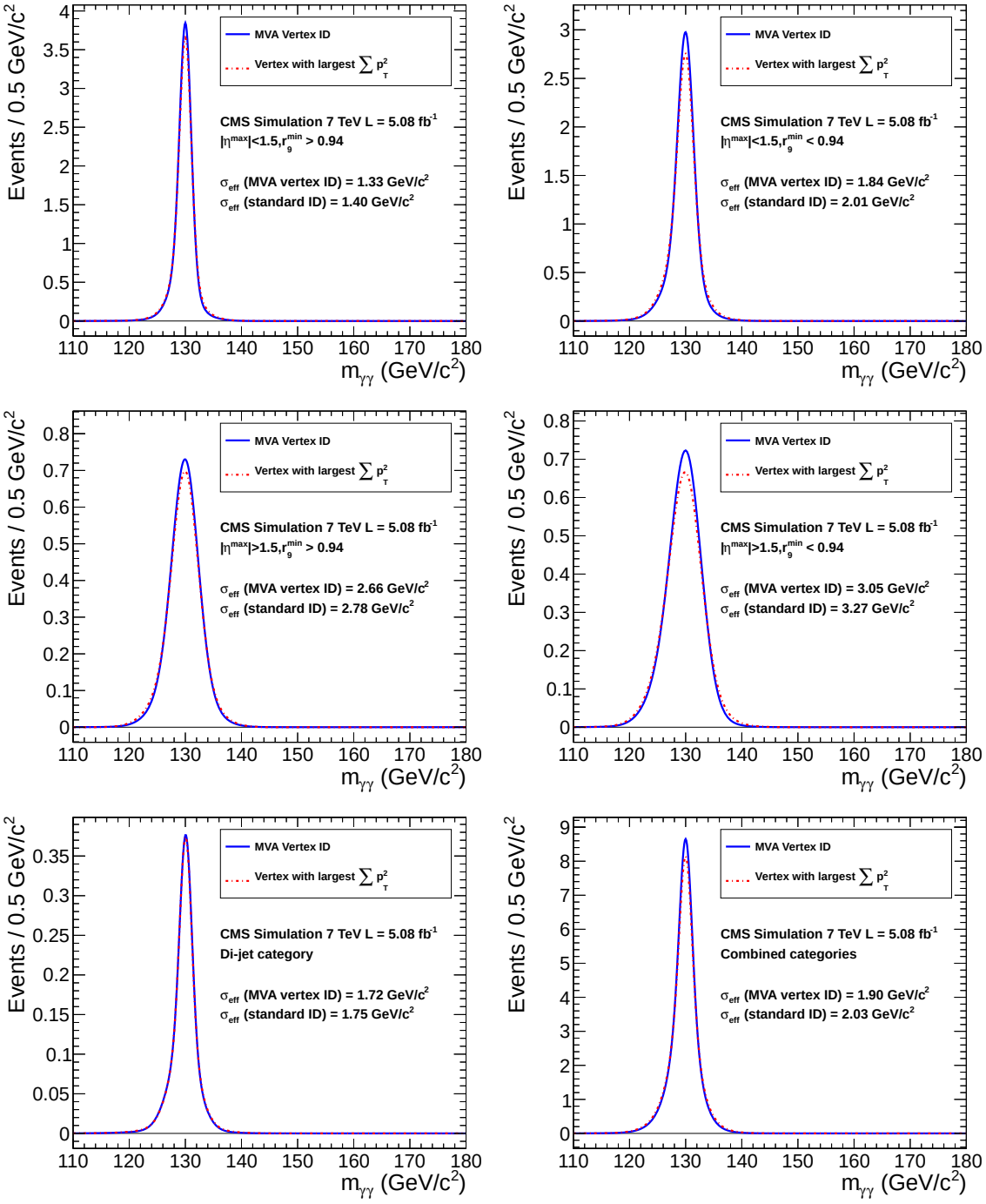

Figure 13.10: Expected H $\rightarrow \gamma\gamma$ invariant mass distributions at $M_H = 130\,\mathrm{GeV}/\,c^2$ in different event categories for the standard and the MVA vertex identification algorithms.

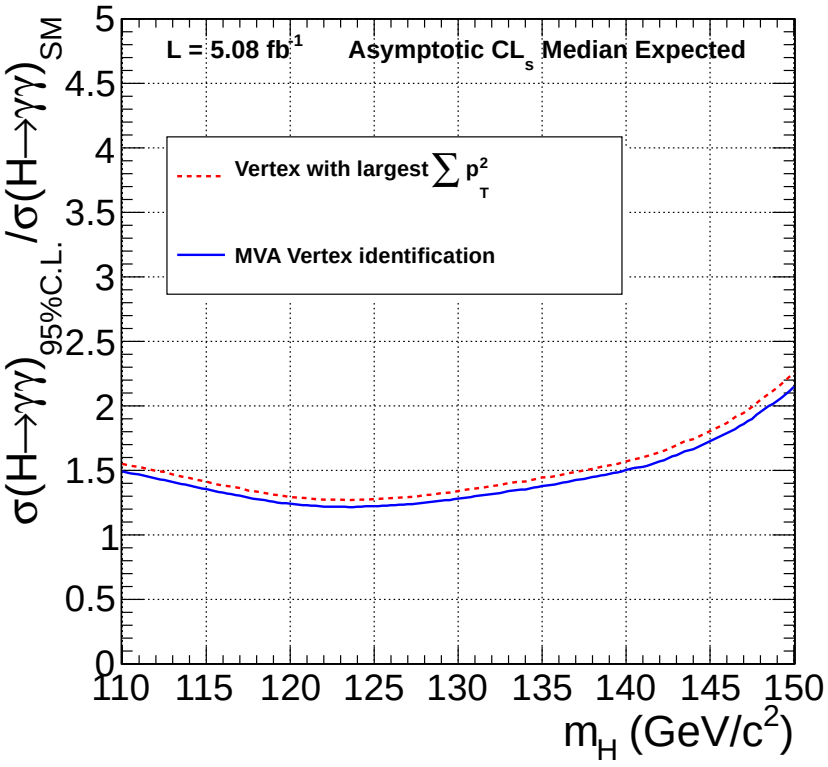

Figure 13.11: Comparison of the 95% CL Exclusion limits on the cross section relative to the Standard Model H $\rightarrow \gamma\gamma$ cross section in the asymptotic $CL_{\rm s}$ approximation, with the standard or the MVA vertex ID.

Chapter 14

Analysis Check of the Regression with Limited Training Statistics

In this thesis we used all available events from the γ+jet MC simulation sample to train the regression for the photon energy correction. In the common analysis [92], only half of the statistics, with events of even event number, was used, while the other half was used to train another regression to estimate the energy error, which is needed for the MVA di-photon analysis. However, this is not needed for the cut-based analysis, which this thesis describes.

In this chapter we study if there is any effect, possibly systematic uncertainties, on the observed limits or the signal strength or significance by using only half of the MC events to train the regression energy correction. There are an infinite number of ways to choose the half of the available sample. For example, one can use the first half or the second half, or events with an even or odd number, or every other two events, etc.

In terms of the energy resolution, there is almost no difference if we use all MC events or only half of them, as shown in figure 14.1. This means that the performance of the regression does not improve by doubling the training sample. However, since there is some arbitrariness in choosing only the half of the events, one should check if such an arbitrary choice would result in statistically different results in this particular dataset we are analyzing. If the difference of the two results is statistically significant, we would need to take that into account as an additional systematic uncertainty when

we report the final result, if and only if the difference could not be fixed [109].

Figures 14.2 and 14.3 show the observed exclusion limits and local p-values as a function of the Higgs boson mass with the photon energy corrected with different regressions, trained with only half of the total MC events, where the half events were chosen by different means: (1) with only even or odd event number, (2) event number mod $4 \leq 1$ or > 1, (3) event number mod $8 \leq$ or > 3. At the mass point 123 GeV/c^2, the difference between the two observed limits from the two regressions in each of the three cases, ranges from 5% to 8%. The observed p-values differ by 9% to 120%.

Given the fact that we have observed some differences due to the arbitrary choices of using only half of the available MC events to train the regression, it is more appropriate to use all of the events than to randomly pick up one of the regressions. However, the number of events is still finite. It is quite likely that if there was another sample with the same number of events, and if we used the regression trained with this sample, that the observed limits or p-values would be different. With a training sample with a finite number of events, there are inevitably statistical fluctuations in the regression, since the parameters in the BDT are determined with limited statistical precision.

We therefore used the "Bootstrapping" [110, 111] method to study the observed difference in the observed limits, the signal strength and the significance, induced from the use of a finite training sample. Starting from the existing MC sample, the bootstrapping technique constructs a number of "resampled" datasets from the observed dataset (of equal size to the observed one), by picking events randomly from it, allowing duplicates among the events that are picked. When the total number of events is large, 63.2% of the events in the existing MC are used to build each bootstrapped sample, with the rest of the event being duplicates. Each of the bootstrapped sample is then subsequently used to train a new regression, and each of these bootstrapped regressions is used to build the distributions of results.

With the bootstrapping approach, we trained 18 bootstrapped regressions. Figure 14.4 shows the distributions of the observed exclusion limits or the local p-values at the Higgs mass $M_H = 123$ GeV/c^2, from these bootstrapped regressions. Figure 14.5

shows the distribution of the best fitted signal strength.

We follow the guideline proposed in section 4.1 of [109], to check if the differences we observed from these bootstrapped regressions are significant or not. According to the guideline, when an analysis is performed in two ways, one in general does not expect the two results to be identical, but one does expect the difference between them to be small. The question arises as to what "small" means when analyzing the same data with two methods.

Suppose one analysis gives a result of $a_1 \pm \sigma_1$, another one gives $a_2 \pm \sigma_2$. Then the difference is $\Delta = a_1 - a_2$, and the error of the difference is given by

$$\sigma_\Delta = \sqrt{\sigma_1^2 + \sigma_2^2 - 2\rho\sigma_1\sigma_2}\,, \tag{14.1}$$

where ρ is the correlation coefficient between the two measurements. Performing one such check between two different analyses is called one analysis check. The decision on whether to take further action depends on the outcome of the analysis check, in terms of Δ/σ_Δ. In general, less than one means the check has passed. Then the correct thing to do is do "nothing". One should not add the difference Δ into the systematic uncertainty when reporting the final result. If the size of the difference is large, for example > 4, then the actions to take are to find the source of the difference and fix it if possible. The last action, if one has not managed to understand or fix the difference, is to add it into the systematic uncertainty of the final result.

We again use the "Bootstrapping" method to measure the correlation coefficient ρ in equation (14.1). First, we make one bootstrapped dataset from the real data corrected with one regression. Second, we make another dataset by applying another regression correction to the same list of events from the bootstrapped dataset obtained in the previous step. Therefore, two bootstrapped datasets are built consisting of the same list of events, but the energy of each photon is corrected with two different regressions. Thirdly, we extract the signal strength from the two bootstrapped datasets. The above procedure is repeated many times.

Figure 14.6 shows the measured correlation between the best fitted signal strengths

obtained with the two regressions. Since we have trained 18 bootstrapped regressions, any two of these regressions can make one analysis check. In total there are 153 checks in the figure. Figure 14.7 shows the results of these analysis checks. Based on these results on Δ/σ_Δ, we conclude that the differences among the bootstrapped regressions are not significant. Therefore there is no further action needed to account for the regression having used a finite training sample. The final result we report in this thesis is from one regression, which is trained with all events of the γ+jet MC sample.

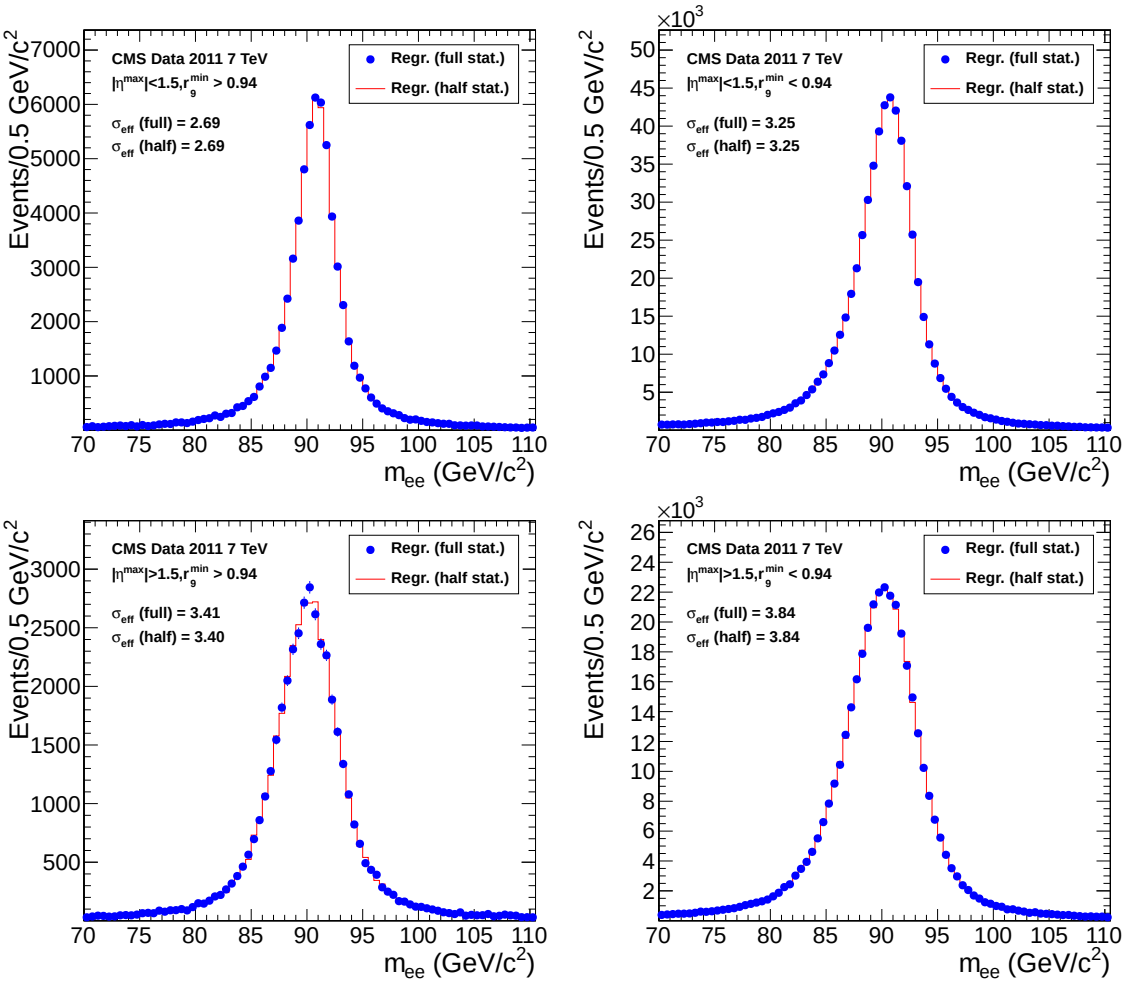

Figure 14.1: Comparison of the $Z \to e^+e^-$ invariant mass distributions in the data between two versions of the regression. One version is trained with the full statistics of the γ+jet MC sample, while the other one is trained with events with even event number.

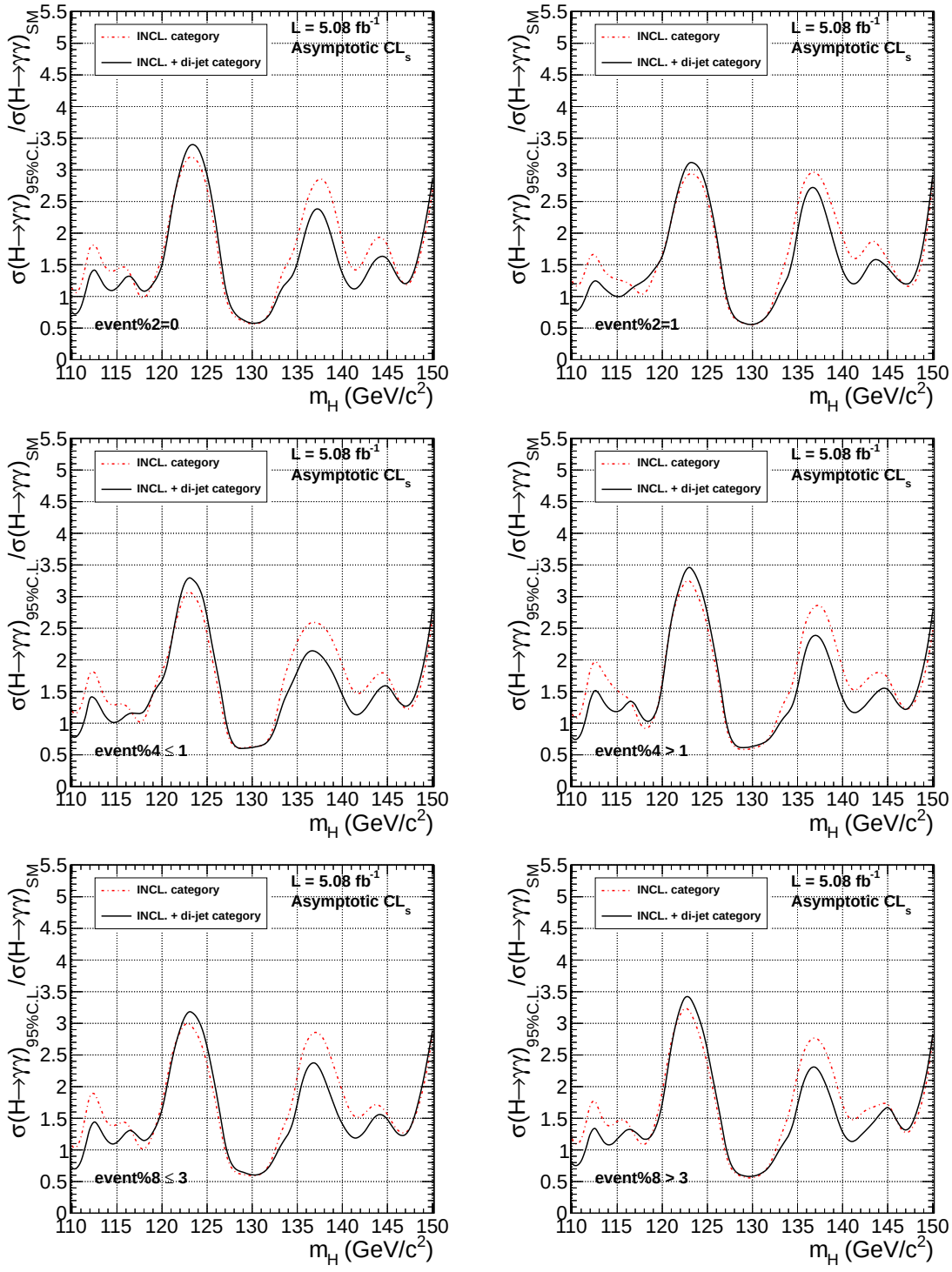

Figure 14.2: Observed 95% CL exclusion limits on the cross section relative to the expected SM cross section in the asymptotic CL_s approximation. Each plot shows the results with photon energy corrected with a regression trained with half of the total MC events. The way to choose only half of the MC sample is indicated in each plot, where the symbol '%" means modulus sign. For example, "event $\%2 = 0$" means only even numbered events are used.

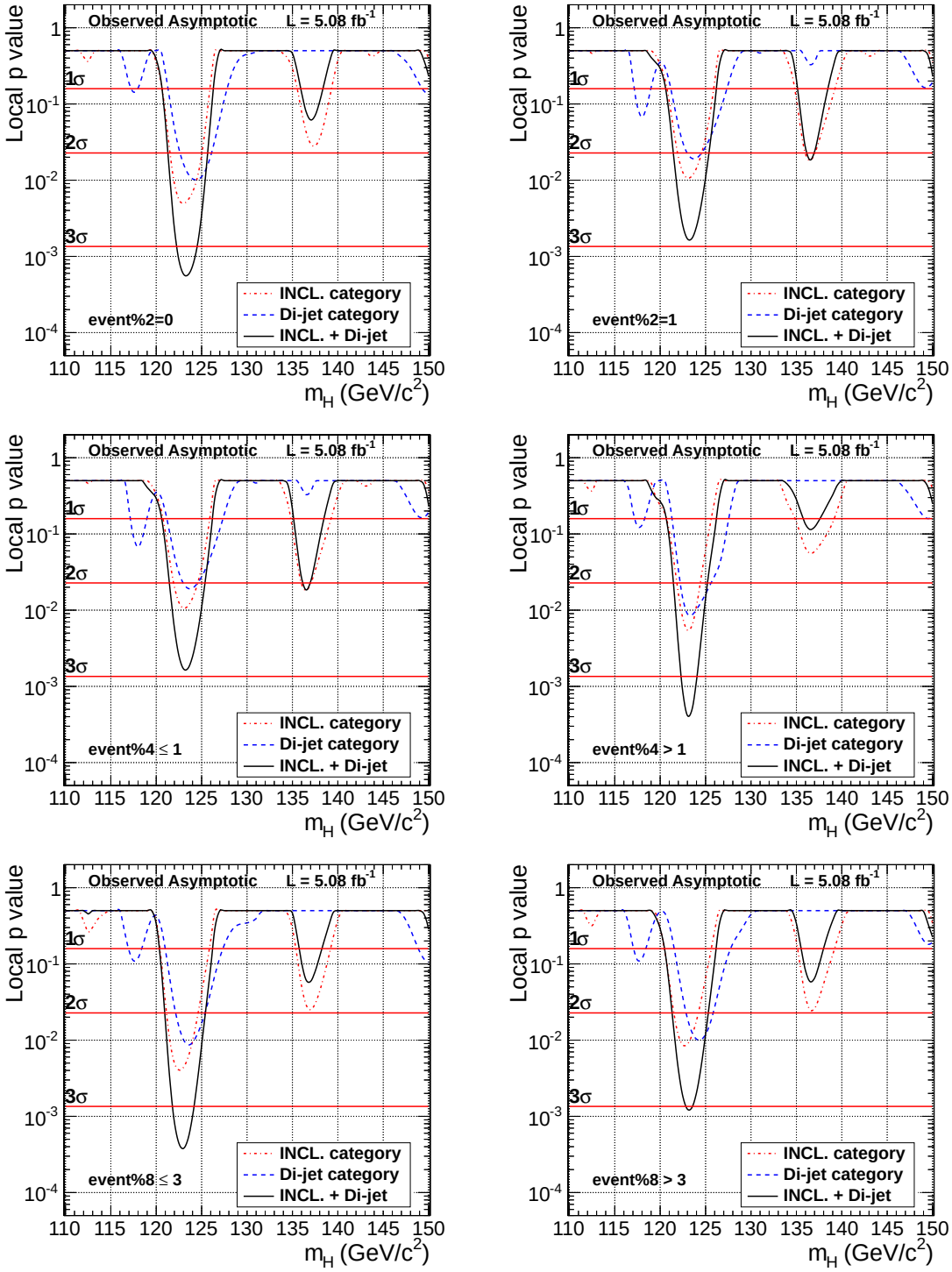

Figure 14.3: Observed local p-values in the asymptotic CL_s approximation as a function of the Higgs boson mass M_H. Each plot shows the results with the photon energy corrected with a regression trained with half of the total MC events. The way to choose only half of the MC sample is indicated in each plot, as in figure 14.2.

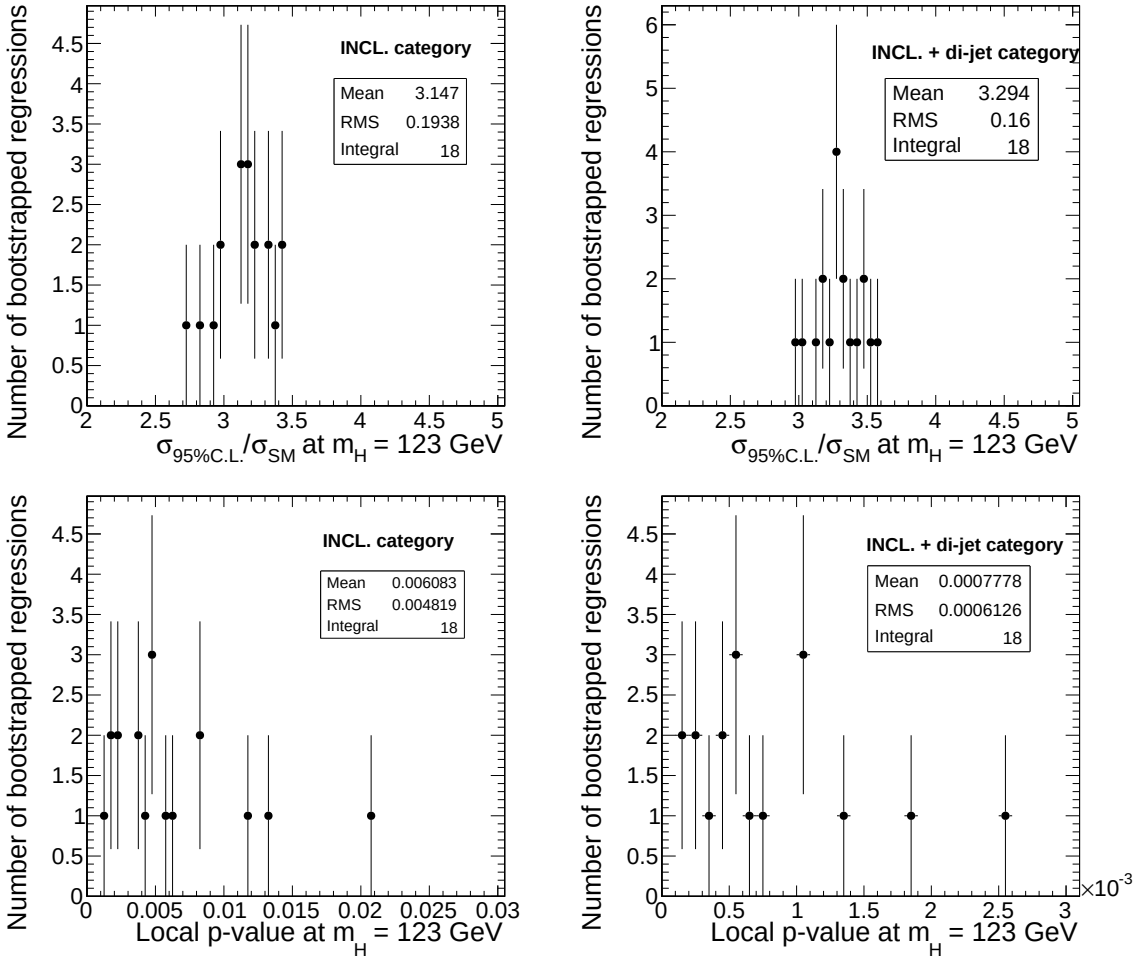

Figure 14.4: Distributions of the observed exclusion limits (top row) and the local p-values (bottom row) from bootstrapped regressions in the asymptotic CL_{s} approximation, at Higgs boson mass $\mathrm{M_H} = 123$ GeV/c^2. In the plots in the left column only the inclusive category is considered. In the right column the di-jet category is added.

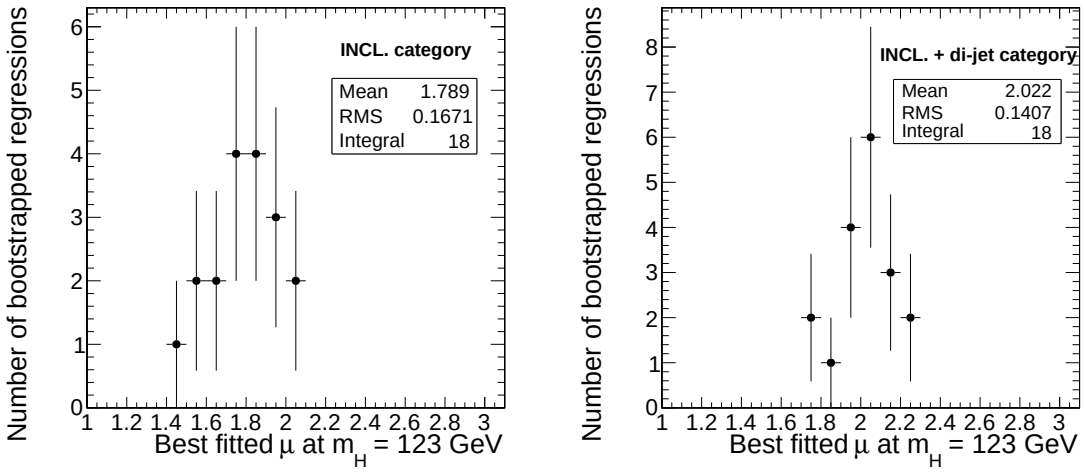

Figure 14.5: Distributions of the best fitted signal strength from the bootstrapped regressions in the asymptotic CL_s approximation at Higgs boson mass $M_H = 123$ GeV/c^2. In the left plot only the inclusive category is considered. In the right plot the di-jet category is added.

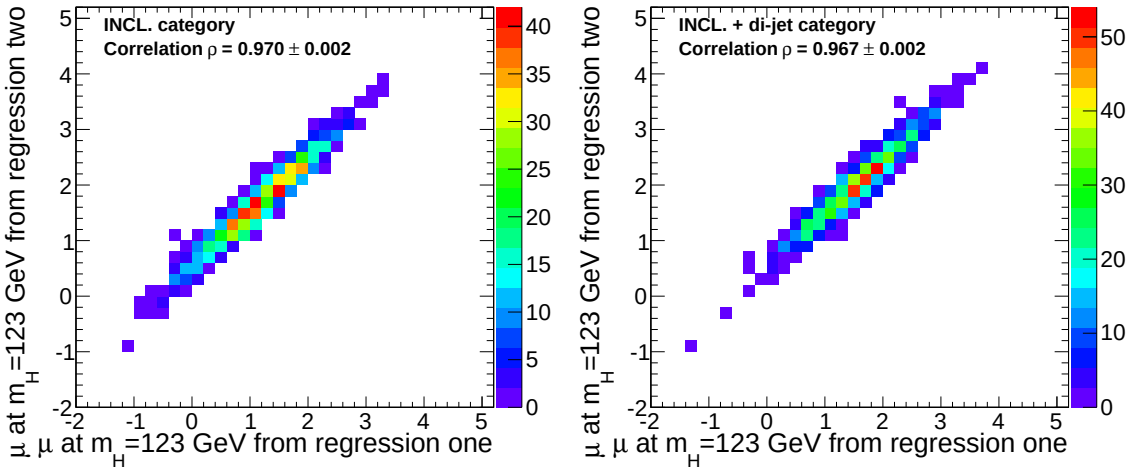

Figure 14.6: Correlation between the two best fitted signal strengths obtained from bootstrapped datasets from two different regressions and the corresponding correlation coefficient ρ. In the left plot only the inclusive category is considered. In the right plot the di-jet category is added.

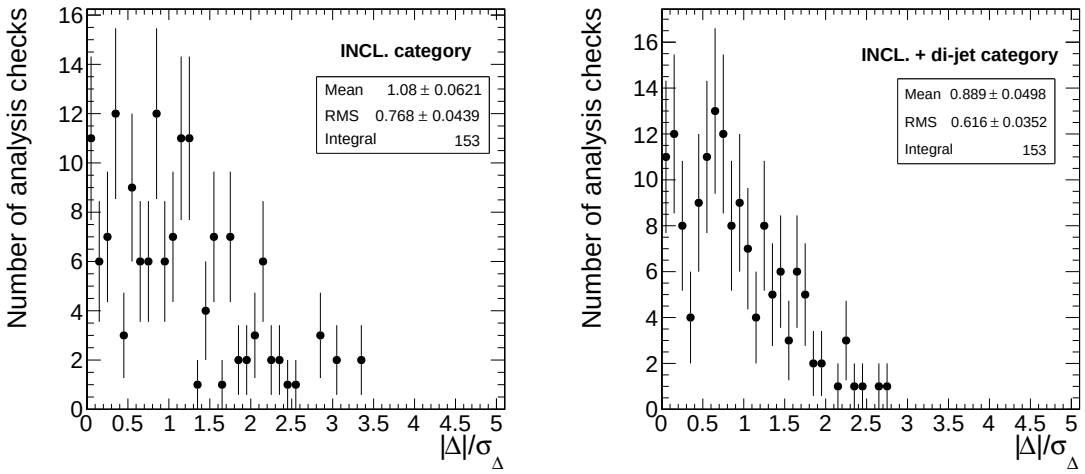

Figure 14.7: The results of 153 analysis checks from 18 bootstrapped regressions. In the left plot only the inclusive category is considered. In the right plot the di-jet category is added.

Chapter 15

$H \to \gamma\gamma$ Search Results

In this chapter, we report the results of the search for a Standard Model Higgs boson decaying into two photons with the CMS detector at $\sqrt{s} = 7$ TeV at the LHC. The result is based on the data collected in 2011, corresponding to a total integrated luminosity of 5.08 fb^{-1}.

15.1 Results

Figure 15.1 shows the invariant mass distribution in each event category, and the background model determined from the data and the expected Standard Model $H \to \gamma\gamma$ signal distributions at $M_H = 120$ GeV/c^2. As previously mentioned, the background model is a fifth order polynomial in the inclusive categories, and a second order polynomial in the di-jet category. The 1σ and 2σ errors bands, corresponding to the 68% and 95% confidence interval of the expected background, are also shown in the figure.

Figure 15.2 left shows the 95% CL exclusion limits on the $H \to \gamma\gamma$ cross section relative to the expected Standard Model $H \to \gamma\gamma$ cross section, in the asymptotic CL_s approximation as a function of the Higgs boson mass M_H for the inclusive categories only. Figure 15.2 right shows the exclusion limits when adding the di-jet category. There is an improvement of about 10% in sensitivity by adding the di-jet category. The Standard Model Higgs boson is excluded at 95% CL in the mass range 127 - 133 GeV/c^2 and 110 - 111.5 GeV/c^2. Other mass ranges from 110 - 150 GeV/c^2 are not excluded by this analysis. In the vicinity of 123 GeV/c^2, the observed upper

limits on $\mu = \frac{\sigma}{\sigma_{\rm SM}}$ are significantly larger than the expected, indicating an excess of events.

Figure 15.3 left and right show the expected and observed local p-value in the asymptotic $CL_{\rm s}$ approximation, respectively. The largest excess is observed at the invariant mass of 123 GeV with a local p-value 5×10^{-4}, where we expect 0.05 on average. The significance of this excess is about 3.3 standard deviation (σ).

Figure 15.4 shows the observed test statistic q_0, defined in equation (12.15), as a function of the Higgs boson mass. The number of up-crossings at the level one is two. According to equation (12.19), the estimated global p-value is 0.0239, corresponding to a significance of approximately 2.0σ.

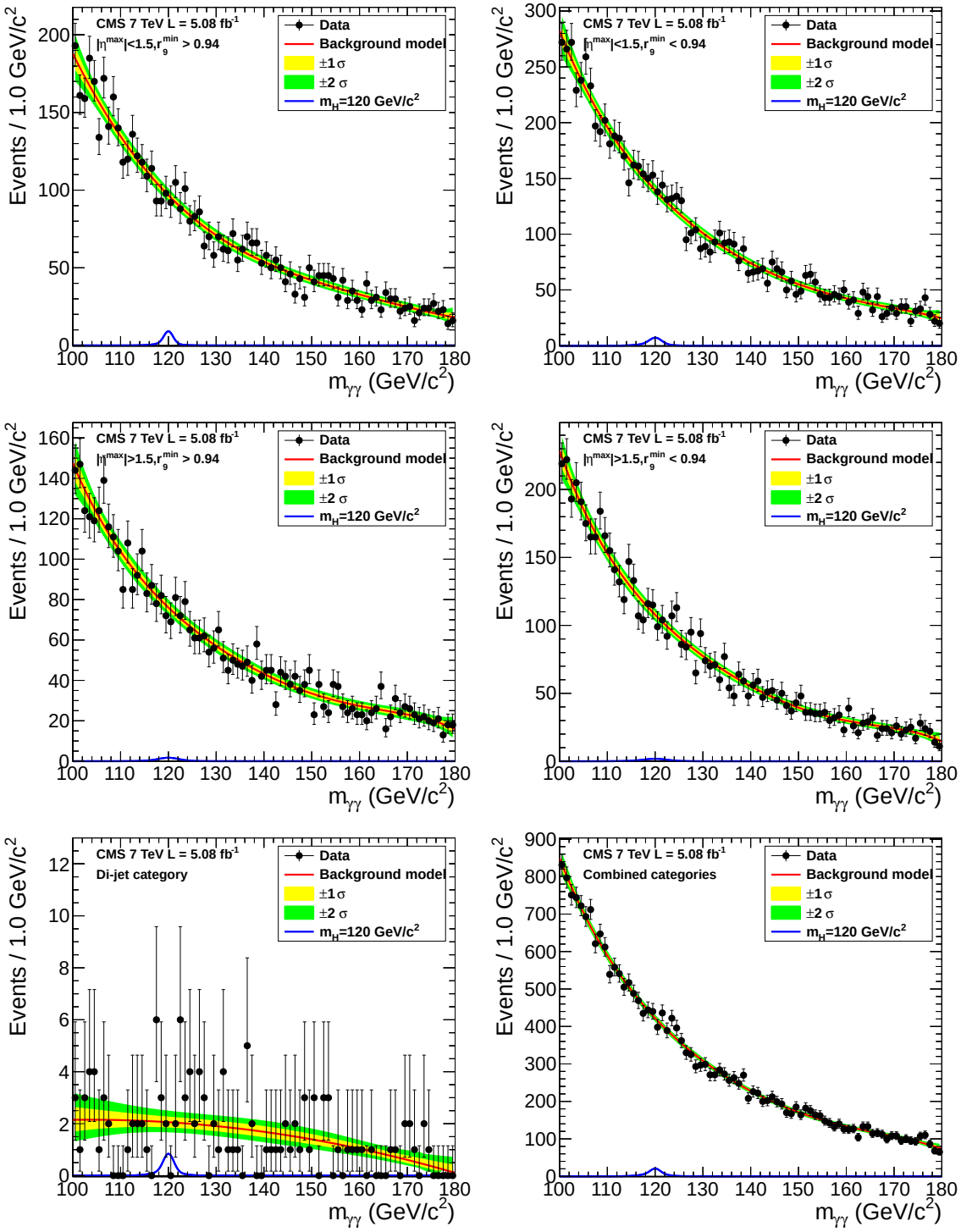

Figure 15.1: Invariant mass distributions in each event category and combined. The overlaid curve on each distribution is the background model, with statistical errors indicated by the 1σ and 2σ bands. A Standard Model H $\to \gamma\gamma$ signal is shown at $M_H = 120$ GeV/c^2, normalized to an integrated luminosity of 5.08 fb^{-1}.

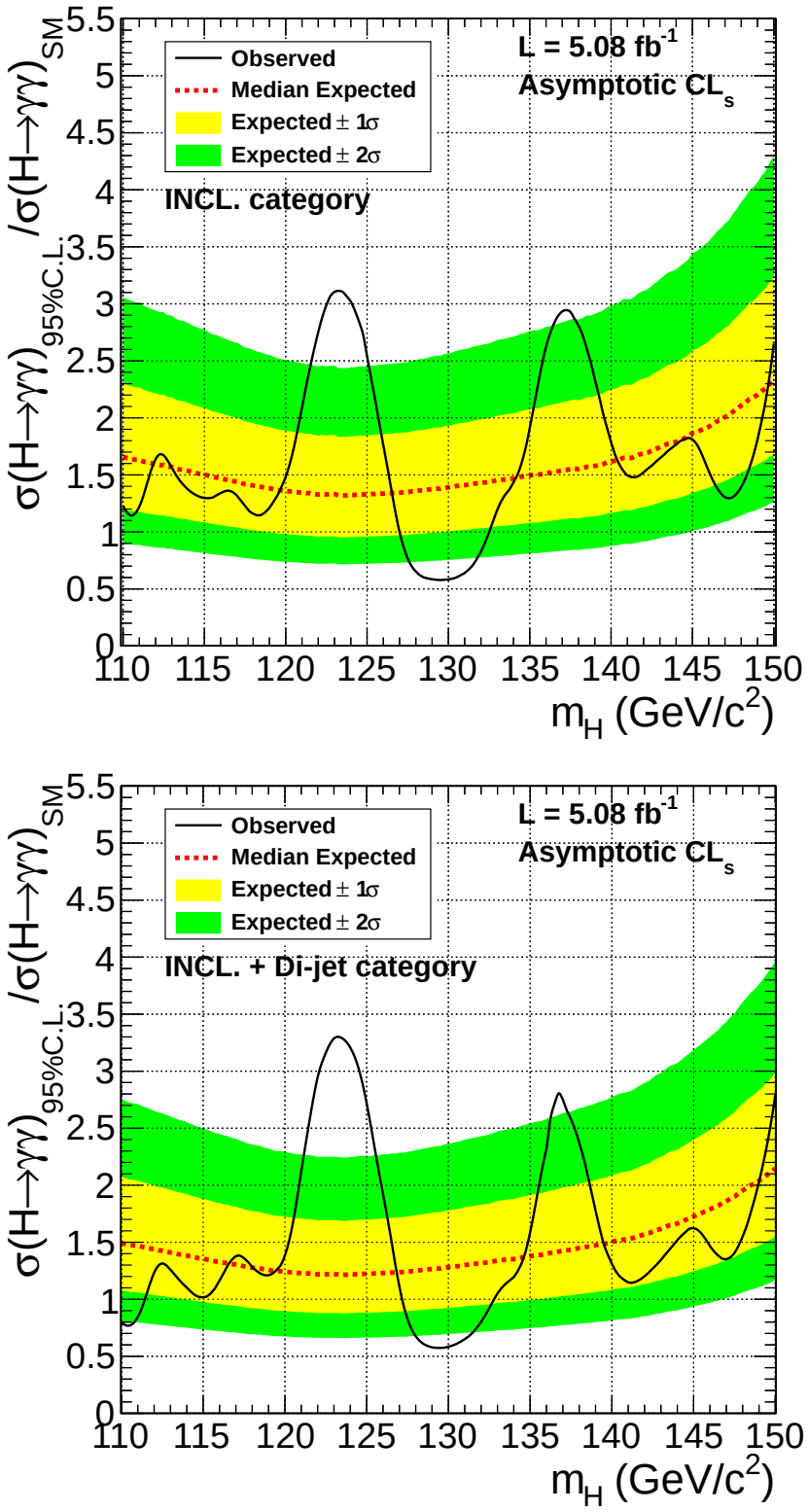

Figure 15.2: 95% CL exclusion limits on the H $\to \gamma\gamma$ cross section relative to the expected Standard Model H $\to \gamma\gamma$ cross section in the asymptotic CL_s approximation. The di-jet category is not used in the top plot but is included in the bottom one.

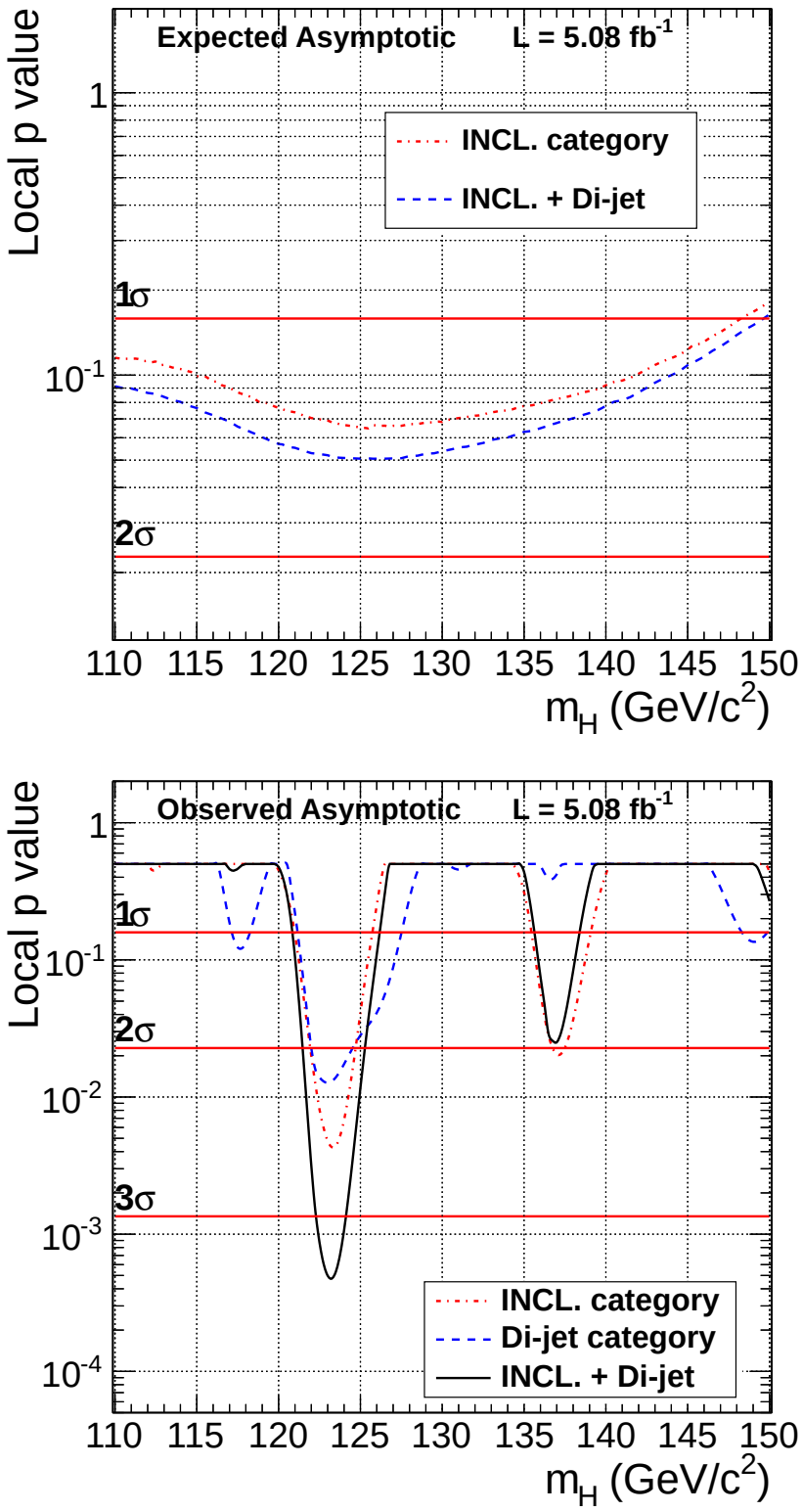

Figure 15.3: Expected (top) and observed (bottom) local p-values in the asymptotic CL_s approximation as a function of the Higgs boson mass M_H.

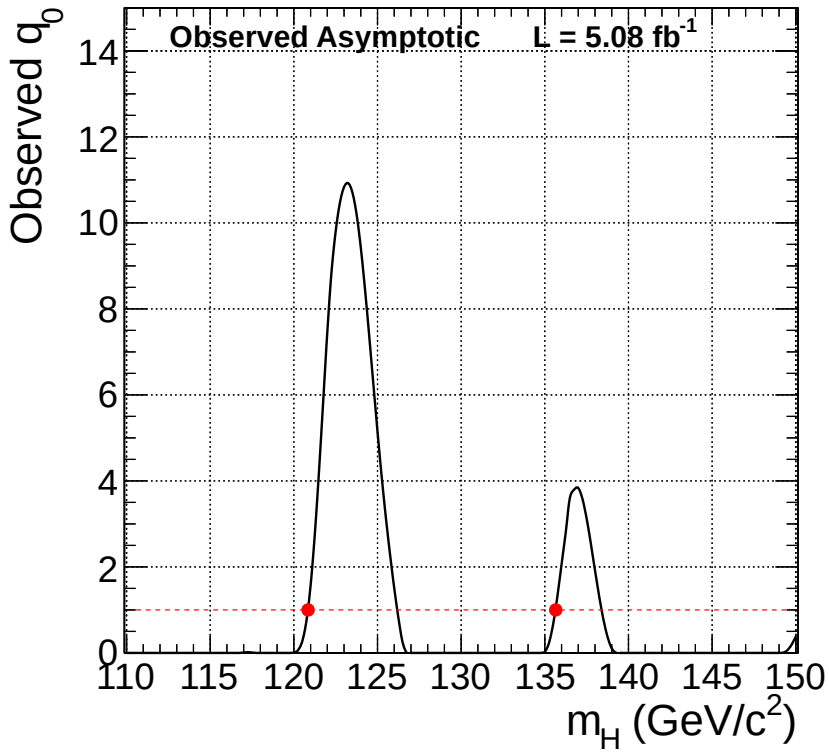

Figure 15.4: Observed q_0 as a function of the Higgs boson mass. There are two up-crossings as indicated by two the intersection points between the dashed red line and the solid black curve.

15.2 Summary and Discussion

We have performed a search for the Standard Model Higgs boson in the di-photon channel with the CMS detector in pp collisions at $\sqrt{s} = 7$ TeV at the LHC. The data we analyzed in this thesis corresponds to an integrated luminosity of 5.08 fb^{-1}, collected in 2011. We observe an excess with a local significance of 3.3σ at the mass about 123 GeV. Taking into account the look elsewhere effect from 100 to 150 GeV, the global significance is 2.0σ.

The new data from 2012 in pp collisions at $\sqrt{s} = 8$ TeV shows a similar excess in the $H \to \gamma\gamma$ channel at about the same mass. During the writing of this thesis, CMS has established the observation [18] of a new particle with a mass of 125 ± 0.6 GeV/c^2, with a local significance of 5σ, by combining a number of search channels using the data from 2011 and 2012. Although the observation is compatible with the hypothesis that the new particle is the Standard Model Higgs boson, more rigorous tests are needed to ascertain whether this new particle is indeed the Standard Model Higgs boson, or if it implies any new physics beyond the Standard Model. For example, decaying into two photons indicates that this new particle has spin different than one, according to the Landau-Yang theorem [112, 113]. The Standard Model Higgs boson has spin 0 and positive parity. With more data from the LHC, it will be possible to discriminate between the $J^P = 0^+$ and 2^+ hypotheses, and between 0^+ and 0^-, by studying the angular correlations among the four leptons in $H \to ZZ^* \to 4l$ decays, as well as between the two photons in $H \to \gamma\gamma$ decays.

Part II

Search for an Excited Muon Decaying to One Muon and One Photon in pp Collisions

Chapter 16

A Search for an Excited Muon with the First LHC Data of 2010

In this chapter we present a search for an excited muon decaying into one muon and one photon, based on 36 pb^{-1} of data collected during 2010, in pp collisions at $\sqrt{s} = 7$ TeV at the LHC with the CMS detector. This exotic particle is predicted in the theory of a compositeness model [36], which was proposed to explain the mass hierarchy of the quark and lepton generations in the Standard Model. This search, which is now published [114], found no evidence for such a particle; however it gives the most stringent limit on the relevant parameters from direct searches at hadron collider experiments to date.

16.1 Introduction

An open question in particle physics is the observed mass hierarchy of the quark and lepton SU(2) doublets in the Standard Model. A commonly proposed explanation for the three generations is a compositeness model [36] of the known leptons and quarks. According to this approach, a quark or lepton is a bound state of three fermions, or of a fermion and a boson [36].

Due to the underlying substructure, compositeness models imply a large spectrum of excited states. The coupling of excited fermions to ordinary quarks and leptons, resulting from novel strong interactions, can be described by contact interactions (CI)

with the effective four-fermion Lagrangian [115]

$$\mathcal{L}_{\rm CI} \;=\; \frac{g^2}{2\Lambda^2}\, j^\mu\, j_\mu\,, \tag{16.1}$$

where j_μ is the fermion current

$$\begin{aligned} j_\mu \;\;&=\;\; \eta_L\, \bar{f}_L \gamma_\mu f_L + \eta'_L\, \bar{f}^*_L \gamma_\mu f^*_L + \eta''_L\, \bar{f}^*_L \gamma_\mu f_L \\ &\quad + h.c. \,+\, (L \to R)\,. \end{aligned}$$

The Standard Model and excited fermions are denoted by f and f^*, respectively; g^2 is chosen to be 4π, the η factors for the left-handed currents are conventionally set to one, and the right-handed currents are set to zero. The compositeness scale is Λ.

Gauge mediated transitions between ordinary and excited fermions can be described by the effective Lagrangian [115]

$$\begin{aligned} \mathcal{L}_{\rm EW} \;\;&=\;\; \frac{1}{2\Lambda} \bar{f}^*_R\, \sigma^{\mu\nu} \\ &\quad \left[g_s f_s \frac{\lambda^a}{2} G^a_{\mu\nu} + g f \frac{\tau}{2} W_{\mu\nu} + g' f' \frac{Y}{2} B_{\mu\nu} \right] f_L + h.c.\,, \end{aligned} \tag{16.2}$$

where $G^a_{\mu\nu}$, $W_{\mu\nu}$, and $B_{\mu\nu}$ are the field strength tensors of the gluon, the SU(2) and U(1) gauge fields, respectively; f_s, f and f' are parameters of order one.

The partial widths for the electroweak decay of excited fermions are

$$\Gamma(f^* \to f + \gamma) = \frac{1}{4} \alpha f_\gamma^2 \frac{m^{*3}}{\Lambda}\,, \tag{16.3}$$

$$\Gamma(f^* \to f + V) = \frac{1}{8} \frac{g_V^2}{4\pi} f_V^2 \frac{m^{*3}}{\Lambda^2} (1 - \frac{m_V^2}{m^{*2}})^2 (2 + \frac{m_V^2}{m^{*2}})\,, \tag{16.4}$$

where V refers to the W or Z gauge boson and

$$f_\gamma = f T_3 + f' \frac{Y}{2}\,, \tag{16.5}$$

$$f_Z = fT_3 cos^2\theta_{\rm W} + f'\frac{Y}{2} sin^2\theta_{\rm W}\,, \tag{16.6}$$

$$f_W = \frac{f}{\sqrt{2}}\,, \tag{16.7}$$

where T_3 denotes the third component of the weak isospin, $g_W = \sqrt{4\pi\alpha}/sin\,\theta_{\rm W}$ and $g_Z = g_W/cos\,\theta_{\rm W}$, and θ is the electroweak mixing angle. f and f' are parameters determined by the composite dynamics. In this analysis, they are set to be unity.

The decay of an excited fermion could also be mediated by the four-fermion contact interaction (CI), the decay width is given by

$$\Gamma(f^* \to f + f'\bar{f}') = \frac{m^*}{96\pi}(\frac{m^*}{\Lambda})^4 N_c S\,, \tag{16.8}$$

where N_c is the number of colors of the fermion and S is an additional combinatorial factor: S = 1 for $f \neq f'$, and S = 2 for $f = f'$ and f being a lepton.

At the LHC, the production of single excited leptons is dominated by the contact interaction (shown in figure 16.1), the cross section of which depends on both the compositeness scale Λ and the mass of the excited lepton m^*

$$\hat{\sigma}(q\bar{q} \to ll^*, l^*\bar{l}) = \frac{\pi}{6\hat{s}}(\frac{\hat{s}}{\Lambda^2})^2(1 + \frac{1}{3}(\frac{\hat{s} - m^{*2}}{\hat{s} + m^{*2}}))(1 - \frac{m^{*2}}{\hat{s}})^2(1 + \frac{m^{*2}}{\hat{s}})\,. \tag{16.9}$$

This analysis considers the single production of an excited muon μ^* in association with a muon via a four-fermion CI, with the subsequent electroweak decay of the μ^* into a muon and a photon (figure 16.2). This decay mode leads to the fully reconstructable, which is almost background-free for large excited muon mass, final state $\mu\mu\gamma$. With the data considered herein, collected with the CMS detector at the LHC in pp collisions at $\sqrt{s} = 7$ TeV, the largest irreducible Standard Model background is from the Drell-Yan (DY) process $p\bar{p} \to Z/\gamma^* \to \mu^+\mu^-(\gamma)$, with the final state photon radiated by either a parton in the initial states (ISR), or from one of the final state muons (FSR).

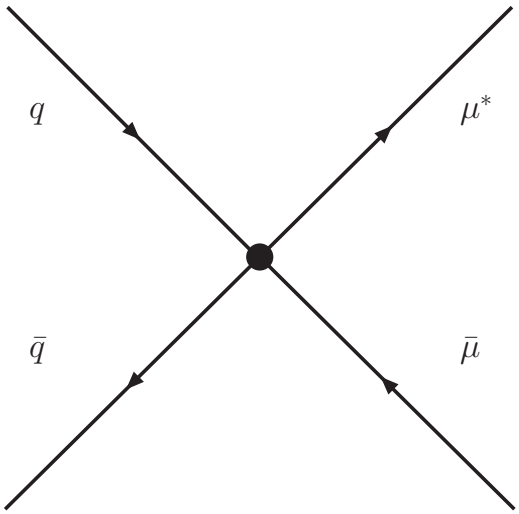

Figure 16.1: Production of single excited muon via contact interactions.

Decays via contact interactions, not implemented in PYTHIA, contribute between a few percent of all decays for $\Lambda \gg M_{\mu^*}$ and 92% for $\Lambda = M_{\mu^*}$ (see figure 16.3). This has been taken into account for the signal expectation in this analysis.

At the time the analysis was performed, searches on excited muons at hadron collider had been previously performed by the D0 and CDF Collaborations [116,117]. At the Tevatron, excited muons were excluded at 95% confidence level in the range $107 < M_{\mu^*} < 853$ GeV ^{2} for $\Lambda = M_{\mu^*}$ by the CDF Collaboration. Using the branching ratios that account for hypothetical contact interaction decays when establishing the limits, a more stringent limit is given by the D0 Collaboration. It excludes the existence of excited muons in the range $M_{\mu^*} < 696$ GeV/c^2 for $\Lambda = M_{\mu^*}$, and $M_{\mu^*} < 618$ GeV/c^2 for $\Lambda = 1$ TeV.

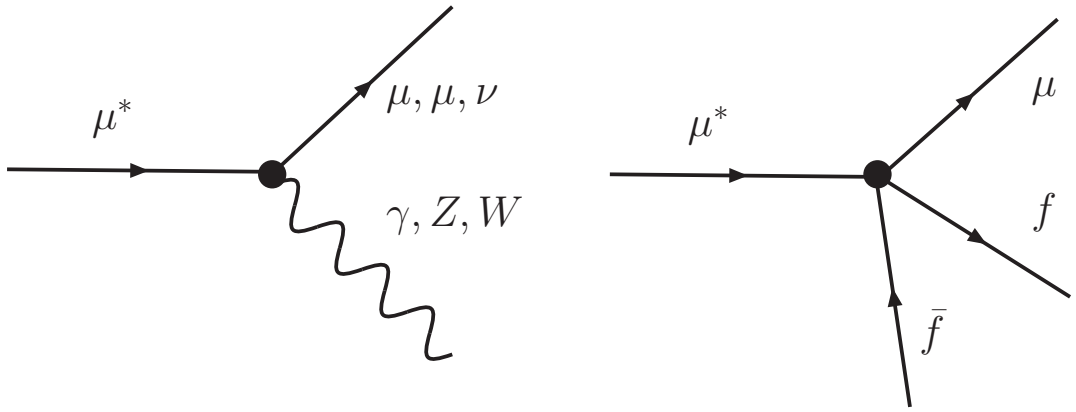

Figure 16.2: Decay channels of an excited muon, via electroweak (left) and contact (right) interactions.

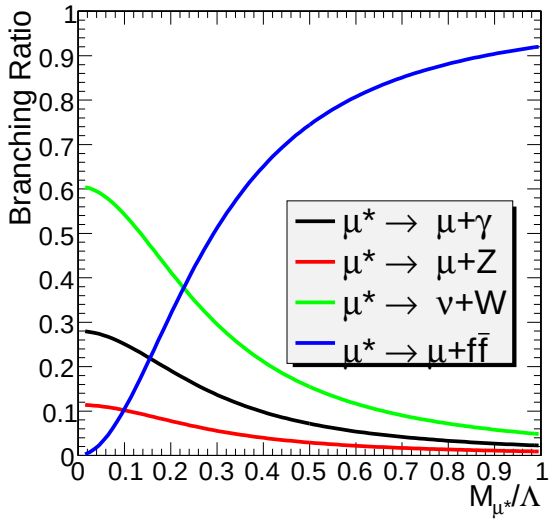

Figure 16.3: Relative contribution to decays of an excited muon via electroweak and contact interactions as a function of M/Λ.

16.2 Data and Monte Carlo Simulation Datasets

16.2.1 Data Samples and Trigger

Table 16.2.1 shows the datasets and run ranges we used in this analysis, corresponding to 36.4 pb^{-1} of data. The label "RECO" is a name that refers to a particular data structure format of the events in these datasets used in CMS. The label "Mu" refers to the single muon primary dataset. The label "Run2010A-Nov4ReReco_v1" refers to the run periods and data reprocessing date (or version).

Dataset	Run Range
/Mu/Run2010A-Nov4ReReco_v1/RECO	136035 to 144114
/Mu/Run2010B-Nov4ReRecov1/RECO	146428 to 149294

Table 16.1: Datasets used for searching for an excited muon $\mu^* \to \mu\gamma$.

In the CMS High Level Trigger (HLT), events are selected by requiring at least one muon with p_{T} above 15 GeV.

16.2.2 Implementation of Excited Muon Generation in PYTHIA

In PYTHIA, the generation of $pp \to \mu\mu^* \to \mu\mu\gamma$ is only available since the official release version 8. However, in this analysis, PYTHIA version 6 is used to generate all Standard Model backgrounds, except the $Z\gamma$ sample which is generated in MADGRAPH. For this sample, the parton fragmentation (showers) is modeled in PYTHIA 6. The parton shower process generates a list of physics particles which are measured in the detector. Therefore, the parton shower model affects the isolation variables, which are frequently used in the particle identifications.

Figure 16.4 shows the comparison of the photon identification efficiency in the barrel between simulations in PYTHIA versions 6 and 8. This difference is not fully understood, but we believe it is due to some different implementations of the parton shower model in these two versions. Therefore, in this analysis, we have to use PYTHIA 6, since all efficiency correction factors are based on PYTHIA 6.

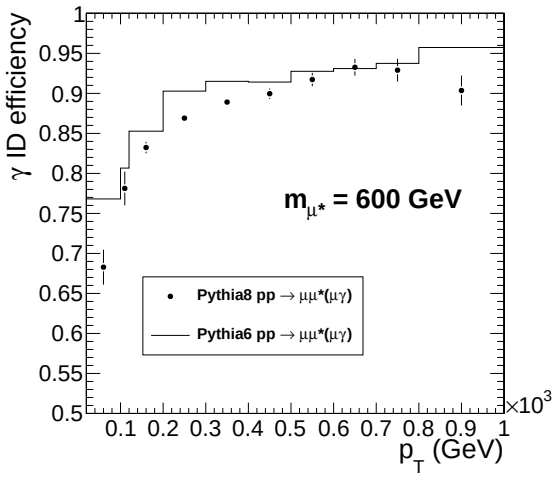

Figure 16.4: Photon identification efficiency as a function of p_{T}^{γ} in the barrel measured in simulation using PYTHIA version 6 or 8.

In PYTHIA 6, the $\mathrm{pp} \to \mathrm{ee}^* \to ee\gamma$ channel is available, which makes the implementation of $\mathrm{pp} \to \mu\mu^* \to \mu\mu\gamma$ relatively easy. Figure 16.5 shows the validation of our implementation, comparing the p_{T} and η spectra of the leptons and photon of $\mathrm{pp} \to \mu\mu^* \to \mu\mu\gamma$ generated in our customized PYTHIA 6 with that of $\mathrm{pp} \to \mathrm{ee}^* \to ee\gamma$ generated in the official release PYTHIA 6. Figure 16.6 shows a further validation by comparing the photon identification efficiency from $\mathrm{pp} \to \mu\mu^* \to \mu\mu\gamma$ and $\mathrm{pp} \to \mathrm{ee}^* \to ee\gamma$ generated separately with our customized and the official PYTHIA 6.

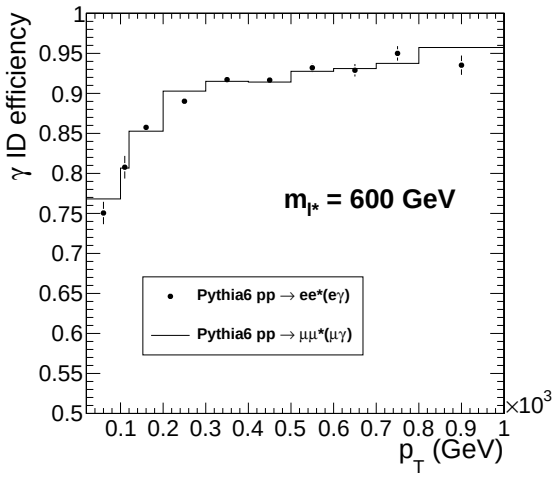

Figure 16.6: Photon identification efficiency as a function of p_{T}^{γ} in the barrel measured in simulation from $\mathrm{pp} \to \mu\mu^* \to \mu\mu\gamma$ implemented in our customized `PYTHIA` 6 and from $\mathrm{pp} \to \mu\mu^* \to \mu\mu\gamma$ implemented in the official `PYTHIA` 6.

16.2.3 Monte Carlo Background Samples

In the $\mathrm{pp} \to \mu\mu^* \to \mu\mu\gamma$ analysis, the Standard Model backgrounds can be subdivided into three distinct categories:

- Background events with two real muons and a real photon in the final state. This contribution is estimated from MC simulation, with the muon and photon efficiency corrected using data-driven methods, and includes:
  - Drell-Yan into dimuons $+\gamma$ production with an FSR or ISR photon. This is the main source of the irreducible backgrounds.
  - Diboson $(\mathrm{WW}, \mathrm{WZ}, \mathrm{ZZ})$ and $t\bar{t}$ production with an ISR or FSR photon.
- Background events with two real muons and one fake photon in the final state. This contribution is estimated from the data using a photon fake rate method, and includes:
  - Drell-Yan, diboson, and $t\bar{t}$ production leading to dimuons + a jet faking a photon in the final state

  - QCD multijet production; for example, where a jet contains a J/ψ or Υ decaying to $\mu^+\mu^-$.

- Background events with one real and one fake muon and a real photon in the final state. This contribution is estimated from the data using a muon fake rate method, and includes:

  - W + jet with an FSR or ISR photon.
  - Jets + photon production.

The Monte Carlo samples used for modeling of the Standard Model backgrounds are listed in table 16.2.3 together with the corresponding NLO cross sections.

The LO-MADGRAPH Zγ sample is used to estimate the main irreducible background. Events are reweighted by a p_{T}^{γ} dependent k factors to match the NLO calculation [118]. The PYTHIA $Z \to \mu\mu$ sample is used for the muon efficiency measurement.

MC Sample	Generator	Cross Section (pb)
$\mathrm{Z} \to \mu^+\mu^- + \gamma$	MADGRAPH	33.7
$W \to \mu\nu + \gamma$	MADGRAPH	121.2
$\mathrm{Z} \to \mu^+\mu^-$	PYTHIA	1666
$\mathrm{Z} \to \tau^+\tau^-$	PYTHIA	1666
WW inclusive decays	PYTHIA	43
WZ inclusive decays	PYTHIA	18.6
ZZ inclusive decays	PYTHIA	5.9
TT	PYTHIA	165

Table 16.2: The Monte Carlo samples and NLO cross sections used in the excited muon analysis.

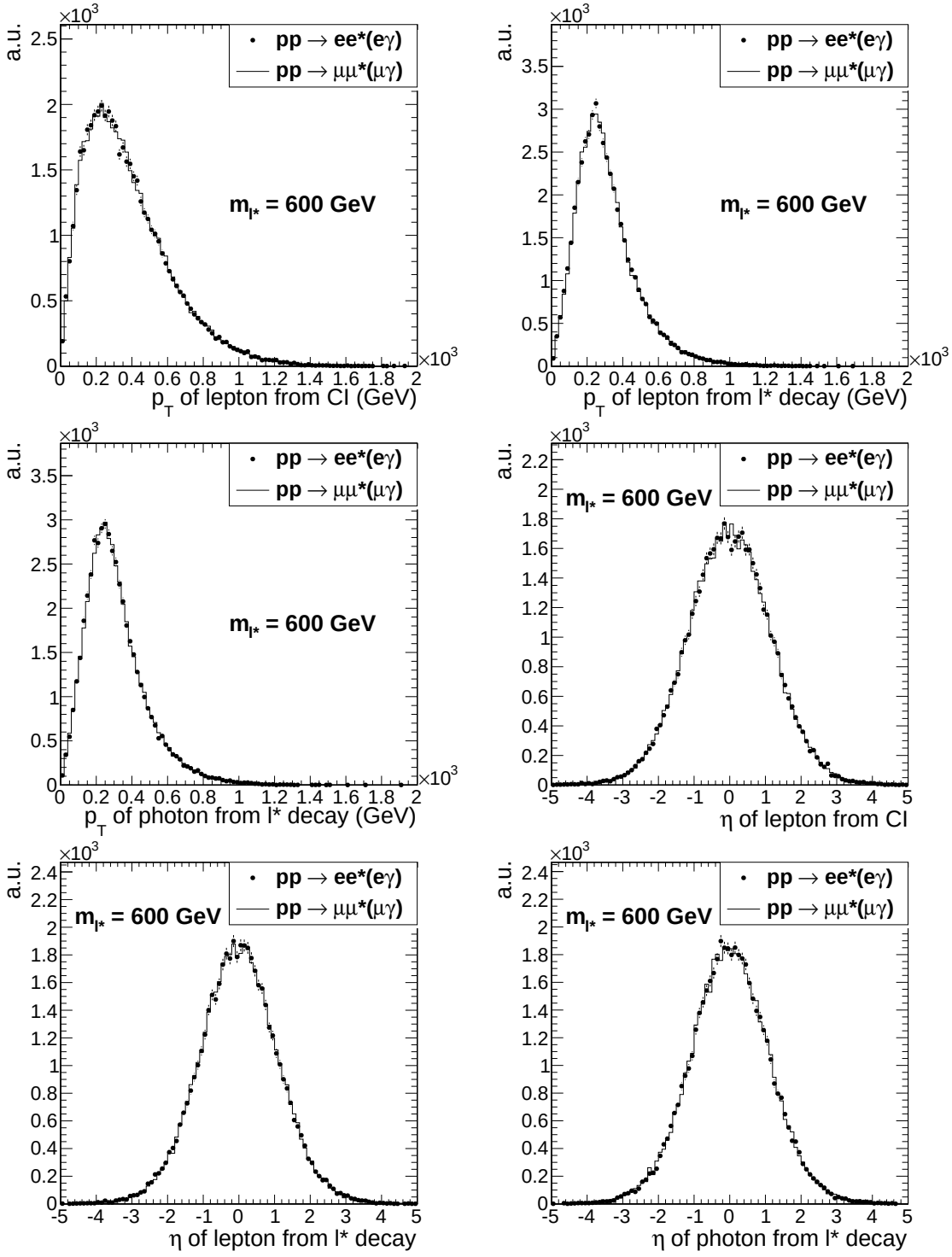

Figure 16.5: Comparison of the generated p_{T} and η spectra of two leptons and one photon from $\mathrm{pp} \to \mu\mu^* \to \mu\mu\gamma$, generated in our customized PYTHIA 6 and $\mathrm{pp} \to \mathrm{ee}^* \to ee\gamma$, generated in the official release PYTHIA 6.

16.3 Objection Identification and Event Selection

In this section we discuss the muon and photon identification (ID) and the event selection criteria used for this analysis.

16.3.1 Muon Reconstruction and Identification

In CMS, muon tracks are first reconstructed independently in the CMS silicon tracker system (tracker track) and in the muon spectrometer (standalone-muon track). Then, two different approaches are taken:

- Global Muon reconstruction. In this approach, the reconstruction is performed in the "outside-in" direction: starting from a standalone muon in the muon system, a matching track in the inner tracker is found and a global-muon track is fitted combining hits from the tracker track and standalone-muon track. In the global muon reconstruction, the measurement of the muon momentum is taken exclusively from the tracker track, for muon transverse momenta up to 200 GeV/c. Above that value, the information of the muon spectrometer is also used, improving the resolution on the muon momentum.

- Tracker Muon reconstruction. This corresponds to the "inside-out" approach, where all tracks measured in the inner tracker with $p_{\mathrm{T}} > 0.5$ GeV/c and p$>$ 2.5 GeV/c are considered as possible muon candidates and are extrapolated to the muon system. The extrapolation takes into account the expected energy loss and multiple scattering suffered by the particle crossing the detector. If a muon segment is found in the muon spectrometer, matching the tracker track, the latter will be considered to be a muon.

In our analysis, we require that all muon candidates are reconstructed both as global and as tracker muons. The muon identification selection in this analysis also includes a few cuts to reject cosmic rays, muons from the decay of hadrons in flight and hadrons misidentified as muons, so-called punch-throughs. The "outside-in" global muon fit is required to have a χ^2/ndf of less than 10, including at least one valid hit

in the muon detector, as well as one station in the muon spectrometer matched to the muon track. The tracker track corresponding to the muon is required to have more than 10 hits. Finally the muon is required to pass a loose isolation cut. We require that the summed p_{T} of the tracks around the muon direction in a cone of $\Delta R < 0.3$ to be less than 10 GeV.

Table 16.3 summarizes the muon identification criteria used in this analysis.

Cut number	Requirements
1	is global and tracker Muon
2	χ^2/ndf of the global muon fit < 10
3	Number of valid μ-detector hits in global fit > 0
4	Track Isolation < 10 GeV
5	Impact parameter w.r.t. the beam spot $\lvert d_0 \rvert < 2$ mm
6	Number of hits in tracker track > 10
7	Number of stations with hits used in the fit > 0

Table 16.3: Muon identification cuts used in the $\mu^* \to \mu\gamma$ analysis.

16.3.2 Photon Reconstruction and Identification

In section 7.1 we have discussed the photon reconstruction. However, there are a few differences in this analysis of $\mu^* \to \mu\gamma$. Here we use the CMS standard photon energy correction. This is because in this analysis the photon energy resolution is not so important as in the $\mathrm{H} \to \gamma\gamma$ analysis, since we are performing a cut-and-count analysis, which is relatively insensitive to the invariant mass resolution. Besides, the standard vertex identification has a very high efficiency in this analysis, because of the presence of the two high p_{T} muon tracks, as well as negligible pileup in the data due to very low instantaneous luminosity at the LHC in 2010.

In this analysis, only photons in the ECAL barrel ($|\eta_{\mathrm{sc}}| < 1.48$) are considered. The following variables are used to reject backgrounds which can be misidentified as photons.

- $\sigma_{\mathrm{i}\eta\mathrm{i}\eta}$ (see section 7.2, equation (7.4)), which characterizes the transverse shape of the electromagnetic shower, is required to be less than 0.013.

- H/E (see section 7.2) is required to be less than 0.05.

- $\text{Iso}^{\text{track}}$. This is defined as the sum p_{T} of all tracks within the cone $\Delta R < 0.4$ around the photon candidate. $\text{Iso}^{\text{track}} < 2\ \text{GeV} + 0.001 \cdot p_{\text{T}}$ is required.

- Iso^{ECAL}. This is defined as the total electromagnetic calorimeter transverse energy measured in all crystals within a cone $\Delta R < 0.4$, around the photon candidate, subtracting the energies in an inner cone of smaller size corresponding to the photon energy itself. $\text{Iso}^{\text{ECAL}} < 4.2\ \text{GeV} + 0.006 \cdot p_{\text{T}}^{\gamma}$ is required.

- Iso^{HCAL}. This is defined as the total hadronic calorimeter transverse energy measured in the HCAL towers between an outer cone $\Delta R < 0.4$ and an inner veto cone $\Delta R > 0.15$, which corresponds to the inner cone used for the calculating the H/E. $\text{Iso}^{\text{HCAL}} < 2\ \text{GeV} + 0.001 \cdot p_{\text{T}}^{\gamma}$ is required.

- Spike rejections. Anomalous signals in the ECAL barrel have been observed in collision data [119]. These signals are caused by the direct ionization of the avalanche photodiode (APD) sensitive volumes due to highly ionizing particles, mainly protons and heavy ions, produced in pp collisions. This kind of signal usually causes a large energy output from the APD, resulting in an isolated "spike" in this single channel, which can be reconstructed as a photon candidate. By definition, nearly all spikes pass all the identification cuts we discussed above. In CMS, a topological selection is used to reject those spikes, by requiring the following variable greater than 0.95:

$$\text{Swiss cross} = (1 - (\text{E}_{\text{Left}} + \text{E}_{\text{Right}} + \text{E}_{\text{Top}} + \text{E}_{\text{Bottom}})/\text{E}_{\text{max}}\,, \tag{16.10}$$

  where E_{max} refers to the energy measured in the seed crystal of the photon, E_{left} is the energy measured in the crystal on the left of the seed crystal, etc., as illustrated in figure 16.7.

  In addition, to remove double spikes which are next to each other, another cut is applied on the variable $\frac{E_2}{E_9} < 0.95$, defined in the following way: the energy

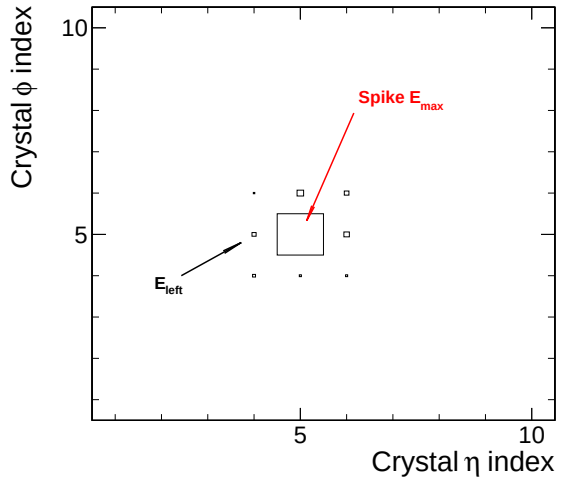

Figure 16.7: Illustration of the spike in the ECAL barrel. Each box refers to a crystal. The size of the box is proportional to the energy measured in that crystal.

collected in the seed crystal is summed with the energy of one of the four closest crystals with the highest energy deposit ("E_2") and then divided by the total energy contained in the 3×3 crystal matrix ("E_9").

Table 16.4 summarizes the photon identification cuts used in this analysis.

Cut #	variable	Value
1	ECAL Isolation	$< 4.2 + 0.006 p_{\mathrm{T}}$
2	HCAL Isolation	$< 2.2 + 0.0025 p_{\mathrm{T}}$
3	Track Isolation	$< 2 + 0.001 p_{\mathrm{T}}$
4	HCAL over ECAL fraction	H/E<0.05
5	Shower shape	$\sigma_{i\eta i\eta}$ <0.013
6	Detector region	barrel
7	Spike removal	(Swiss cross)> 0.95
8	Spike removal	$E_2/E_9 < 0.95$

Table 16.4: Photon identification cuts used in $\mu^* \to \mu\gamma$ analysis.

16.3.3 Event Selection

First of all, the events passing the trigger requirement are required to have at least one good reconstructed primary vertex. More specifically, the transverse and longitudinal

distance of the primary vertex from the beam spot position are required to be less than 2 and 24 cm, respectively. The vertex is required to have 3 degrees of freedom in the vertex fit, which means the fit uses at least 4 tracks, each with weight (determined by the quality of the fit in the reconstruction of each track) ≈ 1. In addition, At least 25% of the tracks are required to have a high purity to remove the beam scraping events.

Secondly, events are selected to have at least two identified muons with p_{T} >20 GeV and $|\eta| < 2.4$. In order to assure a high trigger efficiency, at least one of the two muons is required to match with a trigger muon within $\Delta R < 0.2$. If more than two muons satisfy these criteria, the first two leading p_{T} muons are selected. The invariant mass of the two muons is required to above 60 GeV/c^2, in order to suppress the Drell-Yan and low-mass dimuon resonance backgrounds. This cut also ensures that the generator-level cut of $\sqrt{\hat{s}} > 20$ GeV has no impact on the analysis.

Thirdly, events are further selected by requiring at least one identified photon with p_{T} >20 GeV in the barrel. Meanwhile, this photon is required to be separated from any of the two selected muons by $\Delta R > 0.5$. If more than one photon satisfies those criteria, the one with the highest p_{T} is selected.

The event selections we have described so far refer to a control region selection, from which we can compare the data and background yield with a reasonable amount of statistics. In order to improve the search sensitivity, one of two possible muon and photon invariant mass combinations in each event, with the higher value of $\mathrm{M}_{\mu\gamma}^{\mathrm{max}}$, is used as the final selection variable. We will discuss this selection cut in section 16.8.1.

16.4 Data Driven Efficiency Measurement

The signal selection efficiency estimated from simulation needs to be corrected due to the differences between the data and simulation. In this section, we measure the photon and muon identification efficiency, and the muon trigger efficiency. For photons, the only sample with a high purity is radiative photons in Z decays. However, the rate of this process is very small, making the measurement impractical with

35 pb^{-1} of data. Therefore, we use the $\text{Z} \to \text{e}^+\text{e}^-$ sample, where the electrons are reconstructed as photon candidates as well. To measure the muon efficiencies we use the $\text{Z} \to \mu^+\mu^-$ sample.

16.4.1 The Tag-and-Probe method

A commonly used method is to measure the selection efficiency in a signal enriched sample in the data and simulation by a Tag and Probe (TnP) method.

First, we select one electron (or positron) to pass a tight offline selection cut and trigger selection. Usually a tight cut is needed to reject backgrounds. This electron is called the tag electron. Then we measure the efficiency of the other positron (or electron) passing a particular set of selection criteria of interest. The measurement is usually performed by simultaneously fitting two invariant mass distributions of e^+e^- obtained from the data and the simulation. One distribution is with the probe electron passing the selection criteria. The other one is with the probe electron failing the selection. The distributions from the $\text{Z} \to \text{e}^+\text{e}^-$ simulation are used to model the signal shape in data. In practice, the width of the $\text{Z} \to \text{e}^+\text{e}^-$ distribution in the simulation needs to be broadened to match the data, by adding a Gaussian convolution to the nominal distribution. In data there are usually some nonnegligible backgrounds, which should be subtracted when extracting the efficiency. In practice, the background model is not precisely known. In the case of $\text{Z} \to \text{e}^+\text{e}^-$, a widely used function for the background is an exponential.

We use the same method to measure the efficiency of the muon trigger and the muon identification, but with the $\text{Z} \to \mu^+\mu^-$ sample.

Two efficiency numbers, corresponding to the data and the simulation, are extracted from the simultaneous fit. The ratio of them

$$\text{SF} = \frac{\epsilon_{\text{TnP}}^{\text{Data}}}{\epsilon_{\text{TnP}}^{\text{MC}}}\,, \tag{16.11}$$

is then applied to the relevant objects in the signal sample of $\mu\mu^* \to \mu\mu\gamma$ as a scale factor in the event selection efficiency. For example, if the ratio is 1.05 for the photon

ID, then the event efficiency estimated from simulation

$$\epsilon_{\rm sel} = \epsilon^{\rm evt}_{\rm trig} \cdot \epsilon_{\gamma_{\rm ID}} \cdot \epsilon^2_{\mu_{\rm ID}} \,, \tag{16.12}$$

needs to be scaled up by 5%.

16.4.2 Photon Identification Efficiency

Figure 16.8 and figure 16.9 show the simultaneous fit to the invariant mass distributions of the tag electron (positron) and the probe positron (electron) which pass or fail the photon ID criteria in the barrel and endcaps, respectively. Tag electrons or positrons are required to pass a tight set of electron identification cuts and to be matched with the electron trigger object, while probe positrons or electrons are simply reconstructed electron candidates without additional cuts.

The data-over-MC efficiency factors are measured to be 0.967 ± 0.004 and 0.971 ± 0.006 for the barrel and endcaps, respectively. The systematical uncertainty on these numbers is estimated to be 0.025 [120].

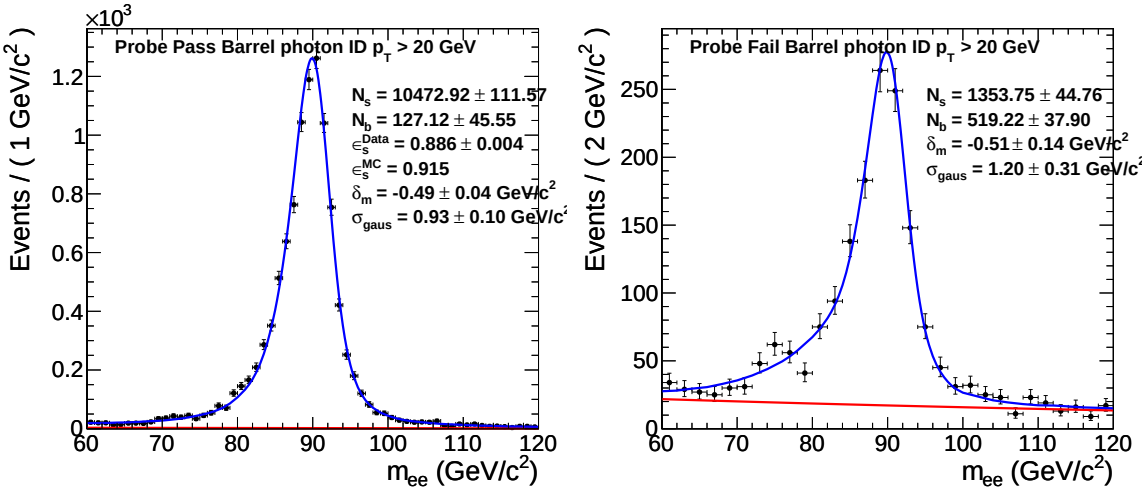

Figure 16.8: Simultaneous fit to the invariant mass distribution of the tag electron (or positron) and the passing probe positron (or electron). The distribution with passing probes is shown on the left, and with failing probes on the right. Both the electron and positron are in the ECAL barrel.

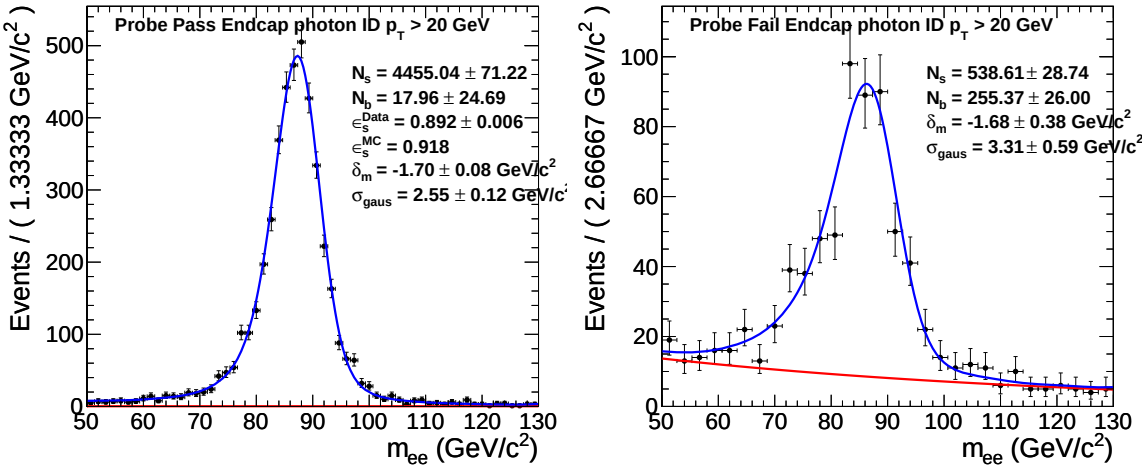

Figure 16.9: Simultaneous fit to the invariant mass distribution of the tag electron (or positron) and the passing probe positron (or electron). The distribution with passing probes is shown on the left, and with failing probes on the right. Both the electron and positron are in the ECAL endcaps.

16.4.3 Muon Trigger and Identification Efficiency

In this section we study the muon related efficiencies with the TnP method using $Z \to \mu^+\mu^-$ events. The tag muon is required to pass the muon ID and the trigger requirements. Besides, the tracker isolation $\mathrm{Iso}^{\mathrm{track}}$ is required to be below 3 GeV in order to reduce the backgrounds.

The efficiency of the track reconstruction, given a reconstructed standalone muon, is found to be 99.9% in the simulation and 99.9 ± 0.1 % in data for p_{T} above 20 GeV/c, thus the starting object for TnP measurements is a reconstructed track. More specifically, we measure the following efficiencies sequentially to derive the overall reconstruction and identification efficiency:

- The efficiency of a muon track reconstructed as a tracker muon. Here, the track is required to pass the isolation cuts, $\mathrm{Iso}^{\mathrm{track}} < 3$ GeV, $\mathrm{Iso}^{\mathrm{ECAL}} < 3$ GeV, and $\mathrm{Iso}^{\mathrm{HCAL}} < 3$ GeV. These cuts are needed to reduce the background in the invariant mass spectrum of tag and failing-probe muon pairs.

- The efficiency of a tracker muon reconstructed as a global muon, passing as well the muon identification criteria.

- The efficiency of an identified muon passing the trigger requirement imposed by the trigger path of HLT_Mu15, which requires at least one muon reconstructed and identified at the HLT with a p_{T} above 15 GeV/c.

Figure 16.10 left and right show the simultaneous fit to the invariant mass distributions of the tag muon and probe muon (tracker muon) which pass or fail the muon ID criteria, respectively.

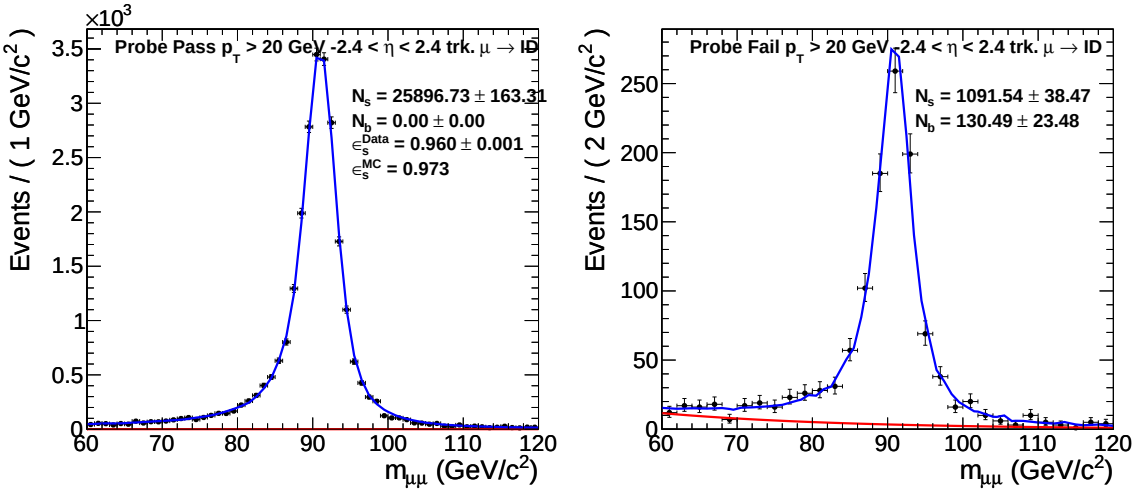

Figure 16.10: Simultaneous fit to extract the efficiency of a tracker muon passing the ID criteria: for passing probes on the left and for failing probes on the right.

Table 16.5 and table 16.6 show the measured TnP efficiencies of a track reconstructed as a tracker muon binned in p_{T} and η in the data and the simulation, respectively. Table 16.7 shows the corresponding Data-over-MC scale factors.

Table 16.8 and table 16.9 show the measured TnP efficiencies of a tracker muon passing the identification cuts binned in p_{T} and η in Data and MC, respectively. Table 16.10 shows the corresponding data-over-MC scale factors.

The overall scale factor is thus estimated to be $0.989 \pm 0.002 \pm 0.010$, where the 1% systematic uncertainty takes into account the variations of the scale factors as functions of the muon p_{T} and η.

Table 16.11 and table 16.12 shows the measured TnP trigger efficiencies in different bins of p_{T} and η, in the data and simulation, respectively. The trigger efficiencies

p_{T}(GeV)\η	(-2.4, -1.2)	(-1.2, 0)	(0, 1.2)	(1.2, 2.4)	(-2.4, 2.4)
$(20, 30)$	100.00 ± 0.12	99.96 ± 0.77	99.05 ± 0.48	100.00 ± 0.28	99.90 ± 0.20
$(30, 40)$	100.00 ± 0.12	99.55 ± 0.17	99.65 ± 0.15	99.56 ± 0.26	99.68 ± 0.10
$(40, 50)$	99.59 ± 0.18	99.71 ± 0.11	100.00 ± 0.05	100.00 ± 0.18	99.85 ± 0.06
$(50, 150)$	99.68 ± 0.47	99.49 ± 0.42	99.48 ± 0.37	99.03 ± 0.61	99.39 ± 0.24
> 20	99.88 ± 0.14	99.65 ± 0.10	99.74 ± 0.10	99.76 ± 0.16	99.76 ± 0.06

Table 16.5: TnP efficiencies (%) of a track reconstructed as a tracker muon in the data, in different p_{T} and η ranges.

p_{T}(GeV)\η	(-2.4, -1.2)	(-1.2, 0)	(0, 1.2)	(1.2, 2.4)	(-2.4, 2.4)
$(20, 30)$	99.67 ± 0.03	99.38 ± 0.04	99.36 ± 0.04	99.66 ± 0.03	99.51 ± 0.02
$(30, 40)$	99.79 ± 0.02	99.36 ± 0.03	99.33 ± 0.03	99.76 ± 0.02	99.52 ± 0.01
$(40, 50)$	99.78 ± 0.02	99.35 ± 0.02	99.37 ± 0.02	99.79 ± 0.02	99.52 ± 0.01
$(50, 150)$	99.85 ± 0.02	99.39 ± 0.04	99.39 ± 0.04	99.81 ± 0.03	99.57 ± 0.02
> 20	99.77 ± 0.01	99.36 ± 0.01	99.36 ± 0.01	99.76 ± 0.01	99.52 ± 0.01

Table 16.6: TnP efficiencies (%) of a track reconstructed as a tracker muon in the simulation.

have significant variations with η, but not with p_{T}. Therefore, we correct the trigger efficiency in the simulation as a function of η, as shown in figure 16.11. Taking into account the fact that both muons have the same chance to pass the trigger requirements, the scale factor, on a event-by-event basis, can be calculated as

$$\mathrm{SF}_{\mathrm{trig}} = \frac{1 - (1 - \epsilon_{\mathrm{data}}(\eta_1))(1 - \epsilon_{\mathrm{data}}(\eta_2))}{1 - (1 - \epsilon_{\mathrm{MC}}(\eta_1))(1 - \epsilon_{\mathrm{MC}}(\eta_2))}\,, \tag{16.13}$$

which is applied to each event in the simulation as a scale factor to the event weight.

p_{T}(GeV)\η	(-2.4, -1.2)	(-1.2, 0)	(0, 1.2)	(1.2, 2.4)	(-2.4, 2.4)
$(20, 30)$	1.003 ± 0.001	1.006 ± 0.008	0.997 ± 0.005	1.003 ± 0.003	1.004 ± 0.002
$(30, 40)$	1.002 ± 0.001	1.002 ± 0.002	1.003 ± 0.002	0.998 ± 0.003	1.002 ± 0.001
$(40, 50)$	0.998 ± 0.002	1.004 ± 0.001	1.006 ± 0.001	1.002 ± 0.002	1.003 ± 0.001
$(50, 150)$	0.998 ± 0.005	1.001 ± 0.004	1.001 ± 0.004	0.992 ± 0.006	0.998 ± 0.002
> 20	1.001 ± 0.001	1.003 ± 0.001	1.004 ± 0.001	1.000 ± 0.002	1.002 ± 0.001

Table 16.7: Data/MC ratio of TnP efficiencies of a track reconstructed as a tracker muon.

p_T(GeV)\η	(-2.4, -1.2)	(-1.2, 0)	(0, 1.2)	(1.2, 2.4)	(-2.4, 2.4)
$(20, 30)$	93.87 ± 0.82	95.96 ± 0.75	96.99 ± 0.72	94.92 ± 0.88	95.48 ± 0.40
$(30, 40)$	95.92 ± 0.50	95.90 ± 0.44	96.76 ± 0.39	94.72 ± 0.61	95.91 ± 0.24
$(40, 50)$	95.87 ± 0.46	96.60 ± 0.33	96.37 ± 0.36	96.31 ± 0.43	96.30 ± 0.20
$(50, 150)$	96.13 ± 0.72	95.32 ± 0.70	96.00 ± 0.03	95.05 ± 0.83	95.66 ± 0.37
> 20	95.54 ± 0.29	96.09 ± 0.25	96.53 ± 0.24	95.39 ± 0.34	95.96 ± 0.14

Table 16.8: TnP efficiencies (%) of tracker muons in the data to pass the identification cuts.

p_T(GeV)\η	(-2.4, -1.2)	(-1.2, 0)	(0, 1.2)	(1.2, 2.4)	(-2.4, 2,4)
$(20, 30)$	96.94 ± 0.09	97.00 ± 0.08	96.67 ± 0.09	97.24 ± 0.08	96.96 ± 0.04
$(30, 40)$	97.47 ± 0.06	97.42 ± 0.05	97.00 ± 0.05	97.59 ± 0.06	97.34 ± 0.03
$(40, 50)$	97.60 ± 0.06	97.48 ± 0.05	97.08 ± 0.05	97.58 ± 0.06	97.40 ± 0.03
$(50, 150)$	96.84 ± 0.11	97.28 ± 0.08	96.92 ± 0.09	97.13 ± 0.10	97.05 ± 0.05
> 20	97.34 ± 0.04	97.37 ± 0.03	96.97 ± 0.03	97.46 ± 0.03	97.26 ± 0.02

Table 16.9: TnP efficiencies (%) of tracker muons in the simulation to pass the identification cuts.

16.4.4 Photon Energy and Muon Momentum Scale

The data we used in this analysis has no laser monitoring correction for the change of the crystal transparency due to radiation damage. Figure 16.12 shows the measured $\pi^0 \to \gamma\gamma$ peak positions in the ECAL barrel as a function of the run number during the data taking in 2010. To perform these measurements, the π^0 calibration trigger, discussed in section 4.3.1, is used. There is a drop of 1.3% in the ECAL response from the first to the last run. This is considered as a systematic uncertainty on the photon energy scale.

The muon momentum scale in data, on the other hand, is found to be matched with simulation quite well, as shown in figure 16.13. The data is fitted with the

p_T(GeV)\η	(-2.4, -1.2)	(-1.2, 0)	(0, 1.2)	(1.2, 2.4)	(-2.4, 2.4)
> 20	0.981 ± 0.003	0.987 ± 0.003	0.995 ± 0.002	0.979 ± 0.004	0.987 ± 0.001
$(20, 30)$	0.968 ± 0.009	0.989 ± 0.008	1.003 ± 0.008	0.976 ± 0.009	0.985 ± 0.004
$(30, 40)$	0.984 ± 0.005	0.984 ± 0.005	0.998 ± 0.004	0.971 ± 0.006	0.985 ± 0.002
$(40, 50)$	0.982 ± 0.005	0.991 ± 0.003	0.993 ± 0.004	0.987 ± 0.004	0.989 ± 0.002
$(50, 150)$	0.993 ± 0.007	0.980 ± 0.007	0.991 ± 0.001	0.979 ± 0.009	0.986 ± 0.004

Table 16.10: Data/MC ratio of the TnP efficiencies of tracker muons to pass the identification cuts.

p_{T}(GeV)|η	(-2.4, -2.1)	(-2.1, -1.2)	(-1.2, -0.8)	(-0.8, 0)
$(20, 30)$	44.13 ± 3.71	90.22 ± 1.17	88.05 ± 1.82	95.80 ± 0.79
$(30, 40)$	46.65 ± 2.75	90.50 ± 0.84	87.48 ± 1.31	95.91 ± 0.50
$(40, 50)$	50.99 ± 2.87	91.47 ± 0.74	85.65 ± 1.20	95.99 ± 0.46
$(50, 150)$	42.74 ± 4.45	88.97 ± 1.42	84.12 ± 2.27	97.57 ± 0.65
> 20	47.05 ± 1.64	90.62 ± 0.47	86.42 ± 0.74	96.15 ± 0.28
p_{T}(GeV)|η	(2.1, 2.4)	(1.2, 2.1)	(0.8, 1.2)	(0,0.8)
$(20, 30)$	38.21 ± 3.12	86.94 ± 1.34	89.44 ± 1.79	95.80 ± 0.80
$(30, 40)$	45.45 ± 2.79	89.59 ± 0.89	88.44 ± 1.27	96.32 ± 0.46
$(40, 50)$	39.68 ± 2.77	89.58 ± 0.81	87.03 ± 1.16	96.17 ± 0.46
$(50, 150)$	46.43 ± 4.69	87.91 ± 1.53	89.74 ± 1.83	97.05 ± 0.70
> 20	41.94 ± 1.57	88.93 ± 0.51	88.22 ± 0.70	96.29 ± 0.27

Table 16.11: TnP trigger efficiencies (%) of HLT_Mu15 in the data, for probe muons which passed the identification cuts.

p_{T}(GeV)|η	(-2.4, -2.1)	(-2.1, -1.2)	(-1.2, -0.8)	(-0.8, 0)
$(20, 30)$	43.43 ± 0.52	93.39 ± 0.15	92.35 ± 0.24	97.96 ± 0.09
$(30, 40)$	42.08 ± 0.42	93.37 ± 0.11	92.06 ± 0.16	97.99 ± 0.05
$(40, 50)$	42.58 ± 0.47	93.72 ± 0.10	92.23 ± 0.14	97.95 ± 0.05
$(50, 150)$	42.70 ± 0.70	93.18 ± 0.18	92.53 ± 0.24	97.82 ± 0.09
> 20	42.61 ± 0.25	93.48 ± 0.06	92.23 ± 0.09	97.95 ± 0.03
p_{T}(GeV)|η	(2.1, 2.4)	(1.2, 2.1)	(0.8, 1.2)	(0,0.8)
$(20, 30)$	41.87 ± 0.53	93.62 ± 0.15	91.71 ± 0.25	97.95 ± 0.09
$(30, 40)$	41.93 ± 0.41	93.50 ± 0.11	92.07 ± 0.16	97.84 ± 0.06
$(40, 50)$	42.70 ± 0.45	93.62 ± 0.10	92.07 ± 0.14	97.89 ± 0.05
$(50, 150)$	42.14 ± 0.74	93.44 ± 0.18	92.36 ± 0.25	97.76 ± 0.09
> 20	42.17 ± 0.25	93.56 ± 0.06	92.06 ± 0.09	97.86 ± 0.03

Table 16.12: TnP trigger efficiencies (%) of HLT_Mu15 in the simulation, for probe muons which passed the identification cuts.

convoluted probability density function (*pdf*) of the $\mathrm{Z} \to \mu^+\mu^-$ invariant mass distribution from the simulation with a Gaussian. The obtained mean of the Gaussian δ_m relative to the peak in simulation is consistent with zero, indicating that the muon momentum scale in the data agrees with the scale in the simulation.

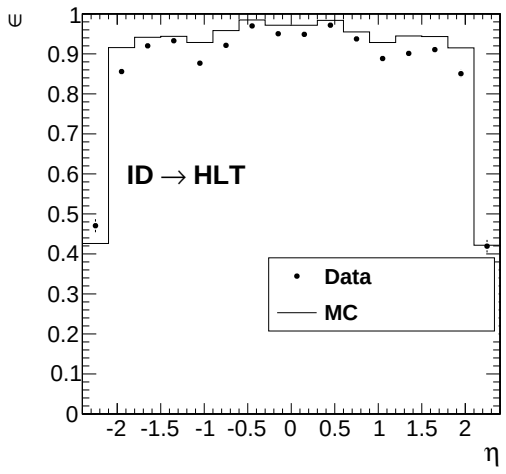

Figure 16.11: TnP trigger efficiency as a function of η.

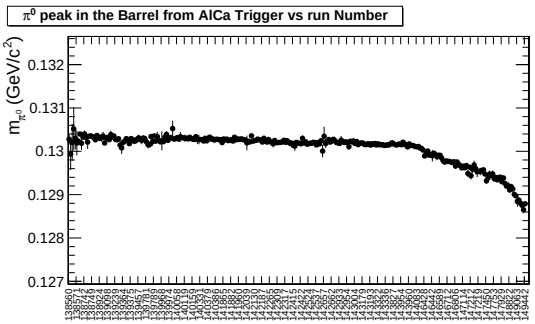

Figure 16.12: Reconstructed $\pi^0 \to \gamma\gamma$ peak positions in ECAL barrel as function of the run number during the data taking in 2010. Each data point corresponds to one measurement from one run.

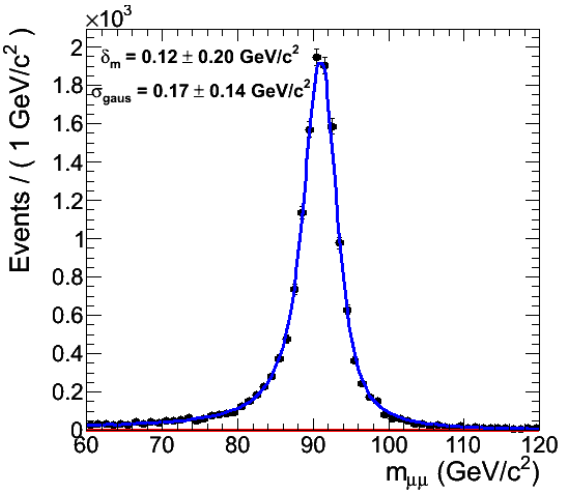

Figure 16.13: $Z \rightarrow \mu^+\mu^-$ invariant mass distribution. The data (black points) is selected in the 35 pb^{-1} of data in 2010. The curve is a fit to the data. The *pdf* is the convolution of the invariant mass distribution from the simulation and a Guassian. The mean of the Gaussian relative to the peak in simulation is δ_m and the width is σ_{gaus}. These two parameters are allowed float in the fit.

16.5 Data Driven Background Estimation

In this section we discuss a data-driven method to estimate the background events with one or more misidentified objects, which are mostly from jets. The dominant background of this type is $Z+$jets, where one of the jets is misidentified as a photon. Estimate of such type of backgrounds is not deemed to be reliable from simulation, because the process of jet misidentified to be a photon is complex and subject to details in the simulation.

16.5.1 The Misidentification Rate Method

The fake rate method uses the number of events in a fake-enriched sample to estimate the number of events after applying the corresponding object identification. The fake-enriched sample is often obtained by applying some loose identification (loose), if we know the efficiency of the nominal identification (tight) in this sample, we can predict the number of events after the tight cut

$$\mathrm{N}_{\mathrm{tight}} = \epsilon_{\mathrm{fake}} \cdot \mathrm{N}_{\mathrm{loose}} \,, \tag{16.14}$$

where ϵ_{fake}, called the misidentification (MisId) rate (or fake rate), is usually measured from a fake-enriched sample, which is orthogonal to the selection sample. In some cases of measuring the fake rate, the object is required to fail the tight ID to suppress signal contamination. This is the case, for example, the photon fake rate which we will discuss in the next section.

Take $Z+$jets as an example to illustrate the application of the fake rate. First of all, we select events with two muons passing the ID cuts. Secondly, we apply some loose ID cut to the photon candidates. Suppose we selected 100 events and we have measured the ϵ_{fake} in another jet-enriched sample, usually from the di-jet process, to be 0.1. Therefore we predict 10 events after the final photon ID selection (tight). One immediate question when using this method is: to what extent can we are sure that we can apply the number of 0.1, measured in another jet sample, to the $Z+$jets

Criteria	variable	Value
1	ECAL Isolation	$< \min\{5 \times (4.2 + 0.006 p_{\mathrm{T}}), 0.2 p_{\mathrm{T}}\}$
2	HCAL Isolation	$< \min\{5 \times (2.2 + 0.0025 p_{\mathrm{T}}), 0.2 p_{\mathrm{T}}\}$
3	Track Isolation	$< \min\{5 \times (2 + 0.001 p_{\mathrm{T}}), 0.2 p_{\mathrm{T}}\}$
4	HCAL over ECAL fraction	H/E <0.05
5	Shower shape	$\sigma_{i\eta i\eta}$ <0.013
6	Veto ID	Failing one of the three isolations or the shower shape cut defined in table 16.4
7	Detector region	barrel
8	Spike removal	(Swiss cross)> 0.95
9	Spike removal	$E_2/E_9 < 0.95$

Table 16.13: The loose photon identification criteria used in the photon MisID rate measurement.

sample? This transfer systematic uncertainty from one sample to another should be estimated if using the fake rate method. Namely, the following equation is not necessarily true for fake photons

$$(\frac{\mathrm{N_{tight}}}{\mathrm{N_{loose}}})_{\mathrm{Z+jets}} = (\frac{\mathrm{N_{tight}}}{\mathrm{N_{loose}}})_{\mathrm{di-jet}} \,. \tag{16.15}$$

16.5.2 Photon Misidentification Rate

In estimating the photon misidentification (misID) rate, we define "loose photons" to be those which satisfy the criteria listed in table 16.13. In particular, the loose photon is required to fail the tight photon ID. The signal contamination with this definition is found to be negligible.

We measure the misID rate as a function of p_{T}^{γ} in single jet-triggered data. To avoid possible bias from the jet trigger requirements, any photon candidate, if matched to the leading p_{T} jet reconstructed at the HLT within a $\Delta R < 0.5$, is not used for the misID rate measurements.

With the tight ID, there is an nonnegligible contamination from real photons, mainly from γ+jet events. To estimate their contribution, we fit the $\sigma_{i\eta i\eta}$ distribution in data with a template of $\mathrm{f_s} pdf_s + (1 - \mathrm{f_s}) pdf_b$, where $\mathrm{f_s}$ refers to the fraction of signal template in data in the overall template, which is a linear combination of a signal template pdf_s and a background template pdf_b. The signal template is taken from the simulation. The background template is obtained from the data, where a modified

tight ID is used. This modified ID is the same as the tight ID, except that the cut on $\mathrm{Iso}^{\mathrm{track}}$ is inverted, $2 + 0.001\mathrm{p_T} < \mathrm{Iso}^{\mathrm{track}} < 4 + 0.001\mathrm{p_T}$, to provide a sideband.

Figure 16.14 shows that the $\sigma_{\mathrm{i}\eta\mathrm{i}\eta}$ distributions of fake photons in the simulation obtained by the sideband tight ID agree well with those obtained using the tight ID. Figure 16.15 shows the example template fit to the data in a number of p_{T}^{γ} bins. In each bin, a different threshold on the jet trigger is used to select the data. This is important to reduce the transfer systematic uncertainty of the misID rate from jet triggered events to muon triggered events. Figure 16.16 shows the measured photon misID rates in different p_{T}^{γ} bins, in events triggered by jet triggers with different p_{T} thresholds. The jet trigger with a threshold of 15 GeV is used to measure the photon misID rate in the p_{T}^{γ} bins $15 < p_{\mathrm{T}} < 20$ and $20 < p_{\mathrm{T}} < 25$ GeV; the threshold of 30 GeV is used for the p_{T}^{γ} bins $25 < p_{\mathrm{T}} < 30$ and $30 < p_{\mathrm{T}} < 40$ GeV; the threshold of 50 GeV is used for p_{T}^{γ} bins $40 < p_{\mathrm{T}} < 50$, $50 < p_{\mathrm{T}} < 60$, and $60 < p_{\mathrm{T}} < 70$ GeV; and the threshold of 70 GeV is used for the bin $70 < p_{\mathrm{T}} < 120$ GeV.

Figure 16.17 left shows the comparison of the photon misID rates between the $Z +$ jets simulation and the jet triggered simulation. The difference as a function of p_{T}^{γ} is considered as a systematic uncertainty in the misID rate.

The photon misID rates have also been measured in the data with single muon triggers. A difference of approximately 20% is observed. This is considered as a systematic uncertainty on the measurement from the data.

16.5.3 Muon Misidentification Rate

We also measure the muon misID rate in jet triggered data. Similarly, any muon candidates overlapping with the leading jet trigger object within a cone of $\Delta R < 0.5$ are excluded from the misID rate measurements. In addition, in order to suppress real muon contamination from W or Z decays, especially for high p_{T} muons, events are rejected if $E_{\mathrm{T}}^{\mathrm{miss}} > 40$ GeV or $M_T > 40$ GeV,[1] or if there are two global muons

[1]Transverse mass M_T is the mass of the body that produced the lepton and missing energy, computed in the plane transverse to the beam since the longitudinal component of the missing energy cannot be measured at hadron colliders.

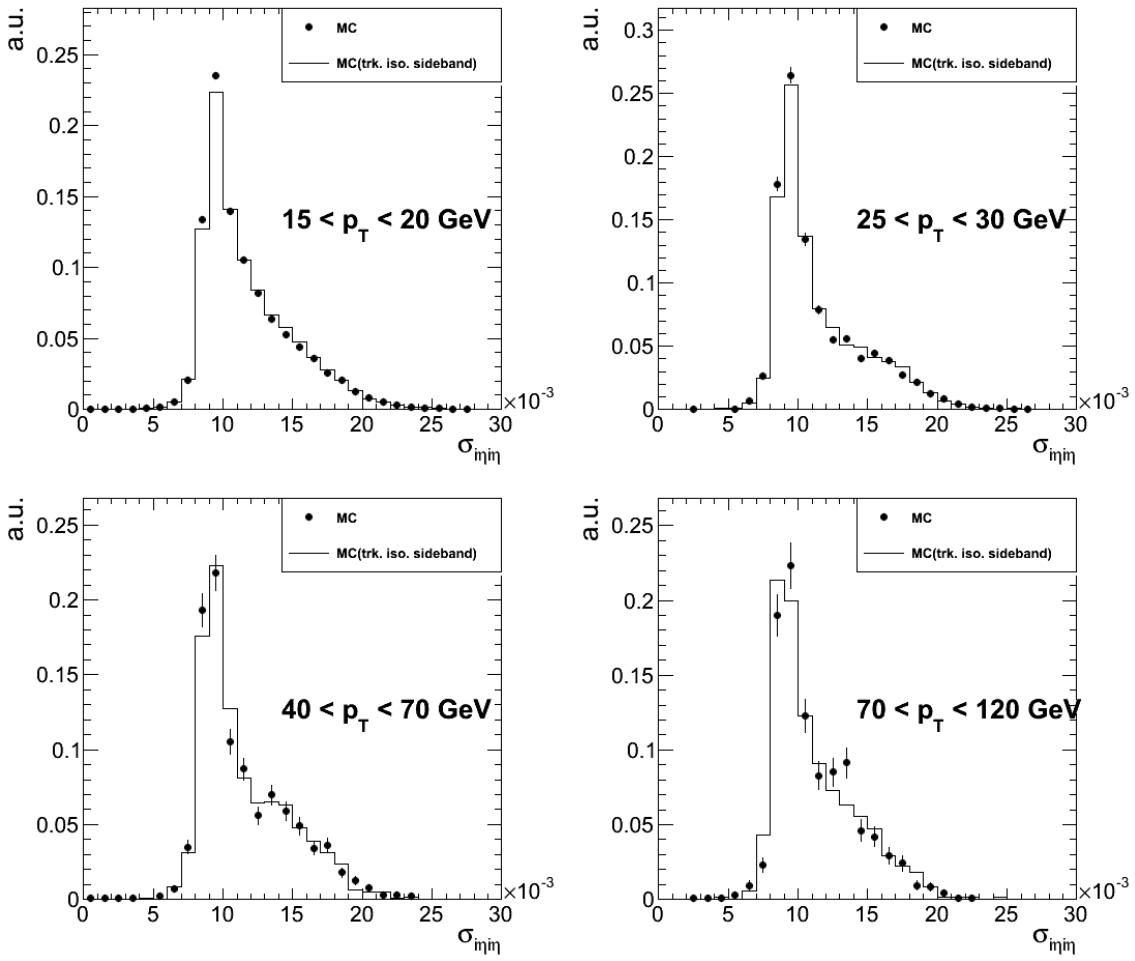

Figure 16.14: Comparison of the $\sigma_{i\eta i\eta}$ distributions of fake photons in different p_{T}^{γ} bins in the simulation, selected by the loose photon ID and by the modified tight photon ID ($\mathrm{Iso}^{\mathrm{track}}$ sideband).

with an invariant mass between 80 and 100 GeV/c^2.

Then the muon misID rate is measured as the ratio of the number of identified muons and the number of tracker muons.

Figure 16.18 shows the measured muon misID rates as a function p_{T} in events triggered by different jet thresholds in the data and the simulation. In each p_{T} bin, the average misID rate from different triggers is taken to be the central value, while half of the maximum difference between different triggers is considered as the systematic uncertainty due to the unknown jet p_{T} spectrum in the W+jets backgrounds. In addition, the maximum difference between the misID rates measured in the jet

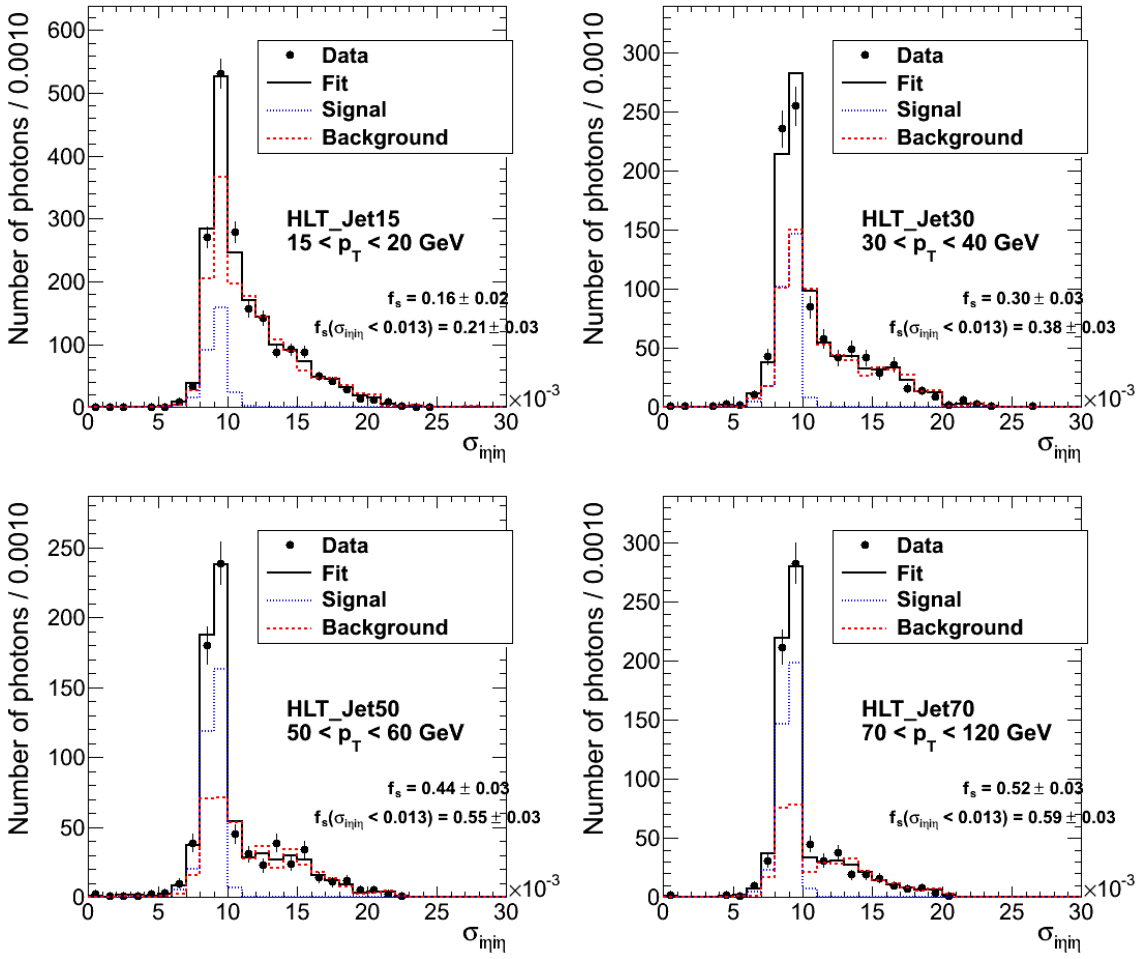

Figure 16.15: Example of the template fit to the data, which is used to extract the signal fraction in the numerator of the misID rate estimation. Each plot shows the $\sigma_{i\eta i\eta}$ distribution in a particular p_{T}^{γ} bin in events triggered by a jet trigger with a different p_{T} threshold.

triggered sample and the W+jets and γ+jets simulation samples is considered as the transfer systematic uncertainty. The average muon misID rates measured in these simulation samples are shown in figure 16.19.

Table 16.14 and table 16.15 show the misID rates in different p_{T} and η bins from the data and the simulation, respectively. We apply the misID rate only as a function of p_{T}, since the variations in η are much smaller and are well covered by the systematic uncertainties.

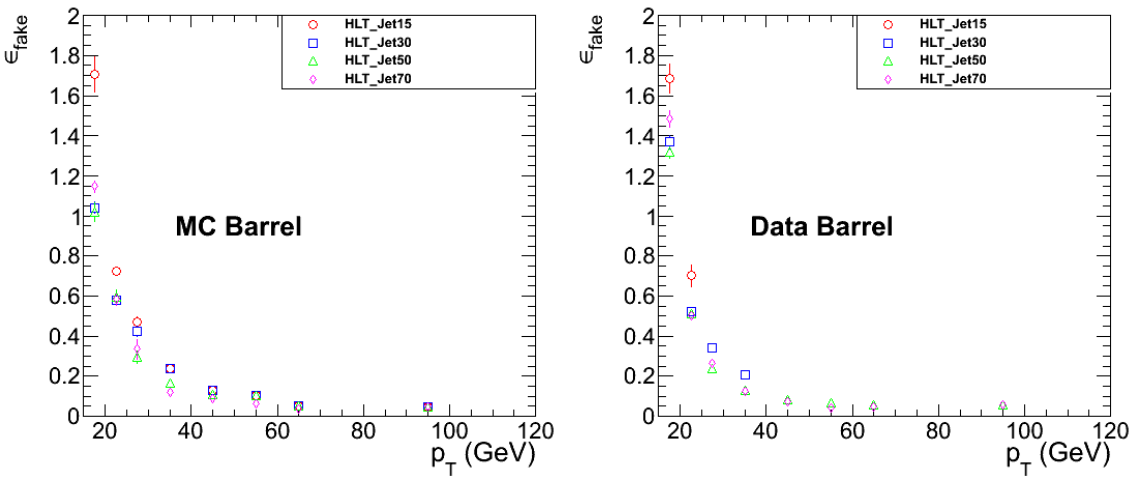

Figure 16.16: Measured photon misID rate as a function of p_{T}^{γ} from different jet triggers with different thresholds, in simulation (left) and in data (right).

p_{T}(GeV) \ η	(-2.4, -1.2)	(-1.2, -0)	(0, 1.2)	(1.2,2.4)	(-2.4,2.4)
$(20, 30)$	0.14 ± 0.14	0.17 ± 0.18	0.17 ± 0.17	0.12 ± 0.12	0.15 ± 0.15
$(30, 40)$	0.10 ± 0.09	0.17 ± 0.19	0.15 ± 0.14	0.07 ± 0.05	0.13 ± 0.12
$(40, 50)$	0.07 ± 0.05	0.12 ± 0.12	0.15 ± 0.16	0.10 ± 0.13	0.10 ± 0.08
$(50, 100)$	0.04 ± 0.02	0.08 ± 0.03	0.09 ± 0.07	0.04 ± 0.03	0.05 ± 0.02

Table 16.14: Measured muon misID rate in jet triggered data in bins of p_{T} and η.

16.5.4 Application of Misidentification Rates

We have measured the photon and muon misID rates from the data. In section 16.5.1 we also gave an example to illustrate the way to apply the photon misID rate to estimate the $Z +$ jets backgrounds. In this section, we discuss in general the method to estimate all types of backgrounds with at least one misidentified object.

According to the number of misidentified objects, there are four possible such backgrounds. In general, to estimate each of them, we begin with a sample of events

p_{T}(GeV) \ η	(-2.4, -1.2)	(-1.2, -0)	(0, 1.2)	(1.2,2.4)	(-2.4,2.4)
$(20, 30)$	0.11 ± 0.13	0.18 ± 0.18	0.18 ± 0.15	0.12 ± 0.15	0.14 ± 0.15
$(30, 40)$	0.08 ± 0.07	0.13 ± 0.11	0.14 ± 0.12	0.06 ± 0.06	0.09 ± 0.08
$(40, 50)$	0.06 ± 0.06	0.09 ± 0.05	0.10 ± 0.05	0.04 ± 0.02	0.07 ± 0.04
$(50, 100)$	0.02 ± 0.01	0.06 ± 0.03	0.05 ± 0.02	0.02 ± 0.01	0.03 ± 0.01

Table 16.15: Measured muon misID rate in jet triggered MC in bins of p_{T} and η.

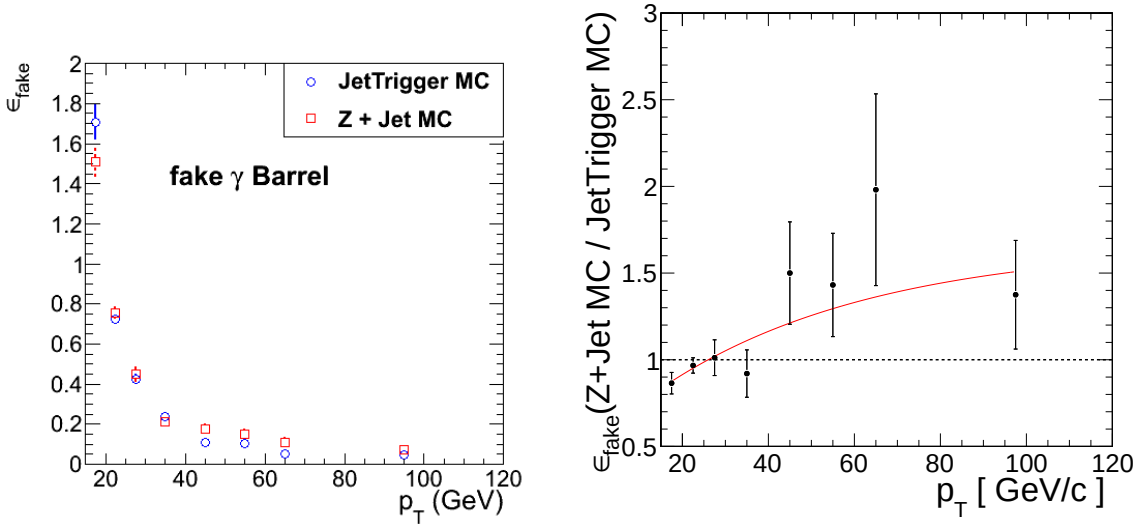

Figure 16.17: Left, comparison of the photon misID rate in the $Z+$jets MC and the jet triggered simulation. Right, the difference as a function of p_{T}^{γ}. The superimposed curve is the best fitted function of the form $p_0 - p_1 e^{-p_2 p_{\mathrm{T}}}$.

selected with one or more loose objects, and weight each event with the corresponding measured misID rates. We discuss below in more detail,

- A: One fake photon. A data sample with two tight muons is selected, and all loose photons are selected in each event, which are weighted by the corresponding photon misID rates. If there is only one loose photon selected, the event weight is simply this photon's misID rate. If there are two loose photons and the misID rate for the photon with higher and lower p_{T} is ϵ_1 and ϵ_2, respectively. Then the event weight is $\epsilon_1 + \max\{1-\epsilon_1, 0\} \cdot \epsilon_2$. By analogy, we can calculate the event weight for any number of loose photons. The reason for doing this is that each loose photon can be promoted to be a tight photon. However, in the event selection, we select the photon with highest p_{T} if more than one photon passes the tight ID. The second loose photon can be promoted only if the first loose photon is not promoted. The resultant estimate includes contributions from $\mu+\mu+$jet, $\mu+$jet$+$jet, and jet$+$jet$+$jet, which is primarily from the $Z \to \mu\mu + jet$, $W \to \mu +$jet$+$jet, and QCD multijets processes, respectively.

- B: One fake muon. A data sample with one tight muon and one loose muon

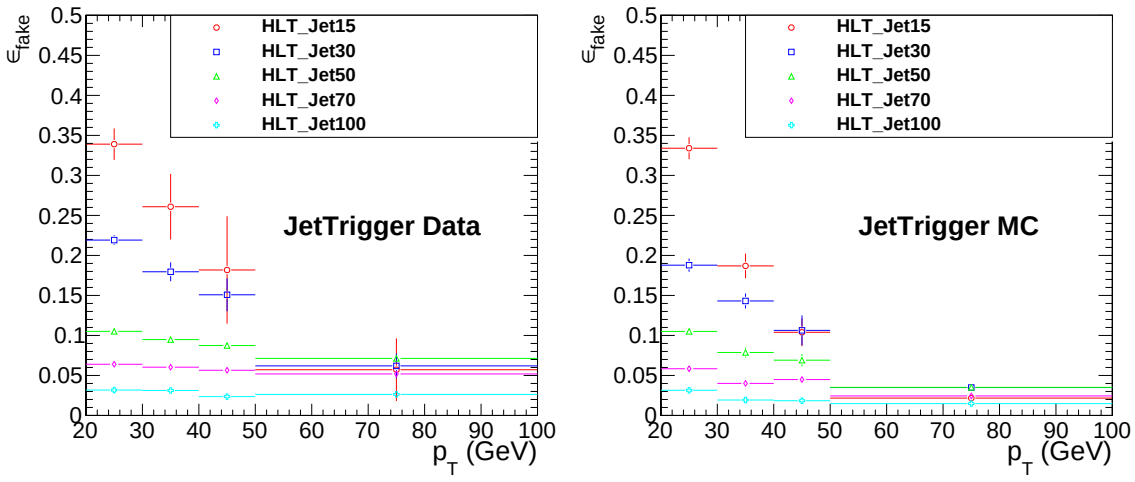

Figure 16.18: Muon misID rate measured in different jet triggers in data (left) and in di-jet MC (right).

is selected. For each loose muon, an event weight is calculated. Then another tight photon is selected. The resultant estimate includes contributions from $\mu + \text{jet} + \gamma$, $2 \times(\text{jet} + \text{jet} + \gamma)$, and $2 \times(\text{jet} + \text{jet} + \text{jet})$, which is primarily from $W \to \mu + \text{jet} + \gamma$, γ+jets and QCD multijet process, respectively. The factor of two comes from the fact that any of the two jets has the same chance to be selected as the tight muon.

- C: Two fake muons. Each event containing two loose muons and one tight photon is weighted with the product of the muon misID rates. The resultant estimate includes contributions from $\text{jet} + \text{jet} + \text{jet}$ and $\text{jet} + \text{jet} + \gamma$, which are primarily from the QCD multijet and γ+jets processes, respectively.

- D: All objects are fake. Each event containing two loose muons and one loose photon is weighted with the product of the three misID rates. The resultant estimate includes contributions from $\text{jet} + \text{jet} + \text{jet}$, which is dominated by the QCD multijet processes.

If we simply add the above four backgrounds, we count three times $\text{jet} + \text{jet} + \gamma$ and four times $\text{jet} + \text{jet} + \text{jet}$. However, if we subtract C+D from A+B, there is no more double counting. Therefore, the total background with fake objects is estimated

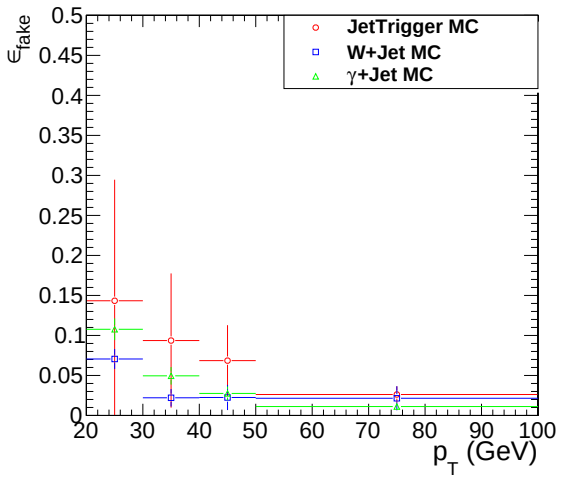

Figure 16.19: The average muon misID rate in di-jet, W+jets and γ+jets MC.

to be A + B − C − D. In this analysis, we refer to A as the misID γ background, and B − C− D as the misID μ background. In case B is smaller than the sum of C and D due to statistical fluctuations, we quote zero for the misID μ background.

16.6 Control Region Studies

As we will see in next section, the expected event yield after the final selection on $M_{\mu\gamma}^{max}$ is very small. Therefore, in this selection, we compare the data and background yield with the event selections described in section 16.3.3 (control region selection).

After this control region event selection, we observe 25 events in the data, in agreement with the expectation 25.3 ± 2.7, out of which 19.1 ± 1.4 $\mu\mu + \gamma$ events are estimated from the simulation, and 5.5 ± 2.1 misID γ background and 0.7 ± 0.9 misID μ background events are estimated from the data.

Figure 16.20 shows the p_T^{γ} and $M_{\mu\gamma}^{max}$ distributions, indicating a good agreement between data and background prediction.

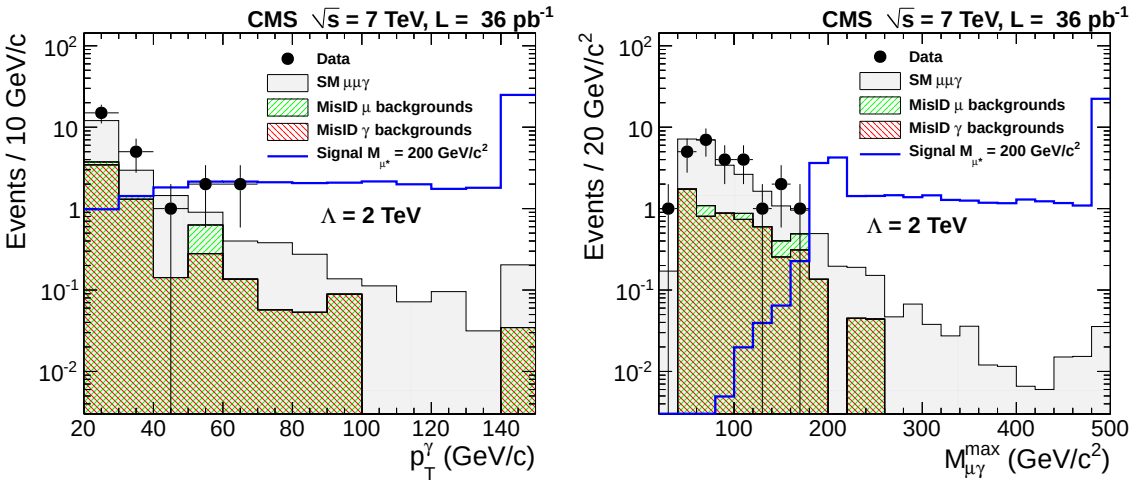

Figure 16.20: p_{T}^{γ} distribution (left) and $\mathrm{M}_{\mu\gamma}^{\mathrm{max}}$ (right) distribution before the final cut. The data are shown as solid circles with error bars and the expected Standard Model background distributions are shown as hatched histograms. The solid-line histogram displays the expected excited muon signal with mass 200 GeV/c^2, $\Lambda = 2$ TeV. In each histogram, the last bin includes the overflows.

16.7 Systematic Uncertainties

In this section we discuss the systematic uncertainty on the signal and the background predictions. Here, the quoted uncertainties are obtained after requiring $\mathrm{M}_{\mu\gamma}^{\mathrm{max}} > 180$ GeV/c^2.

First of all, the normalizations of the spectra are based on the integrated luminosity of the data sample, which is known to a precision of 4% [121]. The theoretical calculations of the background process cross sections are affected by uncertainties in the parton distribution functions (PDF) and the choice of factorization and renormalization scales. The uncertainties on the PDFs are evaluated using a reweighting technique with the CTEQ6M parametrization [122], while the uncertainties on the factorization and the renormalization scales are estimated by varying them simultaneously from half to twice their central values. The resulting uncertainty on the background expectation is found to be 5%.

Secondly, the uncertainty on the number of background events from jets misidentified as muons or photons is estimated by comparing the misID rates measured in

jet-enriched samples collected with different trigger requirements. Another source of uncertainty, estimated using MC simulations, is the difference between the misID rate observed in the jet-triggered samples, where it is measured, and the muon-triggered samples, where it is applied. The photon misID rate uncertainty increases from 20% to 50% with photon p_{T}. This results in an uncertainty on the background prediction of 10%. The uncertainty on the muon misID rate is estimated to be 50%, and the resulting effect on the background expectation is 1%.

Thirdly, the uncertainties on the efficiency correction factors used on the simulated events are included in the systematic uncertainties. They are 1% for muons, and 2.5% for photons. The effect on the signal and background yields due to the ID uncertainties is thus 2% for muons and about 2.5% for photons. The uncertainty on the photon energy scale results in an additional uncertainty of 0.5% for the signal and 1.2% for the background predictions.

Considering all sources of uncertainties mentioned above, the selection efficiencies for excited leptons are known to a precision of 3 - 4%.

16.8 Final Selection Results and Summary

16.8.1 Final Section for $\mathrm{pp} \to \mu\mu^* \to \mu\mu\gamma$

In order to enhance the sensitivity of the analysis, the search is restricted to the high invariant mass region by applying a selection on $\mathrm{M}_{\mu\gamma}^{\mathrm{max}}$ that depends on the excited muon mass hypothesis. For each excited muon mass, the entire analysis is repeated using various search regions, and the region giving the best expected limits is taken. For an excited muon with mass above 600 GeV/c^2, where almost no background is expected, the search region $\mathrm{M}_{\mu\gamma}^{\mathrm{max}} > 500$ GeV/c^2 is used. The number of observed events, and the prediction from the Standard Model backgrounds and from an excited lepton signal, as well as the selection efficiency, are listed in table 16.16 with various excited muon mass hypotheses and fixed Λ=2 TeV. No excited muon candidate events are found in any of the search regions. This lack of events is consistent with the

Standard Model background prediction.

M_{μ^*}(GeV/c^2)	$m_{\mu\gamma}^{max}$ cut	N_{data}	$N_{predicted\ bkg.}$	Signal eff.(%)	$\sigma_{obs}^{lim}(\sigma_{exp}^{lim})(pb)$	N_{signal}
200	180	0	$1.35 \pm 0.15 \pm 0.14$	$44.8 \pm 0.4 \pm 1.5$	0.19(0.28)	47
400	350	0	$0.11 \pm 0.08 \pm 0.03$	$51.0 \pm 0.4 \pm 1.7$	0.16(0.17)	18.6
600	500	0	$0.04 \pm 0.08 \pm 0.03$	$53.9 \pm 0.4 \pm 1.8$	0.15(0.16)	7.3
800	500	0	$0.04 \pm 0.08 \pm 0.03$	$55.6 \pm 0.4 \pm 1.8$	0.15(0.15)	2.8
1000	500	0	$0.04 \pm 0.08 \pm 0.03$	$56.9 \pm 0.4 \pm 1.9$	0.15(0.15)	1.1
1200	500	0	$0.04 \pm 0.08 \pm 0.03$	$56.9 \pm 0.4 \pm 1.9$	0.15(0.15)	0.4
1500	500	0	$0.04 \pm 0.08 \pm 0.03$	$58.5 \pm 0.3 \pm 1.9$	0.14(0.14)	0.1

Table 16.16: For various M_{μ^*} mass hypotheses, the final selection requirement on $m_{\mu\gamma}^{max}$, the number of events observed in the data, and the Standard Model background expectation, the signal efficiency, the observed (expected) upper limits $\sigma_{obs}^{lim}(\sigma_{exp}^{lim})$ on the production cross section times the branching fraction of $\mu^* \to \mu\gamma$, and the expected numbers of signal events, assuming Λ=2 TeV.

16.8.2 $\mu^* \to \mu\gamma$ Search Result

Considering the production of an excited muon via a four-fermion contact interaction as an alternative hypothesis to the Standard Model, upper limits on the pp $\to \mu\mu^*$ production cross section times the branching fraction of $\mu^* \to \mu\gamma$ are set using a Bayesian method with a flat prior [100]. A log-normal prior is used for the integration over the nuisance parameters. The corresponding expected limit is computed as the weighted average of limits over all possible numbers of observed events, where the weight is the Poisson probability to observe a given number of events in data assuming the background-only hypothesis. The systematic uncertainties discussed in the previous section are taken into account in the statistical analysis. Cross sections higher than 0.14 pb to 0.19 pb for μ^* production are excluded at the 95% Confidence Level (CL) for an excited muon with mass ranging from 200 GeV/c^2 to 1500 GeV/c^2, as shown in figure 16.21 left, and as given in table 16.16. At a contact interaction scale of $\Lambda = M_{\mu^*}$, any excited muon with a mass below 1090 GeV/c^2 is excluded. Figure 16.21 right displays the exclusion regions in the $\Lambda - M_{\mu^*}$ plane obtained from these limits, showing an improvement with respect to the previous most stringent limits established at hadron colliders [116] [117].

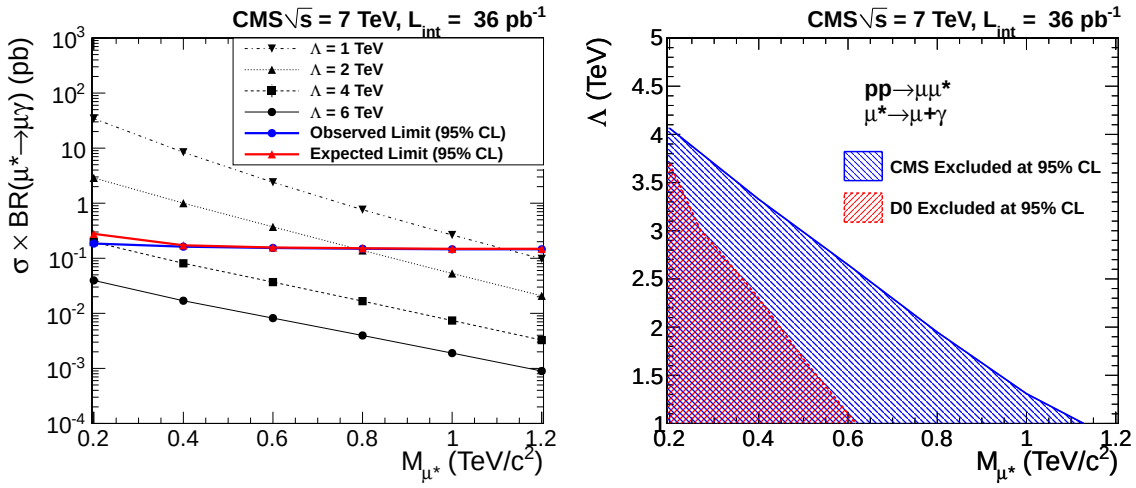

Figure 16.21: Left, observed and expected limits on the excited muon production cross section times branching fraction of $\mu^* \to \mu\gamma$ at 95% CL, as functions of the excited muon mass. The predictions for different Λ values are also shown. Right: the region in the $\Lambda - \mathrm{M}_{\mu^*}$ plane excluded at the 95% CL by this analysis. The previous most stringent limits from the D0 Collaboration [116] are also displayed.

16.8.3 Summary

We have searched for evidence of lepton compositeness in pp collisions at $\sqrt{s} = 7$ TeV at the LHC by looking for the production of an excited muon decaying into to one muon and one photon with the CMS detector. The data sample corresponds to an integrated luminosity of 36 pb^{-1}. No excess of events in the $\mu\mu\gamma$ final state was found above the Standard Model expectation. We report the first upper limits on single μ^* production at this collision energy, and exclude a new region of the $\Lambda - \mathrm{M}_{\mu^*}$ parameter space. At a contact interaction scale of $\Lambda = \mathrm{M}_{\mu^*}$, excited muon masses are excluded at the 95% CL below 1090 GeV/c^2, representing the most stringent limits, as of the date when the analysis was first published [114].

During the writing of this thesis, CMS has updated the search of the excited muon with 5 fb^{-1} of data [123]. At a contact interaction scale of $\Lambda = \mathrm{M}_{\mu^*}$, excited muon masses are excluded up to 1.9 TeV.

Appendix A

Bias studies on the signal strength: more plots

We have discussed in section 10.2.2 the bias on the signal strength due to the wrong choice of the background model, and have shown in Figure 10.11 and 10.12 the distributions of the fitted signal strength and the pull from pseudo-experiments, where the fit model of a 5th order polynomial is tested for different truth background models and the fit range is from 100 to 180 GeV/c^2.

In this appendix we show in figures A.1 to A.22 all the remaining distributions for other choices of the fit models, and a different fit range between 100 and 160 GeV/c^2.

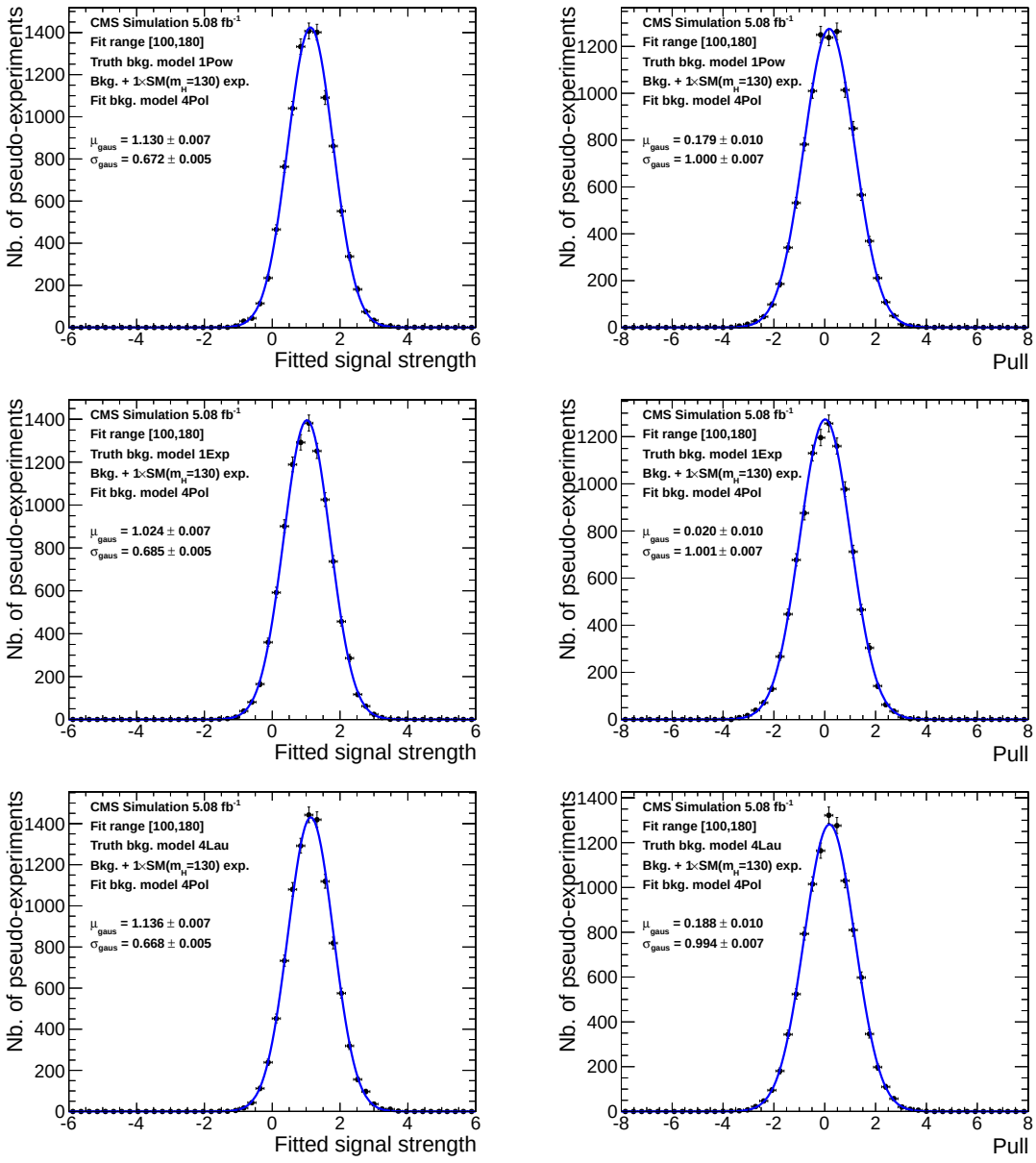

Figure A.1: Distributions of the fitted signal strength and the pull from pseudo-experiments. Different truth background models, 1Pow, 1Exp, and 4Lau, are tested against the fit model of a 5th order polynomial. The invariant mass range is chosen to be 100 to 180 GeV/c^2.

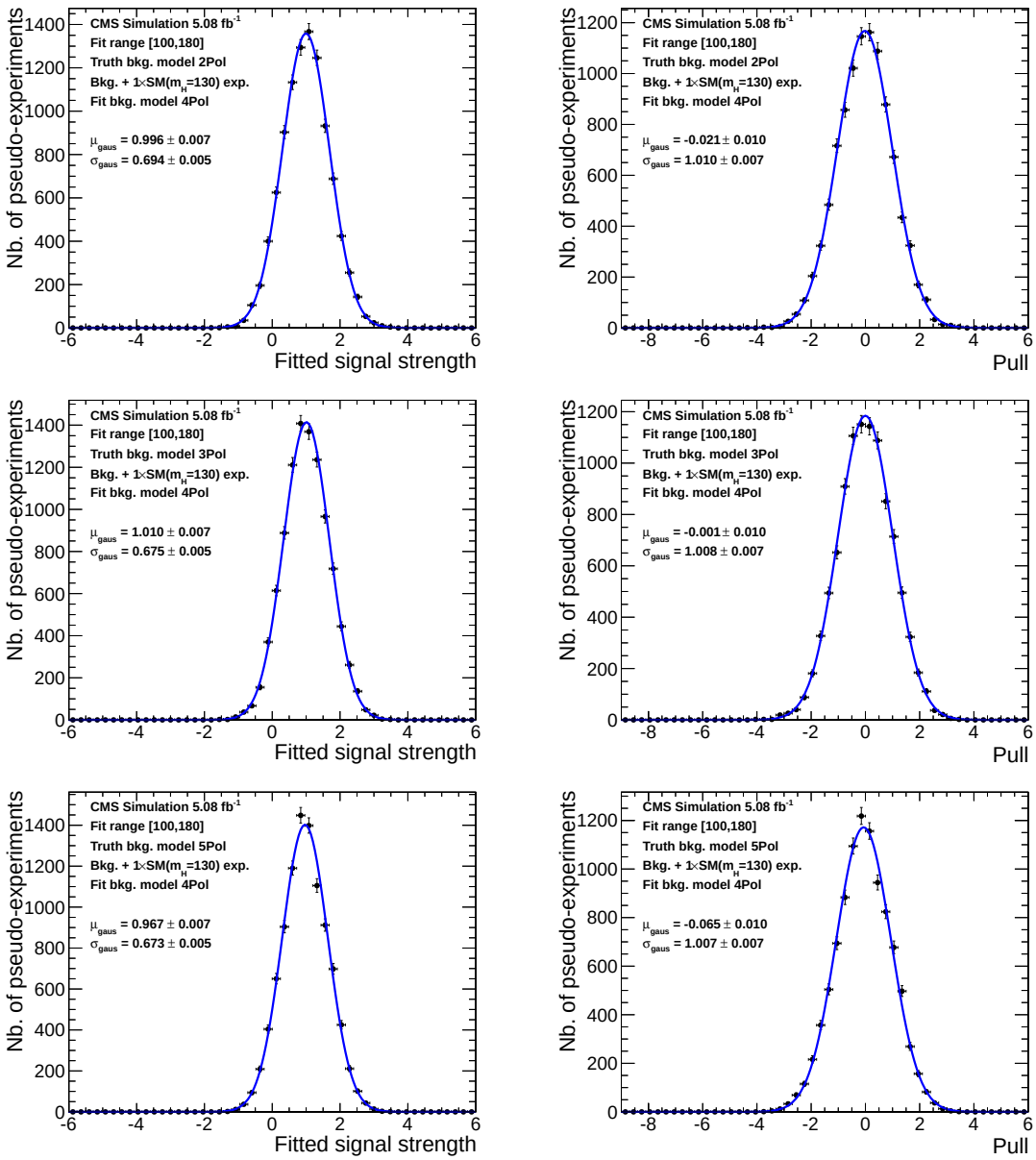

Figure A.2: Same as figure A.1, except that 2Pol, 3Pol, and 5Pol truth background models are used here.

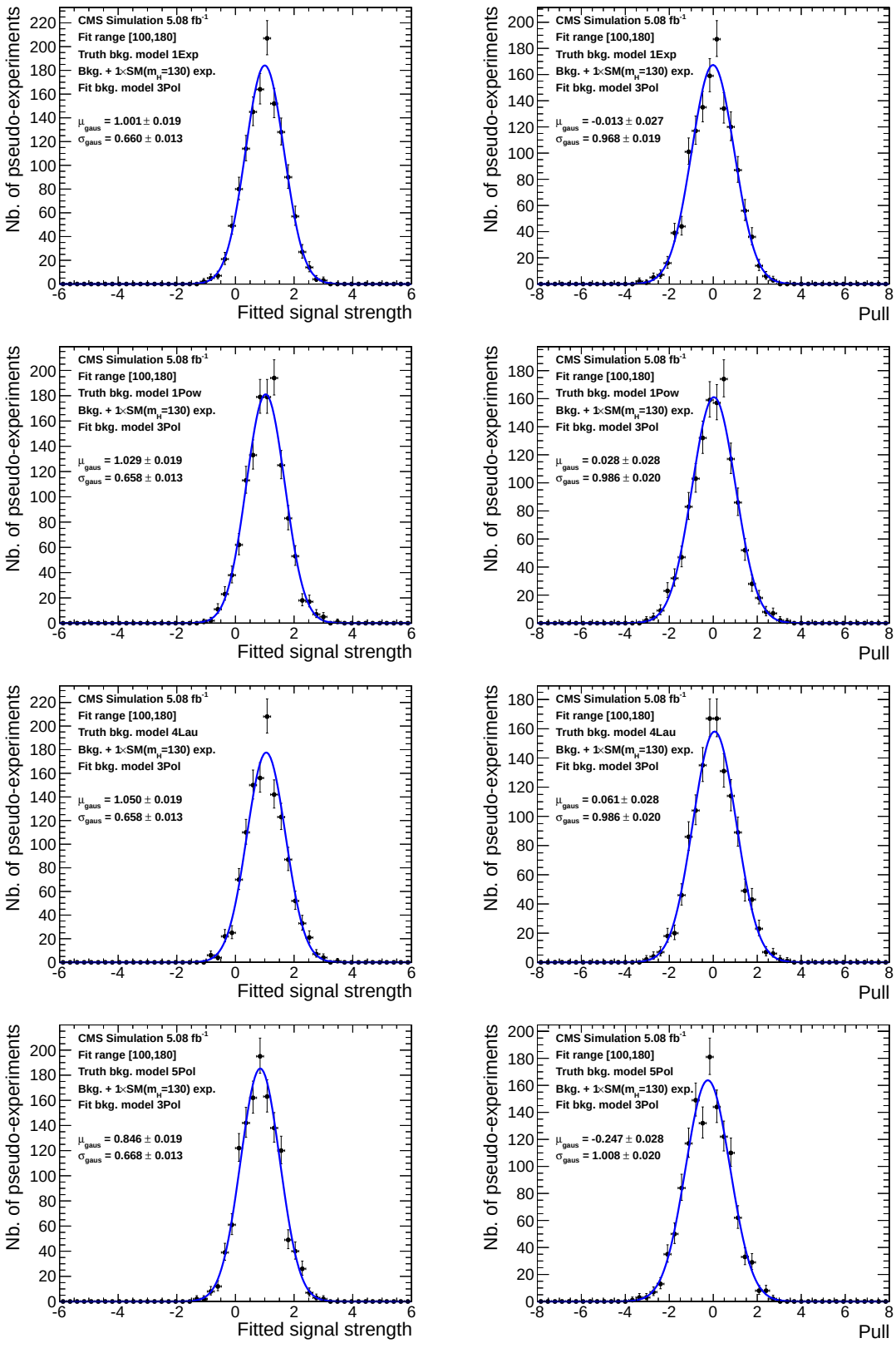

Figure A.3: Same as figure A.1, except that 1Exp, 1Pow, 4Lau and 5Pol truth background models are used to test the fit model of 3Pol.

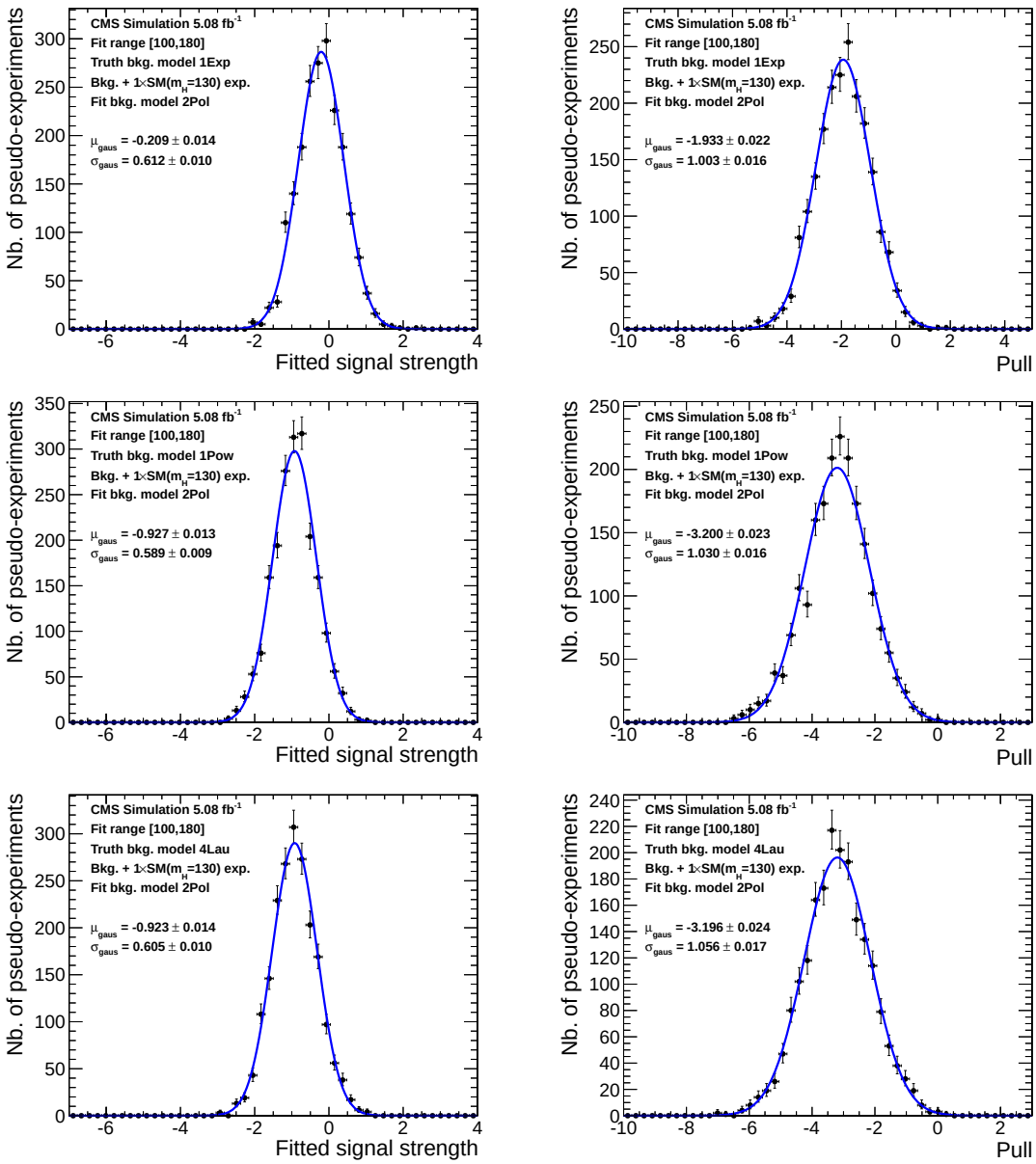

Figure A.4: Same as figure A.1, except that 1Exp, 1Pow and 4Lau truth background models are used to test the fit model of 2Pol.

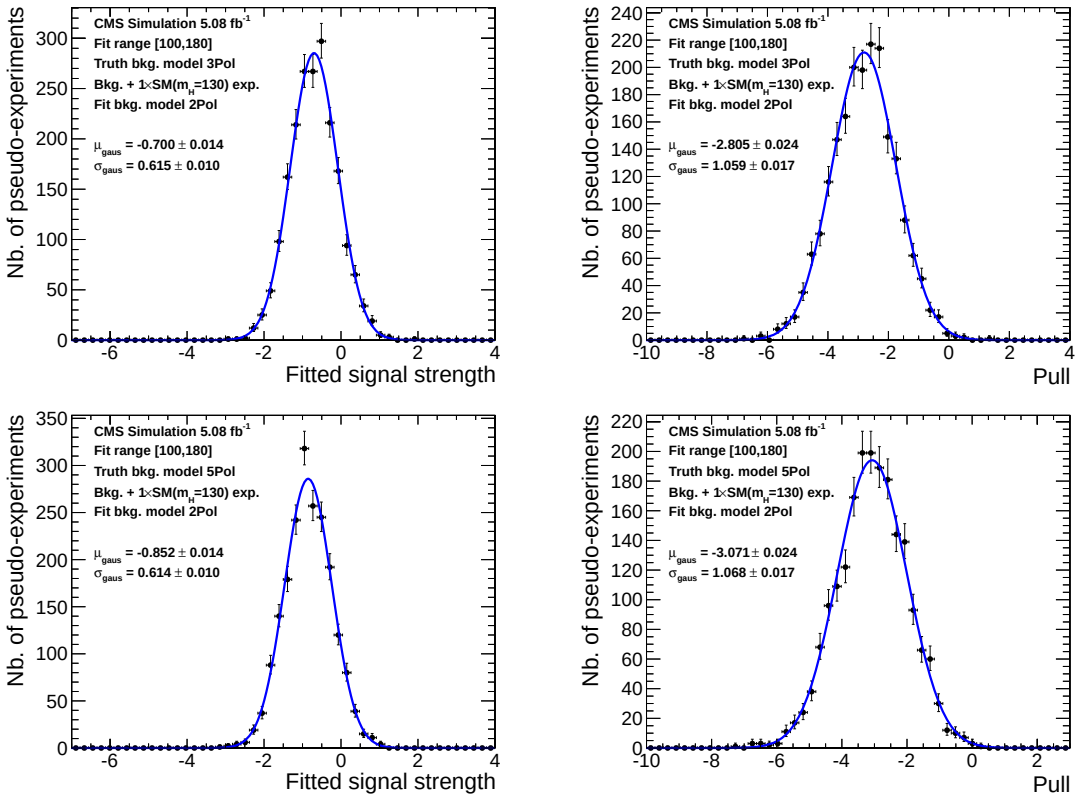

Figure A.5: Same as figure A.1, except that 3Pol and 5Pol truth background models are used to test the fit model of 2Pol.

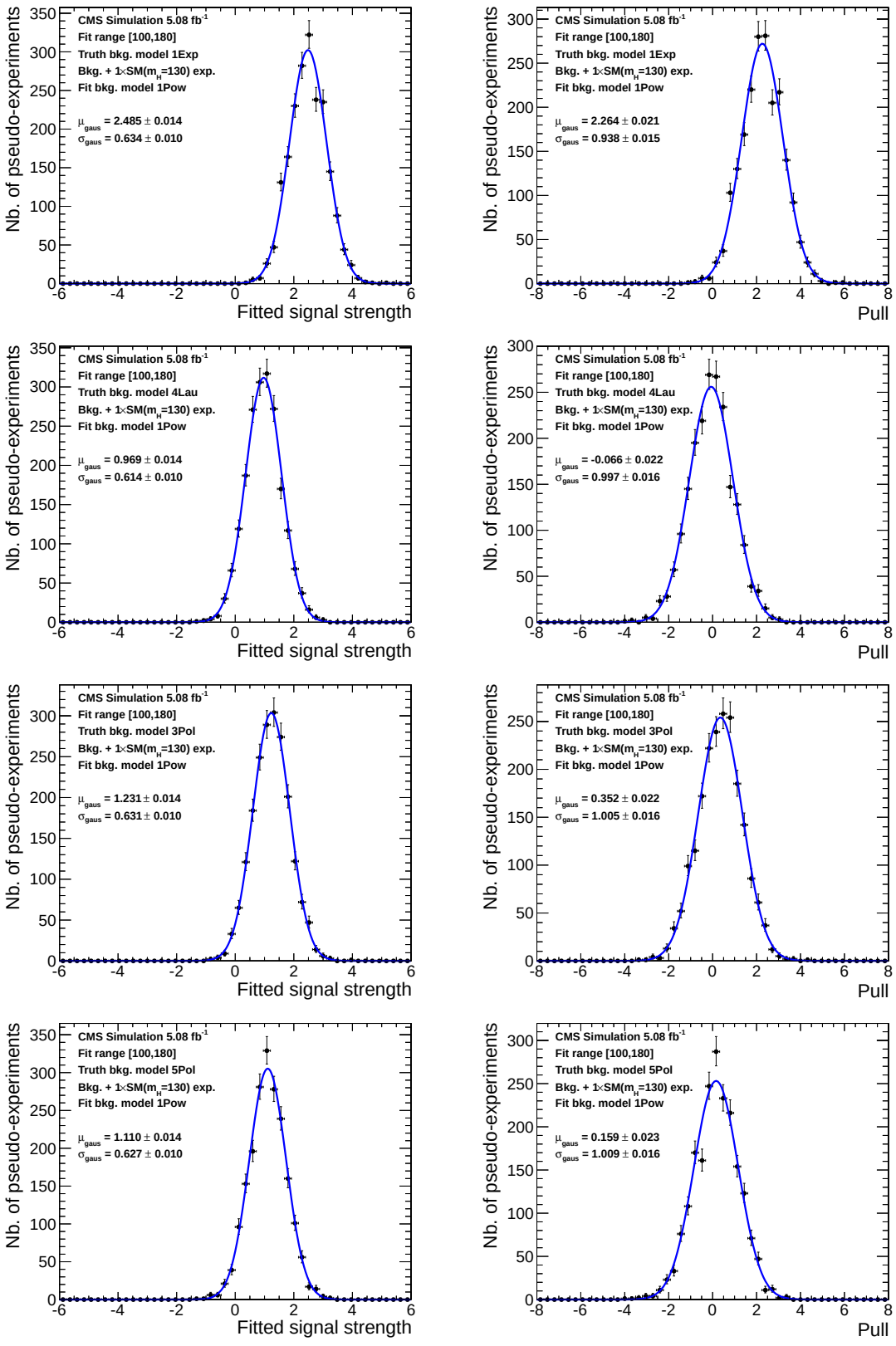

Figure A.6: Same as figure A.1, except that 1Exp, 4Lau, 3Pol and 5Pol truth background models are used to test the fit model of 1Pow.

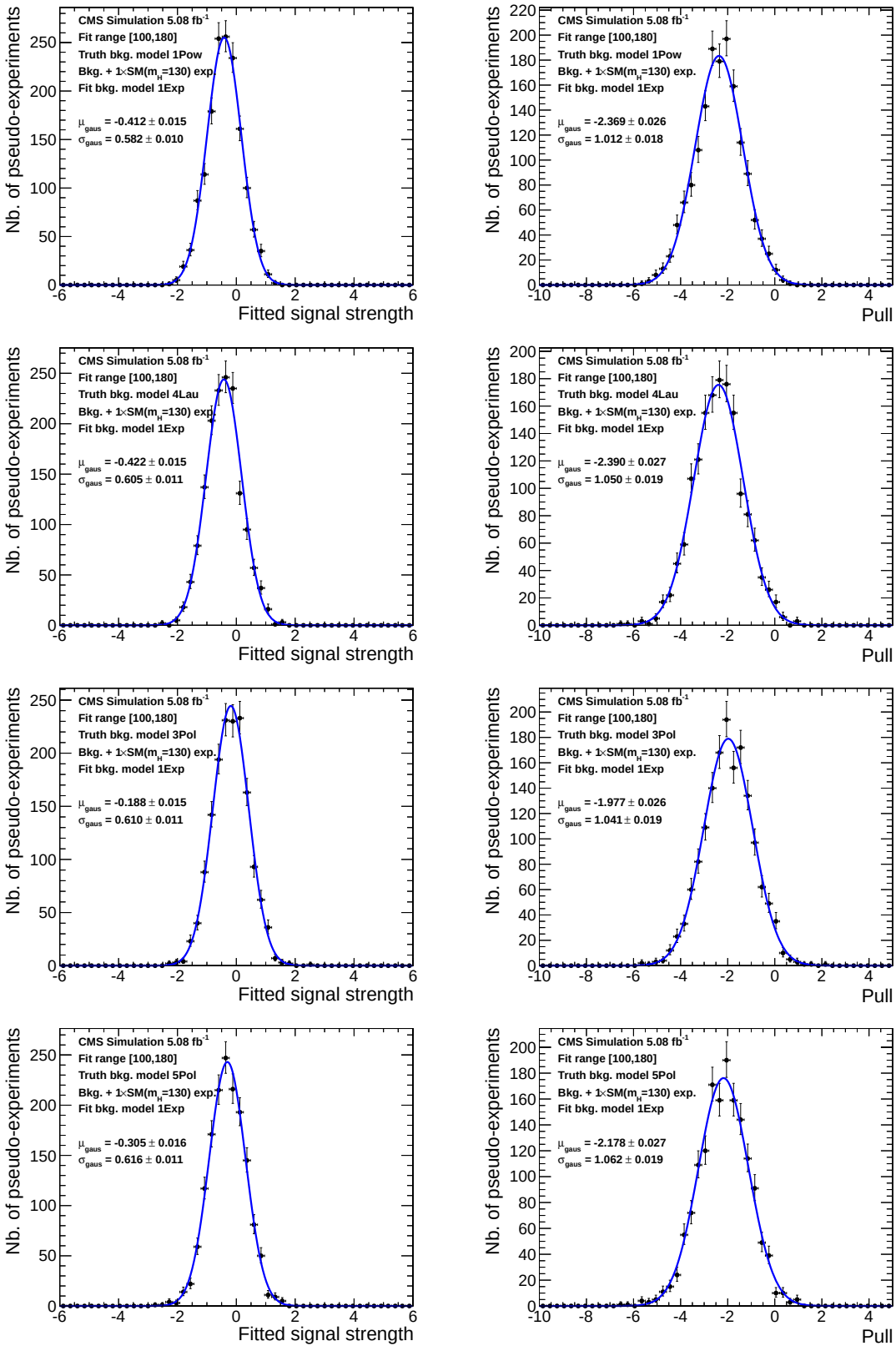

Figure A.7: Same as figure A.1, except that 1Pow, 4Lau, 3Pol and 5Pol truth background models are used to test the fit model of 1Exp.

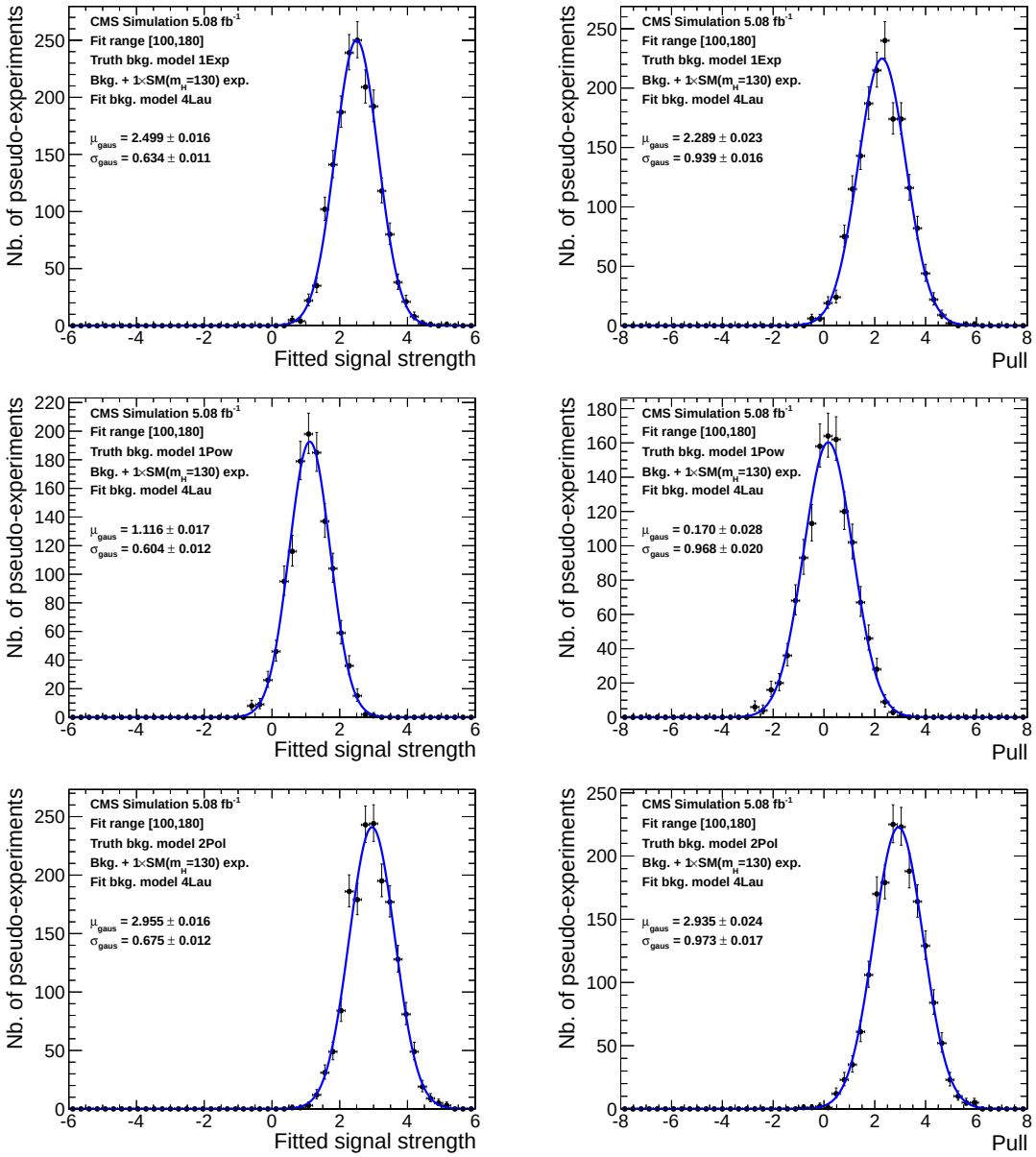

Figure A.8: Same as figure A.1, except that 1Exp, 1Pow, and 2Pol truth background models are used to test the fit model of 4Lau.

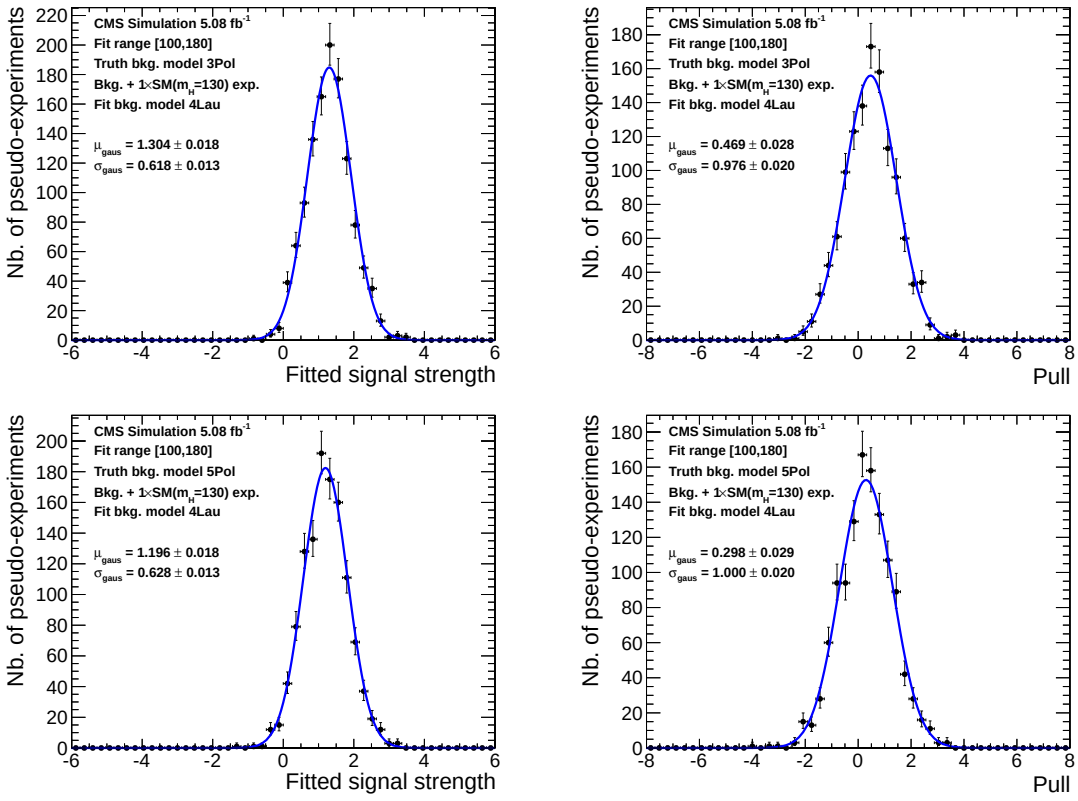

Figure A.9: Same as figure A.1, except that 3Pol and 5Pol truth background models are used to test the fit model of 4Lau.

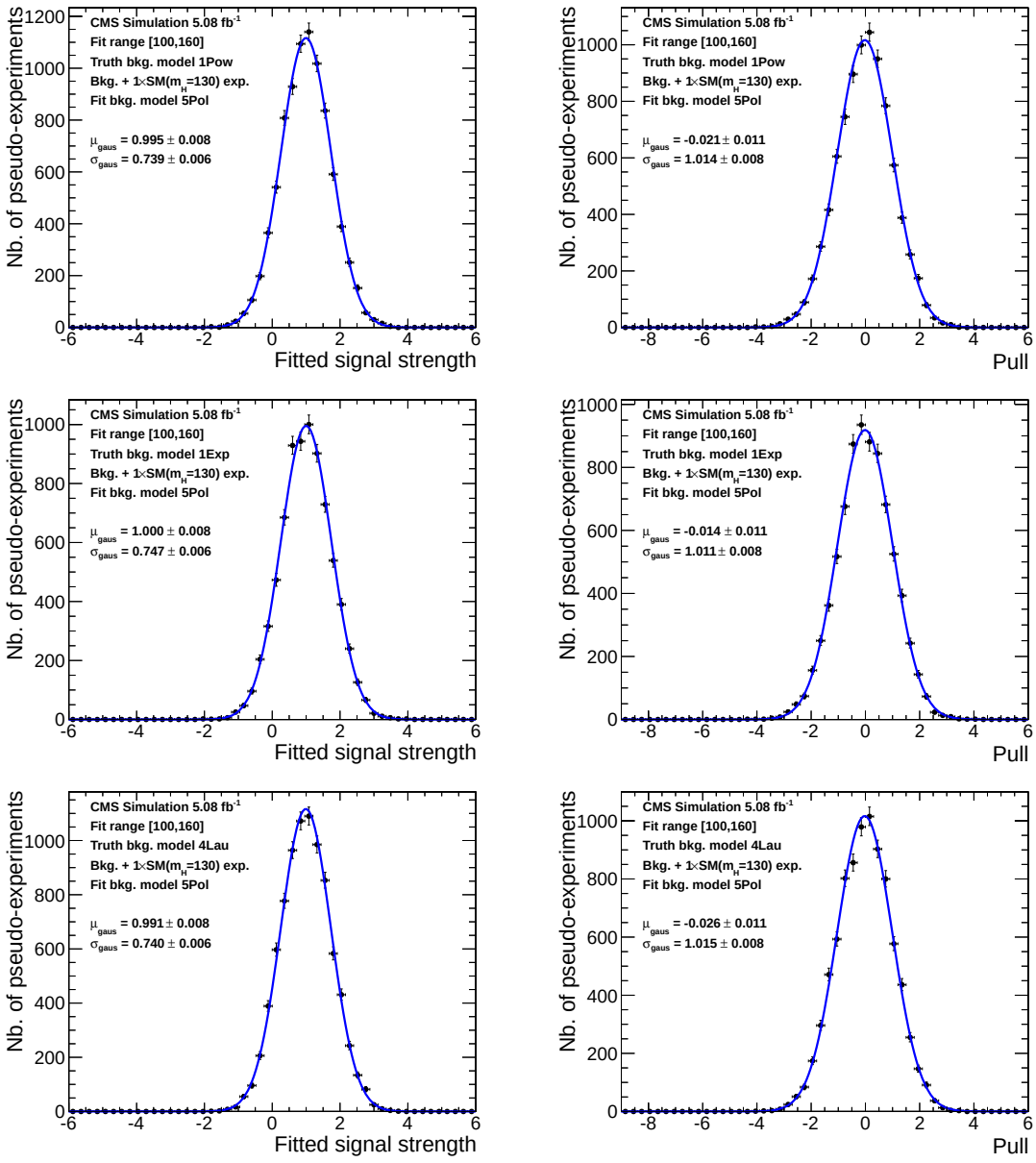

Figure A.10: Distributions of the fitted signal strength and the pull from pseudo-experiments. Different truth background models, 1Pow, 1Exp, and 4Lau, are tested against the fit model of a 5th order polynomial. The invariant mass range is chosen to be 100 to 160 GeV/c^2.

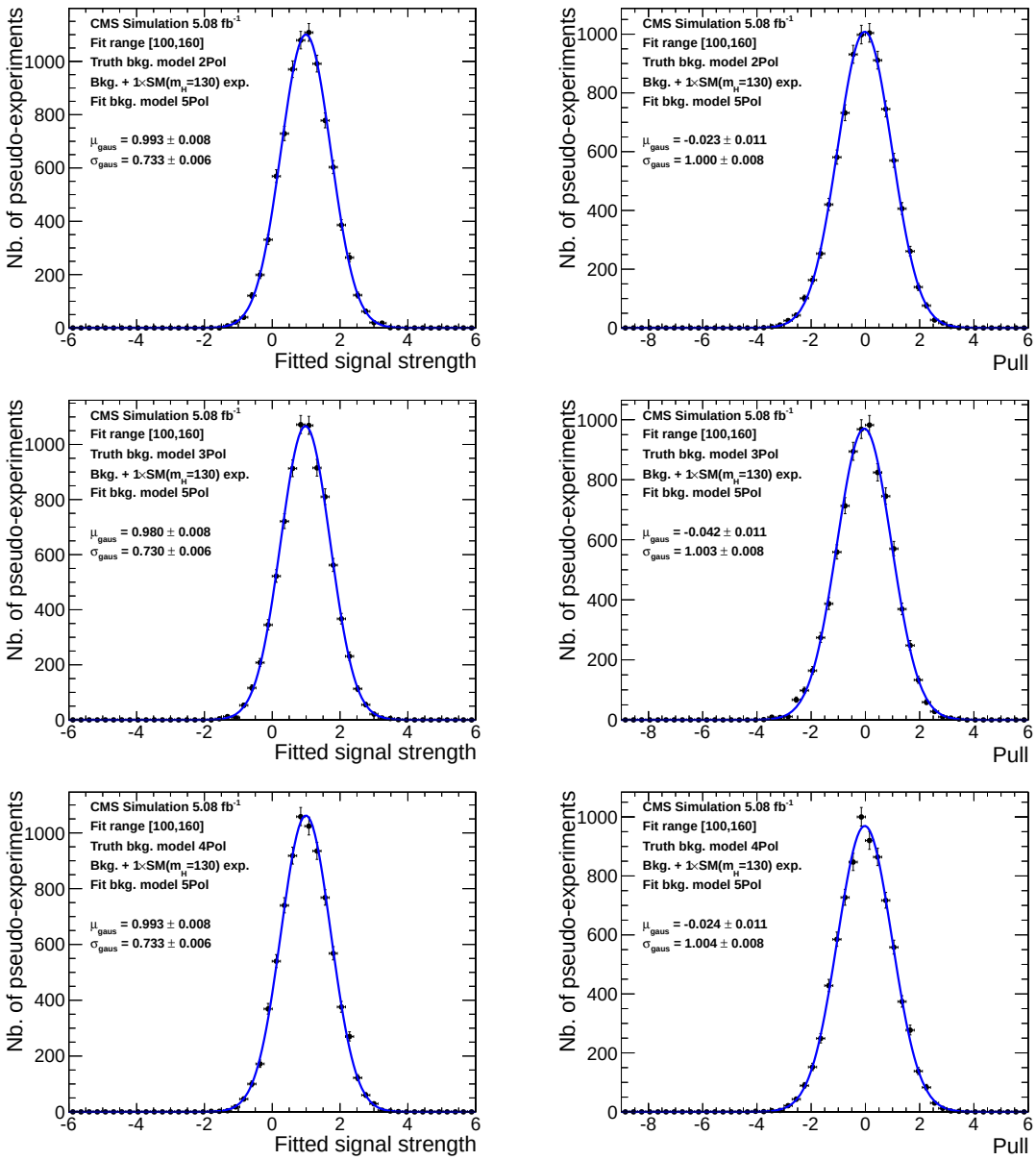

Figure A.11: Same as figure A.10, except that 2Pol, 3Pol, and 4Pol truth background models are used here.

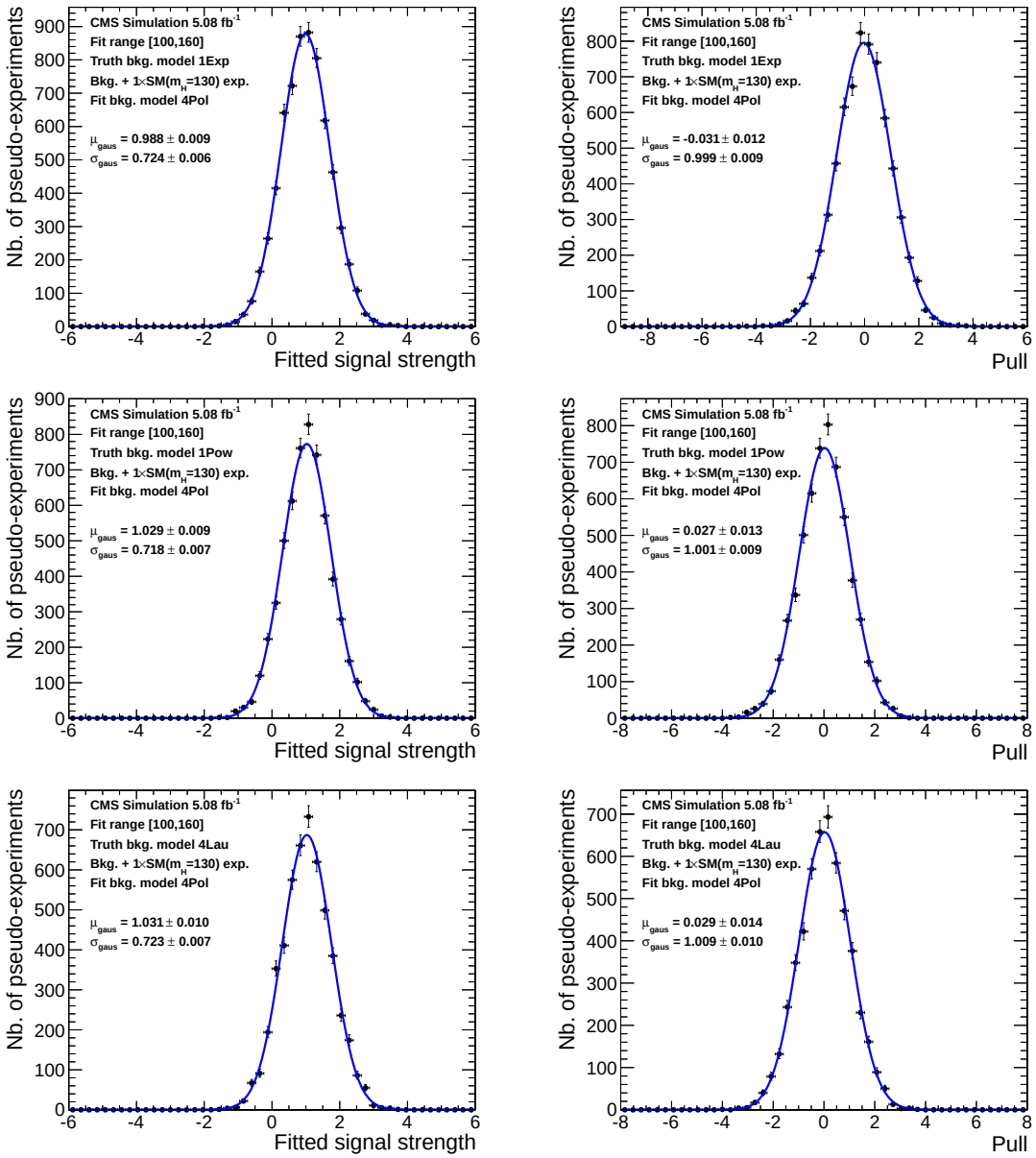

Figure A.12: Same as figure A.10, except that 1Exp, 1Pow, and 4Lau truth background models are used to test the fit model of 4Pol.

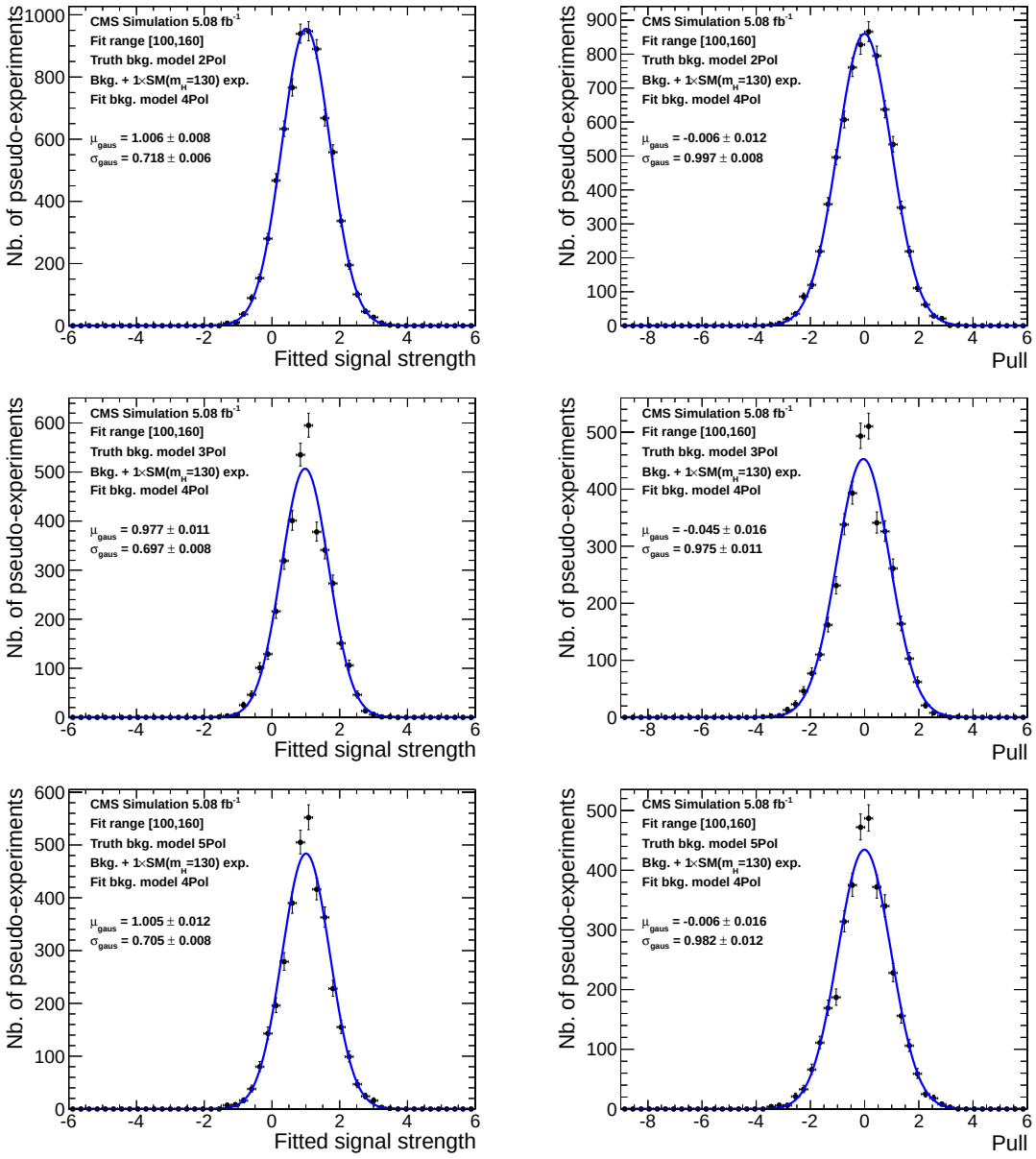

Figure A.13: Same as figure A.10, except that 2Pol, 3Pol, and 5Pol truth background models are used to test the fit model of 4Pol.

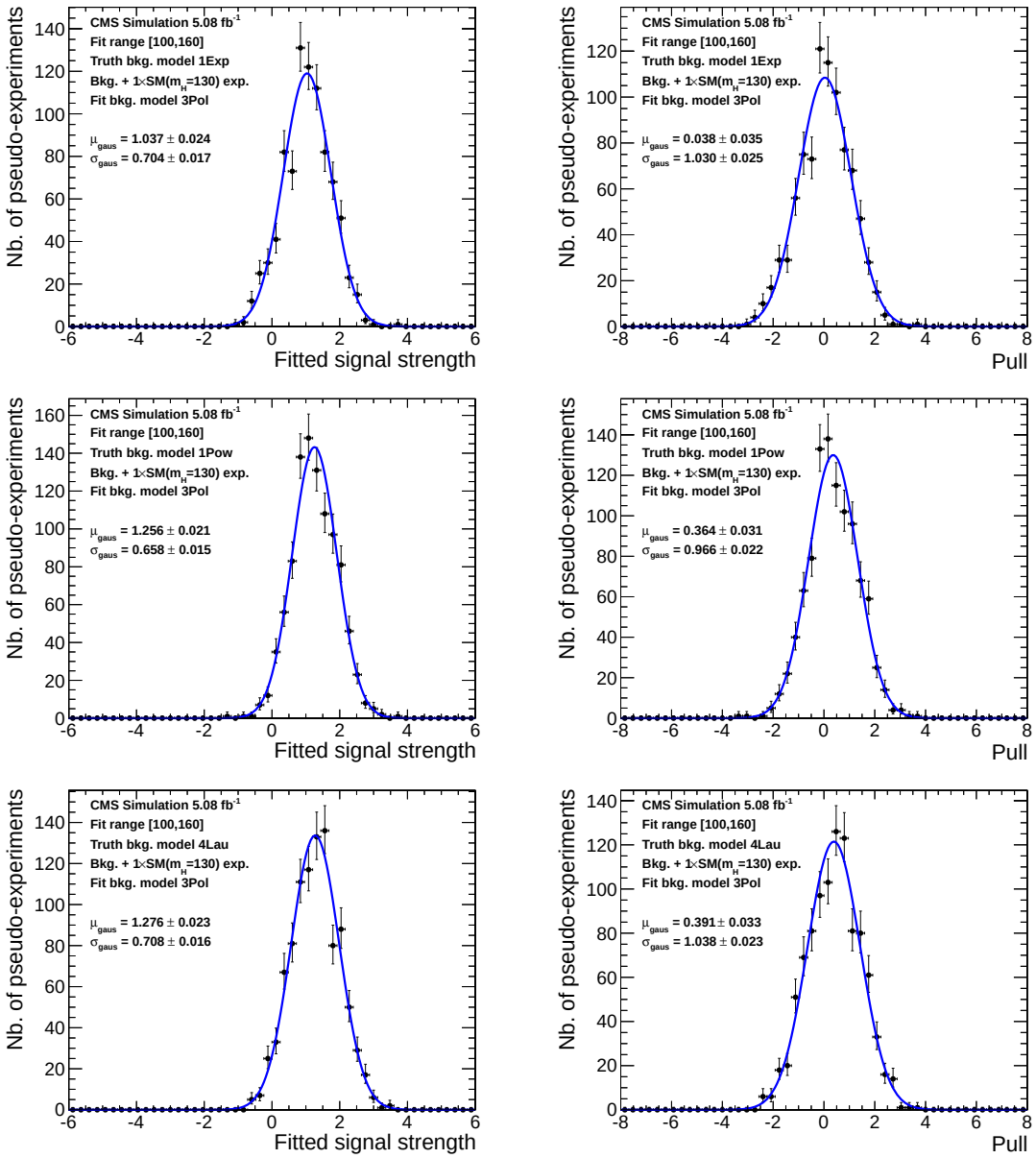

Figure A.14: Same as figure A.10, except that 1Exp, 1Pow, and 4Lau truth background models are used to test the fit model of 3Pol.

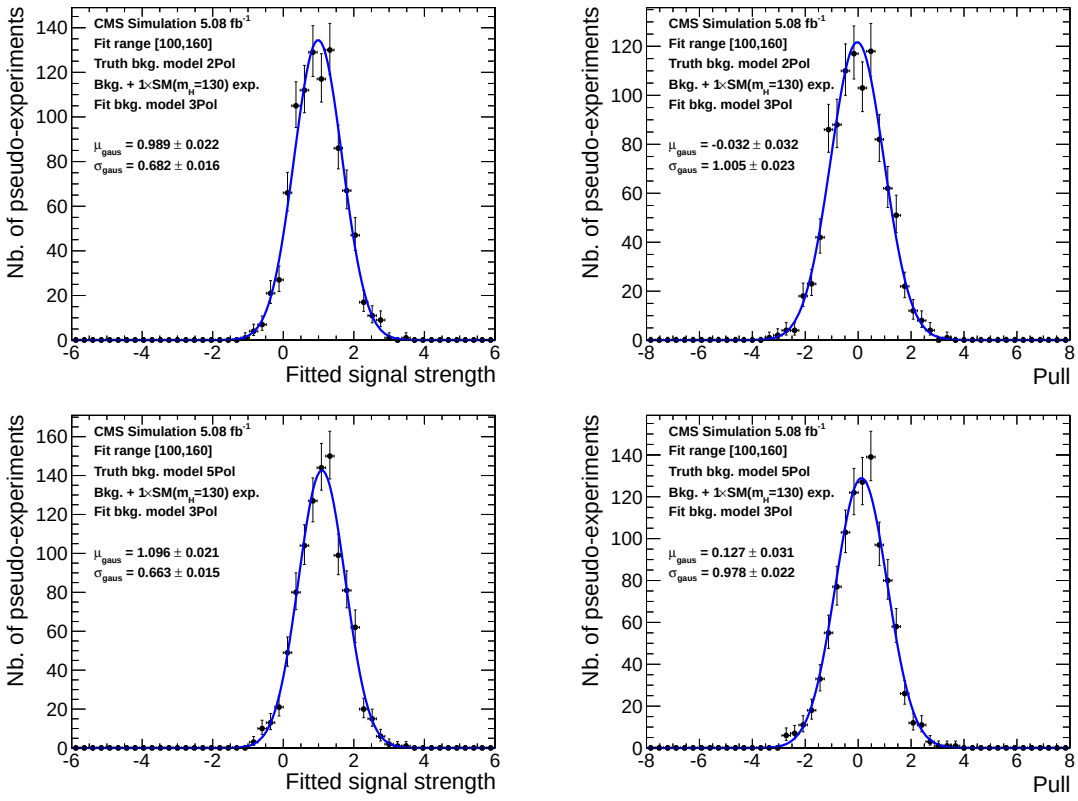

Figure A.15: Same as figure A.10, except that 2Pol and 5Pol truth background models are used to test the fit model of 3Pol.

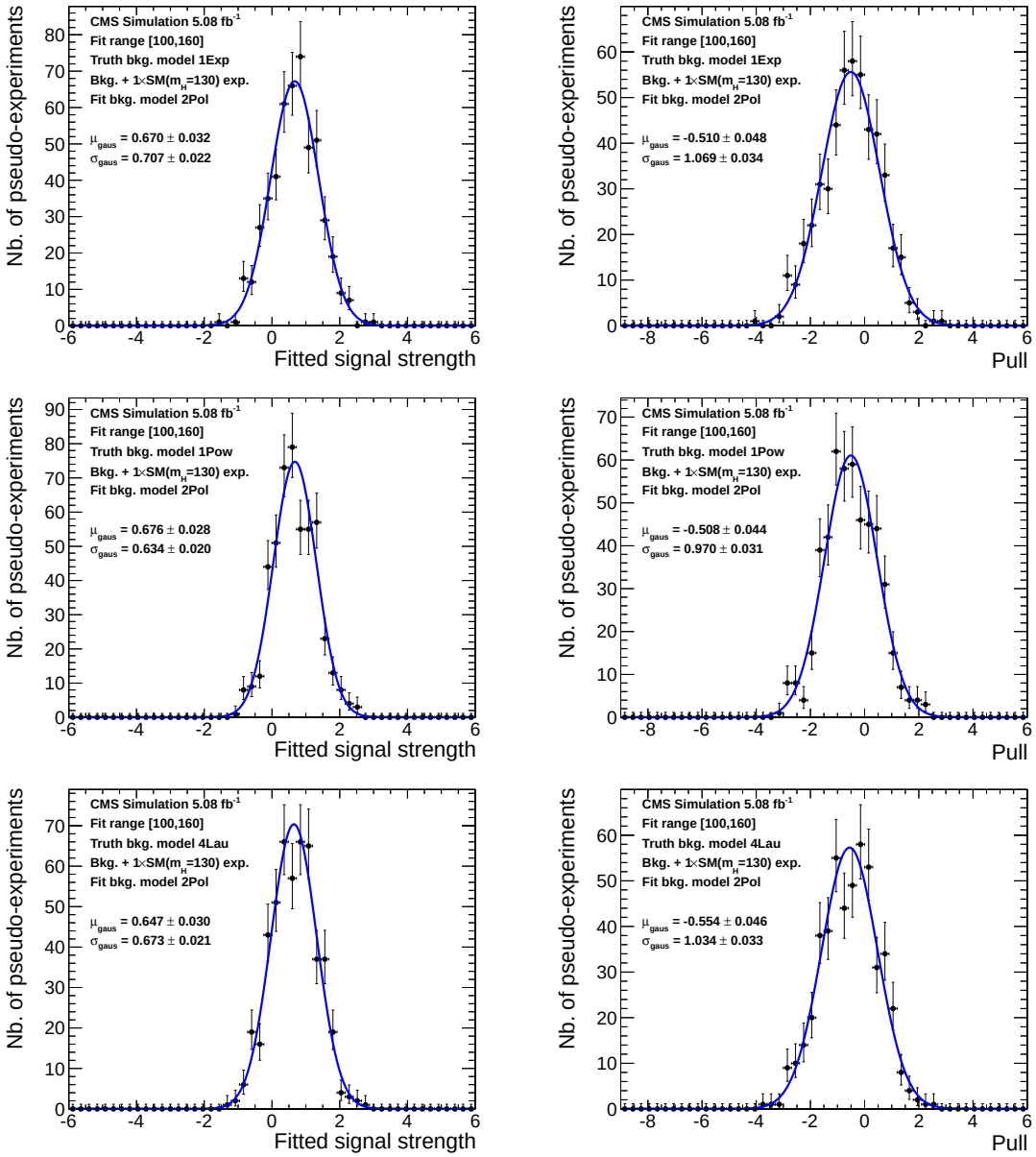

Figure A.16: Same as figure A.10, except that 1Exp, 1Pow and 4Lau truth background models are used to test the fit model of 2Pol.

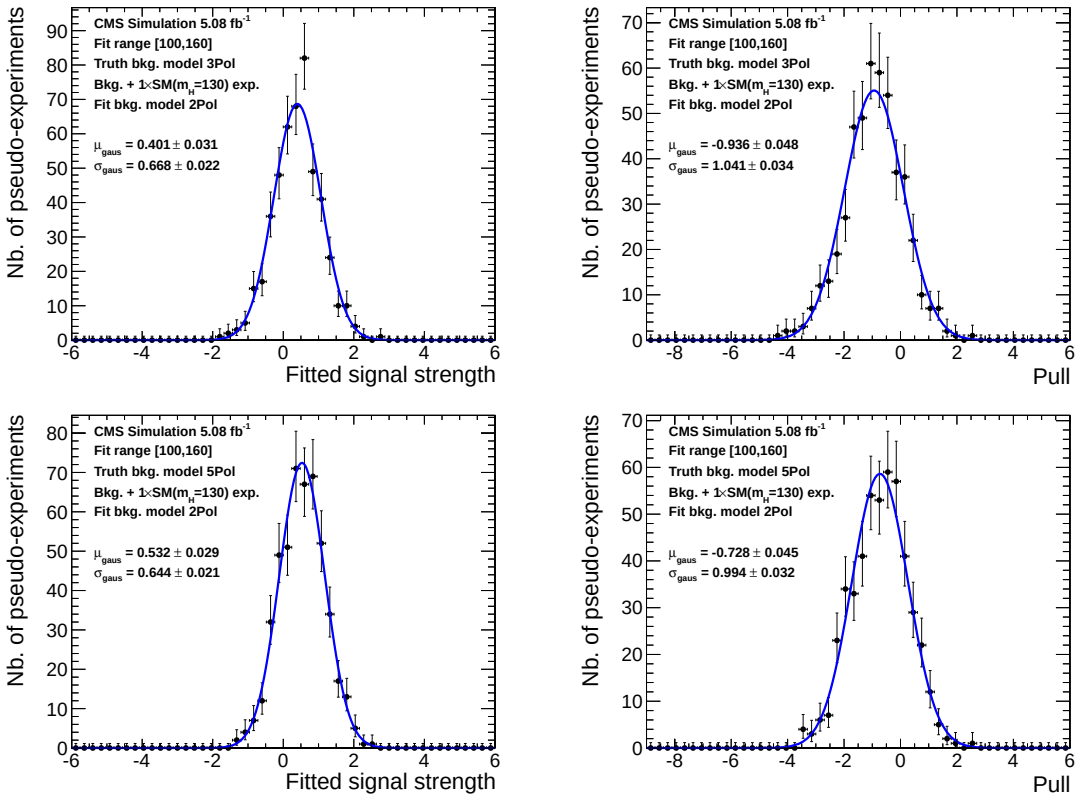

Figure A.17: Same as figure A.10, except that 3Pol and 5Pol truth background models are used to test the fit model of 2Pol.

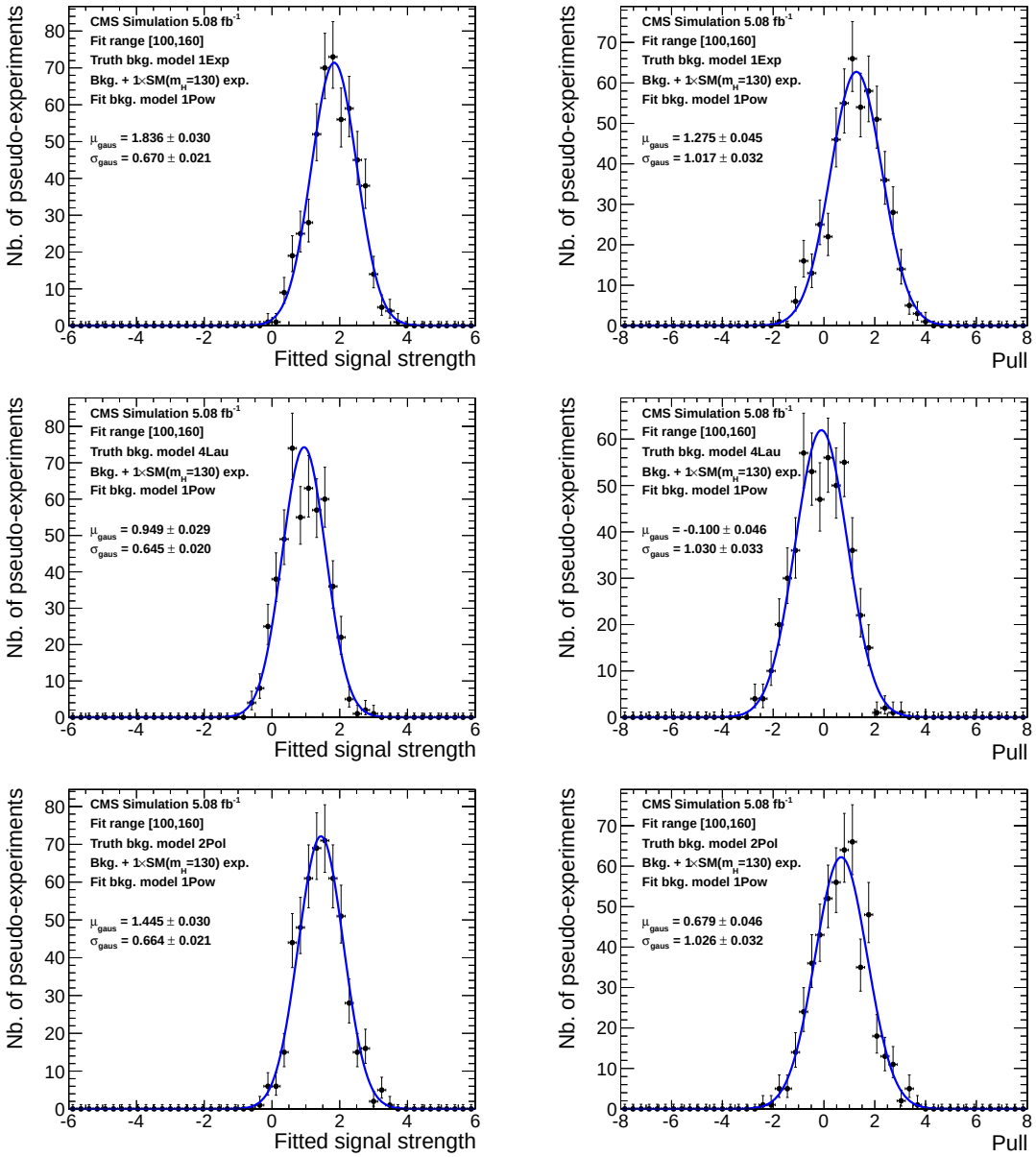

Figure A.18: Same as figure A.10, except that 1Exp, 4Lau and 2Pol truth background models are used to test the fit model of 1Pow.

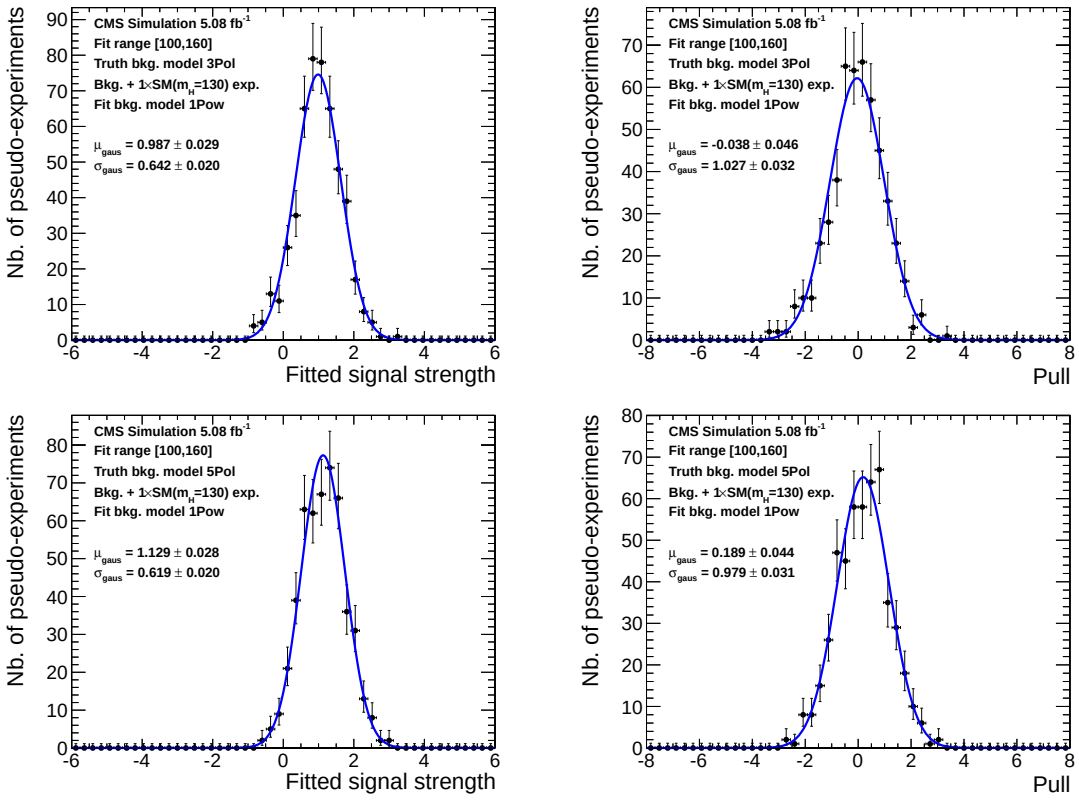

Figure A.19: Same as figure A.10, except that 3Pol and 5Pol truth background models are used to test the fit model of 1Pow.

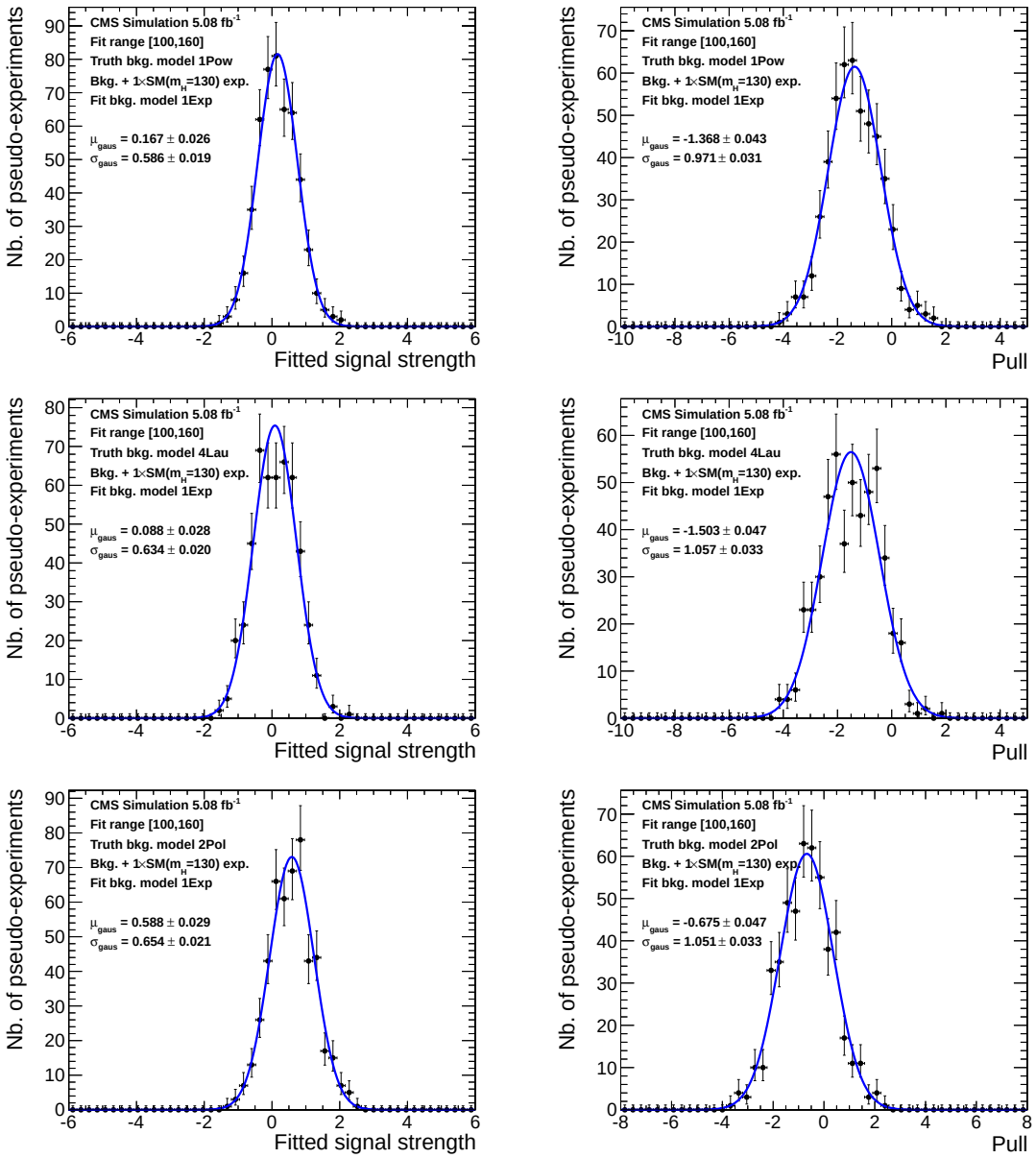

Figure A.20: Same as figure A.10, except that 1Pow, 4Lau and 2Pol truth background models are used to test the fit model of 1Exp.

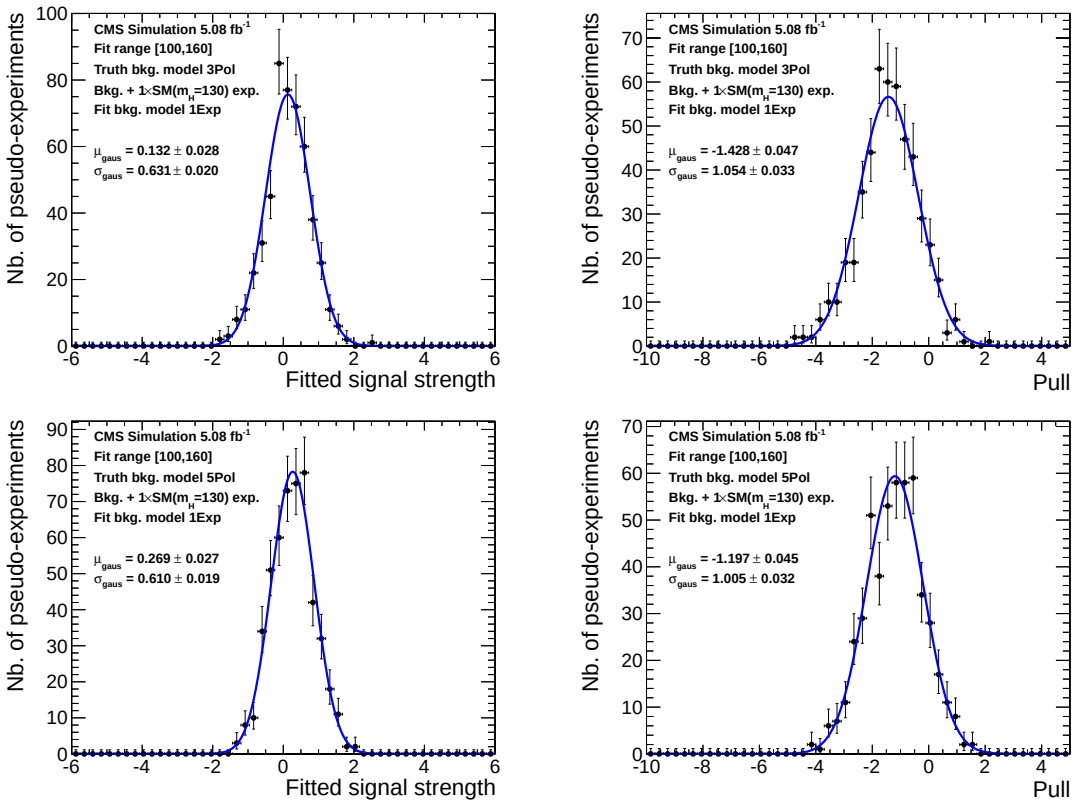

Figure A.21: Same as figure A.10, except that 3Pol and 5Pol truth background models are used to test the fit model of 1Exp.

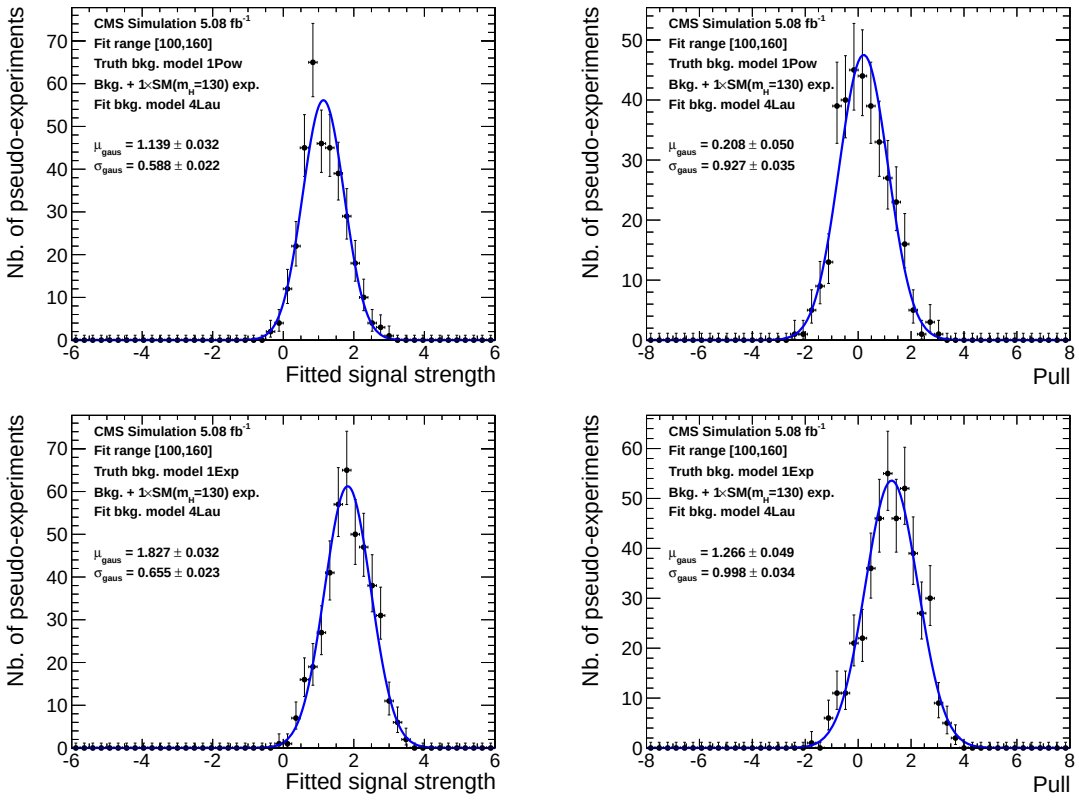

Figure A.22: Same as figure A.10, except that 1Pow and 1Exp truth background models are used to test the fit model of 4Lau.

Bibliography

[1] M. Thomas, *The Shape of Ancient Thought: Comparative Studies in Greek and Indian Philosophies*. Thomas McEvilley, 2002.

[2] J. J. Thomson, "Cathode rays," *Philosophical Magazine*, vol. 44, 1897.

[3] E. Rutherford, "The Scattering of α and β Particles by Matter and the Structure of the Atom," *Philosophical Magazine*, vol. 21, 1911.

[4] E. D. Bloom et al., "High-energy inelastic e-p scattering at 6^o and 10^o," *Phys. Rev. Lett.*, vol. 23, pp. 930–934, 1969.

[5] M. Breidenbach et al., "Observed behavior of highly inelastic electron-proton scattering," *Phys. Rev. Lett.*, vol. 23, pp. 935–939, 1969.

[6] S. L. Glashow, J. Lliopulos, L. Maiani, "Weak interactions with lepton-hadron symmetry," *Phys. Rev. D*, vol. 2, pp. 1285–1292, 1970.

[7] H. Harari, "A new quark model for hadrons," *Phys. Lett. B*, vol. 57, pp. 265–269, 1975.

[8] J.-E. Augustin et al., "Discovery of a narrow resonance in e^+e^- annihilation," *Phys. Rev. Lett.*, vol. 57, pp. 1406–1408, 1974.

[9] J. J. Aubert et al., "Experimental Observation of a Heavy Particle J," *Phys. Rev. Lett.*, vol. 57, pp. 1406–1408, 1974.

[10] S. W. Herb et al., "Observation of a dimuon resonance at 9.5 gev in 400 gev proton-nucleus collisions," *Phys. Rev. Lett.*, vol. 39, pp. 252–255, 1977.

[11] CDF Collaboration, "Observation of top quark production in $\bar{p}$p collisions with the collider detector at fermilab," *Phys. Rev. Lett.*, vol. 74, pp. 2626–2631, 1995.

[12] ALEPH, CDF, D0, DELPHI, L3, OPAL, SLD Collaborations, the LEP Working Group, the Tevatron Electroweak Working Group, and the SLD Electroweak and Heavy flavor Group, "Precision electroweak measurements and constraints on the standard model," *arXiv:1012.2367*, 2010.

[13] R. B. F. Englert, "Broken symmetry and the mass of gauge vector mesons," *Phys. Rev. Lett.*, vol. 13, pp. 321–323, 1964.

[14] P. W. Higgs, "Broken symmetries, massless particles and gauge fields," *Phys. Rev. Lett.*, vol. 12, pp. 132–133, 1964.

[15] P. W. Higgs, "Broken symmetries and the masses of gauge bosons," *Phys. Rev. Lett.*, vol. 13, p. 508, 1964.

[16] ATLAS Collaboration, "ATLAS detector and physics performance: Technical Design Report, volume II," *CERN/LHCC*, vol. 99-15, 1999.

[17] CMS Collaboration, "CMS technical design report, volume II: Physics performance," *J. Phys. G*, vol. 34, pp. 995–1579, 2007.

[18] CMS Collaboration, "Observation of a new boson at a mass of 125 GeV with the CMS experiment at the LHC," *Phy. Lett. B*, vol. 716, no. 1, pp. 30–61, 2012.

[19] S. L. Glashow, "Partial symmetries of weak interactions," *Nucl. Phys.*, vol. 22, pp. 579–588, 1961.

[20] Y. Nambu, "A Superconductor model of elementary particles and its consequences," *Int. J. Mod. Phys.*, vol. A23, p. 4063, 2008.

[21] S. Weinberg, "A Model of Leptons," *Phys. Rev. Lett.*, vol. 19, p. 1264, 1967.

[22] A. Salam, *Elementary Particle Theory*, p. 367. Almquist and Wiksells, Stockholm, 1968.

[23] E. Fermi, "Tentativo di una teoria dei raggi beta," *Nuovo Cimento*, vol. 11, 1934.

[24] T. D. Lee, C. N. Yang, "Question of Parity Conservation in Weak Interactions," *Phys. Rev.*, vol. 104, pp. 254–258, 1956.

[25] C. S. Wu, "Experimental Test of Parity Conservation in Beta Decay," *Phys. Rev.*, vol. 105, pp. 1413–1415, 1957.

[26] R. P. Feynman, M. Gell-Mann, "Theory of the Fermi Interaction," *Phys. Rev.*, vol. 109, pp. 193–198, 1958.

[27] Gargamelle Neutrino Collaboration, "Observation of neutrino-like interactions without muon or electron in the Gargamelle neutrino experiment," *Phys. Lett.*, vol. B46, pp. 138–140, 1973.

[28] M. E. Peskin, D. V. Schroeder, *An Introduction to Quantum Field Theory*. Addison-Wesley Publishing Company, 1995.

[29] J. Schwinger, "A theory of the fundamental interactions," *Ann. Phy.*, vol. 2, pp. 407–434, 1957.

[30] J. Beringer et al., "Review of particle physics," *Phys. Rev.*, vol. D86, p. 010001, 2012.

[31] J. Goldstone, "Field Theories with Superconductor Solutions," *Nuovo Cimento*, vol. 19, pp. 154–164, 1961.

[32] H. Yukawa, "On the Interaction of Elementary Particles," *Proc. Phys. Math. Soc. Japan*, vol. 17, pp. 48–57, 1935.

[33] F. Halzen, A. D. Martin, *Quarks and Leptons: An Introductory Course in Modern Particle Physics*. John Wiley and Sons Inc., 1984.

[34] KamLAND Collaboration, "Measurement of Neutrino Oscillation with KamLAND: Evidence of Spectral Distortion," *Phys. Rev. Lett.*, vol. 94, p. 081801, 2005.

[35] S. P. Martin, "A Supersymmetry Primer," *arXiv:hep-ph/9709356v6*, 1997.

[36] H. Terazawa et al., "Observable effects of the possible substructure of leptons and quarks," *Phys. Lett. B*, vol. 112, pp. 387–392, 1982.

[37] J. Ellis, M. K. Gaillard, D. V. Nanopoulos, "A phenomenological profile of the Higgs boson," *Nuc. Phy. B*, vol. 106, no. 0, pp. 292–340, 1976.

[38] L. L. Camilleri et al., "Physics with very high-energy e^+e^- colliding beams," *CERN report*, vol. 76-18, 1976.

[39] H. M. Georgi, S. L. Glashow, M. E. Machacek, D. V. Nanopoulos, "Higgs Bosons from Two-Gluon Annihilation in Proton-Proton Collisions," *Phys. Rev. Lett.*, vol. 40, pp. 692–694, 1978.

[40] S. L. Glashow, D. V. Nanopoulos, A. Yildiz, "Associated production of Higgs bosons and Z particles," *Phys. Rev. D*, vol. 18, pp. 1724–1727, 1978.

[41] The ALEPH, DELPHI, L3, OPAL, SLD Collaborations, the LEP Electroweak Working Group, the SLD Electroweak and Heavy Flavour Groups, "Precision Electroweak Measurements on the Z Resonance," *Phys. Rept.*, vol. 427, p. 257, 2006.

[42] ALEPH, DELPHI, L3, OPAL Collaborations, and the LEP Working Group for Higgs Boson Searches, "Search for the standard model Higgs boson at LEP," *Phys. Lett. B*, vol. 565, p. 61, 2003.

[43] ATLAS Collaboration, "Combined search for the Standard Model Higgs boson using up to 4.9 fb^{-1} of pp collision data at with the ATLAS detector at the LHC," *Phy. Lett. B*, vol. 710, no. 1, pp. 49–66, 2012.

[44] CMS Collaboration, "Combined results of searches for the standard model Higgs boson in pp collisions at $\sqrt{s} = 7$ TeV," *Phy. Lett. B*, vol. 710, no. 1, pp. 26–48, 2012.

[45] CDF Collaboration and D0 Collaboration, "Evidence for a Particle Produced in Association with Weak Bosons and Decaying to a Bottom-Antibottom Quark Pair in Higgs Boson Searches at the Tevatron," *Phys. Rev. Lett.*, vol. 109, p. 071804, 2012.

[46] ATLAS Collaboration, "Observation of a new particle in the search for the Standard Model Higgs boson with the ATLAS detector at the LHC," *Phy. Lett. B*, vol. 716, no. 1, pp. 1–29, 2012.

[47] LHC Higgs Cross Section Working Group, "Handbook of LHC Higgs Cross Sections: 1. Inclusive Observables," *arXiv:1101.0593*, 2011.

[48] C. Lefèvre, "The CERN accelerator complex. Complexe des accélérateurs du CERN." `https://cdsweb.cern.ch/record/1260465?ln=en`, Dec 2008.

[49] A. Achilli et al., "Total and inelastic cross-sections at LHC at CM energy of 7 TeV and beyond," 2011.

[50] "Drawing of CMS Detector." `https://cdsweb.cern.ch/record/1433717`.

[51] "CMS Slice." `https://cms-docdb.cern.ch/cgi-bin/PublicEPPOGDocDB/ShowDocument?docid=97`.

[52] CMS Collaboration, "The CMS experiment at the CERN LHC," *JINST*, vol. 3, p. S08004, 2008.

[53] G. Gratta, H. Newman, R. Y. Zhu, "Crystal calorimeters in particle physics," *Ann. Rev. Nucl. Part. Sci.*, vol. 44, pp. 453–500, 1994.

[54] CMS Collaboration, "CMS ECAL Technical Design Report," *CERN/LHCC*, vol. 97-33, 1997.

[55] F. Cavallari et al., "Linearity of the CMS Electromagnetic Calorimeter from H2 test beam data," CMS Detector Note 2007/019, 2007.

[56] M. Gataullin et al., "Intercalibration of the CMS Electromagnetic Calorimeter Using $\pi^0 \to \gamma\gamma$ Decays from 2006 Test Beams type =," tech. rep.

[57] R. Y. Zhu, "Radiation damage in scintillating crystals," *Nucl. Instr. and Meth.*, vol. A413, pp. 297–311, 1998.

[58] X. D. Qu, L. Y. Zhang, R. Y. Zhu, "Radiation Induced Color Centers and Light," *Proc. IEEE Trans. Nucl. Sci.*, vol. vol 47 no. 6, pp. 1741–47, 2000.

[59] J. H. Crawford, L. M. Slifkin, "Point Defects in Solids," *Acta Crystallographica*, vol. A29, p. 219, 1973.

[60] The CMS Electromagnetic Calorimeter Group, "Intercalibration of the barrel electromagnetic calorimeter of the CMS experiment at start-up," *JINST*, vol. 3, p. P10007, 2008.

[61] CMS Collaboration, "The Hadron Calorimter Technical Design Report," *CERN/LHCC*, vol. 97-31, 1997.

[62] CMS Collaboration, "Performance of the CMS Hadron Calorimeter with Cosmic Ray Muons and LHC Beam Data," *JINST*, vol. 5, p. T03012, 2010.

[63] CMS HCAL and ECAL Collaboration, "The CMS barrel calorimeter response to particle beams from 2 to 350 GeV/c," *Eur. Phys. J.*, vol. C60, pp. 359–373, 2009.

[64] CMS HCAL Collaboration, "Design, performance and calibration of the CMS forward calorimeter wedges," *Eur. Phys. J.*, vol. C53, pp. 139–166, 2008.

[65] CMS Collaboration, "CMS MUON Technical Design Report," *CERN/LHCC*, vol. 97-32, 1997.

[66] S. Alioli, P. Nason, C. Oleari, and E. Re, "NLO Higgs boson production via gluon fusion matched with shower in POWHEG," *JHEP*, vol. 04, p. 002, 2009.

[67] P. Nason and C. Oleari, "NLO Higgs boson production via vector-boson fusion matched with shower in POWHEG," *JHEP*, vol. 02, p. 037, 2010.

[68] T. Sjostrand, S. Mrenna, P. Skands, "PYTHIA 6.4: Physics and manual," 2006.

[69] G. Bozzi, S. Catani, D. de Florian, and M. Grazzini, "The q(T) spectrum of the Higgs boson at the LHC in QCD perturbation theory," *Phys. Lett.*, vol. B564, pp. 65–72, 2003.

[70] G. Bozzi, S. Catani, D. de Florian, and M. Grazzini, "Transverse-momentum resummation and the spectrum of the Higgs boson at the LHC," *Nucl. Phys.*, vol. B737, pp. 73–120, 2006.

[71] J. Alwall et al., "MadGraph 5: going beyond," *JHEP*, vol. 2011, no. 6, p. 128, 2011.

[72] D. Futyan, "Intercalibration of the CMS Electromagnetic Calorimeter Using Jet Trigger Events," CMS Note 2004/007, 2004.

[73] M. Gataullin et al., "InterCalibration of the CMS Barrel Electromagnetic Calorimeter Using Neutral Pion Decays," CMS Detector Note 2007/013, 2007.

[74] M. Gataullin et al., "Online Selection of $\pi^0 \to \gamma\gamma$ Decays and Performance of the π^0 InterCalibration Method at the LHC Startup," CMS Detector Note 2009/006, 2009.

[75] M. Gataullin et al., "Online Selection of $\eta \to \gamma\gamma$ Decays and Performance of the η InterCalibration Method at the LHC Startup," CMS Detector Note 2009/007, 2009.

[76] L. Agostino et al., "Intercalibration of the CMS Electromagnetic Calorimeter with Isolated Electrons," CMS Note Note-2006/021, 2006.

[77] P. Meridiani and R. Paramatti, "Use of $Z \to e^+e^-$ events for ECAL calibration," CMS Note Note-2006/039, 2006.

[78] CMS Collaboration, "ECAL 2010 performance results," CMS detector performance note 2011/008, 2011.

[79] CMS Collaboration, "ECAL Detector Performance, 2011 Data," CMS detector performance note 2012/007, 2012.

[80] M. Huhtinen, et al., "High-energy proton induced damage in $PbWO_4$ calorimeter crystals," *Nucl. Instr. and Meth.*, vol. A 545, pp. 63–87, 2005.

[81] M. Anfreville, et al., "Laser monitoring system for the CMS lead tungstate crystal calorimeter," CMS Analysis Note AN-2007/028, 2008.

[82] L. Zhang, et al., "Performance of the monitoring light source for the cms lead tungstate crystal calorimeter," *IEEE Trans. Nucl. Sci.*, vol. 52, p. 1123, 2005.

[83] P. Bonamy, et al., "The ECAL Calibration: Use of the Light Monitoring System. Version 2.0," CMS Analysis Note AN-1998/013, 1998.

[84] CMS Collaboration, "Performance of the CMS ECAL with 5 fb^{-1} of data at $\sqrt{s} = 7$ TeV," CMS Physics Analysis Summary EGM-11-001, 2012.

[85] S. Rutherford, "Study of the Effects of Data Reduction Algorithms on Physics Reconstruction in the CMS ECAL," CMS Note Note-2003/001, 2003.

[86] E. Meschi et al., "Electron Reconstruction in the CMS Electromagnetic Calorimeter," CMS Note Note-2001/034, 2001.

[87] U. Chaturvedi et al., "Results of L3 BGO Calorimeter Calibration using an RFQ accelerator," *IEEE Trans. Nucl. Sci.*, vol. 47, p. 2101, 2000.

[88] CMS Collaboration, "Electromagnetic calorimeter calibration with 7 TeV data," CMS Physics Analysis Summary EGM-10-003, 2010.

[89] L. Breiman, J. Friedman, C.J. Stone, R.A. Olshen, *Classification and Regression Trees*. Chapman & Hall, 1984.

[90] J. Breiman, "Greedy Function Approximation: A Gradient Boosting Machine," *The Annals of Statistics*, vol. 29, pp. 1189–1232, 2001.

[91] A. Hoecker, P. Speckmayer, J. Stelzer, J. Therhaag, E. von Toerne, and H. Voss, "TMVA: Toolkit for Multivariate Data Analysis," *PoS*, vol. ACAT, p. 040, 2007.

[92] A. Benaglia et al., "Search for a Higgs boson decaying into two photons in pp collisions recorded by the CMS detector at the LHC," CMS Analysis Note 2011/426, 2011.

[93] M. Cacciari, G. P. Salam, "Pileup subtraction using jet areas," *Phys. Lett.*, vol. B659, pp. 119–126, 2008.

[94] S. Agostinelli et al., "Geant4– a simulation toolkit," *Nuclear Instruments and Methods in Physics Research Section A: Accelerators, Spectrometers, Detectors and Associated Equipment*, vol. 506, no. 3, pp. 250–303, 2003.

[95] A. Apresyan et al., "Search for a Standard Model Higgs boson in the di-photon decay at $\sqrt{s} = 7$ TeV with the CMS detector," CMS Analysis Note 2012/214, 2012.

[96] M. Cacciari1, G. P. Salam1, G. Soyez, "The anti-k_t jet clustering algorithm," *JHEP*, vol. 04, p. 063, 2008.

[97] CMS Collaboration, "Particle-flow event reconstruction in cms and performance for jets, taus, and met," CMS Physics Analysis Summary CMS-PAS-PFT-09-001, 2009.

[98] CMS Collaboration, "Determination of Jet Energy Calibration and Transverse Momentum Resolution in CMS," *JINST*, vol. 6, p. P11002, 2011.

[99] CMS Collaboration, "Absolute Calibration of the Luminosity Measurement at CMS: Winter 2012 Update," CMS Physics Analysis Summary CMS-PAS-SMP-12-008, 2012.

[100] J. Heinrich et al., "Interval estimation in the presence of nuisance parameters. 1. Bayesian approach," *arXiv:physics/0409219v1*, 2004.

[101] A. L. Read, "Presentation of search results: the CLs technique," *J. Phys. G: Nucl. Part. Phys.*, vol. 28, p. 2693, 2002.

[102] T. Junk, "Confidence level computation for combining searches with small statistics," *Nucl. Instrum. Meth.*, vol. A434, p. 435, 1999.

[103] ATLAS and CMS Collaboration, "Procedure for the LHC Higgs boson search combination in Summer 2011," CMS Note Note-2011/005, 2011.

[104] J. Neyman,E. Pearson, "On the Problem of the Most Efficient Tests of Statistical Hypotheses," *Philosophical Transactions of the Royal Society of Londo*, vol. 231, pp. 289–337, 1933.

[105] R. D. Cousins, J. T. Linnemann, and J. Tucker, "Evaluation of three methods for calculating statistical significance when incorporating a systematic uncertainty into a test of the background-only hypothesis for a Poisson process," *Nuclear Instruments and Methods in Physics Research Section A: Accelerators, Spectrometers, Detectors and Associated Equipment*, vol. 595, no. 2, pp. 480–501, 2008.

[106] G. Cowan, "Asymptotic formulae for likelihood-based tests of new physics," *Eur. Phys. J.*, vol. C71, p. 1554, 2001.

[107] S. S. Wilks, "The large-sample distribution of the likelihood ratio for testing composite hypotheses," *Ann. Math. Stat.*, vol. 9, pp. 60–62, 1938.

[108] O. V. E. Gross, "Trial factors for the look elsewhere effect in high energy physics," *Eur. Phys. J.*, vol. C70, pp. 725–530, 2010.

[109] R. Barlow, "Systematic errors: facts and fictions," *arXiv:hep-ex/0207026*, 2002.

[110] B. Efron, "Bootstrap methods: Another look at the jackknife," *The Annals of Statistics*, vol. 7, pp. 1–26, 1979.

[111] B. Efron, R. J. Tibshirani, *An Introduction to the Bootstrap*. Champman & Hall/CRC, 1993.

[112] L. D. Landau, "The moment of a 2-photon system," *Dokl. Akad. Nawk.*, vol. USSR 60, p. 207, 1948.

[113] C. N. Yang, "Selection Rules for the Dematerialization of a Particle Into Two Photons," *Phys. Rev.*, vol. 77, pp. 242–245, 1950.

[114] CMS Collaboration, "A search for excited leptons in pp collisions at $\sqrt{s} = 7$ TeV," *Phys. Lett. B*, vol. 704, no. 3, pp. 143–162, 2011.

[115] U. Baur et al., "Excited-quark and -lepton production at hadron colliders," *Phys. Rev. D*, vol. 42, pp. 815–824, 1990.

[116] D0 Collaboration, "Search for excited muons in ppbar collisions at $\sqrt{s} = 1.96$ TeV," *Phys. Rev. D*, vol. 73, p. 111102, 2006.

[117] CDF Collaboration, "Search for excited and exotic muons in the $\mu\gamma$ decay channel in ppbar collisions at $\sqrt{s} = 1.96$ TeV," *Phys. Rev. Lett.*, vol. 97, p. 191802, 2006.

[118] T. Bolton et al., "Measurement of inclusive Wγ and Zγ cross sections and limits on anomalous trilinear gauge boson couplings at 7 TeV," CMS Analysis Note 2010/279, 2010.

[119] CMS Collaboration, "Electromagnetic calorimeter commissioning and first results with 7 TeV data," CMS Physics Analysis Summary, 2010.

[120] M. Sani, "Photon Efficiency Measurements Using Tag and Probe," CMS Analysis Note 2010/292, 2010.

[121] CMS Collaboration, "Absolute luminosity normalization," CMS Detector Performance Summaries CMS-DP-2011-002, 2011.

[122] J. Pumplin et al., "New Generation of Parton Distributions with Uncertainties from Global QCD Analysis," *JHEP*, vol. 07, p. 012, 2002.

[123] CMS Collaboration, "Search for Excited Leptons in 5 fb^{-1} of pp Collisions at $\sqrt{s}$=7 TeV with the CMS detector," CMS Physics Analysis Summary CMS-PAS-EXO-11-034, 2012.